https://ntrs.nasa.gov/search.jsp?R=19940023914 2020-06-16T14:57:16+00:00Z

NASA Contractor Report 4580

Integrated Active and Passive Control Design Methodology for the LaRC CSI Evolutionary Model

Christopher T. Voth, Kenneth E. Richards, Jr., Eric Schmitz, Russel N. Gehling, and Daniel R. Morgenthaler
Martin Marietta Astronautics Group • Denver, Colorado

National Aeronautics and Space Administration
Langley Research Center • Hampton, Virginia 23681-0001

Prepared for Langley Research Center
under Contract NAS1-19371

April 1994

Abstract

A general design methodology to integrate active control with passive damping has been demonstrated on the NASA LaRC CSI Evolutionary Model (CEM), a ground testbed for future large, flexible spacecraft. Vibration suppression controllers designed for Line-of-Sight (LOS) minimization have been successfully implemented on the CEM. A frequency-shaped H_2 methodology was developed, allowing the designer to specify the roll-off of the MIMO compensator. A closed-loop bandwidth of 4 Hz, including the six rigid-body modes and the first three dominant elastic modes of the CEM, was achieved. Good agreement was demonstrated between experimental data and analytical predictions for the closed-loop frequency response and random tests. Using the Modal Strain Energy (MSE) method, a passive damping treatment consisting of 60 viscoelastic damped struts was designed, fabricated and implemented on the CEM. Damping levels for the targeted modes were more than an order of magnitude larger than for the undamped structure. Using measured loss and stiffness data for the individual damped struts, analytical predictions of the damping levels were very close to the experimental values in the [1–10] Hz frequency range where the open-loop model matched the experimental data. An integrated active/passive controller was successfully implemented on the CEM and was evaluated against an active-only controller. A two-fold increase in the effective control bandwidth and further reductions of 30% to 50% in the LOS RMS outputs were achieved compared to an active-only controller. Superior performance was also obtained compared to a High-Authority/Low-Authority (HAC/LAC) controller.

 PRECEDING PAGE BLANK NOT FILMED

Contents

List of Tables

List of Figures

Chapter 1

Introduction

During the past 15 years, control design methods for space platforms characterized by lightly-damped structural modes have been studied extensively [1]. In the last five years or so the focus of the Controls-Structures Integration (CSI) field has shifted from design to three main areas of endeavor:

1. Implementation and performance assessment of structural, system identification and control design methodologies on realistic ground testbeds of space platforms envisioned in the late 80's by NASA and the Air Force [2, 3, 4, 5, 6].

2. Design of new actuator and sensor hardware for control of flexible structures [7].

3. Detailed assessment of the benefits of CSI technology on near-term programs such as the NASA EOS spacecraft currently in the Phase B stage [8].

The work described in this report addressed the first two areas mentioned above. Its focus is on design and experimental verification of an integrated active and passive damping methodology using the CSI Evolutionary Model (CEM), a ground testbed for large flexible platforms developed at NASA Langley Research Center (LaRC). The testbed shown in Figure 1, equipped with cold-gas thrusters and inertial accelerometers, was used to verify vibration suppression algorithms implemented on a real-time control system. The performance of the control algorithms is evaluated with a set of high-resolution optical line-of-sight (LOS) sensors specifically designed to sense the rigid-body and elastic rotations at several locations along the structure.

PRECEDING PAGE BLANK NOT FILMED

PAGE 14

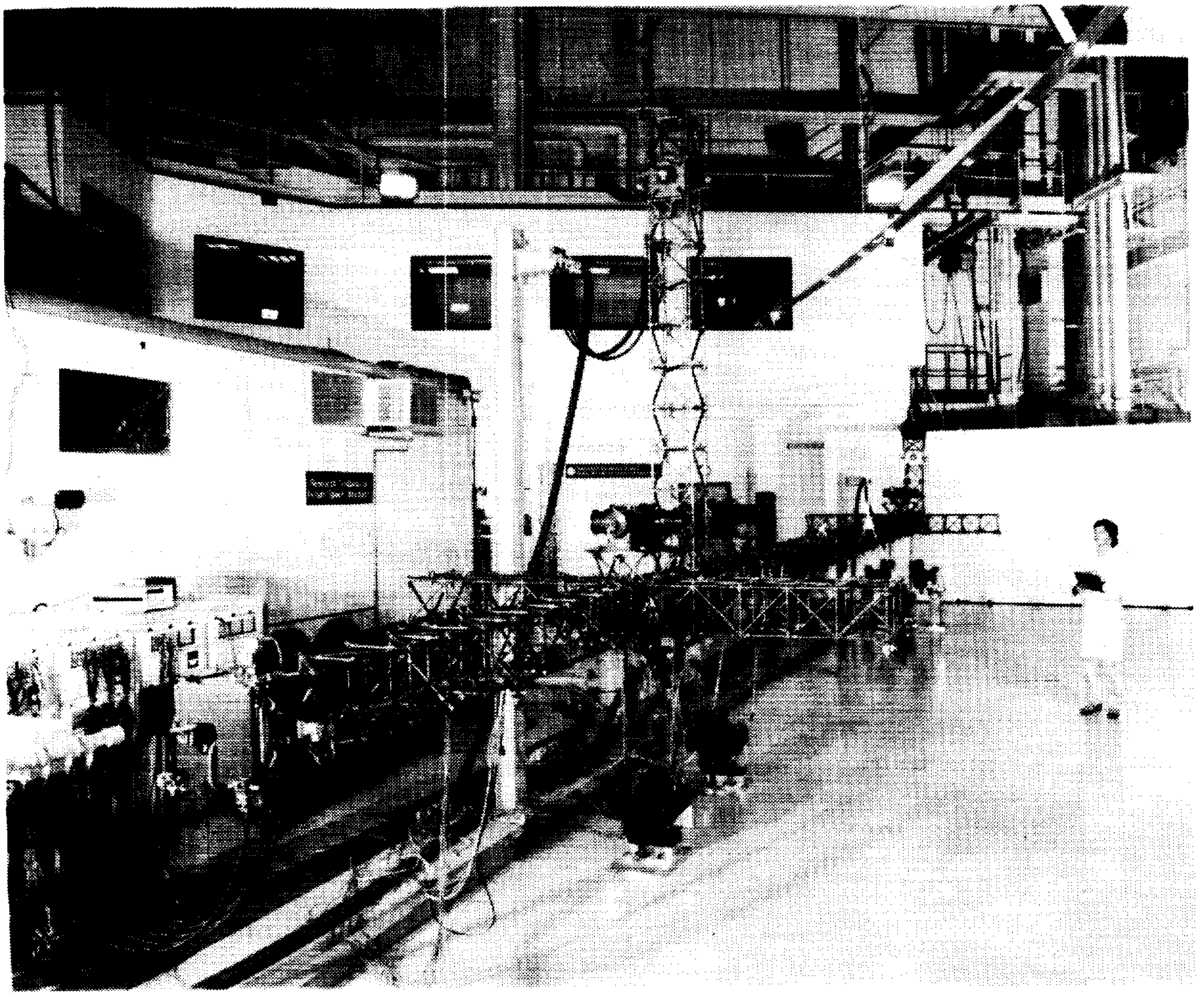

Figure 1.1: Phase 2 Configuration of CSI Evolutionary Model (CEM) Testbed

The control design methodology discussed in the report includes the following two main components:

- an active control design method based on H_2-norm minimization with frequency shaping to capture closed-loop performance, multivariable stability and robustness requirements.
- a passive damping treatment method developed to increase the performance and robustness of the active controller by targeting the highly uncertain modes outside the active control bandwidth.

In contrast to the standard Linear Quadratic Gaussian (LQG) approach, the active control design method developed in this report relies on selection of a set of shaping filters to model both disturbances and frequency dependent closed-loop requirements. The H_2 compensator designs are based on a reduced-order model of the structure, including the rigid-body and dominant structural modes. The compensator high-frequency roll-off is directly adjusted to gain stabilize the high-frequency structural modes of the structure. The control design and analysis methodology is implemented as a set of MATLAB[1] programs developed for this contract.

Using the Modal Strain Energy technique, the passive damping treatment is implemented as a set of extensional viscoelastic shear damped struts at strategic locations in the CEM testbed. The active control design method is applied to the passively damped structure to obtain a combined active/passive control design with increased performance and robustness compared to an active-only control design.

An extensive verification of this general methodology based on a combination of time and frequency domain evaluation techniques is discussed in the report, including the following:

1. verification of and comparison with analytical prediction of the stability and achieved performance for the active control designs using Multi-Input Multi-Output (MIMO) Line-of-Sight (LOS) and accelerometer Frequency Response Functions (FRFs), root-mean-square (RMS) levels computations for random excitation, and sine-excitation tests.

2. verification of the passive damping treatment design based on comparison of achieved damping levels for individual targeted modes and of FRF data with analytical Finite Element Model (FEM) predictions.

3. comparison of the performance of active-only versus active/passive control designs based on closed-loop FRF data and RMS LOS reductions computations.

The report is organized in three main chapters as outlined below.

- In Chapter 2, we give an overview of the CEM, including a detailed description of the hardware testbed, the derivation of the state-space models used for control designs and a summary of the experimental open-loop time-domain and frequency-domain data.

- In Chapter 3, we present a detailed discussion of the active control design methodology. First, the derivation of the control objectives is presented, followed by the design requirements. Two control designs based on different architectures are then discussed, an H_2/Linear-Quadratic-Gaussian (LQG) multivariable controller and a High-Authority/Low-Authority Control (HAC/LAC)

[1]MATLAB is a trademark of The MathWorks, Inc.

controller. For each design the derivation of the synthesis model, the selection of the weighting functions, the design trade-offs and selected experimental results are discussed.

- In Chapter 4, we present the combined active/passive damping design methodology. After establishing the passive damping levels requirements for a set of targeted modes, a detailed discussion of the Modal Strain Energy (MSE) method and its specific implementation for the CEM testbed are given. Two detailed examples of the process developed to select the optimum damper locations are then discussed, concluding with the FEM predictions of the damping levels achieved for the CEM using the damped strut measured properties. A separate discussion of the damped strut designs and a summary of the unit tests follows. The open-loop tests of the passive damping treatment are then presented. Finally the design and tests of the combined active/passive controllers are presented including the comparisons with the active-only controllers discussed in Chapter 3.

Chapter 2

NASA Langley CEM Test Article

2.1 Description of the CSI Evolutionary Model (CEM) Testbed

The active and passive control design methodology discussed in this report was demonstrated on the CSI Evolutionary Model (CEM), a testbed developed at NASA LaRC to serve as a focus for the CSI technology. The CEM is a 50 feet long 3-D truss structure suspended from the ceiling with cables. The CEM was designed as a reconfigurable testbed to emulate the dynamics of future large spacecraft such as large earth-observing platforms and future space stations. During the first year of our contract the CEM was setup in the Phase 1 configuration shown in Figure 2.1 and our work focused on global pointing control based on a a Line of Sight (LOS) sensor. During the second year, the CEM was reconfigured as a multi-payload pointing platform (Phase 2 configuration) shown in Figure 2.2. Each of the three 2-axis gimballed payloads was instrumented with a 2-axis optical scoring system. In order to maintain continuity in the development and verification of the active/passive control design methodology, each gimballed payload was configured locked in its nominal centerline position for the work reported here. In the remainder of this section we describe in some detail the main elements of the CEM testbed, including the structure, the suspension system, the sensors and actuators, and the real-time computer system.

2.1.1 Structure

The Phase 1 CEM structure was based on an integrated structure-control optimization described in Ref. [9]. The major components of the structure, shown in Figure 2.1, includes a 62 bay central truss (cubic bays with 10 inch struts) and two vertical towers, the laser tower with 9 bays where a laser is located and the reflector tower to which is attached a 16 ft diameter reflector. Two horizontal appendages are used as anchoring points for the suspension cables. The dominant bending modes of this structure are in the 2–4 Hz range. A complete description of the modal data of the CEM is given in Section 2.2.1.

The Phase 2 CEM structure, shown in Figure 2.3, was modified from its Phase 1 configuration by removing the reflector appendage, modifying the horizontal appendages and adding three two-axis gimballed payloads with their associated optical scoring system (OSS). Figure 2.4 shows one of the two-axis gimbals (gimbal B of Figure 2.3) and its associated OSS detector mounted on the ground.

Under this contract we have designed a removable passive damping treatment discussed later in the report. The passive treatment consists of damped struts designed to replace some of the original aluminum struts of the structure. A treatment consisting of 60 damped struts was installed on the Phase 2 CEM and is discussed in Chapter 4. A photograph showing some of the damped struts installed near the reflector tower region is shown in Figure 2.5.

2.1.2 Suspension System

The suspension system for the Phase 1 CEM consists of two primary suspension cables, each split into two cables attaching at the corresponding extremities of the horizontal truss appendage. Two extensional springs are attached between the ceiling and the cables to reduce the coupling between suspension and flexible dynamics. With this fairly simple suspension system the 6 rigid-body modes for the structure are in the 0.15–0.9 Hz frequency range. In order to increase the separation between the rigid-body modes and the flexible modes, a more sophisticated suspension system was employed for the Phase 2 CEM. The Phase 2 suspension consists of 4 parallel cables shown in Figures 2.2 and 2.3. Each cable is connected at the ceiling to a suspension device made by CSA Engineering, Inc. The device consists of two parallel subsystems, one pneumatic and one electromagnetic. The passive pneumatic system consists of a frictionless air piston connected to an external air tank with a pressure regulator. The active electromagnetic system consists of a voice-coil actuator with a displacement feedback loop. The combination of frictionless air pistons, carriage airbearings and closed-loop voice-coil actuators render the CSA device virtually frictionless. The resulting six rigid-body frequencies for the CEM are located in the 0.1–0.3 Hz range, significantly lower than for the Phase 1 suspension system.

ORIGINAL PAGE
BLACK AND WHITE PHOTOGRAPH

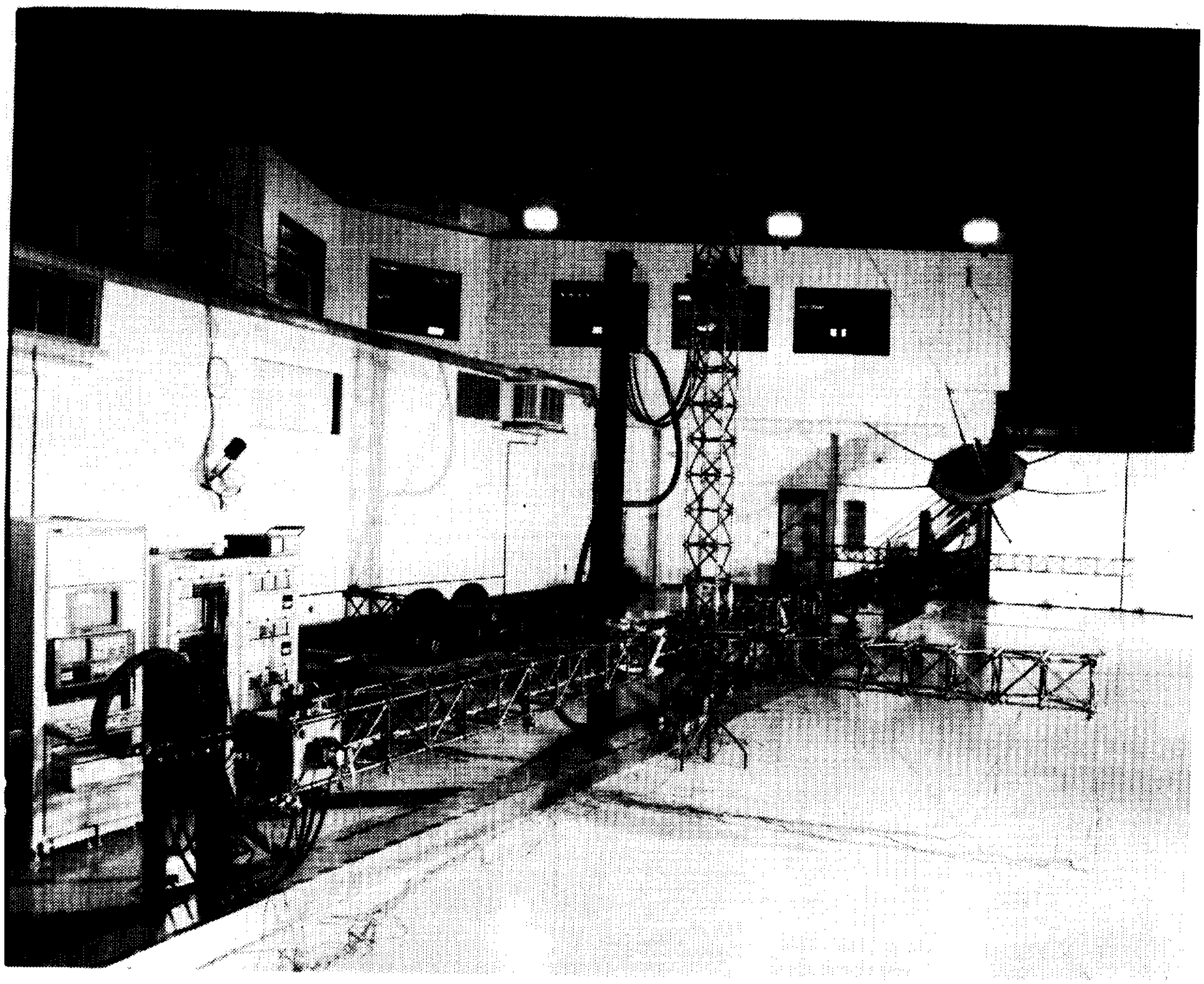

Figure 2.1: CSI Evolutionary Model in its Phase 1 Configuration

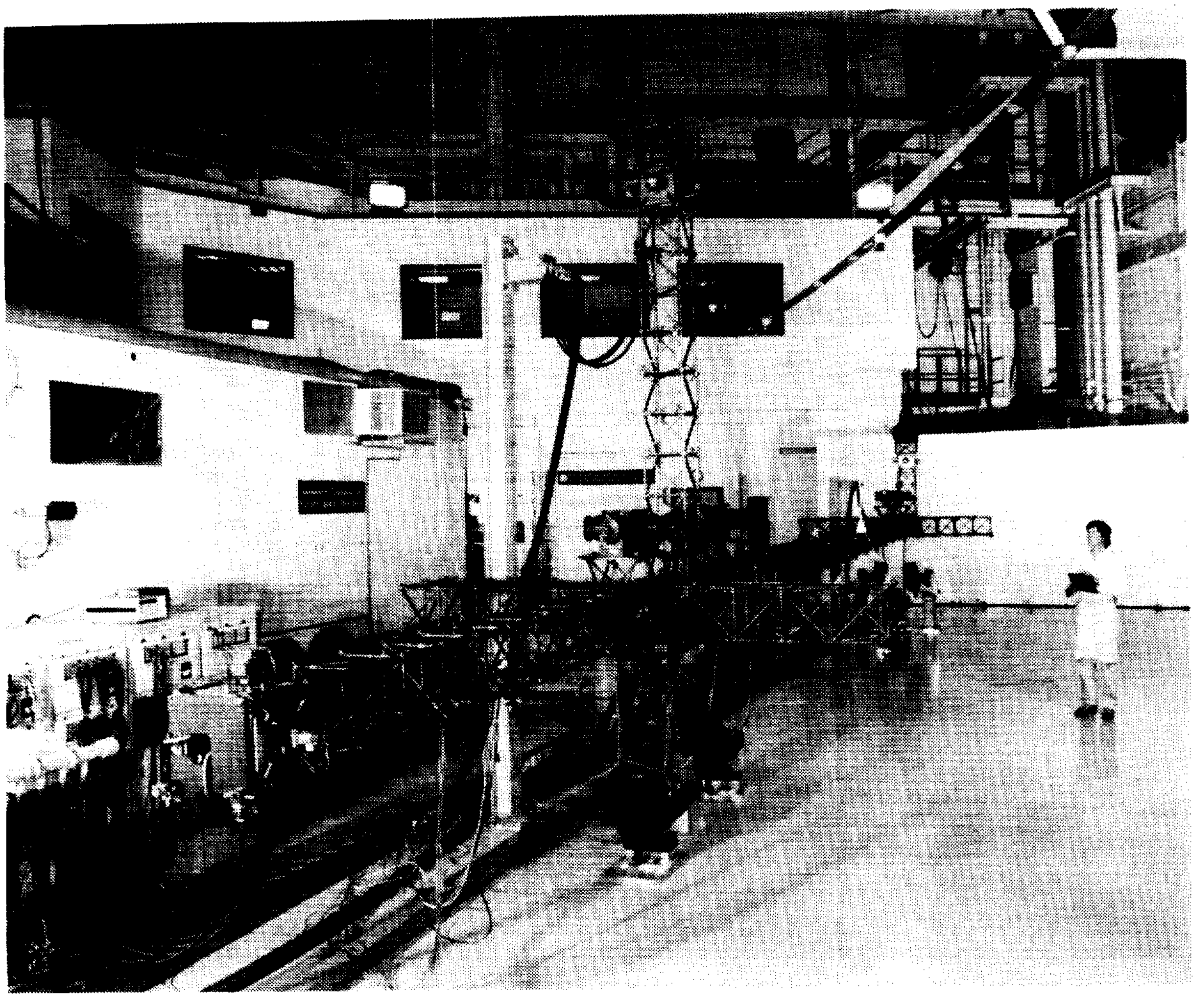

Figure 2.2: CSI Evolutionary Model in its Phase 2 Configuration

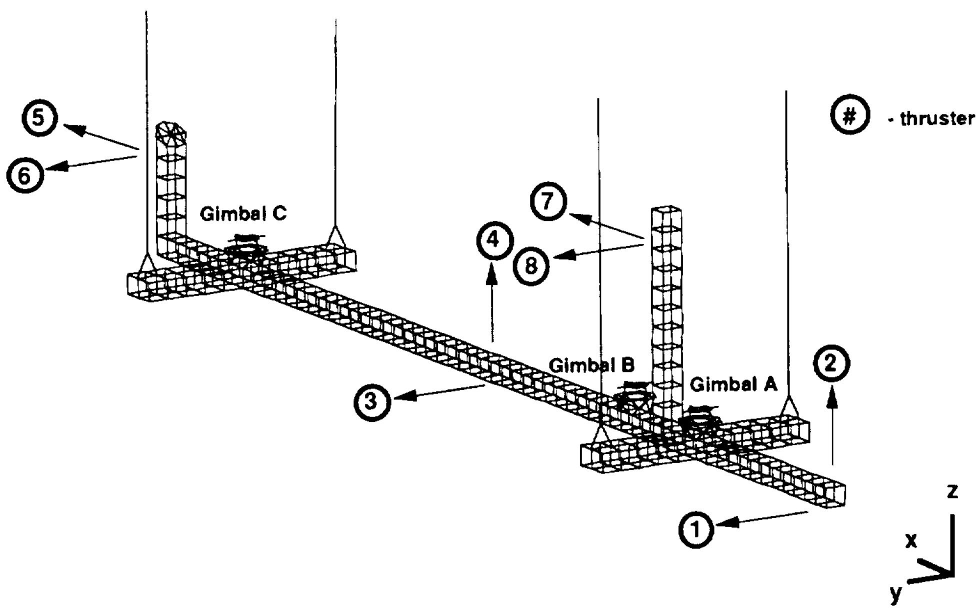

Figure 2.3: Schematic of the Phase 2 CSI Evolutionary Model

2.1.3 Sensors

Two sets of sensors are used, feedback sensors and performance measurement sensors. The feedback sensors consist of 8 Sundstrand model QA–900 servo accelerometers collocated with the cold gas thrusters as shown in Figure 2.3. These sensors have a bandwidth about 300 Hz and were typically used with Bessel analog filters set at a bandwidth of 100 Hz. For the Phase 1 CEM a global LOS pointing scoring system was used to measure performance. The global LOS pointing scoring system consisted of a low-powered laser mounted on the laser tower such that the laser beam is directed to a mirror mounted at the center of the reflector. The beam is reflected to the ceiling where its position is measured by an xy-plane photo-diode array located on the ceiling above the mirror. Typical resolution of the LOS sensor is 0.5 inch. For the Phase 2 CEM, each of the 3 gimbal payloads is instrumented with an optical scoring system which measures two angles, azimuth and elevation, of a laser beam. The optics transforms the angular deflection into a position translation of the laser spot on a two-axes Lateral Effect Detector.

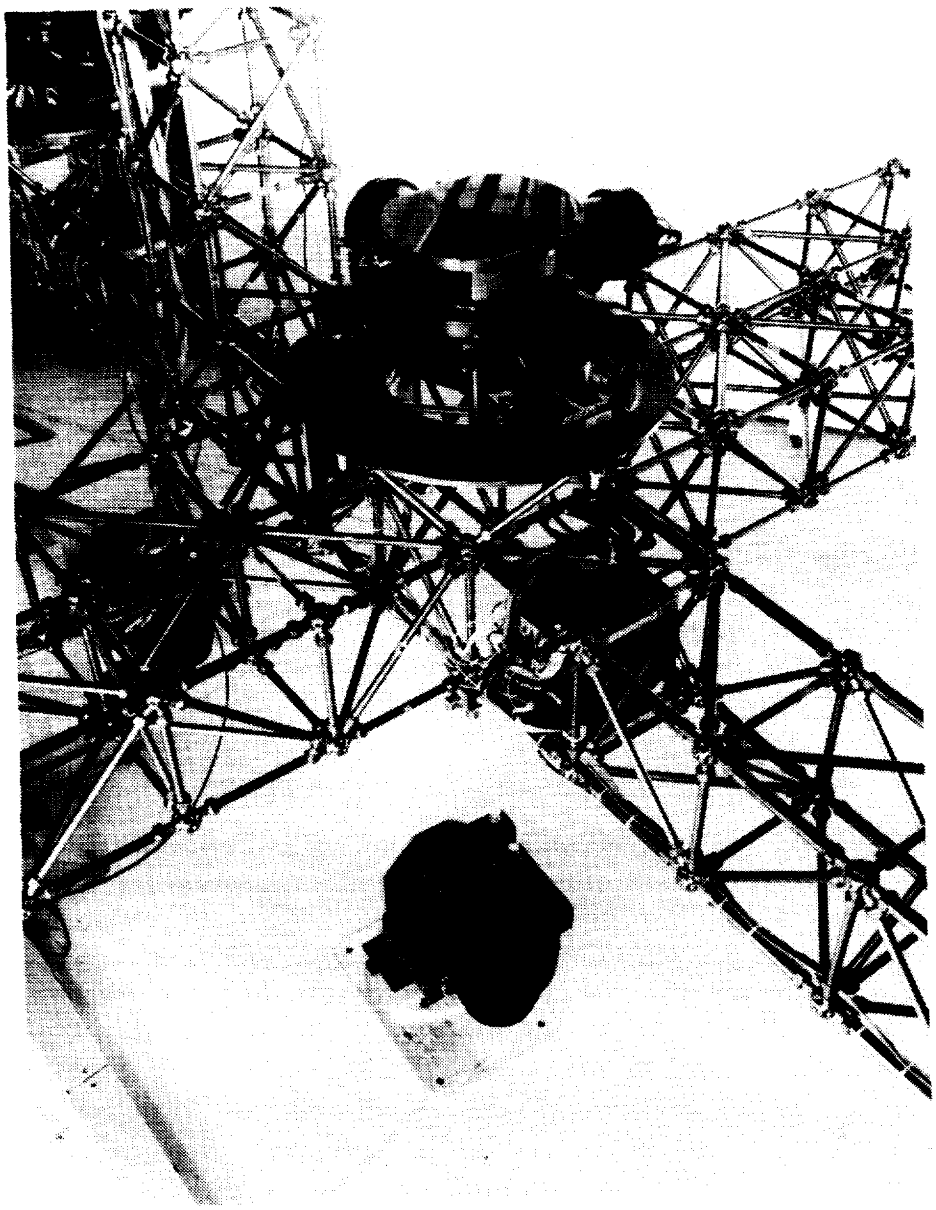

Figure 2.4: 2-Axis Gimbal Science Simulator With Its Optical Scoring System

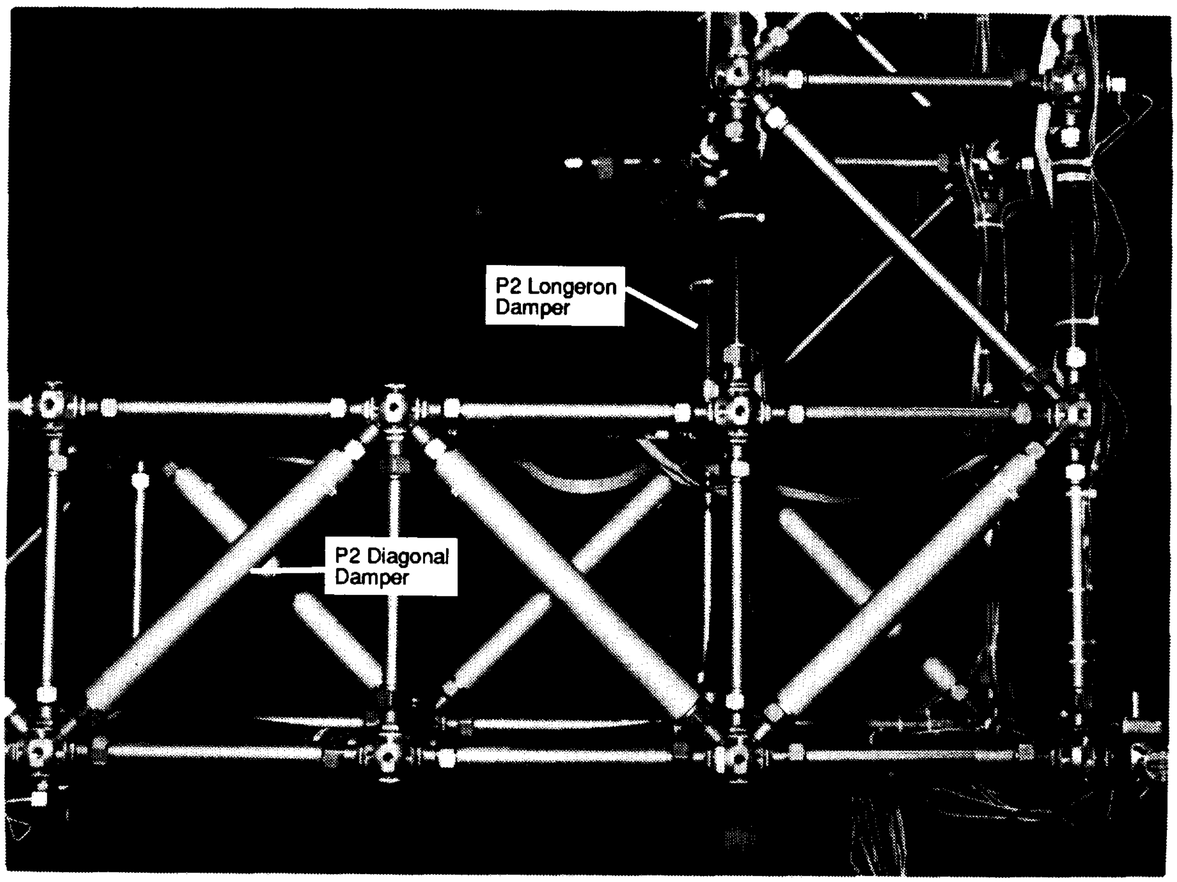

Figure 2.5: Damped Struts Installed on the Phase 2 CEM Near the Reflector Tower

2.1.4 Actuators

The actuator set used for this work are sixteen compressed air thrusters operated in pairs at the 8 locations shown in Figure 2.3. The thrusters are proportional bi-directional force actuators and produce up to 2.2 lbs of force. A local controller is implemented for each thruster to make the response linear with a bandwidth of about 40 Hz. Viscoelastically damped struts designed under this program and discussed later in this report are used to complement the active control actuators.

2.1.5 Real-time Computer System

The open-loop and closed-loop tests described in this report were performed using the real-time control and data acquisition system shown in Figure 2.6 (Phase 2 configuration). The real-time control algorithms are implemented on an IBM RS–6000 computer using a generic user code programmed in FORTRAN. For the Phase 2 tests all the controllers were implemented with a sampling rate of 350 Hz. A standard input file to load the controller matrices and the excitation profiles was used for the tests. The CAMAC (Computer Automated Measurement and Control) based system provides analog-to-digital/digital-to-analog/digital interfaces for the computing platforms and the sensor/actuator electronics. A Zonic System 7000 computer shown also in Figure 2.6 was used to perform the open-loop and closed-loop MIMO frequency response function (FRF) tests.

2.2 Modeling of the CEM Test Article

In this section we discuss the state space models of the CEM used in later sections for the control design analysis. The state space models of the CEM were constructed from the finite-element model (FEM) modal data output by MSC/NASTRAN[1].

2.2.1 Finite Element Model Modes

The modal frequencies and associated mode shapes were obtained from the FEM for modes up to 30 Hz. Table 2.1 shows the frequencies and damping ratios of the Phase 2 CEM rigid and dominant elastic modes up to approximately 10 Hz. Both the frequencies obtained from the FEM and the identified frequencies used in the state space model are given. The identified frequencies of the rigid-body modes were obtained by hand "tuning" the state space model frequencies to approximately match the measured frequency responses. The damping ratios of the rigid-body modes were

[1]MSC is a trademark of the MacNeal-Schwendler Corporation.

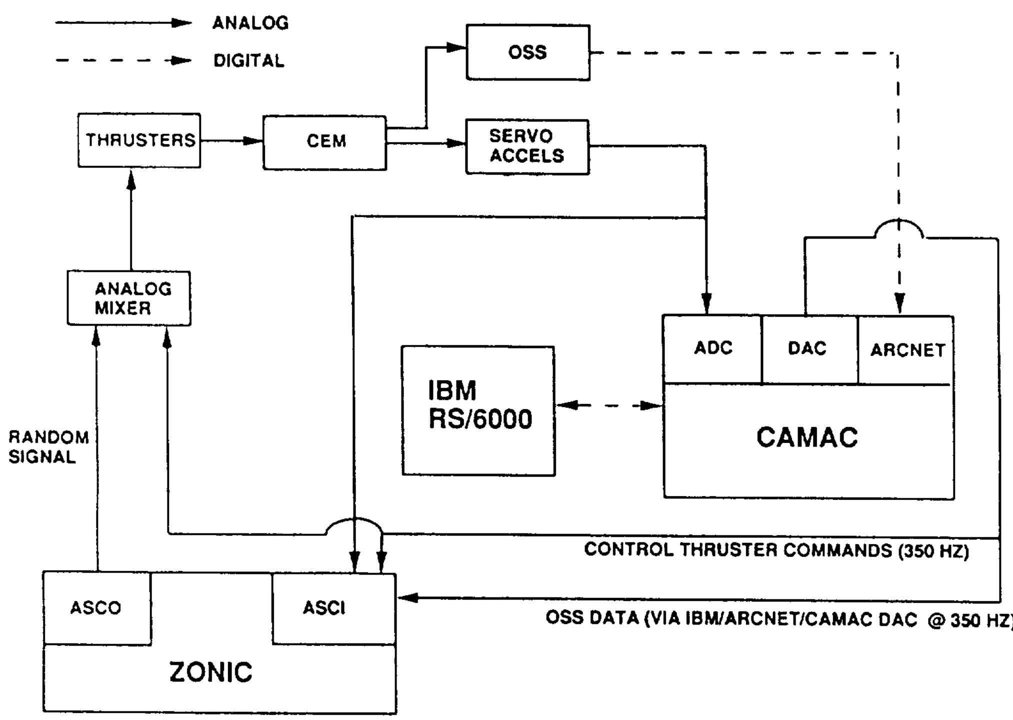

Figure 2.6: Block diagram of the Phase 2 real-time control system

Table 2.1: Phase 2 CEM P2032993 Rigid and Dominant Elastic Modes

Mode Description	FEM Mode #	FEM Freq. (Hz)	ID Freq. (Hz)	ID Damping (Percent)
Lateral Pendulum	1	0.130	0.16	3.5
Longitudinal Pendulum	2	0.132	0.16	3.66
Yaw	3	0.136	0.16	5.0
Reflector-Tower Bounce	4	0.180	0.21	5.88
Laser-Tower Bounce	5	0.181	0.21	5.81
Roll	6	0.303	0.355	2.42
First Torsion	7	1.712	1.775	0.35
Pitch First Bending	8	2.380	2.432	0.22
Yaw First Bending/Torsion	9	2.981	3.042	0.34
Pitch Second Bending	10	5.427	5.675	0.26
Yaw Second Bending/Torsion	11	5.871	6.112	0.30
Laser Tower/Main Truss	20	7.700	7.776	0.45
Second Torsion	21	8.402	8.695	0.31
Pitch Third Bending	22	8.881	9.147	0.23
Laser-Tower/Susp. Truss	23	9.892	10.23	0.22

obtained from a polyreference test analysis of the structure and by further hand tuning to approximately match the measured frequency responses. The frequencies and damping ratios of the dominant elastic structural modes shown in Table 2.1 were obtained using the ERA system identification algorithm to be discussed in a later section. Elastic modes not listed in Table 2.1 were assumed to have 0.1 damping ratio and frequencies from the FEM.

Mode shape plots of the modes in Table 2.1 are shown in Figures 2.7 through 2.21. Mode numbers 1–6 are the rigid-body modes. Mode numbers 7, 8, and 9 are the first dominant bending and torsional modes of the main truss.

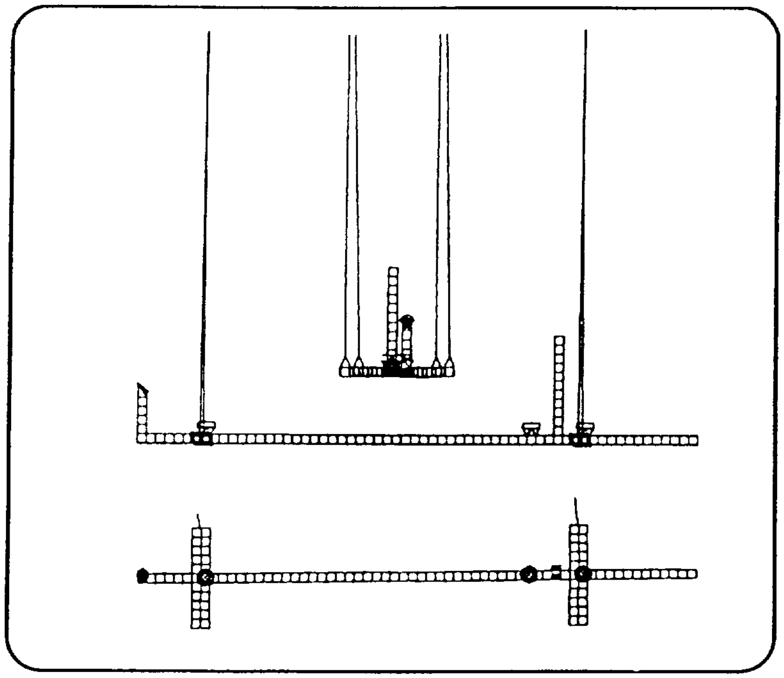

Figure 2.7: Phase 2 CEM 0.130 Hz Lateral Pendulum Mode

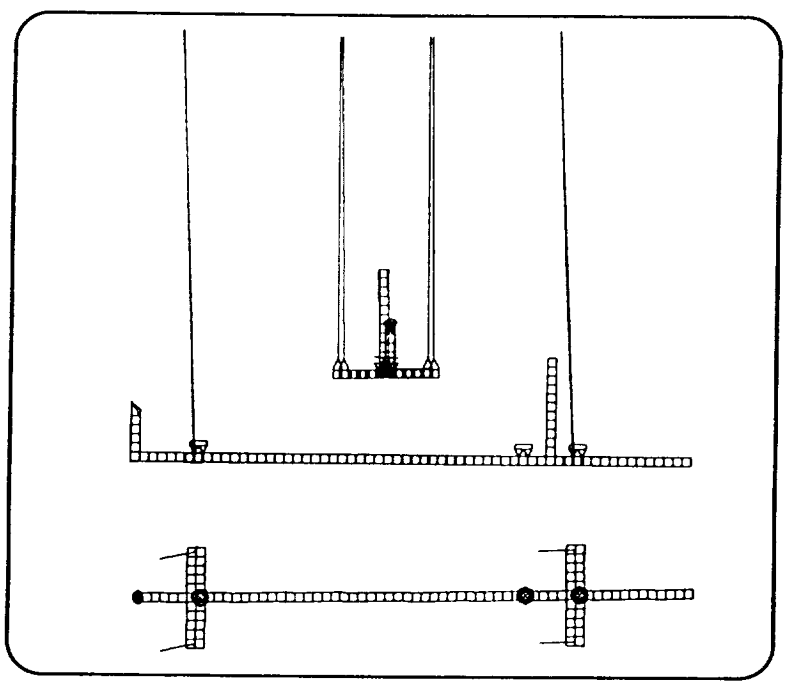

Figure 2.8: Phase 2 CEM 0.132 Hz Longitudinal Pendulum Mode

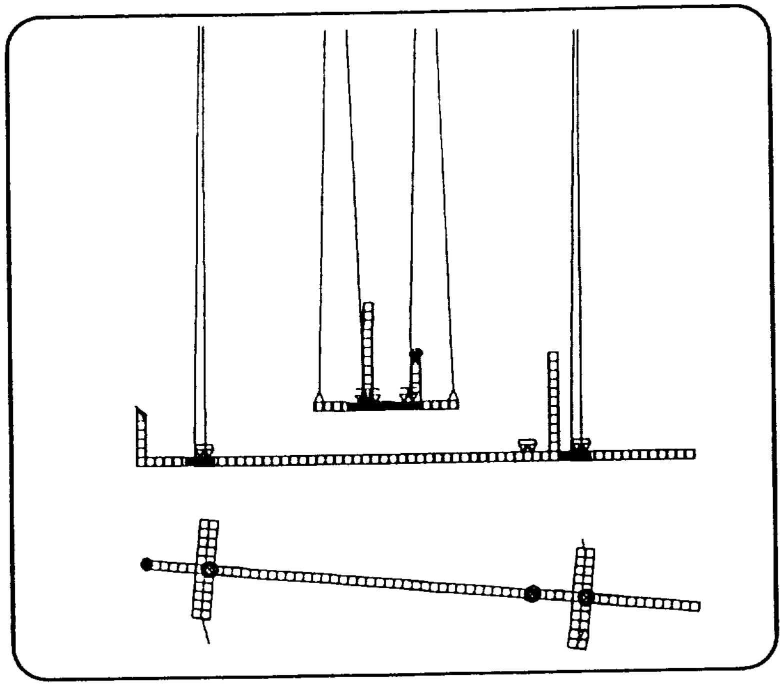

Figure 2.9: Phase 2 CEM 0.136 Hz Yaw Mode

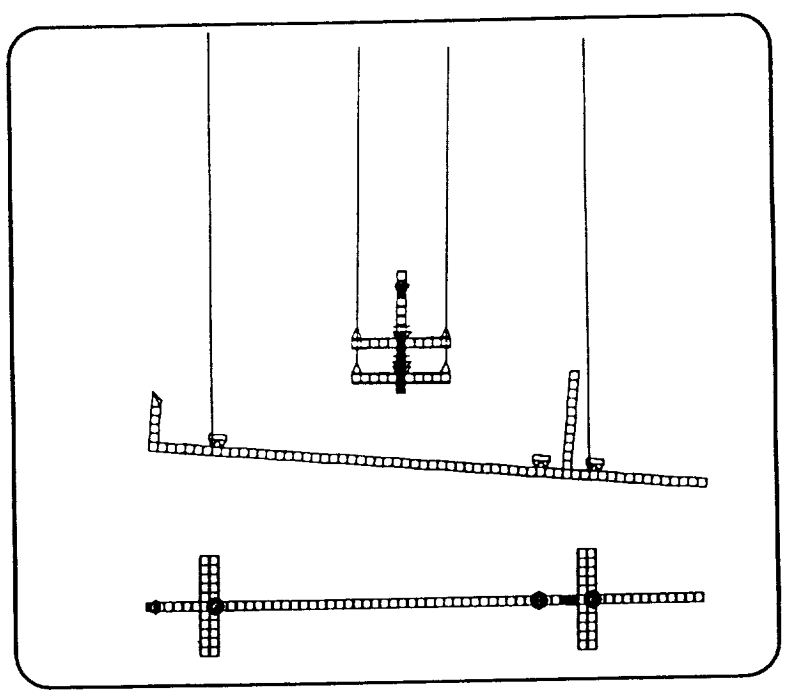

Figure 2.10: Phase 2 CEM 0.180 Hz Bounce Mode Near Reflector Tower

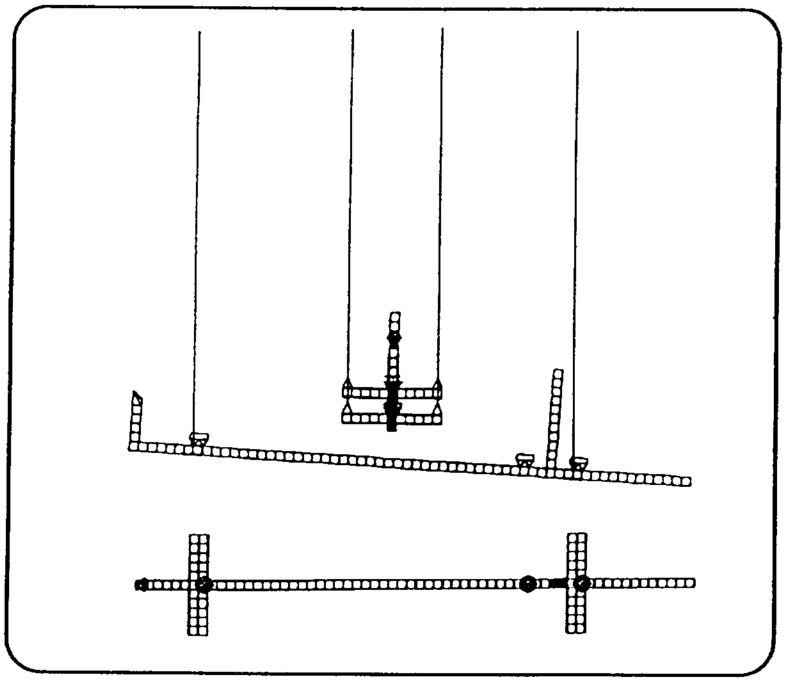

Figure 2.11: Phase 2 CEM 0.181 Hz Bounce Mode Near Laser Tower

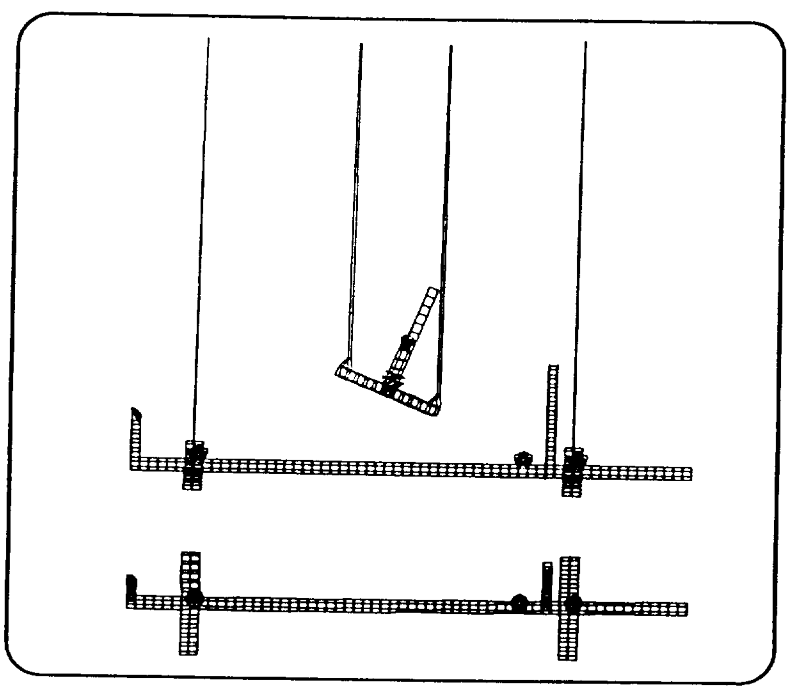

Figure 2.12: Phase 2 CEM 0.303 Hz Roll Mode

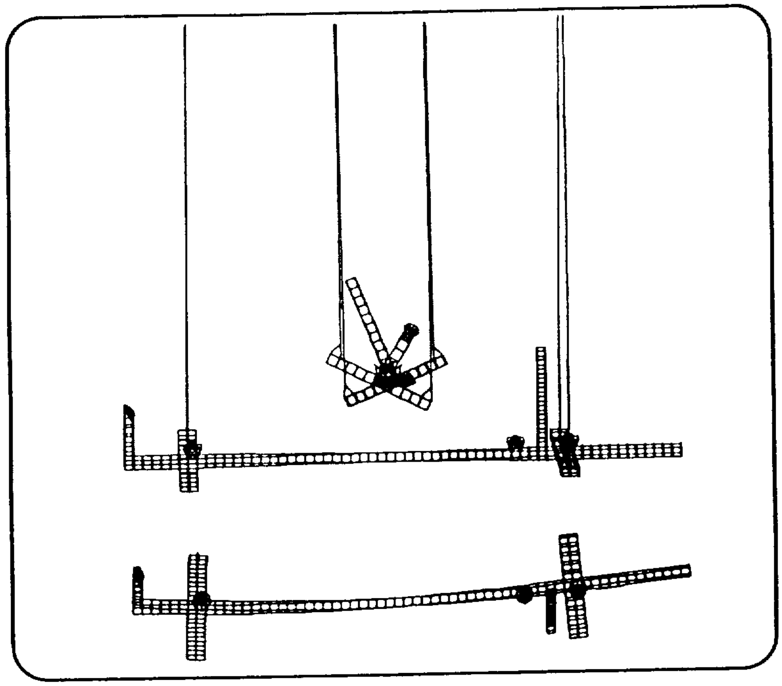

Figure 2.13: Phase 2 CEM 1.712 Hz Main Truss First Torsion Mode

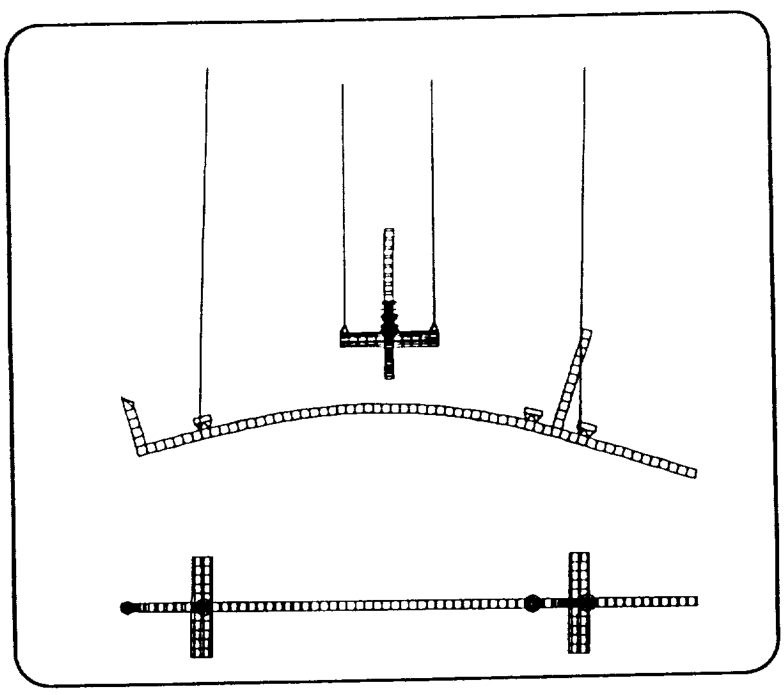

Figure 2.14: Phase 2 CEM 2.380 Hz Main Truss Pitch First Bending Mode

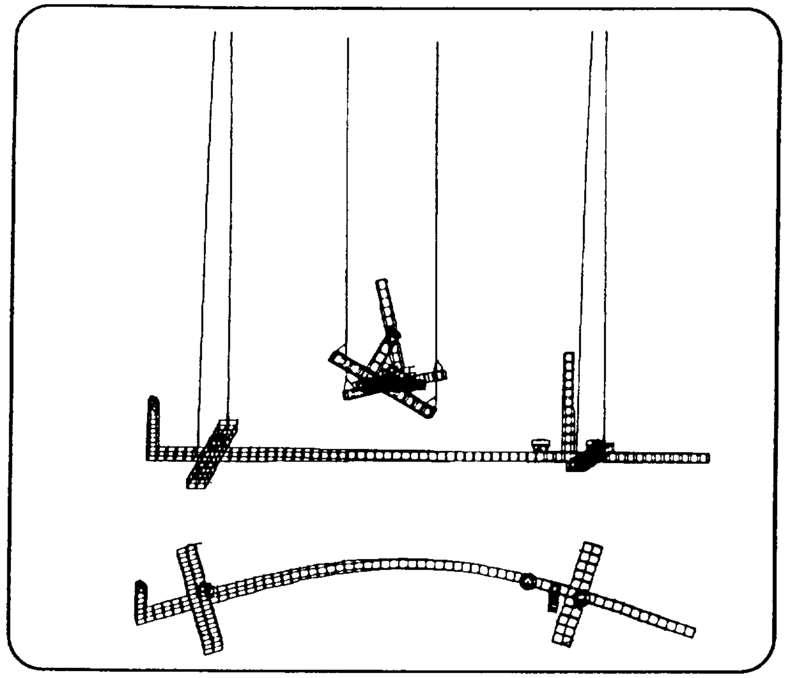

Figure 2.15: Phase 2 CEM 2.981 Hz Main Truss Yaw First Bending/Torsion Mode

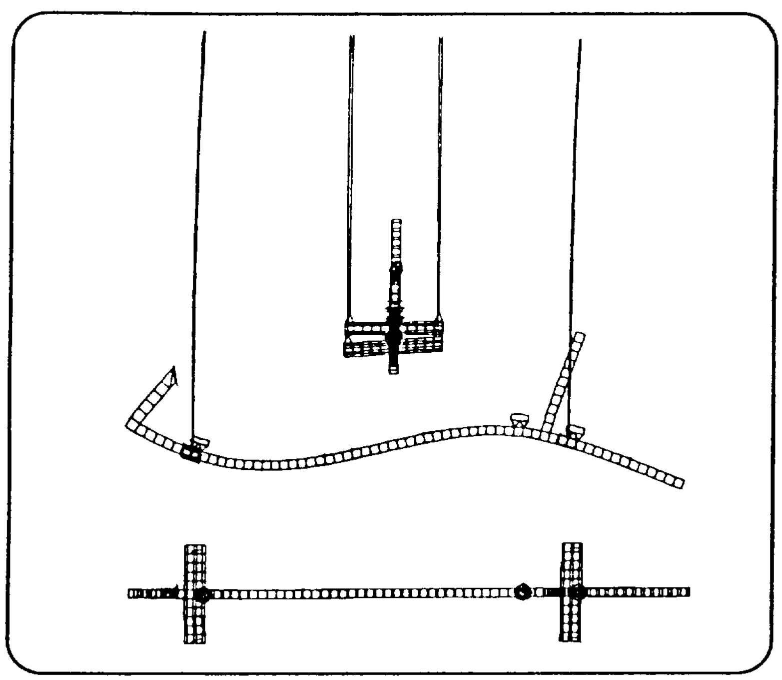

Figure 2.16: Phase 2 CEM 5.427 Hz Main Truss Pitch Second Bending Mode

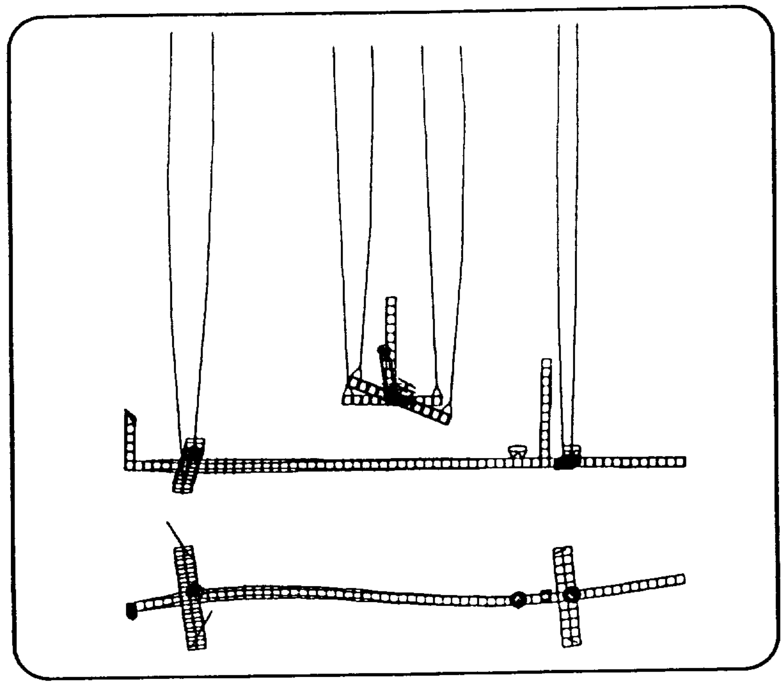

Figure 2.17: Phase 2 CEM 5.871 Hz Main Truss Yaw Second Bending/Torsion Mode

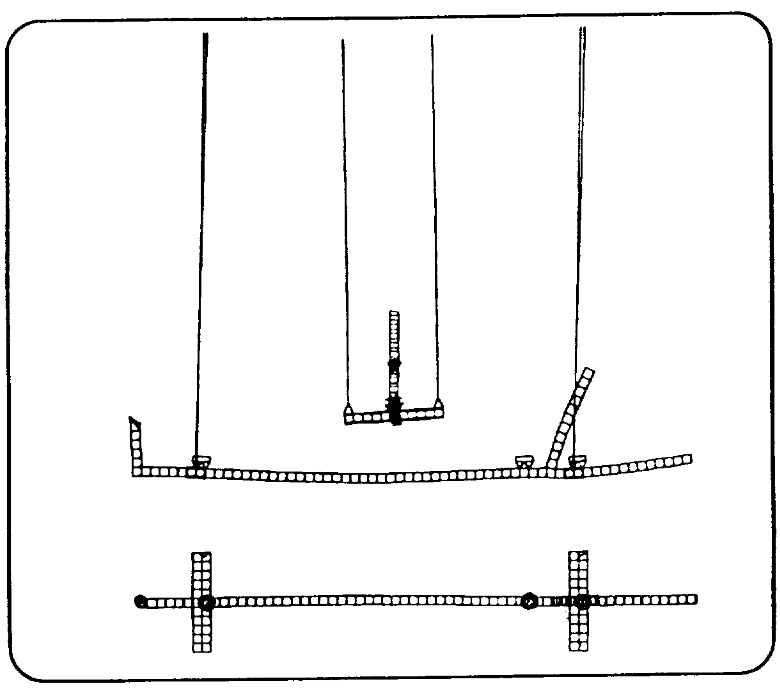

Figure 2.18: Phase 2 CEM 7.700 Hz Laser Tower/Main Truss Mode

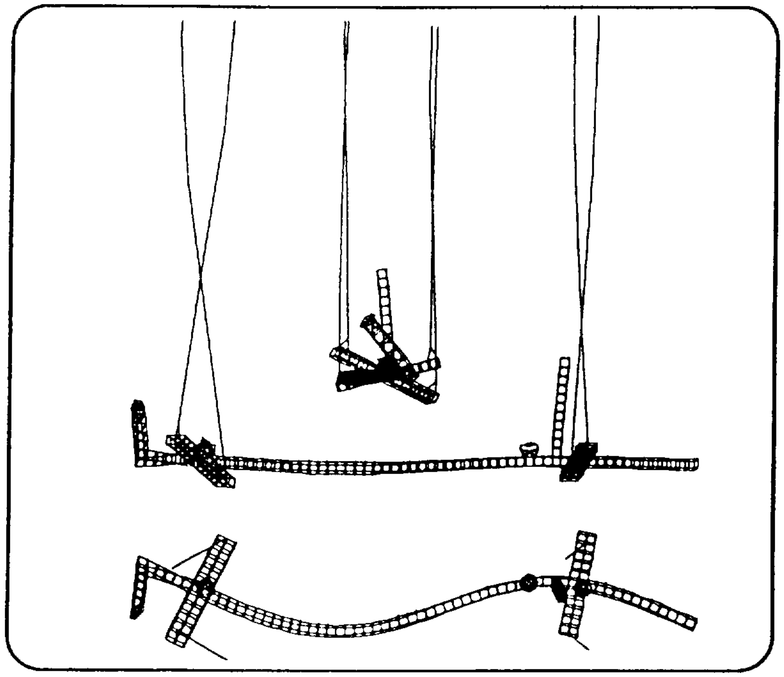

Figure 2.19: Phase 2 CEM 8.402 Hz Main Truss Second Torsion Mode

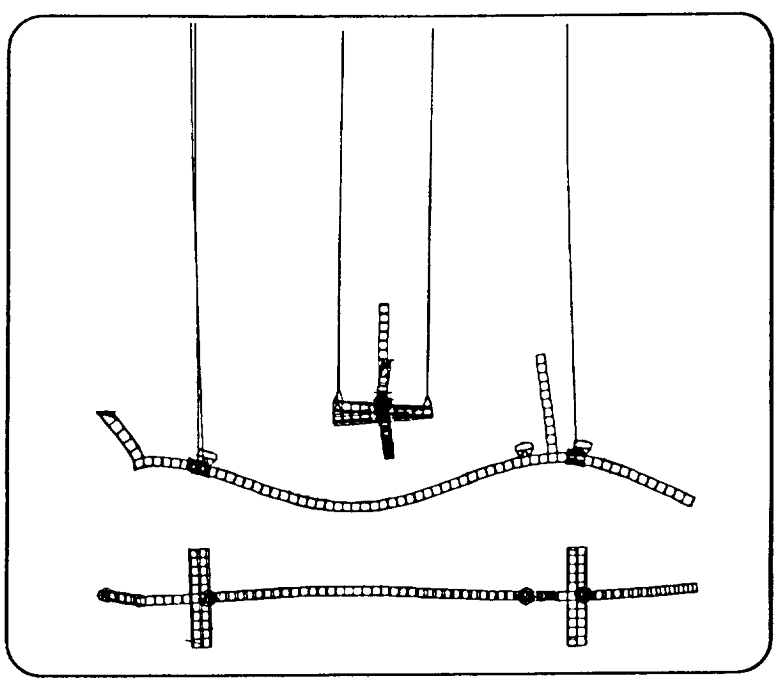

Figure 2.20: Phase 2 CEM 8.881 Hz Main Truss Pitch Third Bending Mode

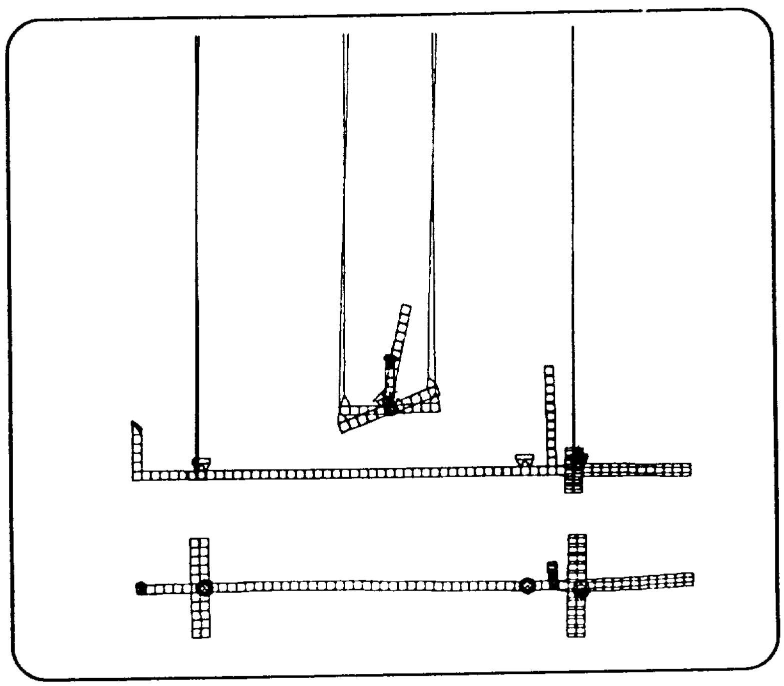

Figure 2.21: Phase 2 CEM 9.892 Hz Laser-Tower/Suspension Truss Mode

2.2.2 State Space Model Equations

The CEM state space equations of motion for the i^{th} mode are constructed in the form:

$$\ddot{x}_i = A_i x_i + B_i T \tag{2.1}$$

where

$$A_i = \begin{bmatrix} 0 & 1 \\ -\omega_i^2 & -2\zeta_i\omega_i \end{bmatrix} \quad B_i = \begin{bmatrix} 0 & \cdots & 0 \\ h_{i1} & \cdots & h_{ip} \end{bmatrix} \tag{2.2}$$

and ω_i and ζ_i are the frequency and damping ratio of the i^{th} mode, respectively. The thruster force inputs are denoted by T and h_{ij} are the modal deflections at the j^{th} thruster location in the direction of the applied force.

The total state space equations including n modes are assembled in block diagonal form as

$$\ddot{x} = \begin{bmatrix} A_1 & & 0 \\ & \ddots & \\ 0 & & A_n \end{bmatrix} x + \begin{bmatrix} B_1 \\ \vdots \\ B_n \end{bmatrix} T \tag{2.3}$$

2.2.3 Modeling of Accelerometers

Eight servo-accelerometers were available for sensing and feedback control on the CEM. The servo-accelerometers were approximately collocated with the applied thruster forces. The j^{th} accelerometer output equation is

$$a_j = \sum_{i=1}^{n} \left[h_{ij}\ddot{\xi}_i + g\sin(\alpha_j + \phi_{ij}\xi_i) \right] \tag{2.4}$$

where a_j is the j^{th} accelerometer output, h_{ij} is the accelerometer displacement due to the i^{th} mode along the j^{th} accelerometer output axis, ξ_i is the i^{th} modal coordinate, g is the gravitational acceleration, α_j is the accelerometer mount angle and ϕ_{ij} is the accelerometer rotation due to the i^{th} mode. The angles α_j and ϕ_{ij} are measured about the vector formed by the cross-product of the gravitational acceleration vector and the vector along the j^{th} accelerometer output axis. The accelerometer mount angle α_j is measured from the plane perpendicular to the gravitational acceleration vector. The notations for α_j and ϕ_{ij} assume that small positive rotation angles result in a component of the gravitational acceleration along the negative accelerometer output axis.

Equation 2.4 can be linearized for small angles $(\phi_{ij}\xi_i)$ as

$$a_j = \sum_{i=1}^{n} \left[h_{ij}\ddot{\xi}_i + g\cos(\alpha_j)\phi_{ij}\xi_i \right]. \tag{2.5}$$

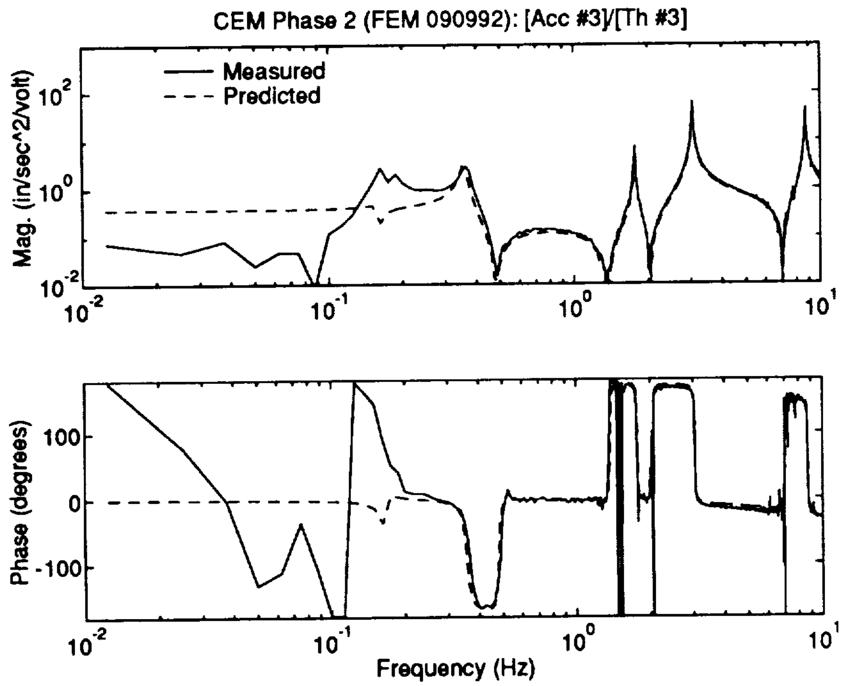

Figure 2.22: Phase 2 CEM 090992 Measured and Predicted Frequency Responses Without Tuned Lateral Pendulum Mode Roll Component

Note that the gravitational term $g\cos(\alpha_j)$ in the accelerometer output equation can be very large for certain modes when the accelerometer mount angle α is zero (or $\cos(\alpha) \simeq 1$). The result is that the accelerometer outputs are dominated by the gravitational components resulting from accelerometer rotations rather than the translational accelerations.

For the Phase 2 CEM this presents a modeling difficulty. The modal rotation component, ϕ_{1x}, about the x-axis for the 0.16 Hz rigid-body lateral pendulum mode (mode #1 in Table 2.1) computed from the FEM is very sensitive to the model of the suspension system. Slight modeling errors in the suspension devices can result in significant accelerometer output errors at the frequency of the rigid-body pendulum modes resulting from the large gravitational terms. This effect is clearly seen in the thruster to accelerometer transfer function $A_3(s)/T_3(s)$ at the rigid-body pendulum mode frequency (Figure 2.22) for the P2090992 FEM[2].

When unaccounted for, this modeling sensitivity resulted in unstable control de-

[2]The measured frequency response phase angles are not very reliable at frequencies where the response amplitudes are very low.

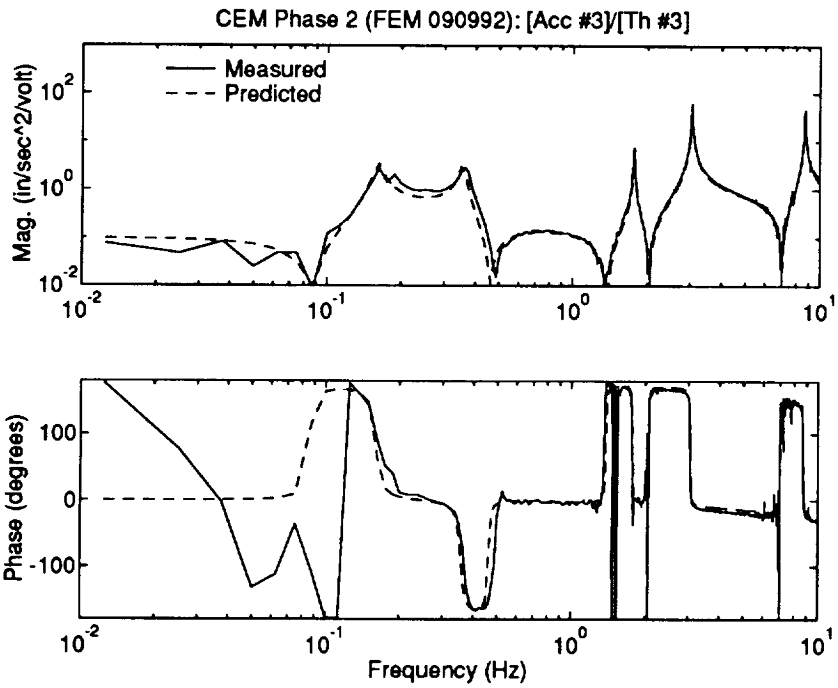

Figure 2.23: Phase 2 CEM 090992 Measured and Predicted Frequency Responses With Tuned Lateral Pendulum Mode Roll Component

signs in actual implementation on the test article (i.e., the controller destabilized the rigid-body lateral pendulum mode). By hand "tuning" the value of ϕ_{1x} a much better match in the frequency responses at low frequencies is obtained (Figure 2.23). The value of ϕ_{1x} obtained from a later FEM (P2032993) more nearly matched the hand tuned value obtained with the P2090992 FEM and the frequency responses were also closer to the measured responses.

2.2.4 Modeling of LOS Outputs

The line-of-sight (LOS) pointing scoring equation for the Phase 1 CEM is computed from a nonlinear equation involving the deflections and rotations at the laser source and reflector mirror locations. A MATLAB M-function is available to compute the nonlinear LOS output equation. A linearized LOS output equation was used for the state space models with the form

$$\begin{pmatrix} x_{\text{LOS}} \\ y_{\text{LOS}} \end{pmatrix} = \sum_{i=1}^{n} \begin{bmatrix} \phi_i^{(x)} \\ \phi_i^{(y)} \end{bmatrix} \xi_i \tag{2.6}$$

Table 2.2: Thruster Dynamic Model Constants

Thruster Number	Gain (lbs/volt)	Frequency (rad/sec)
1	0.412	285.6
2	0.402	302.9
3	0.404	271.1
4	0.406	257.3
5	0.407	263.1
6	0.397	317.4
7	0.399	263.8
8	0.398	247.0

where $\phi_i^{(x)}$ and $\phi_i^{(y)}$ are the equivalent linearized modal deflection components for the i^{th} mode for the x and y LOS outputs, respectively. The equivalent linearized modal deflection components $\phi_i^{(x)}$ and $\phi_i^{(y)}$ were obtained by numerical differentiation using the nonlinear LOS M-function.

For the Phase 2 CEM, the LOS scoring outputs are the gimbal OSS angular rotations. With the gimbals locked in a vertical configuration the LOS output equation for the j^{th} gimbal is

$$\begin{pmatrix} x_{\text{LOS}j} \\ y_{\text{LOS}j} \end{pmatrix} = \sum_{i=1}^{n} \begin{bmatrix} \phi_{ij}^{(x)} \\ \phi_{ij}^{(y)} \end{bmatrix} \xi_i \tag{2.7}$$

where $\phi_i^{(x)}$ and $\phi_i^{(y)}$ are the modal angular rotation components for the i^{th} mode about the x and y axes, respectively.

2.2.5 Actuator and Sensor Dynamic Models

Thruster dynamics were modeled as first-order transfer functions given by

$$T_j^f(s) = \frac{K_j \sigma_j}{s + \sigma_j} T_j^v(s) \tag{2.8}$$

where T_j^f is the j^{th} thruster force in pounds, T_j^v is the j^{th} thruster command in volts, K_j is the thruster gain in pounds/volt, σ_j is j^{th} thruster dynamics break frequency, and $s \in C$. The values for K_j and σ_j are given in Table 2.2.

The accelerometer signals are processed through analog antialiasing filters provided by the CAMAC powered chassis (called a crate) prior to sampling. The analog antialiasing filter transfer functions are modeled as third-order Bessel filters with a 100 Hz break frequency as

$$V_o(s) = -2.7285 \times 10^{-12} \times \frac{(s^2 + 938.67s - 2.5895 \times 10^{20})}{(s + 832.84)(s^2 + 1324.5s + 848340)} V_i(s) \tag{2.9}$$

where $V_i(s)$ and $V_o(s)$ are the input and output signal voltages, respectively.

2.2.6 Modeling of Time Delays and Sampling Effects

Computational time delays were modeled using first-order Padé filter approximations for each thruster loop. The computational delays were assumed to be equal to the length of one sample period.

The effects of the zero-order hold in the digital to analog conversion were modeled by transforming the continuous state space equations in the s-domain to the w-domain using a zero-order hold discretization. The w transform with a zero-order hold discretization has been found to accurately model discrete time and zero-order hold effects for many problems including the TITAN IV launch vehicle.

2.3 CEM Open-Loop Responses

In this section we discuss the open-loop responses of the Phase 1 and Phase 2 CEM configurations. Only selected frequency responses are shown in the text. More complete sets of open-loop frequency responses are given in Appendix B for Phase 1 and Phase 2.

Figure 2.24 shows the measured and predicted (from the state space model) frequency responses of the LOS output maximum singular values to thruster commands for the Phase 1 CEM. The maximum singular values indicate the maximum possible magnitude of the LOS frequency responses for simultaneous thruster commands with an input vector 2-norm less than or equal to one. The modal density of the Phase 1 configuration is seen to be very high. The LOS frequency responses match reasonably well in the frequency range from 0–4 Hz. However, beyond 4 Hz the measured frequency responses deviate significantly from the model.

Figure 2.25 shows the measured and predicted frequency responses of OSS #1 LOS outputs maximum singular values to thruster commands for the Phase 2 CEM. The predicted responses were computed using the FEM modal data without the identified modal frequencies (the damping ratios are the identified values in Table 2.1). The modal density of the Phase 2 configuration, although still quite high, is significantly reduced from the Phase 1 configuration due to the removal of the antenna.

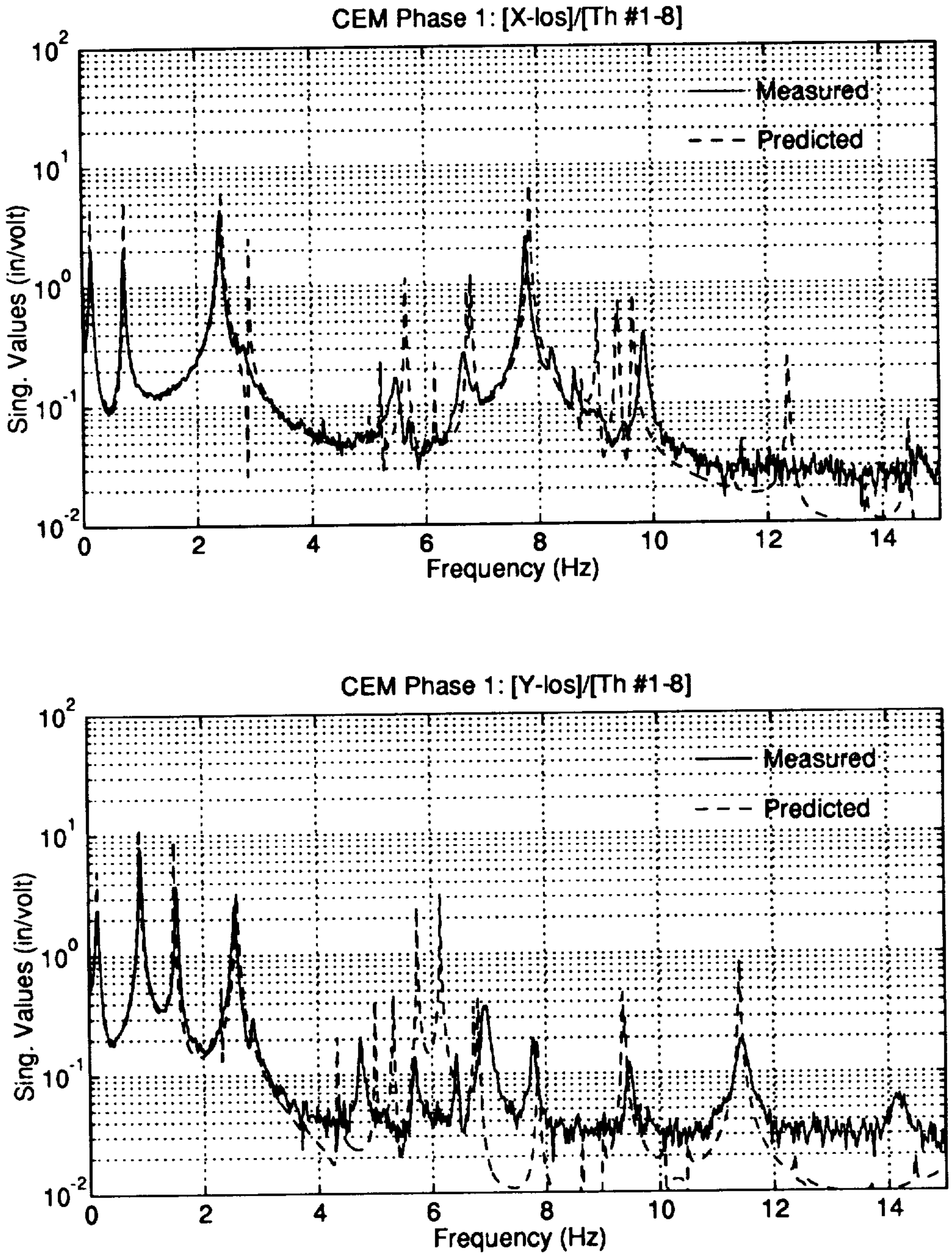

Figure 2.24: Phase 1 CEM Measured and Predicted Open-Loop LOS Frequency Responses

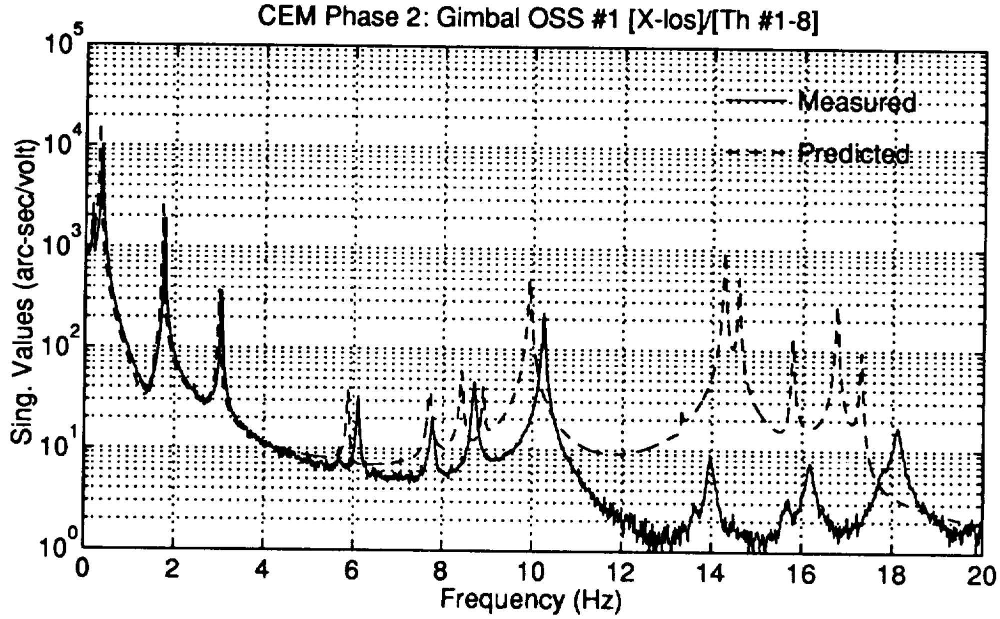

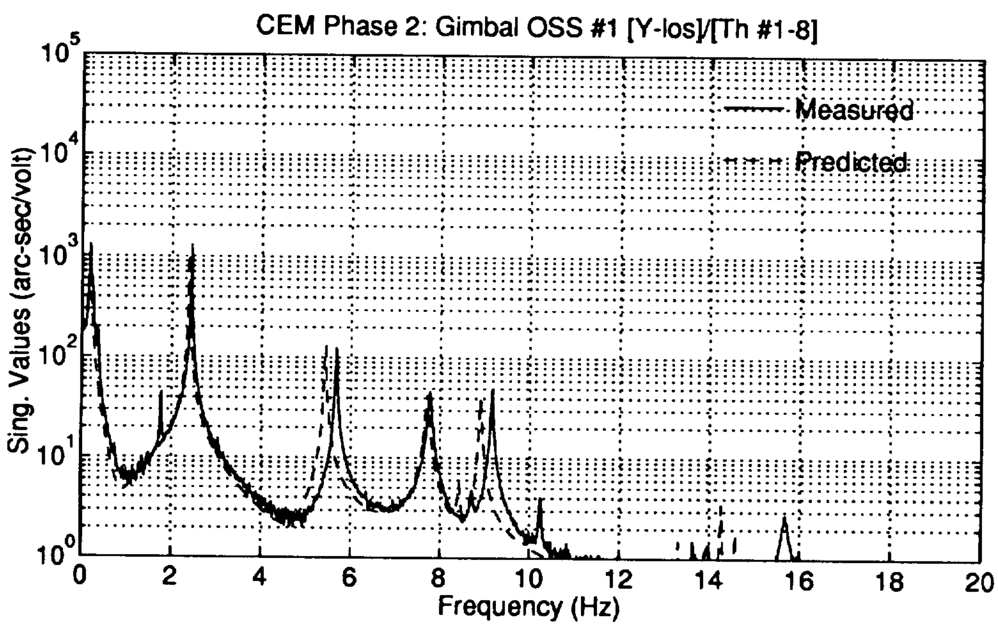

Figure 2.25: Phase 2 CEM Measured and Predicted Open-Loop OSS #1 LOS Frequency Responses Without Identified Modal Frequencies

Figure 2.26 shows the measured and predicted (from the state space model) frequency responses for the Phase 2 CEM. The predicted responses were computed using the identified modal frequencies. The LOS frequency responses for the tuned model match very well in the frequency range from 0–4 Hz and reasonably well from 4–10 Hz. Beyond 10 Hz the measured frequency responses begin to deviate significantly from the model.

Figure 2.27 shows measured open-loop transient responses of gimbal OSS #1 x and y LOS for the Phase 2 CEM. The responses were obtained by exciting the system with sinusoidal thruster inputs for 7 seconds (from 0–7 seconds) with the control loops open. The sinusoidal thruster inputs were chosen at the approximate frequencies of the first three main truss bending/torsional modes.

2.4 Open-Loop System Identification

The Eigensystem Realization Algorithm (ERA) was used to obtain state-space models for the CEM. Two different versions of the ERA have been developed at NASA, one working with time-domain data [10] and another one based on frequency-domain data [11, 12]. These algorithms are implemented in a system identification MATLAB toolbox developed at NASA LaRC [13]. Initial experiments performed with time-domain data generated from open-loop random tests for the Phase 1 CEM showed poor match with the experimental frequency response data. Instead the frequency-domain ERA was used. The algorithm described in [11] is based on a matrix-fraction description of the MIMO transfer function used to fit the frequency response data using the least-squares method. The Markov parameters, derived from the matrix-fraction representation, are then used to develop a state-space model with the Eigensystem Realization Algorithm [10]. Two examples of the frequency-domain fit achieved with ERA are shown in Figures 2.28 (nominal Phase 2 CEM) and 2.29 (Phase 2 CEM with passive damping treatment). The 8×8 matrix of FRF experimental data for the 8 accelerometer/thruster pairs was used to identify a discrete time state-space model. As shown from the figures the fit obtained with the elastic data is excellent. In Figure 2.29, the fit in the rigid-body region is poor in comparison to Figure 2.28. This is a result of selecting a lower-order state-space model for the damped model (80 versus 160 states).

The discrete time state-space models derived with ERA are obtained for a sampling frequency equal to twice the maximum frequency in the FRF data (15 or 20 Hz for our tests). In order to use the state-space model for control design and analysis, a discrete model needs to be obtained for much higher sampling rate (at least 150 Hz). Initial attempts to obtain higher sampling rate models were not successful. Because there was already quite good agreement between FEM predictions and experimental

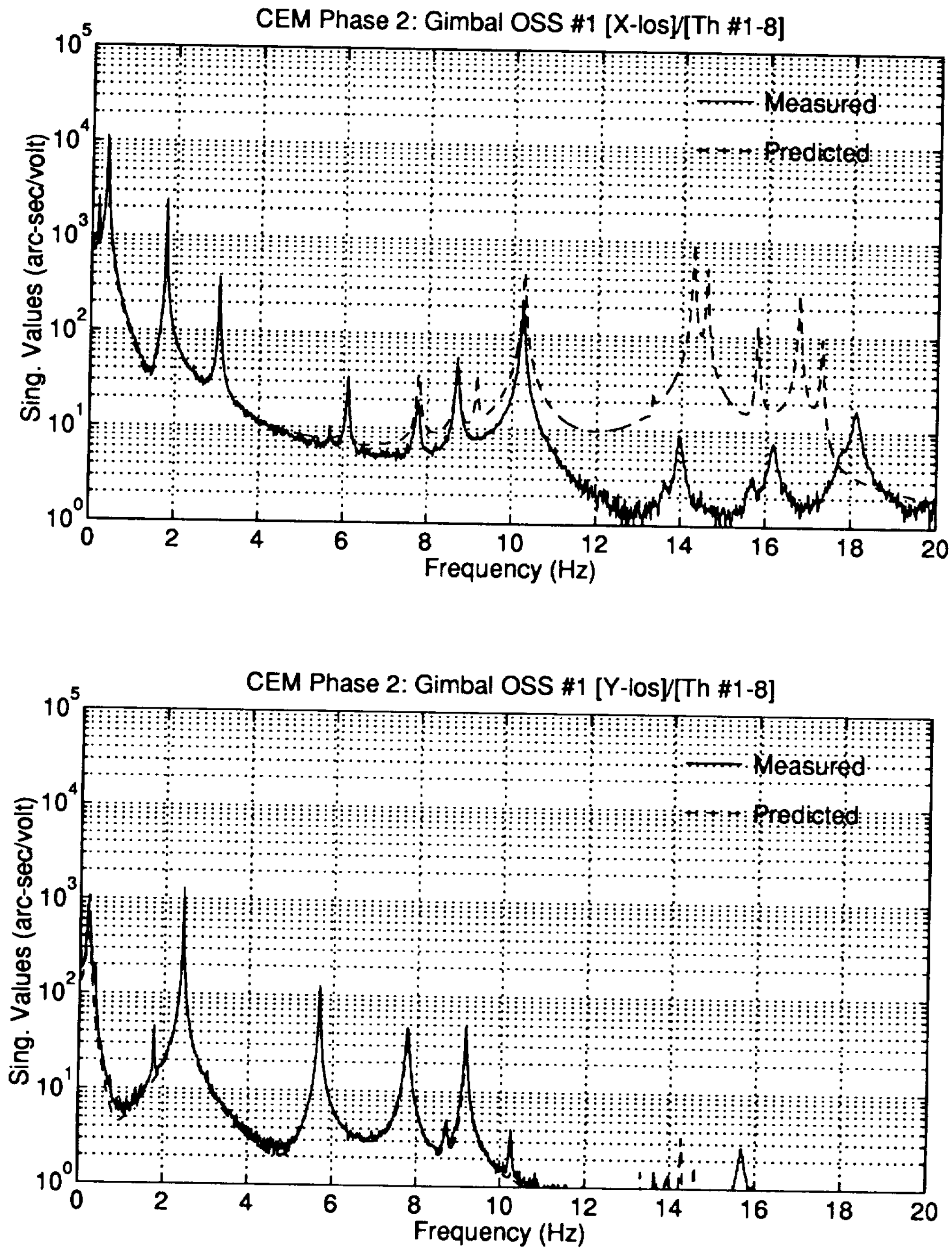

Figure 2.26: Phase 2 CEM Measured and Predicted Open-Loop OSS #1 LOS Frequency Responses With Identified Modal Frequencies

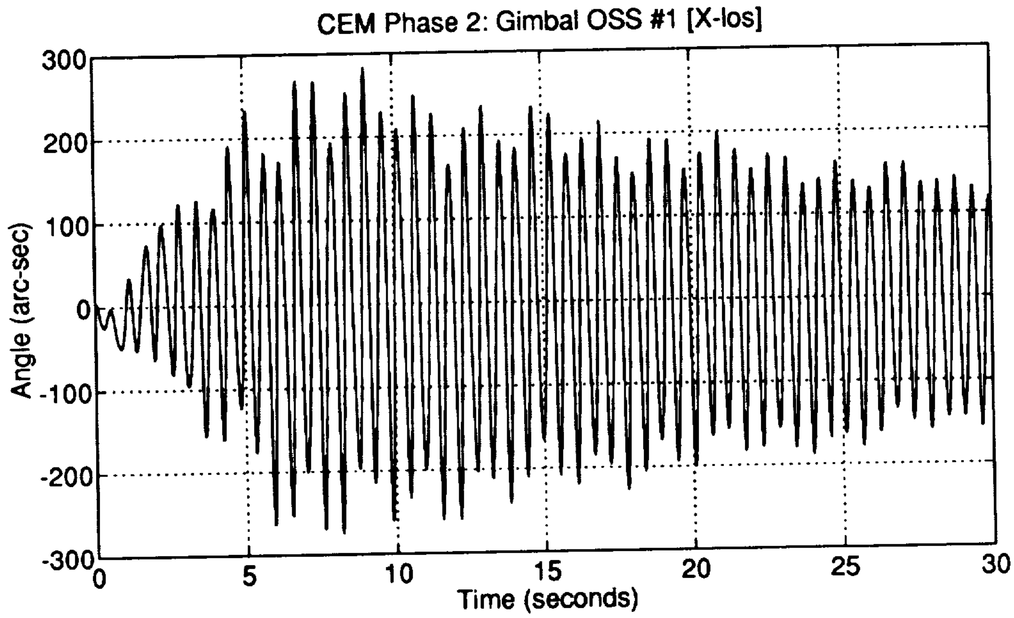

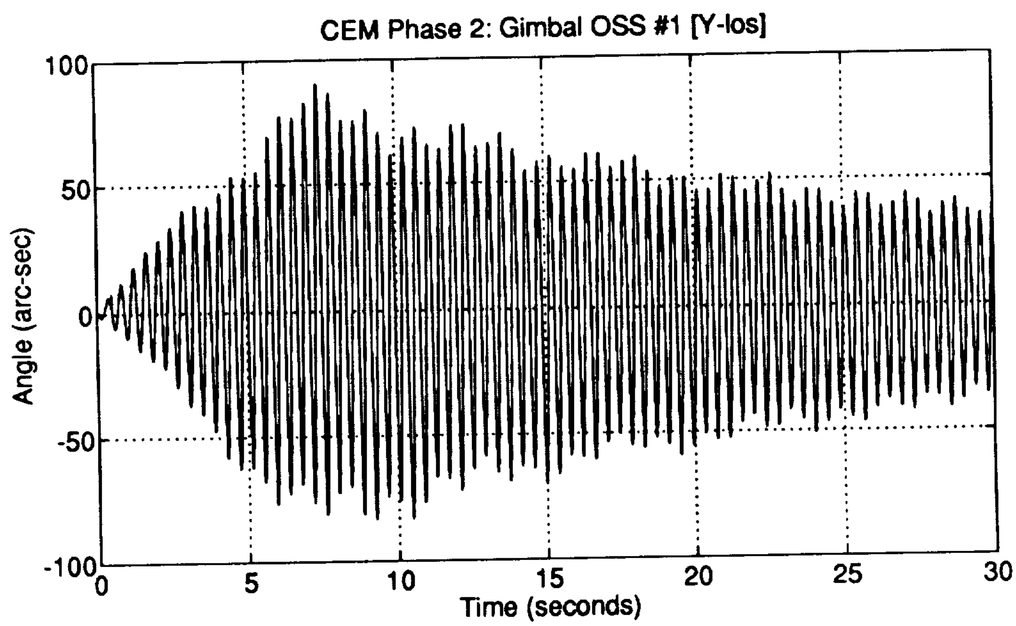

Figure 2.27: Phase 2 CEM Measured Open-Loop Transient Responses

data for the Phase 2 CEM in the [0–10] Hz region, it was decided to use the FEM-derived state-space models. The frequencies and damping ratios of the CEM elastic modes were calculated from the ERA identified state-space models and used to update the FEM-derived state-space models. Identified frequencies and damping ratios for the undamped Phase 2 CEM are given in Table 2.1. Identified frequencies and damping from the open-loop damped FRF data discussed in Section 4.5 are shown in Table 2.3.

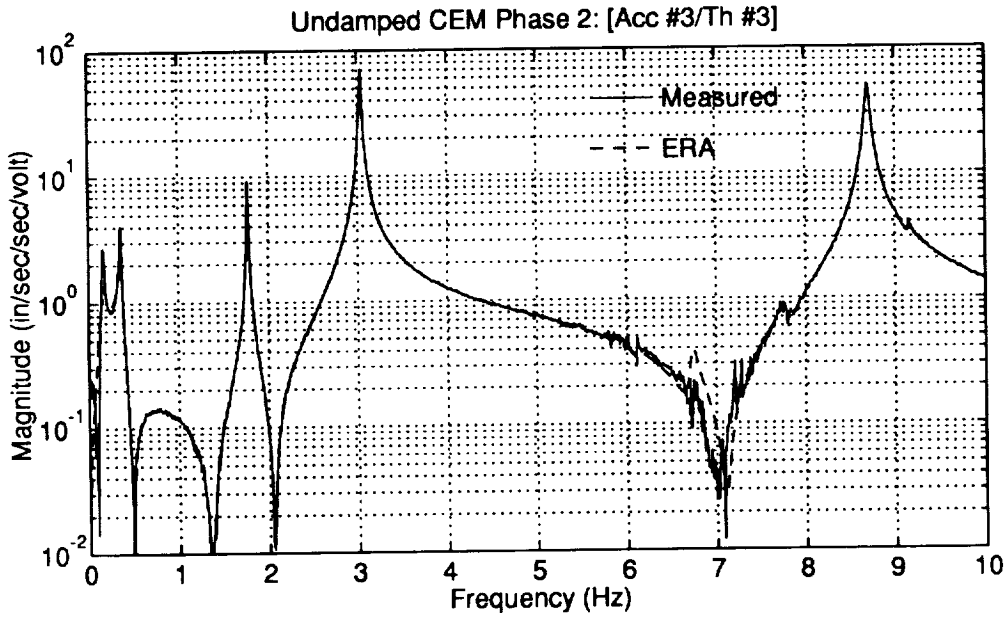

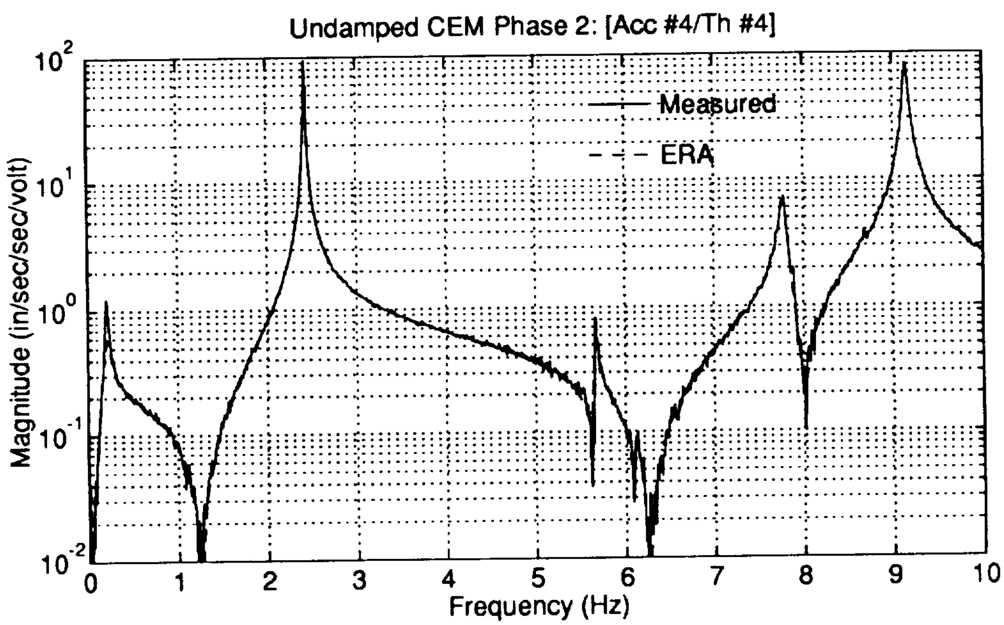

Figure 2.28: Undamped Phase 2 CEM Measured and Identified Frequency Responses for Accelerometers #3 and #4

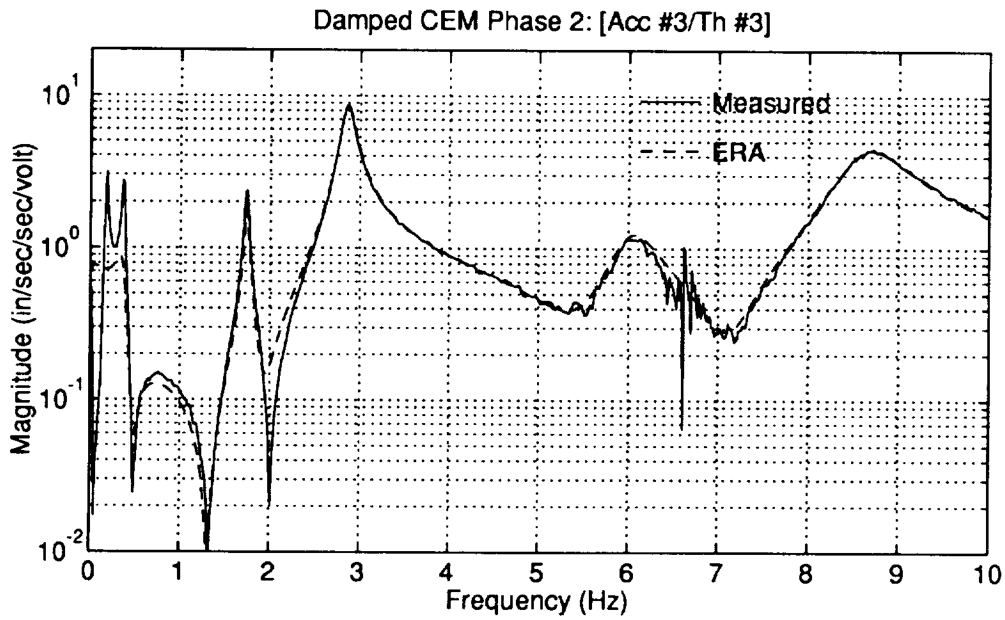

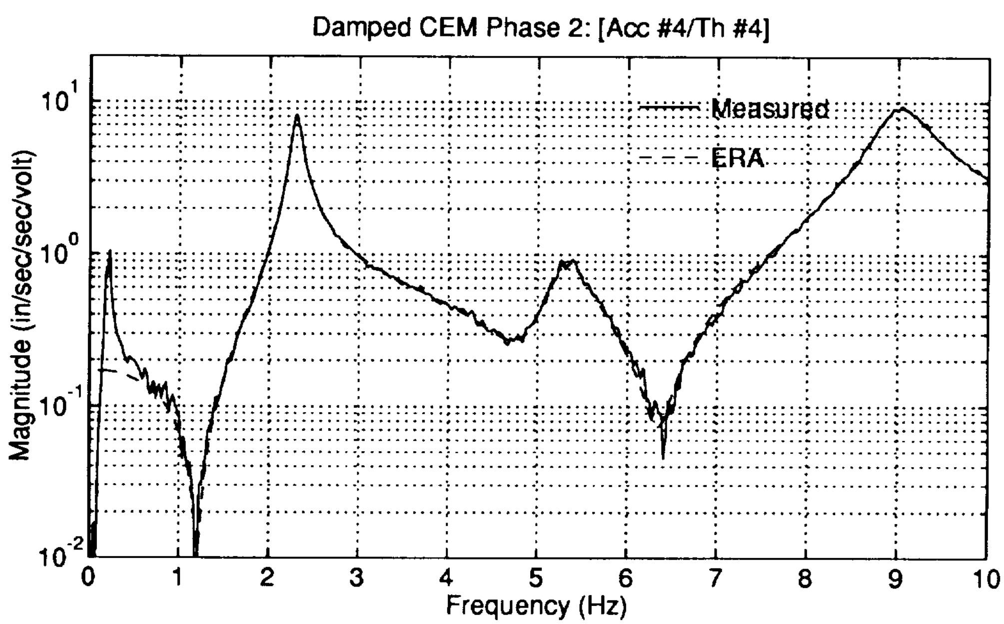

Figure 2.29: Damped Phase 2 CEM Measured and Identified Frequency Responses for Accelerometers #3 and #4

Table 2.3: Frequencies and Damping from the Identified CEM Phase 2 Damped Model

Elastic Mode Number	Frequency (Hz)	Damping (Percent)
1	1.74	1.31
2	2.29	2.42
3	2.86	2.53
4	5.30	4.00
5	6.03	4.65
6	7.86	7.89
7	8.65	4.35
8	9.20	3.20
9	10.64	4.20
10	13.16	3.40
11	13.40	2.31
12	13.98	1.82
13	14.59	2.81
14	15.12	2.00
15	15.86	1.62
16	17.94	2.06
17	18.12	2.14
18	18.58	9.21

Chapter 3

Active Control Design

3.1 Control Objective and Requirements

In this section the objective and associated requirements for the active control design are discussed. The objective function is defined in terms of an H_2 transfer function norm or equivalent LQG cost. Requirements on multivariable gain and phase margins, parametric stability margins, and other requirements are given. The role of the requirements in the design process is to ensure that the control law will be compatible with hardware limitations and to ensure that the design will be insensitive to the expected model uncertainties.

3.1.1 Design Objective

In broad terms, the active control design objective for the CEM Phase 1 and 2 configurations was to minimize the disturbance responses of the LOS (line-of-sight) measurements. For the CEM Phase 1 configuration, the x and y global LOS outputs were used in the control design objective. While for the CEM Phase 2 configuration the gimbals OSS #1, #2 and #4 x and y LOS outputs were used with the gimbals locked in a rigid configuration.

The system was disturbed by random thruster commands added to the controller feedback commands. The disturbances were considered to be zero-mean Gaussian random signals within a frequency bandwidth from 0 to 10 Hz and of equal intensity for each thruster. All eight thruster commands were used for disturbances and control.

The control design objective defines the performance of the closed-loop system. To quantify the design objective we define an objective function (or cost function) J_p

Table 3.1: Phase 2 CEM Open-Loop OSS LOS RMS of Random Responses

Output	Measured	Predicted
Gimbal OSS #1 x LOS (arc-sec)	146.1	167.3
Gimbal OSS #1 y LOS (arc-sec)	75.08	69.52
Gimbal OSS #2 x LOS (arc-sec)	127.6	142.5
Gimbal OSS #2 y LOS (arc-sec)	71.31	57.14
Gimbal OSS #4 x LOS (arc-sec)	202.6	220.9
Gimbal OSS #4 y LOS (arc-sec)	75.77	63.73

as

$$J_p = \|H_{z_{\mathrm{LOS}} w_u}\|_2{}^2 \tag{3.1}$$

where $H_{z_{\mathrm{LOS}} w_u}$ is the closed-loop transfer function matrix from the thruster disturbance model inputs w_u to the weighted LOS outputs z_{LOS}. The equivalent LQG objective function is

$$J_p = \lim_{t\to\infty} E\left[z_{LOS}^T(t) z_{LOS}(t)\right] \tag{3.2}$$

where $z_{LOS}(t)$ is the vector or LOS measurements. The objective function is inversely related to the system performance.

Equation 3.2 is equivalent to the sum of the mean-squared random LOS responses. Table 3.1 shows the root-mean-squared (RMS) values of the OSS LOS outputs for the open-loop Phase 2 CEM. Both measured and predicted values were computed from the OSS LOS responses over a 120 second time interval. The disturbances used were Gaussian random thruster commands in a frequency band from 1–10 Hz[1].

3.1.2 Design Requirements

As always, the plant models used for the control law design and analysis are not exact representations of the test article (i.e., there are uncertainties and approximations inherent in the model). An acceptable control design must achieve a design objective J_p which is insensitive or robust over a range of model variations. Traditionally, robustness requirements are specified for closed-loop *stability* to model variations rather than the *sensitivity* of the design objective. However, a system may be stable over the expected range of model variations and not possess sufficient performance

[1] A 1–10 Hz random disturbance frequency band was used in the experiments and analysis instead of 0–10 Hz so that the responses of the structural modes would not be swamped by the rigid-body motions.

at every point in this range. To ensure sufficient performance, the assumed range of model variations is often taken to be larger than what is reasonably expected. The selection of stability margin requirements (i.e., the assumed range of model variations) is based primarily upon past experiences.

Both nonparametric and parametric stability margin requirements were defined for the CEM. These requirements include:

- Multivariable gain/phase stability margins at the control inputs and sensor outputs for modes within the control bandwidth.
- Multivariable gain stability margins (roll-off) at the control inputs and sensor outputs for modes outside of the control bandwidth.
- Univariable modal frequency stability margins within the control bandwidth.

For both the Phase 1 and 2 CEM designs, the control bandwidth was limited to approximately 4 Hz due to large uncertainties in the higher frequency modes and limitations on the controller order. This bandwidth included the six rigid-body modes and the first three main truss bending modes of the structure.

Multivariable Gain/Phase Stability Margins

Traditionally, for a single loop, gain/phase margins are computed from the magnitude of the return difference transfer function responses $|1 + L(j\omega)|$ where $L(s)$ is the loop transfer function (negative feedback). For the multiloop case, we assume a diagonal gain/phase perturbation matrix $D(s)$ in the feedback loop given by

$$D(s) = \begin{bmatrix} k_1 e^{\theta_1} & & 0 \\ & \ddots & \\ 0 & & k_n e^{\theta_n} \end{bmatrix} \tag{3.3}$$

where the gain $k_q \in \Re$ or phase $\theta_q \in \Im$ of each loop, q, can vary simultaneously. The nominal system is given by $k_q = 1$ and $\theta_q = 0$ in each loop. The multivariable gain or phase margin is defined as the real interval on k or θ for which the perturbed closed-loop system is guaranteed stable. Lower and upper bounds on the multivariable gain/phase margins can be calculated from the minimum singular values of the return difference matrix[14] using the inequality relation

$$\max_{1 \le q \le m} \sqrt{\left(1 - \frac{1}{k_q}\right)^2 + \frac{2}{k_q}\left(1 - \cos\theta_q\right)} \le \min_{\omega} \underline{\sigma}\left(I + L(j\omega)\right) \tag{3.4}$$

where $\underline{\sigma}(\bullet)$ denotes the minimum singular value operator.

The requirement for multiloop stability margins was defined as

$$\underline{\sigma}\,(I + L(j\omega)) \geq 0.5 \tag{3.5}$$

at both the control inputs and sensor outputs[2]. The corresponding gain margins are $[-3.52, +6.02]$ dB and the corresponding phase margins are ± 28.96 degrees.

High-Frequency Gain Stabilization

Robust gain stabilization, or roll-off, of uncertain modes (typically high frequency) is achieved through the use of broad band roll-off filters in the compensator (as opposed to notch filters which are not robust to frequency variations). For single-loop systems, the loop gain $|L(j\omega)|$ is restricted to be less than one. For multiloop systems, the maximum loop gain is given by the maximum singular value of the loop transfer function matrix frequency response $\bar{\sigma}\,(L(j\omega))$. The roll-off gain margin K_{rgm} is defined as

$$K_{rgm} = \frac{1}{1 - \sup_\omega |L(j\omega)|} \tag{3.6}$$

for single-loop systems and

$$K_{rgm} = \frac{1}{1 - \sup_\omega \bar{\sigma}\,(L(j\omega))} \tag{3.7}$$

for multiloop systems where ω is within the frequency band of interest.

The minimum roll-off gain margin requirement at the control inputs and the sensor outputs was 10 dB for modes with frequencies greater than the control bandwidth.

Modal Frequency Stability Margins

The stability margin requirement for modal frequency uncertainties was based upon variations in the frequencies of individual modes one-at-a-time and was extended to all modes within the control bandwidth. The requirement was that the closed-loop system remain stable for modal frequencies within $\pm 15\%$ of nominal when varied one-at-a-time. Analysis of the modal frequency stability margins for a control law was performed by checking the system stability along a fine grid of frequency points for each mode.

[2] Note that Osborne's method for diagonal scaling of matrices was used to improve the stability margin bounds.

Miscellaneous Design Requirements

Other design requirements stemmed from physical limitations of various hardware components or from operational considerations. These requirements were:

- the control law must be open-loop stable,
- the sampling rate was 150 Hz for Phase 1 and 350 Hz for Phase 2,
- the maximum state dimension of the control law was ≈ 60 states,
- and thruster commands could not exceed 10 volts absolute value.

Note that the limitation on the control law state dimension and the maximum sampling rate limitation are interdependent.

3.2 Design/Analysis Process Overview

The control objectives and requirements defined in the previous section form the basis for the design process. The goal of the designer is to find a control law which optimizes (minimizes) the objective function within the constraints imposed by the design requirements. The design requirements act as constraints on the control design to ensure that the design is feasible and robust.

In a conventional design process, the designer selects a control law structure (architecture) and adjusts the feedback gains and filter parameters to optimize the objective while satisfying the design requirements. The selection of the controller gains and filters as well as the controller architecture is an iterative, and often tedious, process which relies heavily on the designers' experience. The advantages of this approach are its simplicity and applicability to a wide range of problems.

Figure 3.1 shows a concept for a control law design process using a modern frequency domain based optimal control design method such as H_2/LQG, H_∞, or μ-synthesis. The design process is more involved than the conventional design process because the designer must transform the original design objectives and requirements into closed-loop frequency domain objectives and requirements. The transformation to the closed-loop requirements involves defining frequency dependent weighting functions which represent penalties or bounds on the closed-loop responses. The design process is also iterative since the objectives and requirements are combined with relative weightings into a *total objective function* and because some design requirements may be difficult to define precisely in the frequency domain. The main advantage in this approach is that the designer works directly with weightings among the design objectives and requirements, resulting in fewer design iterations.

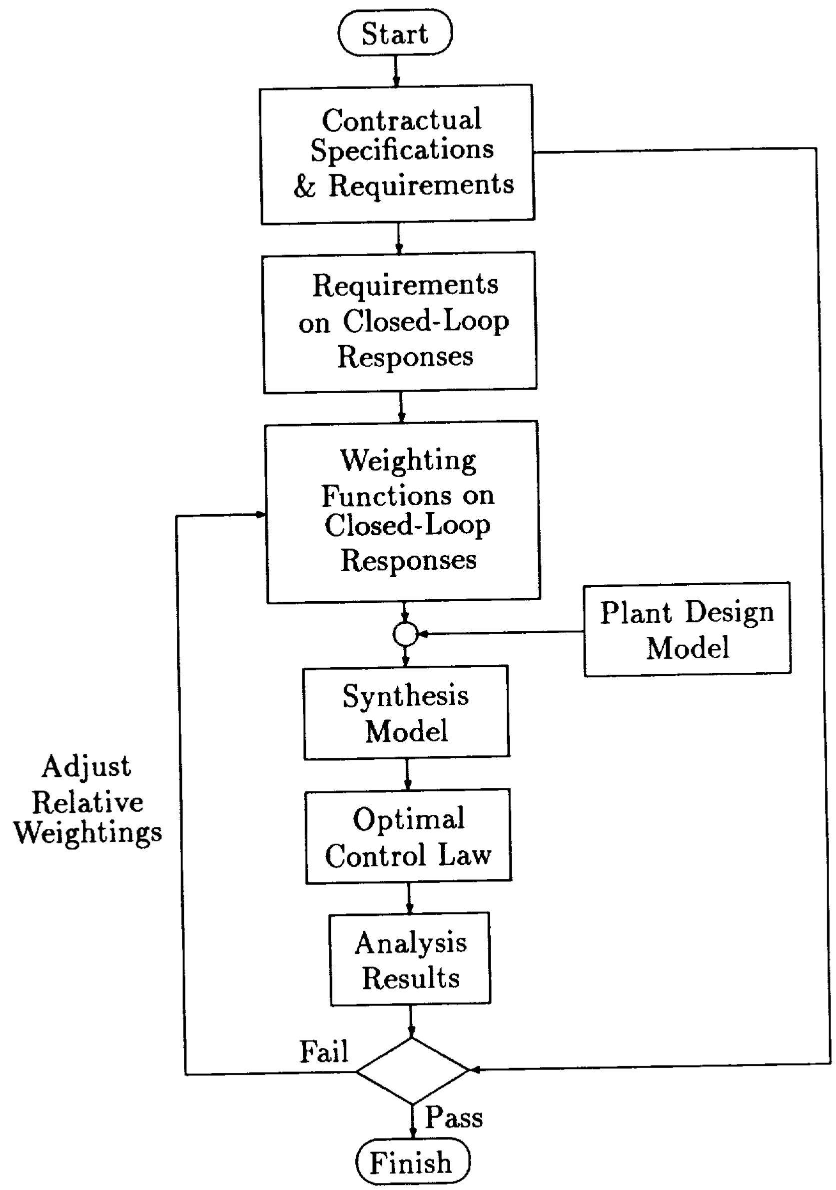

Figure 3.1: A Frequency Domain Based Optimal Control Law Design Process

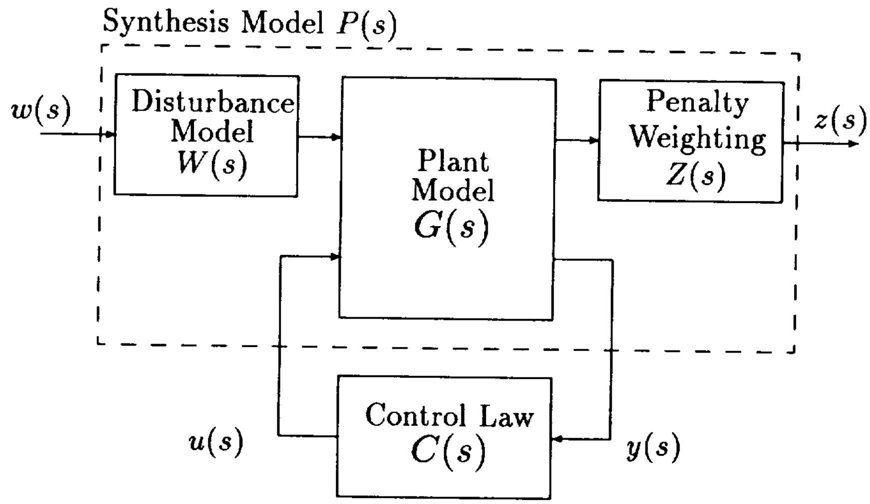

Figure 3.2: Block diagram depicting a standard H_2/LQG optimal control problem.

We would like to emphasize here that the translation of the original design objectives and requirements into closed-loop frequency domain objectives and requirements is perhaps the most crucial step in the design process. In the application of modern control synthesis methods, it is often the case that the designer neglects to include one or more important design requirements in the total objective function. The resulting control law may not satisfy all of the original requirements.

3.3 H_2/LQG Control Law Design

In this section we discuss the design of feedback control laws using the H_2/LQG control design algorithm. First we discuss, in general terms, the formulation of design requirements in the closed-loop frequency domain and incorporation in the synthesis model. Next we discuss the selection of weighting functions and some design tradeoffs and limitations. Finally we present analytical and experimental results from the designs.

3.3.1 Synthesis Model

Figure 3.2 is a block diagram depicting a standard H_2/LQG optimal control problem. $G(s)$ is the plant design model, $P(s)$ is the synthesis model, $W(s)$ and $Z(s)$ are diagonal weighting function models, and $C(s)$ is the controller model. The inputs u and outputs y are the control inputs and sensor outputs, respectively. The inputs w and outputs z are design inputs and outputs, respectively. Recall that the H_2-norm or LQG optimal control law $C(s)$ minimizes the closed-loop objective function

J given by

$$J = \|H_{zw}\|_2^{\,2} \tag{3.8}$$

where $H_{zw}(s)$ is the closed-loop transfer function matrix from w to z, or equivalently

$$J = \lim_{t\to\infty} E\left[z^T(t)z(t)\right] \tag{3.9}$$

where $w(t)$ is a zero mean Gaussian random process with $E[w(t-\tau)w^T(t)] = W\delta(\tau)$. The role of the weighting functions $W(s)$ and $Z(s)$ in the synthesis model is to shape the magnitudes of the closed-loop frequency responses.

The first step in developing the synthesis model for the H_2/LQG optimal control problem was to reformulate the design requirements as given in Section 3.1.2 in terms of the magnitudes of closed-loop frequency responses. We will consider how to formulate requirements for:

- multivariable gain/phase margins,
- roll-off of the control law transfer function responses,
- and robustness to modal frequency uncertainties

from the closed-loop frequency responses. The discussions on gain/phase margins and controller roll-off are for the requirements at the control inputs. The formulation for gain/phase margins and roll-off at the sensor outputs is similar and straight forward.

Multivariable Gain and Phase Margins

Consider a plant $G(s)$ with an output feedback control law $C(s)$. And recall from Section 3.1.2 that a measure of the multivariable gain and phase margins (MVGPM) at the control inputs is given by the minimum singular values of the return difference matrix $\underline{\sigma}\,(I + C(j\omega)G(j\omega))$. Using the identity $\underline{\sigma}(A) = 1/\bar{\sigma}(A^{-1})$, the MVGPM are inversely related to $\bar{\sigma}\,(S(j\omega))$ where

$$S(s) = [I + C(s)G(s)]^{-1} \tag{3.10}$$

is the sensitivity transfer function matrix at the control inputs.

To maximize the MVGPM at the control inputs we need to minimize $\|S(s)\|_\infty$. In practice, it is usually sufficient to minimize $\|Z(s)S(s)W(s)\|_2$ where $Z(s)$ and $W(s)$ are frequency dependent weighting functions. The weighting functions are required since $S(s)$ is not strictly proper and the H_2-norm $\|S(s)\|_2$ is not defined. The weighting functions must be selected such that the transfer function matrix

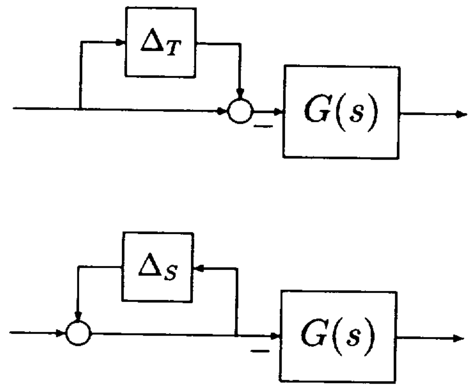

Figure 3.3: Δ-block representations of the multivariable gain and phase uncertainties at the control inputs.

$Z(s)S(s)W(s)$ is strictly proper. The weighting functions $Z(s)$ and $W(s)$ can also be used to adjust the amount of stability margins obtained at different frequencies.

Alternatively, one can choose to minimize $\|T(s)\|_\infty$ or $\|T(s)\|_2$ where

$$T(s) = C(s)G(s)\left[I + C(s)G(s)\right]^{-1} \tag{3.11}$$

is the complementary sensitivity transfer function matrix at the control inputs. So long as $\|C(s)G(s)\|_\infty$ cannot go to zero in the frequency range of interest, the effect will be to maximize the MVGPM since

$$T(s) = C(s)G(s)S(s). \tag{3.12}$$

The advantage to this approach is that no weighting functions are required since $T(s)$ is strictly proper and the resulting control law will be of lower order.

From the perspective of the small gain theorem, minimizing the sensitivity and complementary sensitivity at the control inputs corresponds to maximizing the robustness to the Δ-block uncertainties shown in Fig. 3.3. In both cases Δ is a complex matrix representing multiplicative gain and/or phase uncertainties at the control inputs of the plant model.

High Frequency Roll-off

Again consider the plant $G(s)$ with output feedback control law $C(s)$. The control law is considered to be gain stabilized or rolled off at the control inputs within a

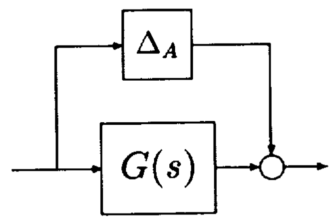

Figure 3.4: Δ-block representation of the additive uncertainty for gain stabilization or roll-off.

frequency band if

$$\bar{\sigma}\left(C(j\omega)G(j\omega)\right) \leq \frac{1}{K_{\mathrm{rgm}}} \tag{3.13}$$

where K_{rgm} is the roll-off gain margin. We define the transfer function matrix $R(s)$ as

$$R(s) = C(s)\left[I + G(s)C(s)\right]. \tag{3.14}$$

If the control law is sufficiently rolled off within the given frequency band (e.g., $\bar{\sigma}\left(G(j\omega)C(j\omega)\right) \ll 1$) then $R(s) \approx C(s)$. We can maximize the control law roll-off within a frequency band by minimizing $\bar{\sigma}\left(C(j\omega)\right)$ or equivalently $\bar{\sigma}\left(R(j\omega)\right)$ within the given frequency band. In practice we find that the requirement can be satisfied by minimizing $\|Z(s)R(s)W(s)\|_2$ where $Z(s)$ and $W(s)$ are weighting functions which penalize most the frequencies outside the control bandwidth.

From the perspective of the small gain theorem, minimizing $\|R(s)\|_\infty$ corresponds to maximizing the robustness to the Δ-block uncertainty shown in Fig. 3.4. The uncertainty Δ_A represents an additive uncertainty across the plant model.

Modal Frequency Stability Margins

Consider a system with a lightly damped mode shown in Fig. 3.5. From a classical perspective, robustness to modal uncertainties within the control bandwidth is obtained through phase stabilization. The effect of phase stabilizing a mode is mainly to increase the damping of the mode in the closed loop or to reduce the responses to external disturbances. We can infer that minimizing the closed-loop responses of the mode to external excitations will result in robustness to uncertainties in the frequency and/or damping ratio of the mode.

Applying the small gain theorem to the problem of minimizing the closed-loop responses of a mode to external excitations we find that the robustness to the Δ-block

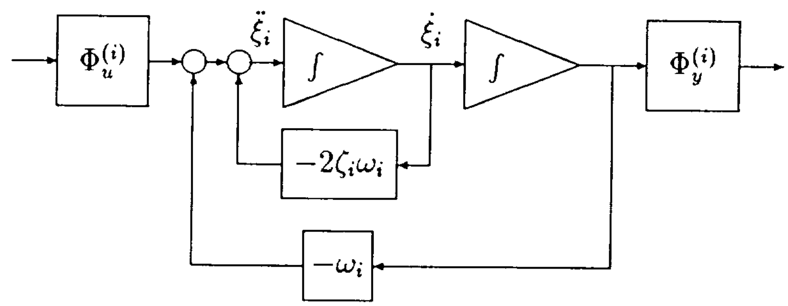

Figure 3.5: Block diagram of a system comprised of a single lightly damped mode.

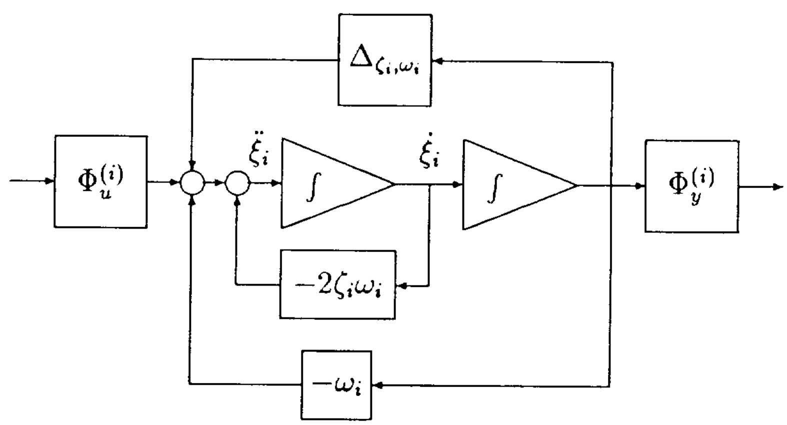

Figure 3.6: Δ-block representation of modal frequency and/or damping ratio uncertainty.

uncertainty in Fig. 3.6 is maximized. In this case $\Delta_{\zeta_i,\omega_i}$ represents frequency and/or damping ratio uncertainties in the i^{th} mode of the plant model.

Development of the Synthesis Model

Fig. 3.7 is a block diagram of the H_2/LQG control law synthesis model $P(s)$ and controller $C(s)$ for the CEM Phase 2 configuration using acceleration feedback. The inputs to the synthesis model are the commanded thruster inputs u and disturbance

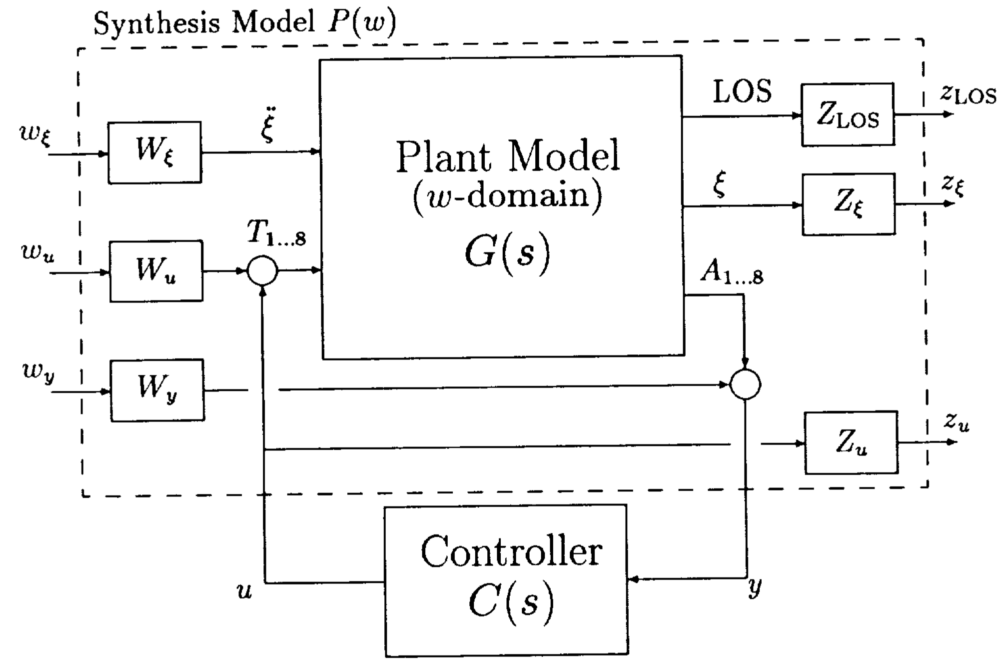

Figure 3.7: H_2/LQG control law synthesis model using acceleration feedback.

inputs $w = \{w_\xi, w_u, w_y\}$ where w_ξ is a vector of disturbances to the modal states[3], w_u is a vector of disturbances to the thruster commands, and w_y is a vector of "noise" disturbances to the accelerometer sensor outputs. The outputs from the synthesis model are the accelerometer sensor outputs y and the criterion outputs $z = \{z_{\text{LOS}}, z_\xi, z_u\}$ where z_{LOS} are the LOS scoring system outputs, z_ξ are modal state outputs, and z_u are the thruster commands from the controller.

A reduced-order model of the plant is used for the design model $G(s)$. Since any modes outside of the control bandwidth will be gain stabilized, $G(s)$ need only provide an accurate representation of the plant within the control bandwidth. As such, the plant design model was obtained by truncating any modes outside of the desired control bandwidth.

The synthesis model combines the closed-loop objective function and requirements as formulated above into a *total* design objective function. Recall the definition of

[3]The modal disturbance inputs $\ddot{\xi}_i$ are normalized by ω_i^2 in the plant model $G(s)$, where ω_i are the modal frequencies.

the H_2 norm

$$\|H(s)\|_2{}^2 = \frac{1}{2\pi}\int_{-\infty}^{\infty} \mathrm{tr}\left[H^*(j\omega)H(j\omega)\right] d\omega \tag{3.15}$$

where $H(s)$ is an $m \times n$ transfer function matrix

$$H(s) = \begin{bmatrix} h_{11} & \cdots & h_{1n} \\ \vdots & \ddots & \vdots \\ h_{m1} & \cdots & h_{mn} \end{bmatrix}. \tag{3.16}$$

Since the trace of a matrix product A^*A is the sum of the magnitudes squared of the elements of A we can rewrite Eqn. 3.15 as

$$\|H(s)\|_2{}^2 = \frac{1}{2\pi}\int_{-\infty}^{\infty} \sum_{\substack{i=1\\j=1}}^{m,n} \left[h_{ij}^*(j\omega)h_{ij}(j\omega)\right] d\omega \tag{3.17}$$

or

$$\|H(s)\|_2{}^2 = \sum_{\substack{i=1\\j=1}}^{m,n} \|h_{ij}(s)\|_2{}^2. \tag{3.18}$$

Expanding the closed-loop transfer function of the synthesis model (with weighting functions) and controller gives

$$H_{zw}(s) = \begin{bmatrix} z_{\mathrm{LOS}}(s)/w_\xi(s) & z_{\mathrm{LOS}}(s)/w_u(s) & z_{\mathrm{LOS}}(s)/w_y(s) \\ z_\xi(s)/w_\xi(s) & z_\xi(s)/w_u(s) & z_\xi(s)/w_y(s) \\ z_u(s)/w_\xi(s) & z_u(s)/w_u(s) & z_u(s)/w_y(s) \end{bmatrix}. \tag{3.19}$$

The total objective function is then

$$\begin{aligned} J &= \|H_{zw}(s)\|_2{}^2 \\ &= \|z_{\mathrm{LOS}}(s)/w_\xi(s)\|_2{}^2 + \|z_{\mathrm{LOS}}(s)/w_u(s)\|_2{}^2 + \|z_{\mathrm{LOS}}(s)/w_y(s)\|_2{}^2 \\ &+ \|z_\xi(s)/w_\xi(s)\|_2{}^2 + \|z_\xi(s)/w_u(s)\|_2{}^2 + \|z_\xi(s)/w_y(s)\|_2{}^2 \\ &+ \|z_u(s)/w_\xi(s)\|_2{}^2 + \|z_u(s)/w_u(s)\|_2{}^2 + \|z_u(s)/w_y(s)\|_2{}^2 \end{aligned} \tag{3.20}$$

The penalty $\|z_{\mathrm{LOS}}(s)/w_u(s)\|_2{}^2$ is simply the original objective function for performance, J_p, from Eqn. 3.1 weighted by the transfer functions W_u and Z_{LOS}. While the other terms comprising the objective function are penalties representing the design requirements.

The terms $\|z_u(s)/w_\xi(s)\|_2{}^2$ and $\|z_u(s)/w_u(s)\|_2{}^2$ in the total objective function are penalties for the MVGPM requirements at the control inputs. The transfer function matrix $z_u(s)/w_u(s)$ is the weighted complementary sensitivity at the control inputs.

The weighting functions W_u and Z_u are used to increase the MVGPM at the control inputs. The transfer function matrix $z_u(s)/w_\xi(s)$ is similar to the complementary sensitivity, but is composed of the responses from the individual modes of the plant. Therefore the magnitudes of the weighting function $W_\xi(s)$ can be used to independently increase the MVGPM's of individual plant modes at the control inputs.

The complementary sensitivity at the sensor outputs, representing the MVGPM requirements at the sensor outputs, is not included in the synthesis model. However, the transfer function matrix $z_{\mathrm{LOS}}(s)/w_y(s)$ is similar to the weighted complementary sensitivity and the terms $\|z_{\mathrm{LOS}}(s)/w_y(s)\|_2^2$ and $\|z_\xi(s)/w_y(s)\|_2^2$ in the objective function were used to obtain the MVGPM requirements in the sensor loops. The transfer function matrix $z_\xi(s)/w_y(s)$ is similar to the complementary sensitivity at the sensor outputs, but is composed of the responses from the individual modes of the plant. The magnitudes of the weighting function $Z_\xi(s)$ can be used to independently increase the MVGPM's of individual plant modes at the sensor outputs.

The term $z_u(s)/w_y(s)$ in the total objective function is the transfer function matrix $R(s)$ weighted by $Z_u(s)$ and $W_y(s)$ and is used to roll-off the responses of the controller outside the control bandwidth. The magnitudes of the weighting functions $W_y(s)$ or $Z_u(s)$ are increased outside the control bandwidth to increase the roll-off of the controller.

The quantities $\|z_{\mathrm{LOS}}(s)/w_\xi(s)\|_2^2$, $\|z_\xi(s)/w_\xi(s)\|_2^2$, and $\|z_\xi(s)/w_u(s)\|_2^2$ all represent penalties on the modal frequency stability margins as discussed in Section 3.3.1. The associated weighting functions determine the robustness of the controller to uncertainties in the modal frequencies[4]. If the sensitivity of the i^{th} mode frequency is too high, the magnitude of the weighting function $W_\xi(s)$ or $Z_\xi(s)$ can be increased for the i^{th} mode to decrease the sensitivity.

Note that by carefully selecting the inputs and outputs for the synthesis model we have eliminated extraneous transfer functions which would add unwanted terms to the total objective function. This is essentially what would be achieved by using a μ-synthesis design algorithm.

3.3.2 Selection of Weighting Functions

Recall that the original design requirements were specified as constraints. These requirements have been incorporated into the H_2/LQG synthesis model along with the design objective as a *combined* minimization problem instead of a constrained

[4]As will be seen later, the modal disturbances w_ξ were not used in the control designs (i.e., $W_\xi(s) = 0$) since the disturbances w_u provided sufficient excitation to all the modes within the control bandwidth. The modal disturbance input and associated weighting function are retained in the synthesis model of Figure 3.7 for completeness.

minimization problem. For this reason, selection of the weighting functions in the synthesis model is an iterative process. The goal in adjusting the weighting functions is to obtain a design such that the performance is maximized (J_p is minimized) while still satisfying the requirements. At each iteration in the design process, the designer identifies the most severely violated or over satisfied requirement and adjusts the corresponding weighting functions.

In deciding which weighting functions to adjust and how they should be adjusted, the designer must consider the cross couplings between the weighting functions and the design penalties comprising the total objective as given in Eqn. 3.20. For example, increasing the gain of the weighting function $W_u(s)$ in the synthesis model will increase the weighting on the MVGPM requirement at the control inputs in the design. However, unless the gain of the weighting function $Z_{\mathrm{LOS}}(s)$ is also reduced by the same proportion, the weighting on the controller performance will be increased at the same time.

For the H_2/LQG control design the weighting functions $W_\xi(s)$, $W_u(s)$, $Z_{\mathrm{LOS}}(s)$, and $Z_\xi(s)$ were chosen to be pure gains. Frequency dependent transfer functions, such as shown in Fig. 3.8, were used for the weighting functions $W_y(s)$ and $Z_u(s)$ to obtain the necessary roll-off of the controller. The frequency of the filter zeros, 3.0 Hz, was approximately equal to the desired control bandwidth while the frequency of the poles was well beyond the control bandwidth at 50.0 Hz. The filter tuning parameters were the d.c. gain and the filter order.

The selection and adjustment of $W_y(s)$ and $Z_u(s)$ weighting filter parameters is driven by the roll-off requirement

$$\bar{\sigma}\left(C_{uy}(j\omega)G_{yu}(j\omega)\right) \leq \frac{1}{K_{\mathbf{rgm}}} \tag{3.21}$$

for the control loops and

$$\bar{\sigma}\left(G_{yu}(j\omega)C_{uy}(j\omega)\right) \leq \frac{1}{K_{\mathbf{rgm}}} \tag{3.22}$$

for the sensor loops where $G_{yu}(s)$ is the plant model transfer function matrix from the control inputs to the sensor outputs and $C_{uy}(s)$ is the controller transfer function matrix. The matrix products $C_{uy}(j\omega)G_{yu}(j\omega)$ and $G_{yu}(j\omega)C_{uy}(j\omega)$ can be expanded as

$$C_{uy}(j\omega)G_{yu}(j\omega) = \sum_{i=1}^{n} C_{uy_i}(j\omega)G_{y_iu}(j\omega) \tag{3.23}$$

for the i^{th} sensor loop and

$$G_{yu}(j\omega)C_{uy}(j\omega) = \sum_{i=1}^{m} G_{yu_i}(j\omega)C_{u_iy}(j\omega) \tag{3.24}$$

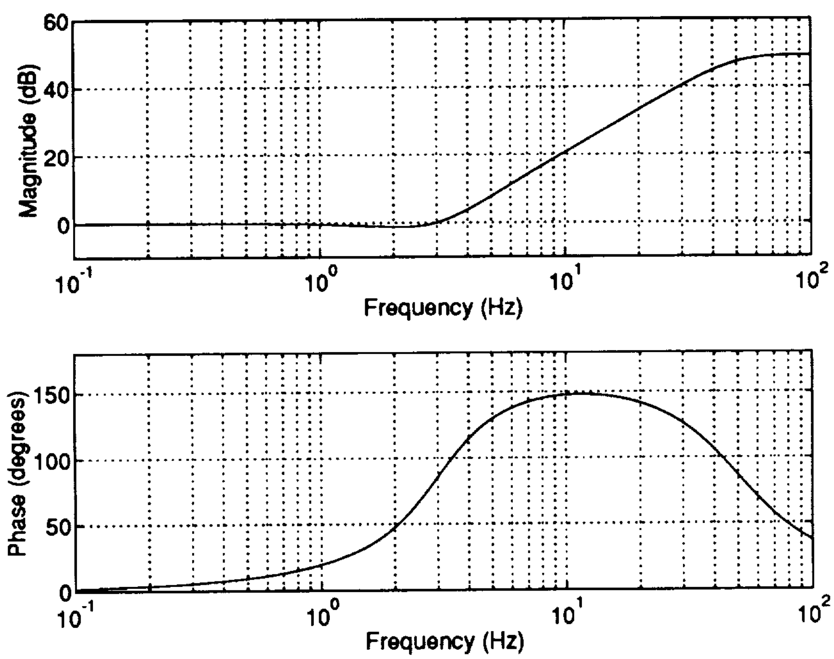

Figure 3.8: Frequency response of a typical $W_{y_i}(s)$ or $Z_{u_i}(s)$ weighting filter transfer function.

for the i^{th} control loop. Substituting into the previous two equations and exchanging the order of the summation and singular value operators gives the conservative roll-off requirements

$$\sum_{i=1}^{n} \bar{\sigma}\left(C_{uy_i}(j\omega)G_{y_iu}(j\omega)\right) \leq \frac{1}{K_{\text{rgm}}} \tag{3.25}$$

for the control loops and

$$\sum_{i=1}^{m} \bar{\sigma}\left(G_{yu_i}(j\omega)C_{u_iy}(j\omega)\right) \leq \frac{1}{K_{\text{rgm}}} \tag{3.26}$$

for the sensor loops. Inspection of the singular value plots of $\bar{\sigma}\left(C_{uy_i}(j\omega)G_{y_iu}(j\omega)\right)$ for each sensor loop reveals which $W_{y_i}(s)$ weighting filter to adjust. The selection of the $Z_{u_i}(s)$ weighting filters is based on inspection of the singular value plots of $\bar{\sigma}\left(G_{yu_i}(j\omega)C_{u_iy}(j\omega)\right)$.

3.3.3 Some Design Tradeoffs & Limitations

Several tradeoffs are of concern in the controller design process. These tradeoffs include:

- control bandwidth versus controller order,
- controller gain versus controller order,
- acceleration feedback versus pseudo-velocity feedback.

The performance of a controller is to some degree related to the control bandwidth. Modes outside the control bandwidth are gain stabilized (rolled off) and the controller provides little additional damping to (or may even be destabilizing to) these modes. By increasing the controller bandwidth, addition modes can be damped and the performance increased. This of course requires that the additional modes to be damped are sufficiently well modeled. Increasing the control bandwidth also requires adding modes to the design model. When using design algorithms such as the full-order H_2/LQG this results in an increase in the controller order (e.g. the dimension of the control law state vector). The controller order can also increase if additional roll-off is required (e.g. higher-order weighting functions) due to the increased bandwidth. For the CEM control design a control bandwidth of approximately 4 Hz was chosen as an appropriate tradeoff between control bandwidth and increasing controller order. As will be discussed in Chapter 4, by combining active control with passive damping, the modes outside the control bandwidth can also be damped, effectively increasing the control bandwidth in a robust fashion.

For a given control bandwidth, the controller performance, in loose terms, is determined by the controller 'gain'. Increasing the controller gain requires increasing the order of the roll-off weighting filters in the synthesis model, resulting in a higher order controller. Accordingly, lower controller orders are possible by reducing the gain (and performance) of the controller. For the CEM control designs, the controller performance was maximized subject to the limitation of 60 controller states.

Another tradeoff involves the choice of sensor signals for feedback. The available sensors are the 8 servo-accelerometers. Preconditioning of the servo-accelerometer signals with pseudo-integrators (e.g. an integrator with a low-frequency washout to reduce sensor measurement bias) has the advantage of adding roll-off to the plant and increasing the signal gain at the rigid-body frequencies. This allows greater control of the rigid-body modes while sacrificing some damping of the actively controlled elastic modes. The influence on the controller order is minimal since the size of the plant model increases but the size of the roll-off weighting filters decreases by nearly the same amount. Controllers were designed and tested using both types of sensor signals for feedback.

3.3.4 Design Results

The H_2/LQG design process developed above was successfully implemented on the CEM test article in its Phase 1 and Phase 2 configurations. Experimental results obtained with the Phase 1 controller designs are documented in Appendix C. A detailed discussions of two different designs implemented on the Phase 2 CEM is given below. Only selected results are shown here; the complete set of results for the Phase 2 designs are given in Appendix D.

The first control design (H_2/LQG A1.4) used the eight servo-accelerometer measurements available for feedback. The feedback outputs for the second control design (H_2/LQG V1.1) were obtained by preconditioning the eight servo-accelerometer measurements with pseudo-integrators filters according to

$$\tilde{v}_i(s) = \frac{1}{s + \omega_I} a_i(s). \tag{3.27}$$

where $\tilde{v}_i$ is the i^{th} loop pseudo-velocity feedback output computed from the i^{th} accelerometer measurement a_i. The pseudo-integrator washout frequency ω_I was set to 0.5 Hz. Figure 3.9 shows the frequency responses of the pseudo-integrator filter. The eight thruster commands were the control inputs for both control designs.

The synthesis models were as shown in Figure 3.7. The weighting functions in the synthesis model were selected using the approach described above. The final

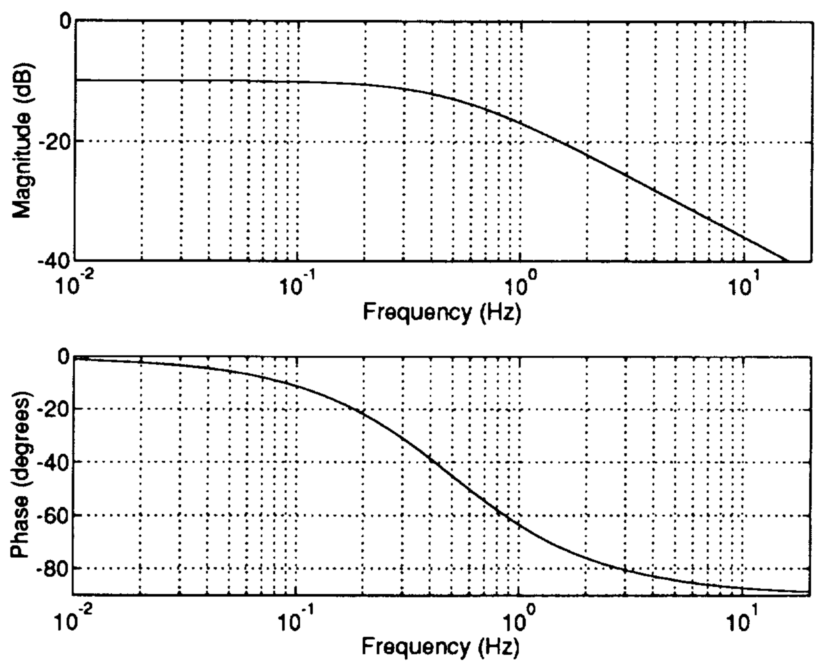

Figure 3.9: Phase 2 CEM H_2/LQG V1.1 Pseudo-Integrator Filter Transfer Function Frequency Response

weighting functions arrived at for H_2/LQG A1.4 were

$$Z_{\text{LOS}} = 350 I_{6\times6}, \quad W_\xi = 0_{9\times9}, \quad W_u = I_{8\times8} \tag{3.28}$$

$$Z_\xi \;=\; \text{diag}\{60, 60, 60, 0, 0, 0, 120, 0, 120\} \tag{3.29}$$

$$W_y = \text{diag}\left\{\begin{array}{c} 10.5 f_{2a}(s) \\ 6.3 f_{2a}(s) \\ 3.0 f_{2a}(s) \\ 3.0 f_1(s) \\ 3.0 f_{2a}(s) \\ 6.0 f_{2a}(s) f_1(s) \\ 3.6 f_{2a}(s) f_1(s) \\ 3.0 f_{2a}(s) \end{array}\right\} \quad Z_u = \text{diag}\left\{\begin{array}{c} 0.35 f_{2a}(s) f_{2b}(s) \\ 0.21 f_{2a}(s) f_{2b}(s) \\ 0.15 f_{2a}(s) \\ 0.1 f_{2a}(s) \\ 0.1 f_{2a}(s) \\ 0.2 f_{2a}(s) f_{2b}(s) \\ 0.1 f_{2a}(s) f_{2b}(s) \\ 0.1 f_{2a}(s) f_1(s) \end{array}\right\} \tag{3.30}$$

where the roll-off weighting filters $f_1(s)$, $f_{2a}(s)$, and $f_{2b}(s)$ are given with frequencies in Hertz by

$$f_1(s) \;=\; \frac{50(s+3)}{3(s+50)} \tag{3.31}$$

$$f_{2a}(s) \;=\; \frac{50^2(s^2 + 2(0.5)(3) + 3^2)}{3^2(s^2 + 2(0.6)(50) + 50^2)} \tag{3.32}$$

$$f_{2b}(s) \;=\; \frac{50^2(s^2 + 2(0.5)(3) + 3^2)}{3^2(s^2 + 2(0.7)(50) + 50^2)}. \tag{3.33}$$

The units in the design model of the OSS LOS outputs were radians, the thruster commands were in volts, the accelerometer outputs were in in/sec^2, and the modal states were in inches. The modal disturbance inputs are given in order of increasing frequencies starting with the first rigid-body mode.

For H_2/LQG V1.1 the final weighting functions were

$$Z_{\text{LOS}} = 350 I_{6\times6}, \quad W_\xi = 0_{9\times9}, \quad W_u = I_{8\times8} \tag{3.34}$$

$$Z_\xi \;=\; \text{diag}\{60, 60, 60, 10, 10, 0, 120, 0, 120\} \tag{3.35}$$

$$W_y = \text{diag}\left\{\begin{array}{c} 0.66 f_{2a}(s) \\ 0.36 f_1(s) \\ 0.45 f_1(s) \\ 0.3 f_1(s) \\ 0.3 f_1(s) \\ 0.75 f_{2a}(s) \\ 0.3 f_{2a}(s) \\ 0.54 f_1(s) \end{array}\right\} \quad Z_u = \text{diag}\left\{\begin{array}{c} 0.14 f_{2a}(s) f_1(s) \\ 0.15 f_{2a}(s) \\ 0.13 f_1(s) \\ 0.1 f_1(s) \\ 0.13 \\ 0.18 f_{2a}(s) \\ 0.1 f_{2a}(s) \\ 0.12 f_{2a}(s) \end{array}\right\}. \tag{3.36}$$

Most of the effort involved in choosing the weighting functions was in selecting the roll-off weighting functions $W_y(s)$ and $Z_u(s)$. The approach taken was to ignore the roll-off requirements for modes outside the bandwidth at first while adjusting the performance and stability margins inside the control bandwidth. Afterwards, the roll-off weighting functions were selected according to the procedure in Section 3.3.2. Only if the required roll-off could not be achieved was it necessary to readjust the weightings inside the control bandwidth.

Both control designs satisfied the requirements in Section 3.1.2. The H_2/LQG A1.4 controller had 60 states while the H_2/LQG V1.1 controller had 59 states (51 controller states and 8 pseudo-integrator filter states).

Multivariable Gain and Phase Margins

Figure 3.10 shows the singular values of the return difference transfer function matrix frequency responses at the control inputs and sensor outputs for H_2/LQG A1.4[5]. The frequency range for the responses covers only the active control bandwidth (0–4 Hz) since the stability margins outside the control bandwidth are measured with a different test. The minimum gain/phase margins are seen to occur in the region between the rigid-body modes and the first torsional mode. The corresponding multivariable gain and phase margins (Eqn. 3.4) are $[-3.83, +7.03]$ dB and ± 32.22 degrees at the control inputs and $[-3.90, +7.25]$ dB and ± 32.88 degrees at the sensor outputs. The H_2/LQG V1.1 MVGPM analysis results are shown in Figure 3.11. The corresponding multivariable gain and phase margins are $[-4.10, +8.04]$ dB and ± 35.14 degrees at the control inputs and $[-4.09, +8.00]$ dB and ± 35.02 degrees at the sensor outputs.

High Frequency Roll-off Gain Margins

Figures 3.12–3.13 show the singular values of the open-loop transfer function matrix frequency responses for the H_2/LQG A1.4 and H_2/LQG V1.1 control laws. The responses are shown for the loops opened at the control inputs and the sensor outputs. The minimum roll-off gain margins are 20 dB for H_2/LQG A1.4 and 25 dB for H_2/-LQG V1.1.

[5]Osborne's method for diagonal scaling of matrices was applied to the return difference frequency response matrices to improve the stability margin bounds.

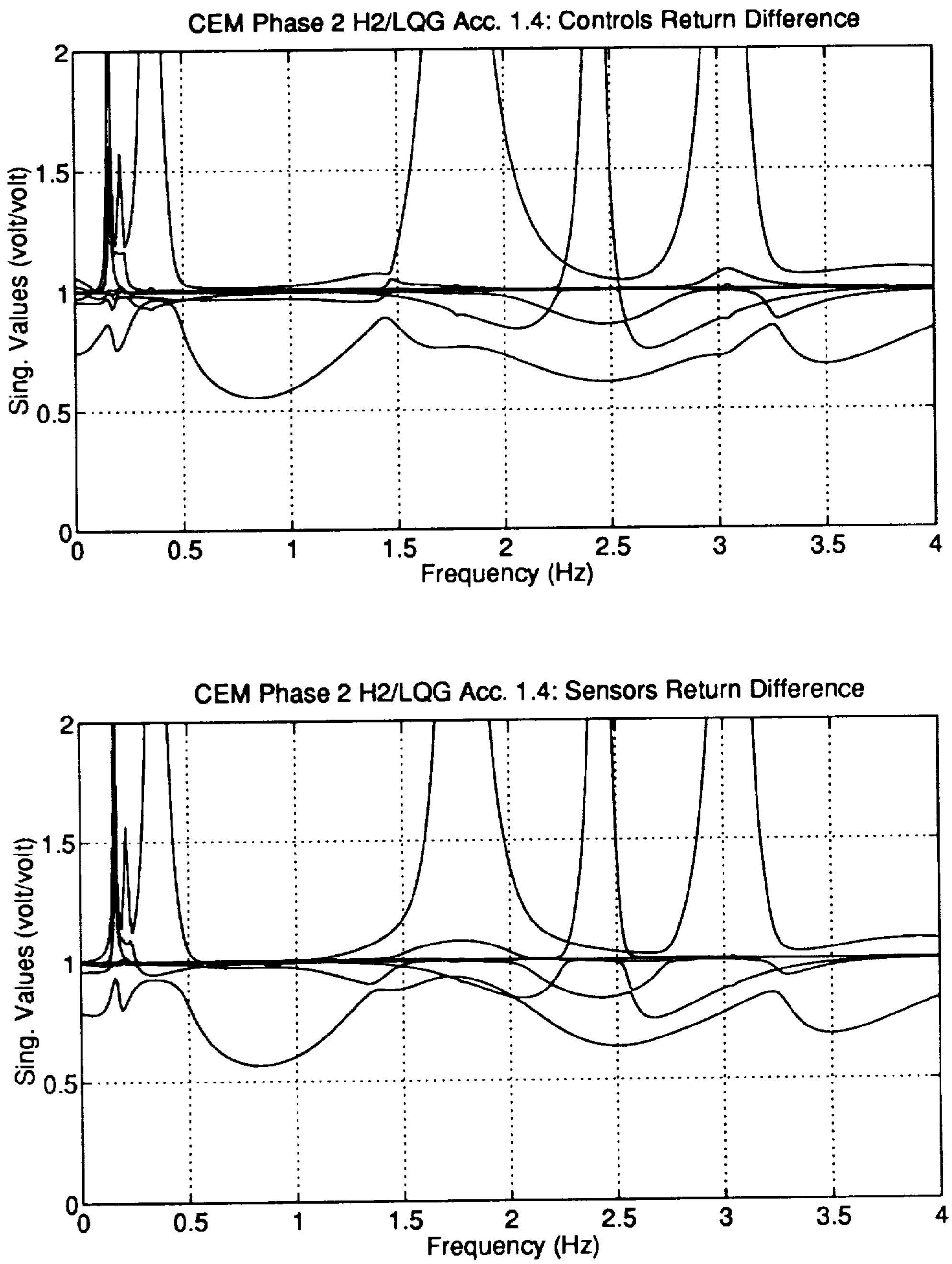

Figure 3.10: Phase 2 CEM H_2/LQG A1.4 Return Difference Transfer Function Matrix Frequency Response

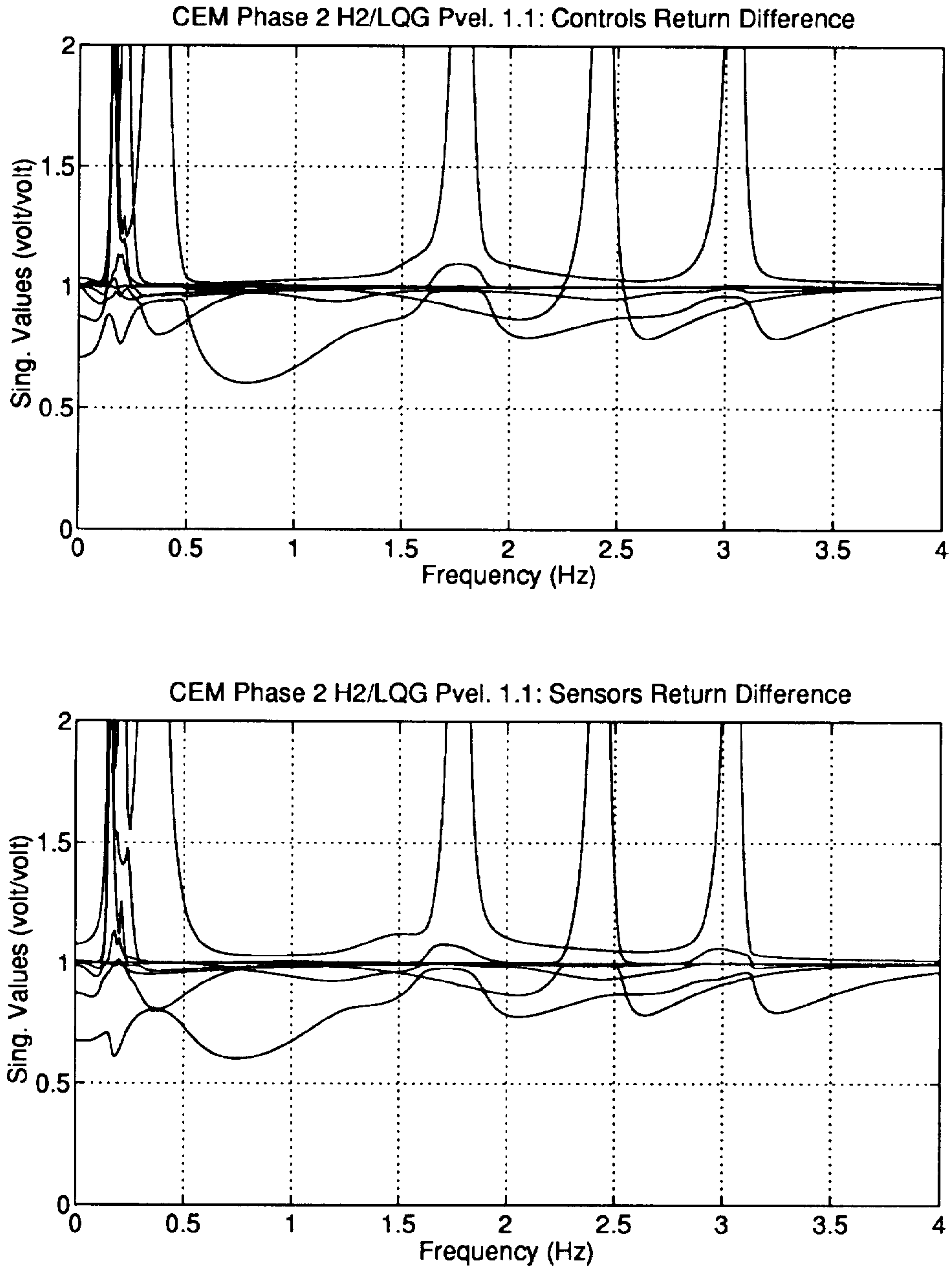

Figure 3.11: Phase 2 CEM H_2/LQG V1.1 Return Difference Transfer Function Matrix Frequency Response

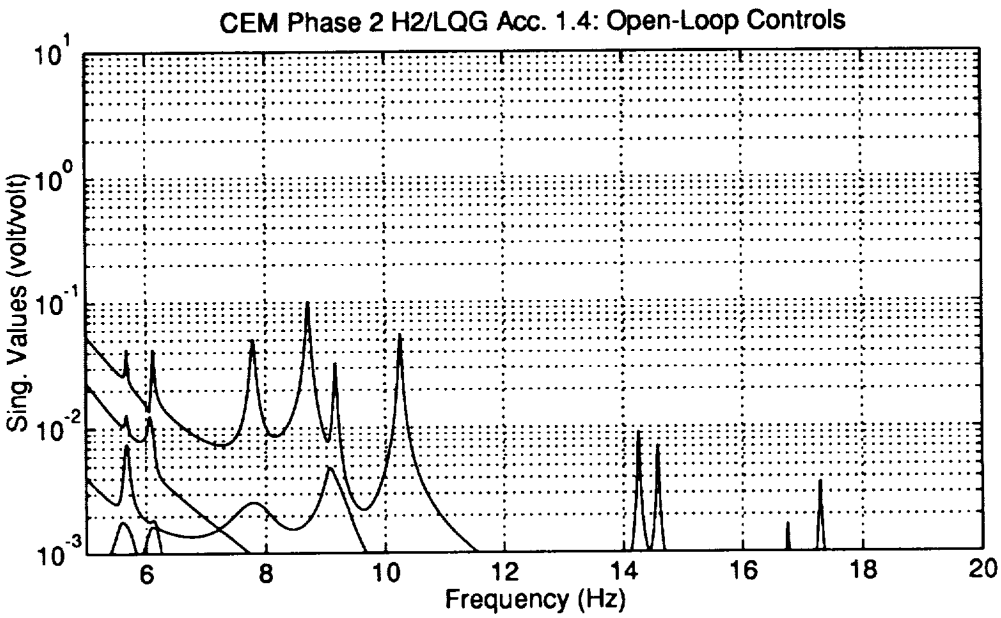

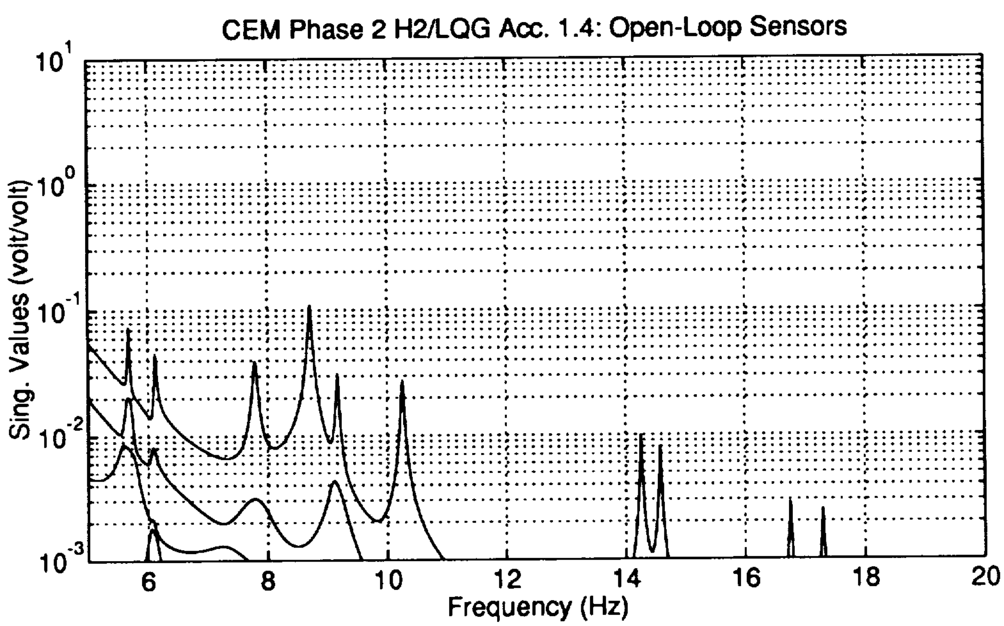

Figure 3.12: Phase 2 CEM H_2/LQG A1.4 Open-Loop Frequency Response Singular Values

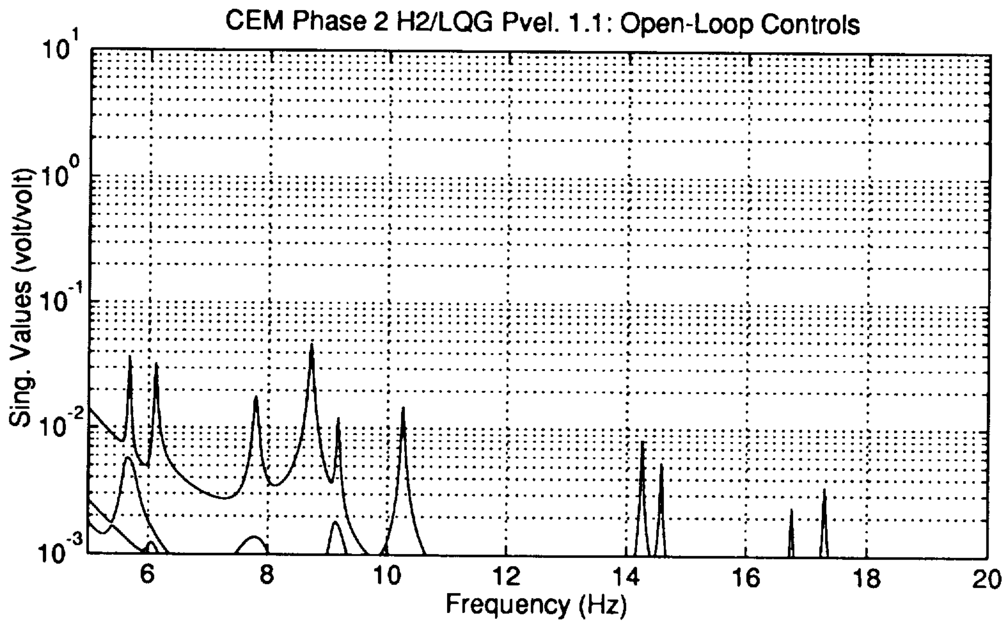

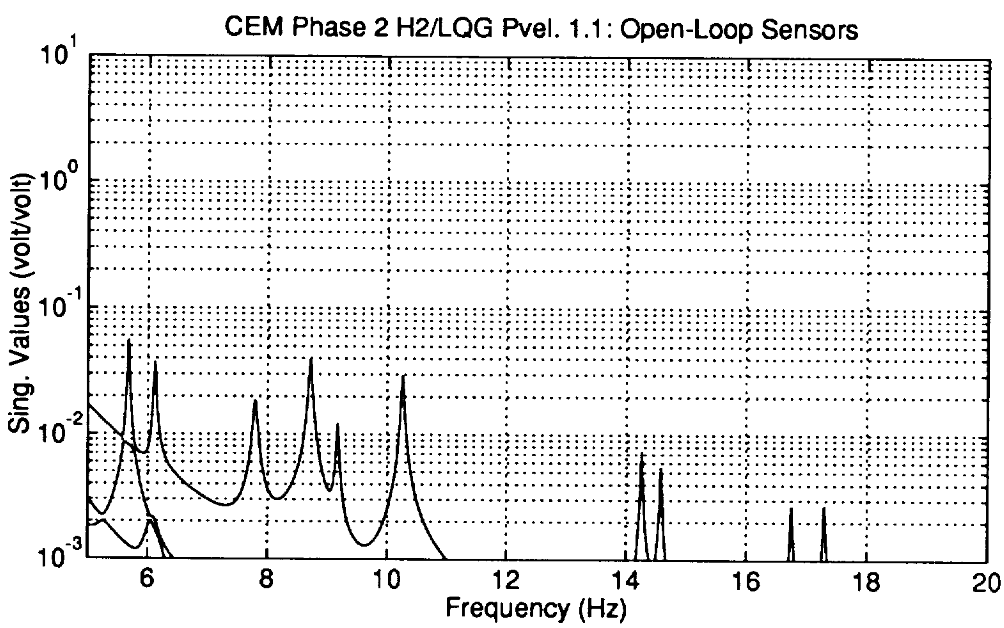

Figure 3.13: Phase 2 CEM H_2/LQG V1.1 Open-Loop Frequency Response Singular Values

Experimental Closed-Loop Performance

To access the closed-loop performance experimentally, three types of tests were performed:

1. closed-loop free-decay transient responses after open-loop excitation of the first three main truss elastic modes,
2. closed-loop MIMO frequency responses using the ZONIC computer, and
3. closed-loop RMS calculations of responses to random excitations.

Both control designs provided strong attenuation of the first three main truss structural bending/torsional modes. Results from each of the test are discussed below.

Figure 3.14 show the measured closed-loop transient responses of gimbal #1 OSS x and y LOS for the H_2/LQG A1.4 control design. The measured responses for H_2/LQG V1.1 are shown in Figure 3.15. The responses were obtained by exciting the system with sinusoidal thruster inputs for 7 seconds with the control loops open. The sinusoidal thruster inputs were chosen at the approximate frequencies of the first three bending/torsional modes. The control loops were then closed at 10 seconds.

Figures 3.16 and 3.17 show the measured open and closed-loop frequency responses for the two control laws. H_2/LQG A1.4 provides greater than 10:1 attenuation of the peak responses of the first three main truss bending/torsional modes. The Eigensystem Realization Algorithm (ERA) was used to derive a state-space model from the closed-loop MIMO frequency response data. The identified damping ratios for the first three elastic modes are 14.8%, 5.0% and 7.6%, respectively (the corresponding open-loop damping ratios are all less than 0.35%). As shown from the frequency response plots, no active damping is added to the elastic modes beyond 4 Hz. These modes are gain stabilized by the H_2 controllers as discussed in Section 3.3.2. The controller using the preconditioned pseudo-velocity measurements (H_2/LQG V1.1) provides slightly more damping to the rigid-body modes and less damping to the structural bending modes from 2–4 Hz than the controller using the unfiltered accelerometer measurements for feedback (H_2/LQG A1.4). This effect is due to the obvious fact that the unfiltered accelerometer signals inherently tend to pick up the high frequency signals much more than the low frequency rigid-body signals.

A quantitative measure of the closed-loop performance is obtained from the RMS (root-mean-squared) values of the OSS LOS responses to random disturbances. The disturbances used were Gaussian random thruster commands in a frequency band from 1–10 Hz Tables 3.2 and 3.3 list the measured and predicted RMS values of the OSS LOS outputs and the controller commands for both control designs. The

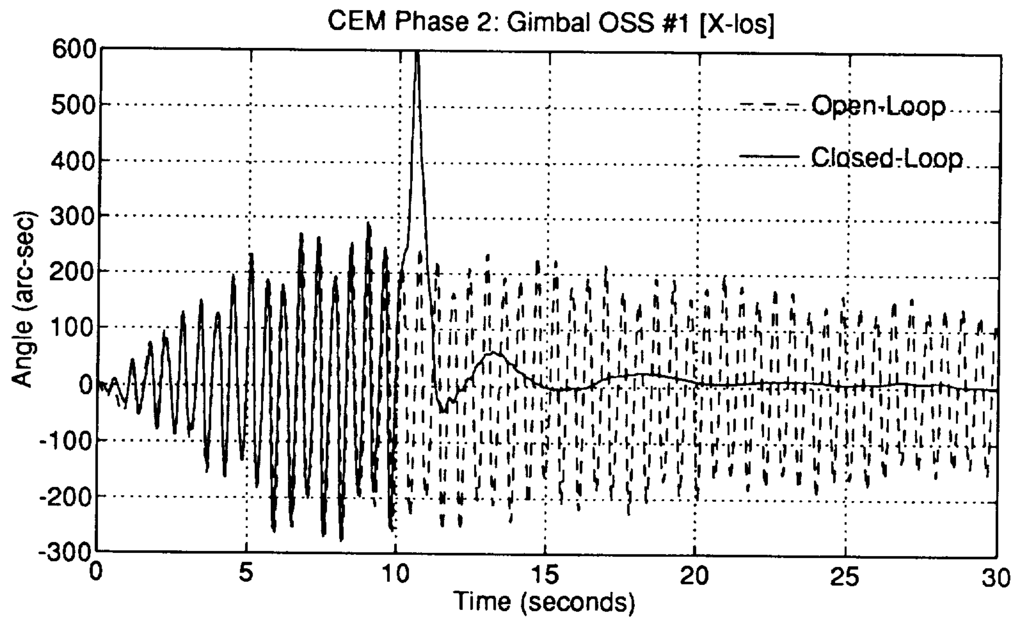

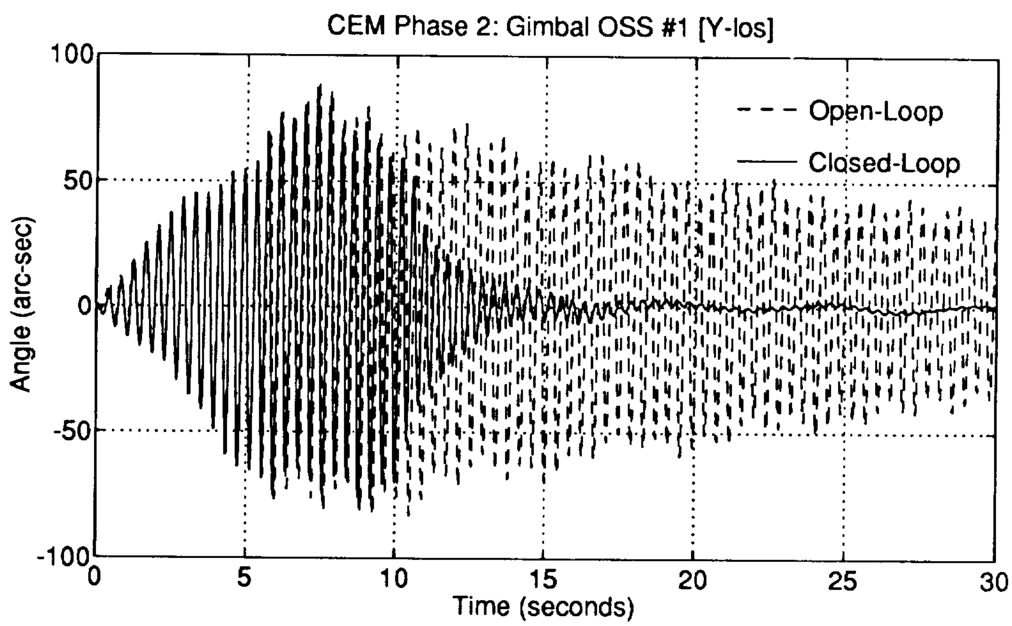

Figure 3.14: Phase 2 CEM H_2/LQG A1.4 Measured Closed-Loop Transient Responses

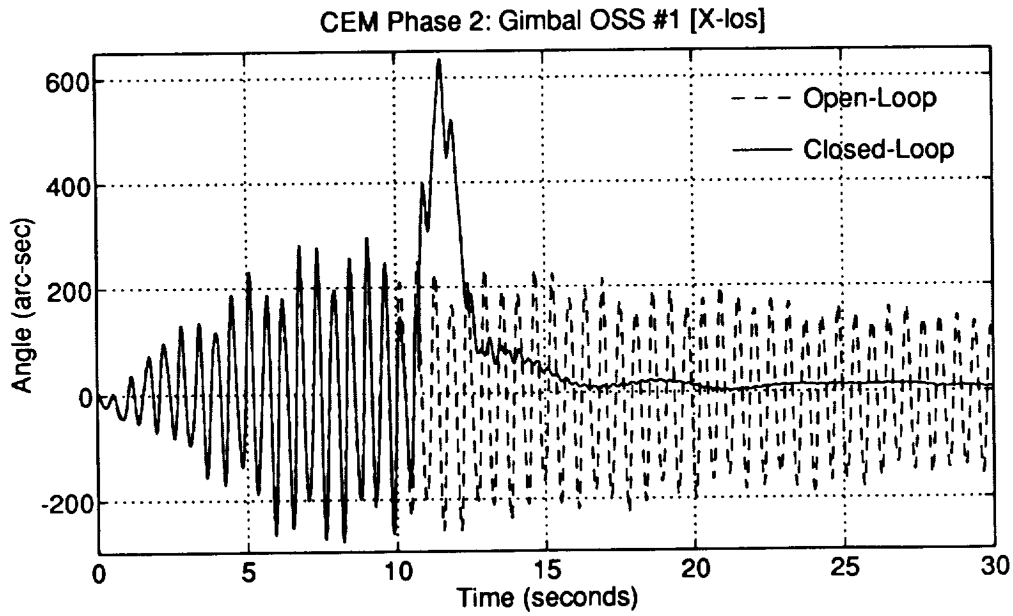

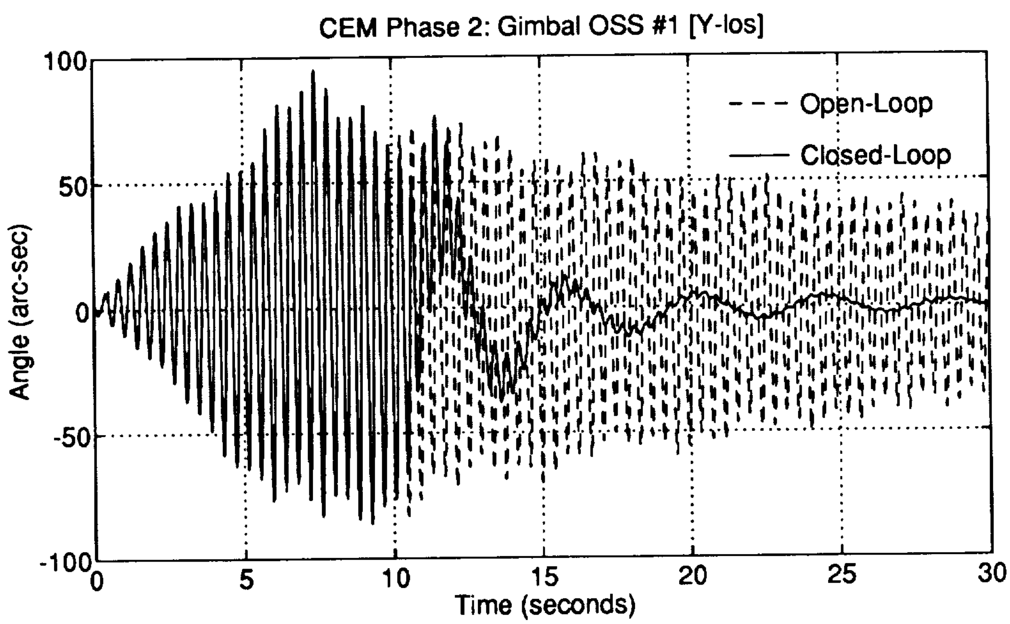

Figure 3.15: Phase 2 CEM H_2/LQG V1.1 Measured Closed-Loop Transient Responses

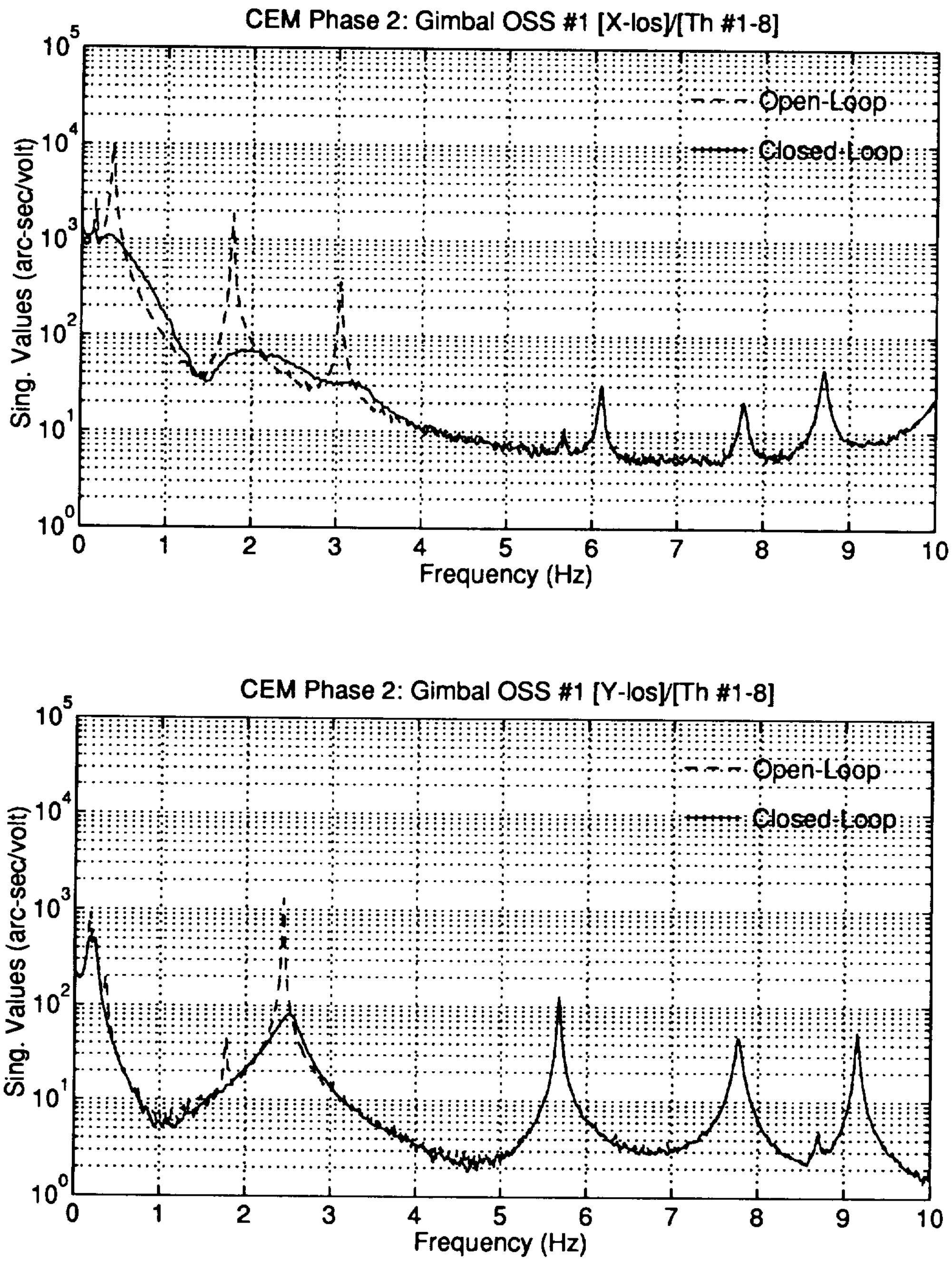

Figure 3.16: Phase 2 CEM H_2/LQG A1.4 Measured Open and Closed Loop Frequency Responses

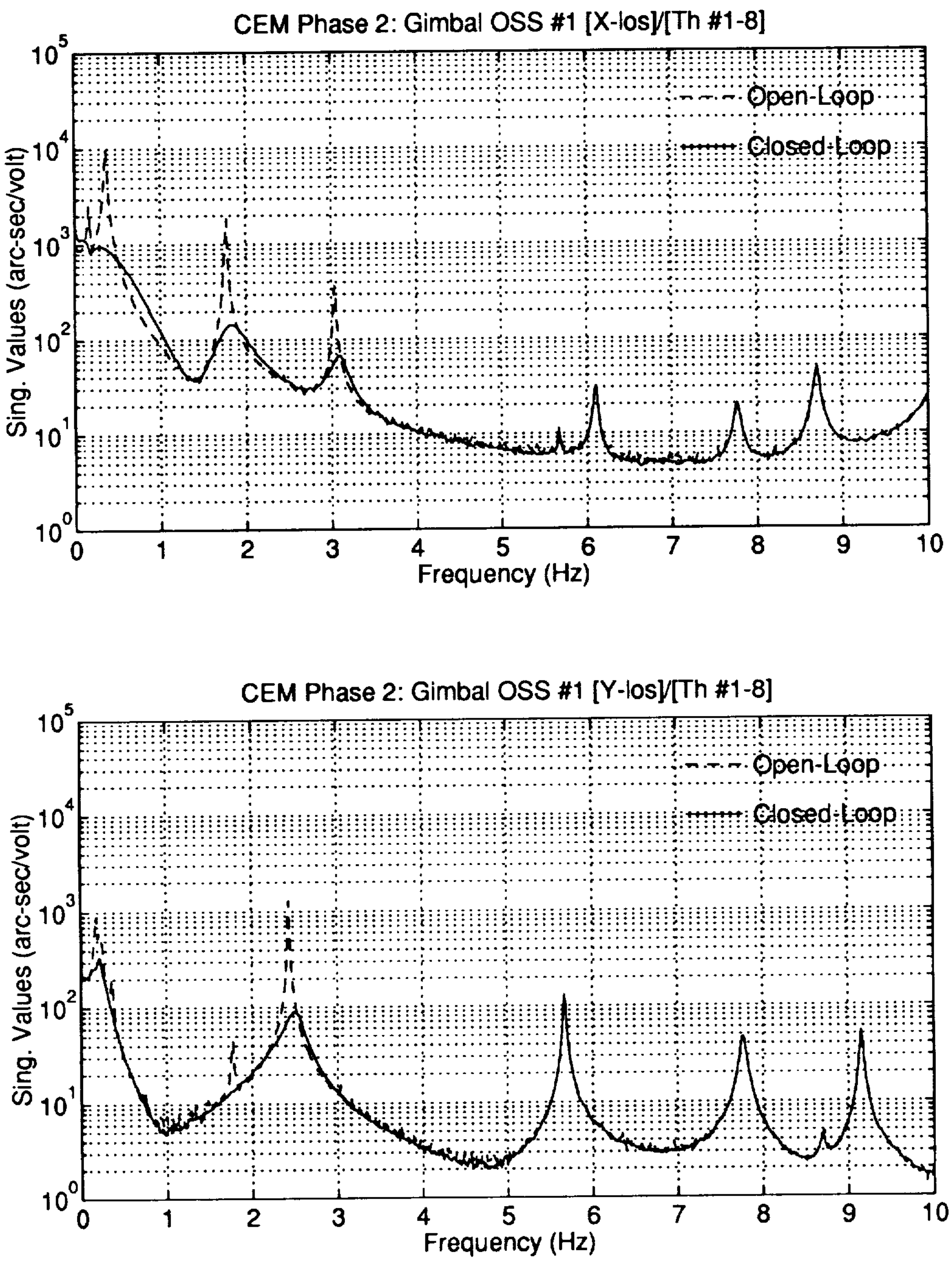

Figure 3.17: Phase 2 CEM H_2/LQG V1.1 Measured Open and Closed Loop Frequency Responses

Table 3.2: Phase 2 CEM H_2/LQG A1.4 Closed-Loop RMS Values of Random Disturbance Responses

Output/Control Command	Measured Open-Loop	Measured Closed-Loop	Predicted Closed-Loop
Gimbal OSS #1 x LOS (arc-sec)	146.1	60.01	80.76
Gimbal OSS #1 y LOS (arc-sec)	75.08	19.16	19.01
Gimbal OSS #2 x LOS (arc-sec)	127.6	56.68	68.54
Gimbal OSS #2 y LOS (arc-sec)	71.31	16.49	13.86
Gimbal OSS #4 x LOS (arc-sec)	202.6	78.25	82.01
Gimbal OSS #4 y LOS (arc-sec)	75.77	20.68	20.04
Thruster #1 Command (volts)	0.0	0.0843	0.0759
Thruster #2 Command (volts)	0.0	0.0507	0.0483
Thruster #3 Command (volts)	0.0	0.4371	0.3991
Thruster #4 Command (volts)	0.0	0.1472	0.1402
Thruster #5 Command (volts)	0.0	0.0673	0.0640
Thruster #6 Command (volts)	0.0	0.3068	0.2734
Thruster #7 Command (volts)	0.0	0.1559	0.1502
Thruster #8 Command (volts)	0.0	0.3638	0.3295

open-loop RMS values are also shown for comparison. The average RMS LOS output reductions achieved with H_2/LQG A1.4 are 60% for the x LOS output and 75% for the y LOS output. The measured and predicted RMS values for the OSS LOS show generally close agreement. Some discrepancies are known to result from signal drift in OSS LOS measurements observed during the tests.

Experimental Verification of Control Law Sensitivity

The control design robustness requirements discussed in Section 3.1.2 were chosen to ensure that the closed-loop performance, as defined by the objective function J_p (Eqn. 3.1), be insensitive to the inherent model uncertainties and approximations. Recall that J_p is a function of the LOS disturbance responses. As such, the relative agreement between the measured and predicted LOS disturbance responses can be used to infer the sensitivity of the control design. An insensitive control design will show close agreement between the measured and predicted closed-loop LOS disturbance responses.

Figures 3.18 and 3.19 show the measured and predicted closed-loop frequency

Table 3.3: Phase 2 CEM H_2/LQG V1.1 Closed-Loop RMS Values of Random Disturbance Responses

Output/Control Command	Measured Open-Loop	Measured Closed-Loop	Predicted Closed-Loop
Gimbal OSS #1 x LOS (arc-sec)	146.1	57.71	67.74
Gimbal OSS #1 y LOS (arc-sec)	75.08	20.43	19.40
Gimbal OSS #2 x LOS (arc-sec)	127.6	53.17	48.77
Gimbal OSS #2 y LOS (arc-sec)	71.31	17.72	14.25
Gimbal OSS #4 x LOS (arc-sec)	202.6	76.93	79.06
Gimbal OSS #4 y LOS (arc-sec)	75.77	22.27	19.56
Thruster #1 Command (volts)	0.0	0.1474	0.1329
Thruster #2 Command (volts)	0.0	0.0975	0.0900
Thruster #3 Command (volts)	0.0	0.1529	0.1388
Thruster #4 Command (volts)	0.0	0.0795	0.0751
Thruster #5 Command (volts)	0.0	0.0371	0.0327
Thruster #6 Command (volts)	0.0	0.1326	0.1193
Thruster #7 Command (volts)	0.0	0.1529	0.1432
Thruster #8 Command (volts)	0.0	0.1964	0.1770

responses for both control laws. The responses show excellent agreement for the frequencies within the control bandwidth (0–4 Hz) and good agreement up to 10 Hz. The agreement between the predicted and measured RMS values of the LOS responses in Tables 3.2 and 3.3 are also generally good.

The sensitivity of the control designs to artificial gain variations at the control inputs was also tested. The tests involved increasing the feedback gains simultaneously in all control loops (using the CPOT parameter in the real-time software) from the nominal value (CPOT=1.0) until an instability or limit-cycle was observed. For the H_2/LQG A1.4 design, a limit-cycle was observed at a CPOT gain of 1.7 involving the rigid-body roll-mode. For the H_2/LQG V1.1 design, a similar limit-cycle was observed at a CPOT gain of 1.9 involving the rigid-body roll-mode.

3.4 HAC/LAC Control Law Design

In this section we discuss the design of a feedback control law which combines a low authority control (LAC) inner loop, for damping the overall vibrations, with a high authority control (HAC) outer loop, for obtaining stringent point accuracy. Figure 3.20 shows a block diagram of a HAC/LAC concept for the CEM. The LAC is designed using the numerical parameter optimization algorithm SANDY[6]. The HAC is designed using the H_2/LQG control design algorithm discussed in Section 3.3.

Typically, high performance controllers for lightly damped systems designed with H_2/LQG or H_∞ design algorithms must contain high-order filters to roll-off the plant responses outside the control bandwidth. The HAC/LAC approach capitalizes on the principle that a low authority control law incorporating minimal information from the plant model will be more robust to model uncertainties than a high authority controller which takes full advantage of the available information. The LAC is used as a robust inner loop for suppressing the plant responses outside the bandwidth of the HAC in place of the usual high-order roll-off filters. A similar approach has been successfully employed by the LaRC CSI group on the Phase 0 CEM. Their results for an active vibration absorber low-authority controller are discussed in [15]. Here we use a different method to automatically design the LAC controller.

The SANDY algorithm was applied to the design of a local (collocated) velocity feedback (LVF) LAC for the CEM. Before discussing the HAC/LAC design for the CEM we first give a brief overview of the SANDY control design algorithm [16, 17].

[6]SANDY is a trademark of A. J. Controls, Inc.

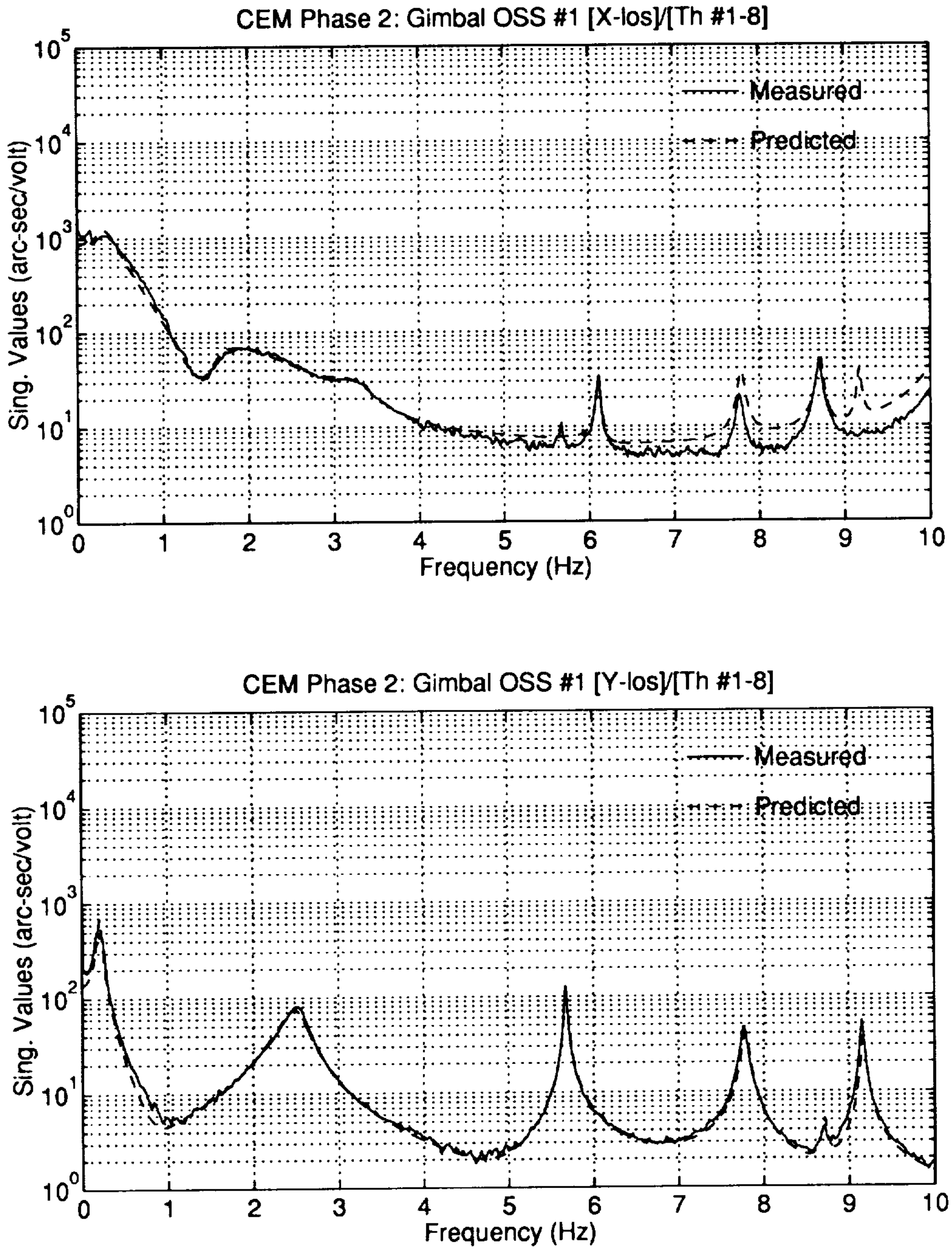

Figure 3.18: Phase 2 CEM H_2/LQG A1.4 Measured and Predicted Closed-Loop Frequency Responses

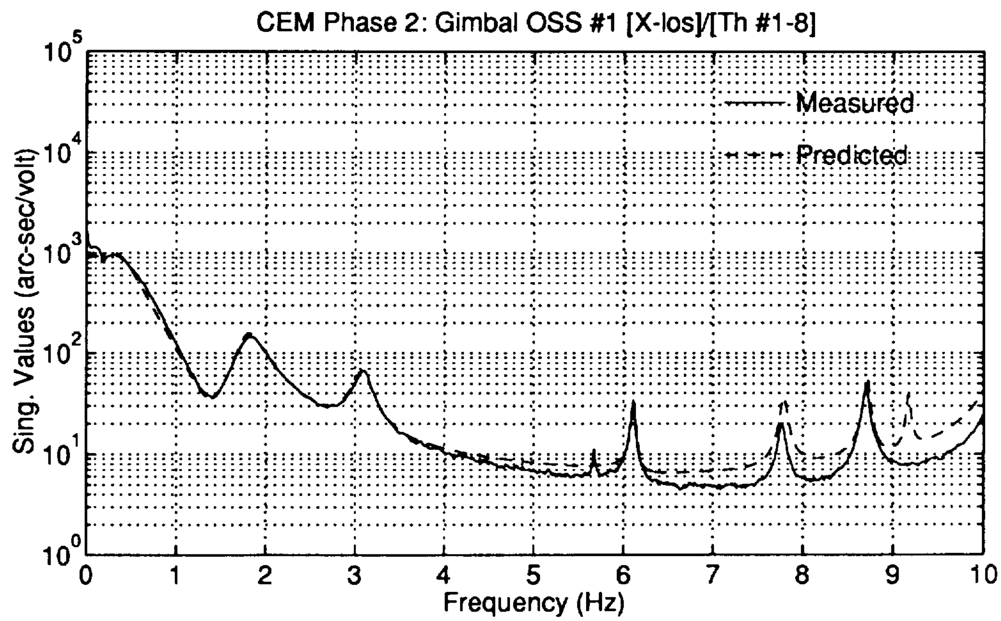

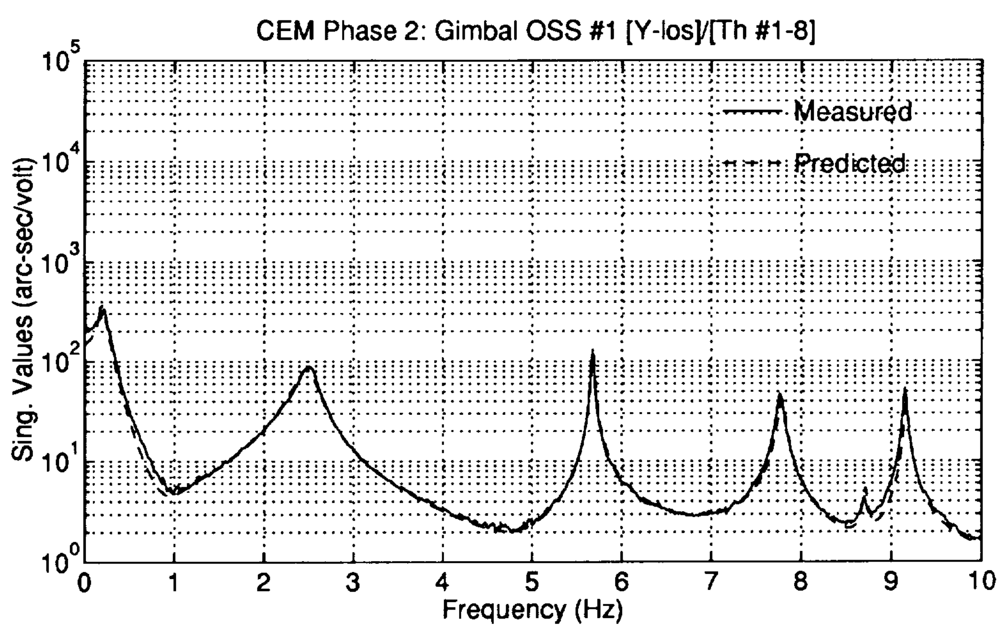

Figure 3.19: Phase 2 CEM H_2/LQG V1.1 Measured and Predicted Closed-Loop Frequency Responses

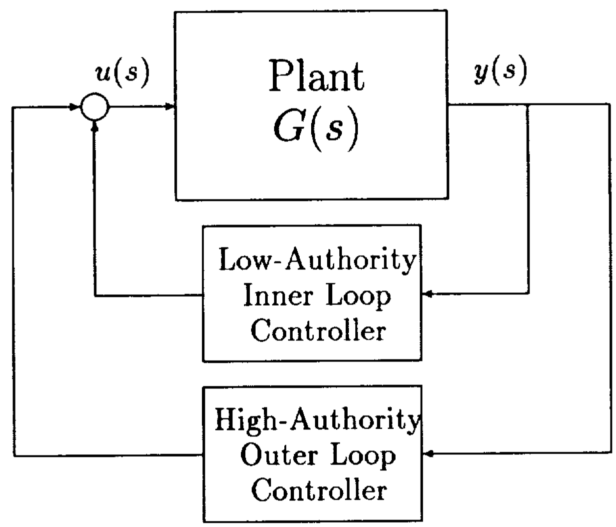

Figure 3.20: High Authority Control/Low Authority Control (HAC/LAC) Concept for the CEM

3.4.1 The SANDY Control Design Software

Advanced control design theories such as H_2/LQG and H_∞ provide practical solutions to control law design for complex multivariable systems. A major drawback to these techniques is that they are only applicable to the design of centralized control laws and the resulting controllers are generally complex and high-order. The algorithm implemented in the SANDY design software [16, 17] provides a solution for the design of low-order, constrained architecture controllers. The SANDY algorithm allows for MIMO closed-loop shaping of H_2-norm or equivalent LQG criteria.

The SANDY problem formulation is based on the numerical minimization of a composite objective function $J(t_f)$ formed by the sum of quadratic performance indices (e.g. H_2-norm optimization) for multiple plant models. The minimization is subject to various types of linear and nonlinear constraints specified by the user. The objective function incorporates performance indices over multiple plants to facilitate the design of parameter insensitive controllers. The design software provides direct nonlinear constraints on closed-loop stability and covariance responses and allows the user to define new sets of design constraints.

Figure 3.21 illustrates the overall control problem. The plant design models $P_i(s)$

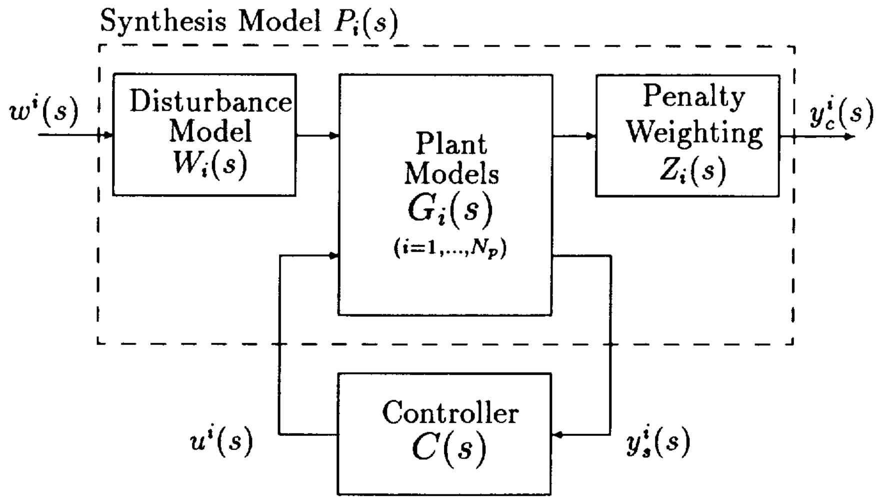

Figure 3.21: A block diagram representation of the SANDY feedback control design problem formulation.

are represented by the state space system of linear differential equations

$$\dot{x}^i(t) = F^i x^i(t) + G^i u^i(t) + \Gamma^i w^i(t) \tag{3.37}$$
$$y_s^i(t) = H_s^i x^i(t) + D_{su}^i u^i(t) + D_{sw}^i w^i(t) \tag{3.38}$$
$$y_c^i(t) = H_c^i x^i(t) + D_{cu}^i u^i(t) + D_{cw}^i w^i(t) \tag{3.39}$$

where $x^i(t)$ is a state vector, $u^i(t)$ is a control vector, $w^i(t)$ is a disturbance vector, $y_s^i(t)$ is a sensor output vector, $y_c^i(t)$ is a criteria output vector, and i for $i = 1 \ldots N_p$ is the index of the i^{th} plant model (note that G^i is the control input distribution matrix while $G_i(s)$ is the plant transfer function matrix).

The excitations to the closed-loop system model are through the disturbance/command input vector $w^i(t)$. Different interpretations of the objective function apply for different types of disturbance/command inputs (e.g., impulse functions, or random noises). Design problems to initial conditions and step commands are formulated with the use of impulse inputs.

The SANDY objective function $J(t_f)$ is defined as the weighted sum over individual performance indices

$$J(t_f) = \sum_{i=1}^{N_p} w_{pi} J_i(t_f) \tag{3.40}$$

for each plant design model weighted by the factor w_{pi}. The performance indices $J_i(t_f)$ are defined for different types of disturbance/command inputs, including random impulsive disturbances and initial conditions or random white noise disturbances:

1. **Random Impulsive Disturbances and Initial Conditions:** Disturbances defined by $w^i(t) = w_0^i\delta(t)$ are random impulses where $\delta(t)$ is the usual Dirac delta function. Initial conditions on the state vector $x(t)$ are established by defining the input disturbance/command vector $w^i(t) = x_0^i(t)\delta(t)$ with the matrix $W^i = I_n$. The objective function is defined as

$$J_i(t_f) = \frac{1}{2}\int_0^{t_f} E_{\alpha_i}\left[y_c^{iT}(t)Q^i y_c^i(t) + u^{iT}(t)R^i u^i(t)\right] dt \tag{3.41}$$

where the E_{α_i} is the expectation operator on the closed-loop system destabilized by α_i.

2. **Random White-Noise Disturbances:** The objective function to white-noise disturbances with covariance $E[w^i(t)w^{iT}(\tau)] = W^i\delta(t-\tau)$ is defined as

$$J_i(t_f) = \frac{1}{2}E_{\alpha_i}\left[y_c^{iT}(t_f)Q^i y_c^i(t_f) + u^{iT}(t_f)R^i u^i(t_f)\right] dt \tag{3.42}$$

In the limit as $t_f \to \infty$ an equivalent performance index can be expressed using the H_2-norm as

$$J_i(t_f) = \frac{1}{2}\left\| \begin{array}{c} Q^{i1/2}H^i_{y_cw}(s) \\ R^{i1/2}H^i_{uw}(s) \end{array} \right\|_2^2 \tag{3.43}$$

where $H^i_{y_cw}(s)$ and $H^i_{uw}(s)$ are the transfer function matrices between the disturbances $w^i(s)$ and the criterion outputs $y_c^i(s)$ and the controls $u^i(s)$ for the closed-loop system destabilized by α_i.

The controller model $C(s)$ is represented by the linear differential equations

$$\dot{z}(t) = Az(t) + By_s(t) \tag{3.44}$$

$$u(t) = Cz(t) + Dy_s(t) \tag{3.45}$$

where $z(t)$ is the controller state vector. The controller design parameters are selected from the state matrices of the controller structure. Direct inequality constraints among the design parameters of the form

$$lb_{d_i} \leq \frac{p_{c_i}}{\beta_i} \leq ub_{d_i} \quad (1 \leq i \leq n_c) \tag{3.46}$$

are specified by the user where p_c is the vector of design parameters of length n_c, β is a vector of parameter scalings, and lb_d and ub_d are vectors of lower and upper bounds respectively. Linear inequality constraints among the design parameters of the form

$$lb_{l_i} \leq \sum_{j=1}^{n_c} L_{ij}\beta_j\frac{p_{c_i}}{\beta_i} \leq ub_{l_i} \tag{3.47}$$

can also be specified where L is a matrix of linear coefficients and lb_l and ub_l are vectors of lower and upper bounds respectively.

SANDY provides three types of nonlinear constraints:

1. nonlinear constraints on covariance responses,
2. nonlinear constraints on closed-loop stability,
3. user-defined nonlinear constraints.

Nonlinear constraints on the covariance responses of the closed-loop plant criterion outputs y_c and controller outputs u to Gaussian random disturbances are specified as

$$lb_{c_i}^{(k)} \leq E_{\alpha_i}\left[y_{c_i}^{(k)^2}(t_f)\right] \leq ub_{c_i}^{(k)} \tag{3.48}$$

and

$$lb_{u_i}^{(k)} \leq E_{\alpha_i}\left[u_i^{(k)^2}(t_f)\right] \leq ub_{u_i}^{(k)} \tag{3.49}$$

where $y_{c_i}^{(k)}$ is the i^{th} criterion output of the k^{th} plant design model and $u_i^{(k)}$ is the i^{th} control input to the k^{th} plant design model.

3.4.2 LVF LAC Design with SANDY

Here we discuss the design of a LAC inner loop control law for the CEM using the SANDY design software. The purpose of the LAC inner loop is to increase the robustness of the HAC controller to modes in the frequency region just outside the bandwidth of the HAC controller (which in this case is approximately 4 Hz). The HAC control law must gain stabilize these modes to be robust. To increase the roll-off gain margins, the LAC controller is designed to suppress the responses of these modes as seen in the transfer function responses from the control inputs to the feedback sensor outputs of the HAC controller.

The eight servo-accelerometers of the CEM available for control are approximately collocated with the thrusters. It is a well known property of collocated or local velocity feedback (LVF) for structural elastic systems that closed-loop stability is guaranteed regardless of uncertainties in the plant model parameters. This stability property holds provided that the sensed feedback signal is the true velocity and the feedback command is a true force. There can be no additional dynamics in the feedback paths such as those resulting from sensors/actuators or time delays. Note that the LVF controller is a direct gain feedback controller and does not possess any feedback compensation or noise reduction filters.

The inherent robustness of LVF allows vibration suppression across a wide bandwidth. For this reason LVF was chosen as the basis for the LAC controller.

Velocity feedback outputs for the LVF controller can be obtained by integrating the accelerometer measurements. Note, however, that the accelerometer measurements include components of the gravitational acceleration and are not equivalent to the inertial accelerations. As a result, the guaranteed stability property of the closed-loop LVF design is lost. Since the gravitational effects are greatest at the rigid-body frequencies of the CEM and diminish rapidly with increasing frequency this does not present a significant problem. The important vibration suppression and robustness properties of the LVF controller is retained for the elastic structural modes.

The destabilizing effects of the LVF controller on the rigid-body modes can be reduced by using pseudo-integrator filters (integrator filters with a low frequency washout) instead of true integrators. The HAC controller can then be designed to restabilize any rigid-body modes which may be slightly destabilized by the LVF LAC controller. Another reason for using pseudo-integrators instead of true integrators is to reduce the effects of DC sensor offsets in the closed-loop system.

The LVF control equation for the i^{th} feedback loop is given by

$$u_i = -k_i \tilde{v}_i \tag{3.50}$$

where $\tilde{v}_i$ is the i^{th} loop pseudo-velocity feedback output computed from the i^{th} accelerometer measurement a_i as

$$\tilde{v}_i(s) = \frac{1}{s+\omega_I} a_i(s) = \frac{1}{\tilde{s}} a_i(s). \tag{3.51}$$

The pseudo-integrator washout frequency ω_I is the same for each feedback loop. The design parameters optimized with SANDY are the feedback gains k_i.

Selection of the pseudo-integrator washout frequencies is important for the HAC design. If the washout frequency is too low the rigid-body stability margins of the HAC controller will be poor because large controller gains will be required to overcome the destabilizing effects of the LVF inner loop. On the other hand, if the washout frequency is too high, the elastic mode stability margins of the HAC controller may be degraded for the same reason.

The presence of sensors/actuator dynamics and time delays in the CEM also affects the stability and robustness of the LVF controller. These effects are minimal at low frequencies and increase with increasing frequency. The fact that the integrated accelerometer outputs roll-off with increasing frequency alleviates this effect. However, the effects of sensors/actuators dynamics and time delays are the major limiting factors on the allowable LVF feedback gains.

Figure 3.22 is a block diagram of the SANDY LVF LAC synthesis problem. The transfer function matrix $1/\tilde{s}$ is a diagonal matrix of pseudo-integrator filter transfer functions. The matrix K_{LVF} is a diagonal LVF feedback gain matrix. The plant

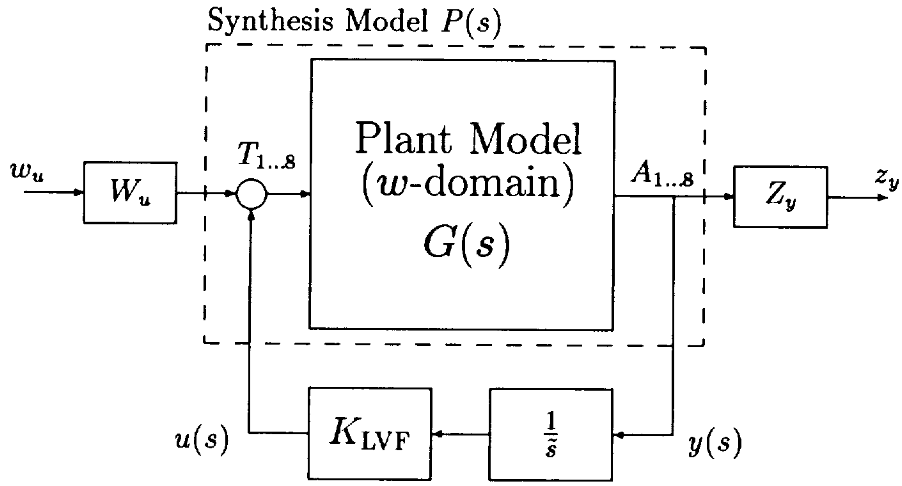

Figure 3.22: Local Velocity Feedback LAC Controller SANDY Synthesis Problem

design model $G(s)$ includes all the dominant elastic modes up to 30 Hz (in contrast to the H_2/LQG design models which included only the rigid-body and first 3 elastic modes). The objective function is the H_2-norm of the closed-loop responses from thruster command inputs to the accelerometer outputs weighted by the diagonal weighting functions $W_u(s)$ and $Z_y(s)$ respectively. Note that the closed-loop transfer function matrix $z_y(s)/w_u(s)$ must be strictly proper for the H_2-norm to be defined. Covariance constraints on the controller thruster feedback commands were used to limit the controller gains. The covariance constraints were for Gaussian white-noise disturbance processes w_u with zero mean and unit covariance.

3.4.3 H_2/LQG HAC Design

The H_2/LQG design procedure developed in Section 3.3 was applied to the design of a HAC control law. The synthesis model for the HAC design is shown in Figure 3.23. The synthesis model is formed from the nominal plant model $G(s)$ and weighting functions by closing the LVF LAC inner loop. The pseudo-velocity outputs $\tilde{V}$ are used as feedback outputs for the HAC. By feeding back the pseudo-velocity outputs to the HAC instead of the accelerometer outputs lower order roll-off weighting filters can be used and the resulting controller state dimension is reduced.

The design procedure for selecting the synthesis model weighting functions to minimize the OSS LOS responses while meeting the design requirements is the same as described in Section 3.3.2. In addition, the pseudo-integrators washout frequency

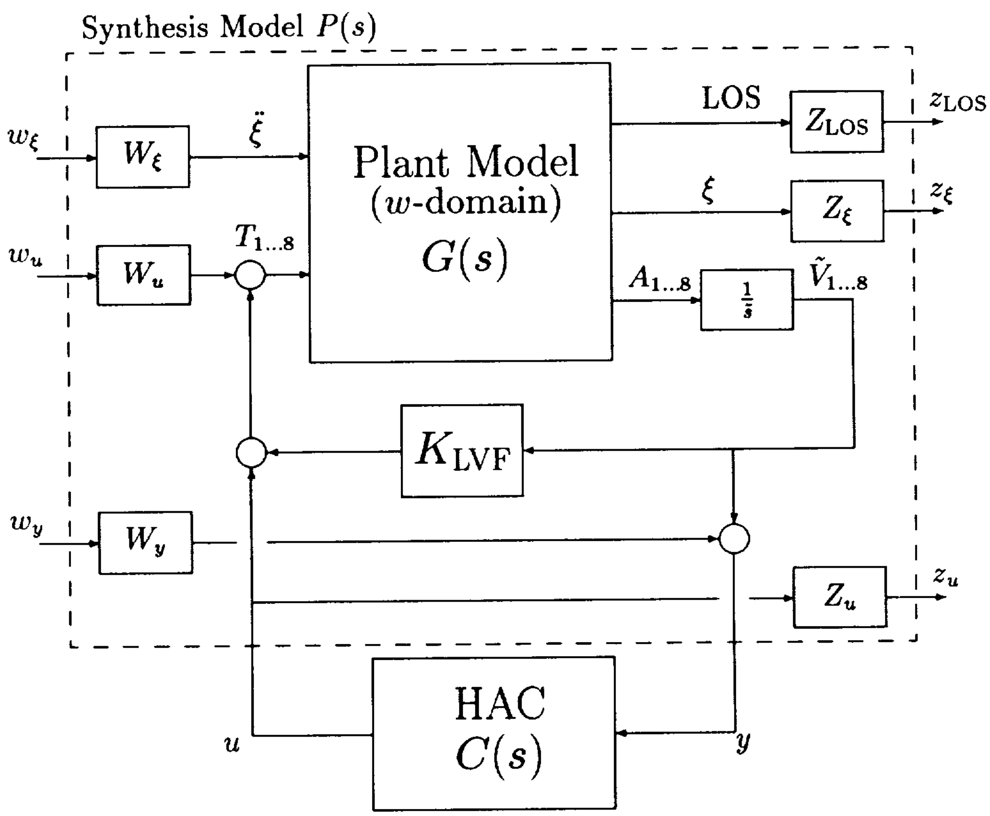

Figure 3.23: HAC H_2/LQG control law synthesis model using pseudo-velocity feedback.

(ω_I) must be adjusted to so that the MVGPM requirements are achieved. Increasing the washout frequency improves the MVGPM's at the rigid-body frequencies. In the case that the MVGPM's at the elastic mode frequencies are too low then the washout frequency should be reduced.

3.4.4 Design Results

The HAC/LAC design process developed above was successfully implemented on the CEM test article in its Phase 1 and Phase 2 configurations. Results obtained with one of the Phase 1 controller designs are given for reference in Appendix C. The results from the Phase 2 controller designs are discussed here in detail. Two different HAC/LAC controllers were designed and tested on the Phase 2 CEM. Complete experimental results from the Phase 2 designs are given in Appendix D.

Two different sets of LVF controller gains were designed for the Phase 2 CEM using SANDY (Table 3.4). For the first design, LVF 1.1, the plant design model included the CEM rigid-body modes and dominant structural modes up to 30 Hz. The second design, LVF 1.2, used a plant design model which included only the dominant structural modes up to 30 Hz (i.e., the rigid-body modes were not included). The reason for leaving the rigid-body modes out of the second design plant model was to allow SANDY to optimize the vibration suppression properties of the design while disregarding the destabilizing effects on the rigid-body modes. In both designs the sensors/actuators dynamic models and time-delay approximations were included in the design models.

The weighting functions were chosen as $W_u(s) = I_{8\times8}$ and $Z_y(s) = f(s)I_{8\times8}$ where

$$f(s) = \frac{35^2}{s^2 + 2(0.5)(35)s + 35^2} \tag{3.52}$$

with frequencies in Hertz. The upper limit of the individual controller thruster output command covariances was 0.5 volts^2.

The LVF feedback gains in Table 3.4 were designed using a second-order pseudo-integrator filter instead of the first-order filter in Eqn. 3.51. The pseudo-velocity output equation used for the SANDY design was

$$\tilde{v}_i(s) = \frac{s}{s^2 + 2\zeta_I\omega_I + \omega_I^2} a_i(s) \tag{3.53}$$

where $\zeta_I = 0.707$ and the washout frequency ω_I was set to a nominal value of 0.03 Hz. The pseudo-integrator filter was later changed to the first-order filter in Eqn. 3.51 to reduce the total state dimension of the HAC/LAC controller[7]. The washout frequency ω_I was also readjusted to improve the stability margins of the HAC controller.

[7]The LVF feedback gains were not redesigned using the first-order pseudo-integrator filters.

Table 3.4: Phase 2 CEM LAC Local Velocity Feedback Gains

Feedback Loop	LVF 1.1 (volts/in/sec)	LVF 1.2 (volts/in/sec)
Thruster/Accelerometer # 1	0.18661	0.66041
Thruster/Accelerometer # 2	0.46938	0.53823
Thruster/Accelerometer # 3	0.20798	0.85381
Thruster/Accelerometer # 4	0.67587	0.73593
Thruster/Accelerometer # 5	0.81016	1.13340
Thruster/Accelerometer # 6	0.00000	1.48720
Thruster/Accelerometer # 7	0.34957	0.38864
Thruster/Accelerometer # 8	0.14429	0.71314

H_2/LQG HAC controllers, HAC 1.1 and HAC 1.2, were designed for each of the LVF LAC controllers in Table 3.4. The combined HAC/LAC control law corresponding to LVF 1.1 is denoted by HAC/LAC 1.1 while the HAC/LAC control law corresponding to LVF 1.2 is denoted by HAC/LAC 1.2. The plant design model used for the H_2/LQG HAC synthesis (Figure 3.23) was the same as for the H_2/LQG control designs in Section 3.3.4. The pseudo-integrator filter washout frequency was set to 0.6 Hz for HAC/LAC 1.1 and 0.8 Hz for HAC/LAC 1.2.

The final weighting functions for HAC 1.1 and HAC 1.2 were selected as

$$Z_{\text{LOS}} = 350 I_{6\times6}, \quad W_\xi = 0_{9\times9}, \quad W_u = I_{8\times8} \tag{3.54}$$

$$Z_\xi = \text{diag}\{60, 60, 60, 0, 0, 0, 120, 0, 120\} \tag{3.55}$$

$$W_y = \text{diag}\left\{\begin{array}{c} 1.05 f_{2a}(s) f_1(s) \\ 0.45 f_1(s) \\ 0.3 f_{2a}(s) \\ 0.3 \\ 0.3 f_1(s) \\ 0.75 f_{2a}(s) \\ 0.3 f_1(s) \\ 0.3 f_1(s) \end{array}\right\} \qquad Z_u = \text{diag}\left\{\begin{array}{c} 0.25 f_{2a}(s) f_1(s) \\ 0.15 f_1(s) \\ 0.15 f_1(s) \\ 0.1 \\ 0.13 \\ 0.2 f_{2a}(s) f_{2b}(s) \\ 0.1 f_1(s) \\ 0.12 f_{2a}(s) \end{array}\right\} \tag{3.56}$$

where the weighting filters $f_1(s)$, $f_{2a}(s)$, and $f_{2b}(s)$ are given in Section 3.3.4. The units in the design model of the OSS LOS outputs were radians, the thruster commands were in volts, the accelerometer outputs were in in/sec^2, and the modal states were in inches. The modal disturbance inputs are given in order of increasing frequencies starting with the first rigid-body mode.

The Phase 2 HAC/LAC controllers satisfied the design requirements in Section 3.1.2. Both HAC/LAC controllers had 57 states (including the pseudo-integrator filter states). Analysis and experimental results for the Phase 2 HAC/LAC control designs are discussed below.

Multivariable Gain and Phase Margins

Multivariable gain and phase margins of the LVF LAC controllers and HAC/LAC controllers were analyzed at the plant model control inputs and sensor outputs.

Analysis predicted that both LVF LAC controllers for Phase 2 should be closed-loop stable independent of the HAC controllers. However, tests showed that LVF 1.2 in fact caused a low frequency rigid-body instability. Figures 3.24 and 3.25 show the singular values of the return difference transfer function matrix frequency responses at the control inputs and sensor outputs for LVF 1.1[8] and LVF 1.2. The minimum gain/phase margins for LVF 1.1 and LVF 1.2 occur at approximately 0.34 Hz and 0.29 Hz frequency respectively which corresponds to the rigid-body roll mode. The LVF 1.1 minimum gain/phase margins are $[-4.52, +9.96]$ dB and ± 39.88 degrees at both the control inputs and sensor outputs. The LVF 1.2 minimum gain/phase margins are $[-2.87, +4.31]$ dB and ± 22.56 degrees at both the control inputs and sensor outputs. The effects of actuators/sensors dynamics and time delays causes the gain/phase margins of the elastic modes to be reduced, with the greatest loss occurring at approximately 15 Hz frequency.

Figures 3.26 and 3.27 show the singular values of the return difference transfer function matrix frequency responses at the thruster command inputs and accelerometer sensor outputs for HAC/LAC 1.1 and HAC/LAC 1.2. The gain/phase margins for HAC/LAC 1.1 are $[-3.81, +6.95]$ dB and ± 31.96 degrees at the control inputs and $[-3.72, +6.64]$ dB and ± 31.01 degrees at the sensor outputs. The gain/phase margins for HAC/LAC 1.2 are $[-4.02, +7.72]$ dB and ± 34.24 degrees degrees at the control inputs and $[-3.76, +6.77]$ dB and ± 31.42 degrees at the sensor outputs.

In conclusion, the multivariable gain/phase margins of the HAC/LAC designs satisfied the original requirements of $[-3.52, +6.02]$ dB and ± 28.96 degrees.

[8]To apply Osborne's scaling to the frequency responses of LVF 1.1, the feedback gain for accelerometer/thruster #6 was perturbed from zero to a value of 10^{-5} to avoid an irreducible transfer matrix.

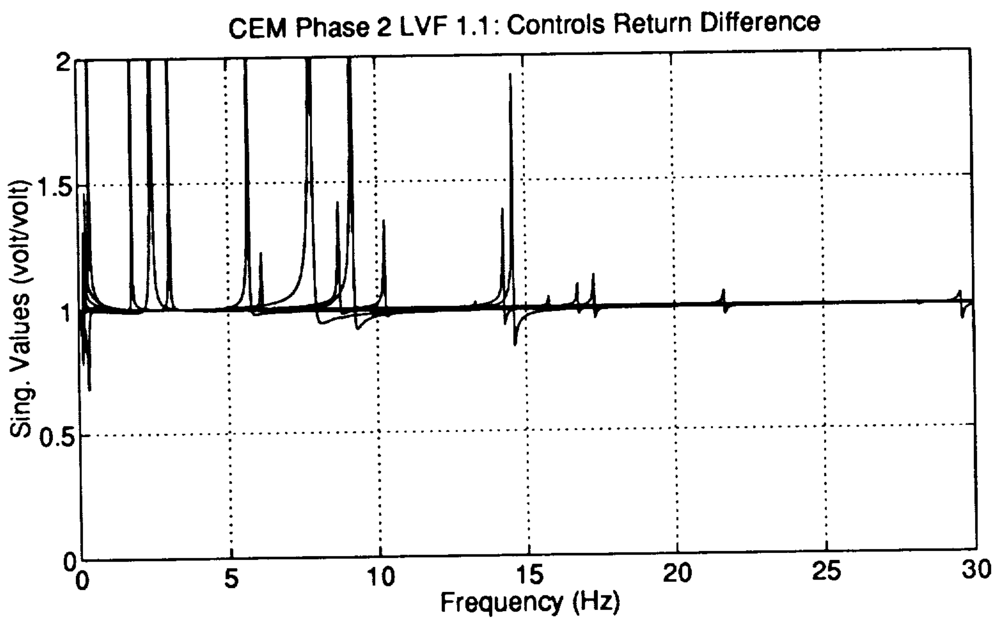

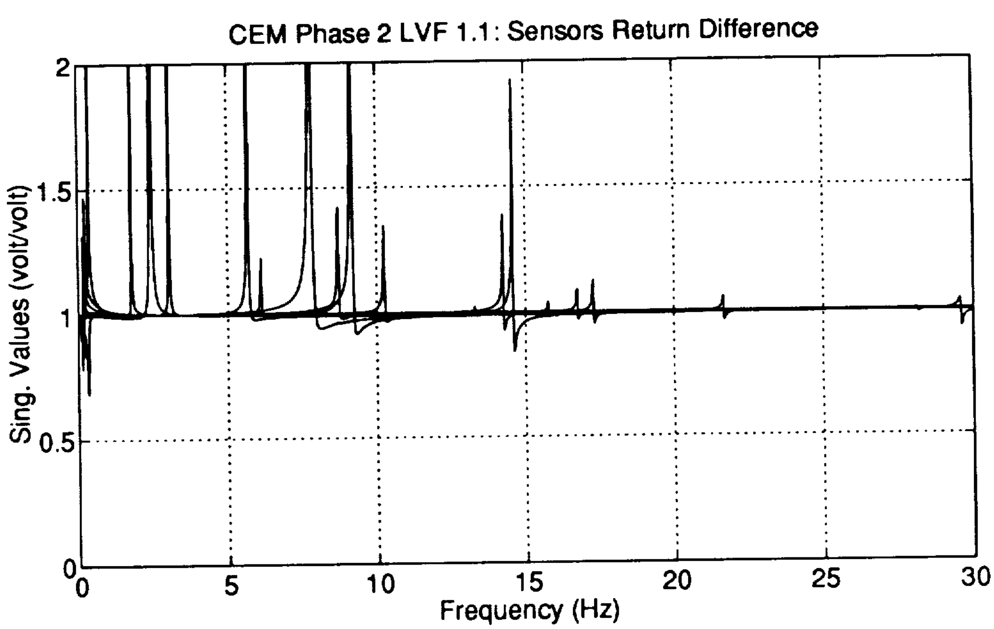

Figure 3.24: Phase 2 CEM LVF 1.1 Return Difference Transfer Function Matrix Frequency Response

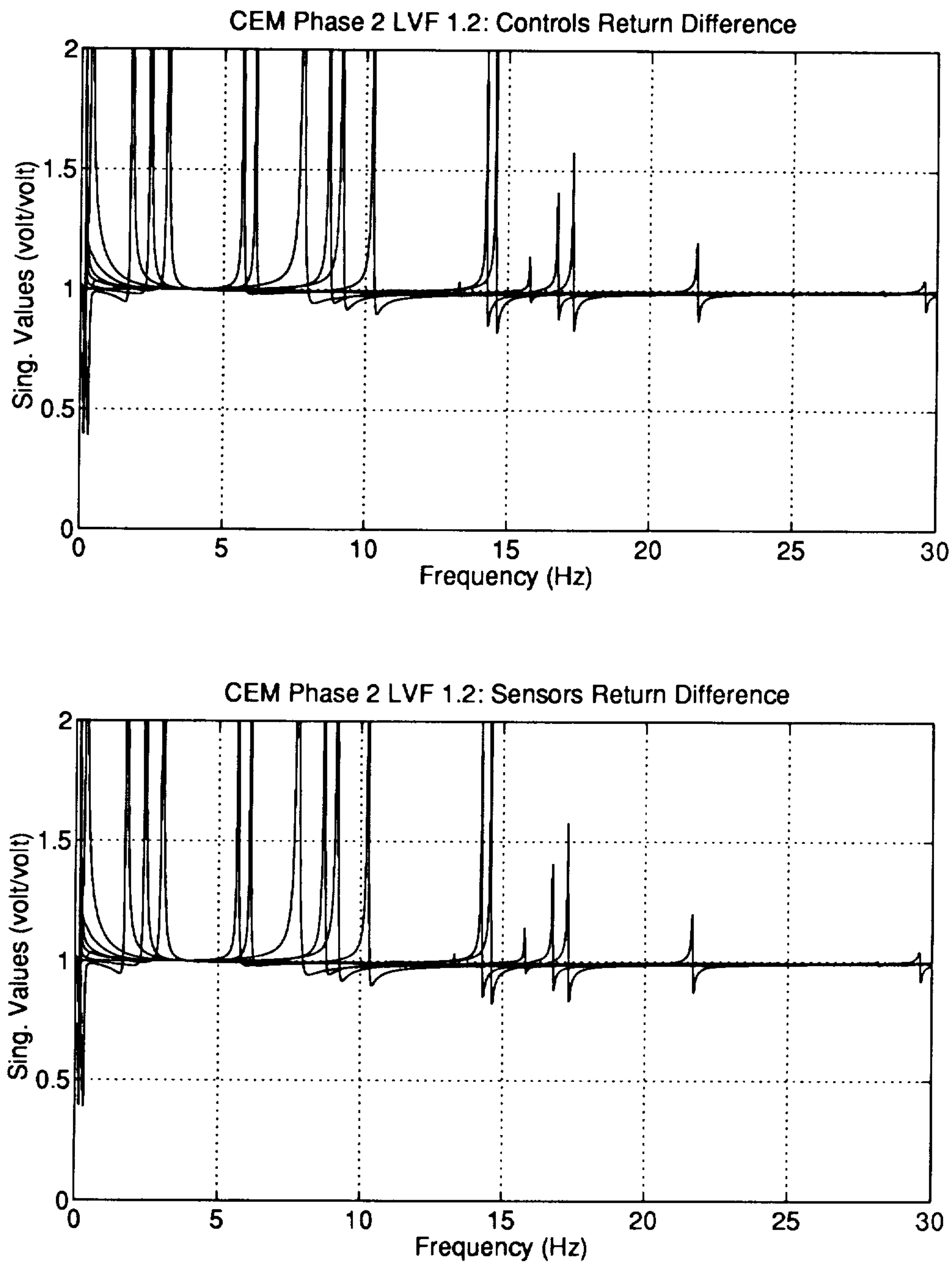

Figure 3.25: Phase 2 CEM LVF 1.2 Return Difference Transfer Function Matrix Frequency Response

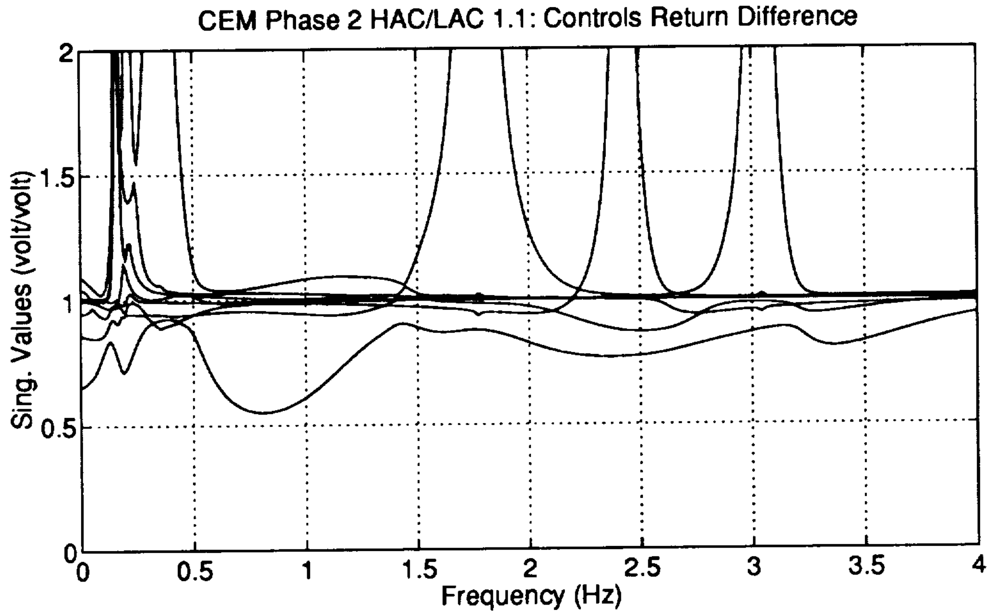

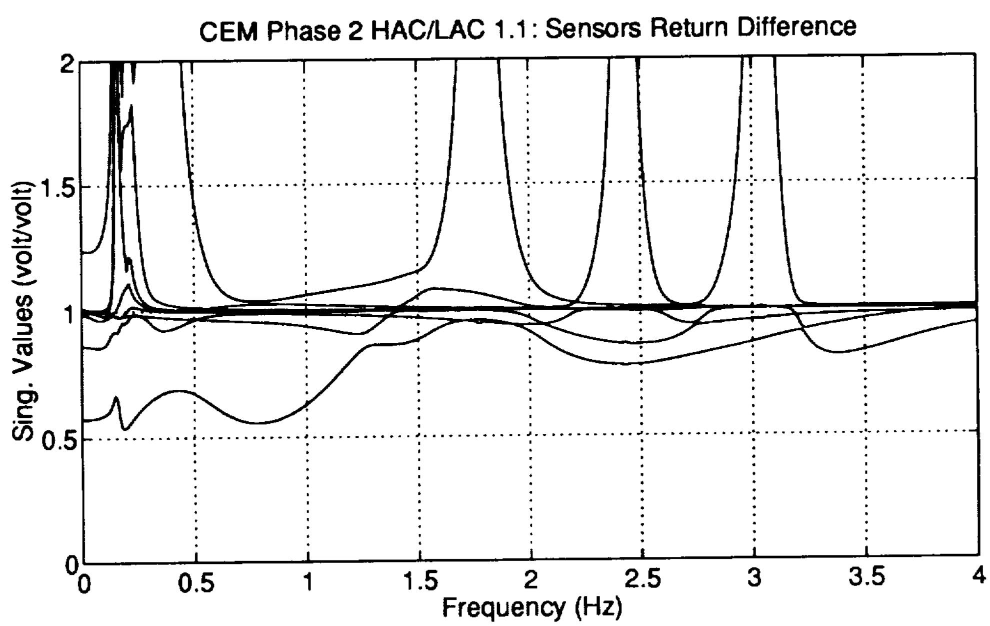

Figure 3.26: Phase 2 CEM HAC/LAC 1.1 Return Difference Transfer Function Matrix Frequency Response

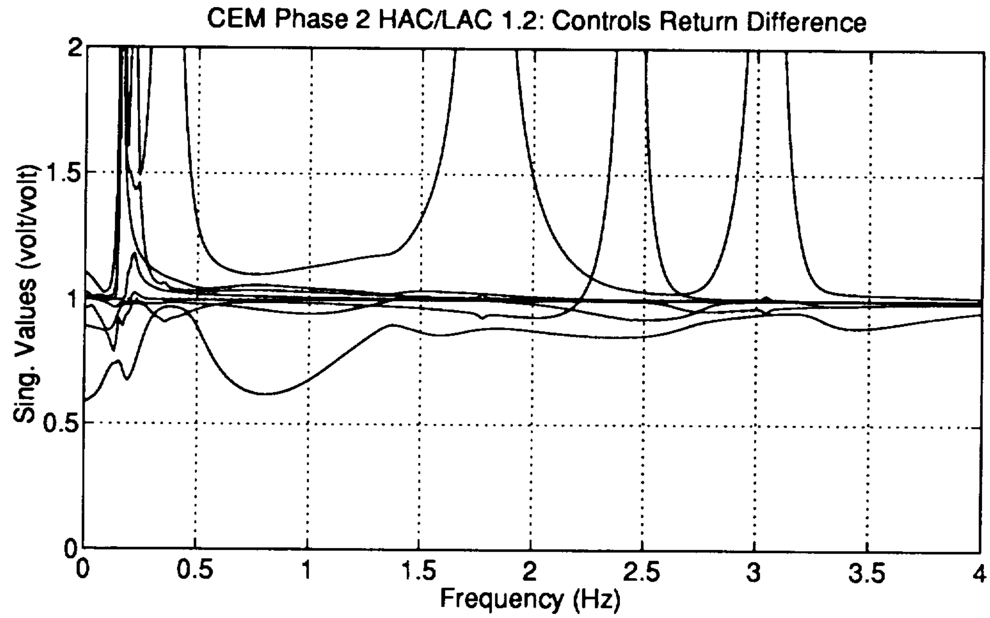

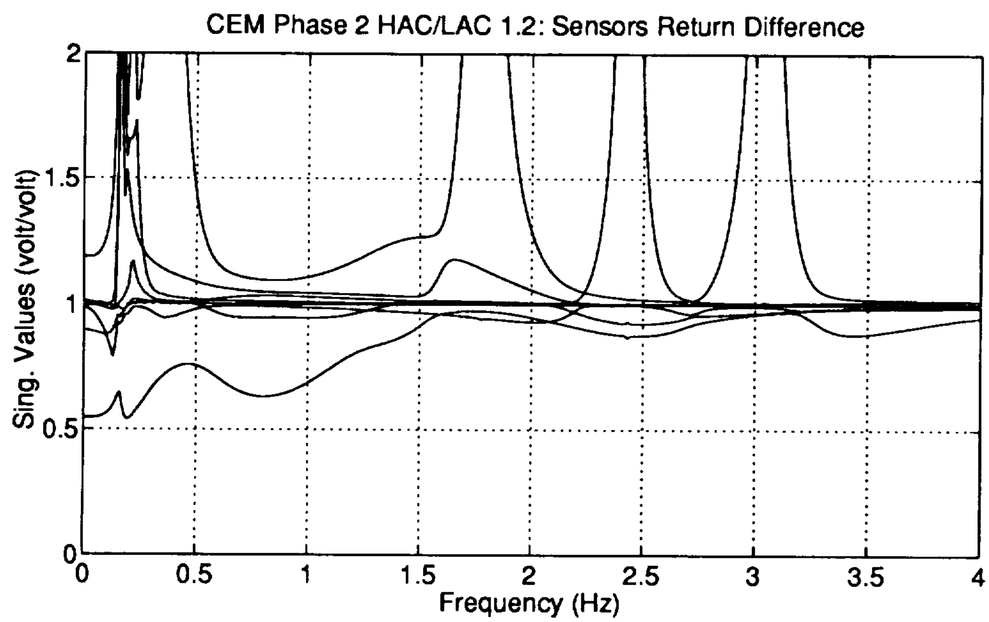

Figure 3.27: Phase 2 CEM HAC/LAC 1.2 Return Difference Transfer Function Matrix Frequency Response

High Frequency Roll-off Gain Margins

The multivariable roll-off gain margins of the HAC controllers was analyzed at the inputs and outputs of the HAC controller. Recall that the LVF LAC controller is not required to gain stabilize the elastic modes just outside the bandwidth of the HAC. Thus the roll-off analysis is only applied to the inputs and outputs of the HAC controller and not to the combined HAC/LAC. Figures 3.28–3.29 show the singular values of the open-loop transfer function matrix frequency responses for the HAC 1.1 and HAC 1.2 control laws. The responses are shown for the loops opened at the inputs and outputs of the HAC controllers. The minimum roll-off gain margins are 28 dB for HAC 1.1 and 31 dB for HAC 1.2. The roll-off gain margins are greater than those of the H_2/LQG designs due to the vibration suppression properties of the LAC inner loop.

Experimental Closed-Loop Performance

The same tests were performed to access the closed-loop performance as was performed for the H_2/LQG control designs. The test results showed that the HAC/LAC control designs provided strong attenuation of the first three main truss structural bending/torsional modes. The higher frequency elastic mode responses outside the bandwidth of the HAC were also attenuated by a lesser amount due to the action of the LAC LVF inner loop. Results from each of the test are discussed below.

Figure 3.30 show the measured closed-loop transient responses of gimbal #1 OSS x and y LOS for the HAC/LAC 1.1 control design. The measured responses for HAC/LAC 1.2 are shown in Figure 3.31. The responses were obtained by exciting the system with sinusoidal thruster inputs for 7 seconds with the control loops open. The sinusoidal thruster inputs were chosen at the approximate frequencies of the first three bending/torsional modes. The control loops were then closed at 10 seconds.

Figures 3.32 and 3.33 show the measured open and closed-loop frequency responses for the two control laws. HAC/LAC 1.2 provides greater than 10:1 attenuation of the peak responses of the first three main truss bending/torsional modes. Due mostly to the higher LVF gains of the inner loop LAC controller, HAC/LAC 1.2 is seen to have slightly better performance than HAC/LAC 1.1. As seen from the frequency response plots, the LAC controller provides active damping to the elastic modes above 4 Hz. Identified damping levels for the modes in the 4–10 Hz range are increased by a factor of 2 to 3 from the open-loop values.

Closed-loop responses to random disturbances were measured for the HAC/LAC designs. The disturbances were Gaussian random thruster commands in a frequency band from 1–10 Hz. The measured and predicted RMS values were computed from the OSS LOS responses over a 120 second time interval. Tables 3.5 and 3.6 list

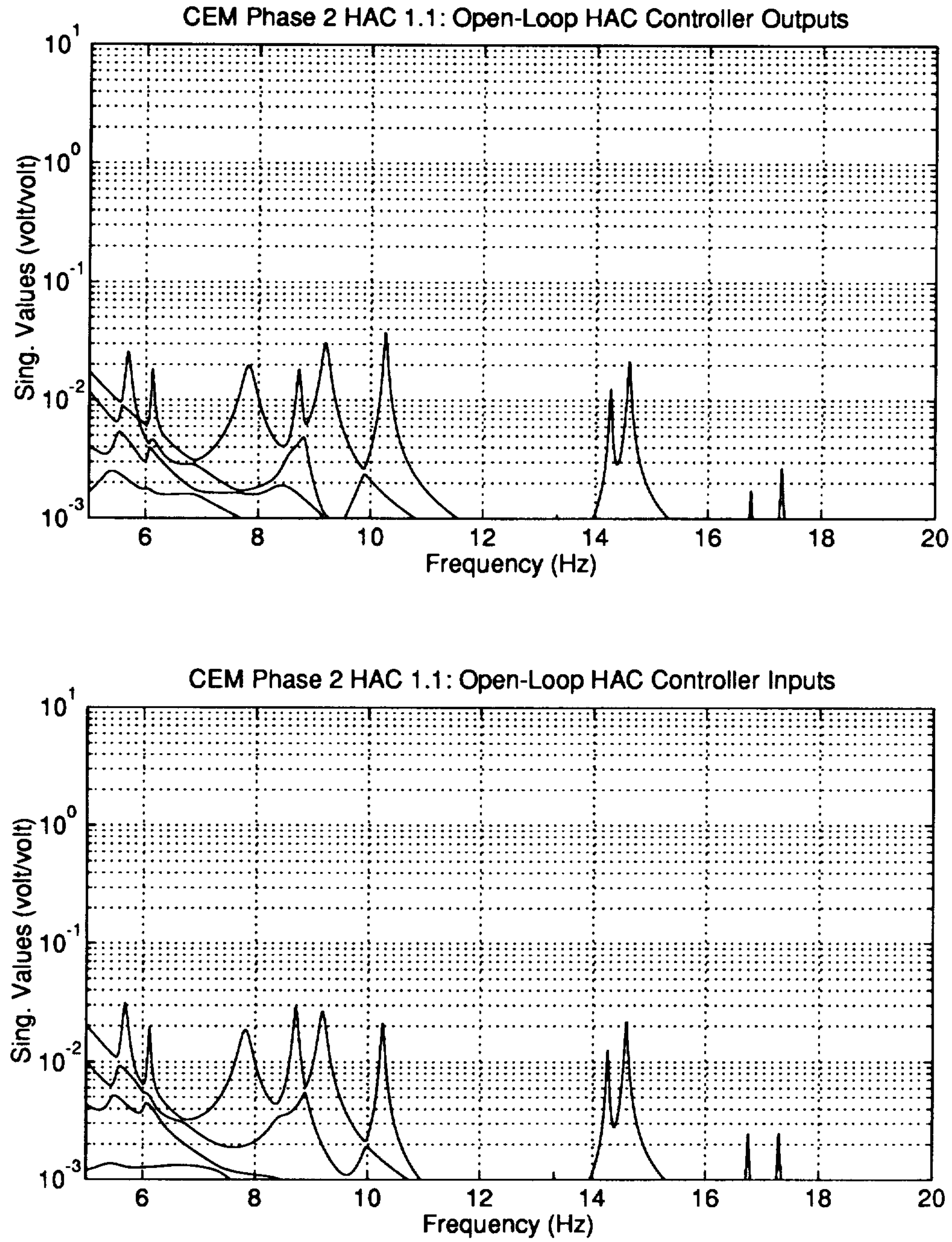

Figure 3.28: Phase 2 CEM HAC 1.1 Open-Loop Frequency Response Singular Values

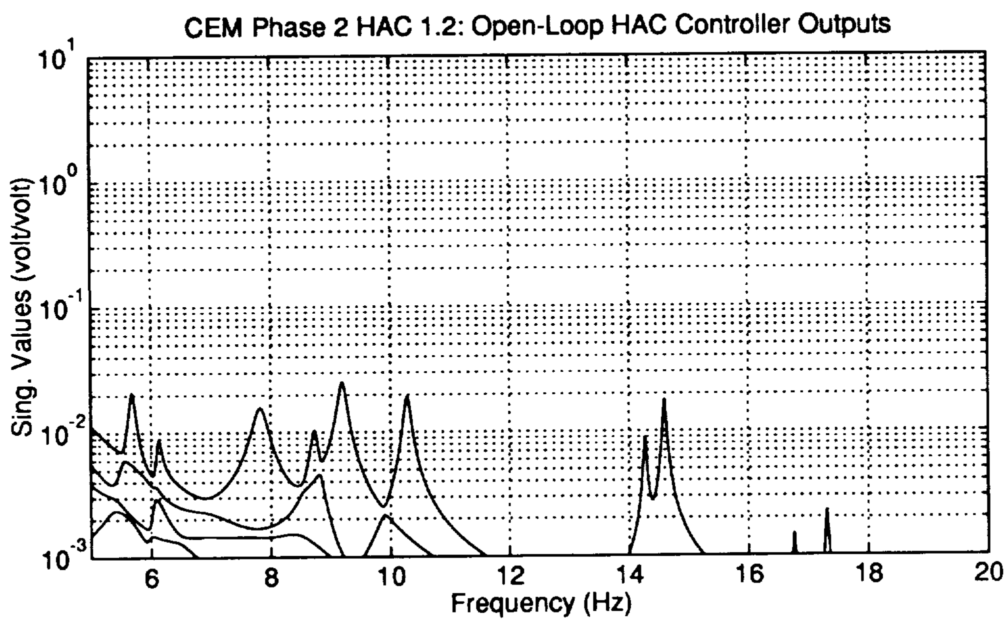

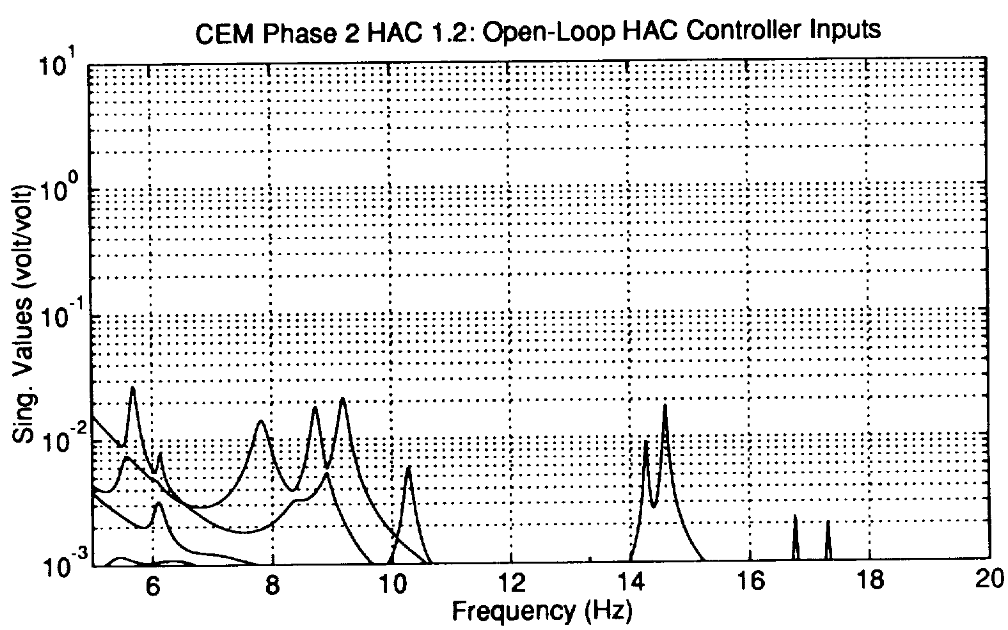

Figure 3.29: Phase 2 CEM HAC 1.2 Open-Loop Frequency Response Singular Values

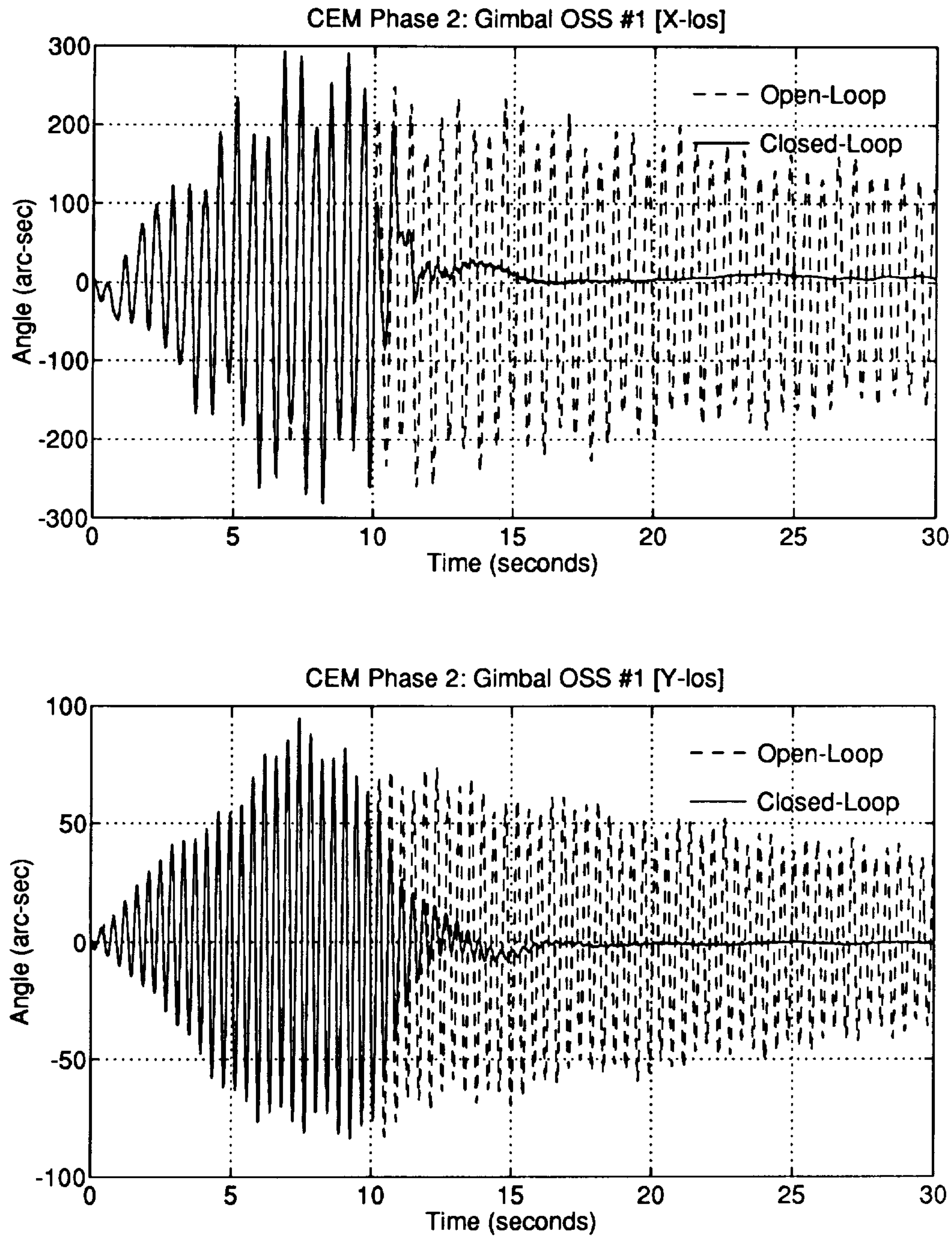

Figure 3.30: Phase 2 CEM HAC/LAC 1.1 Measured Open and Closed Loop Transient Responses

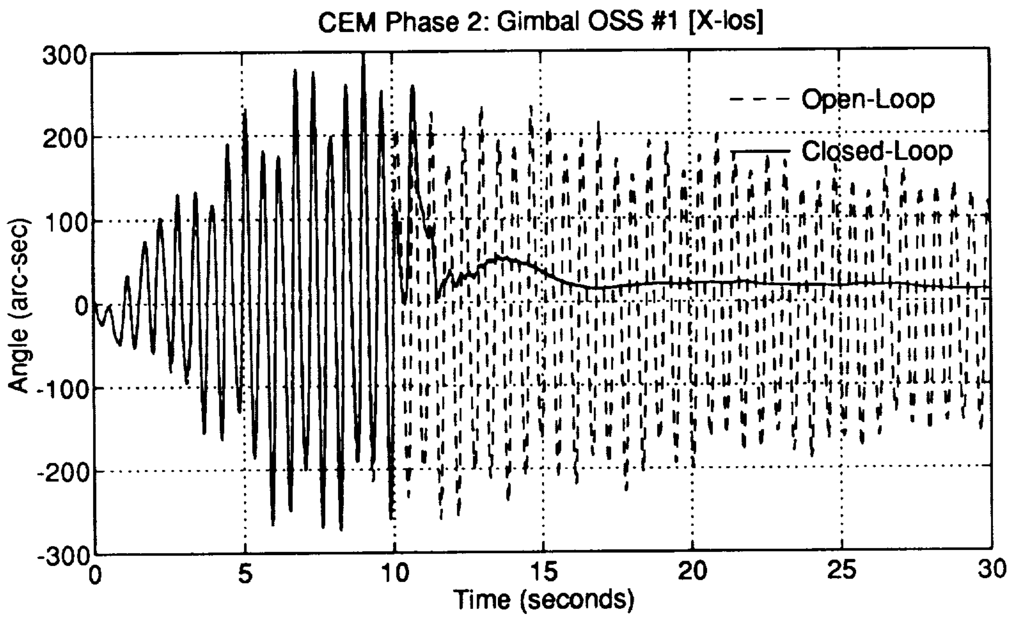

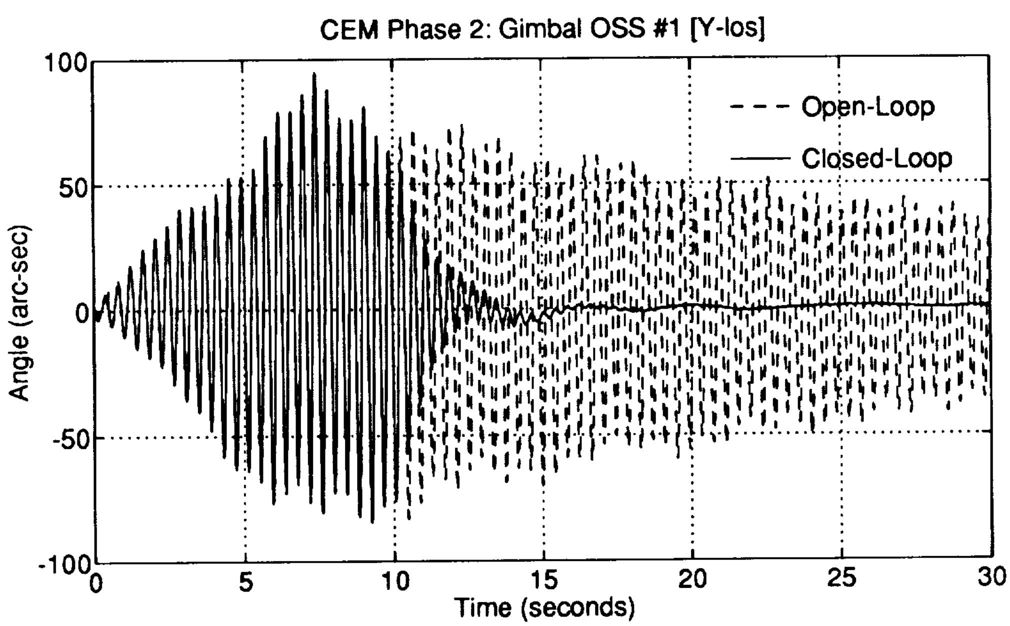

Figure 3.31: Phase 2 CEM HAC/LAC 1.2 Measured Open and Closed Loop Transient Responses

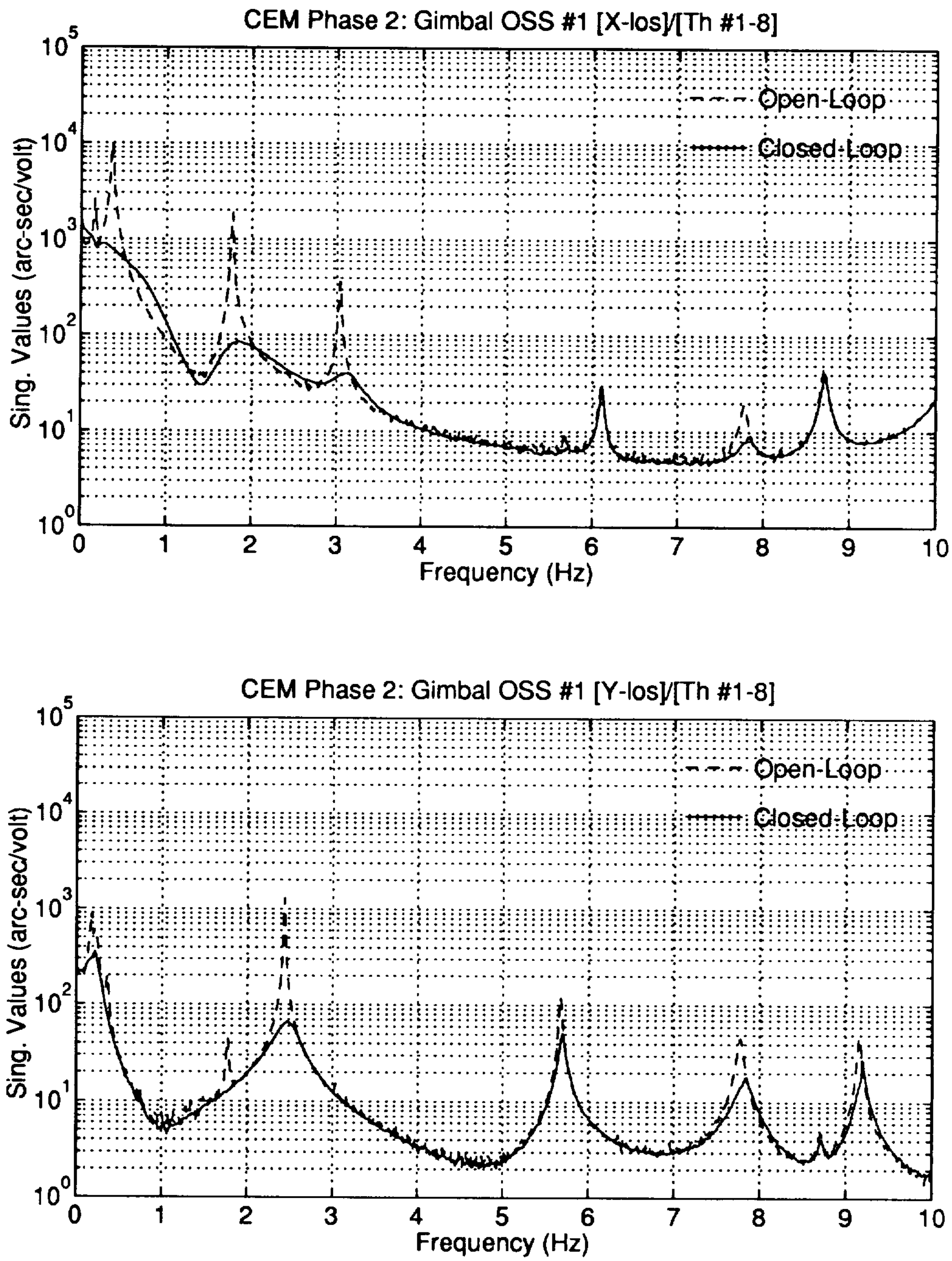

Figure 3.32: Phase 2 CEM HAC/LAC 1.1 Measured Open and Closed Loop Frequency Responses

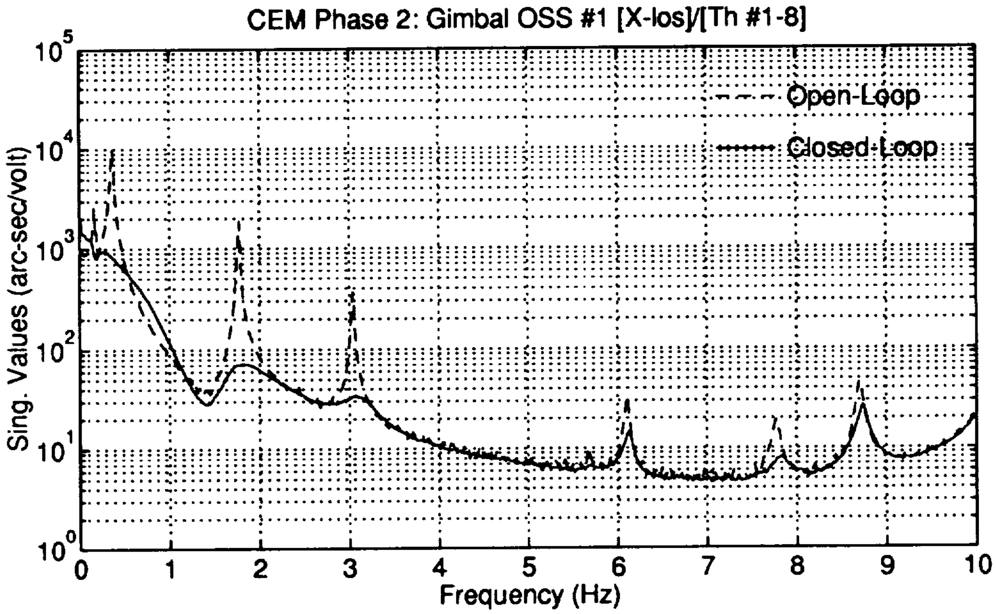

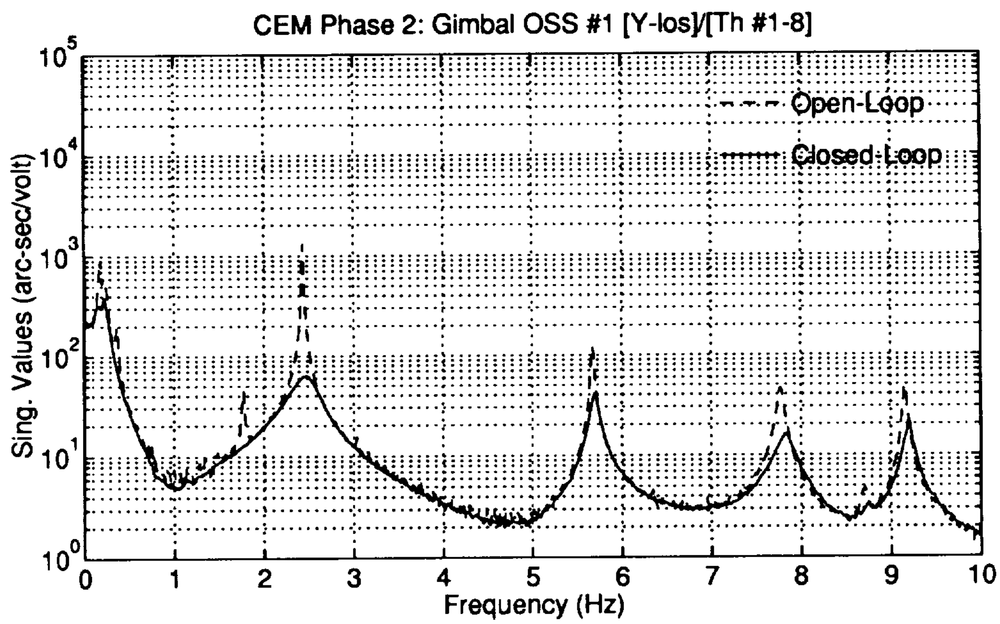

Figure 3.33: Phase 2 CEM HAC/LAC 1.2 Measured Open and Closed Loop Frequency Responses

Table 3.5: Phase 2 CEM HAC/LAC 1.1 Closed-Loop RMS Values of Random Disturbance Responses

Output/Control Command	Measured Open-Loop	Measured Closed-Loop	Predicted Closed-Loop
Gimbal OSS #1 x LOS (arc-sec)	146.1	57.31	60.11
Gimbal OSS #1 y LOS (arc-sec)	75.08	14.96	14.50
Gimbal OSS #2 x LOS (arc-sec)	127.6	54.71	44.86
Gimbal OSS #2 y LOS (arc-sec)	71.31	14.29	11.58
Gimbal OSS #4 x LOS (arc-sec)	202.6	75.87	72.95
Gimbal OSS #4 y LOS (arc-sec)	75.77	16.16	14.27
Thruster #1 Command (volts)	0.0	0.1165	0.1044
Thruster #2 Command (volts)	0.0	0.1240	0.1256
Thruster #3 Command (volts)	0.0	0.2512	0.2246
Thruster #4 Command (volts)	0.0	0.1701	0.1586
Thruster #5 Command (volts)	0.0	0.0985	0.0976
Thruster #6 Command (volts)	0.0	0.1886	0.1660
Thruster #7 Command (volts)	0.0	0.1275	0.1190
Thruster #8 Command (volts)	0.0	0.2960	0.2648

the measured and predicted RMS values of the OSS LOS outputs and the controller commands for both control designs. The open-loop RMS values are also shown for comparison. The average RMS LOS output reductions achieved with HAC/LAC 1.2 are 66% for the x LOS output and 80% for the y LOS output.The measured and predicted values for the OSS LOS and controller commands show generally close agreement.

Experimental Verification of Control Law Sensitivity

The close agreement between the predicted and measured RMS values of the LOS responses in Tables 3.5 and 3.6 indicate that the closed-loop LOS responses were relatively insensitive to the model inaccuracies. Figures 3.34 and 3.35 show the measured and predicted closed-loop frequency responses for both control laws. The measured and predicted frequency responses show excellent agreement for the frequencies within the control bandwidth (0–4 Hz) and good agreement up to 10 Hz.

The sensitivity of the control designs to artificial gain variations at the control inputs was tested. The tests involved increasing the feedback gains simultaneously

Table 3.6: Phase 2 CEM HAC/LAC 1.2 Closed-Loop RMS Values of Random Disturbance Responses

Output/Control Command	Measured Open-Loop	Measured Closed-Loop	Predicted Closed-Loop
Gimbal OSS #1 x LOS (arc-sec)	146.1	48.48	52.55
Gimbal OSS #1 y LOS (arc-sec)	75.08	14.60	14.09
Gimbal OSS #2 x LOS (arc-sec)	127.6	47.37	41.26
Gimbal OSS #2 y LOS (arc-sec)	71.31	14.08	11.35
Gimbal OSS #4 x LOS (arc-sec)	202.6	66.85	66.05
Gimbal OSS #4 y LOS (arc-sec)	75.77	15.74	13.83
Thruster #1 Command (volts)	0.0	0.1409	0.1384
Thruster #2 Command (volts)	0.0	0.1313	0.1329
Thruster #3 Command (volts)	0.0	0.2334	0.2157
Thruster #4 Command (volts)	0.0	0.1673	0.1552
Thruster #5 Command (volts)	0.0	0.1234	0.1234
Thruster #6 Command (volts)	0.0	0.2052	0.1906
Thruster #7 Command (volts)	0.0	0.1321	0.1225
Thruster #8 Command (volts)	0.0	0.2785	0.2581

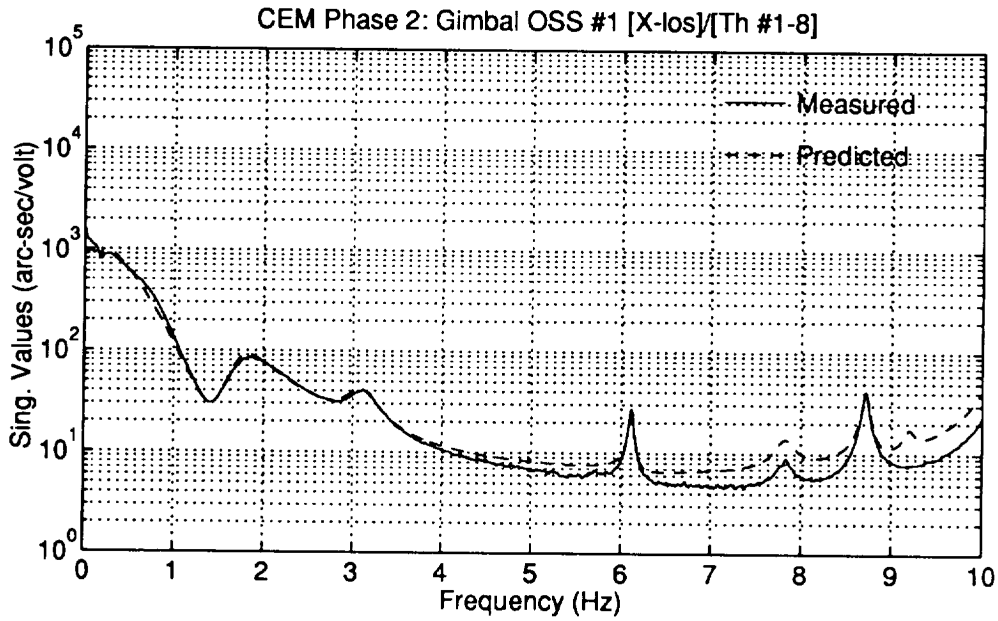

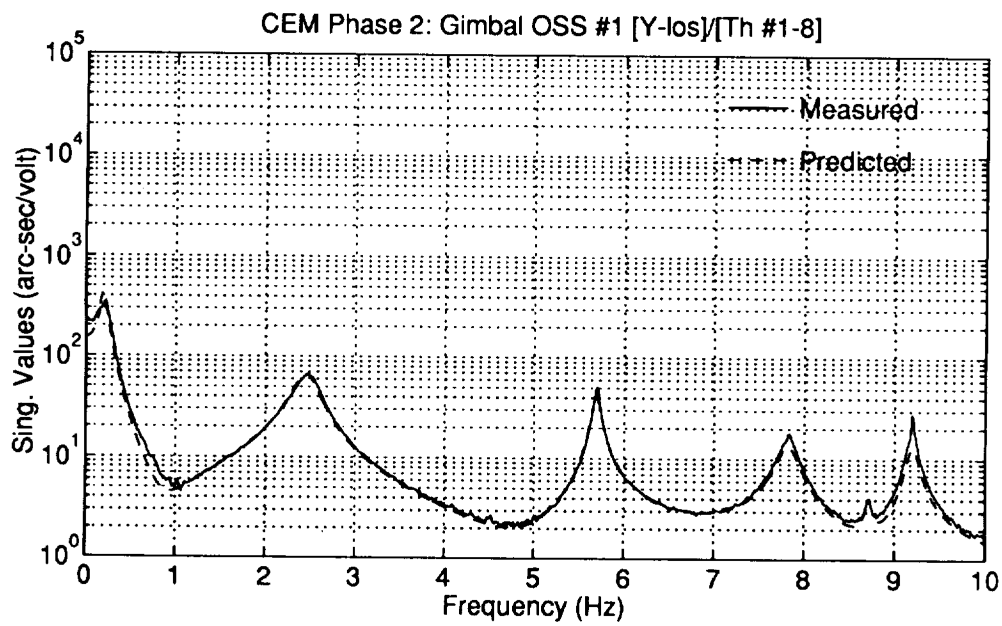

Figure 3.34: Phase 2 CEM HAC/LAC 1.1 Measured and Predicted Closed-Loop Frequency Responses

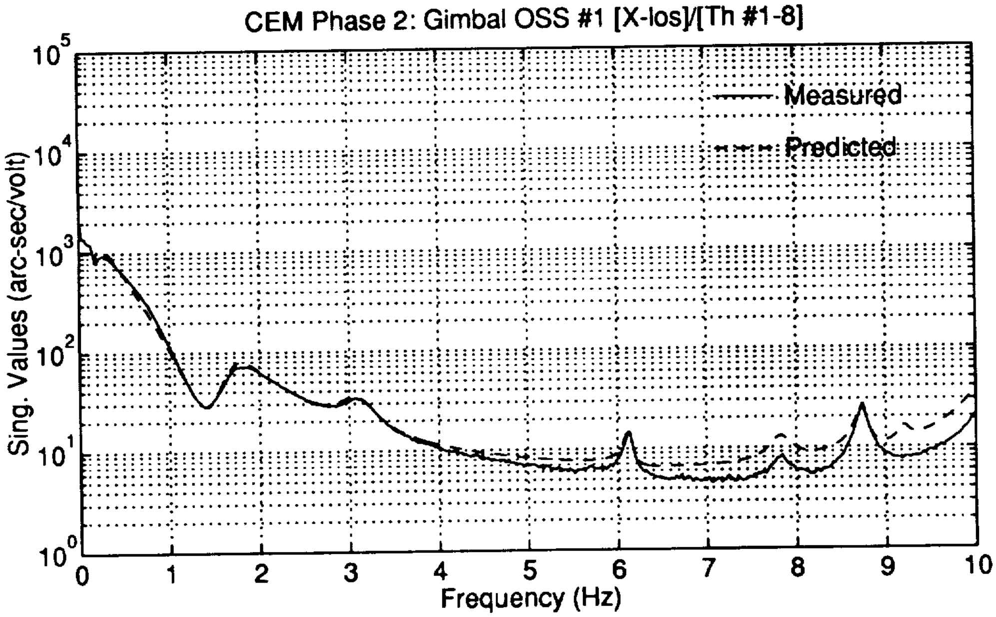

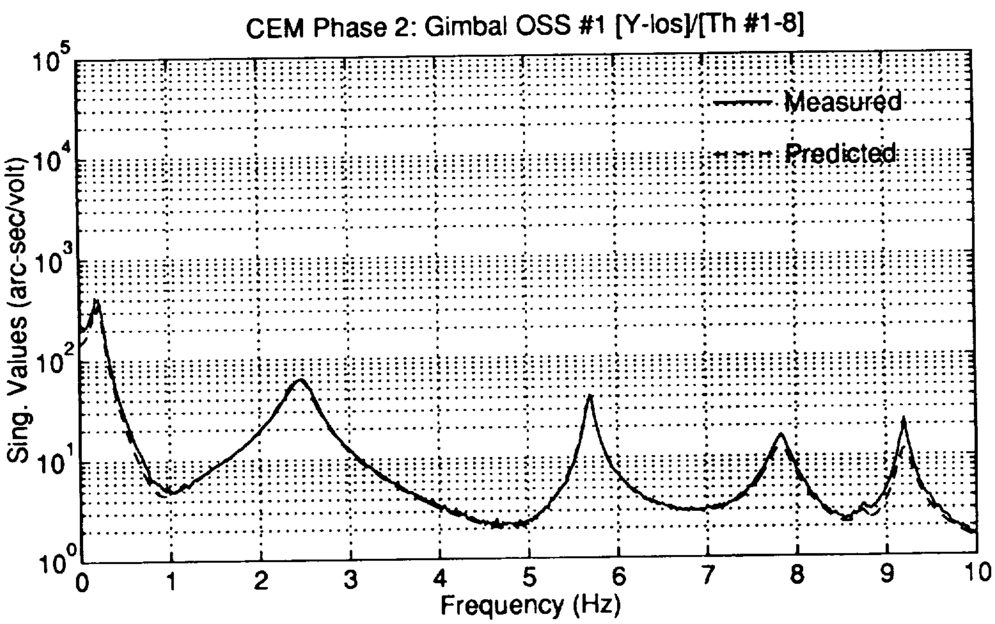

Figure 3.35: Phase 2 CEM HAC/LAC 1.2 Measured and Predicted Closed-Loop Frequency Responses

Table 3.7: Phase 2 CEM HAC/LAC 1.2 and H_2/LQG A1.4 Closed-Loop Damping Levels for the Dominant Elastic Modes

Mode Description	OL Freq. (Hz)	OL Damping (Percent)	HAC/LAC 1.2 Damping (Percent)	H_2/LQG A1.4 Damping (Percent)
First Torsion	1.8	0.3	12.3	14.8
Pitch First Bending	2.4	0.2	5.6	5.0
Yaw First Bending/Torsion	3.0	0.3	5.8	7.6
Pitch Second Bending	5.7	0.3	0.8	0.2
Yaw Second Bending/Torsion	6.1	0.3	0.8	0.3
Laser Tower/Main Truss	7.8	0.4	1.3	0.4
Second Torsion	8.7	0.3	0.7	0.3
Pitch Third Bending	9.1	0.2	0.5	0.2
Laser-Tower/Susp. Truss	10.2	0.2	0.4	0.2

in all control loops (using the CPOT parameter in the real-time software) from the nominal value (CPOT=1.0) until an instability or limit-cycle was observed. For the HAC/LAC 1.2 design, a limit-cycle was observed at a CPOT gain of 1.9 involving the 7.93 Hz laser tower/main truss mode. The peak amplitude for this limit-cycle response was approximately 0.6 in/sec^2 as measured by accelerometer #7. The laser tower/main truss mode limit cycle is most likely due to unmodeled actuator/sensor dynamics affecting the LVF inner loop stability.

Comparison with the H_2/LQG Controller

Figure 3.36 shows a comparison of the closed-loop frequency responses for the H_2/-LQG A1.4 with those of the HAC/LAC 1.2 controller. The HAC/LAC controller provides similar attenuation of the modes from 1–4 Hz (within the active control bandwidth of the H_2/LQG and HAC controllers) compared with the H_2/LQG controller while providing additional damping to the modes above 4Hz. The identified closed-loop damping levels for the elastic modes below 12 Hz are given in Table 3.7 for each controller.

No significant difference in the RMS LOS level reductions is observed between the two controllers.

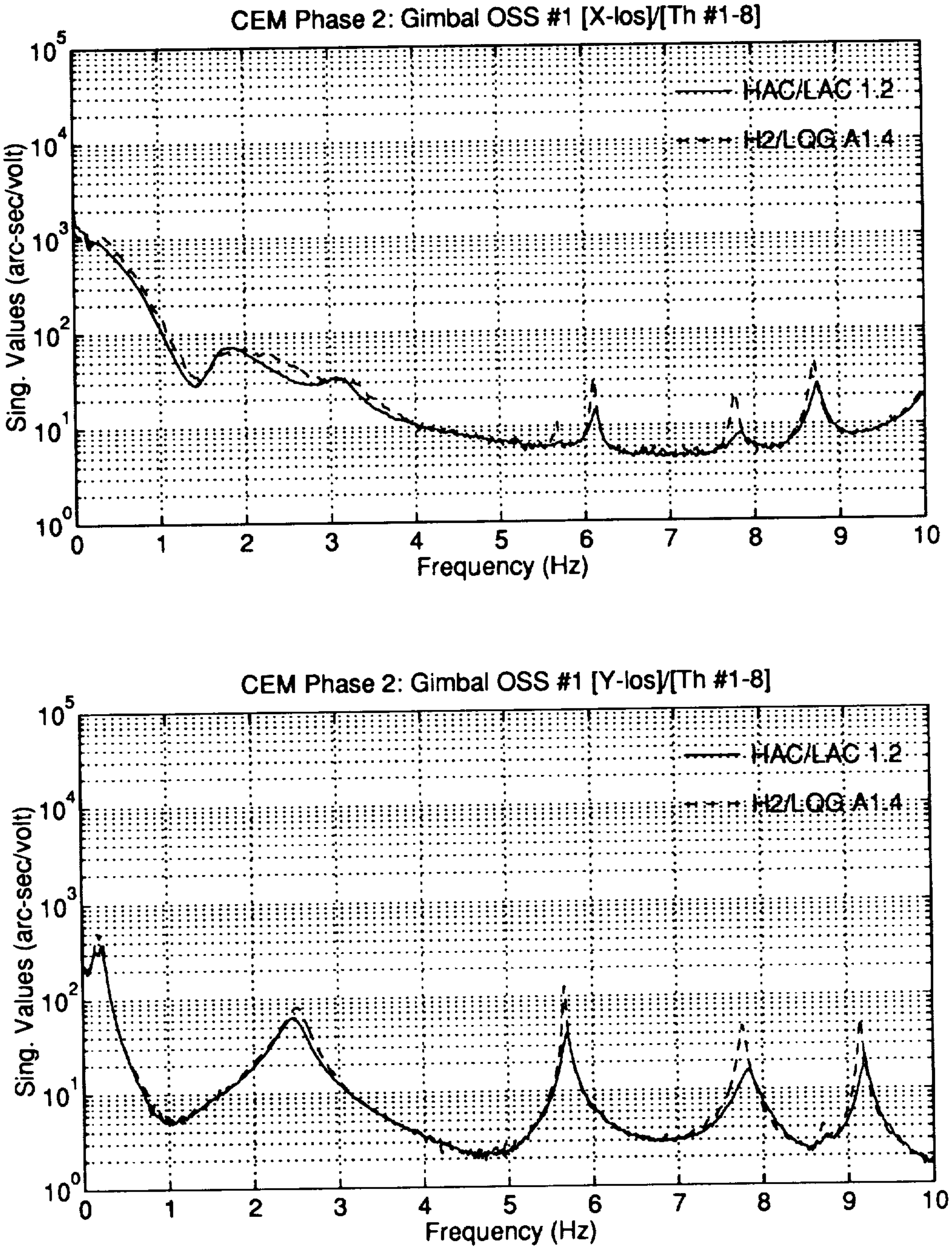

Figure 3.36: Phase 2 CEM HAC/LAC 1.2 and H_2/LQG A1.4 Measured Closed-Loop Frequency Responses

Chapter 4

Active/Passive Damping Design Methodology

4.1 Motivation

For future large space systems with stringent control requirements, sufficient performance is not obtainable using either active or passive techniques alone. In these cases it is often possible to combine high authority active control with passive damping treatments to achieve greater performance than with either technique alone.

A fundamental requirement of any control scheme is a certain level of knowledge about the system which is to be controlled. Without this minimum level of knowledge, it is likely that the closed-loop system objectives will not be achieved. Passive damping techniques and certain control schemes like local velocity feedback (LVF) can inherently tolerate high levels of plant uncertainties. The main drawback to these techniques is that the system performance is often less than can be obtained using optimal control techniques such as H_2/LQG or H_∞ which rely on having more information about the plant.

Often for large space systems, considerably more information is available about the plant dynamics than is required for the application of robust control schemes such as LVF or passive damping alone. The central problem is to determine which aspects of the dynamics are known accurately and which are considered uncertain. A high authority active controller (HAC) can then be designed to control the known dynamics while robust techniques are employed to control the uncertain dynamics.

To ensure stability, uncertain dynamics must be robustly gain stabilized by the high performance active controller. Robust gain stabilization can be achieved in one of two ways: 1) by using roll-off filters in the controller or 2) by reducing the gain of the uncertain dynamics through the use of a robust low authority control technique such as an LVF inner loop, or passive damping treatments. Roll-off filters, as opposed to notch filters, provide wide-band gain reduction to account for frequency uncertainties. The use of roll-off filters, for obvious reasons, is generally restricted to frequencies outside the bandwidth of the high authority active controller. Roll-off filters have the undesirable effect of increasing the controller order and complexity and they can severely limit the performance of the HAC controller.

The option of using a LAC inner loop to reduce the gain of uncertain dynamics (vibration suppression) was explored in Section 3.4. The LAC inner loop also serves to increase performance by damping vibrations outside the bandwidth of the HAC controller in a robust fashion. The use of a LAC controller suffers from the same drawbacks as the use of roll-off filters of increased controller order and complexity. As we demonstrate in this chapter, the use of passive damping treatments offers a potentially better solution to gain reduction of uncertain modes as compared to a LAC inner loop. While the vibration suppression ability of an LVF controller decreases rapidly with increasing frequency because of the effects of actuators/sensors dynamics, passive damping techniques can provide high levels of damping over a broad range of frequencies.

The discussion of an integrated active/passive damping controller for the CEM is presented in the next sections. After deriving the passive damping level requirements, the passive damping treatment design is discussed, followed by the detailed damped struts designs. The experimental verification of the passive damping treatment is then presented, followed by the design and experimental performance of the active/passive controller.

4.2 Derivation of Requirements

A design process for the combined active HAC controller and passive damping treatment proceeds as follows:

1. A high authority control law is designed to satisfy the design objective and requirements within the bandwidth of the known dynamics[1].

2. Uncertain modes are targeted for passive damping treatment and damping requirements are derived based on performance goals and robustness requirements of the active controller (assuming that the desired modal damping ratios can be achieved directly without modifying the mode shapes).

[1]The known dynamics refers to modes which are sufficiently well modeled to be robustly phase stabilized. The bandwidth of known dynamics may also include modes which are too uncertain to phase stabilize.

3. The damping requirements are used as the damping goals to design a damping treatment for the targeted modes.

4. A damped FEM is generated from the damping design.

5. The closed-loop performance objective and robustness are analyzed. If the design is not satisfactory then the process returns to step (1) using the latest damped model.

More than one iteration may be necessary if the passive damping requirements are not achievable or if the addition of the passive treatment significantly modifies the known dynamics.

The approach described above for the combined design of an active high authority controller with passive damping treatments was successfully applied to the Phase 2 CEM test article. The CEM dynamics at frequencies greater than 4 Hz were considered too uncertain to be actively controlled (e.g. phase stabilized) by the HAC controller and could not be rolled off without decreasing performance within the control bandwidth. To obtain the required roll-off, these modes were targeted for passive damping.

An H_2/LQG HAC controller was designed to suppress the disturbance responses of the OSS LOS outputs for modes in the 0–4 Hz frequency band. The controller design requirements and design process were the same as described in Sections 3.1 and 3.3. On the first iteration of the passive damping requirements derivation, the undamped model was used for the controller design. The roll-off gain margin requirement was reduced to 0 dB with the undamped model, and the design weights were adjusted to obtain a higher performance controller than the designs in Chapter 3. In subsequent iterations of the passive damping requirements derivation, the damped model from the previous iteration was used for the controller design.

For each controller design, the modal damping ratios of the targeted modes in the model were tuned by hand to obtain the required passive damping values. The criteria for selecting the modal damping ratios were derived from the OSS LOS disturbance frequency responses and from the roll-off of the high authority controller. The peak values of the maximum singular values of the disturbance frequency response to each OSS LOS output were required to be less than 60 arc–seconds (approximately equal to the peak value of the closed-loop responses in the 1–4 Hz frequency range). The minimum roll-off gain margin requirement was 20 dB (although the active controller was later redesigned with less roll-off gain margin). The required modal damping ratios were selected as the minimal values necessary to satisfy both the performance and the roll-off requirements.

Only two iterations were required to obtain a satisfactory design. After the initial design iteration the active controller authority was increased and the damping treatments redesigned to take advantage of achievable passive damping values in excess of the initial damping requirements[2]. The final design damping requirements are listed in Table 4.1. Modes greater than 4 Hz frequency not listed in Table 4.1 did not require any additional damping greater than what was inherent to the structure (assumed to be at least 0.1 percent).

4.3 Passive Damping Treatment Design

As discussed above, the motivation for incorporation of passive damping treatments into mechanical or structural systems is to enhance or enable the achievement of performance goals or requirements. The performance objectives are as diverse as the candidate systems. An automobile manufacturer wants to reduce passenger compartment noise. A computer manufacturer wants to decrease settling time for his disk drive head components. Sporting goods companies want to reduce vibrations of their products, such as baseball bats and tennis racquets. Launch vehicle companies want to reduce the severity of payload and instrument environments. Spacecraft manufacturers want to increase reliability of their satellites, and increase their capabilities, such as pointing accuracies.

In spite of the diversity of the examples listed above and the corresponding differences in design requirements and constraints, the process of arriving a satisfactory damping design is surprisingly similar for all these cases. An overview of the process used for the CEM will be presented here. This process is somewhat less general than could be applied if damping treatments were included at the beginning of the CEM design process, but the CEM design was substantially complete at the beginning of this project. The PACOSS (Passive and Active Control of Space Structures) program [18, 19, 20, 6] developed and demonstrated a more general approach applicable to systems when more design latitude is available.

This discussion assumes that the reader is familiar with finite element modeling, the representation of structural systems in modal coordinates, and has the ability to calculate performance metrics from system modes. The remaining analytic component of the process, the modal strain energy (MSE) method, is not widely known except to individuals involved in damping design. The MSE method will therefore be discussed before the damping design process is presented.

[2]The passive damping treatment and active controller were later redesigned to reduce the total number of dampers from 72 elements to 60 elements and to place the strongest elements at the locations in the structure with the highest static loads.

Table 4.1: CEM Phase 2 Final Passive Damping Requirements Derived From P2090992 Model

FEM Mode Number	FEM Frequency (Hz)	Damping Requirement (Percent)
10	5.497	1.35
11	5.928	2.1
20	7.632	1.25
21	8.495	1.5
22	9.022	0.5
23	10.177	2.1
28	12.741	2.3
33	13.589	1.7
34	13.796	1.2
35	14.122	0.9
36	14.353	1.7
38	15.684	0.2
39	16.447	1.0
44	18.097	0.2
49	18.517	0.2
50	18.771	0.2

4.3.1 Modal Strain Energy Method

The literature contains numerous justifications of the MSE method. Johnson and Kienholz[21] are generally credited with first putting heuristic arguments on a more firm ground. This discussion is based on their presentation.

A common model for viscoelastic materials is given by

$$\bar{G} = G(1 + i\eta_\nu), \tag{4.1}$$

where

$\bar{G}$ = the complex shear modulus,

$i = \sqrt{-1}$,

G = real part of the shear modulus,

η_ν = viscoelastic material loss factor.

Typically, both the shear modulus and loss factor are functions of frequency and temperature. For purposes of this discussion, we will initially assume that these quantities are constant.

The equations of motion for free vibration for a finite element representation of a structure containing viscoelastic elements is given by

$$M\ddot{x} + \bar{K}x = 0 \tag{4.2}$$

where

M = the mass matrix,

x = the physical degrees of freedom,

$\bar{K}$ = the complex stiffness matrix.

The complex stiffness matrix has three components,

$$\bar{K} = K_e + K_{\nu R} + iK_{\nu I}, \tag{4.3}$$

where

K_e = is the component representing the purely elastic elements,

$K_{\nu R}$ = is the component representing the real part of the viscoelastic elements,

$K_{\nu I}$ = is the component representing the imaginary part of the viscoelastic elements.

Implicit in this representation is the assumption that viscoelastic materials are the only complex elements in the structure.

Let

$$K_R = K_e + K_{\nu R}, \tag{4.4}$$

$$K_I = K_{\nu I}. \tag{4.5}$$

First consider the more familiar problem consisting of the real portion of 4.2

$$M\ddot{x} + K_R x = 0. \tag{4.6}$$

We assume a solution of the form

$$X = \phi e^{ipt}, \tag{4.7}$$

the solution to which is a set of eigenvectors ϕ and eigenvalues p. The r^{th} eigenvalue and eigenvector are related by the Raleigh quotient

$$p_r^2 = \frac{\phi^{(r)T} K_R \phi^{(r)}}{\phi^{(r)T} M \phi^{(r)}} \tag{4.8}$$

We also note that the numerator of the above expression represents twice the strain energy for the structure as it deforms in the r^{th} mode shape. The strain energy may be in the form of elastic strain energy, potential energy due to geometric stiffness in the structure, or a combination of the two. Johnson and Kienholz did not consider strain energy sources other than from elastic deformation. Modifications to the MSE method for cases where geometric stiffness contributes to the strain energy of a mode will be presented in a later section.

Returning to the complex problem represented by 4.2, we assume a solution of the form

$$X = \bar{\phi} e^{i\bar{p}t} \tag{4.9}$$

which has as a solution a set of complex eigenvalues and eigenvectors. The r^{th} members of the set are represented by

$$\bar{\phi}^{(r)} = \phi_R^{(r)} + i\phi_I^{(r)}, \tag{4.10}$$

$$\bar{p}_r = p_{(r)}\sqrt{1 + i\eta^{(r)}}. \tag{4.11}$$

In 4.11, $\eta^{(r)}$ is the loss factor for the r^{th} mode, which is numerically equal to twice the modal viscous damping.

The Rayleigh quotient for the complex modes is given by

$$p_r^2\left(1+i\eta^{(r)}\right)=\frac{\bar{\phi}^{(r)T}K_R\bar{\phi}^{(r)}}{\bar{\phi}^{(r)T}M\bar{\phi}^{(r)}}+i\frac{\bar{\phi}^{(r)T}K_I\bar{\phi}^{(r)}}{\bar{\phi}^{(r)T}M\bar{\phi}^{(r)}} \tag{4.12}$$

We regard K_I as a perturbation of the real stiffness matrix, and assume that the real eigenvectors derived by neglecting the imaginary portion of the stiffness matrix are a good approximation to the complex eigenvectors. This approximation is valid for low damping levels, where "low" depends on the intended use of the mode shapes. Frequently, this approximation is sufficiently accurate for modes with damping levels of up to 10 percent.

Then it follows that

$$p_r^2=\frac{\bar{\phi}^{(r)T}K_R\bar{\phi}^{(r)}}{\bar{\phi}^{(r)T}M\bar{\phi}^{(r)}} \tag{4.13}$$

and

$$p_r^2\eta^{(r)}=\frac{\bar{\phi}^{(r)T}K_I\bar{\phi}^{(r)}}{\bar{\phi}^{(r)T}M\bar{\phi}^{(r)}}. \tag{4.14}$$

From 4.13 and 4.14 it follows that

$$\eta^{(r)}=\frac{\bar{\phi}^{(r)T}K_I\bar{\phi}^{(r)}}{\bar{\phi}^{(r)T}K_R\bar{\phi}^{(r)}}. \tag{4.15}$$

If we restrict our attention to structures which contain only a single viscoelastic material, it follows from 4.1 and 4.5 that

$$K_I=\eta_\nu K_{\nu R}. \tag{4.16}$$

Thus,

$$\eta^{(r)}=\eta_\nu\left[\frac{\bar{\phi}^{(r)T}K_{\nu R}\bar{\phi}^{(r)}}{\bar{\phi}^{(r)T}K_R\bar{\phi}^{(r)}}\right]. \tag{4.17}$$

Now we consider the bracketed expression. The denominator represents twice the modal strain energy contained in the r^{th} mode for the real eigenproblem formed by neglecting the imaginary portion of the stiffness matrix. The numerator represents twice the modal strain energy contained in the viscoelastic material in the real eigenproblem. Thus, under the assumptions listed above, we can obtain an approximation to the modal loss factor by forming the real eigenproblem, calculating the portion of the modal strain energy contained in the viscoelastic elements, and multiplying by the loss factor of the viscoelastic material.

The argument above makes several assumptions which, in practice, are almost always violated. Most serious is the fact that the frequency dependency of the viscoelastic material properties has been neglected. Ref. [21] suggests a method of modifying the damping ratios to account for this variation, but a much better practice is to divide the frequency range of interest into small bands, use the average value of the viscoelastic properties within each band to form the corresponding eigenproblem, and combine the results for all the bands. Caution must be used near the boundaries of the bands to ensure that modes that have "crossed over" into the next band are not included twice. Because of the temperature dependency of the viscoelastic material, it may be necessary to repeat this process for several temperature values to obtain a model valid over the anticipated operational temperature range of the structure.

It is also common practice to apply more than one viscoelastic treatment to a structure, again a violation of the assumption made above. In practice for such cases, the numerator of 4.17 is formed by adding the contributions for each viscoelastic material, and the modal viscous damping for each mode is calculated by

$$\zeta^{(r)} = \frac{1}{2} \sum_{k=1}^{N} \eta_k^{(r)} \left[V_k^{(r)} / V^{(r)} \right], \tag{4.18}$$

where

$\zeta^{(r)}$ = the modal viscous damping for the r^{th} mode,

$\eta_k^{(r)}$ = the loss factor for k^{th} viscoelastic material at the r^{th} modal frequency,

$V_k^{(r)}$ = the modal strain energy in the k^{th} viscoelastic material in the r^{th} mode,

$V^{(r)}$ = the total modal strain energy in the r^{th} mode.

The expression in brackets in 4.18 is the fraction of the modal strain energy contained in the viscoelastic materials. That fraction multiplied by 100 is the percent of modal strain energy in the viscoelastic materials.

The MSE method, though approximate, is often sufficiently accurate for practical damping designs. For many applications required damping levels are low, and the real modes do provide an adequate approximation to the complex modes. Even in cases where complex modes or direct solutions to the complex dynamics problem may be required, the MSE method still provides a valuable, intuitive tool for designing damping treatments, and the more sophisticated analysis techniques are only required in the final stages of design.

4.3.2 Modification of the MSE Method for the CEM

The equations given above apply for structures wherein all the modal strain energy is due to elastic deformation. In the case of the CEM, many modes such as the pendulum-like suspension modes and suspension cable modes have a high percentage of their potential energies due to geometric stiffness. Obviously, no amount of damping treatment applied to a suspension cable will produce significant damping to the pendulum modes, but other modes may also contain a significant portion of their strain energy arising from geometric stiffness. If that strain energy is included in the strain energy in the numerator of 4.18, the damping predictions so obtained will be erroneously high. The above equations must be modified to compensate for the geometric strain energy by removing it from the damping calculations. This modification is accomplished by calculating the modal damping by applying the loss factors only to the elastic portion of the modal strain energies as follows:

$$\zeta^{(r)} = \frac{1}{2}\sum_{k=1}^{N}\eta_k^{(r)}\left[V_{ek}^{(r)}/V^{(r)}\right], \tag{4.19}$$

where

$\zeta^{(r)}$ = the modal viscous damping for the r^{th} mode,

$\eta_k^{(r)}$ = the loss factor for k^{th} viscoelastic material at the r^{th} modal frequency,

$V_{ek}^{(r)}$ = the elastic component of modal strain energy in the k^{th} viscoelastic material in the r^{th} mode,

$V^{(r)}$ = the total modal strain energy in the r^{th} mode.

The importance of this correction depends on the particular mode. For this program, MSC/NASTRAN was used for modeling. Straight recovery of modal strain energies for the CEM produces results which include the geometric stiffness portions. We have included elsewhere in this report DMAPs and procedures to perform the required calculations.

4.3.3 Overview of the CEM Damping Design Process

The process used to design the CEM damping treatment is shown in Figure 4.1. A FEM obtained from LaRC was used to calculate modes required for the control design process. As part of the process, described in Section 4.2, the control designer established modal damping goals. Note that these goals were established on a mode-by-mode basis, a practice that is more weight and cost efficient than merely specifying the same requirement for all modes. In addition to modes, modal strain energy distributions and static element loads are calculated.

The next step in the process is motivated by 4.19, which tells us that the most efficient way to damp selected modes is to place damping treatments in regions of high modal strain energy for modes targeted for passive damping. There are obviously other constraints, such as static loads, dynamic loads, or instrument locations, which might require a compromise in damping treatment placement. In the case of the CEM, the Phase 1 reflector ribs provided a good location for passive damping, but LaRC researchers decided to eliminate those ribs from the Phase 2 version. The ribs were therefore eliminated from consideration to maximize the carryover benefits to the Phase 2 model. Thus, only truss members were considered as candidates for damping treatments.

Once candidate locations have been selected, the damping treatment design process begins. Details of the damper designs are presented in Section 4.4. This discussion assumes that the design equations which predict the loss factors, stiffnesses, static stresses, and dynamic stresses of the strut dampers as a function of frequency are available. Note that for simple damping struts, 4.19 can be applied so that the loss factor and strain energies in the equation are for the damping struts as units, rather than for finite elements representing the struts.

From the candidate locations, a subset is selected which will provide the required damping for the targeted modes and will also satisfy other constraints. The struts in the original FEM are replaced with beam elements dynamically similar to the dampers for each selected frequency band. Modes, strain energies, modal damping, and loads are calculated. The modes are then used in the control simulation to verify performance and constraints are examined to ensure they are satisfied. Modifications to the design are made as required until a satisfactory solution is found.

4.3.4 Phase 1 CEM Damping Design

The design of the Phase 1 CEM damping treatment will be used as an example to clarify the process. The Phase 1 model would only be available for a short period of time, so it was decided to install only a small subset of the dampers to gain some experience with the structure and test a few prototype dampers before fabricating the entire complement. As mentioned above, the only candidate locations were in the trusses.

Previous investigators had identified the 7.8 Hz laser tower/main truss mode, shown in Figure 4.2, as being problematic for active control implementation. This mode would limit cycle or go unstable with a variety of active control approaches, so it was selected as the target mode for the Phase 1 structure. Our control design process identified this mode as being one for which passive damping would be beneficial, but it did not predict any instability.

We adopted the following set of design requirements as a conservative approach for the initial design:

1. The dampers would be able to replace any similar length strut in the CEM.

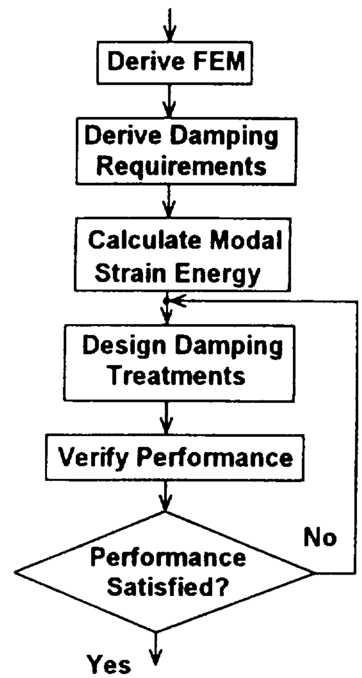

Figure 4.1: CEM Damping Design Process

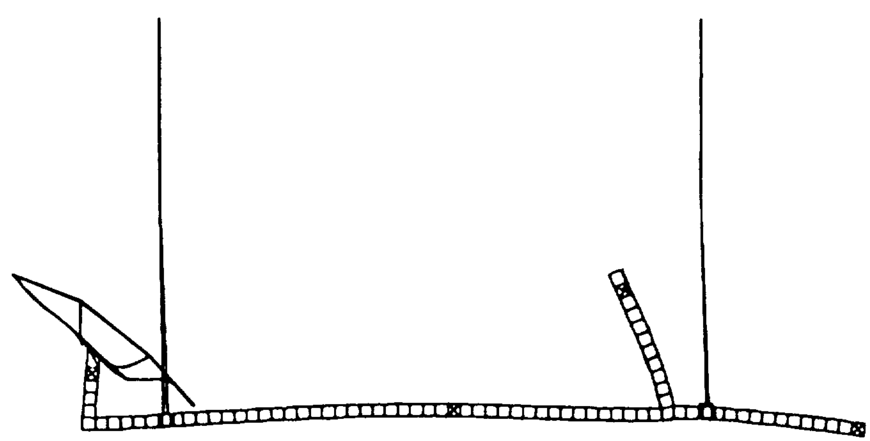

Figure 4.2: Phase 1 CEM 7.8 Hz Laser Tower/Main Truss Mode Shape

Table 4.2: Modal Strain Energy Distribution In Phase 1 CEM 7.8 Hz Laser Tower Mode

Major Contributing Elements	Percent Strain Energy	Percent Elastic Strain Energy
Main Truss, 20 Bays, Longerons	19.7	19.6
Main Truss, 42 Bays, Longerons	5.1	5.1
Main Truss, 20 Bays, Battens	7.2	7.1
Main Truss, 20 Bays, Side Diagonals	25.3	25.2
Tower Truss Longerons	32.7	32.6

2. The damper stiffness would approximately match that of the strut it replaced at 5 Hz.

3. The damper would withstand a 1600 lb. dynamic load.

4. The stress in the aluminum components would be less than 80 percent of yield.

Modal strain energies were calculated from the LaRC Phase 1 model. Results of those calculations, listed by major element group, are listed in Table 4.2.

Only those element groups having significant strain energies in the laser tower/-main truss mode are listed in Table 4.2. We note that the total strain energies and the elastic strain energies listed above are very nearly the same, indicating that geometric stiffness is not a significant component of stiffness in this mode. Clearly, the main truss 20 bay group of longerons, the main truss 20 bay group of side diagonals, and the tower truss longerons are all potentially good locations for the damper locations. In addition to having the highest strain energy of any group, the tower truss longerons have very low static loads. Because this was the first attempt at applying damping struts to the CEM and damper ultimate load testing would be completed only a short time before installation, a conservative approach was taken, and the tower truss was selected for the initial damper installation.

The data in Table 4.2 indicate the general locations for damper placement. To select the exact locations, we further decompose the strain energy calculations into totals for the four longerons in each bay, calculating the strain energy for each bay and then accumulating the total. In the following table, the bays are numbered beginning at the root of the laser tower. Note that there is some disagreement in the last decimal place due to rounding.

The results in Table 4.3 show that the lower bays are the most efficient locations for the dampers, with the first two bays accounting for over half of the strain energy

Table 4.3: Laser Tower Longeron Modal Strain Energy Distribution In 7.8 Hz Mode

Laser Tower Bay No.	Percent Elastic Strain Energy	Cumulative Percent Elastic Strain Energy
1	9.8	9.8
2	7.5	17.2
3	5.6	22.8
4	4.0	26.8
5	2.7	29.5
6	1.7	31.2
7	0.9	32.1
8	0.4	32.5
9	0.1	32.7
10	0.0	32.7
11	0.0	32.7

Table 4.4: Predicted Phase 1 CEM Laser Tower 7.8 Hz Modal Damping

Temperature (deg F)	Stiffness (lb/in)	Damper Elastic Strain Energy (Percent)	Damper Loss Factor	Added Damping (Percent)
70.0	212320	23.8	0.224	2.7
79.5	175250	27.1	0.170	2.3

contained in the tower. We elected to damp the first three bays to permit testing 12 struts. The locations of the dampers are shown in Figure 4.3.

Recall that the damper properties are a function of both temperature and frequency. The data in Table 4.3 are only approximations for the damped truss because the strain energy of each damper will depend on its stiffness. Table 4.4 lists the damper properties and predicted modal damping for two different temperatures for the 12 damper configuration which were calculated using 4.19.

One common misconception about damping treatments is that they soften a structure. The stiffness of the nominal laser tower longerons is 175000 lb/in, so in this case the damping treatment actually stiffens the truss. It must be noted that the DYAD 606 viscoelastic properties used in the above predictions were measured several years apart on different batches of the viscoelastic material, and should be viewed with

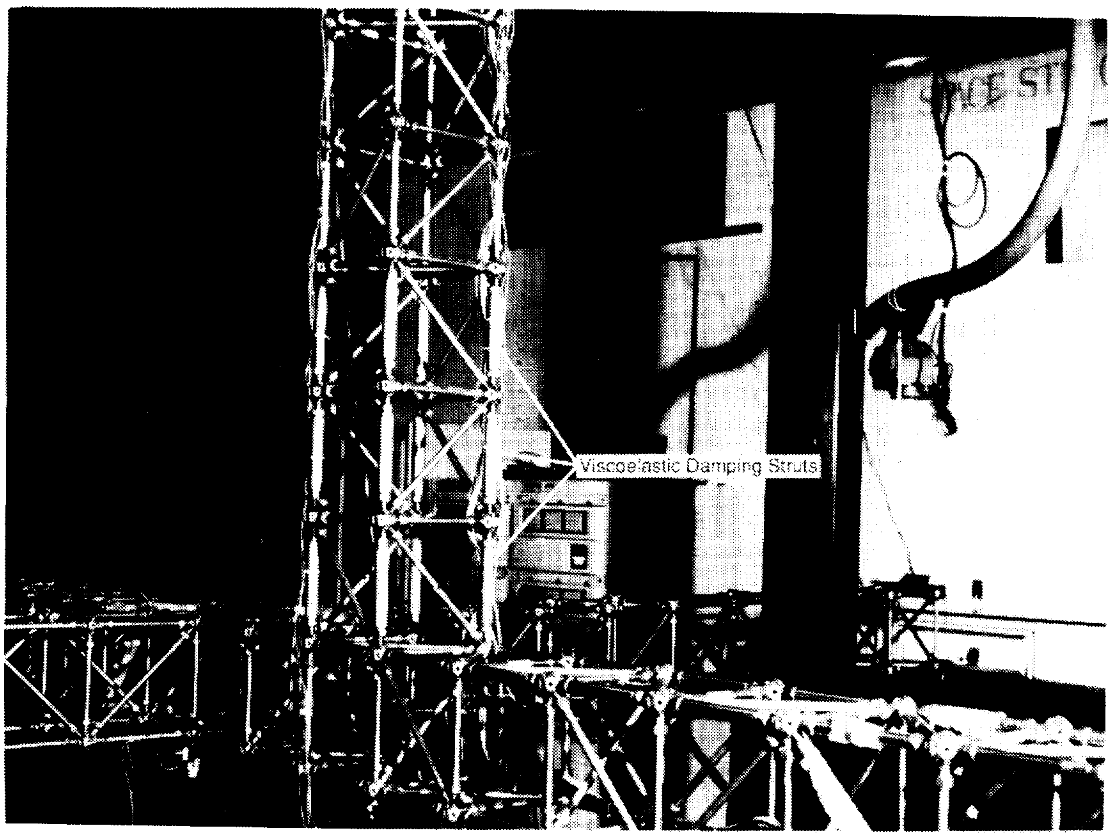

Figure 4.3: Phase 1 CEM Damper Locations

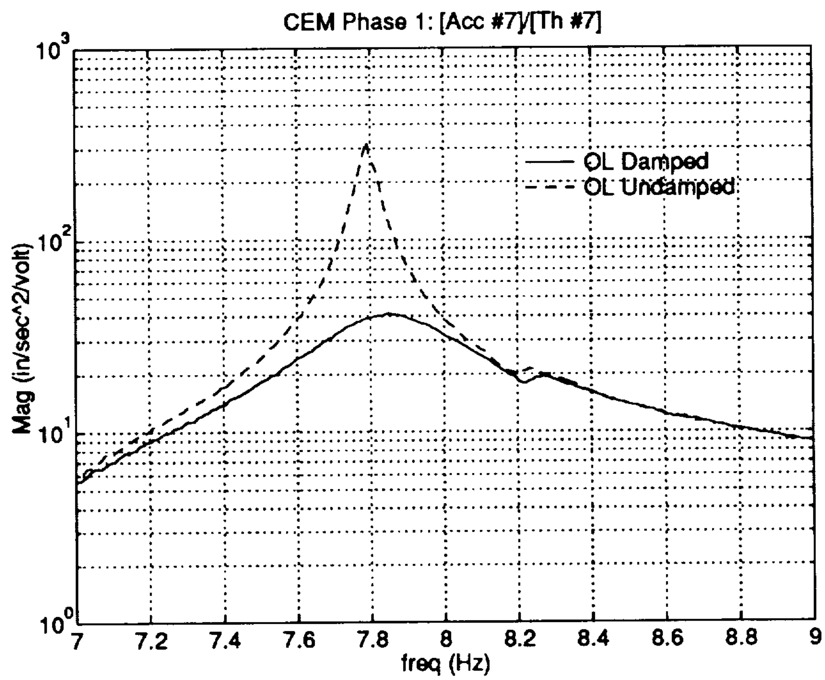

Figure 4.4: Phase 1 CEM Measured Open-Loop Undamped and Damped Frequency Responses of Accelerometer #7 to Thruster #7.

caution, as there is frequently a significant batch-to-batch variation in properties.

As mentioned above, these calculations should be repeated for the entire frequency range of interest, with the range divided into small bands. That process was done for the Phase 1 structure, dividing the frequency range of zero to 30 Hz into six bands. In this frequency range, the dampers had only a small effect on the modes other than the laser tower/main truss mode, so those results will not be presented here.

Open-loop tests were performed with the damped structure to verify the predictions of Table 4.4. Both tuned decay tests and frequency response tests were done, using the colocated pair accelerometer #7/thruster #7 mounted at the top of the laser tower. The corresponding damped and undamped experimental FRF's are shown in Figure 4.4 (obtained at 79.5 deg F). Using ERA, the identified damping ratio for the laser tower mode is 2.5%. The total predicted damping is the sum of the structure inherent damping and the added damping from the damping treatment (2.3%). Using the identified modal damping of 0.2% obtained for the *undamped* structure, the total predicted damping agrees precisely with the measured value.

Table 4.5: Phase 2 CEM Damping Requirements For Modes 10, 11, And 20 Derived From CEM Model P2090992

Mode	Description	Frequency (Hz)	Required Damping (Percent)
10	Pitch Second Bending	5.427	1.35
11	Yaw Second Bending/Torsion	5.871	2.10
20	Laser Tower/Main Truss	7.700	1.25

4.3.5 Phase 2 CEM Damping Design

The damping design for the Phase 2 CEM was done following the procedure described in the tower truss example. Unlike the tower truss example, this design is driven by damping requirements derived during the controller design, and targets modes throughout the frequency range of interest.

The derivation of the damping requirements is given in Section 4.2. Twenty-four modes in the five to 30 Hz range were targeted for passive damping. In this section, the details of the design process for three of the modes with higher damping requirements, modes 10, 11, and 20, are presented. A summary of the results for all modes within the frequency range of interest is also given.

The requirements for modes 10, 11, and 20 as derived from the September, 1992 CEM model (P2090992) are listed in Table 4.5. The corresponding mode shape plots are shown in Section 2.2.

Modal Strain Energy Distribution

The elastic modal strain energy distribution by element was calculated for each targeted mode. The CEM elements were divided into major groups based on group definitions supplied by LaRC, and elastic modal strain energy distributions were calculated for each group for each targeted mode. The element groups are defined in Table 4.6. Results of the strain energy calculations for modes 10, 11, and 20 are summarized in Appendix E. Results for groups with high strain enery in the targeted modes (10, 11, and 20) have been extracted and are displayed in Table 4.7.

Table 4.6: Phase 2 CEM Element Group Definitions

Set Name	First Element	Last Element
Main Truss,20 Bays,Longerons	1	80
Main Truss,42 Bays,Longerons	81	248
Main Truss,20 Bays,Battens	249	332
Main Truss,42 Bays,Battens	333	500
Main Truss,20 Bays,Batten Diagonals	501	521
Main Truss,42 Bays,Batten Diagonals	522	563
Main Truss,20 Bays,Top,Bottom Diagonals	564	603
Main Truss,42 Bays,Top,Bottom Diagonals	604	687
Main Truss,20 Bays,Side Diagonals	690	727
Main Truss,42 Bays,Side Diagonals	728	811
Laser Tower Truss Longerons	812	855
Laser Tower Truss Battens	856	899
Laser Tower Truss Batten Diagonals	900	909
Laser Tower Truss Front,Back Diagonals	911	932
Laser Tower Truss Side Diagonals	933	954
Reflector Truss Longerons	955	970
Reflector Truss Battens	971	986
Reflector Truss Batten Diagonals	987	990
Reflector Truss Side Diagonals	991	996
Reflector Truss Front,Back Diagonals	999	1004
Front Suspension Truss Longerons +Y	1007	1036
Front Suspension Truss Longerons -Y	1037	1066
Front Suspension Truss Battens +Y	1072	1106
Front Suspension Truss Battens -Y	1112	1146
Front Suspension Truss Batten Diagonals +Y	1167	1176
Front Suspension Truss Batten Diagonals -Y	1177	1186
Front Suspension Truss Front,Back Diagonals +Y	1187	1201
Front Suspension Truss Front,Back Diagonals -Y	1207	1221
Front Suspension Truss Top,Bottom Diagonals +Y	1227	1246
Front Suspension Truss Top,Bottom Diagonals -Y	1247	1266
Back Suspension Truss Longerons +Y	1267	1296

continued on next page

continued from previous page

Set Name	First Element	Last Element
Back Suspension Truss Longerons -Y	1307	1336
Back Suspension Truss Battens +Y	1347	1381
Back Suspension Truss Battens -Y	1387	1421
Back Suspension Truss Batten Diagonals +Y	1427	1436
Back Suspension Truss Batten Diagonals -Y	1437	1446
Back Suspension Truss Front,Back Diagonals +Y	1447	1461
Back Suspension Truss Front,Back Diagonals -Y	1467	1481
Back Suspension Truss Top,Bottom Diagonals +Y	1487	1506
Back Suspension Truss Top,Bottom Diagonals -Y	1507	1526
Reflector Support Brackets	1531	1542
Front Suspension Cables	1551	1557
Front Suspension Cables	1561	1567
Front Cable Standoffs	1558	1559
Front Cable Standoffs	1568	1569
Back Suspension Cables	1571	1577
Back Suspension Cables	1581	1587
Back Cable Standoffs	1578	1579
Back Cable Standoffs	1588	1589
Gimbal 1 Supports	1601	1608
Gimbal 1 Rings	1609	1646
Gimbal 1 Posts	1647	1648
Gimbal 1 Laser Supports	1651	1654
Gimbal 1 Plate Backup	1661	1672
Gimbal 1 Plates	1681	1688
Gimbal 1 Control Board	1691	1694
Gimbal 2 Supports	1701	1708
Gimbal 2 Rings	1709	1746
Gimbal 2 Posts	1747	1748
Gimbal 2 Laser Supports	1751	1754
Gimbal 2 Plate Backup	1761	1772
Gimbal 2 Plates	1781	1788
Gimbal 2 Control Board	1791	1794
Gimbal 3 Supports	1801	1808

continued on next page

continued from previous page		
Set Name	First Element	Last Element
Gimbal 3 Rings	1809	1846
Gimbal 3 Posts	1847	1848
Gimbal 3 Laser Supports	1851	1854
Gimbal 3 Plate Backup	1861	1872
Gimbal 3 Plates	1881	1888
Gimbal 3 Control Board	1891	1894
Small Reflector Plate	1900	1900
Forward Thruster Plate	1901	1916
Tower Thruster Plate	1921	1936
Middle Thruster Plate	1941	1956
Reflector Thruster Plate	1961	1976
Laser Plate	1981	1984
Controller Board Plate	1991	1992
Weightless Beams	2000	2043
Reflector Spacer Plate	2045	2048
Spacer Plate	2051	2058
PESD Springs	2201	2204
Thruster Tubes	2241	2252

Table 4.7: Phase 2 CEM Model P2090992 Modal Strain Energy Distribution For Groups With High Strain Energy in Modes 10, 11, and 20

Set Name	Percent Elastic Strain Energy In Set		
	Mode #10	Mode #11	Mode #20
Main Truss,20 Bays,Longerons	20.56	13.57	22.15
Main Truss,42 Bays,Longerons	62.35	37.12	3.08
Main Truss,42 Bays,Top, Bottom Diagonals	0.09	20.35	0.21
Main Truss,20 Bays,Side Diagonals	1.66	0.11	26.09
Main Truss,42 Bays,Side Diagonals	6.51	18.23	1.17
Laser Tower Truss Longerons	1.22	0.04	33.87
Reflector Truss Longerons	3.99	2.65	0.78

The main truss longeron groups contain over 83 percent of the strain energy in this mode. These groups should be examined further to identify which longerons within the groups are the best locations. The main truss side diagonals in the 42 bay group and the reflector truss longerons together have over 10 percent of the strain energy in this mode. Although these latter two groups are not prime locations to damp mode 10, if members in these groups are selected to damp other modes, they will also provide damping to mode 10. This effect, members contributing damping to modes other than the one for which they were selected as damper locations, is termed "damping spillover."

The main truss longeron groups and the diagonal groups from the 42 bay section are potential locations for damping struts for mode 11. If the reflector truss longerons were selected to damp other modes, they would also contribute to damping mode 11.

The main truss 20 bay section longerons, the main truss 20 bay side diagonals, and the laser tower longerons are candidate groups for damping mode 20.

Passive Damping Design Constraints

Like most design problems, there were practical constraints levied on the damping design. The major constraint was our decision to confine damping treatments to truss strut members. The purpose of this constraint was to minimize the impact of modifications on other investigators. Damped truss struts are easily replaced by their nominal counterparts, whereas it would be more difficult to restore the nominal configuration if damping treatments were applied to the gimbal hardware or thruster mounts. The disadvantage of this decision is that modes which have a significant portion of their strain energy in locations other than struts, such as gimbal ring modes, can not be given high levels of passive damping.

Another constraint is that the truss members must be able to withstand the static and dynamic loads during normal CEM operation. Potentially, this constraint can limit the candidate locations for the dampers.

A major constraint is that of cost. The amount of strain energy in a particular damper for a given mode depends on the location of the damper and its dynamic stiffness at the modal frequency. Thus, the most efficient design might require a large number of different damper designs to optimize the stiffnesses of the dampers for the targeted modes. Such a scheme would increase the unit costs of the dampers, and could potentially restrict the ability of the investigator to change the damper configuration. In practice, the accuracy of FEMs and viscoelastic material properties probably do not justify precise mathematical tuning of a damping system design. After considering the options, it was decided to design two new types of dampers, a second longeron damper and a diagonal damper. These dampers were designed to be strong enough to be used at any truss location, thereby giving investigators total freedom in damping design.

For this program, budget considerations dictated that 65 additional struts consisting of a more efficient longeron and a diagonal could be manufactured. With the Phase 1 struts and allowing for destructive testing of some Phase 2 struts and some off-nominal outliers, this would permit the installation of a total of 60 struts on the Phase 2 CEM.

Selection of Damper Locations

Examining the strain energy distributions of the truss members from zero to 30 Hz showed that a majority of the truss elements had significant strain energy in at least one of the modes. Therefore, the truss elements were grouped by bay and type as listed in Appendix F for strain energy calculations by bay to identify bays with high strain energy content.

Results of the strain energy calculations for each bay and group of struts for modes 10, 11, and 20 are summarized in Appendix G. Results for groups and bays with high strain energy in the targeted modes (10, 11, and 20) have been extracted and are displayed in Table 4.8.

Table 4.8: Phase 2 CEM Model P2090992 Beam Modal Strain Energy Distribution By Bay And Member Type For Groups and Bays With High Strain Energy in Modes 10, 11, and 20

Beam Element Set	Percent Elastic Strain Energy In Set		
	Mode #10	Mode #11	Mode #20
Main Truss,20 Bays,Longeron Group	20.56	13.57	22.15
Bay 7	0.25	0.20	0.50
Bay 8	0.35	0.28	0.71
Bay 9	0.48	0.39	0.96
Bay 10	0.62	0.50	1.25
Bay 11	0.79	0.63	1.59
Bay 12	0.98	0.78	1.97
Bay 13	1.07	0.79	2.32
Bay 14	1.20	1.02	2.81
Bay 15	1.42	1.35	4.33
continued on next page			

continued from previous page

Beam Element Set	Percent Elastic Strain Energy In Set		
	Mode #10	Mode #11	Mode #20
Bay 16	2.14	1.50	3.14
Bay 17	2.90	1.47	1.28
Bay 18	2.86	1.50	0.32
Bay 19	2.72	1.47	0.18
Bay 20	2.42	1.41	0.11
Main Truss,42 Bays,Longeron Group	62.35	37.12	3.08
Bay 1	2.70	1.60	0.09
Bay 2	2.34	1.40	0.06
Bay 3	2.00	1.22	0.03
Bay 4	1.68	1.03	0.02
Bay 5	1.38	0.86	0.01
Bay 6	1.10	0.69	0.01
Bay 7	0.84	0.54	0.02
Bay 8	0.61	0.40	0.03
Bay 9	0.42	0.28	0.04
Bay 10	0.26	0.18	0.06
Bay 11	0.14	0.11	0.08
Bay 12	0.06	0.05	0.10
Bay 13	0.00	0.00	0.00
Bay 14	0.01	0.02	0.14
Bay 15	0.04	0.04	0.14
Bay 16	0.10	0.07	0.14
Bay 17	0.20	0.13	0.14
Bay 22	1.05	0.66	0.10
Bay 23	1.25	0.79	0.09
Bay 24	1.47	0.91	0.07
Bay 25	1.68	1.04	0.05
Bay 26	1.89	1.17	0.04
Bay 27	2.10	1.29	0.02
Bay 28	2.30	1.40	0.01
Bay 29	2.49	1.51	0.01
Bay 30	2.67	1.61	0.01
Bay 31	2.83	1.70	0.01

continued on next page

continued from previous page			
Beam Element Set	Percent Elastic Strain Energy In Set		
	Mode #10	Mode #11	Mode #20
Bay 32	2.99	1.78	0.01
Bay 33	3.13	1.86	0.02
Bay 34	3.28	1.95	0.04
Bay 35	3.06	1.70	0.05
Bay 36	2.85	1.36	0.06
Bay 37	2.78	1.72	0.09
Bay 38	2.38	1.40	0.14
Bay 39	2.06	1.17	0.13
Bay 40	1.72	1.01	0.19
Bay 41	1.51	0.93	0.20
Bay 42	0.68	0.08	0.11
Main Truss,42 Bays,Top, Bottom Diagonal Group	0.09	20.35	0.21
Bay 36	0.00	0.70	0.00
Bay 37	0.01	3.42	0.04
Bay 38	0.01	3.56	0.04
Bay 39	0.01	3.47	0.04
Bay 40	0.01	3.40	0.04
Bay 41	0.02	2.89	0.03
Bay 42	0.01	0.29	0.00
Main Truss,20 Bay, Side Diagonal Group	1.66	0.11	26.09
Bay 13	0.01	0.00	0.08
Bay 14	0.02	0.00	0.12
Bay 15	0.03	0.02	0.07
Bay 16	1.02	0.02	24.59
Bay 17	0.01	0.00	0.08
Bay 18	0.00	0.00	0.07
Bay 19	0.03	0.01	0.05
Main Truss,42 Bay, Side Diagonal Group	6.51	18.23	1.17
Laser Tower Truss Longeron Group	1.22	0.04	33.87
Bay 1	0.36	0.02	10.19
			continued on next page

continued from previous page			
Beam Element Set	Percent Elastic Strain Energy In Set		
	Mode #10	Mode #11	Mode #20
Bay 2	0.28	0.01	7.76
Bay 3	0.21	0.01	5.80
Bay 4	0.15	0.00	4.13
Bay 5	0.10	0.00	2.78
Bay 6	0.06	0.00	1.72
Bay 7	0.04	0.00	0.94
Reflector Truss Longeron Group	3.99	2.65	0.78
Bay 1	2.11	1.48	0.41
Bay 2	1.25	0.78	0.24
Bay 3	0.64	0.38	0.12
Bay 4	0.00	0.00	0.00

Table 4.8 shows that good locations for dampers for mode 10 would be in the longerons of bays 12 through 20 of the 20 bay portion of the main truss, in the longerons of bays 22 through 41 of the 42 bay portion of the main truss, and in the longerons of bay 1 of the reflector truss.

Table 4.8 shows that good locations for dampers for mode 11 would be in the longerons of bays 12 through 20 of the 20 bay portion of the main truss, in the longerons of bays 1 through 4 and bays 27 through 41 of the 42 bay portion of the main truss, in the top and bottom diagonals of bays 37 through 41 of the 42 bay portion of the main truss, in the side diagonals of bays 37 through 41 of the 42 bay portion of the main truss, and in the longerons of bay 1 of the reflector truss.

Table 4.8 shows that good damper locations for mode 20 would be in the longerons of bays 9 through 17 of the 20 bay portion of the main truss, in the side diagonals of bay 16 of the 20 bay portion of the main truss, and in the longerons of bays 1 through 6 in the tower truss. Note that the single pair of diagonals in bay 16 contain almost 25 percent of the modal strain energy in this mode.

Tables identical in form to the complete version of Table 4.8 as listed in Appendix G were prepared for all targeted modes, and locations were selected for damper placement. This process involves several trades. If only one mode were targeted for passive damping, the best location would be in the highest modal strain energy locations available, assuming that the damper static and dynamic strength is sufficiently high to withstand design loads. For the more practical cases where more than one mode is targeted for damping, the best choice of locations is not necessarily as obvious. Frequently, several members will have significant but not the highest modal strain energy in more than one targeted mode, and a mix of those members may produce a design requiring fewer members than if a design were achieved by choosing only the highest strain energy members in each mode.

Another trade involves reducing the sensitivity of the design to model error. Selecting a very few high strain energy elements to damp a mode will produce a design which minimizes the number of required dampers. However, if the model is inaccurate, a strain energy error in a single member can result in damping which is too low. A better choice might be a larger set of lower strain energy elements distributed along a truss, the rationale being that the exact bay for the highest strain energy might be questionable, but a reasonably accurate model will predict the high strain energy location within a region of several bays. Following this practice will produce a less efficient design if the model is accurate, but a lower risk design if it is not. Risk can be further reduced by applying a factor of safety to damping, i.e., designing in more damping than is required to compensate for model errors.

Finally, it was desirable to furnish a mix of damper types to provide some flexibility in damping design for other investigators. Considering all these aspects, the damper selection shown in Table 4.9 was chosen. Figure 4.5 shows the locations of the 60 dampers installed on the Phase 2 CEM. Figure 4.6 shows some of the dampers installed on the CEM in the region near the laser tower.

Predicted Passive Damping Levels

It must be remembered that the strain energy carried in a particular member in a particular mode is a function of the stiffness of the member. The results shown above are for the nominal truss members. However, damper stiffnesses are functions of frequency and temperature because of the dependence of the VEM properties on those variables. Thus, the tables above serve as good indicators for damper placement, but the analysis must be repeated with the actual damper properties incorporated in the FEM.

The frequency range of interest, in this case from 0 to 30 Hz, is divided into bands. The selection of the number of bands and the frequency boundary for each band is based on the shapes of the damper stiffness and loss factor curves. Enough bands are chosen to avoid larges changes with the band. The dampers in the FEM are represented as beams with the appropriate axial stiffnesses for the frequency band being analyzed. Modes from each band are combined to represent the damped structure. The bands, together with the predicted damper properties that were used with the P2090992 model, are given in Table 4.10.

The P2090992 damping predictions as assembled from the six frequency bands are summarized in Table 4.11 and were calculated according to Equation 4.19. The added damping is that due to the dampers, and should be combined with the inherent

Table 4.9: Phase 2 CEM Damper Types And Locations

Damper Group/Bay	First Element	Last Element	Damper Type	Number
Main Truss,20 Bays,Longeron Group				
Bay 12	45	48	Phase 1 Longeron	4
Bay 13	49	52	Phase 1 Longeron	4
Bay 14	53	56	Phase 1 Longeron	4
Bay 15	57	60	Phase 2 Longeron	4
Bay 16	61	64	Phase 2 Longeron	4
Bay 17	65	68	Phase 2 Longeron	4
Bay 18	69	72	Phase 2 Longeron	4
Bay 19	73	76	Phase 2 Longeron	4
Main Truss,42 Bays,Top,Bottom Diagonal Group				
Bay 38	678	679	Phase 2 Diagonal	2
Bay 39	680	681	Phase 2 Diagonal	2
Bay 40	682	683	Phase 2 Diagonal	2
Main Truss,20 Bay,Side Diagonal Group				
Bay 15	716	717	Phase 2 Diagonal	2
Bay 16	718	719	Phase 2 Diagonal	2
Main Truss,42 Bay,Side Diagonal Group				
Bay 40	806	807	Phase 2 Diagonal	2
Bay 41	808	809	Phase 2 Diagonal	2
Bay 42	810	811	Phase 2 Diagonal	2
Tower Truss Longeron Group				
Bay 1	812	815	Phase 2 Longeron	4
Bay 2	816	819	Phase 2 Longeron	4
Reflector Truss Longeron Group				
Bay 1	955	958	Phase 2 Longeron	4
Total Dampers By Type				
Phase 1 Longeron				12
Phase 2 Longeron				32
Phase 2 Diagonal				16
Total Dampers All Types				60

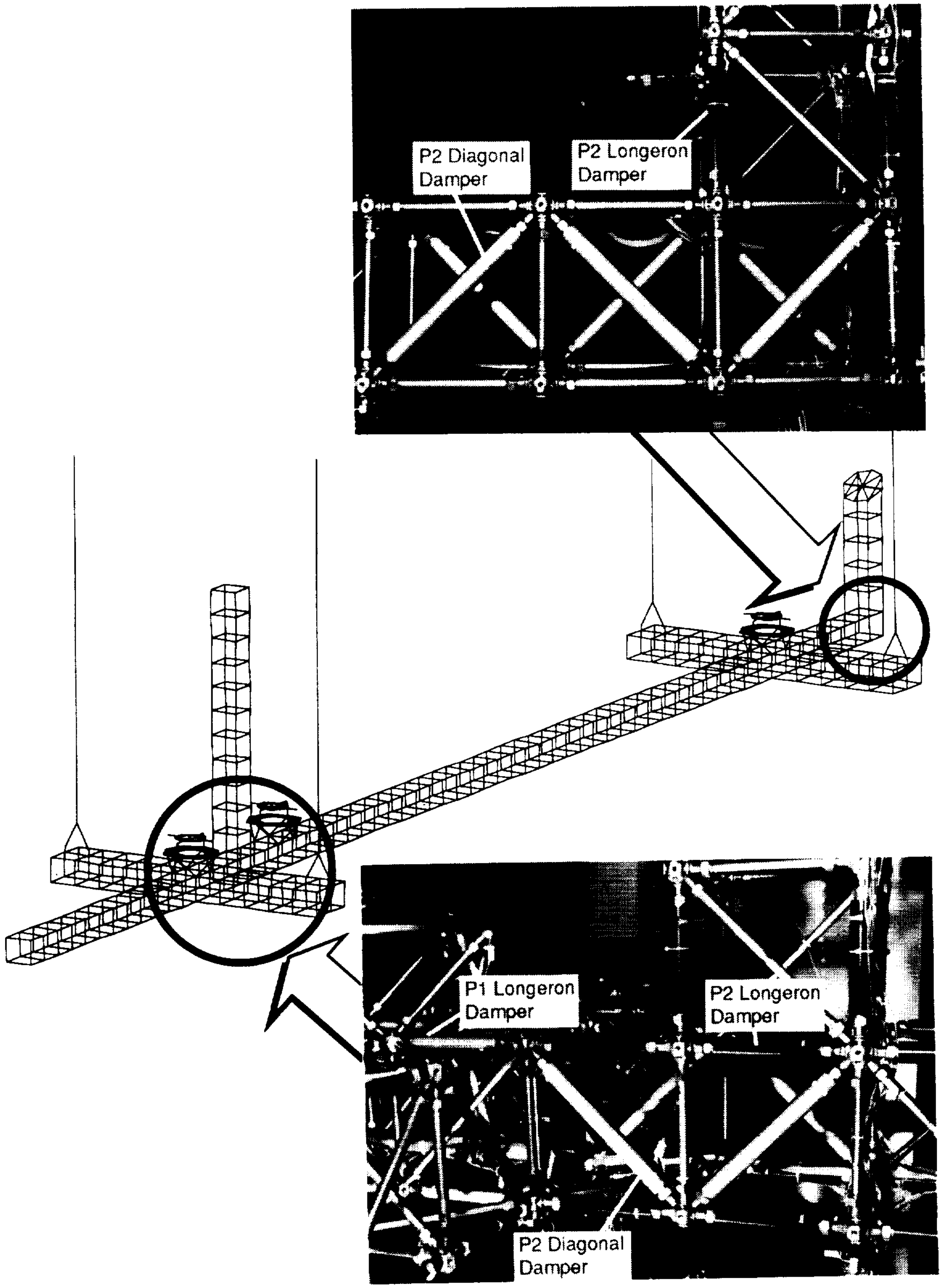

Figure 4.5: Phase 2 CEM Damper Locations

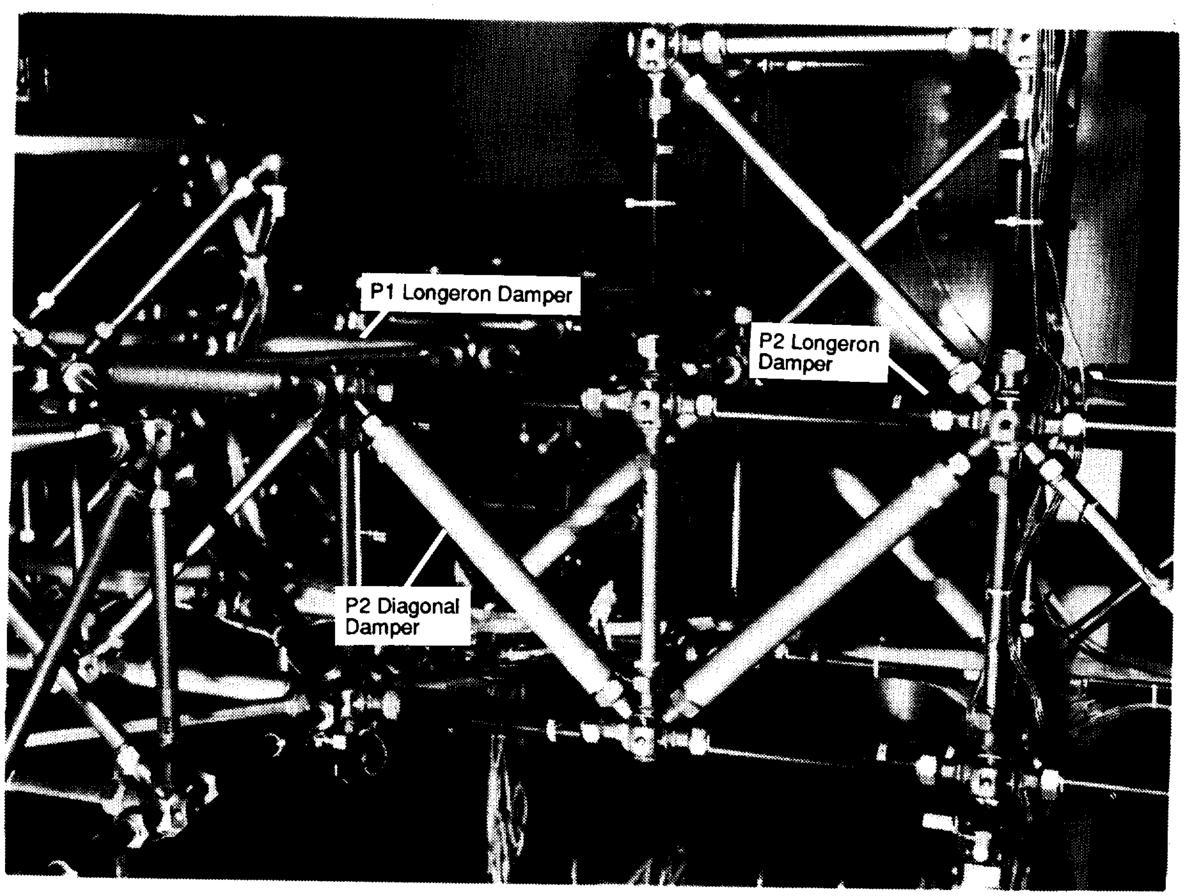

Figure 4.6: Detail of the laser tower region for the Phase 2 CEM

Table 4.10: Phase 2 CEM Analysis Bands and Predicted Damper Properties

Band	Reference Frequency (Hz)	Frequency Band (Hz)	Damper Type Stiffness	Predicted Loss (kip/in)	Predicted Factor
1	2.0	0.0–3.0	Phase 1 Longeron	176.6	0.196
			Phase 2 Longeron	133.4	0.255
			Phase 2 Diagonal	77.4	0.435
2	4.5	3.0–6.0	Phase 1 Longeron	194.0	0.219
			Phase 2 Longeron	151.3	0.287
			Phase 2 Diagonal	94.3	0.415
3	8.0	6.0–10.0	Phase 1 Longeron	212.3	0.224
			Phase 2 Longeron	169.3	0.289
			Phase 2 Diagonal	109.8	0.368
4	12.5	10.0–15.0	Phase 1 Longeron	224.0	0.212
			Phase 2 Longeron	181.8	0.274
			Phase 2 Diagonal	119.8	0.322
5	17.5	15.0–20.0	Phase 1 Longeron	235.0	0.195
			Phase 2 Longeron	193.2	0.257
			Phase 2 Diagonal	128.5	0.284
6	25.0	20.0–30.0	Phase 1 Longeron	246.3	0.185
			Phase 2 Longeron	205.2	0.240
			Phase 2 Diagonal	137.1	0.250

damping in the CEM. As an approximation, the inherent damping in the untreated CEM is accepted as the inherent damping in the treated CEM. Furthermore, because the levels of inherent damping in the CEM are relatively low, the total damping can be approximated as the sum of the inherent and added damping.

Table 4.11: Phase 2 CEM Model P2090992 Damping Predictions For 70 Degrees F

System Mode	Band	Number	Frequency (Hz)	Added Damping (Percent)
1	1	1	0.1393	0.00
2		2	0.1405	0.00
3		3	0.1487	0.00
4		4	0.1600	0.00
5		5	0.1640	0.00
6		6	0.2790	0.23
7		7	1.720	1.17
8		8	2.263	2.67
9		9	2.803	2.45
10	2	1	5.131	4.38
11		2	5.764	4.91
12	3	1	6.441	0.02
13		2	6.462	0.03
14		3	6.525	0.02
15		4	6.547	0.03
16		5	6.912	0.01
17		6	6.941	0.01
18		7	7.003	0.00
19		8	7.032	0.00
20		9	7.619	8.76
21		10	8.345	5.32
22		11	8.932	4.01
23	4	1	10.54	5.06
24		2	12.09	2.41

continued on next page

continued from previous page

System Mode	Band	Number	Frequency (Hz)	Added Damping (Percent)
25		3	12.29	0.08
26		4	12.32	0.07
27		5	12.41	0.00
28		6	12.45	0.00
29		7	13.18	0.00
30		8	13.24	0.00
31		9	13.32	0.00
32		10	13.38	0.00
33		11	13.53	1.05
34		12	13.96	1.94
35		13	14.13	0.25
36		14	14.24	0.42
37		15	15.04	0.12
38		16	15.72	0.65
39	5	1	16.14	0.83
40		2	16.97	0.00
41		3	17.03	0.00
42		4	17.08	0.00
43		5	17.13	0.00
44		6	18.16	0.52
45		7	18.22	0.10
46		8	18.29	0.04
47	6	1	18.33	0.00
48		2	18.41	0.02
49		3	18.47	0.96
50		4	18.71	1.32
51		5	20.03	0.00
52		6	20.07	0.00
53		7	20.09	0.00
54		8	20.13	0.00
55		9	21.12	1.70

continued on next page

continued from previous page				
System Mode	Band	Number	Frequency (Hz)	Added Damping (Percent)
56		10	21.51	0.04
57		11	21.54	0.00
58		12	21.60	0.04
59		13	21.63	0.00
60		14	22.25	2.19
61		15	23.10	0.55
62		16	24.69	0.38
63		17	25.68	0.34
64		18	27.53	0.93
65		19	29.20	0.55

A large population of each type of damper was tested at 75 degrees F, the temperature that LaRC technical personnel thought was within the capability of the laboratory air conditioning system in the summer. Properties of the three damper types are listed in Table 4.12. Note that the stiffnesses shown for the diagonal dampers are higher than the analytic values shown above because the inner tube of the dampers as fabricated was thicker than originally modeled. For more details on the damper design, refer to Section 4.4.

In March 1993, a new model of the CEM became available. This model, denoted P2032993, was examined and found to represent measured CEM modes as provided by LaRC somewhat better than did P2090992 , although both models deviate significantly from measured transfer functions for frequencies higher than about 10 Hz. We elected to perform our final pretest analysis using model P2032993 and the measured damper properties. Unfortunately, for modes above about 10 Hz, the mode shapes between the two models differ enough as determined from modal strain energy comparisons so that comparison of modal damping predictions between the two models is not meaningful for the higher modes. Because of the differences between predicted and measured transfer functions above 10 Hz and budget limitations, it was decided not to rerun the analysis using P2090992 and measured damper properties.

Table 4.12: Phase 2 CEM Analysis Frequency Bands And Measured Damper Properties

Band	Reference Frequency (Hz)	Frequency Band (Hz)	Damper Type	Stiffness (kip/in)	Loss Factor
1	2.0	0.0–3.0	Phase 1 Longeron	174.6	0.193
			Phase 2 Longeron	130.9	0.227
			Phase 2 Diagonal	95.9	0.353
2	4.5	3.0–6.0	Phase 1 Longeron	194.7	0.197
			Phase 2 Longeron	148.9	0.232
			Phase 2 Diagonal	117.0	0.331
3	8.0	6.0–10.0	Phase 1 Longeron	210.6	0.188
			Phase 2 Longeron	163.4	0.222
			Phase 2 Diagonal	133.6	0.298
4	12.5	10.0–15.0	Phase 1 Longeron	222.5	0.175
			Phase 2 Longeron	175.1	0.207
			Phase 2 Diagonal	146.2	0.267
5	17.5	15.0–20.0	Phase 1 Longeron	231.4	0.164
			Phase 2 Longeron	183.6	0.194
			Phase 2 Diagonal	155.5	0.243
6	25.0	20.0–30.0	Phase 1 Longeron	240.5	0.153
			Phase 2 Longeron	192.3	0.180
			Phase 2 Diagonal	164.7	0.218
Avg	15.0	0.0–30.0	Phase 1 Longeron	227.5	0.169
			Phase 2 Longeron	179.8	0.200
			Phase 2 Diagonal	151.3	0.253

Table 4.13: Phase 2 CEM Model P2032993 Damping Predictions

System Mode	Band	Number	Frequency (Hz)	Added Damping (Percent)
1	1	1	0.1299	0.00
2		2	0.1318	0.00
3		3	0.1357	0.00
4		4	0.1785	0.00
5		5	0.1808	0.00
6		6	0.3040	0.17
7		7	1.698	0.86
8		8	2.262	2.09
9		9	2.802	1.98
10	2	1	5.114	3.42
11		2	5.793	3.79
12	3	1	6.461	0.02
13		2	6.486	0.02
14		3	6.551	0.01
15		4	6.577	0.02
16		5	6.866	0.01
17		6	6.904	0.00
18		7	6.962	0.00
19		8	7.000	0.00
20		9	7.792	6.62
21		10	8.336	4.02
22		11	8.813	3.11
23	4	1	10.34	3.56
24		2	12.10	1.84
25		3	12.89	0.02
26		4	12.94	0.02
27		5	13.01	0.62
28		6	13.10	0.00
29		7	13.15	0.00

continued on next page

continued from previous page

System Mode	Band	Number	Frequency (Hz)	Added Damping (Percent)
30		8	13.24	0.08
31		9	13.38	0.43
32		10	13.71	0.00
33		11	13.79	0.00
34		12	13.86	0.02
35		13	13.93	0.00
36		14	14.00	0.02
37		15	14.05	0.30
38		16	14.69	1.56
39	5	1	15.61	0.43
40		2	16.78	0.99
41		3	17.10	0.98
42		4	18.67	1.02
43		5	19.32	0.00
44		6	19.40	0.00
45		7	19.67	0.00
46		8	19.75	0.00
47	6	1	20.24	0.89
48		2	20.59	0.05
49		3	20.87	0.54
50		4	20.91	0.06
51		5	21.02	0.00
52		6	22.76	1.25
53		7	23.08	0.49
54		8	24.54	0.26
55		9	25.62	0.11
56		10	25.72	0.09
57		11	25.78	0.03
58		12	26.29	0.00
59		13	26.39	0.00
60		14	27.15	0.70

continued on next page

continued from previous page				
System Mode	Band	Number	Frequency (Hz)	Added Damping (Percent)
61		15	27.30	0.03
62		16	27.45	0.01
63		17	27.94	0.00
64		18	28.09	0.00
65		19	28.90	0.40

4.4 Damper Design

Three different types of damping struts were designed, fabricated, unit tested, and installed on the LaRC CEM. The damper types were a longeron damper designed for the Phase 1 CEM, a more efficient longeron damper for the Phase 2 CEM, and a diagonal damper, also for the Phase 2 CEM. This section provides background to and outlines the design process, provides the equations used to predict damper performance, and describes the three individual designs.

4.4.1 General Viscoelastic Damping Design Considerations

Viscoelastic material (VEM) damping treatments provide an inexpensive, reliable source of passive damping for structures. Properly designed, these treatments will enhance the performance of a system with minimum added weight penalty while maintaining adequate structural integrity. Depending on the performance requirements for a given system, it is even possible that passive damping can reduce the overall weight of the system by reducing control actuator sizes and energy requirements.

To avoid undue cost and weight penalties, it is important to design efficient damping devices and to place them in effective locations. It is also important to determine what the required damping levels are, for excessively high levels increase system cost and weight while providing little incremental benefit over required levels. The controls section of this report discusses the establishment of damping requirements for the CEM, and the MSE section describes efficient damper placement.

DYAD 606

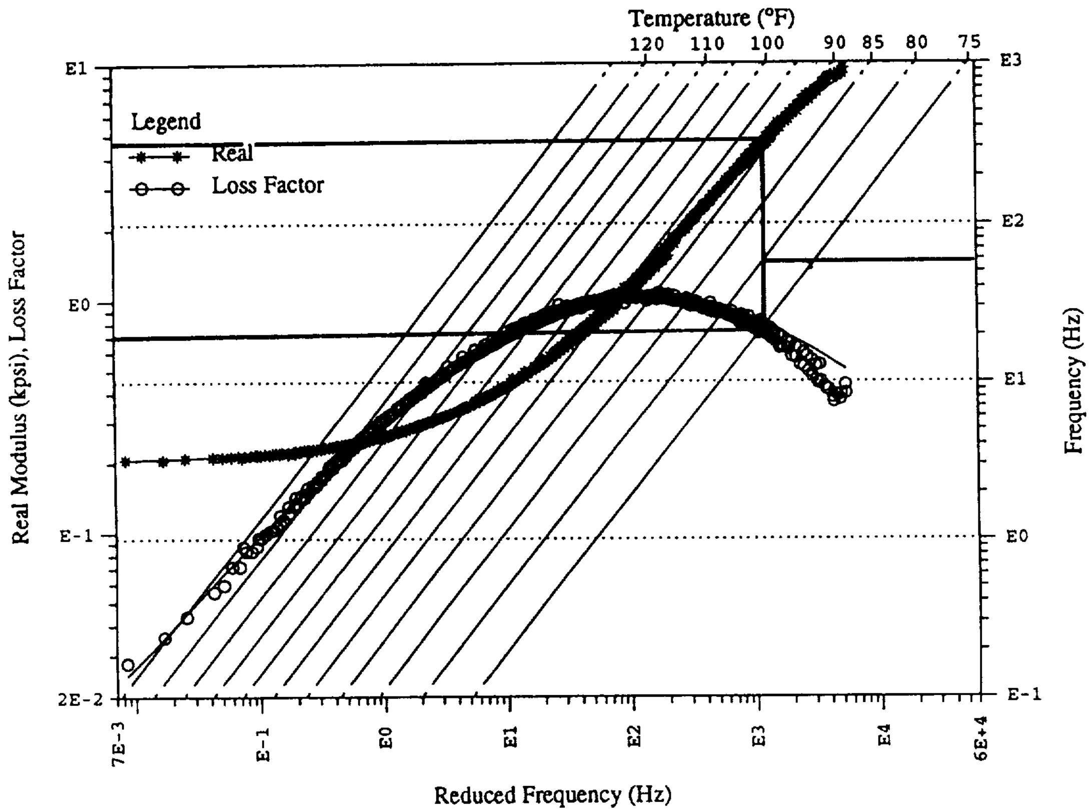

Figure 4.7: VEM International Plot

4.4.2 VEM Properties

VEM mechanical properties, such as shear modulus and loss factor, are also temperature and frequency dependent. It is therefore impractical to test VEMs over all the frequency and temperature values of potential interest. To overcome this difficulty, specimens are tested at discrete temperatures and frequencies, and an analytic relationship (curve fit) is developed to characterize the material at all other temperatures and frequencies within the limits of the test range. The form of the relationship varies. One frequently used curve fit is in the form of a ratio of factored polynomials [22].

One common way of presenting VEM properties derived from tests is the International plot, an example of which is shown in Figure 4.7. To use the plot, select the desired frequency on the right axis. Draw a horizontal line. Choose the constant temperature line corresponding to the desired operational temperature. At the intersection of the selected temperature line and the horizontal frequency line, draw a vertical line. The values for shear modulus and loss factor are read from the left axis at the intersections of the vertical line with the corresponding curves.

Because of the logarithmic scales, it is obvious that a small error in performing this process can easily lead to a very large error in the selected values. For this reason, it is the author's preference to use linear plots of the modulus and loss factor test data at the desired temperature if available. If direct measurements are not available, the analytic relationship developed for the material curve fit should be used whenever possible. For this program, International plots were used to choose the damping material. Direct measurements for the selected material were available and used for analysis and design.

It is important to realize that VEM testing and characterization are as much of an art as they are a science. It is not unusual for different laboratories to produce significantly different test results on identical samples of VEM [23]. Obviously, using only analytic results based on measured VEM properties to predict system performance is simply not prudent, even if the system FEMs are perfectly accurate. The recommended practice is to use the MSE method and analytic damper models for initial design, manufacture prototype dampers and test them, and then use the test results together with the MSE method for final system predictions. This process will not compensate for a poor system FEM, but it will reduce the impact of questionable VEM data and damper models.

VEMs generally creep under load, so as a general practice it is advisable to provide a load path of elastic materials parallel to the VEM load path. A conservative but common practice is also to assume that the VEMs carry no static load when calculating factors of safety.

4.4.3 Phase 1 Longeron Damper Design

As discussed in the Section 4.3.3, it was decided to limit CEM damping treatment design to damping struts. For the Phase 1 longeron damper, the following design requirements were adopted:

1. The damper must interface with the truss in precisely the same manner as a nominal member.

2. The damper must be capable of replacing any CEM strut of the same length.

3. The damper will withstand a 1600 pound dynamic load.

4. The stress in aluminum components must be less than 80 percent of yield stress to ensure linearity.

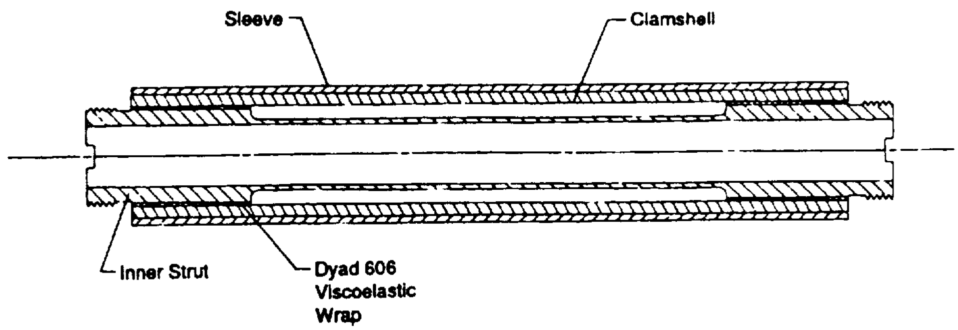

Figure 4.8: Phase 1 CEM Damper Design Concept

The first concept considered and eventually selected is shown in Figure 4.8, an assembly drawing of the Phase 1 damper. The interface requirements were satisfied by designing a damper section which replaces the strut section of a nominal member. The damper design duplicates the geometry of the ends of a nominal strut, and the envelope of the damper can be made sufficiently compact to avoid interference with other struts and dampers in the trusses. The inner tube provides a parallel elastic load path. The VEM wraps are bonded to the hubs on the ends of the inner tube. Two clamshells are then bonded to the VEM, followed by a sleeve which is bonded to the clamshells. The clamshell/tube assembly provides restraint for the VEM.

Loads applied to the ends of the tube divide between the tube itself and the tube/VEM/clamshell/sleeve path, thereby straining the VEM. The higher percentage of strain energy in the VEM relative to the rest of the damper, the more efficient the damper. The center tube must be strong enough, however, to withstand static loads neglecting the VEM path. This is a prudent practice not only because VEM creeps, but it also serves to protect the CEM if the bonds fail.

Another similar, and aesthetically more pleasing concept was considered. It would utilize the existing tubes with reduced center wall thickness, and then insert a tube with hubs and VEM wraps inside the existing tube. The appeal of this design is that it would be much smaller in outside diameter and would closely resemble the existing struts, but it would be much more difficult to fabricate. Preliminary analysis also showed that it was not possible to obtain high efficiency with the design due to the limited volume available for the VEM.

4.4.4 Damper Design Equations

From experience gained on the PACOSS program and on IR&D D–65D, a simplified mechanics of materials approach provides sufficient accuracy for most practical designs, particularly when the challenge of VEM characterization is considered. Thus, it was decided to design, fabricate and test the Phase 1 CEM longeron damper based on a simple analytic model, deferring the development of a damper FEM until it could be determined if the expense of developing such a model was justified.

The axial stiffnesses of large populations of each of the nominal undamped truss struts, which is adequate for accurate modeling of the nominal CEM, was measured at NASA LaRC. The nominal truss elements are represented in the LaRC FEM by beams with equivalent cross-sectional areas. However, the axial stiffness of the node ball/standoff/screw/nut/threaded end assembly is required for damper design, but it is not known from direct measurement. The required axial stiffness was derived from the measured node-to-node stiffness of a laser tower longeron by subtracting the analytic stiffness of the constant cross-section portion of the strut, which is in series with the stiffnesses of the two end assemblies.

Let

A_{eq} = the cross-sectional area of the equivalent FEM beam,

E_{eq} = Young's modulus of the equivalent beam,

L = the node-to-node length of the equivalent beam element,

k_{eq} = the node-to-node stiffness of the equivalent member,

k_e = the stiffness of one end assembly,

k_c = the stiffness of the constant cross-section portion of the strut,

E = Young's modulus of the strut material,

l_c = the length of the constant cross-section portion of the strut,

then, the axial stiffness of an equivalent uniform rod is

$$k_{eq} = \frac{A_{eq}E_{eq}}{L}. \tag{4.20}$$

The stiffness of the uniform center portion of the constant cross-section of the tube is

$$k_c = \frac{A_c E}{l_c}. \tag{4.21}$$

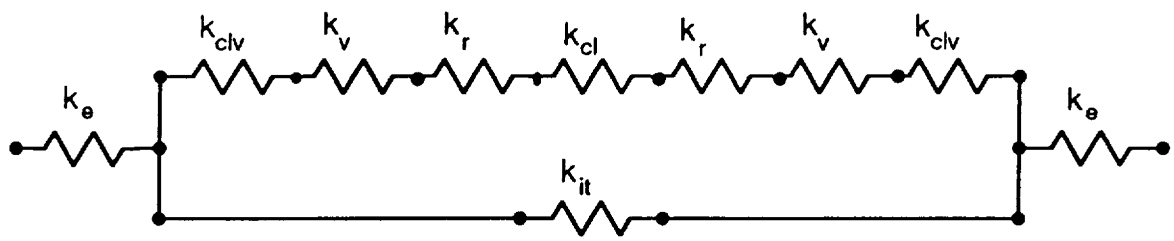

Figure 4.9: Damper Equivalent Spring Network

Two end assemblies are in series with the center portion. For springs in series, the equivalent stiffness of the series arrangement is

$$\frac{1}{k_{eq}} = \frac{2}{k_e} + \frac{1}{k_c}. \tag{4.22}$$

Thus,

$$k_e^{-1} = 0.5\left(k_{eq}^{-1} - k_c^{-1}\right). \tag{4.23}$$

Figure 4.9 is a spring network equivalent to the damper. We will derive approximate equations for the damper stiffness and loss factor in a form convenient for programming in PC MATLAB.

The VEM wrap is much softer than the ring and clamshell. Thus, it is assumed that the VEM wrap acts as a uniform cylinder in shear.

Let

G_ν = the VEM shear modulus

l_ν = the length of one VEM wrap

$r_{\nu o}$ = the outer radius of the VEM wrap

$r_{\nu i}$ = the inner radius of the VEM wrap

k_ν = the stiffness of a single VEM wrap

F = the resultant shear force carried by the VEM

$\Delta =$ the axial displacement of the outer VEM surface relative to the inner VEM surface

$\gamma(r) =$ shear strain in the VEM, a function of the radial position

$\tau(r) =$ shear stress in the VEM, a function of the radial position

then

$$\Delta = \frac{1}{G_\nu} \int_{r_{\nu i}}^{r_{\nu o}} \gamma(r)\, dr. \tag{4.24}$$

Assuming the shear stress is uniform over any radius in the VEM,

$$\tau(r) = \frac{F}{2\pi r l_\nu}. \tag{4.25}$$

But

$$\tau(r) = G_\nu \gamma(r). \tag{4.26}$$

Thus

$$\Delta = \frac{F}{2\pi G_\nu l_\nu} \int_{r_{\nu i}}^{r_{\nu o}} \frac{dr}{r} = \frac{F}{2\pi G_\nu l_\nu} \ln\left(\frac{r_{\nu o}}{r_{\nu i}}\right). \tag{4.27}$$

But

$$F = k_\nu \Delta. \tag{4.28}$$

Thus, from 4.27 and 4.28 it follows that

$$k_\nu = \frac{2\pi G_\nu l_\nu}{\ln\left(r_{\nu o}/r_{\nu i}\right)}. \tag{4.29}$$

The loading conditions on the portion of the clamshell/sleeve assembly in contact with the VEM are more complicated, as are the loads on the ring or hub. Both of these portions of the damper are very stiff with respect to the VEM and center tube. The damper equations are therefore not particularly sensitive to these stiffnesses if the clamshell/sleeve assembly is sufficiently stiff. We will use relationships similar to those used for the VEM as an adequate approximation.

Let

$G_{cl} =$ the shear modulus of the clam shell/sleeve assembly

$r_{clo} =$ the outer radius of the clamshell/sleeve assembly

$r_{cli} =$ the inner radius of the clamshell/sleeve assembly

$k_{cl\nu} =$ the stiffness of the clamshell/sleeve assembly on the VEM

$G_r =$ the shear modulus of the ring

r_{ro} = the ring outer radius

r_{ri} = the ring inner radius

k_r = the ring stiffness

$$k_{cl\nu} = \frac{2\pi G_{cl} l_\nu}{\ln\left(r_{clo}/r_{cli}\right)} \tag{4.30}$$

$$k_r = \frac{2\pi G_r l_\nu}{\ln\left(r_{ro}/r_{ri}\right)} \tag{4.31}$$

Let

l_{cl} = effective clamshell/sleeve assembly length

A_{cl} = cross-sectional area of clamshell/sleeve assembly

E_{cl} = Young's modulus of clamshell/sleeve assembly

l_{it} = length of inner damper tube

A_{it} = cross-sectional area of inner damper tube

E_{it} = Young's modulus of inner damper tube

k_{it} = stiffness of inner damper tube

k_{dd} = stiffness of damper portion of damper strut

k_{ddit} = damper stiffness exclusive of ends

k_{eqd} = end-to-end damper strut stiffness

The length of the portion of the clamshell/sleeve assembly not in contact with the VEM is

$$l_{cl} = l_c - 2l_\nu. \tag{4.32}$$

Treating this portion as an axially loaded member,

$$k_{cl} = \frac{A_{cl} E_{cl}}{l_{cl}}. \tag{4.33}$$

For the damper portion, the equivalent springs are in series as shown in Figure 4.9. Thus,

$$k_{dd} = \left[2\left(k_{cl\nu}^{-1} + k_\nu^{-1} + k_r^{-1}\right) + k_{cl}^{-1}\right]^{-1}. \tag{4.34}$$

The axial stiffness of the inner tube is

$$k_{it} = \frac{A_c E}{l_{it}}. \tag{4.35}$$

The inner tube is in parallel with the damper portion of the strut. Therefore,

$$k_{ddit} = k_{dd} + k_{it}. \tag{4.36}$$

The two branches in parallel have a total stiffness given by

$$k_{eqd} = \left(2k_e^{-1} + k_{ddit}^{-1}\right)^{-1}. \tag{4.37}$$

Equation 4.37 is the equation for the damper node-to-node stiffness. Note that, because it depends implicitly on the VEM shear stiffness, it is a function of temperature and frequency.

The damper loss factor for a given temperature and frequency is equal to the percentage of strain energy in the VEM multiplied by the VEM loss factor. The loss factor is calculated as follows:

Let

E_{s1} = strain energy in the damper due to an applied unit force

δ = damper elongation due to an applied unit force

F_{dd} = force in the damping portion due to an applied unit force

δ_{ddit} = elongation of inner tube and damper portion due to unit applied force, equal because they are in parallel

$E_{s\nu}$ = total strain energy in VEM (both wraps) due to load

η_ν = VEM loss factor

η_d = loss factor of damper

The strain energy stored in an axial member with stiffness equal to the equivalent damper stiffness due to an elongation δ is

$$E_{s1} = 0.5k_{eqd}\delta^2. \tag{4.38}$$

For a unit load,

$$\delta = k_{eqd}^{-1}. \tag{4.39}$$

Thus, for a unit load

$$E_{s1} = 0.5k_{eqd}^{-1}. \tag{4.40}$$

The inner tube and the damping portion are in parallel. For a unit load, the elongation of these components is given by

$$\delta_{ddit} = \left(k_{dd} + k_{it}\right)^{-1}. \tag{4.41}$$

The force in the damping portion is calculated from its deformation and equivalent spring constant.

$$F_{dd} = k_{dd}\delta_{ddit} \tag{4.42}$$

The sum of the strain energies in the two VEM wraps is

$$E_{s\nu} = 2\left(0.5F_{dd}^2/k_\nu\right) = F_{dd}^2/k_\nu. \tag{4.43}$$

The damper loss factor is thus

$$\eta_d = \eta_\nu \left(E_{s\nu}/E_{s1}\right). \tag{4.44}$$

Equation 4.44 is the equation for the damper loss factor. As in the case of the damper stiffness, the damper loss factor is a function of temperature and frequency.

The equations above are used to design extensional shear dampers. The important messages they contain are as follows:

1. The loss factor of the damper is a function of the fraction of the strain energy contained in the VEM and the loss factor of the VEM.
2. The fraction of the strain energy in the VEM is a function of the relative stiffness of the VEM portion compared to the rest of the damper.
3. The stiffness of the VEM portion depends on the shear modulus of the VEM and the length and thickness of the VEM wraps.
4. Increasing the length of the VEM wraps increases the VEM wrap stiffness.
5. Increasing the thickness of the VEM wraps decreases the VEM wrap stiffness.

Thus, even though it is not generally possible to select the "perfect" VEM, adjustments in damper design parameters can be made to produce a satisfactory damper.

4.4.5 VEM Selection

There are literally hundreds of VEM's, of which only a small subset are well characterized. Selecting VEM properties from the open literature can be risky if one does not know the source of the test data. On the other hand, some damping houses treat their data base as proprietary and charge a fee for the data. For this program, we selected a data base being developed under Air Force contract by CSA Engineering, Inc. [24] to search for a suitable VEM.

The following physical characteristics are considered when selecting a VEM for a particular application:

1. Loss factor and shear modulus in the frequency and temperature range of interest.

2. Form (adhesive, thin film, tape, sheets).

3. Bonding method (self adhesive or requiring bonding).

Thin films and adhesives (typically 2–4 mils thick) are convenient to apply and generally are very uniform in thickness. Their self adhesive nature minimizes bonding problems, and they are particularly suited for integral and constrained damping treatments. For damping strut applications, however, this type of VEM has some significant disadvantages. Equation 4.29 shows that the sensitivity of the VEM stiffness to thickness increases rapidly with decreasing thickness. Thus, it is very important to control the VEM layer thickness for uniform results from unit to unit. Control of the VEM thickness is relatively easy in constrained damping treatments formed by bonding flat plates together. In strut applications such as the small ones required for the CEM, however, using stock materials where tolerances are on the order of the VEM thickness would produce large variations from unit to unit, and machining the inner surfaces of the clam shells to the required accuracy for thin films would drastically increase costs. Therefore, the use of thin films or adhesives was rejected, and a minimum thickness of 10 mils was established.

The design equations were programmed and used to obtain preliminary sizes for the damper design, and to select VEM properties. For the zero to 30 Hz frequency range of interest and room temperature conditions, it is relatively easy to find VEMs with loss factors of between 0.6 and 1.0, so a value of 0.7 was assumed for purposes of initial sizing. Geometric parameters and VEM shear moduli were varied to obtain dampers with stiffnesses approximating those of the nominal laser tower truss longerons and having good loss factors. The objective of this process is to arrive at reasonable VEM requirements with enough latitude remaining in the design to accommodate variations from the desired properties.

One VEM in particular, 3M Acrylic Core Foam Tape, received particular attention. It is 40 mils thick, has a good loss factor in the anticipated operating range, and is self adhesive. It was used with great success in the PACOSS program. However, calculations showed that its modulus was much too low for this application.

Further study led to the preliminary selection of DYAD606 in a 24 mil thickness. Dyad606 had been used on PACOSS in two applications. It is very tough, and tolerates large strains well. According to Soundcoat, the manufacturer, it will not deteriorate at temperatures up to 150 degrees F. One significant drawback, however, is that it requires bonding with an epoxy adhesive, our choice being Scotchweld adhesive.

Our experience with respect to predictability of DYAD606 applications on PACOSS was mixed. For the PACOSS applications, the DYAD606 was bonded to large flat areas. Generally, damping assembly stiffnesses were well predicted, but damping levels were over predicted by a factor about two. The bond line thickness was difficult to control well, and probably varied to from 1 to 5 mils or more in thickness. Bond line elasticity terms do not appear in the above equations because it is assumed that they are very stiff compared to the VEM, a condition satisfied by epoxy bond lines which are thin relative to the VEM thickness. Thick bond lines will degrade the assembly loss factor, and non uniform bonds will produce significant unit to unit variations.

After considering VEMs for which recent data were available and finding that none had properties as suitable as DYAD606, we selected DYAD606 and accepted the challenge of forming thin, uniform bonds. The assembly process is documented in Appendix H. A description of problems in fabrication and their solutions are summarized in the next section.

4.4.6 Summary Of Test Results And Issues

Sixteen of the Phase 1 longeron dampers were fabricated, unit tested, and tested successfully on the Phase 1 CEM. This activity proceeded so smoothly that it could have been a textbook example. As described in the damper testing portion of this report, the measured properties matched the predicted properties well, and the measured damping levels on the Phase 1 CEM were very close to predicted values.

For the Phase 2 effort, a more efficient longeron damper and diagonal dampers were designed. The Phase 2 designs are identical in concept to the Phase 1 longeron dampers, but have narrower VEM wraps and thinner inner tubes in an attempt to force more strain energy into the VEM. In addition, of course, the diagonal dampers are longer. The Phase 2 designs are shown in Figures 4.10 and 4.11. To take advantage of the knowledge gained during Phase 1, the same personnel performed the same tasks as they did during Phase 1, specifically damper design, damper fabrication, and damper unit testing. Figure 4.12 shows typical Phase 1 and Phase 2 completed dampers.

The damper fabrication and testing activities met with several setbacks during the program. The first problem encountered was discovered during unit testing. There was a major difference between Phase 2 damper predicted and measured performance, and the shapes of the measured stiffness and loss factor curves did not resemble the shapes predicted and measured during Phase 1 testing. These deviations motivated a major effort to reexamine virtually all aspects of the damper design, fabrication, and test processes. The details of the test activities are described in Appendix I, and

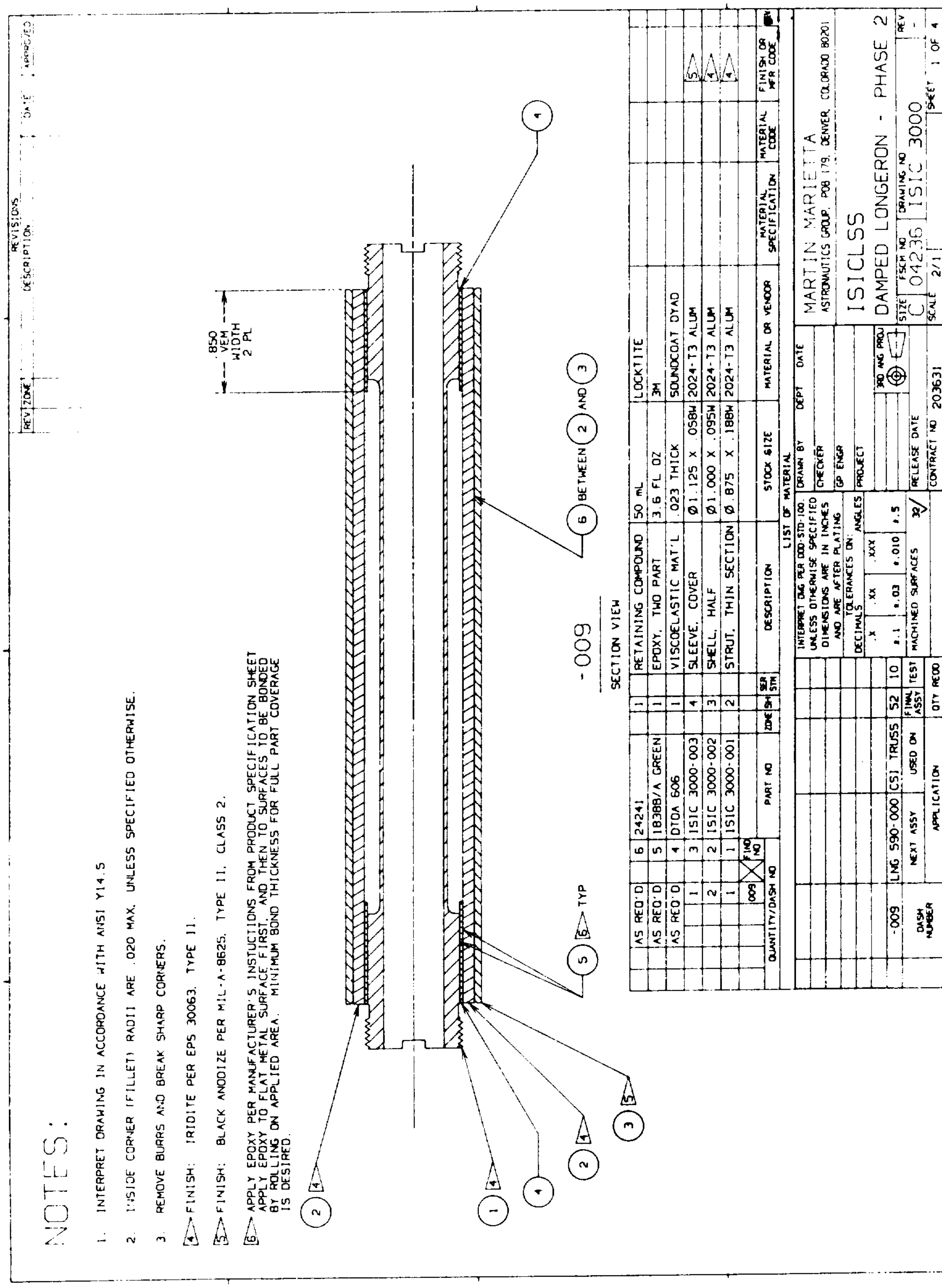

Figure 4.10: Phase 2 CEM Longeron Damper Design

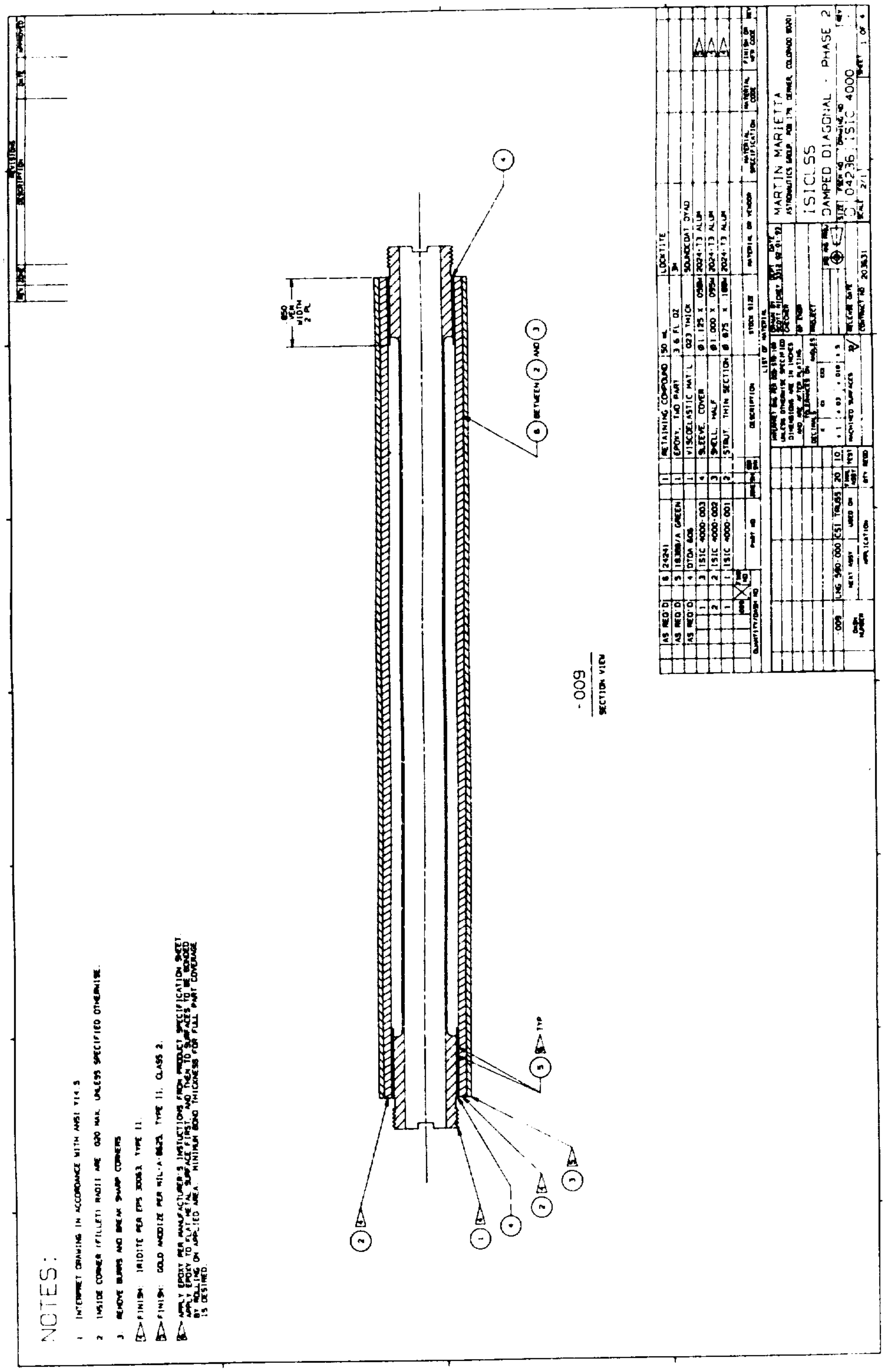

Figure 4.11: Phase 2 CEM Diagonal Damper Design

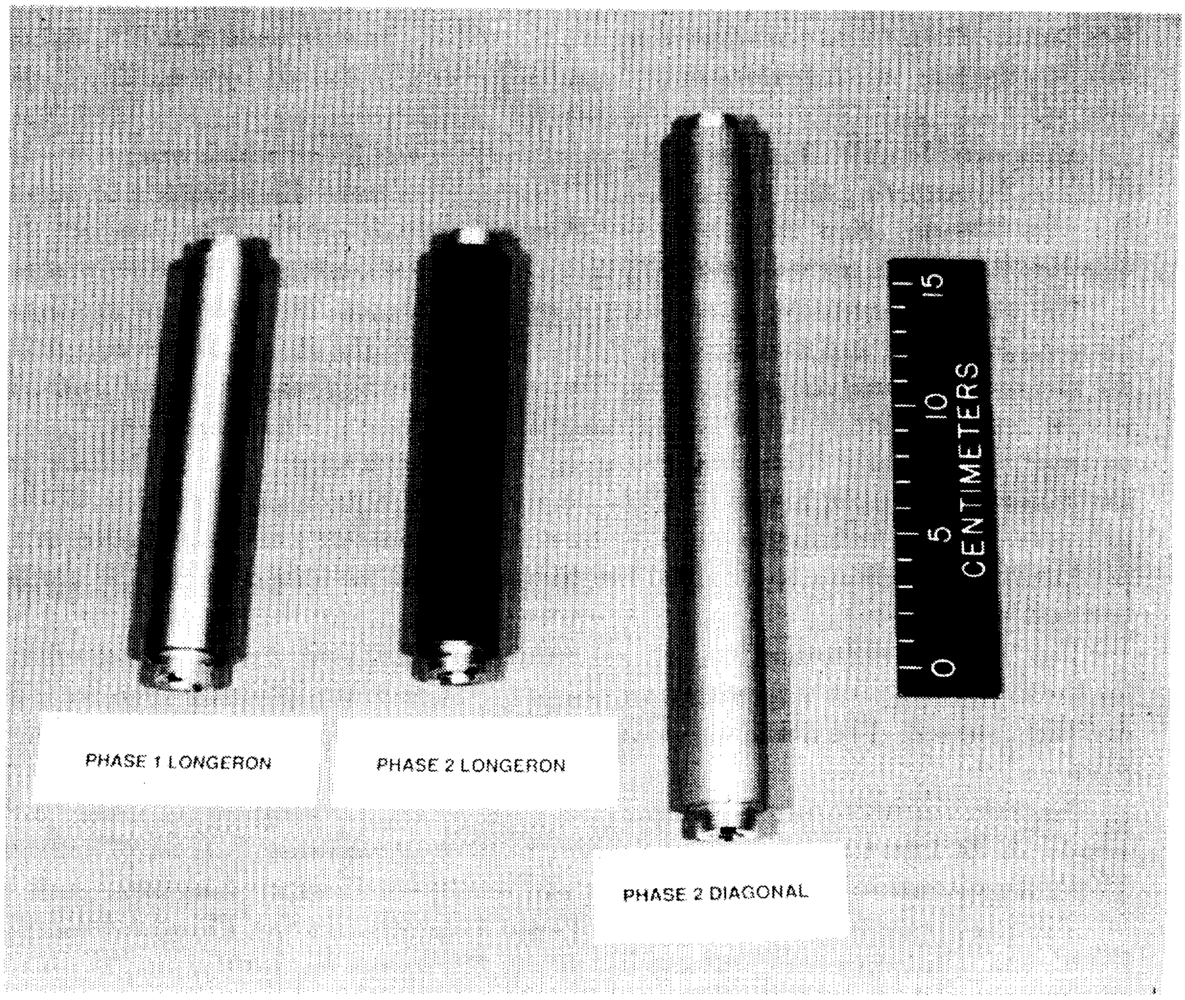

Figure 4.12: Phase 1 and 2 Assembled Dampers

will not be repeated here.

The damper design does not permit full inspection of the bonds, so a damper was cut apart. Examination of the interior revealed that excessive adhesive had been used, and the excess had flowed and bridged the DYAD606 VEM. Bridging effectively "shorts out" the VEM, increasing the damper stiffness and decreasing the damper loss factor. Both these phenomena were observed in the unit tests, but it is difficult to quantify how much performance degradation can be caused by a small adhesive bridge.

After considerable effort, an epoxy paint stripper was found which was moderately effective in removing the adhesive, and the dampers were disassembled to salvage the core portion. New clamshells and sleeves were fabricated. The dampers were reassembled with a refined process and extra care used during the bonding process.

The unit tests were repeated, with slight improvement but still poor agreement between predicted and measured properties. However, the shapes of the curves still did not resemble analytic predictions. Two different testing machines were used with similar results. Finally, the Phase 1 dampers were tested. The Phase 1 test results deviated significantly from those obtained in 1992, exhibiting greater stiffness and lower loss factor, both a sign of VEM deterioration. Significant effort was devoted to improving test techniques and investigating the possibility of deterioration of the DYAD606. The efforts to improve the test technique are described in the damper test section.

The VEM manufacturer was consulted, and verified that the storage conditions for the DYAD606 were well within allowable limits, so it was doubtful that the VEM had deteriorated. The next issue considered was that of the available VEM property data.

Program resources had not permitted VEM testing, so existing data were used. The DYAD606 data which were available were from two different batches of material. These data consisted of measurements at 70 degrees F which had been used on PACOSS and which were used for the Phase 1 design. During Phase 1 testing at LaRC, the laboratory temperature was nearly 80 degrees F, so we obtained data at 79.5 degrees F from CSA Engineering, Inc. We anticipated a laboratory temperature of around 75 degrees F during the Phase 2 testing, and the Martin Marietta Materials Test Lab was controlled to 75 degrees for Phase 2 unit testing. However, the particular batch of DYAD606 used for the dampers had not been tested at temperatures below 79.5 degrees F, and it is not advisable to extrapolate data beyond the test range, or try to interpolate between the two temperatures for data from two different batches of material.

CSA volunteered to provide a limited material characterization at 75 degrees without charge, which would not only provide data at the required temperature but also determine if the VEM had deteriorated. Figures 4.13 and 4.14 show the DYAD606 shear modulus and loss factor data values from the three sets of data. The June '93 data have not been smoothed. Note that we would expect the June '93 75 degree shear modulus to fall between the old 70 and 79.5 degree curves, but it was dramatically higher than the previous data. We would also expect the June '93 loss factor data to fall between the old data sets, which it did for most of the frequency range. It appears high throughout much of the range, however, when compared to the old data. The CSA test apparatus had just been modified, so the reliability of the test apparatus had not been reestablished.

Finally, as described in the damper unit test section, a flaw in calibration procedures was discovered, and testing was repeated for a sizable population of all damper types. The shapes of the curves matched predicted shapes and the shapes measured during Phase 1 testing, although the refined test technique and higher temperature for the Phase 2 testing resulted in somewhat different measurements than during Phase 1 testing.

Figures 4.15 and 4.16 show the Phase 1 longeron damper test data with outliers removed compared to the predicted stiffness and loss factor. The predicted stiffness is about five percent above the average measured value at seven Hz, and the corresponding predicted loss factor is about 20 percent high. Figures 4.17 and 4.18 show the corresponding Phase 2 longeron damper data. The predicted stiffness at seven Hz is about six percent higher than the average measured value, and the corresponding predicted loss factor is about 30 percent high. Figures 4.19 and 4.20 show that the predicted seven Hz stiffness of the Phase 2 diagonal dampers is about eight percent low, and the corresponding predicted loss factor is about 17 percent high.

In addition to the somewhat high loss factor achieved in the recent material test, another cause may be weak sleeve bonding in the case of the Phase 2 longeron dampers. The same cleaning process was used to clean the black anodized sleeves as was done on the gold sleeves, and no gold sleeves have ever debonded. It has since been learned that residual material, called smut, is left on surfaces by the anodizing process. Gold anodizing produces much less smut, so the cleaning process was adequate for the gold sleeves, but not thorough enough for the black sleeves. The larger deviation in loss factor than measured with the other damper types may be in part due to achieving less than full effective stiffness from the sleeves. These units were repaired prior to final installation on the CEM, but were not retested due to schedule and budget constraints.

As shown in Sections 4.3.4 and 4.5, however, using the measured damper properties to predict open loop system damping levels yielded excellent results over the frequency range for which the FEM was accurate, so it is possible that the bonds were performing satisfactorily for the load levels used in unit testing. As has been

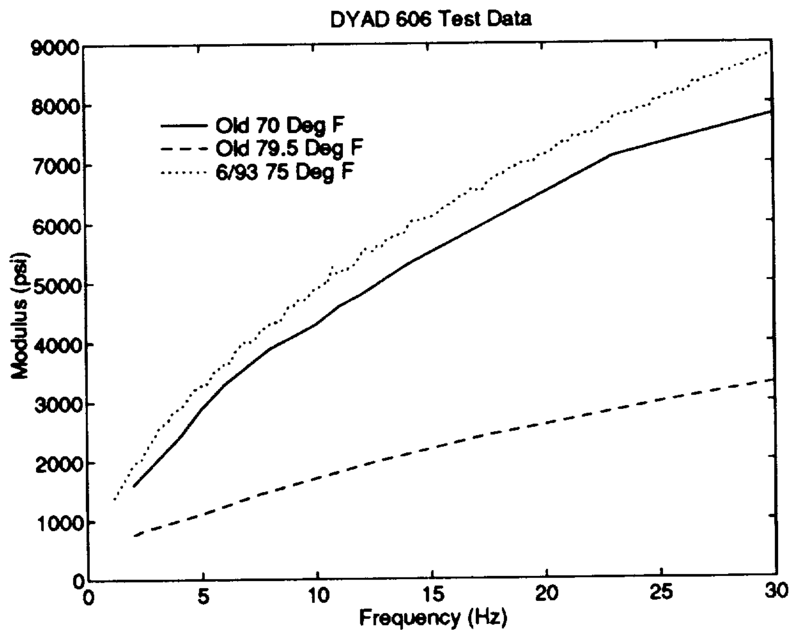

Figure 4.13: DYAD606 Shear Modulus

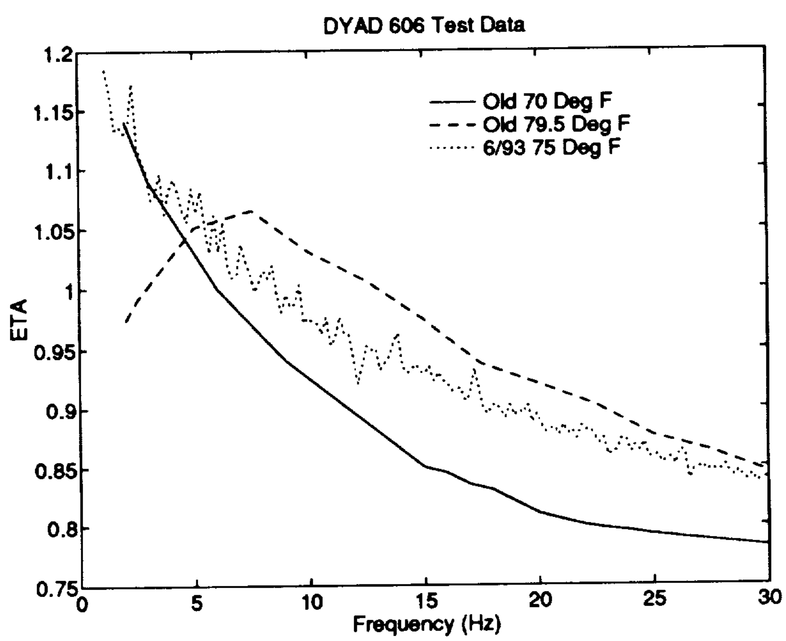

Figure 4.14: DYAD606 Loss Factor

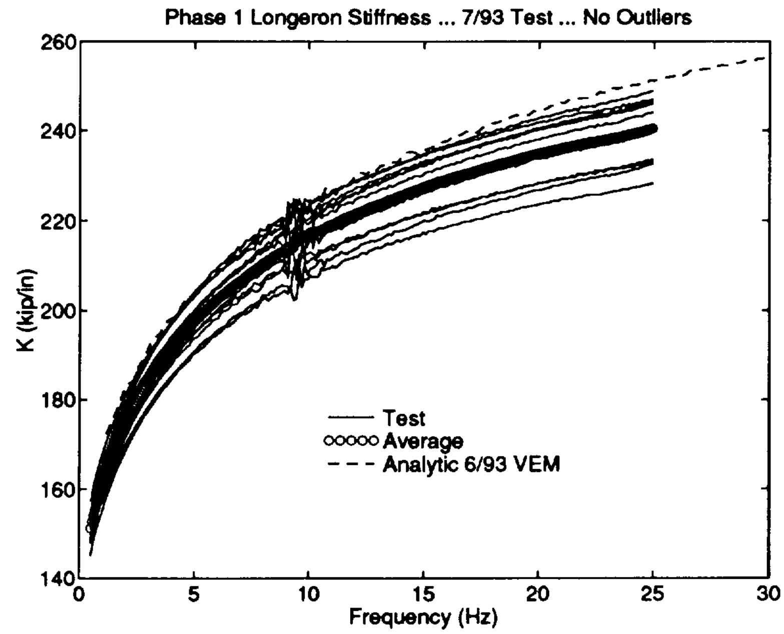

Figure 4.15: Phase 1 Longeron Stiffnesses

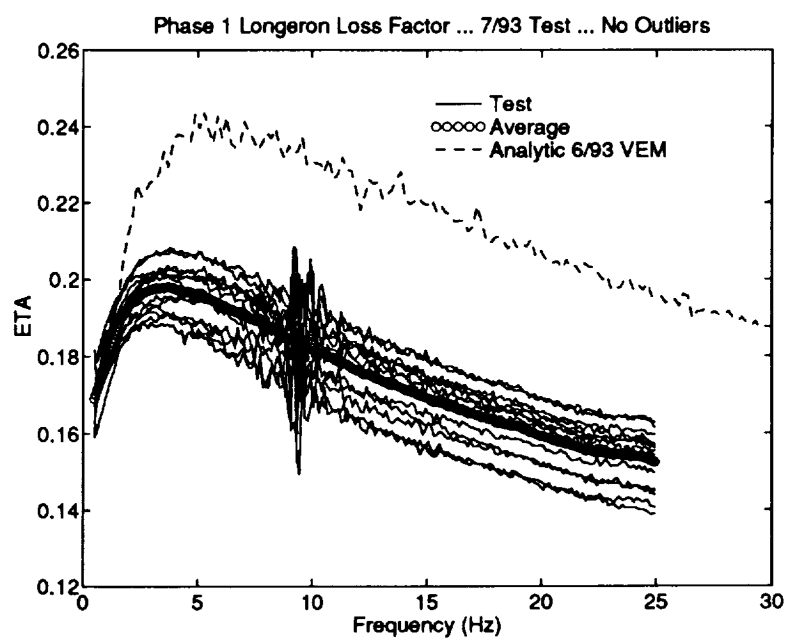

Figure 4.16: Phase 1 Longeron Loss Factors

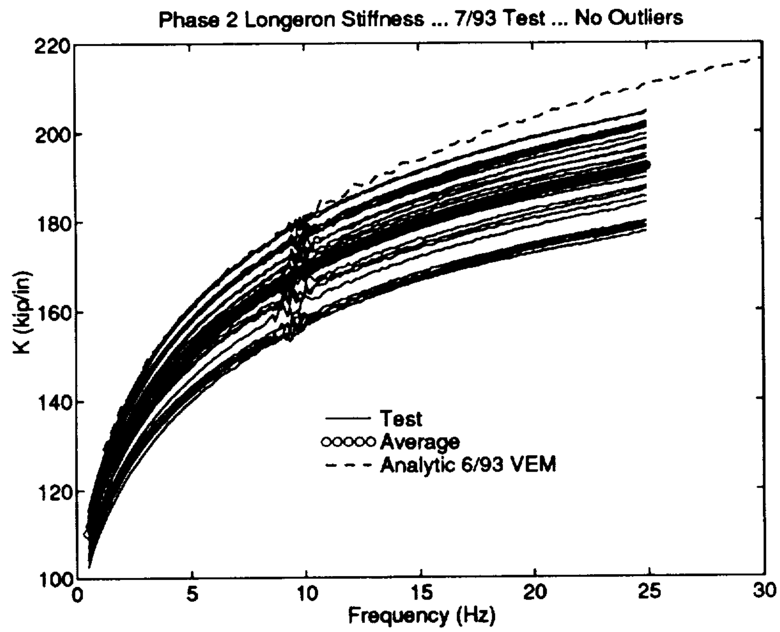

Figure 4.17: Phase 2 Longeron Stiffnesses

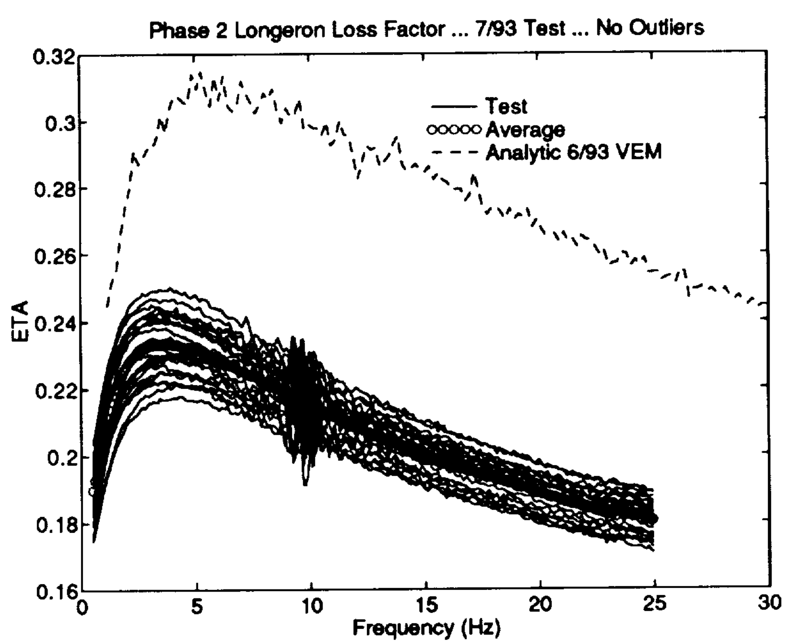

Figure 4.18: Phase 2 Longeron Loss Factors

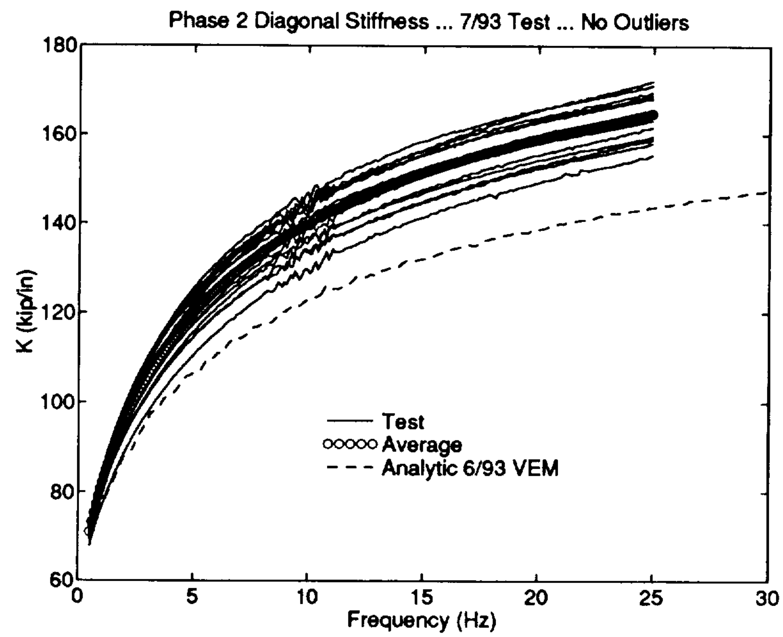

Figure 4.19: Phase 2 Diagonal Stiffnesses

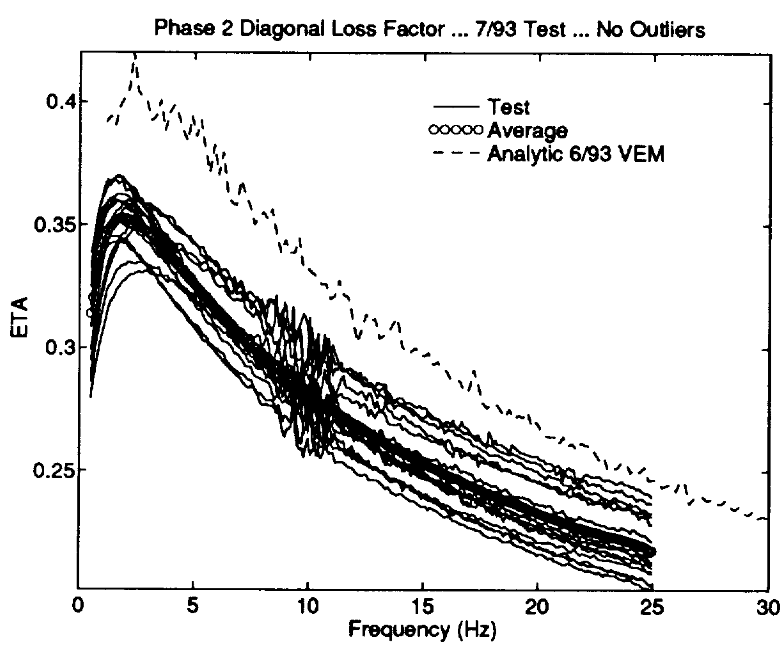

Figure 4.20: Phase 2 Diagonal Loss Factors

stated above, past predictions of damping with DYAD606 have been problematic, and the results obtained for this program are a decided improvement over results for components using this material on PACOSS.

It appears highly probable that the flaw in testing procedures may actually have been the only significant problem apart from the sleeve bonding, but all of the Phase 2 dampers had been refabricated, so it was not possible, even if resources had permitted, to investigate this theory.

An objective disclosure of the damper fabrication and testing problems has been provided as an aid to others who might experience the same difficulties if not forewarned. The problems described above were somewhat disruptive to the program schedule as originally planned, but they were investigated and solved in a systematic fashion. The program finished with very good results, so the major impact was probably a heightened sense of anxiety among the guest investigators.

4.5 Open-Loop Damping Results

The passive damping designs discussed above were successfully implemented on the CEM test article in its Phase 1 and Phase 2 configurations. The Phase 1 damping results were discussed in Section 4.3.4. Recall that the objective of the passive damping design for Phase 1 was only to damp the 7.8 Hz laser tower/main truss mode. In contrast, the Phase 2 damping treatment was designed in combination with the high authority active controller to obtain increased performance and to provide robust stabilization of uncertain modes.

Open loop testing was done to obtain estimates of modal damping. Selected modes were driven at resonance by the thrusters. The thrusters were then turned off, and the mode allowed to damp out. Damping levels were estimated from logarithmic decrement calculations. Experience has shown that, for modes that can be tuned well, this method provides accurate damping measurements. Damping values measured by this technique consist of added damping plus inherent modal damping.

For the Phase 2 damping design modal tests were performed to estimate the damping ratios of selected modes in the 1–11 Hz frequency range. Table 4.14 shows the predicted and measured damping values. The measured damping should be compared to the sum of the measured inherent damping in column 5 and the predicted added damping in column 4. As can be seen, in most cases the comparison is excellent.

The ERA algorithm was also used to estimate the modal damping ratios and frequencies. The results from the ERA algorithm are shown in Table 4.15.

Table 4.16 shows the measured damping ratio values obtained from the ERA algorithm versus the damping requirements. The damping ratios for modes beyond 13 Hz could not be compared individually to the modes of the FEM due to significant

Table 4.14: Phase 2 CEM P2032993 Frequencies and Passive Damping Values Estimated From Resonance Responses

Mode Number	FEM Freq. (Hz)	Resonant Freq. (Hz)	Predicted Added Damping (Percent)	Measured Inherent Damping (Percent)	Measured Total Damping (Percent)
7	1.698	1.739	0.86	0.32	1.07–1.17
8	2.262	2.292	2.09	0.22	2.35–2.44
9	2.802	2.865	1.98	0.33	2.29–2.31
10	5.114	5.385†	3.42	0.27	4.0–4.3
11	5.793	6.17 †	3.79	0.30	3.24–4.96
20	7.792	7.924	6.62	0.45	7.7–8.2
21	8.336	–	4.02	0.31	–
22	8.813	9.00	3.11	0.23	2.97–3.28
23	10.34	10.76	3.56	0.22	3.58–3.95

†Denotes modes for which good frequency tuning was not achieved.
Entries marked '–' indicate modes for which an isolated resonance response could not be obtained.

Table 4.15: Phase 2 CEM P2032993 Frequencies and Passive Damping Values Identified From MIMO FRF's (ERA)

Mode Number	FEM Freq. (Hz)	ERA Freq. (Hz)	Predicted Added Damping (Percent)	Measured Inherent Damping (Percent)	ERA Total Damping (Percent)
7	1.698	1.738	0.86	0.32	1.31
8	2.262	2.295	2.09	0.22	2.42
9	2.802	2.863	1.98	0.33	2.53
10	5.114	5.301	3.42	0.27	4.00
11	5.793	6.033	3.79	0.30	4.65
20	7.792	7.864	6.62	0.45	7.89
21	8.336	8.652	4.02	0.31	4.35
22	8.813	8.831	3.11	0.23	3.20
23	10.34	10.366	3.56	0.22	3.44

variations in the mode shapes and frequencies. Nevertheless, the measured damping ratios obtained from ERA for the lightly-damped modes in the [13–20] Hz region were all larger than 1.6 percent.

While the damping values in Table 4.16 give some indication as to the success of the passive damping design, the true measure of success is determined by the open-loop responses, from which the damping requirements were derived. Figures 4.21 through 4.25 show the measured and predicted open-loop frequency responses of the passively damped Phase 2 CEM. The peak maximum singular values of the OSS LOS frequency responses are all well below the 60 arc-seconds requirement. The peaks of the measured collocated thruster to accelerometer frequency responses are all well below the predicted values, indicating that the minimum roll-off gain margins for the active controller were also exceeded.

Table 4.17 lists the measured and predicted RMS values of the OSS LOS outputs. The disturbances were Gaussian random thruster commands in a frequency band from 1–10 Hz. The RMS values were computed from the OSS LOS responses over a 120 second time interval. The measured and predicted RMS values for the OSS LOS show generally close agreement. Some of the discrepancies are attributed to signal drift of the OSS LOS detector outputs observed during the tests.

The sensitivity of the Phase 2 damping design to ambient temperature variations

Table 4.16: Phase 2 CEM P2090992 Required Versus Achieved Passive Damping

Mode Number	FEM Freq. (Hz)	ERA Freq. (Hz)	Required Damping (Percent)	ERA Damping (Percent)
10	5.497	5.301	1.35	4.00
11	5.928	6.033	2.1	4.65
20	7.632	7.864	1.25	7.89
21	8.495	8.652	1.5	4.35
22	9.022	9.018	0.5	3.20
23	10.18	10.639	2.1	3.44
28	12.74	–	2.3	–
33	13.59	–	1.7	–
34	13.80	–	1.2	–
35	14.12	–	0.9	–
36	14.35	–	1.7	–
38	15.68	–	0.2	–
39	16.45	–	1.0	–
44	18.10	–	0.2	–
49	18.52	–	0.2	–
50	18.78	–	0.2	–

Entries marked '–' indicate modes which could not be compared to the model due to significant variations in the mode shapes.

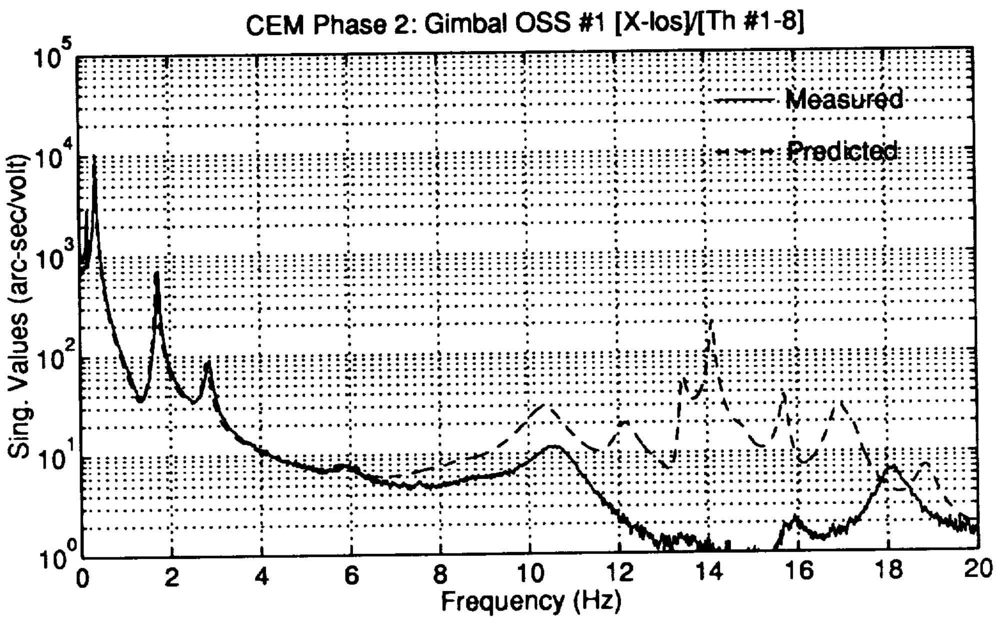

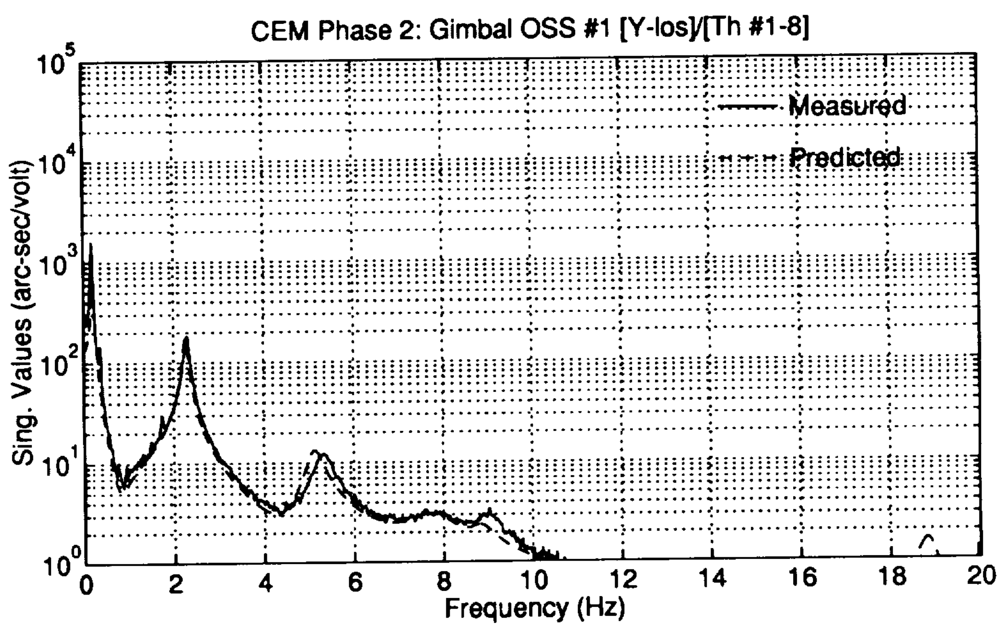

Figure 4.21: Phase 2 CEM Measured and Predicted Open-Loop Passively Damped Frequency Responses of OSS #1 LOS Outputs to Thrusters 1–8

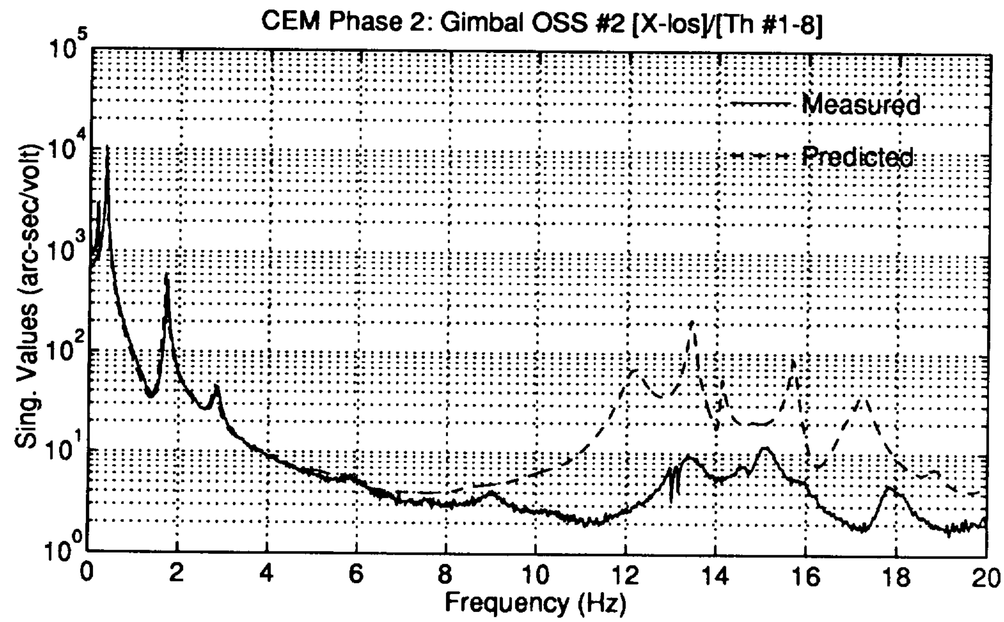

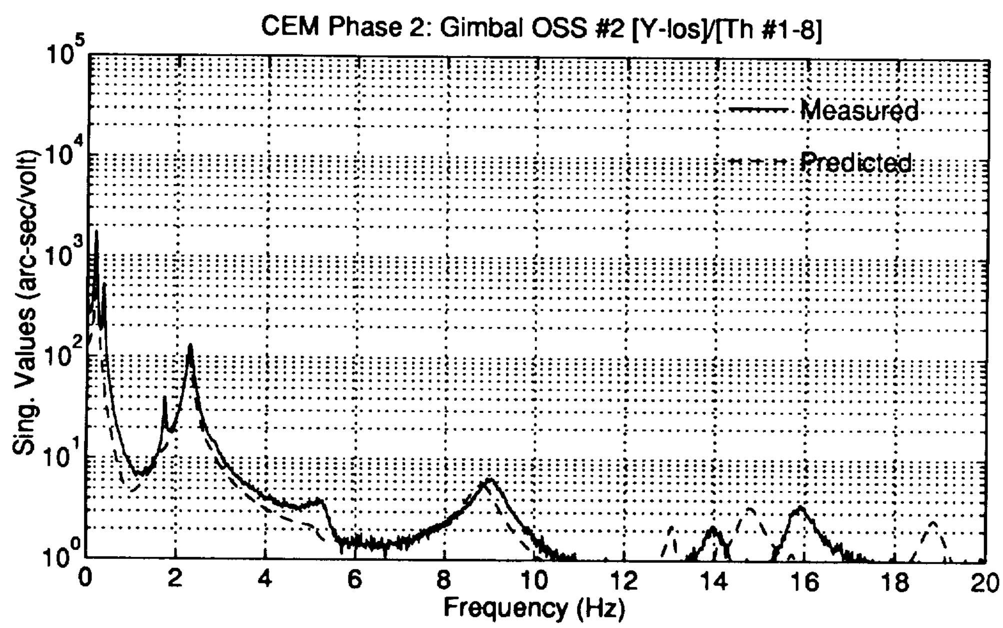

Figure 4.22: Phase 2 CEM Measured and Predicted Open-Loop Passively Damped Frequency Responses of OSS #2 LOS Outputs to Thrusters 1–8

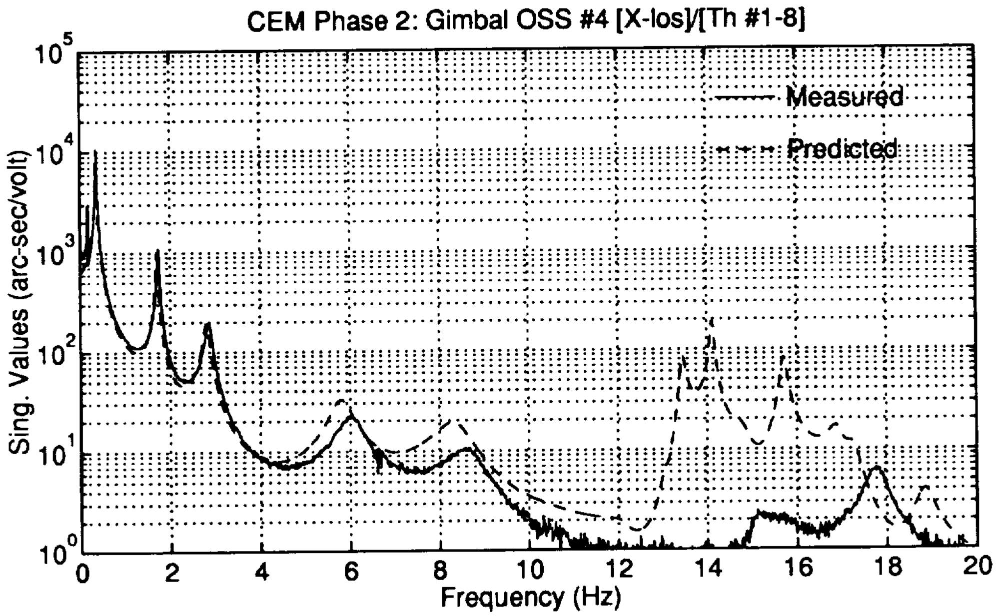

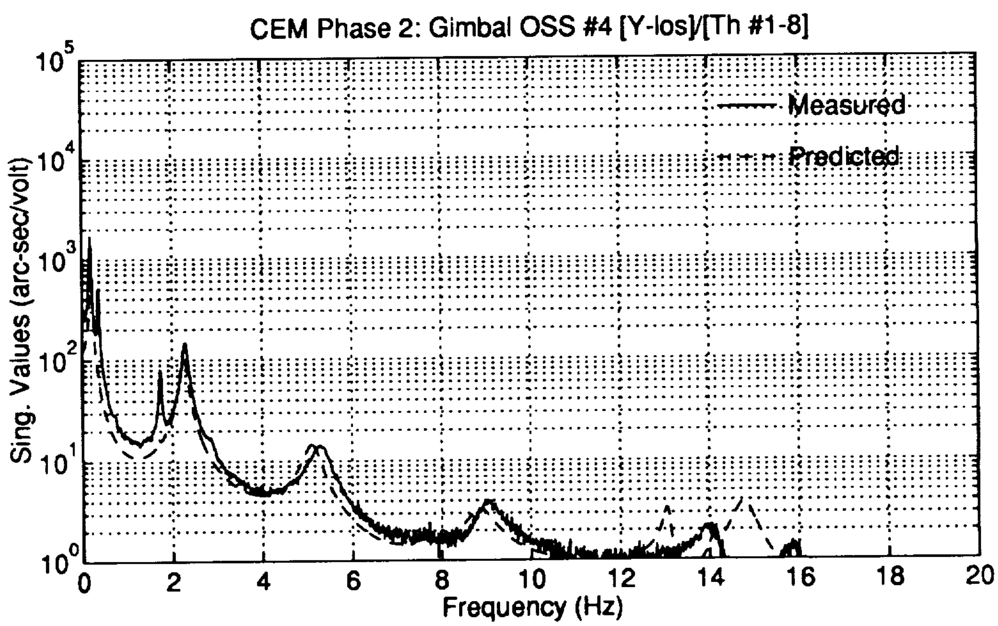

Figure 4.23: Phase 2 CEM Measured and Predicted Open-Loop Passively Damped Frequency Responses of OSS #4 LOS Outputs to Thrusters 1–8

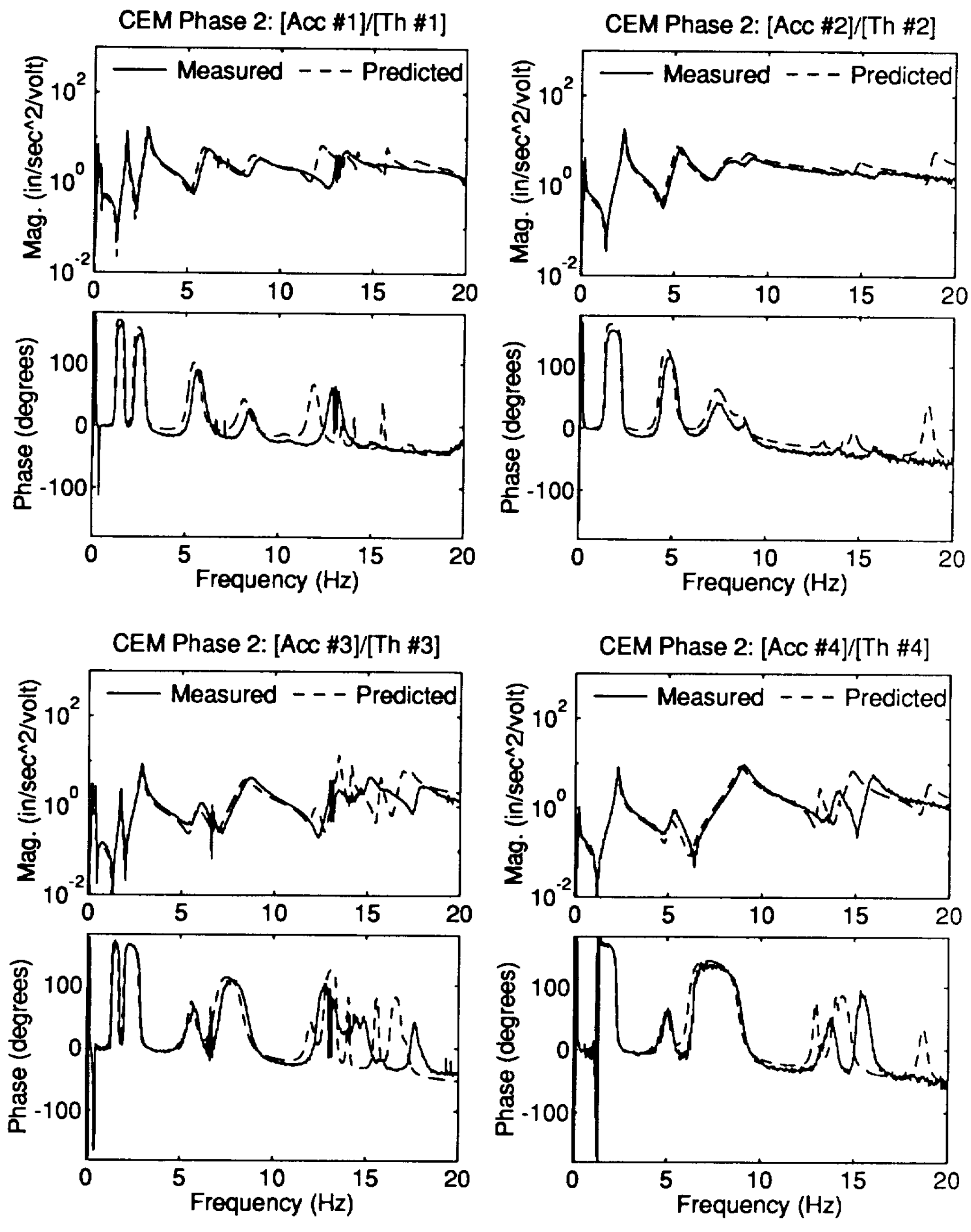

Figure 4.24: Phase 2 CEM Measured and Predicted Open-Loop Passively Damped Frequency Responses of Accelerometers #1–#4 to the Collocated Thrusters

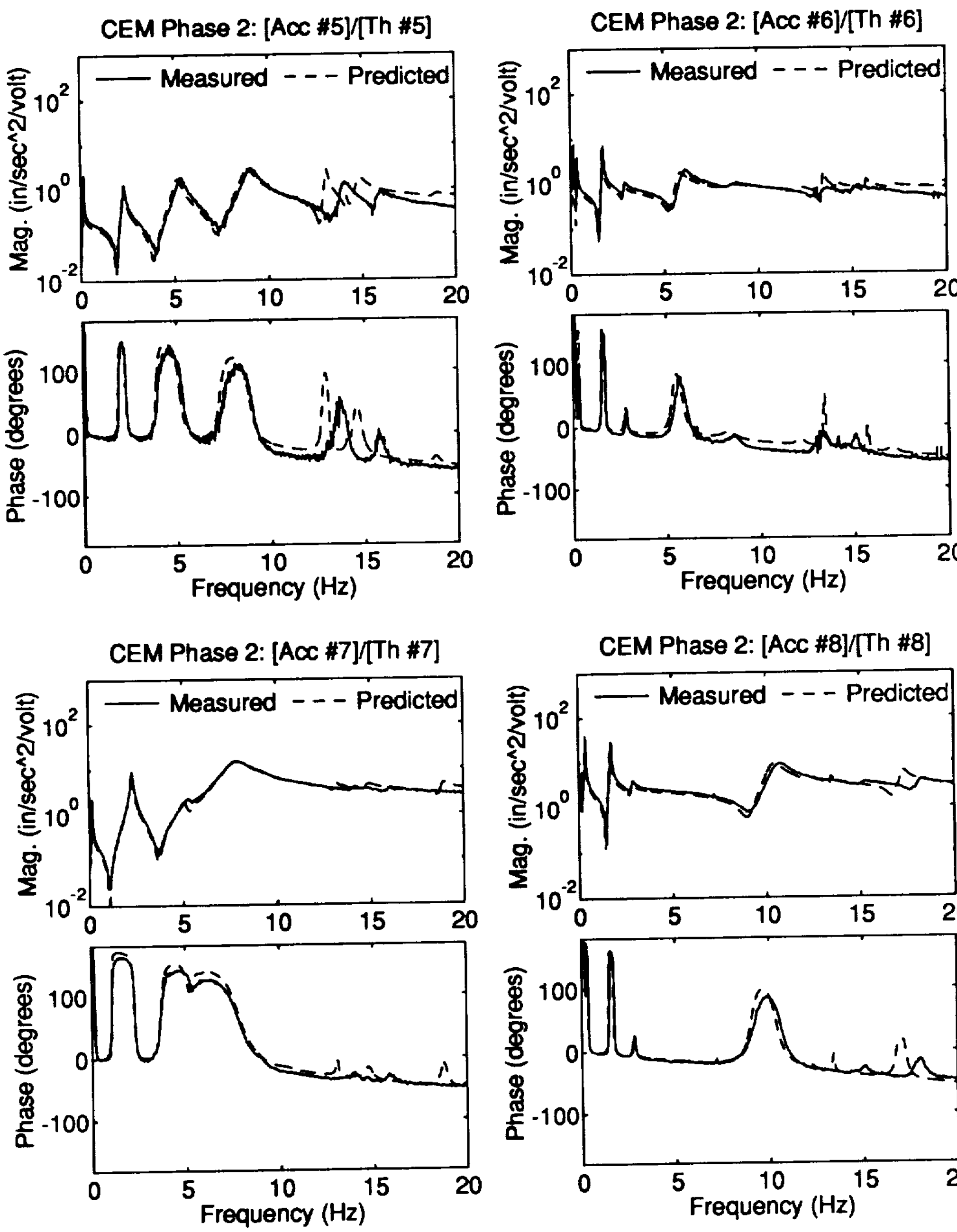

Figure 4.25: Phase 2 CEM Measured and Predicted Open-Loop Passively Damped Frequency Responses of Accelerometers #5–#8 to the Collocated Thrusters

Table 4.17: Phase 2 CEM Open-Loop Passively Damped RMS Values of Random Disturbance Responses

Output/Control Command	Measured Undamped	Measured Damped	Predicted Damped
Gimbal OSS #1 x LOS (arc-sec)	146.1	98.55	92.83
Gimbal OSS #1 y LOS (arc-sec)	75.08	20.92	21.28
Gimbal OSS #2 x LOS (arc-sec)	127.6	93.06	88.57
Gimbal OSS #2 y LOS (arc-sec)	71.31	17.25	14.59
Gimbal OSS #4 x LOS (arc-sec)	202.6	119.0	111.3
Gimbal OSS #4 y LOS (arc-sec)	75.77	19.60	16.55

was investigated. The frequency responses of the passively damped structure were obtained at an ambient temperature of approximately 80 degrees Fahrenheit, corresponding to 5 degrees above the design temperature of 75 degrees. The frequency responses for the Gimbal OSS #1 are shown in Figure 4.26 for the nominal and elevated temperatures. The slight variation in modal frequencies and peak responses indicates that the damper properties varied slightly with temperature.

4.6 Closed-Loop Active/Passive Results

The approach for combining high authority active control with passive damping discussed above was successfully implemented on the CEM test article in its Phase 1 and Phase 2 configurations. Selected results from the Phase 1 and Phase 2 combined active/passive designs are discussed here. Complete experimental results from the Phase 2 designs are given in Appendix D.

4.6.1 Phase 1 Active/Passive Results

For the Phase 1 design the damping treatment was designed to increase the controller robustness to the 7.8 Hz laser tower/main truss mode. A high gain HAC/LAC controller was designed for the undamped CEM with relatively small roll-off gain margins of approximately 6 dB (the HAC controller was an H_2/LQG design and the LAC inner loop was an LVF design). The small stability margins resulted in a high-frequency limit cycle of the laser tower/main truss mode (Figure 4.27). Addition of the 12 passive struts to the base of the laser tower was sufficient to robustly stabilize this mode with the HAC/LAC controller (also Figure 4.27).

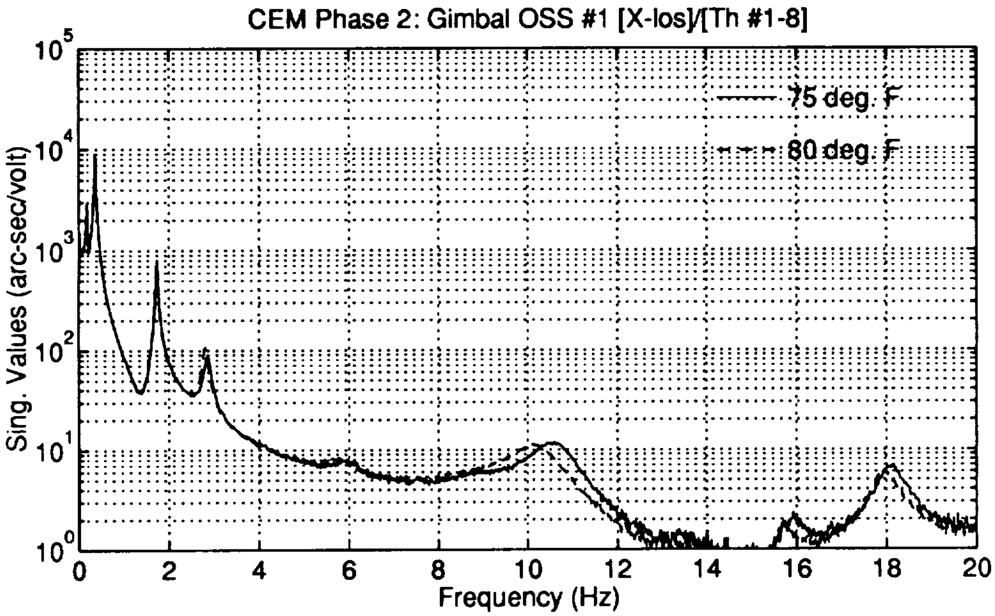

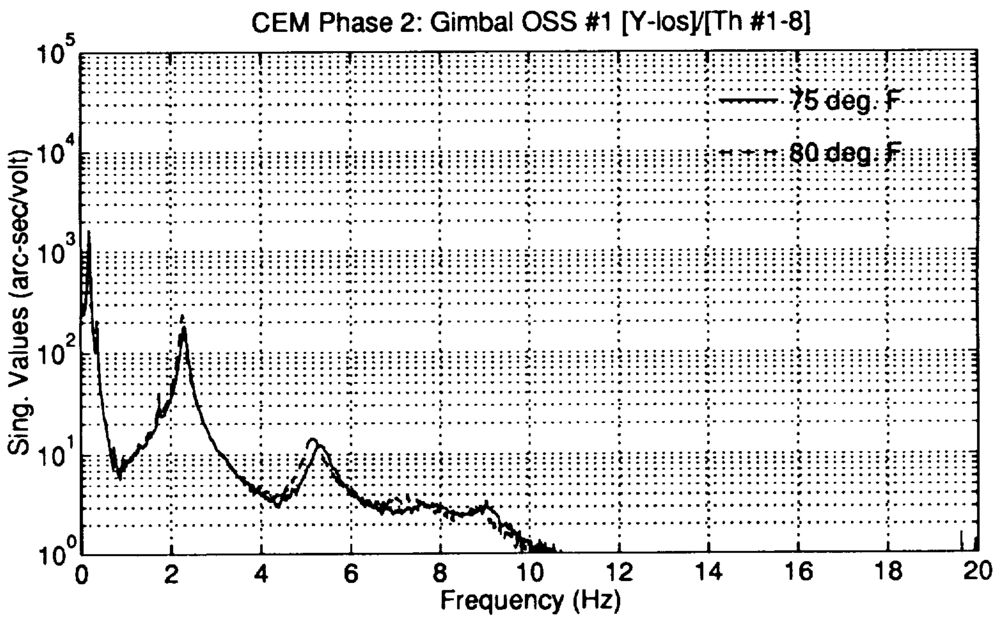

Figure 4.26: Phase 2 CEM Measured Open-Loop Passively Damped Frequency Responses for the Nominal and Elevated Ambient Temperatures

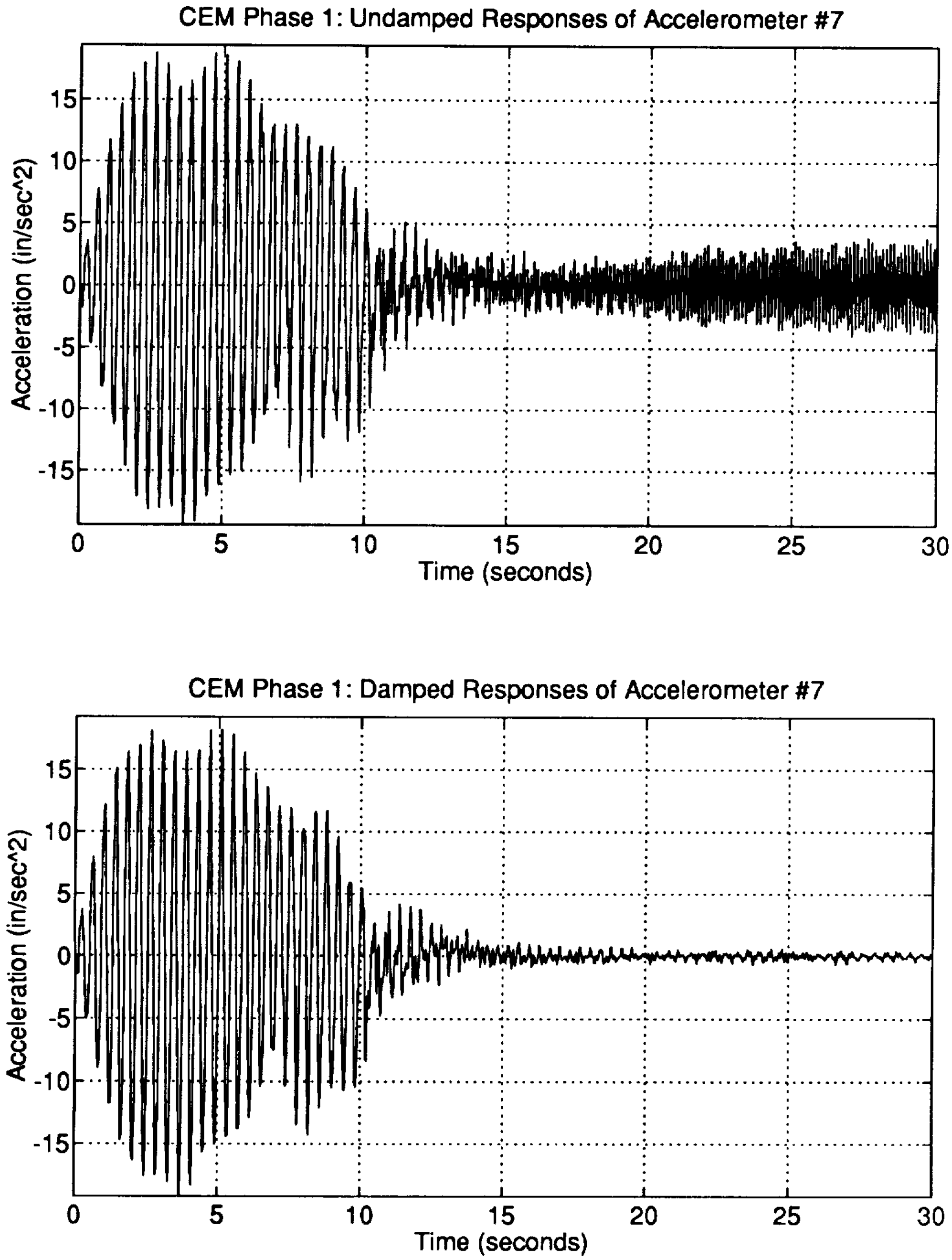

Figure 4.27: Phase 1 CEM Measured Closed-Loop Time Responses of a HAC/LAC Controller With and Without Passive Damping Treatments

4.6.2 Phase 2 Active/Passive Results

An H_2/LQG HAC controller, HAC/PAS 1.6.1.2, was designed in combination with the passive damping treatment for the Phase 2 CEM. The plant design model used for the H_2/LQG HAC synthesis (Figure 3.23) was the same as for the H_2/LQG control designs in Section 3.3.4 except that the passively damped FEM was used instead of the undamped FEM.

The final weighting functions for HAC/PAS 1.6.1.2 were selected as

$$Z_{\text{LOS}} = 600 f_{\text{LOS}}(s) I_{6\times6}, \quad W_\xi = 0_{9\times9}, \quad W_u = 1.7 I_{8\times8} \tag{4.45}$$

$$Z_\xi \; = \; \text{diag}\{60, 60, 60, 0, 0, 0, 0, 0, 0\} \tag{4.46}$$

$$W_y = \text{diag}\left\{\begin{array}{c} 3.6 f_1(s) \\ 6.0 f_{2a}(s) \\ 2.7 f_1(s) \\ 3.6 \\ 3.0 \\ 2.7 f_1(s) \\ 3.0 f_{2a}(s) \\ 3.9 f_1(s) \end{array}\right\} \qquad Z_u = \text{diag}\left\{\begin{array}{c} 0.18 f_{2a}(s) \\ 0.25 f_{2a}(s) \\ 0.12 f_1(s) \\ 0.13 f_1(s) \\ 0.1 f_1(s) \\ 0.14 f_{2a}(s) \\ 0.08 f_{2a}(s) f_1(s) \\ 0.08 f_{2a}(s) f_1(s) \end{array}\right\} \tag{4.47}$$

where the weighting filters $f_1(s)$, $f_{2a}(s)$, and $f_{2b}(s)$ are given in Section 3.3.4. The LOS weighting function $f_{\text{LOS}}(s)$ given by

$$f_{\text{LOS}}(s) = \frac{1.3^2(s^2 + 2(0.6)(0.5) + 0.5^2)}{0.5^2(s^2 + 2(0.5)(1.3) + 1.3^2)} \tag{4.48}$$

was used to increase the LOS disturbance attenuation for the elastic modes separately from the rigid-body responses.

The weighting functions for the HAC controller synthesis model were chosen to satisfy the design requirements in Section 3.1.2. The final controller had 53 states. Analysis and experimental results for the Phase 2 HAC active/passive control design are discussed below.

Multivariable Gain and Phase Margins

Multivariable gain and phase margins of the HAC controller were analyzed at the plant model control inputs and sensor outputs with the damped CEM model. Figure 4.28 shows the singular values of the return difference transfer function matrix frequency responses at the thruster command inputs and accelerometer sensor outputs for the active/passive controller. The gain/phase margins for HAC/PAS 1.6.1.2 are $[-3.84, +7.04]$ dB and ± 32.25 degrees at the control inputs and $[-4.05, +7.83]$ dB and ± 34.54 degrees at the sensor outputs. The multivariable gain/phase margins of the HAC active/passive design satisfied the requirements of $[-3.52, +6.02]$ dB and ± 28.96 degrees.

High Frequency Roll-off Gain Margins

The guaranteed roll-off gain margins of the active/passive controller was analyzed at the control inputs and sensor outputs. Figure 4.29 shows the singular values of the open-loop transfer function matrix frequency responses. The minimum roll-off gain margins is 4.87 dB at approximately 5 Hz. While this does not meet the original requirements, the roll-off gain margin requirements are met or exceeded for all modes beyond 5.5 Hz. Since the roll-off requirement tends to be conservative and the uncertainties in the 5.11 Hz main truss bending mode were not expected to be very large, the original roll-off requirement was relaxed for this mode.

Experimental Closed-Loop Performance

The tests described in Section 3.3.4 to assess the closed-loop performance of the active only controllers were performed to access the closed-loop performance of the combined active/passive approach. The test results showed that the combined active/passive control design provided strong attenuation of the elastic structural mode responses from 1 Hz to frequencies beyond 10 Hz.

Figure 4.30 show the measured closed-loop transient responses of gimbal #1 OSS x and y LOS for the HAC/PAS 1.6.1.2 active/passive control design. The responses were obtained by exciting the system with sinusoidal thruster inputs from 0–7 seconds with the control loops open. The sinusoidal thruster inputs were at the same frequencies and amplitudes as for the undamped H_2/LQG controller tests. The control loops were then closed at 8 seconds.

Figure 4.31 shows the measured open and closed-loop frequency responses. The attenuation of the peak responses of the first three main truss bending/torsional modes generally better than for the H_2/LQG and HAC/LAC designs (the identified damping ratios for these three modes are 17.8%, 26.7% and 13.7%, respectively). More importantly, the responses from 4–10 Hz are significantly reduced for the HAC/-PAS 1.6.1.2 active/passive design.

Table 4.18 lists the measured and predicted RMS values of the OSS LOS outputs and the controller commands. The disturbances were Gaussian random thruster commands in a frequency band from 1–10 Hz. The measured and predicted RMS

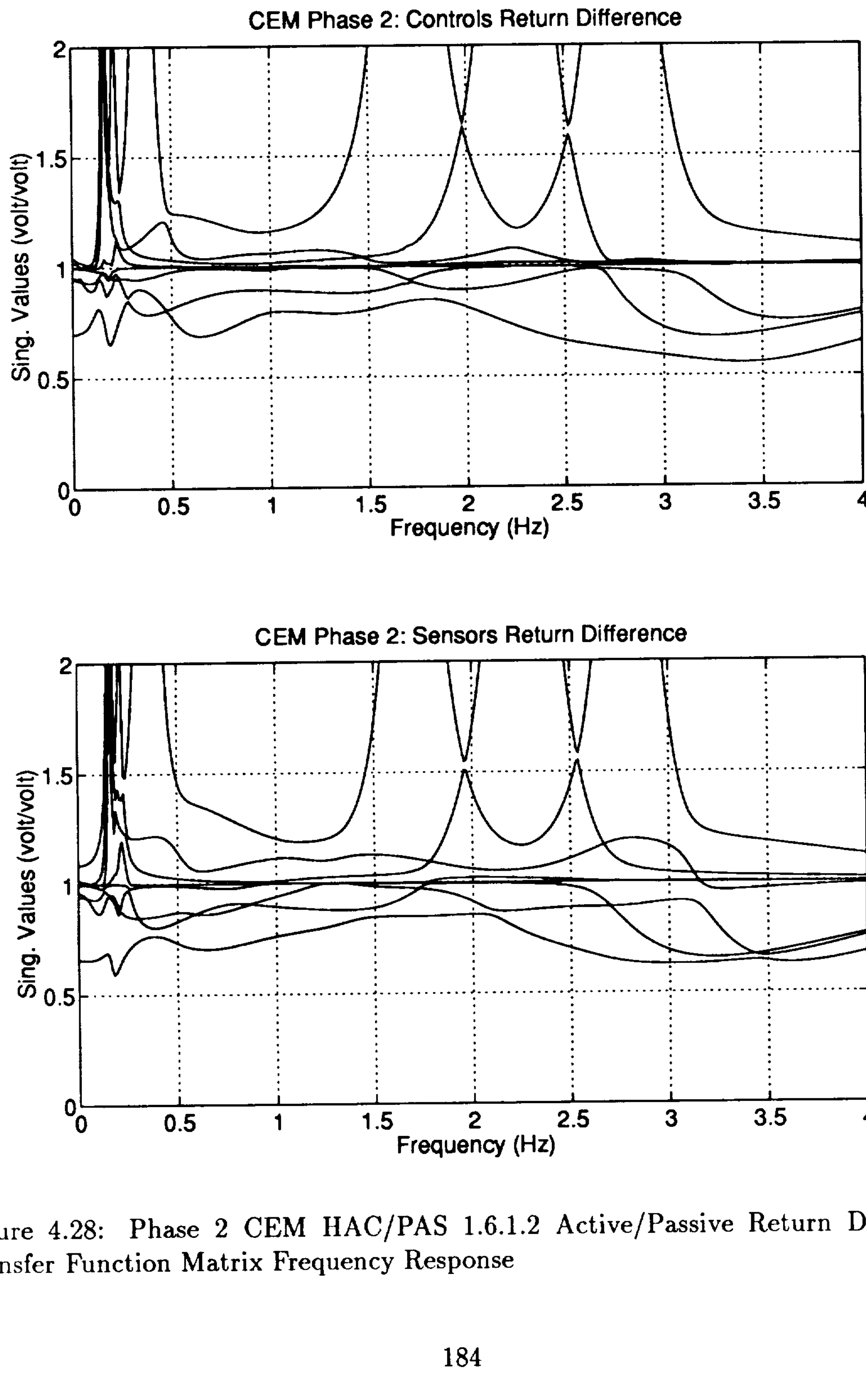

Figure 4.28: Phase 2 CEM HAC/PAS 1.6.1.2 Active/Passive Return Difference Transfer Function Matrix Frequency Response

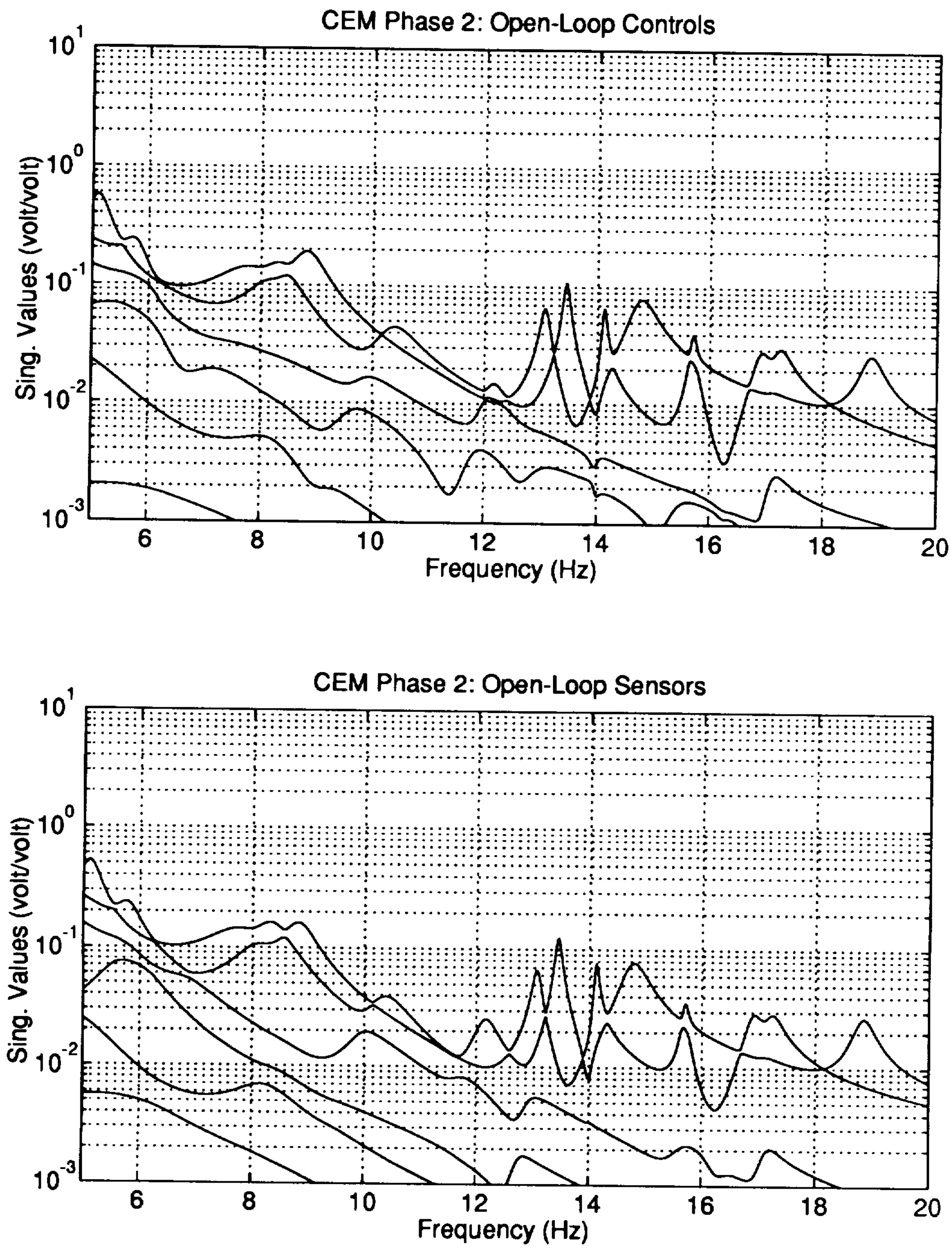

Figure 4.29: Phase 2 CEM HAC/PAS 1.6.1.2 Active/Passive Open-Loop Frequency Response Singular Values

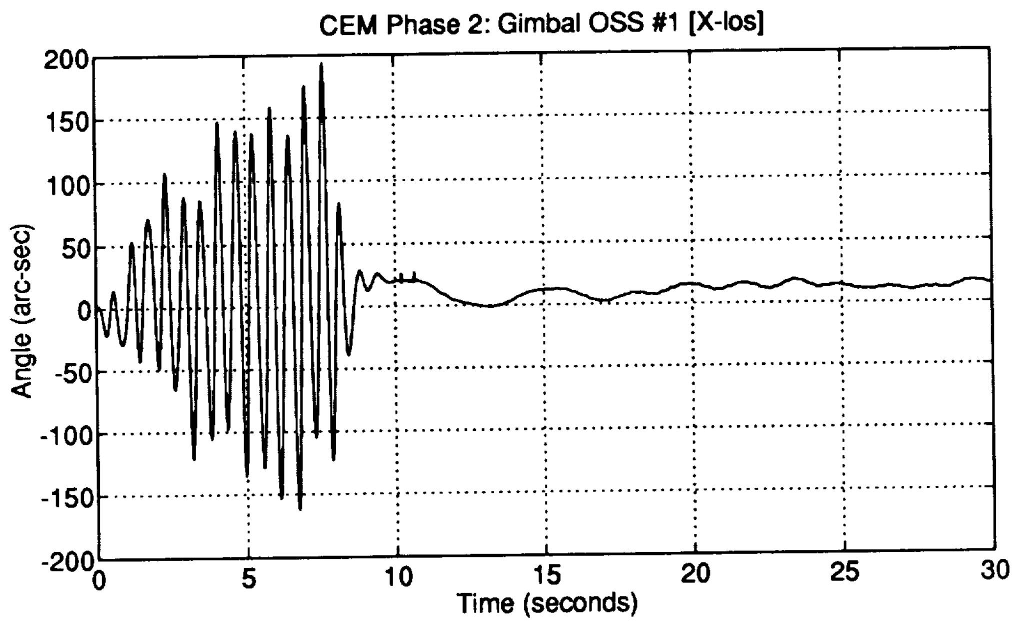

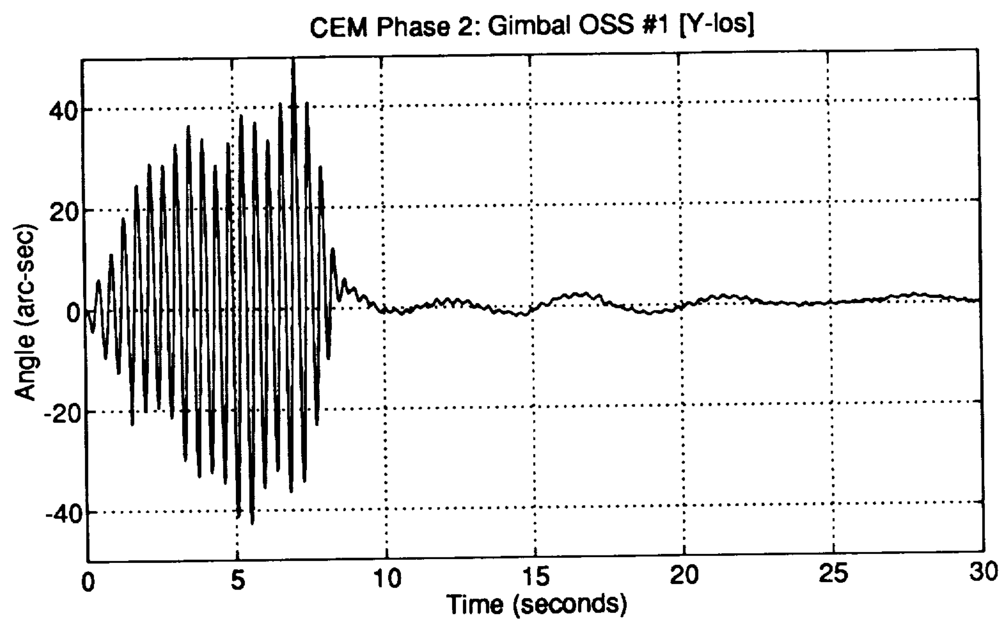

Figure 4.30: Phase 2 CEM HAC/PAS 1.6.1.2 Measured Closed-Loop Transient Responses for the Damped Test Article

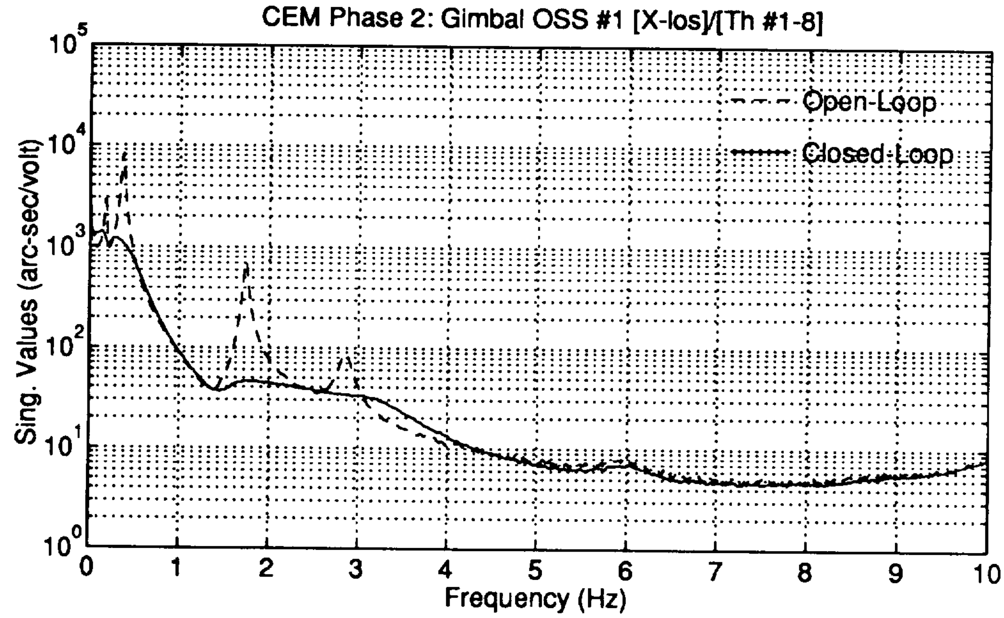

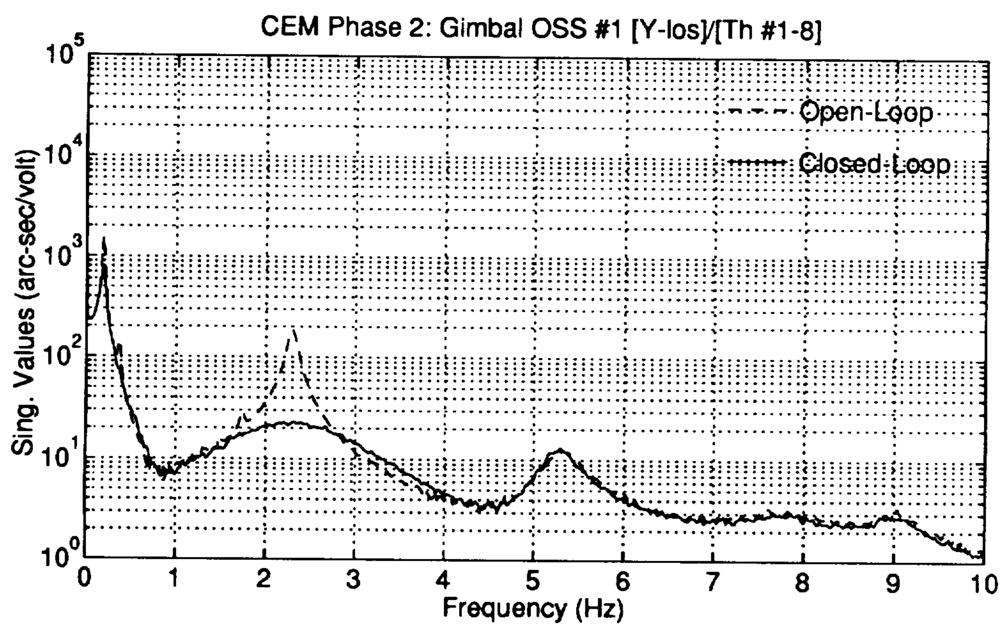

Figure 4.31: Phase 2 CEM HAC/PAS 1.6.1.2 Measured Open and Closed Loop Frequency Responses for the Damped Test Article

Table 4.18: Phase 2 CEM HAC/PAS 1.6.1.2 RMS Values of Random Disturbance Responses

Output/Control Command	Measured Open-Loop Undamped	Measured Closed-Loop Damped	Predicted Closed-Loop Damped
Gimbal OSS #1 x LOS (arc-sec)	146.1	43.23	41.75
Gimbal OSS #1 y LOS (arc-sec)	75.08	10.02	9.391
Gimbal OSS #2 x LOS (arc-sec)	127.6	41.57	42.56
Gimbal OSS #2 y LOS (arc-sec)	71.31	8.523	6.431
Gimbal OSS #4 x LOS (arc-sec)	202.6	53.59	51.52
Gimbal OSS #4 y LOS (arc-sec)	75.77	10.49	8.309
Thruster #1 Command (volts)	0.0	0.1724	0.1578
Thruster #2 Command (volts)	0.0	0.1171	0.1106
Thruster #3 Command (volts)	0.0	0.3191	0.2932
Thruster #4 Command (volts)	0.0	0.2366	0.2230
Thruster #5 Command (volts)	0.0	0.2629	0.2475
Thruster #6 Command (volts)	0.0	0.4882	0.4345
Thruster #7 Command (volts)	0.0	0.1999	0.1894
Thruster #8 Command (volts)	0.0	0.2594	0.2227

values were computed from the OSS LOS responses over a 120 second time interval. The average RMS LOS output reductions from the undamped open-loop values were 71% for the x LOS output and 87% for the y LOS output The measured and predicted RMS values for the OSS LOS show generally close agreement.

Experimental Verification of Control Law Sensitivity

Figure 4.32 shows the measured and predicted closed-loop frequency responses for both control laws. The responses show excellent agreement for the frequencies within the control bandwidth (0–4 Hz) and good agreement up to 10 Hz. The close agreement between the predicted and measured frequency responses and the RMS values of the LOS responses in Table 4.18 indicate that the closed-loop LOS responses were relatively insensitive to the model inaccuracies.

The sensitivity of the HAC control design to artificial gain variations at the control inputs was tested. The tests involved increasing the feedback gains simultaneously in all control loops (using the CPOT parameter in the real-time software) from the nom-

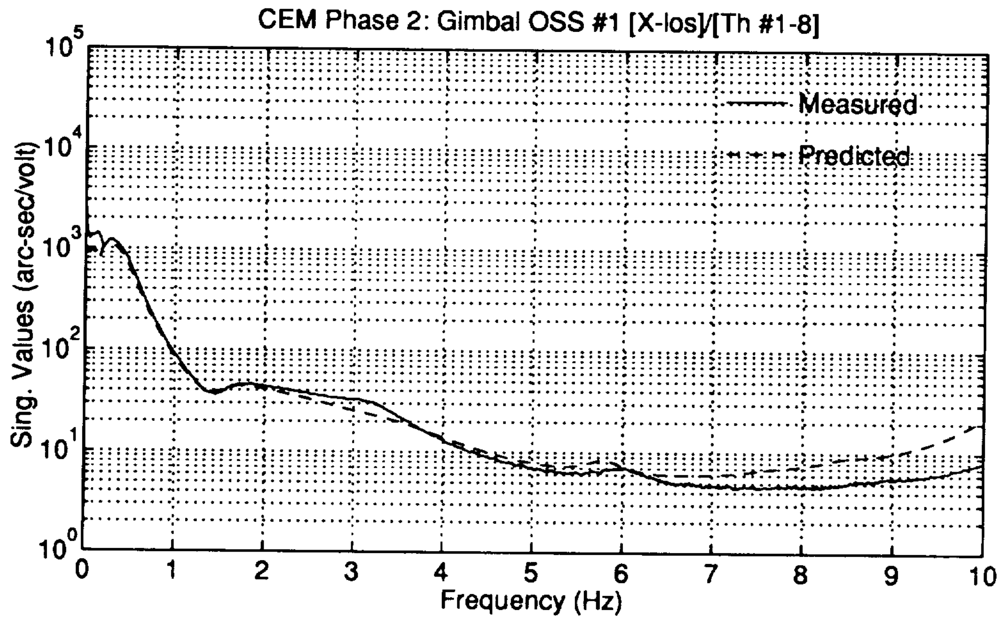

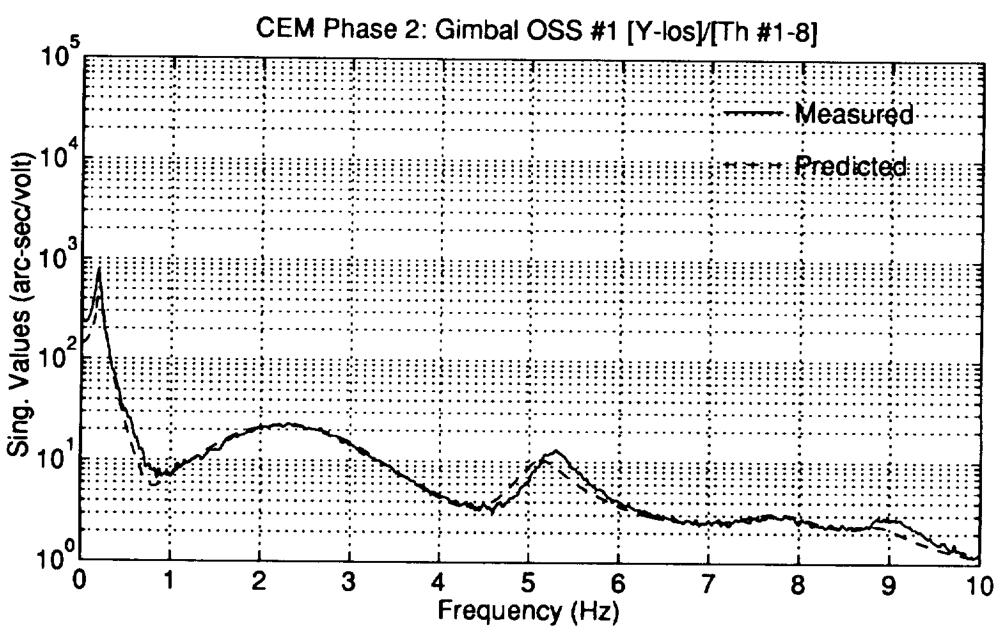

Figure 4.32: Phase 2 CEM HAC/PAS 1.6.1.2 Active/Passive Measured and Predicted Closed-Loop Frequency Responses

inal value (CPOT=1.0) until an instability or limit-cycle was observed. A limit-cycle was observed at a CPOT gain of 1.9 involving the yaw plane first bending/torsion mode at approximately 3.45 Hz. The peak amplitude for this limit-cycle response was approximately 0.75 in/sec^2 as measured by accelerometers #1, #3, and #8.

Comparison with the H_2/LQG and HAC/LAC Designs

Figures 4.33 and 4.34 show comparisons of the closed-loop frequency responses for the HAC/PAS 1.6.1.2 with those of the H_2/LQG A1.4 and HAC/LAC 1.2 controllers. The three controllers provides similar attenuation of the modes from 1–4 Hz (within the active control bandwidth of the H_2/LQG and HAC controllers). The passive damping treatment, however, results in significantly more disturbance attenuation at frequencies greater than 4 Hz for the HAC/PAS 1.6.1.2 active/passive design. In the 4–20 Hz bandwidth, a 10:1 reduction in the peaks of the maximum singular values of the OSS x and y LOS frequency responses is achieved with the active/passive controller compared to the active-only H_2/LQG A1.4 design. Figure 4.35 compares the average RMS LOS level reductions obtained for the open-loop and closed-loop systems[3]. Compared to the H_2/LQG A1.4 design, a 30% and 50% reduction in the LOS RMS outputs is achieved for the x and y components, respectively.

[3]Data for the Active Control label corresponds to the H_2/LQG A1.4 design. Reduction levels achieved with the HAC/LAC 1.2 design would fall in between the H_2/LQG A1.4 and the combined active/passive designs.

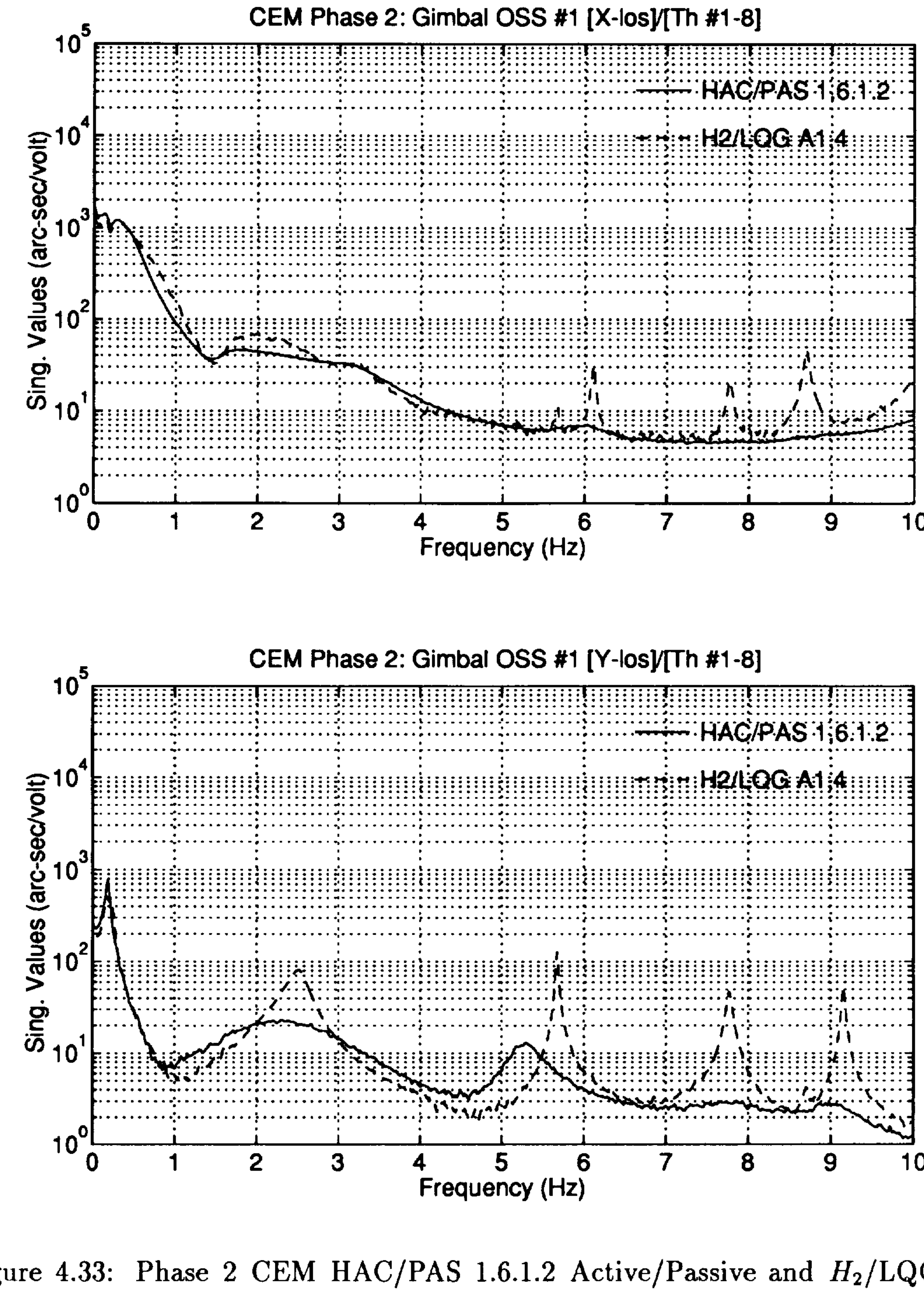

Figure 4.33: Phase 2 CEM HAC/PAS 1.6.1.2 Active/Passive and H_2/LQG A1.4 Measured Closed-Loop Frequency Responses

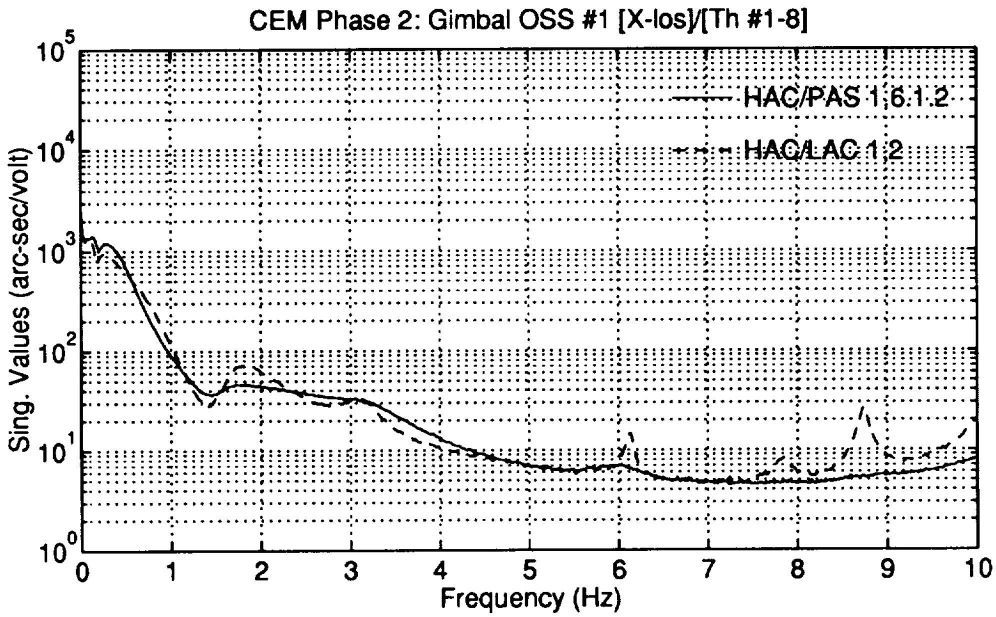

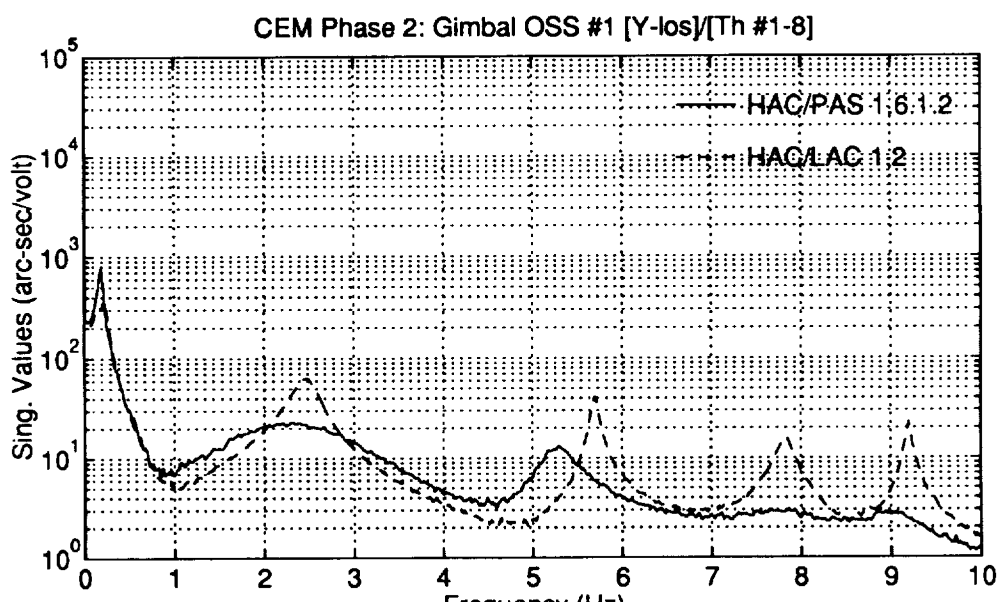

Figure 4.34: Phase 2 CEM HAC/PAS 1.6.1.2 Active/Passive and HAC/LAC 1.2 Measured Closed-Loop Frequency Responses

C-3

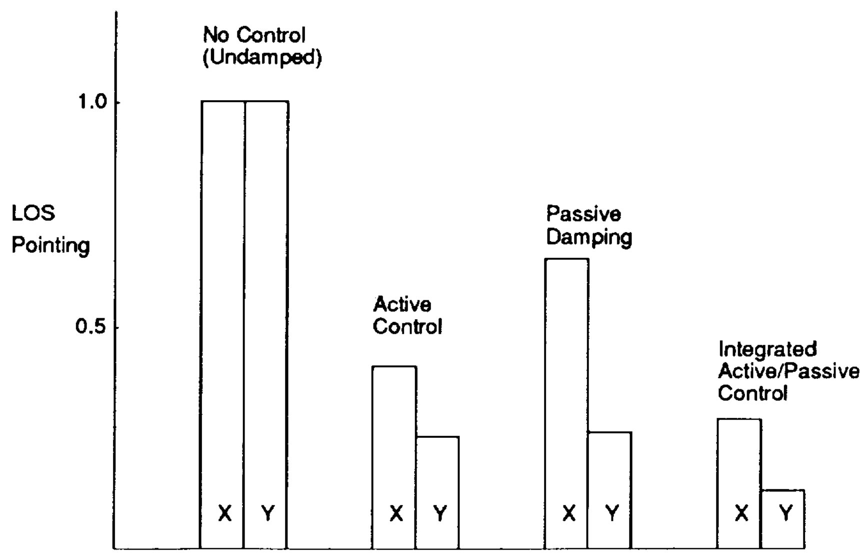

Figure 4.35: Comparison of Average RMS Experimental Values for OSS LOS x and y outputs with Band-limited Random Inputs

Chapter 5

Conclusions and Lessons Learned

In this chapter, we summarize the main results of this program and outline the lessons learned from the control designs, closed-loop tests, fabrication and tests of the damped struts for the CSI CEM testbed.

5.1 Main Results

We have developed a general methodology, integrating active control with passive damping for control of a large, flexible spacecraft.

Each component of this methodology, design of a MIMO vibration suppression controller for LOS minimization and design of a passive damping treatment, has been successfully implemented and verified on the CEM testbed. Significant performance improvements have been demonstrated experimentally with a vibration suppression controller designed for the damped CEM.

MIMO vibration suppression control

A novel technique to design a vibration suppression controller for a flexible structure has been developed. It allows the designer to incorporate the necessary amount of roll-off in the MIMO compensator to achieve a prescribed amount of multivariable high-frequency stability margins. Tailoring of the multivariable margins within the active control bandwidth and robustness to modal data are also included in the design process. Using this method, MIMO controllers designed to provide active damping of the rigid-body modes and main truss elastic modes were successfully tested on the CEM in its Phase 1 and Phase 2 configurations. An order of magnitude peak reduction in the LOS outputs was demonstrated for the dominant structural modes up to 4 Hz. The achieved RMS LOS output reductions for random inputs limited

PRECEDING PAGE BLANK NOT FILMED

to 1–10 Hz were about 60% for the x LOS output and 75% for the y LOS output. Experimental closed-loop frequency responses for LOS and accelerometer outputs showed good agreement with the analytical predictions up to 10 Hz.

Passive damping treatment

Using the MSE method specifically tailored for the CEM, a passive damping treatment was designed based on damping level requirements for a set of targeted modes in the high-frequency band [4–30] Hz. The damping levels were selected to achieve the same level of performance in the high-frequency band as in the [0–4] Hz active control bandwidth and to improve the HAC robustness (roll-off). A set of 60 viscoelastically damped struts was designed and fabricated for the CEM. Identified damping levels from 3% to 5% were achieved for the dominant targeted modes in the [4–10] Hz frequency band; about twice the targeted levels and about an order of magnitude larger than the damping levels for the untreated structure. After having incorporated the measured stiffness and loss factor data for the individual damped struts into the FEM model, the predicted damping levels for the structural modes in the [1–10] Hz region agreed within 10% of the experimentally identified levels. The MIMO experimental frequency responses for LOS and accelerometers outputs showed good agreement in the [0–10] Hz region with the analytical FRFs derived from the damped FEM mode.

Integrated active/passive vibration control

For the Phase 1 CEM, a passive damping treatment of the laser tower was successfully used to eliminate a high-frequency limit cycle occurring with an active-only low-order controller. Other investigators had found that the same high-frequency laser tower/main truss mode was easily destabilized with active-only control.

An integrated active/passive vibration suppression controller was successfully designed and tested on the Phase 2 damped CEM. As with the previous open and closed-loop tests, good agreement between predicted and measured FRF data was obtained in the [0-10] Hz region. An effective increase of the active bandwidth from 4 to 10 Hz was demonstrated. Compared to an active-only H_2/LQG controller, the following performance increase was achieved with the active/passive controller:

1. a reduction of the peak LOS outputs by a factor of 5 and 10 respectively for the x and y components in the [4–10] Hz region.

2. a 30% and 50% reduction in the LOS RMS outputs for the x and y components respectively for band-limited random inputs.

The integrated active/passive controller was also evaluated against an HAC/LAC active-only controller. The LAC component based on local velocity feedback played the same role as the passive damping treatment by adding damping to a set of targeted modes outside the HAC controller bandwidth. The active/passive controller was shown to have overall superior performance compared to the HAC/LAC controller. In particular peak reduction achieved for the LOS outputs in the high-frequency [4–10] Hz region were still higher by a factor of 2 to 3.

5.2 Lessons Learned

Based on the extensive amount of control designs and tests performed for several configurations of the CEM testbed, the following recommendations can be made:

1. Incorporating frequency shaping techniques in the design of active controllers for complex elastic structures is essential to achieve stability and performance.

2. Early in the design process the open-loop models derived from FEM data should be evaluated against experimental data using MIMO frequency response tests relating the feedback *and* the performance evaluation sensors to the actuator sets.

3. For ground testbeds, it is important to account for gravity components in modeling of accelerometer outputs. For the CEM this step was essential to match the FRF responses in the rigid-body frequency region. Actually some initial LVF controller designs were unstable if these effects were not accounted for.

4. Both time and frequency domain tests should be used to evaluate performance of the closed-loop controllers. For this work we performed sine excitation and random input tests as well as closed-loop frequency responses. Closed-loop FRF tests are quite useful to verify proper implementation of the real-time active vibration suppression controller.

5. The ability to transfer back and forth through E-Mail the experimental data acquired on the testbed is very important for debugging and tuning of closed-loop controllers. In the case of the CEM, this was possible because there was a well-established procedure by the LaRC team to exchange input and output data.

Based on the experience gained in the design, fabrication and tests of the damped struts, the following suggestions are given:

1. VEM properties can have a significant batch-to-batch variation, and VEM characterization test results can vary widely from lab to lab. Secure a sufficient quantity of the selected VEM at the beginning of the program, have it characterized by a reliable lab for the temperature and frequency range of interest, and store it according to the manufacturer's recommendations. This practice will provide the most reliable VEM data for the program and will eliminate any questions about the pedigree of the VEM.

2. Direct complex stiffness testing is difficult to perform well. The dampers fabricated for this program were quite stiff, and exceeded the capacity of our normal strut test system. When developing a new test system, obtain enough measurements from different parts of the test apparatus to verify that all measurements are consistent with each other. Question all experimental results, even those which agree well with predictions. Self-canceling errors are possible.

3. Bonding presents a challenge to fabrication of small struts. Seemingly trivial changes in the damper design, such as the color of anodize used, can impact a process. Verify by test that changes in the design do not require process modification. Obsessively clean surfaces to be bonded. Inspect bond quality at each step where possible, and consider including inspection holes in the design to facilitate inspection of hidden bonds.

4. When determining the number and placement of dampers, design in more damping than required. A damping "factor of safety" will help ensure that performance goals are achieved, even in the presence of reasonable FEM errors and unit-to-unit variations in dampers.

5. Unit testing of a large population of each type of damper is essential for discovering fabrication problems.

6. Use measured damper properties in the FEM for final predictions. Excellent agreement between prediction and system test results can be obtained for frequency ranges where the system FEM is accurate.

Bibliography

[1] Jerry Newsom, W.E. Layman, H.B. Waites, and R.J. Hayduk. The NASA controls-structures interaction technology program. In *Proceedings of the 1990 International Astronautics Federation Conference*, number IAF–90–290, October 1990.

[2] W. Keith Belvin, K.E. Elliott, Anne Brunner, Jeff Sulla, and Jim Bailey. The LaRC CSI Phase-0 evolutionary model testbed: Design and experimental results. In *Proceedings of the 4th NASA/DoD Controls-Structures Interaction Technology Conference*, pages 594–612, November 1990.

[3] John Spanos and Zahidul Rahman. Optical pathlength control on the JPL phase B interferometer testbed. In *Proceedings of the 5th NASA/DoD Controls-Structures Interaction Technology Conference*, pages 343–357, March 1992.

[4] Alok Das, Joel L. Berg, et al. ASTREX — a unique testbed for CSI research. In *Proceedings of the 29th IEEE Conference on Decision and Control*, December 1990.

[5] V. L. Jones, A. P. Buckley, and A. F. Patterson. NASA/MSFC large space structures ground test facility. In *Proceedings of the AIAA Guidance and Control Conference*, August 1991.

[6] Russel N. Gehling, Daniel R. Morgenthaler, and Kenneth E. Richards, Jr. *Passive And Active Control Of Space Structures (PACOSS): Final Report for Period Nov 88–Apr 91.* Technical Report WL-TR-91-3052, Martin Marietta Astronautics Group, June 1991.

[7] Gregory W. Neat et al. Joint Langley Research Center/Jet Propulsion Laboratory CSI experiment. In *Proceedings of the 15th Annual AAS Guidance and Control Conference*, February 1992.

[8] John Chionchio and Michael Garnek. CSI/MMC studies for improving jitter performance for large multi-payload platforms. In *Proceedings of the 5th*

NASA/DoD Controls-Structures Interaction Technology Conference, pages 569–615, March 1992.

[9] Peiman Maghami, Suresh M. Joshi, and E. S. Armstrong. An optimization-based integrated controls-structures design methodology for flexible space structures. Technical Report NASA Technical Paper 3283, NASA Langley Research Center, January 1993.

[10] Jer-Nan Juang and Richard Pappa. An eigensystem realization algorithm. *AIAA Journal*, Vol 20(No. 9):1284–1290, September 1982.

[11] C. W. Chen, Jer-Nan Juang, and Gordon Lee. Frequency domain state-space system identification. Technical Report NASA Technical Memorandum 107659, NASA Langley Research Center, 1992.

[12] M. Phan, Lucas Horta, Jer-Nan Juang, and R. W. Longman. Linear system identification via an asymtotically stable observer. In *Proceedings of AIAA Guidance and Control Conference*, pages 1180–1194, August 1991.

[13] Jer-Nan Juang, Lucas G. Horta, and Minh Phan. System/observer/controller identification toolbox. NASA Technical Memorandum 107566, NASA Langley Research Center, Hampton, VA, 1992.

[14] Richard Y. Chiang and Michael G. Safonov. *Robust Control Toolbox.* The MathWorks, Inc., 24 Prime Park Way, Natick, MA 01760–1520, 1992.

[15] Anne M. Bruner, W. Keith Belvin, Lucas G. Horta, and Jer-Nan Juang. Active vibration absorber for the CSI evolutionary model: Design and experimental results. In *Proceedings of AIAA Structural Dynamics and Materials Conference*, pages 2929–2938. American Institute of Aeronautics and Astronautics, April 1991.

[16] U. Ly. *A Design Algorithm for Robust Low-Order Controllers.* PhD thesis, Stanford University, Department of Aeronautics and Astronautics, November 1982.

[17] U. Ly. H^2 and H^∞-design tools for linear time-invariant systems. In *Third Annual Conference on Aerospace Computational Control*, Oxnard, California, August 1989.

[18] Russel N. Gehling, Daniel R. Morgenthaler, and Kenneth E. Richards, Jr. *PACOSS Final Report: Damping Design Methodology.* Technical Report WRDC-TR-90-3044, Martin Marietta Astronautics Group, September 1990. Vol 1.

[19] Russel N. Gehling, Daniel R. Morgenthaler, and Kenneth E. Richards, Jr. *PA-COSS Final Report: Dynamic Test Article Modal Survey — Test and Analysis Results.* Technical Report WRDC-TR-90-3044, Martin Marietta Astronautics Group, September 1990. Vol 2.

[20] Russel N. Gehling, Daniel R. Morgenthaler, and Kenneth E. Richards, Jr. *PA-COSS Final Report: DTA Finite Element Model.* Technical Report WRDC-TR-90-3044, Martin Marietta Astronautics Group, September 1990. Vol 3.

[21] Conor D. Johnson and David A. Kienholz. Finite element prediction of damping in structures with constrained viscoelastic layers. *AIAA Journal*, Vol 20(No. 9):1284–1290, September 1982.

[22] B. R. Allen and E. D. Pinson. Complex stiffness test data for three viscoelastic materials by the direct complex stiffness method. In *Proceedings of Damping '91, Vol II*, pages EAE–1—EAE–14, August 1991.

[23] D. I. G. Jones. Results of a round robin test series to evaluate complex moduli of a selected damping material. In *Proceedings of Damping '91, Vol II*, pages EBD–1—EBD–18, August 1991.

[24] Bryce Fowler. VEM property referency guide, release 1.1. Technical Report No. 93–01–05, CSA Engineering, Inc., July 1993.

Appendix A

CSI MATLAB Programs Reference Guide

This appendix is a reference guide to the MATLAB[1] functions developed specifically for constructing the CEM state space models and for analyzing the controller designs. Many of these functions make use of a toolbox of generic controls design and analysis functions developed in the Advanced Controls group at Martin Marietta.

The following tables give brief descriptions of the MATLAB functions. The first two tables describe functions specific to the CEM. Online help is available for each function by executing the `help` command on the function name.

CSI Evolutionary Models	
cem	Build state space CSI Evolutionary Model (CEM).
cemact	Build thruster actuators model.
cemsen	Build analog sensor filter model.
fem2sys	Build state space model from finite element model outputs.
loslin	Equivalent linearized global LOS modal matrices.
lvf	Local velocity feedback (LVF) controller.
lvf1	First-order LVF controller.

[1] MATLAB is a trademark of The MathWorks, Inc.

PRECEDING PAGE BLANK NOT FILMED

CEM Controller Analysis	
cemtresp	Open/closed loop time response analysis.
lacperf	Low authority control (LAC) freq. resp. analysis.
losperf	LOS frequency response analysis.
mimomarg	Multivariable gain/phase stability margins.
pfreq	Univariable modal frequency stability margins.
rolloff	Multivariable roll-off gain margins.
sisomarg	Univariable gain/phase stability margins.

State Space Systems	
brkloop	Open loop system connections.
compsens	Complementary sensitivity system connection.
issys	True if a matrix is a state space system.
lft	Linear Fractional Transformation.
modecrit	Add modal disturbance inputs and criterion outputs.
s2z	s-domain to z-domain system transform.
sadd	Parallel system connection.
sappend	Append state space systems.
sbalanc	Numerical conditioning of state space systems.
sbalreal	State space system balanced realization.
scovar	State space system covariance analysis.
select	Select state space system inputs/outputs.
sensitiv	Sensitivity system connection.
sgram	Controllability/observability grammians.
sinfo	Display state space system information.
sinterc	General system connections.
smodal	State space system modal form transformation.
smult	Series system connection.
split	Extract A, B, C, D state matrices from a system.
strans	State transformations.
sys2tf	State space to transfer function conversion.
sys2zp	State space to transfer zero–pole conversion.
system	Build a state space system from A, B, C, D matrices.
tf2sys	Transfer function to state space conversion.
w2z	w-domain to z-domain system transform.
z2w	z-domain to w-domain system transform.

Matrix Manipulation	
balanc	Balance matrix 1-norm.
magphase	Magnitude and phase angles of a complex matrix.
osborne	Precondition a matrix by diagonal similarity transform.
riccati	Solve matrix Riccati equation.

Linear System Analysis	
freqvec	Variable density frequency analysis vector.
fresp	State space system frequency responses.
sigma	Frequency response singular values.
spoles	Poles of a state space system.
szeros	Transmission zeros of a state space system.
tresp	State space system time responses.
tresp2	Open/closed loop time responses.
warpspace	Variable density frequency vector from poles/zeros.

Linear Controller Design	
h2lqg	H_2-norm or LQG optimal control problem.
h2norm	Compute the H_2-norm.
hinfnorm	Compute the H_∞-norm.
hinftest	Test system H_∞-norm.

Plotting Functions	
plotbode	Bode diagrams.
plotmag	Magnitude response diagrams.
plotnich	Nichols diagrams.

The following pages contain detailed descriptions of the MATLAB functions specific to the CEM. The functions are listed in alphabetical order by name. Online help for each function can be accessed by executing the `help` command on the function name.

The following format is used for the function references:

Purpose	Provides short concise descriptions.
Synopsis	Shows calling format of the function or command.
Parameters	Describes the function input parameters.
Return Values	Describes the function outputs.

Description	Describes what the function/command does and any rules or restrictions that apply.
Algorithm	Associated algorithms and routines.
Examples	Provides examples of how the function/command can be used.
See Also	Refers the user to other related functions/commands.
References	Additional information.

The convention used for the format of function parameters was as follows: required parameters are shown in `typewriter` type while optional parameters are in *italics.* Function parameters shown in quotations are string values used as flags. Function return values shown in `typewriter` type are always returned regardless of whether an output data variable is specified or not. Function return values shown in *italics* are returned only if an output data variable is specified in the function call.

cem

Purpose

Calculate the linear state space CSI Evolutionary Model (CEM).

Synopsis

[*Sp*, *wfreq*] = `cem(fname,`*modes*, *Ts*, *options*)

Parameters

`fname`	file name with FEM modal data outputs.
modes	modal indices to keep (the default is `Inf` which includes all available modes).
Ts	sample period (sec). If Ts is nonzero, the system is discretized and transformed to the w-domain.
'nodyn'	flag which causes the actuators, sensors or time delays approximation dynamics to *not* be included in the CEM.
'nodelay'	flag which causes the padé time delay approximations to *not* be included in the CEM.
'loslin'	flag to create the linearized X and Y line-of-sight outputs in the model.
'los'	flag to create the outputs (laser source and mirror) for calculating the nonlinear line-of-sight.
'gmbl'	flag to create the gimbal OSS linearized X and Y line-of-sight outputs in the model.
'reduce'	flag to perform balanced order reduction on the CEM. The user is prompted for the number of states to keep.
'velocity'	flag to create velocity outputs at the accelerometer locations instead of the usual accelerometer measurement outputs.

Return Values

Sp	linear state space CEM.
wfreq	frequency vector for analysis.

Description

The CEM data file must contain the following variables:

- **Fn** FEM (finite-element-model) modal frequencies (in Hz).
- **Zeta** modal damping ratios corresponding to the modal frequencies in Fn.
- **Phi** modal matrix of "eigenvectors" in columns for each mode in Fn. The rows of Phi correspond to the individual degrees-of-freedom in the FEM.
- **Philos** modal matrix of "eigenvectors" in columns for each mode in Fn. The rows of Philos correspond to the laser tower and reflector mirror degrees-of-freedom in the FEM.
- **Philoslin** modal matrix of "eigenvectors" in columns for each mode in Fn. The rows of Philos correspond to the equivalent linearized global LOS degrees-of-freedom in the FEM.
- **Phigmbl** modal matrix of "eigenvectors" in columns for each mode in Fn. The rows of Phi correspond to the gimbal OSS LOS rotational degrees-of-freedom in the FEM.
- **iTh** row indicates of thruster input degrees-of-freedom in the modal matrix Phi.
- **iAcc** row indicates of accelerometer output degrees-of-freedom in the modal matrix Phi.
- **iLOS** row indicates of laser source and reflector mirror degrees-of-freedom in the modal matrix Philos.
- **iLOSlin** row indicates of linearized global LOS output degrees-of-freedom in the modal matrix Philoslin.
- **iGmbl** row indicates of gimbal OSS LOS output rotational degrees-of-freedom in the modal matrix Phigmbl.

The order of the outputs of the state space model is: linearized global LOS outputs, laser tower and reflector mirror degrees-of-freedom outputs, gimbal OSS LOS outputs, and accelerometer outputs. The thruster gains are included in the model even if the 'nodyn' option is specified. The thruster commands are in units of volts. Computational time delays on the sensor outputs are assumed to be Ts (sec). This is a reasonable assumption if the sample rate is near the computational upper limit. The user is prompted for the output file name if no output arguments are given.

Examples

The following command returns a state space model with nine modes, as sample rate of 350 Hz, gimbal OSS outputs and no sensor/actuator or time delay dynamics:

```
[Sp,freq] = cem('femdata',[1:9],1/350,'gmbl','nodyn')
```

See Also

`fem2sys`, `cemact`, `cemsen`

cemact

Purpose

Create the CEM thruster actuators model.

Synopsis

```
[Sact] = cemact(Ithrust)
```

Parameters

`Ithrust` thruster indices.

Return Values

`Sact` state space actuator model.

Description

Thrusters dynamics are modeled as first-order transfer functions given by

$$T_j^f(s) = \frac{K_j \sigma_j}{s + \sigma_j} T_j^v(s) \tag{A.1}$$

where T_j^f is the j^{th} thruster force in pounds, T_j^v is the j^{th} thruster command in volts, K_j is the thruster gain in pounds/volt, and σ_j is j^{th} thruster dynamics break frequency.

cemsen

Purpose

Create the CEM analog sensor filter model.

Synopsis

```
[Ssen] = cemsen(omega)
```

Parameters

omega filter break frequency. The available frequencies are: 10, 20, 50 and 100 Hz.

Return Values

Ssen state space analog filter model.

Description

The analog filters are modeled as third-order Bessel filters.

cemtresp

Purpose

Time domain analysis of closed-loop performance and control activity.

Synopsis

`[`*Crit*`,`*Sen*`,`*Ctl*`] = cemtresp(Sp,`*Sc*`,`*Time*`,`*Dist*`,`*Tcon*`)`

Parameters

`Sp`	state space plant model with disturbance inputs and criterion outputs (in addition to the control inputs and sensor outputs). The disturbance inputs and criterion outputs must be the first inputs and outputs respectively. If there are no disturbance inputs the control inputs are used as the disturbances.
Sc	state space controller model.
Time	simulation time vector in seconds. The default is `[0:0.01:30]` seconds.
Dist	disturbance inputs. The default is unity covariance white-noise.
Tcon	the time at which the controller feedback loops are closed (i.e., the controller is turned on). By default, the controller is turned on at the initial time.

Return Values

Crit	the criterion outputs time responses.
Sen	the sensor outputs time responses.
Ctl	the controller outputs time responses.

Description

All optional input arguments must be given in the listed order except for *Sc* which may be left out of the argument list. If no return values are requested the responses are plotted. Also, the first two outputs are assumed to be the global X & Y LOS (in), while the next six are assumed to be the gimbals X & Y LOS outputs (rad).

fem2sys

Purpose

Convert finite element model parameters to a state-space system model.

Synopsis

`S = fem2sys(Fn,Zeta,Phi,iU,iY,YType,`*Keep*`)`

Parameters

- `Fn` Vector containing system frequencies (in Hz) obtained from Finite Element Model (`length(Fn)=Nmodes`).
- `Zeta` Damping ratio(s) to use. If `Zeta` is scalar, it is applied to all modes; if `Zeta` is a vector (of length `Nmodes`), then elements of `Zeta` specify damping ratios for each mode.
- `Phi` Modal "gains" or eigenvectors matrix from FEM model. The rows of `Phi` are the mode shape deflections/rotations for each DOF (`dim(Phi)=Ndof x Nmodes`).
- `iU` Vector of row indices for `Phi` corresponding to the input DOF's.
- `iY` Vector of row indices for `Phi` corresponding to the measurement DOF's. For accelerometer measurements, `iY` is a complex vector. The real parts are the row indices for `Phi` correspond to the deflections, and the imaginary parts are zero if the measurement axis is parallel to the gravitational field, otherwise the imaginary parts (absolute value) are the row indices of `Phi` corresponding to the rotations at the accelerometer locations. The sign of the imaginary part, if positive, indicates that a positive rotation points the accelerometer positive axis "up", resulting in a positive gravitational component, and if negative, indicates that a positive rotation points the accelerometer positive axis "down", resulting in a negative gravitational component.
- `YType` Describes the type of measurements specified in `iY`, where `YType = [1|2|3]` indicates `[Pos|Vel|Acc]`. If `YType` is scalar, all measurements are assumed to be the same; if a vector (must be same length as `iY`), then `YType` can be used to individually specify the measurement types in `iY`.
- *Keep* Vector of indices specifying which modes of `Phi` to keep. If not specified, all modes will be retained.

Return Values

- `S` state space structural model.

Description

The return value is a state space model of the CEM structural dynamics.

See Also

`cem`

lacperf

Purpose

Analyze Low Authority Control (LAC) performance.

Synopsis

[*sigmaTh*,*sigmaAcc*,*sigmaThOL*,*sigmaAccOL*,*freq*] = `lacperf(Sp,Sc,`*freq*`)`

Parameters

- `Sp` plant model with thruster inputs and accelerometer outputs.
- `Sc` LAC controller model.
- *freq* analysis frequency vector.

Return Values

- *sigmaTh* closed-loop frequency response maximum singular values from each thruster input to the accelerometer outputs.
- *sigmaAcc* closed-loop frequency response maximum singular values from the thruster inputs to each accelerometer output.
- *sigmaThOL* open-loop frequency response maximum singular values from each thruster input to the accelerometer outputs.
- *sigmaAccOL* open-loop frequency response maximum singular values from the thruster inputs to each accelerometer outputs.
- *freq* analysis frequency vector.

Description

If no return values are requested then the responses are plotted. Also, if only three output args are requested the third output is *freq*.
The purpose of the LAC controller is to suppress the peak responses from the thruster inputs to the accelerometer outputs. Both open-loop and closed-loop responses are returned for comparison. The singular values to individual accelerometer output are also returned.

loslin

Purpose

Calculate the equivalent linearized global line-of-sight (LOS) modal matrices (eigenvectors) using the nonlinear function `los`.

Synopsis

```
[Philoslin] = loslin(Philos)
```

Parameters

`Philos` laser source and reflector modal eigenvector matrices (see the function `los`).

Return Values

`Philoslin` modal matrix of "eigenvectors" in columns for each mode in `Fn`. The rows of `Philos` correspond to the equivalent linearized global LOS degrees-of-freedom in the FEM.

Description

The function `los` simply calls the function `los2`.

Algorithm

The equivalent modal matrices are obtained by numerical differentiation.

See Also

`los, los2`

losperf

Purpose

Analyze Line-of-Sight (LOS) performance (frequency domain).

Synopsis

`[`*sigmaLOS*`,`*freq*`] = losperf(Sp,`*Sc*`,`*freq*`,`*nLOS*`)`

Parameters

`Sp`	state space plant model with disturbance inputs and line-of-sight outputs (in addition to the control inputs and sensor outputs). If there are no disturbance inputs the control inputs are used as the disturbances.
`Sc`	state space controller model.
`freq`	analysis frequency vector.
`nLOS`	number of LOS outputs (the default is 2).

Return Values

sigmaLOS	singular values of each LOS output frequency responses to the disturbance inputs.
freq	analysis frequency vector.

Description

If the optional argument *Sc* is not given then `Sp` is assumed to be the closed-loop plant model. If no return values are requested then the responses are plotted. The first two criterion outputs are assumed to be the Global X & Y LOS while the next six are assumed to be gimbals OSS #1, #2, and #4 X & Y LOS outputs.

lvf

Purpose

Construct a CEM local velocity feedback (LVF) controller model.

Synopsis

`[Sc,Aid,Bid,Cid,Did,nLincoef,Lincoef,Linbnds] =`
`lvf(Ko,` *OmegaWashOut*`)`

Parameters

`Ko`	initial controller gains.
OmegaWashOut	low-frequency washout break frequency (Hz).

Return Values

`Sc`	state space controller model.
`Aid`	A-matrix parameter identity information.
`Bid`	B-matrix parameter identity information.
`Cid`	C-matrix parameter identity information.
`Did`	D-matrix parameter identity information.
`nLincoef`	number of linear coefficients in each linear constraint.
`Lincoef`	linear coefficients of the linear constraints.
`Linbnds`	lower and upper bounds on the linear constraints.

Description

Returns a CEM local velocity feedback (LVF) controller model. The assumed controller inputs are accelerations. The controller integrates the accelerations to get velocity. Optional second-order low-frequency washout filters on each sensor are available to cancel out effects from sensor drift.

The controller design parameter (gains) information is returned for optimization with SANDY[a].

[a]SANDY is a trademark of A. J. Controls, Inc.

lvf1

Purpose

Construct a CEM local velocity feedback (LVF) controller model with first-order pseudo-integrator filters.

Synopsis

`[Sc,Aid,Bid,Cid,Did,nLincoef,Lincoef,Linbnds] = lvf1(Ko,`*OmegaInt*`)`

Parameters

`Ko`	initial controller gains.
OmegaInt	pseudo-integrator filter break frequency (Hz). The default value is 1×10^{-8}.

Return Values

`Sc`	state space controller model.
`Aid`	A-matrix parameter identity information.
`Bid`	B-matrix parameter identity information.
`Cid`	C-matrix parameter identity information.
`Did`	D-matrix parameter identity information.
`nLincoef`	number of linear coefficients in each linear constraint.
`Lincoef`	linear coefficients of the linear constraints.
`Linbnds`	lower and upper bounds on the linear constraints.

Description

Returns a CEM local velocity feedback (LVF) controller model. The assumed controller inputs are accelerations. The controller uses first-order pseudo-integrator filters on the accelerometer outputs to get velocity.

The controller design parameter (gains) information is returned for optimization with SANDY.

mimomarg

Purpose

Analyze multivariable gain/phase stability margins at the control inputs and sensor outputs.

Synopsis

[*sigCtlRtd*, *sigSenRtd*, *sigCtlIrtd*, *sigSenIrtd*, *freq*] = `mimomarg(Sp,Sc,`*freq*`)`

Parameters

`Sp`	state space plant model with control inputs and sensor outputs.
`Sc`	state space controller model.
freq	analysis frequency vector.

Return Values

sigCtlRtd	singular values of the return difference transfer function matrix frequency responses at the control inputs.
sigSenRtd	singular values of the return difference transfer function matrix frequency responses at the sensor outputs.
sigCtlIrtd	singular values of the inverse return difference transfer function matrix frequency responses at the control inputs.
sigSenIrtd	singular values of the inverse return difference transfer function matrix frequency responses at the sensor outputs.
freq	analysis frequency vector.

Description

If only three output arguments are requested the third output is the frequency vector `freq`. The singular values of the return difference transfer function matrices are plotted if there are no output arguments.

References

Richard Y. Chiang and Michael G. Safonov. *Robust Control Tollbox.* The MathWorks, Inc., 24 Prime Park Way, Natick, MA 01760–1520, 1992.

pfreq

Purpose

Univariable modal frequency stability margin analysis. Perturbs modal frequencies of the CEM model and test for closed-loop stability.

Synopsis

`[result] = pfreq(fname,Sc,pfact,`*modes*`,`*pmodes*`)`

Parameters

fname file name with FEM modal data outputs.

Sc state space controller model.

pfact perturbational factors to apply to each mode.

modes mode indices to include in the perturbed plant model (default is to include all available modes).

pmodes mode indices to perturb in the plant model (default is to perturb all modes). Note *pmodes* must be a subset of *modes*.

Return Values

result stability test results matrix where a "1" in the i^{th} row and j^{th} column indicates that the i^{th} mode was stable for the j^{th} perturbation factor. A "0" indicates that the closed-loop system was unstable.

Description

The closed-loop stability of a controller can be tested along a grid of model frequency perturbations taken one-at-a-time.

Examples

The following command analyzes the stability of a controller for ±20% variations in the individual frequencies of the first nine modes:

```
pfreq('femdata',Sc,[-0.2:0.01:+0.2],1:9,1:9)
```

See Also

cem, fem2sys

rolloff

Purpose

Synopsis

[*sigCtl*, *sigSen*, *sigCtlIsen*, *sigSenIctl*, *freq*] = `rolloff(Sp,Sc,`*freq*`)`

Parameters

- `Sp` state space plant model with control inputs and sensor outputs.
- `Sc` state space controller model.
- *freq* analysis frequency vector.

Return Values

- *sigCtl* singular values of the open-loop frequency responses from control inputs to the control outputs $C_{uy}(j\omega)G_{yu}(j\omega)$.
- *sigSen* singular values of the open-loop frequency responses from sensor inputs to the sensor outputs $G_{yu}(j\omega)C_{uy}(j\omega)$.
- *sigCtlIsen* maximum singular values of the open-loop frequency responses $C_{uy_i}(j\omega)G_{y_iu}(j\omega)$ in columns.
- *sigSenIctl* maximum singular values of the open-loop frequency responses $G_{yu_i}(j\omega)C_{u_iy}(j\omega)$ in columns.
- *freq* analysis frequency vector.

Description

The singular values of the open-loop frequency responses are plotted if no output arguments are requested.

sisomarg

Purpose

Analyze SISO gain/phase stability margins at the control inputs and sensor outputs.

Synopsis

[*gCtlOL*,*gSenOL*,*freqCtlOL*,*freqSenOL*] = `sisomarg(Sp,Sc,`*freq,options*`)`

Parameters

`Sp`	state space plant model with control inputs and sensor outputs.
`Sc`	state space controller model.
freq	analysis frequency vector.
'mesh'	flag to use a variable density "mesh" of frequency points.

Return Values

`gCtlOl`	open-loop frequency responses in columns for each control input. The i^{th} column contains the responses for the i^{th} control input.
`gSenOl`	open-loop frequency responses in columns for each sensor output. The i^{th} column contains the responses for the i^{th} sensor output.
`freqCtlOL`	analysis frequencies for the control inputs.
`freqSenOL`	analysis frequencies for the sensor outputs.

Description

The SISO gain/phase stability margins for each control/sensor loop may be computed from the open-loop frequency responses at each loop. The Nichols diagrams for each loop are plotted if there are no output arguments.

Appendix B

CEM Open-Loop Responses

The following figures show the open-loop undamped frequency responses of the Phase 1 and Phase 2 CEM configurations. Both measured and predicted responses are shown in each figure. Responses are shown for both the original untuned models obtained from the FEM modal data and for the tuned models where the modal frequencies and damping ratios of certain modes were adjusted based on system identification results or hand tuning.

PRECEDING PAGE BLANK NOT FILMED

224

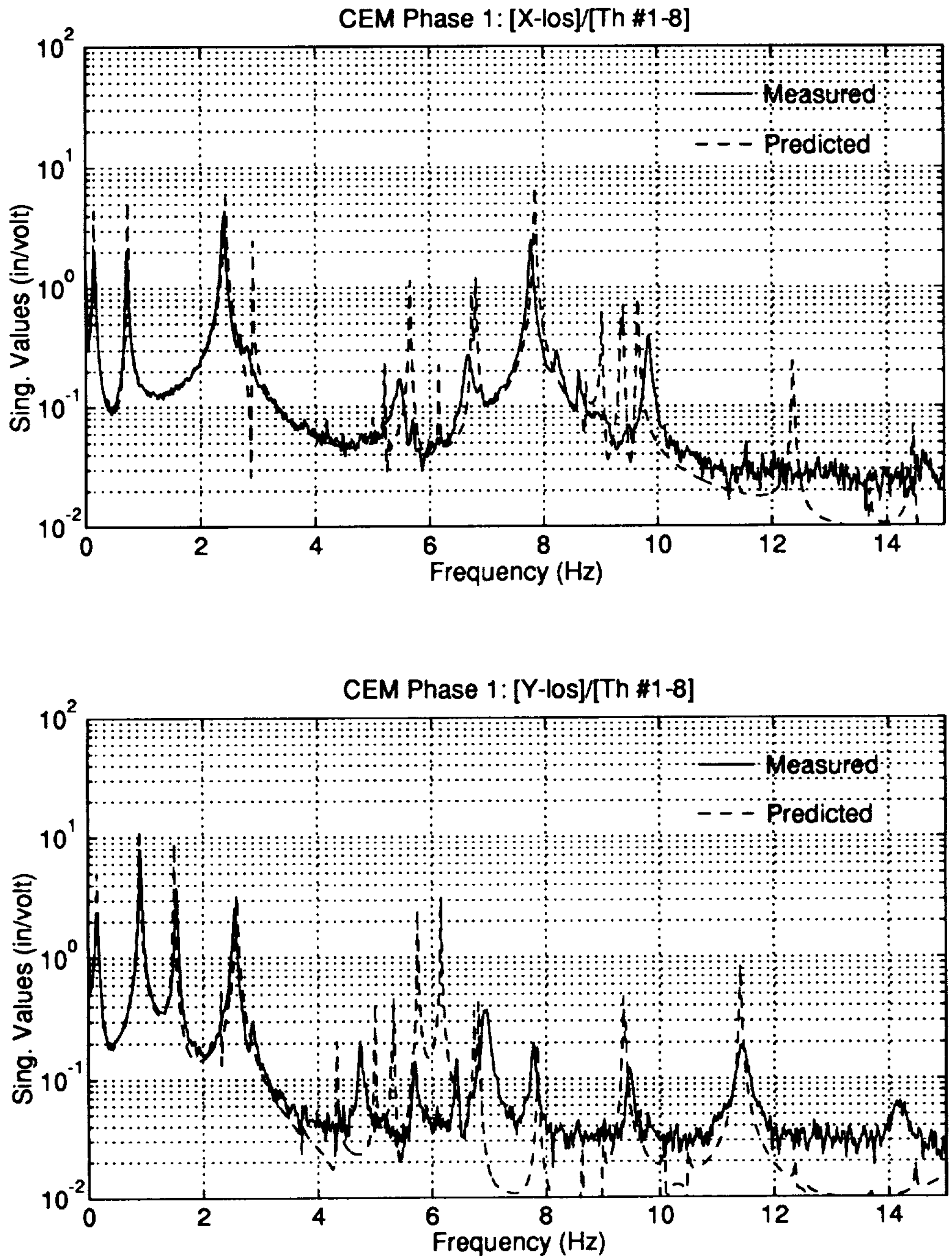

Figure B.1: Phase 1 CEM Measured and Predicted Open-Loop LOS Frequency Responses Using FEM Modes

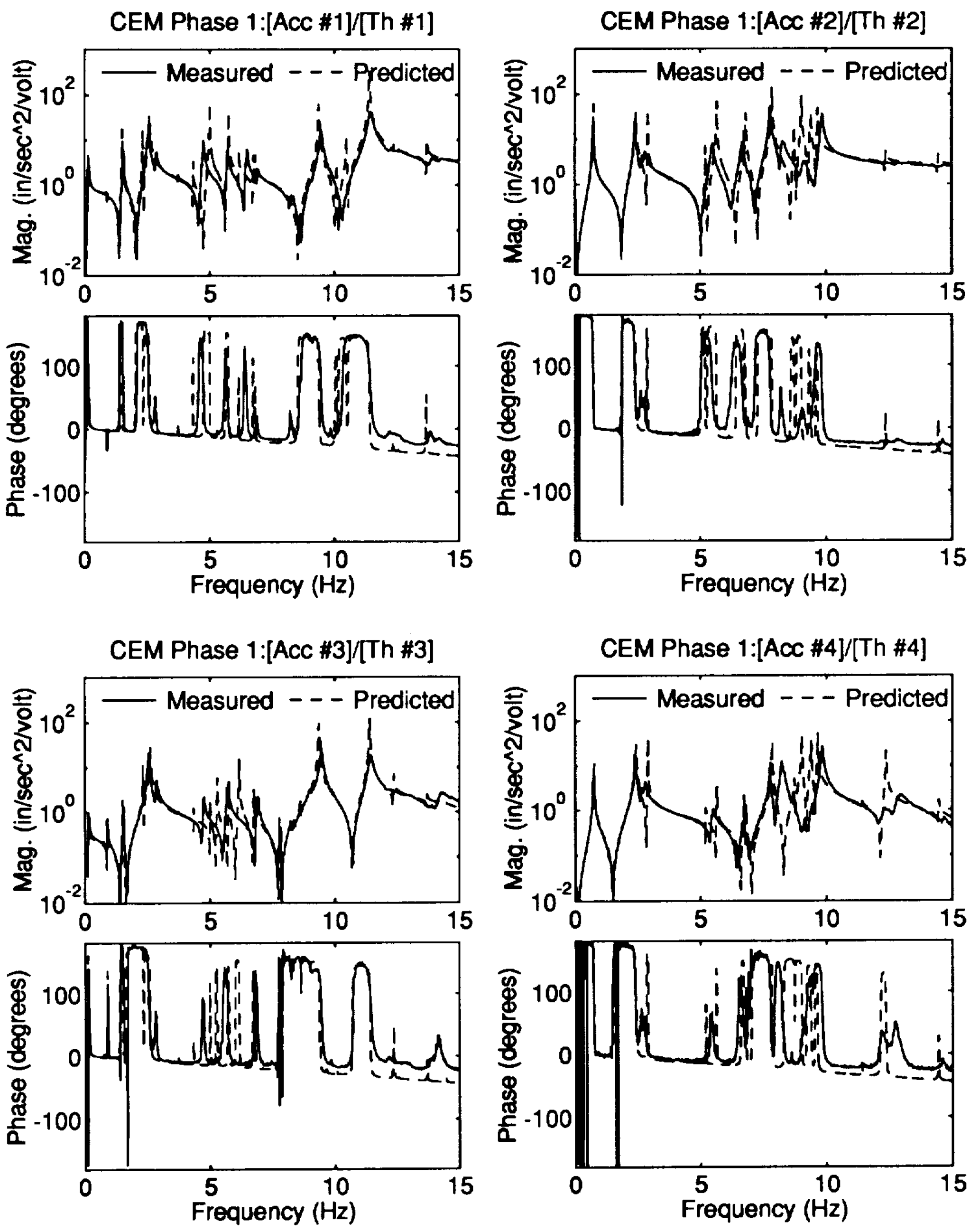

Figure B.2: Phase 1 CEM Measured and Predicted Open-Loop Accelerometer Frequency Responses Using FEM Modes

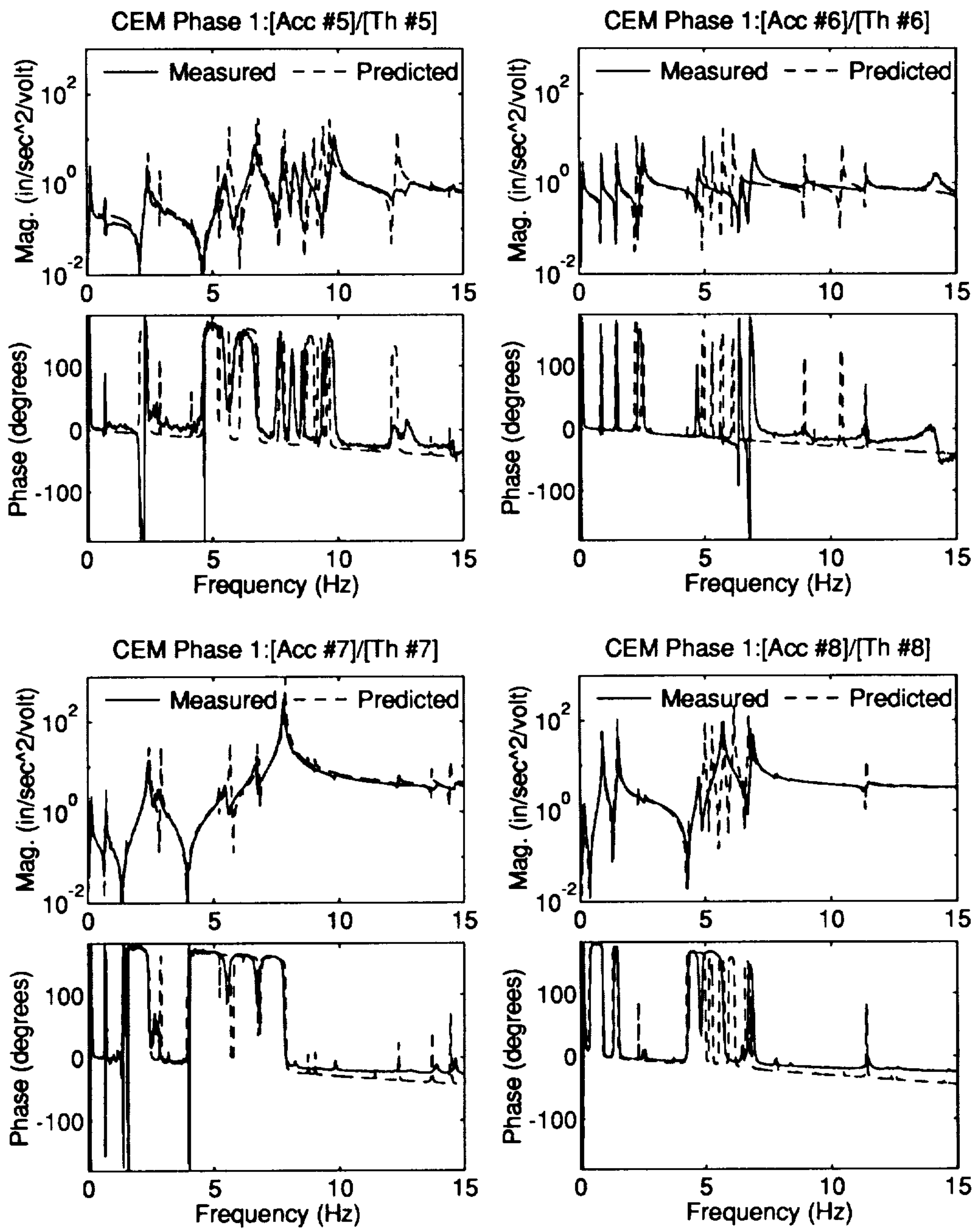

Figure B.3: Phase 1 CEM Measured and Predicted Open-Loop Accelerometer Frequency Responses Using FEM Modes

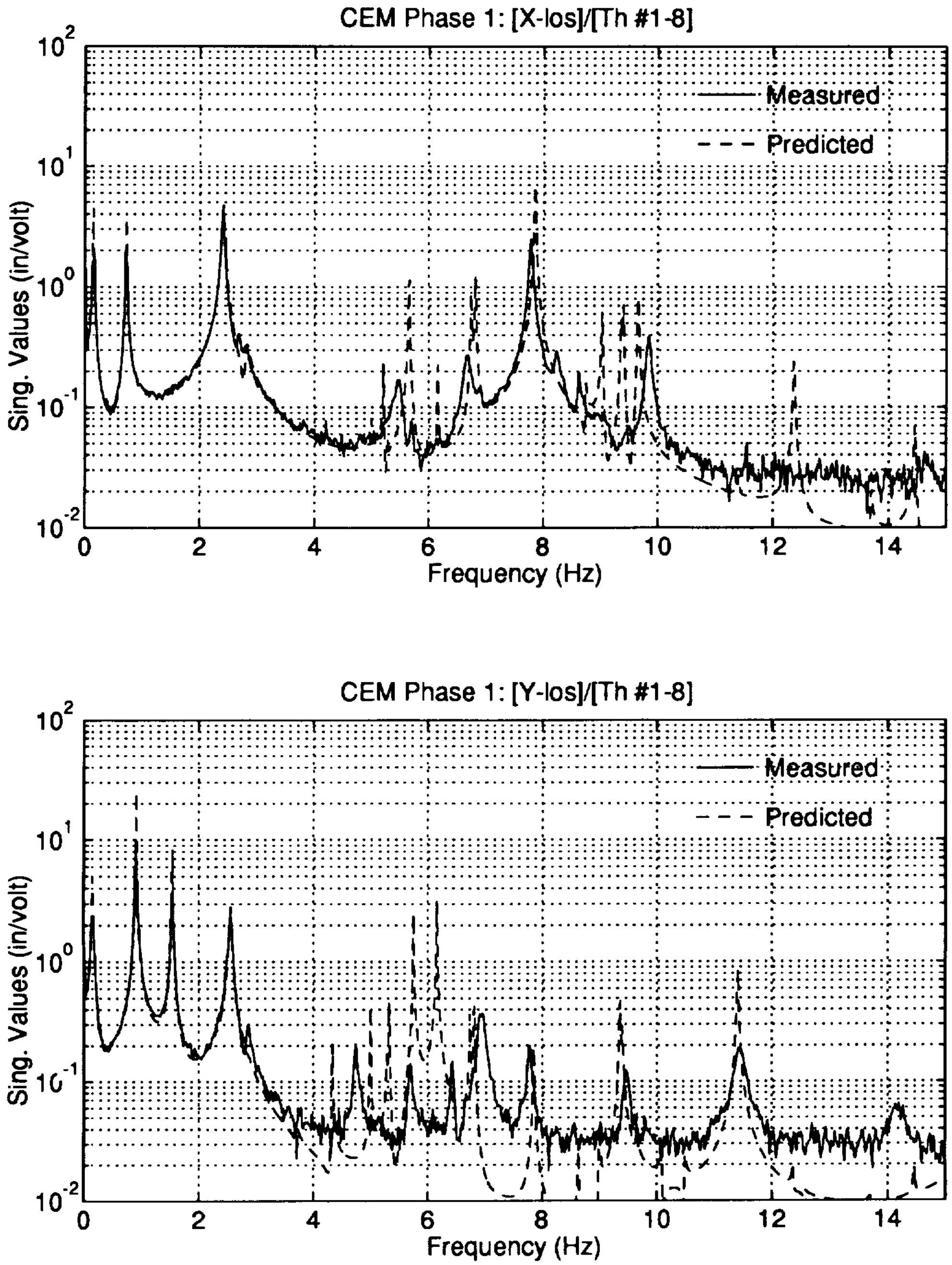

Figure B.4: Phase 1 CEM Measured and Predicted Open-Loop LOS Frequency Responses Using Identified Modes

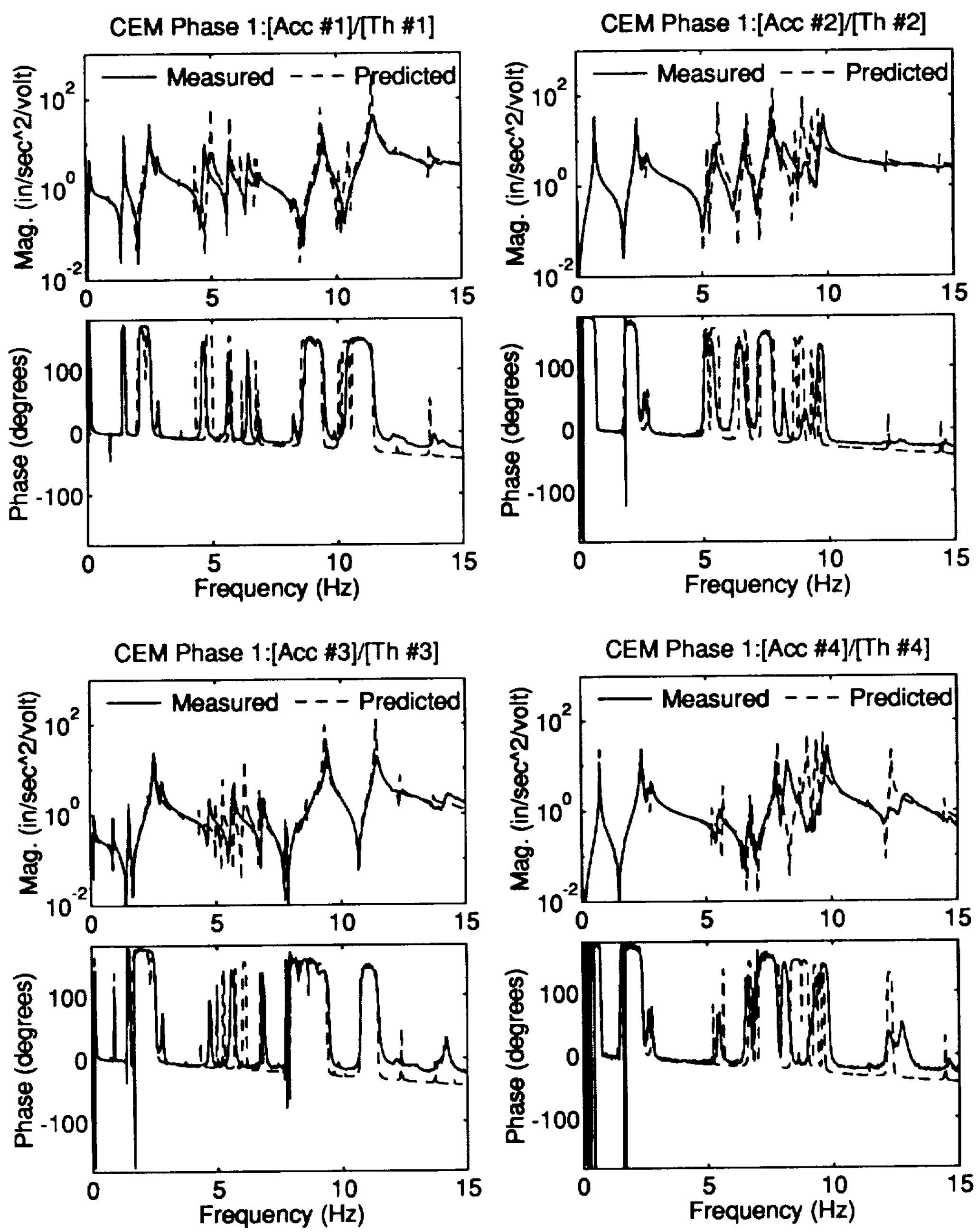

Figure B.5: Phase 1 CEM Measured and Predicted Open-Loop Accelerometer Frequency Responses Using Identified Modes

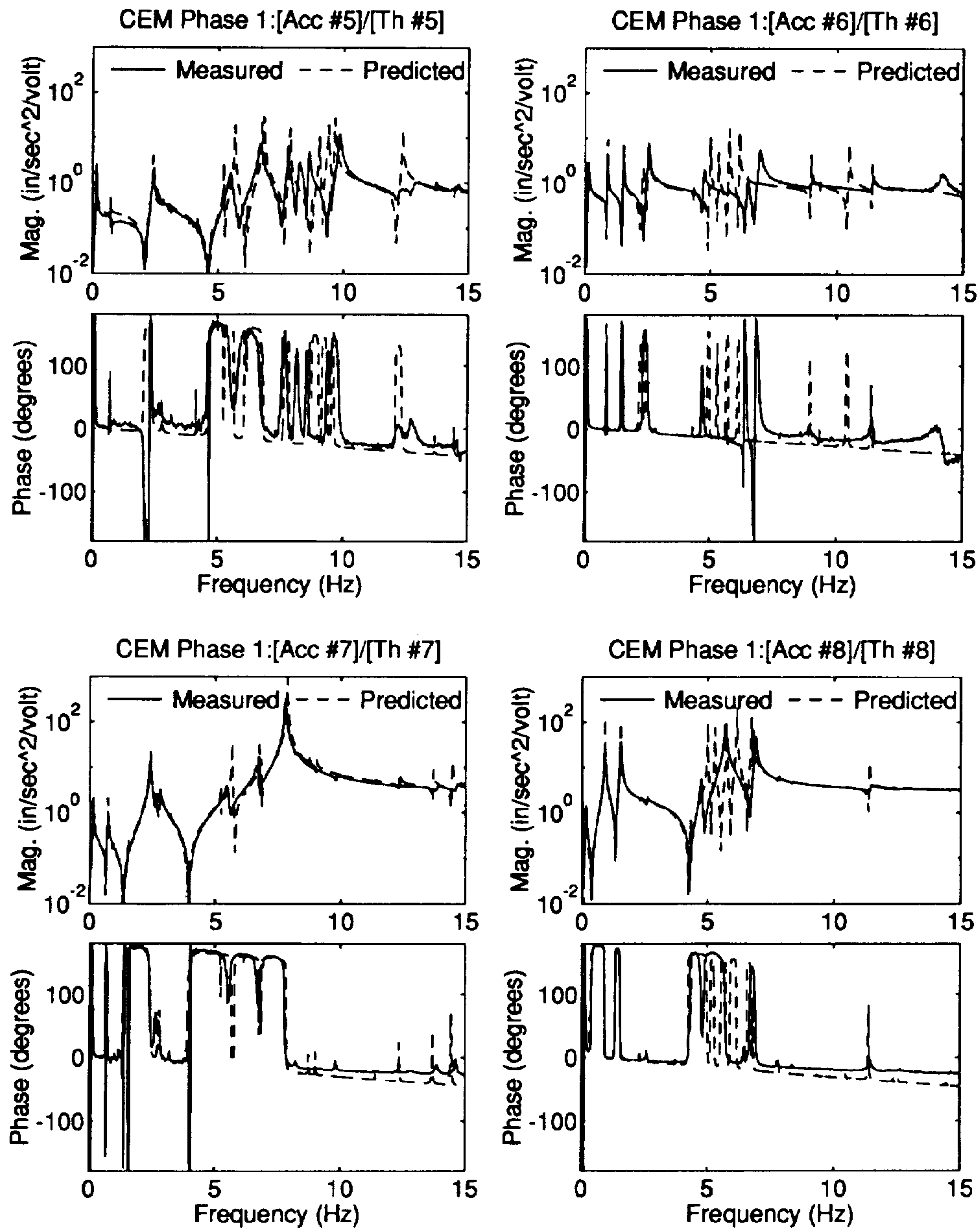

Figure B.6: Phase 1 CEM Measured and Predicted Open-Loop Accelerometer Frequency Responses Using Identified Modes

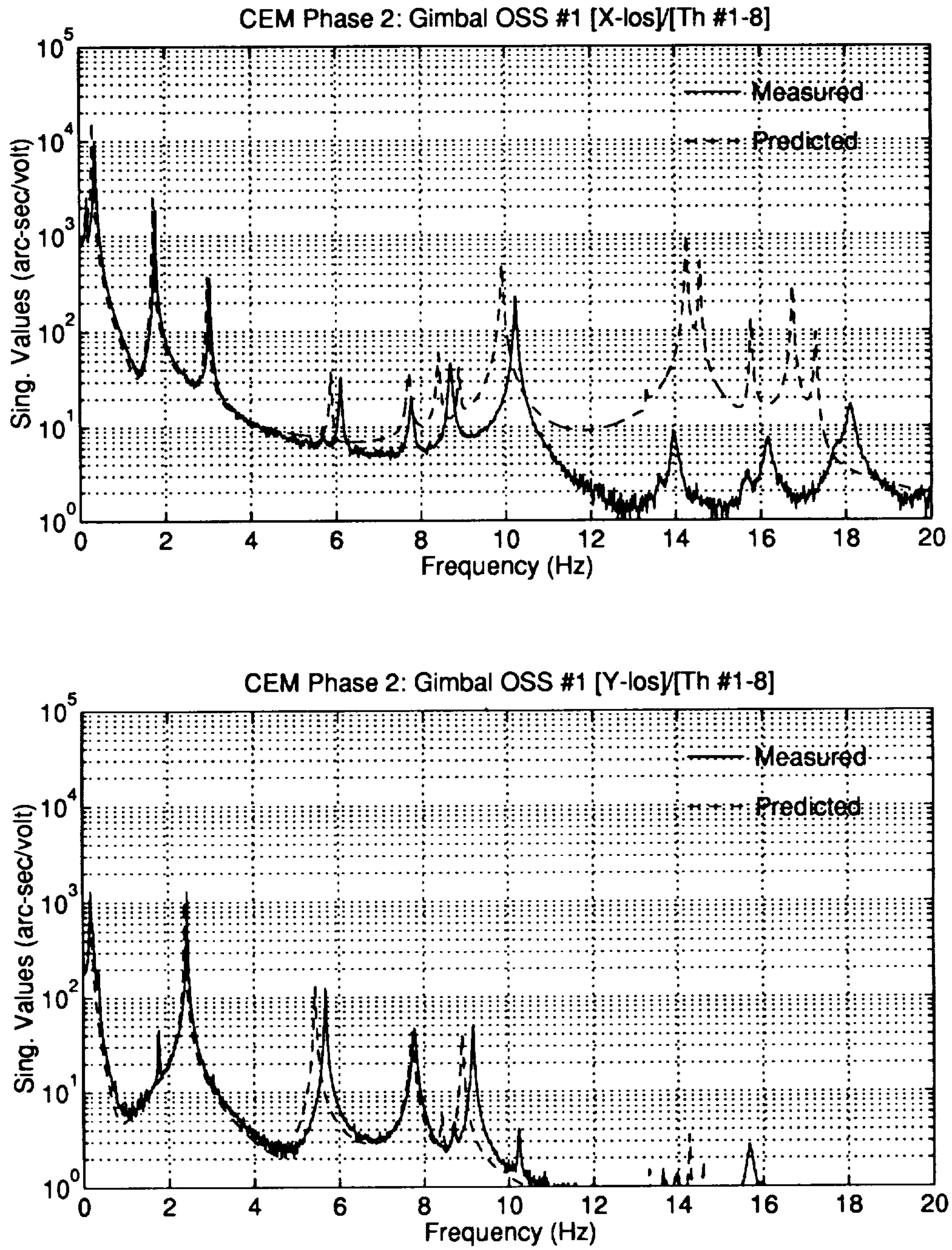

Figure B.7: Phase 2 CEM Measured and Predicted Open-Loop OSS #1 LOS Frequency Responses Using FEM Modes

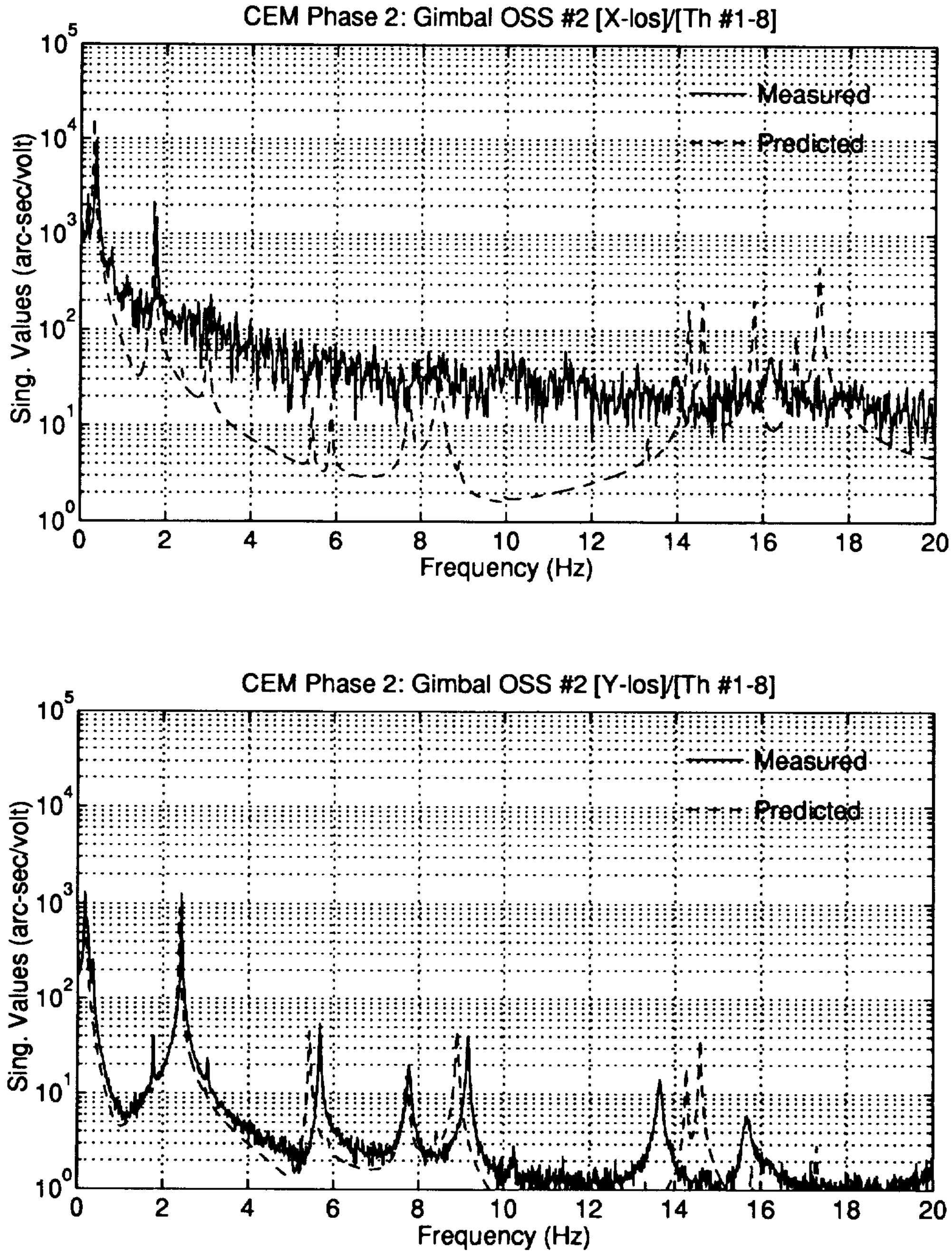

Figure B.8: Phase 2 CEM Measured and Predicted Open-Loop OSS #2 LOS Frequency Responses Using FEM Modes

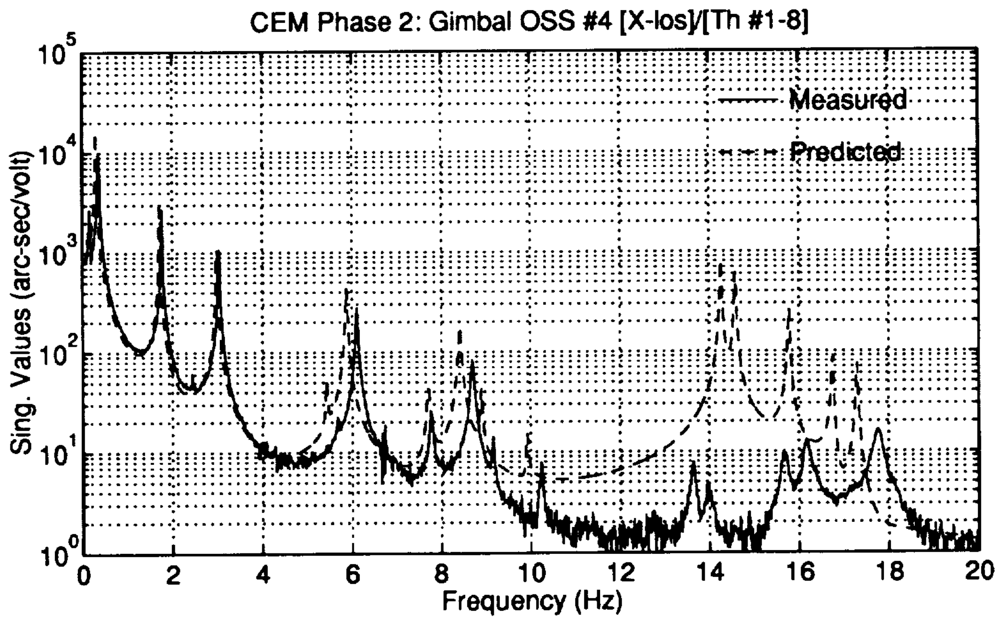

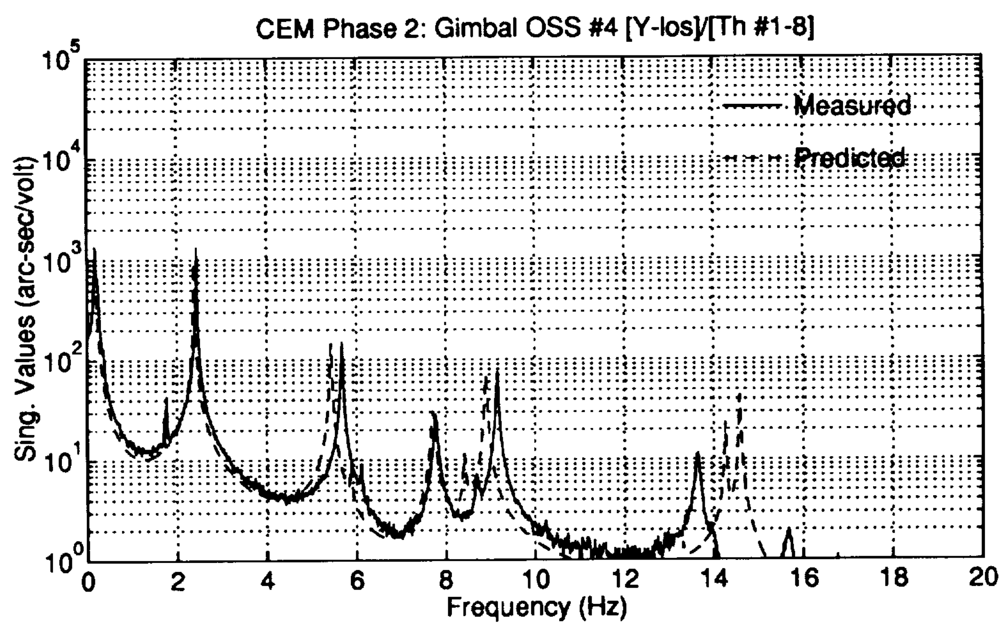

Figure B.9: Phase 2 CEM Measured and Predicted Open-Loop OSS #4 LOS Frequency Responses Using FEM Modes

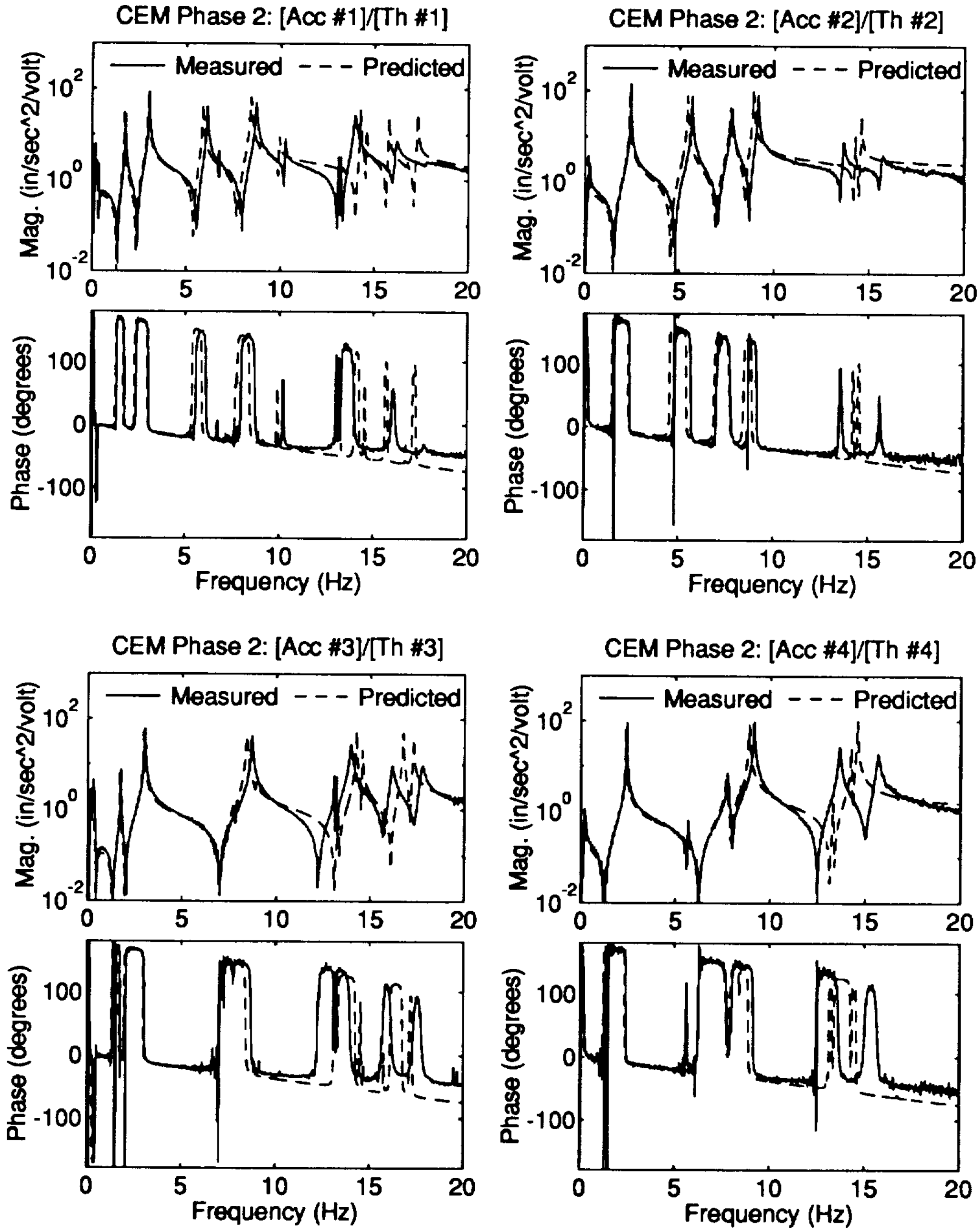

Figure B.10: Phase 2 CEM Measured and Predicted Open-Loop Accelerometer Frequency Responses Using FEM Modes

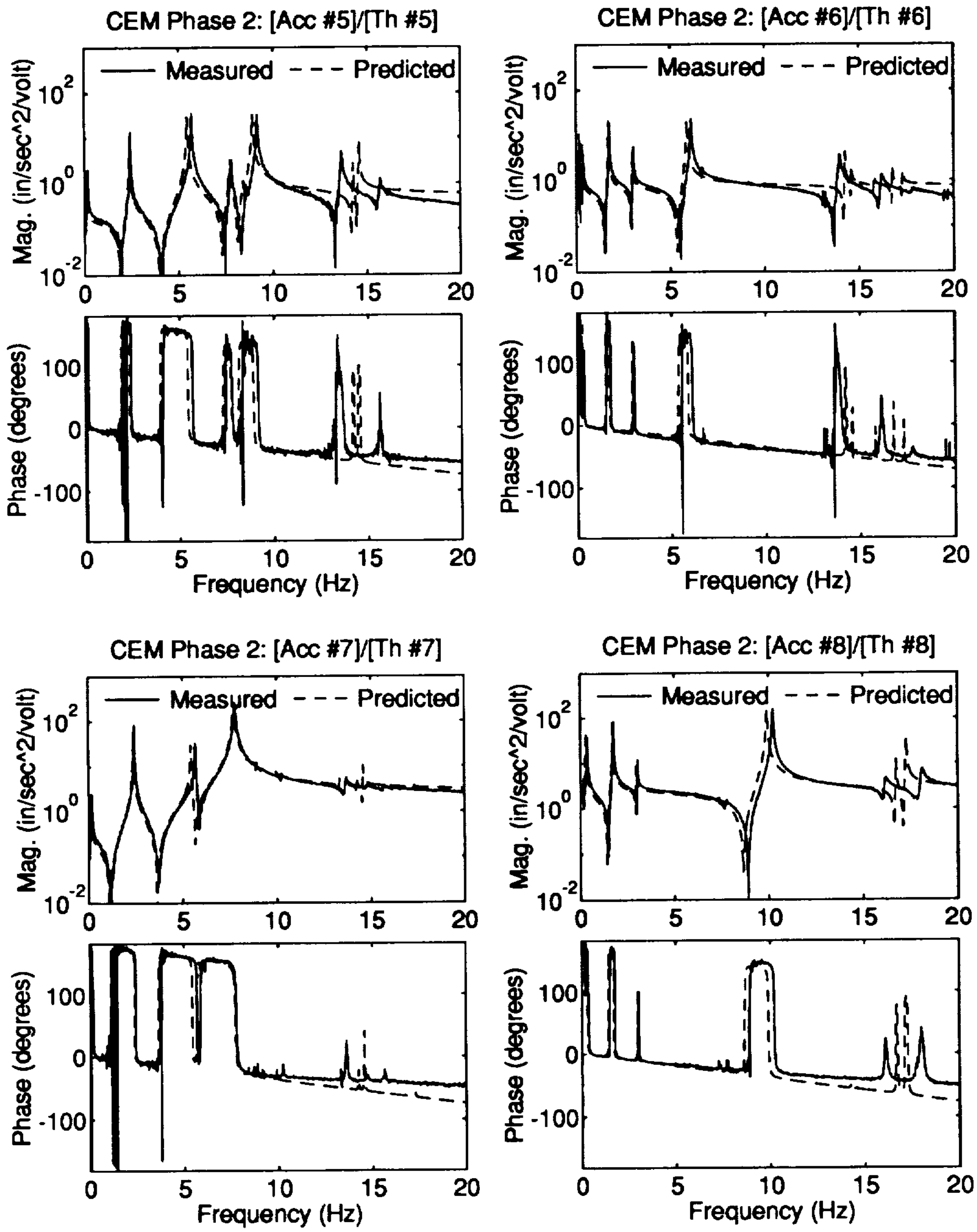

Figure B.11: Phase 2 CEM Measured and Predicted Open-Loop Accelerometer Frequency Responses Using FEM Modes

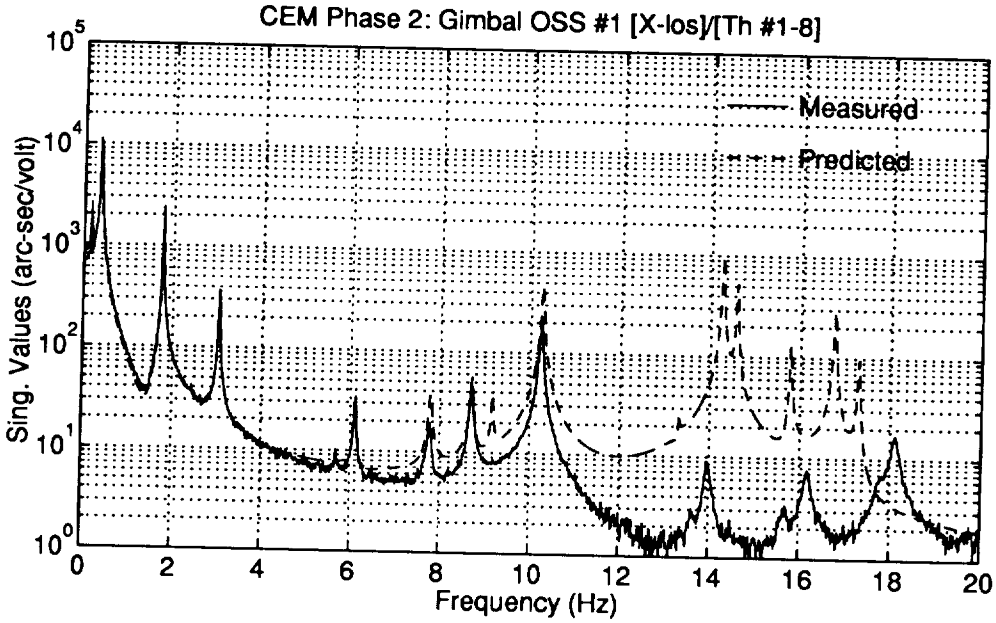

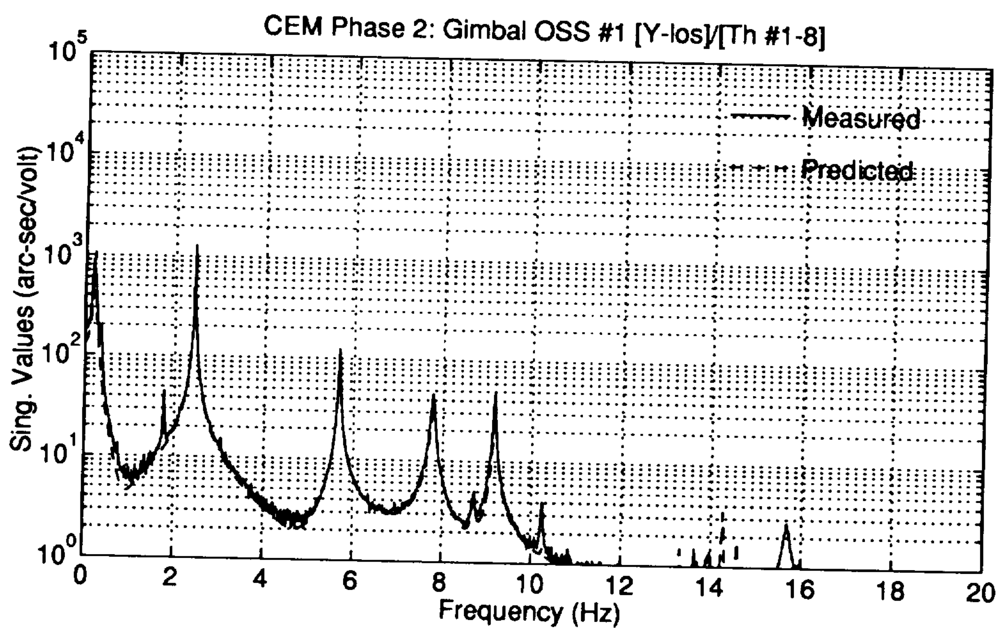

Figure B.12: Phase 2 CEM Measured and Predicted Open-Loop OSS #1 LOS Frequency Responses Using Identified Modes

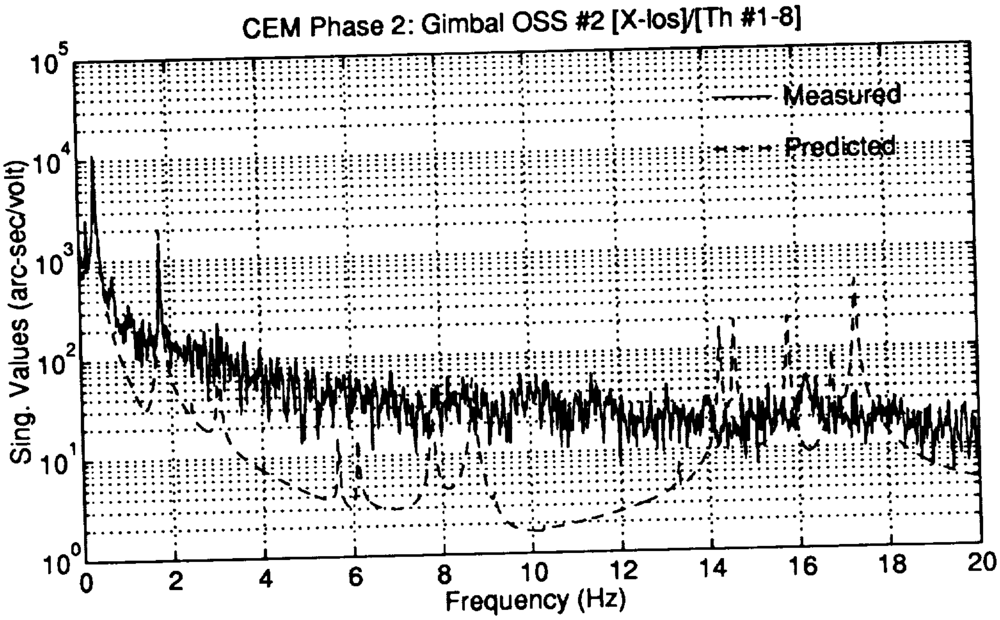

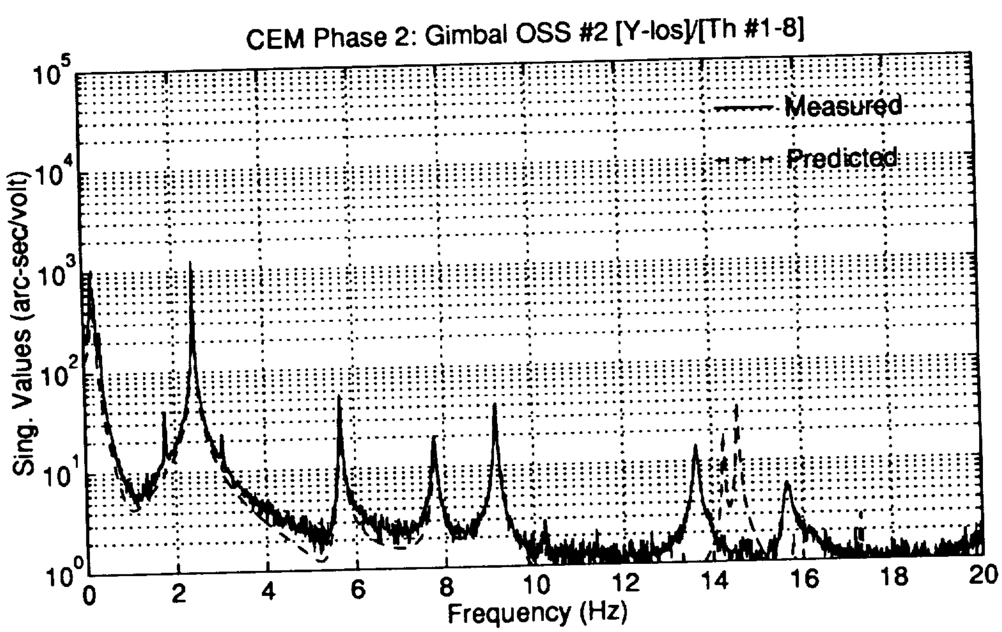

Figure B.13: Phase 2 CEM Measured and Predicted Open-Loop OSS #2 LOS Frequency Responses Using Identified Modes

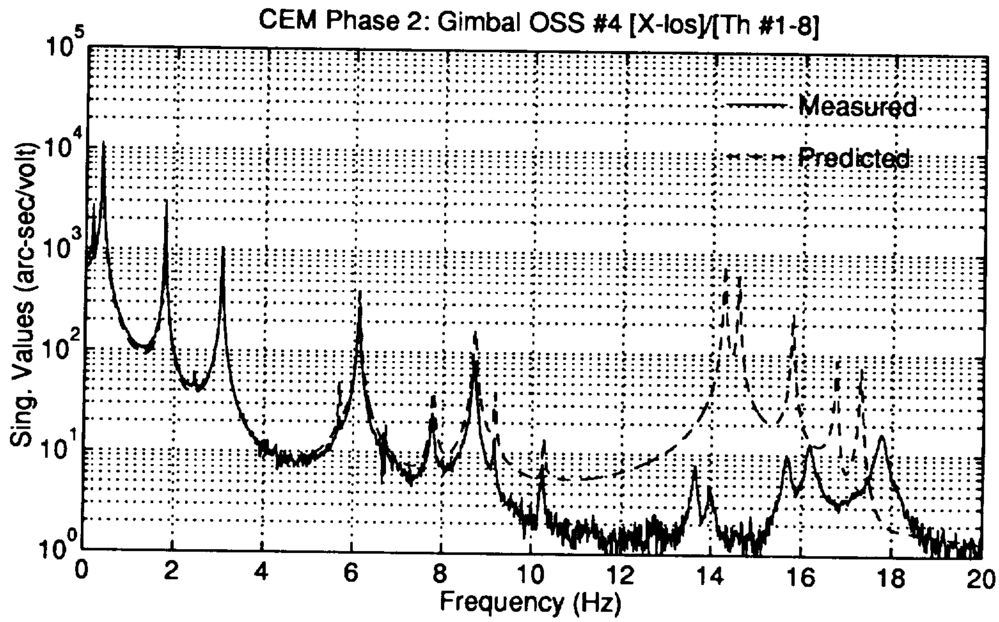

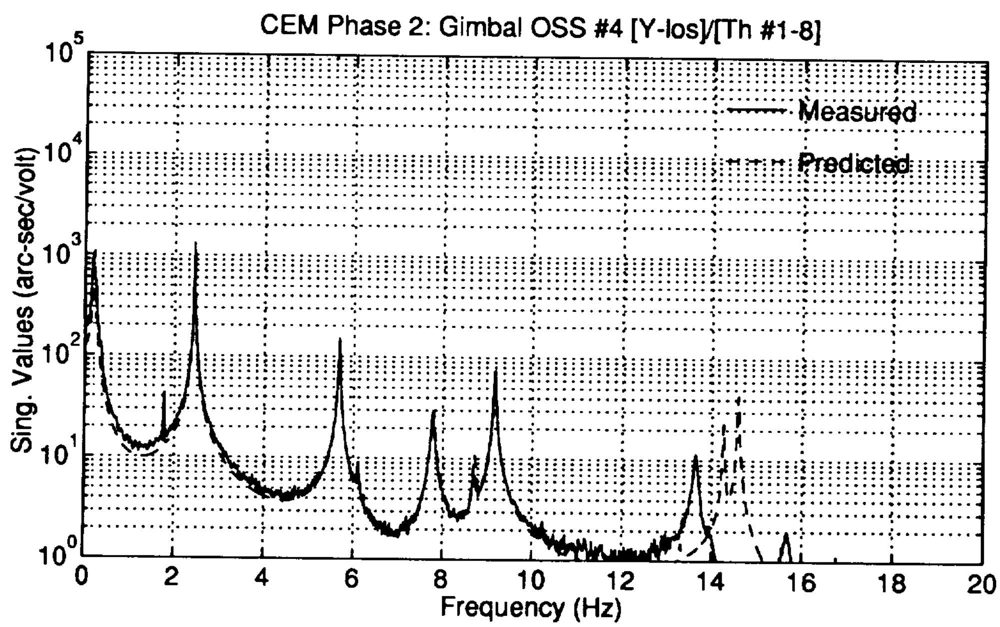

Figure B.14: Phase 2 CEM Measured and Predicted Open-Loop OSS #4 LOS Frequency Responses Using Identified Modes

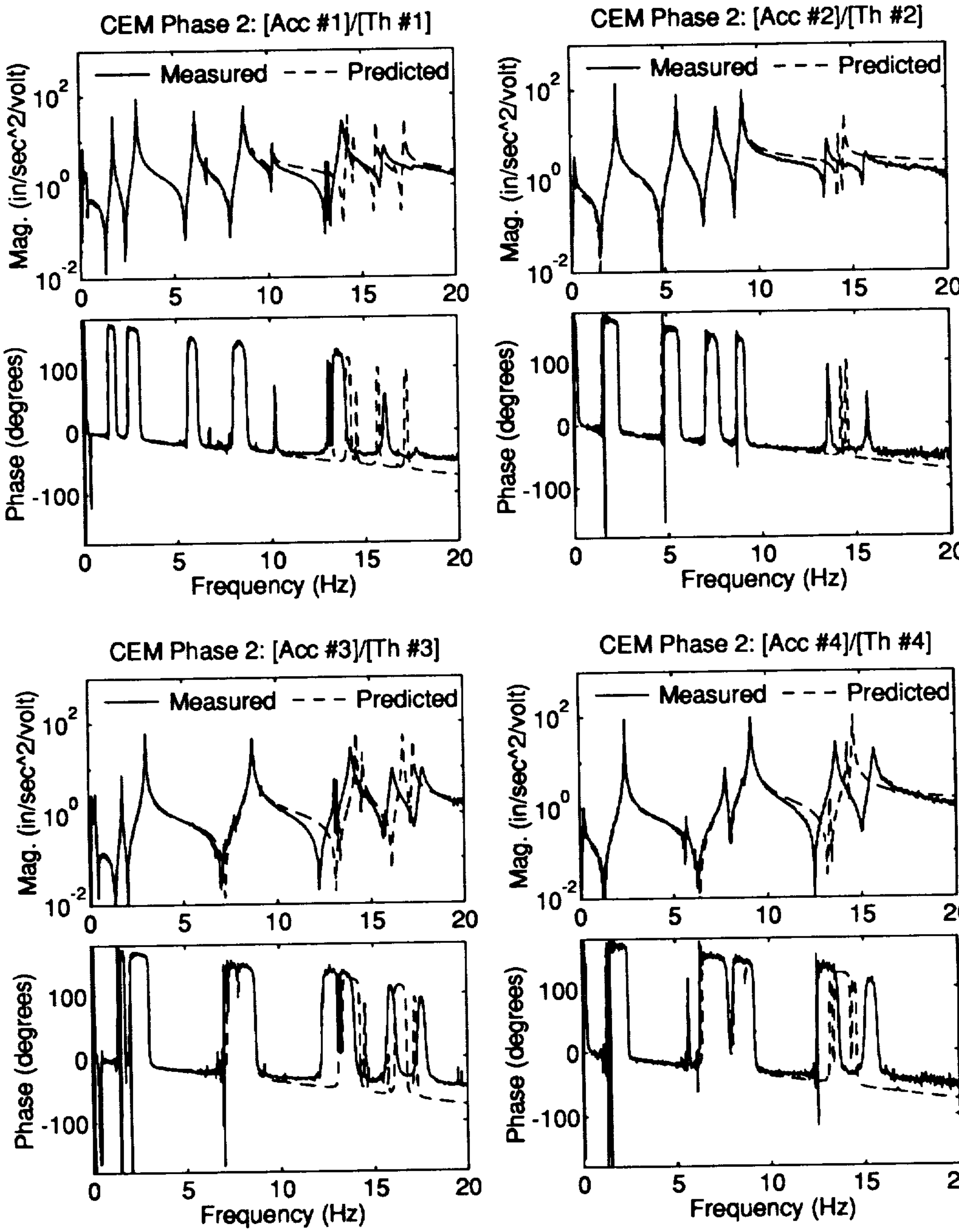

Figure B.15: Phase 2 CEM Measured and Predicted Open-Loop Accelerometer Frequency Responses Using Identified Modes

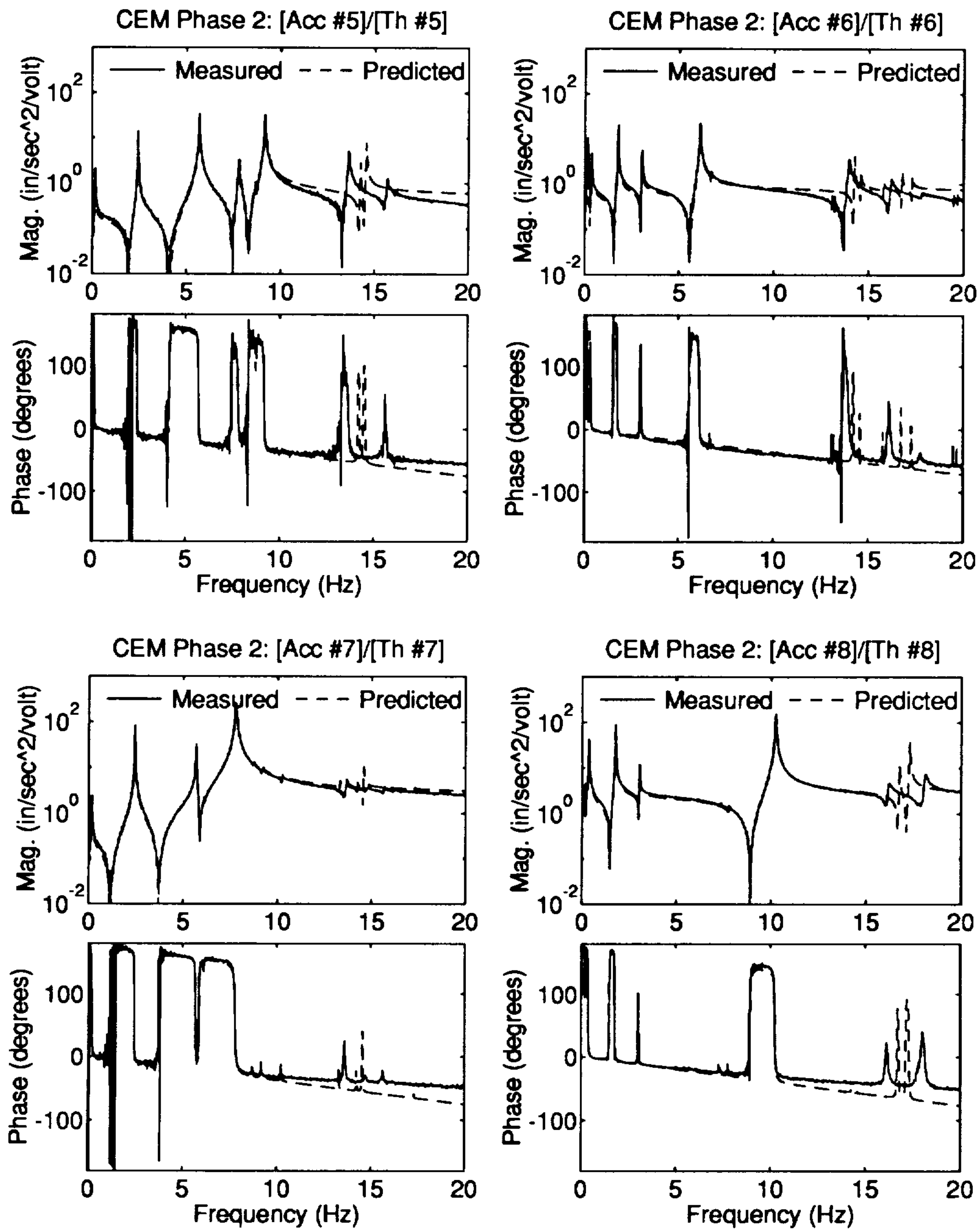

Figure B.16: Phase 2 CEM Measured and Predicted Open-Loop Accelerometer Frequency Responses Using Identified Modes

Appendix C

Phase 1 Control Design Results

The figures in this section show the experimental results of the active controller tests on the Phase 1 CEM. The first two control designs shown are an H_2/LQG controller (150b) and a HAC/LAC controller (150h) for the undamped structure. The last controller is a HAC/LAC controller using 12 damped struts (i.e., 3 bays) installed at the base of the laser tower to provide robust stabilization of the laser tower/main truss mode. The state dimensions of all three controllers was 61 states. All three control laws were implemented at a sampling rate of 150 Hz. The HAC/LAC designs were similar to the Phase 2 HAC/LAC designs in that they used an LVF inner loop to provide wide band gain reduction and an H_2/LQG outer loop to provide high authority control of the rigid-body and elastic modes up to 4 Hz. The Phase 1 LVF LAC's, however, used second-order pseudo-integrator filters with a 0.03 Hz low-frequency washout to eliminate DC sensor bias.

PRECEDING PAGE BLANK NOT FILMED

PAGE 242 INTENTIONALLY BLANK

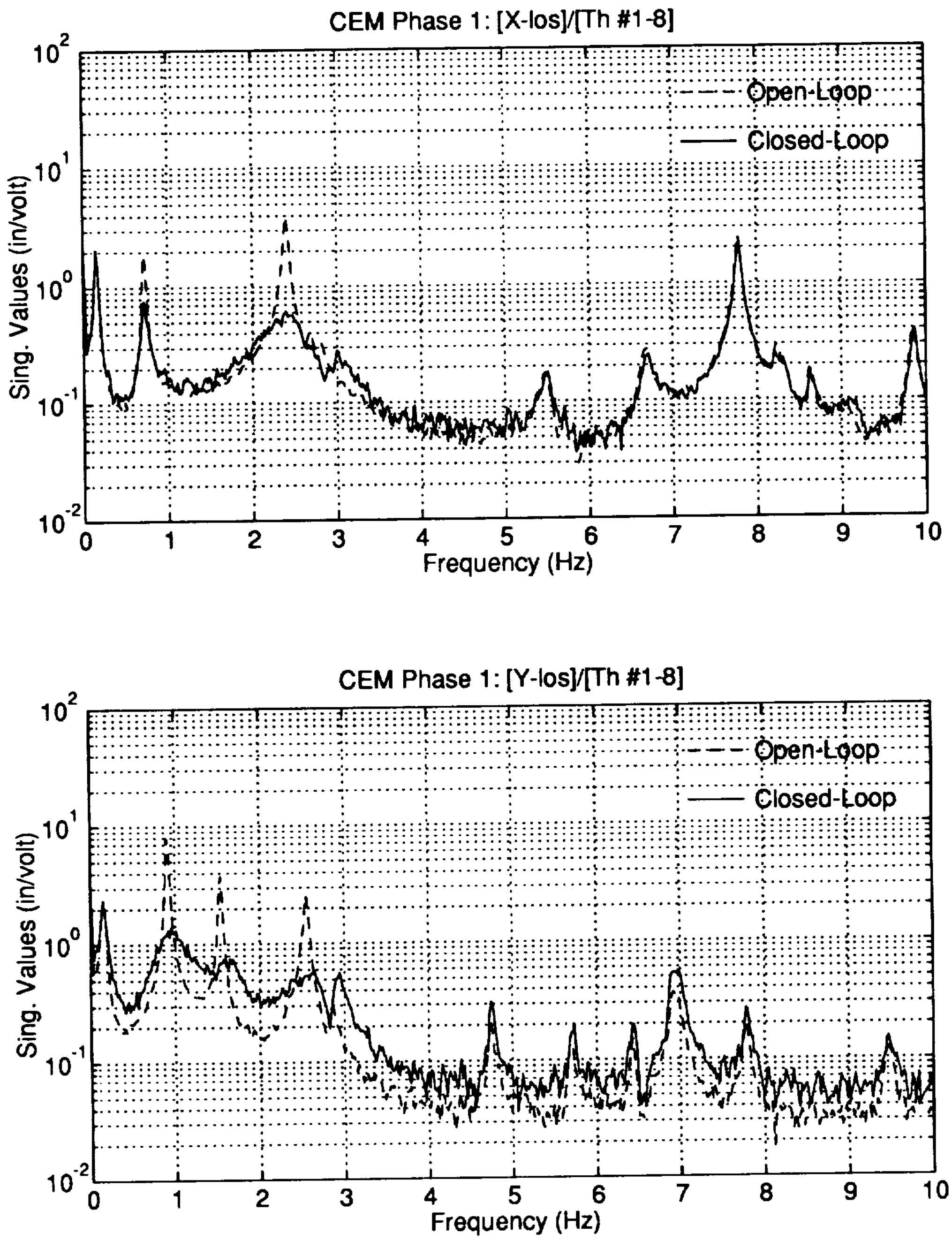

Figure C.1: Phase 1 CEM H_2/LQG 150b Measured Open and Closed Loop LOS Frequency Responses

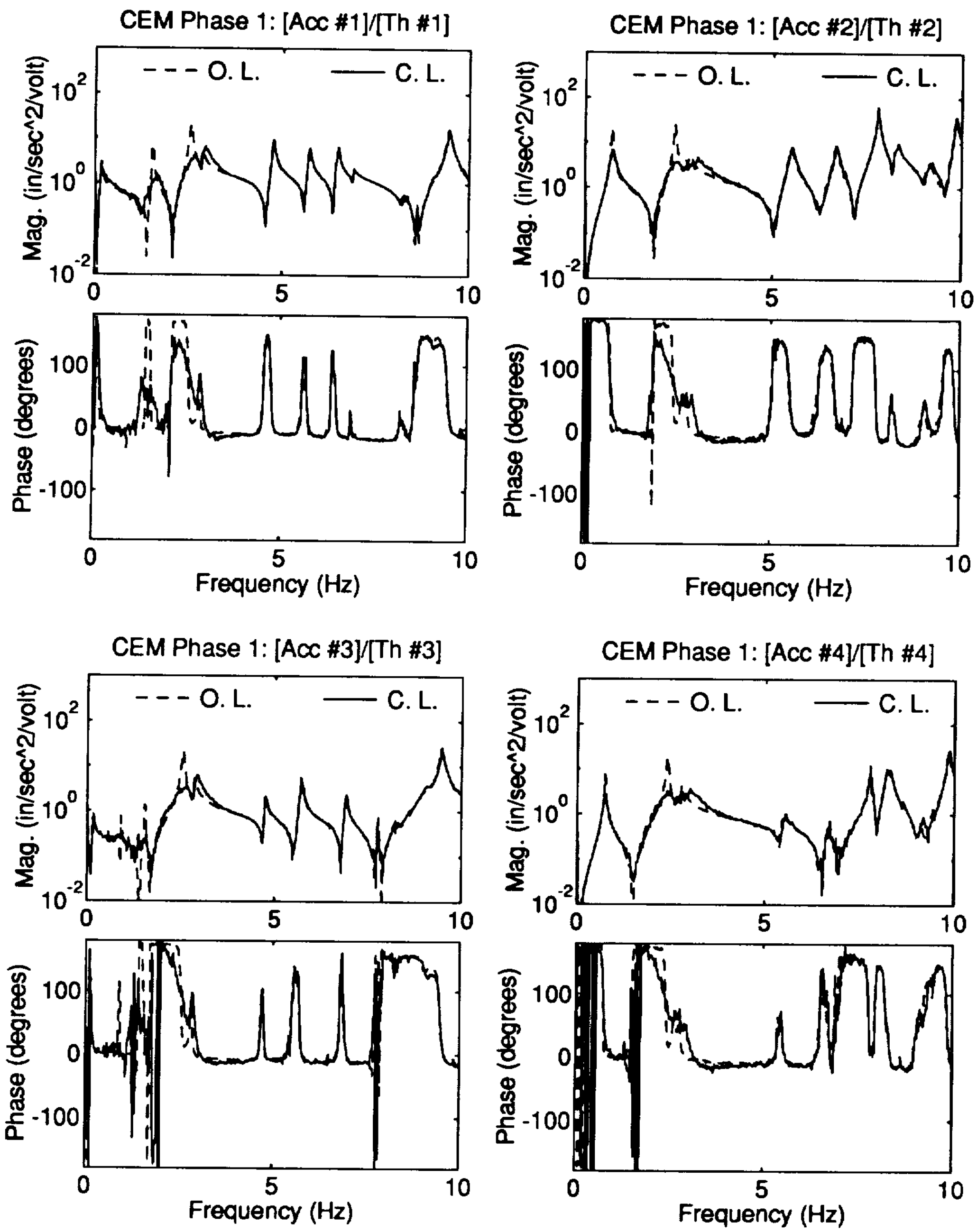

Figure C.2: Phase 1 CEM H_2/LQG 150b Measured Open and Closed Loop Accelerometer Frequency Responses

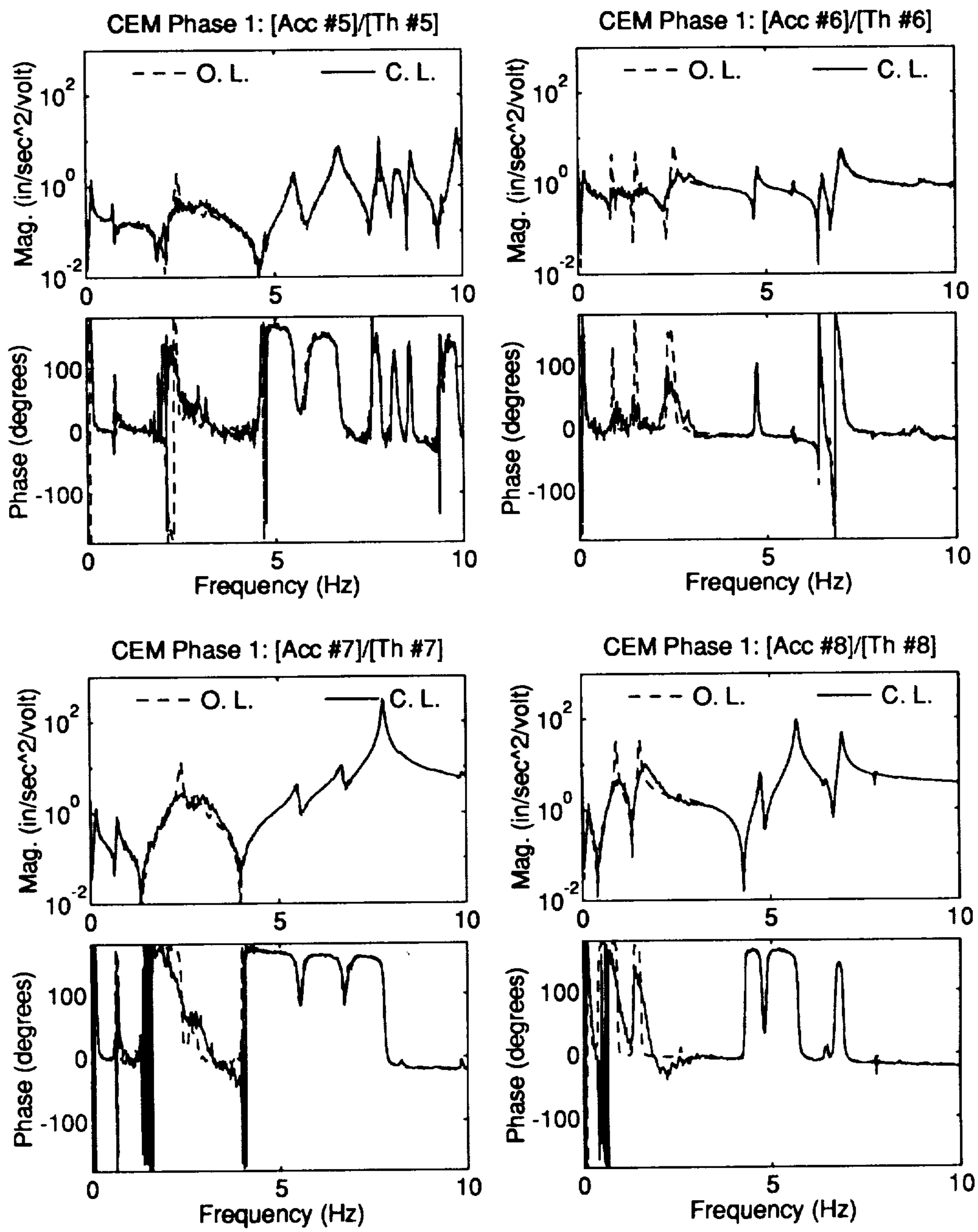

Figure C.3: Phase 1 CEM H_2/LQG 150b Measured Open and Closed Loop Accelerometer Frequency Responses

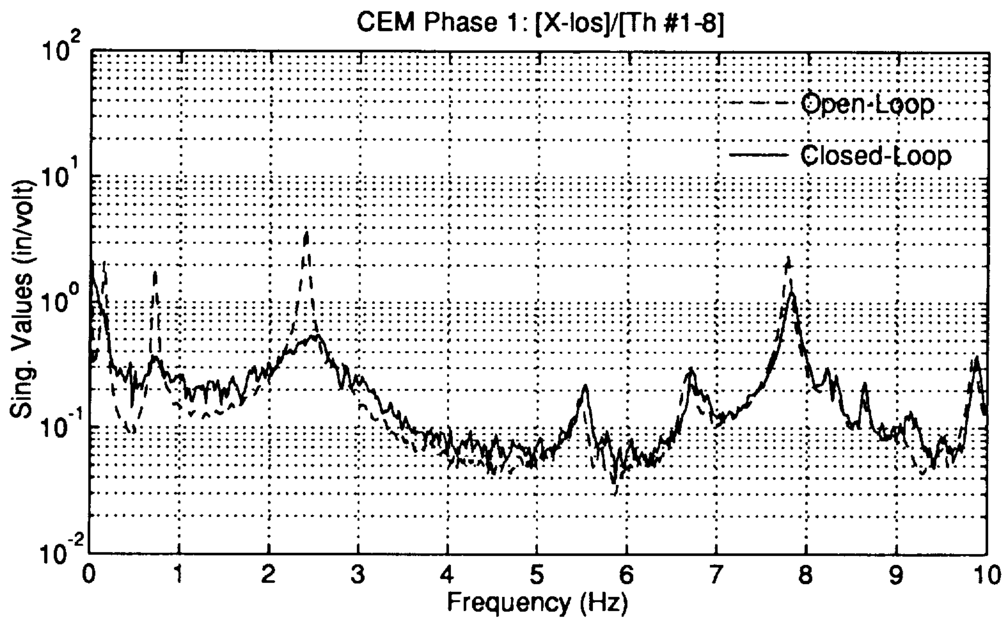

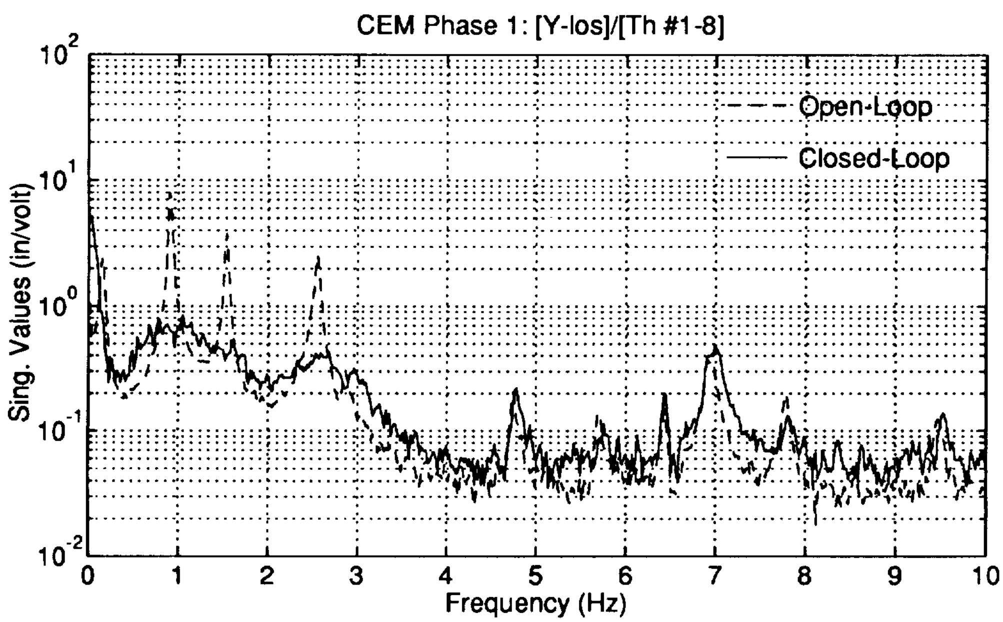

Figure C.4: Phase 1 CEM HAC/LAC 150h Measured Open and Closed Loop LOS Frequency Responses

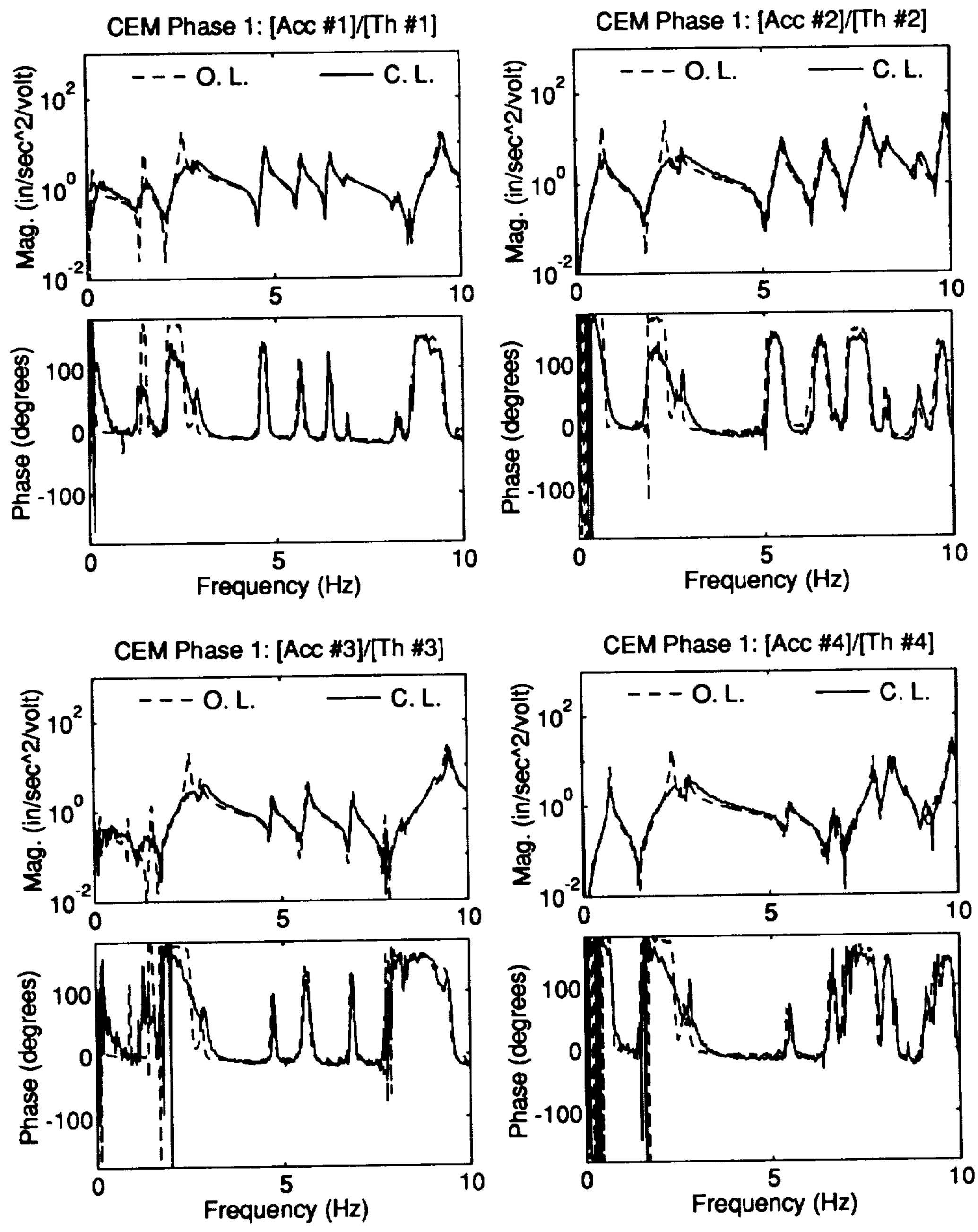

Figure C.5: Phase 1 CEM HAC/LAC 150h Measured Open and Closed Loop Accelerometer Frequency Responses

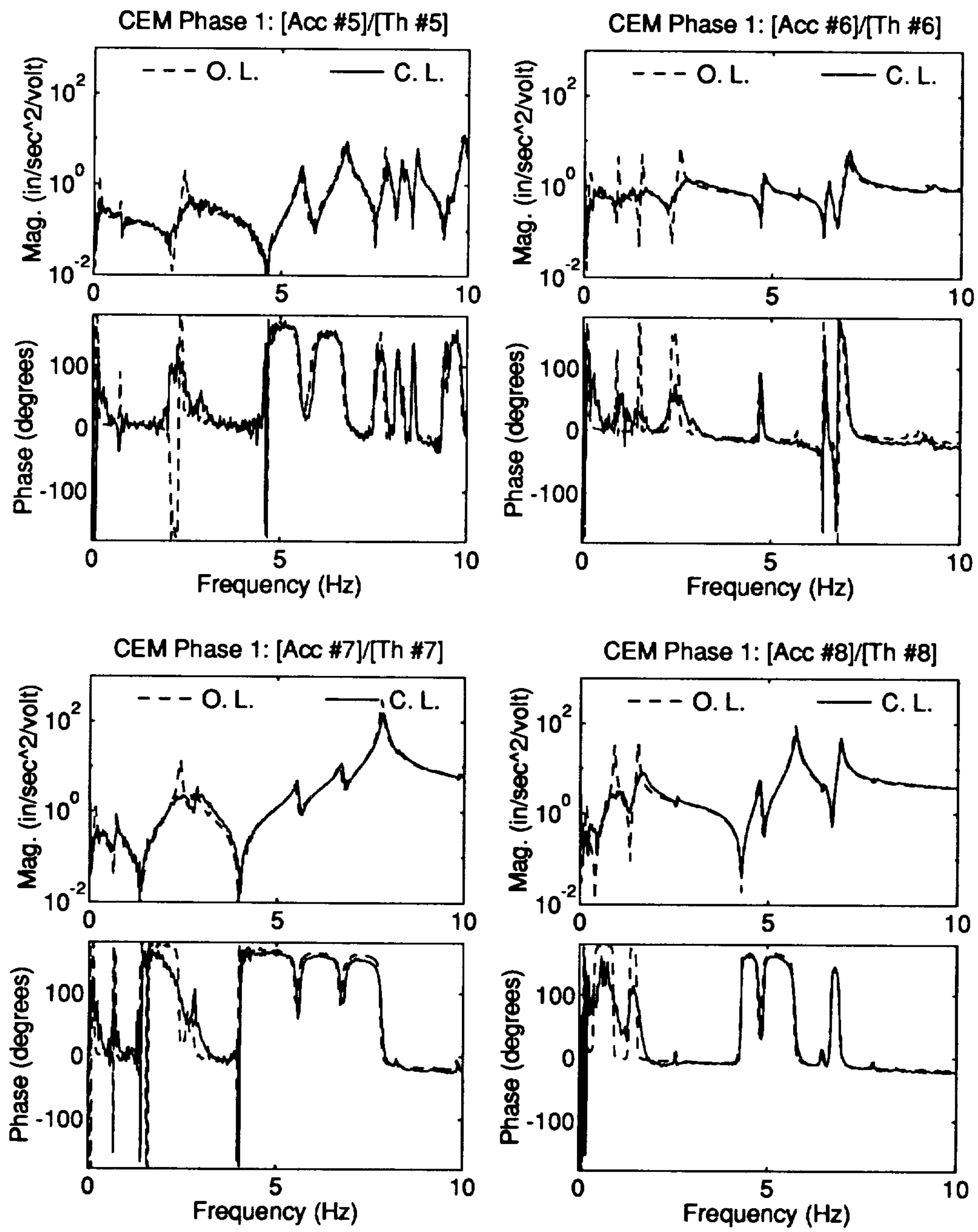

Figure C.6: Phase 1 CEM HAC/LAC 150h Measured Open and Closed Loop Accelerometer Frequency Responses

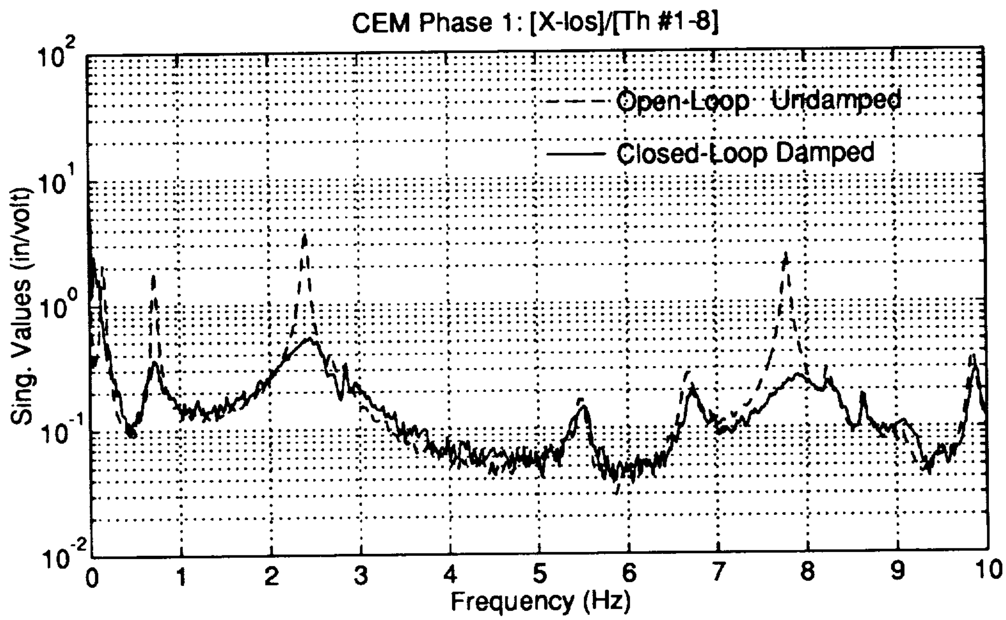

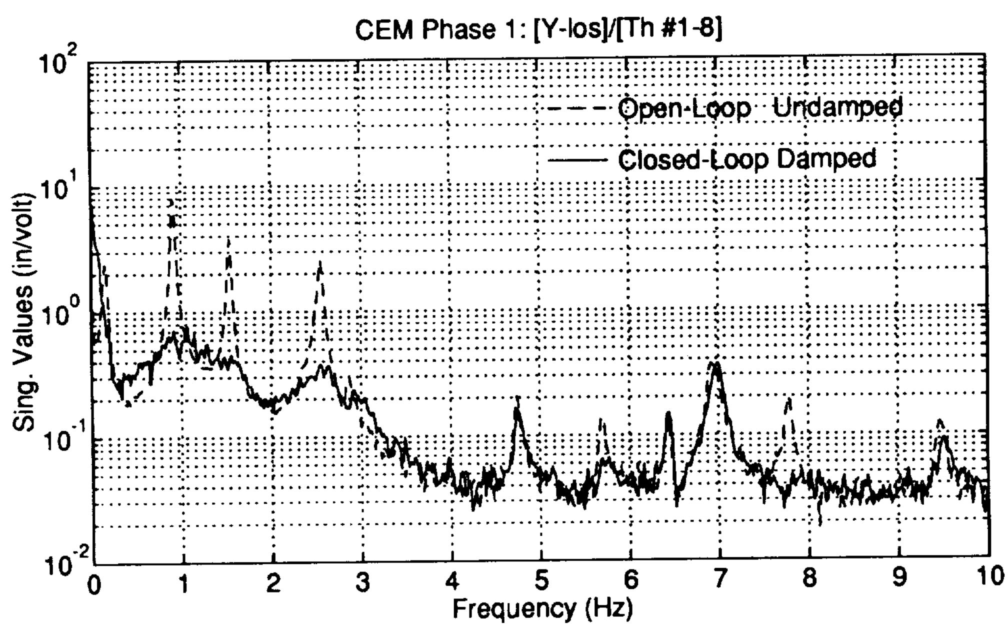

Figure C.7: Phase 1 CEM HAC/LAC 150c Measured Open and Closed Loop LOS Frequency Responses

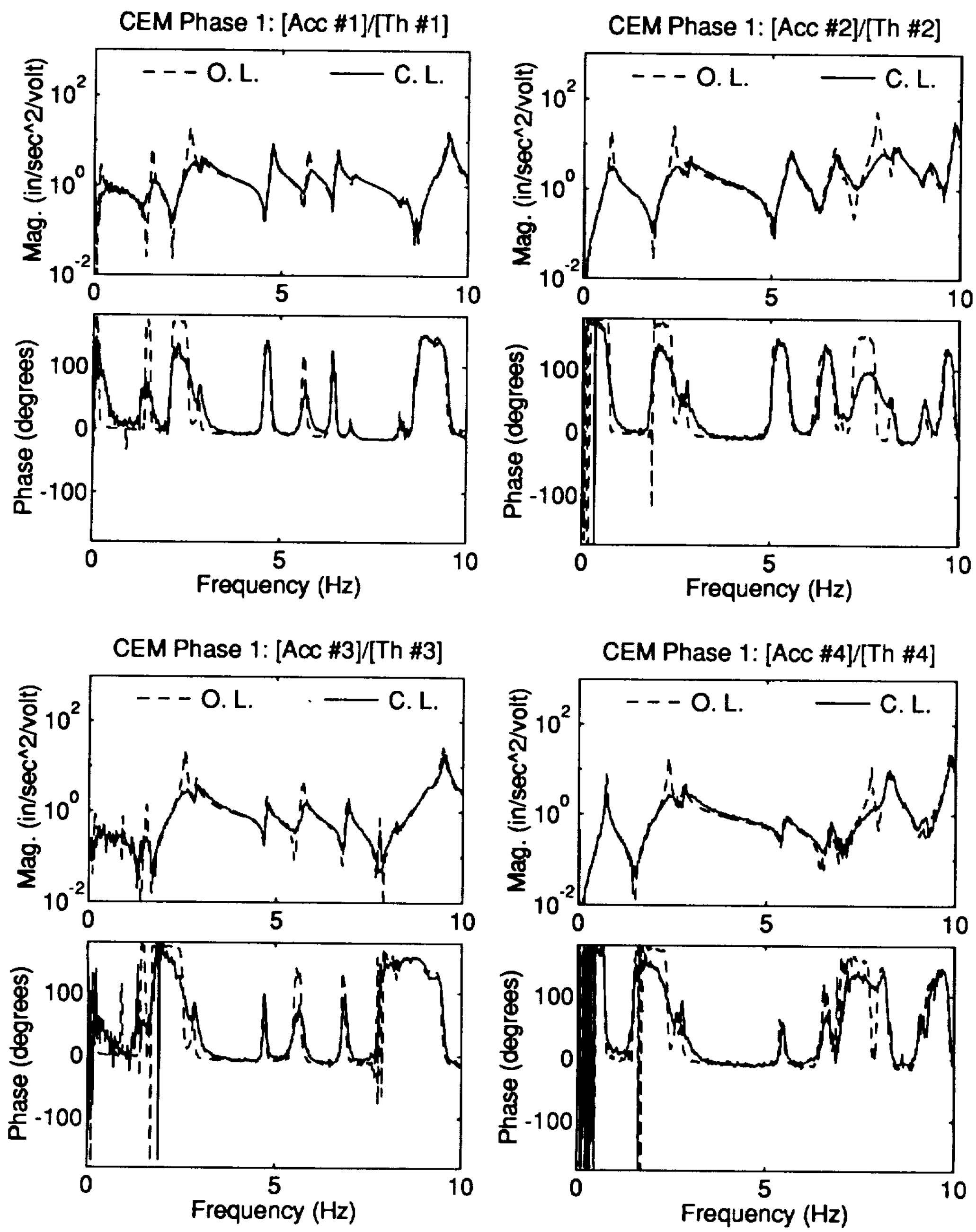

Figure C.8: Phase 1 CEM HAC/LAC 150c Measured Open and Closed Loop Accelerometer Frequency Responses

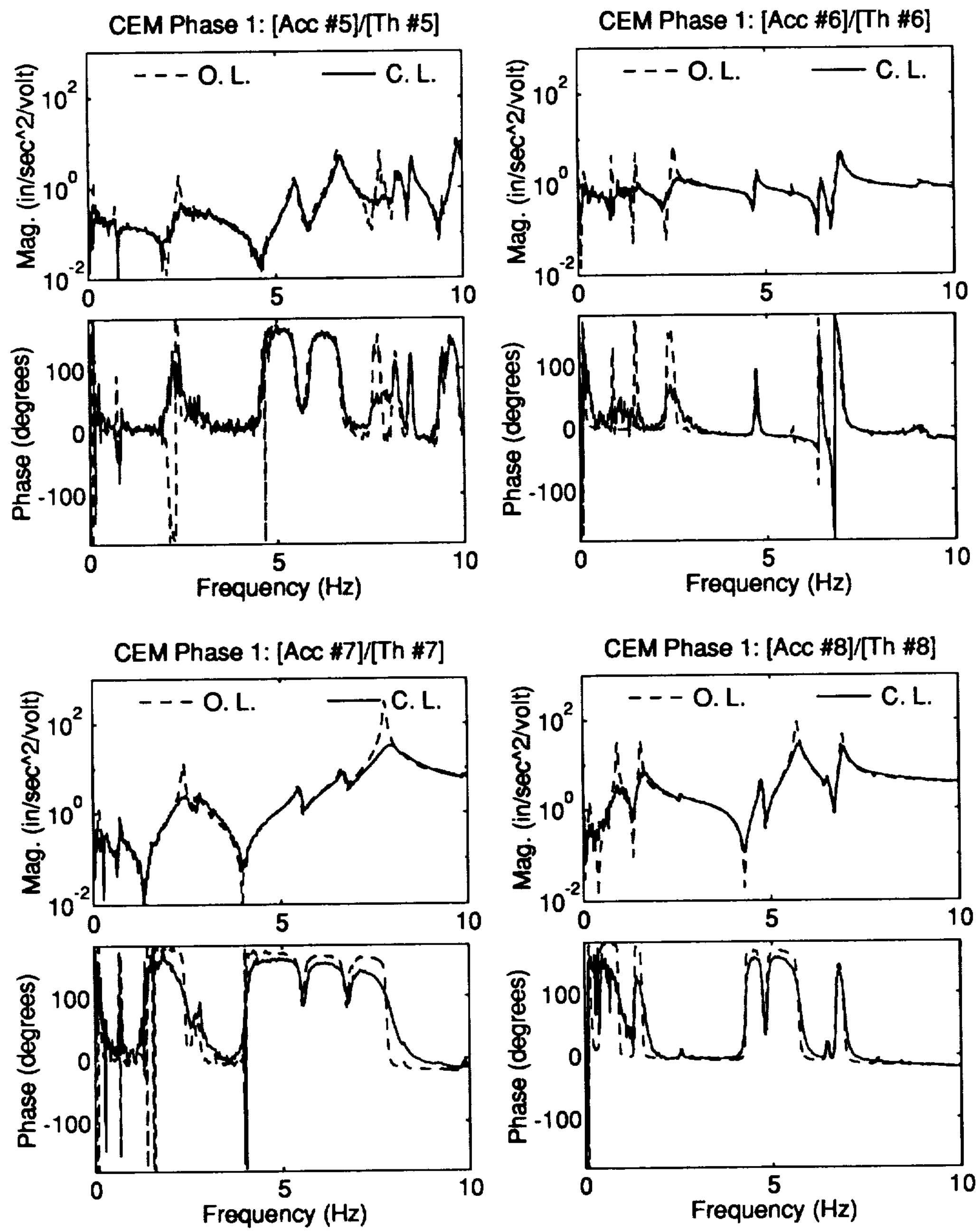

Figure C.9: Phase 1 CEM HAC/LAC 150c Measured Open and Closed Loop Accelerometer Frequency Responses

Appendix D

Phase 2 Control Design Results

The figures in this section show the experimental results of the active controller tests on the Phase 2 CEM. The first two control designs shown are for H_2/LQG A1.4 and H_2/LQG V1.1 controllers discussed in Section 3.3. The next two control designs are the HAC/LAC 1.1 and HAC/LAC 1.2 controllers discussed in Section 3.4. The final controller, HAC/PAS 1.6.1.2, is the combined active/passive controller discussed in Section 4.6.2.

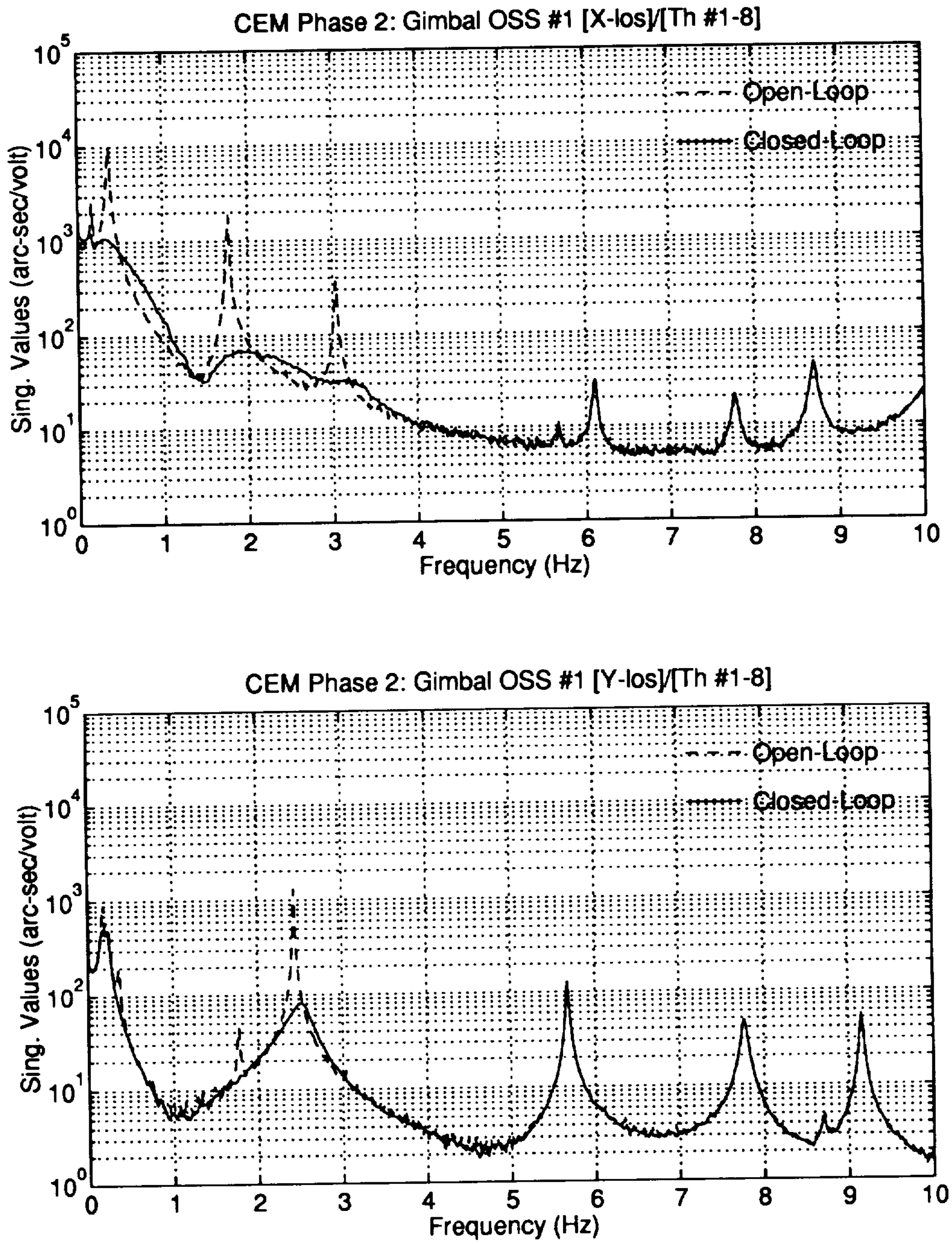

Figure D.1: Phase 2 CEM H_2/LQG A1.4 Measured Open and Closed Loop OSS #1 LOS Frequency Responses

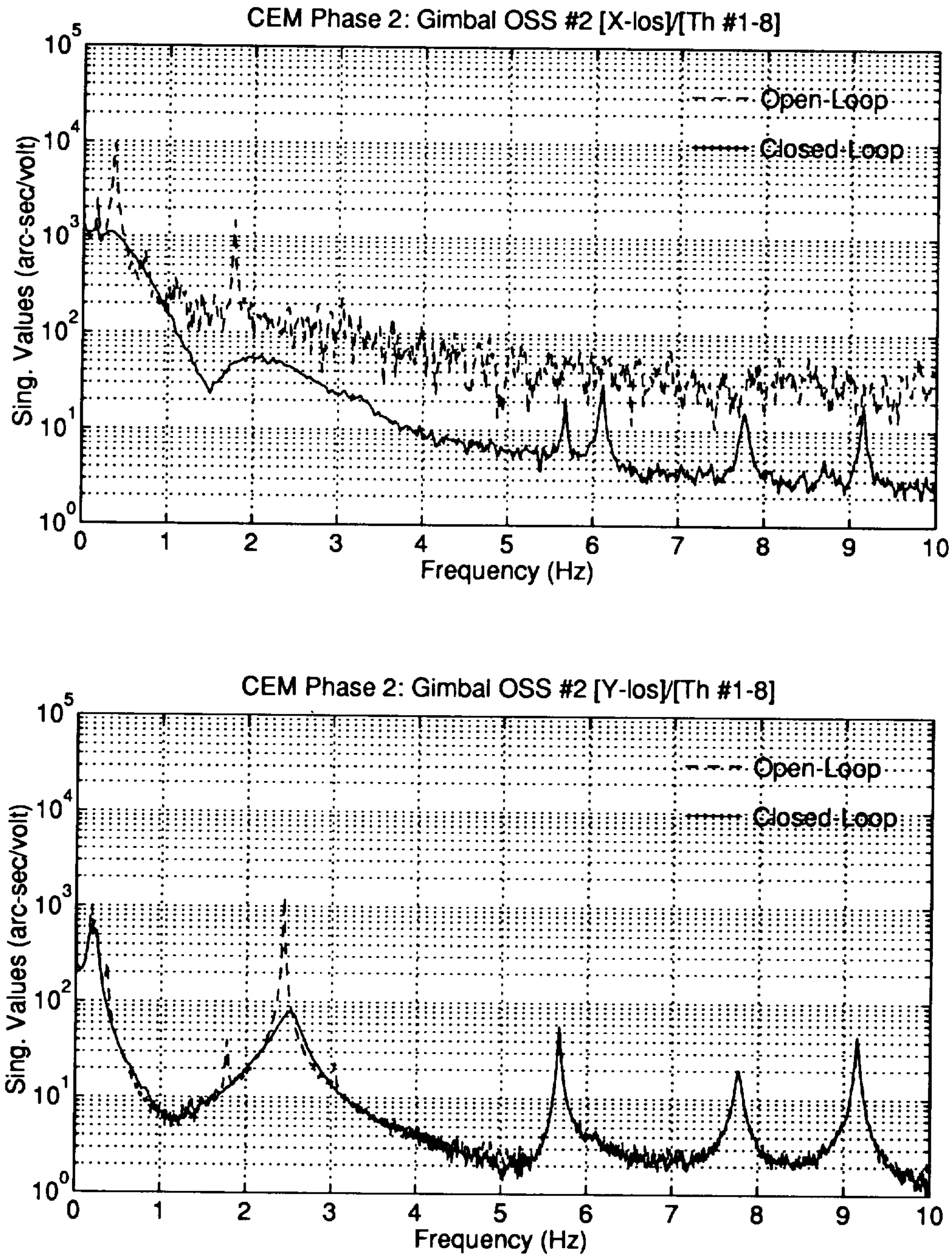

Figure D.2: Phase 2 CEM H_2/LQG A1.4 Measured Open and Closed Loop OSS #2 LOS Frequency Responses

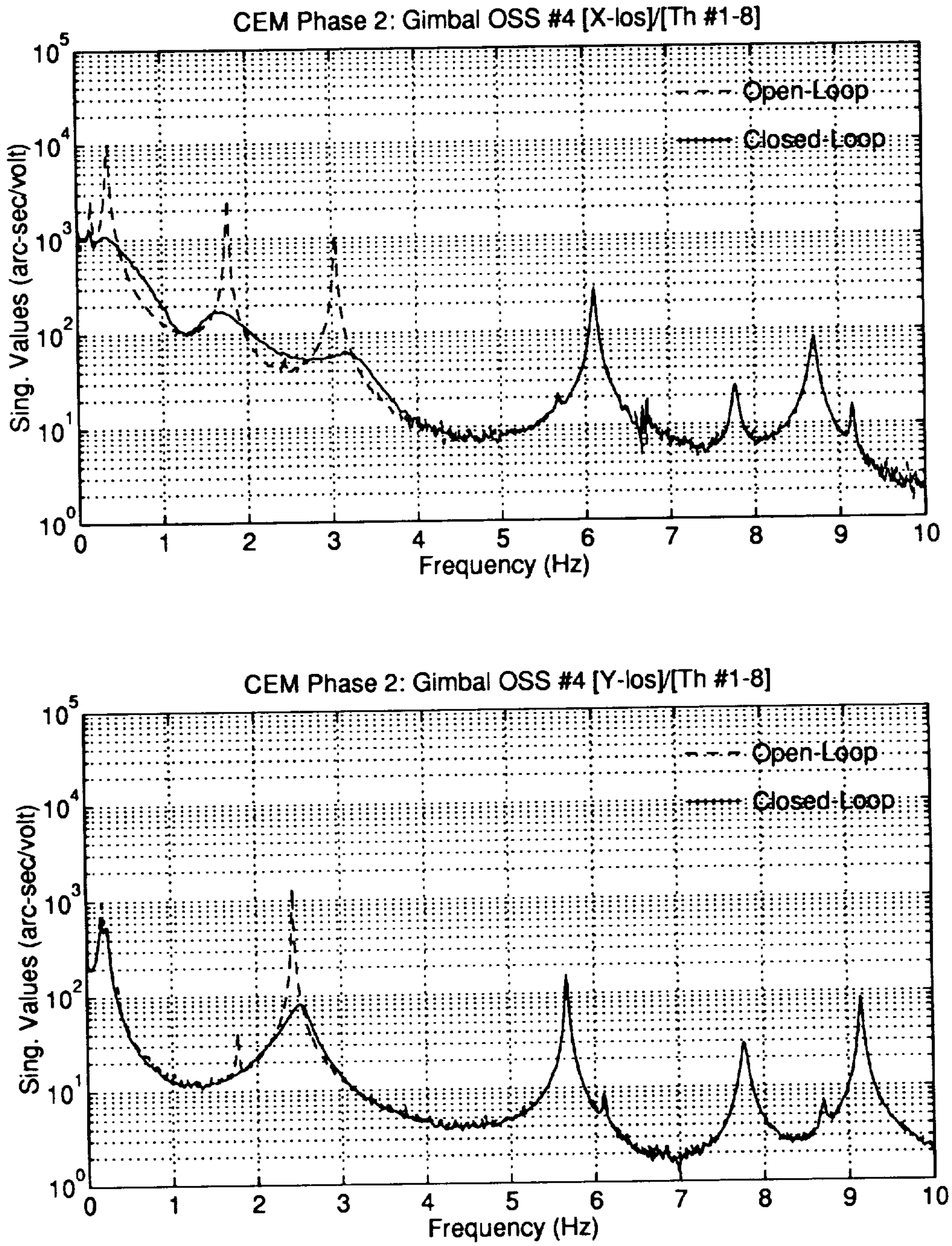

Figure D.3: Phase 2 CEM H_2/LQG A1.4 Measured Open and Closed Loop OSS #4 LOS Frequency Responses

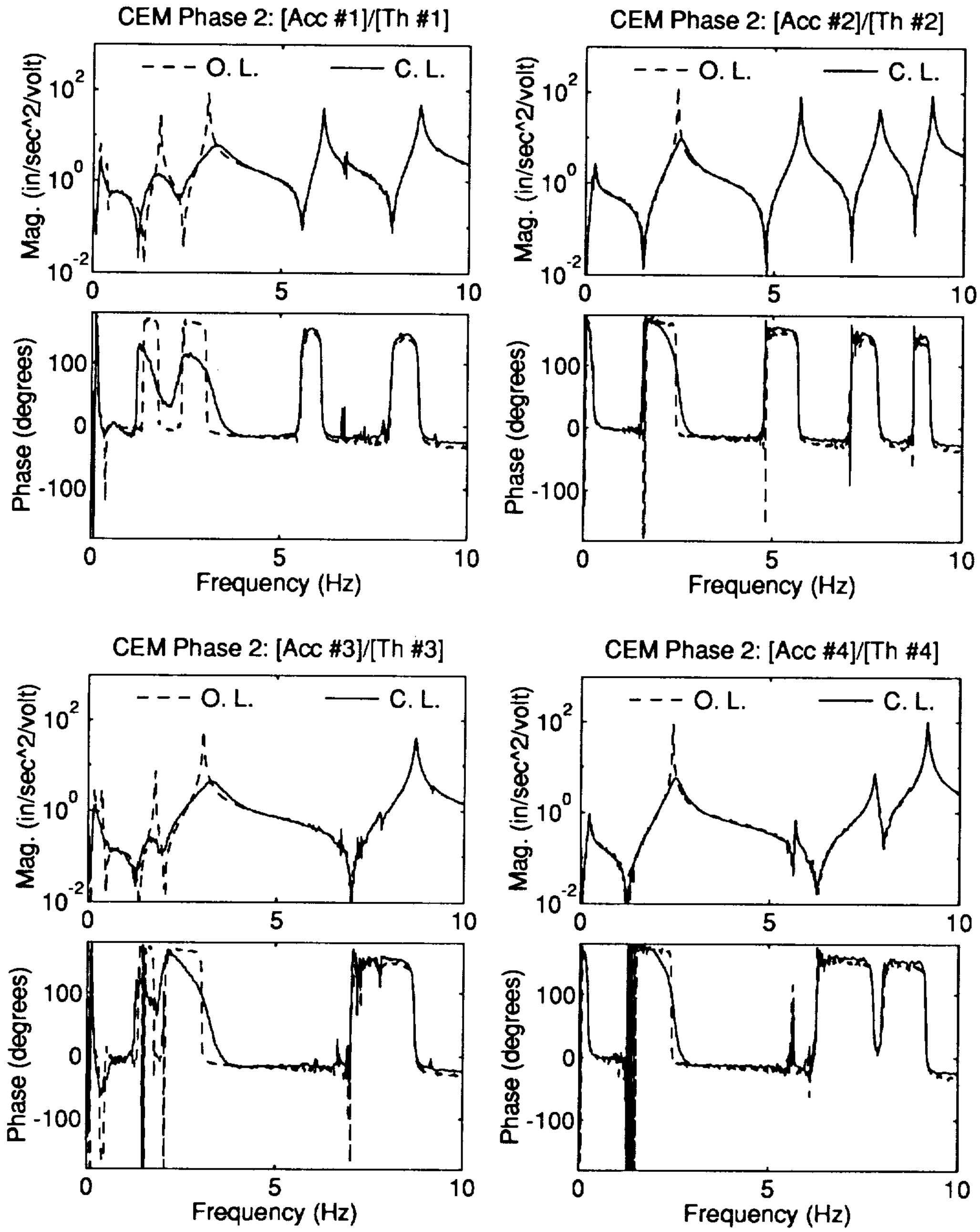

Figure D.4: Phase 2 CEM H_2/LQG A1.4 Measured Open and Closed Loop Accelerometer Frequency Responses

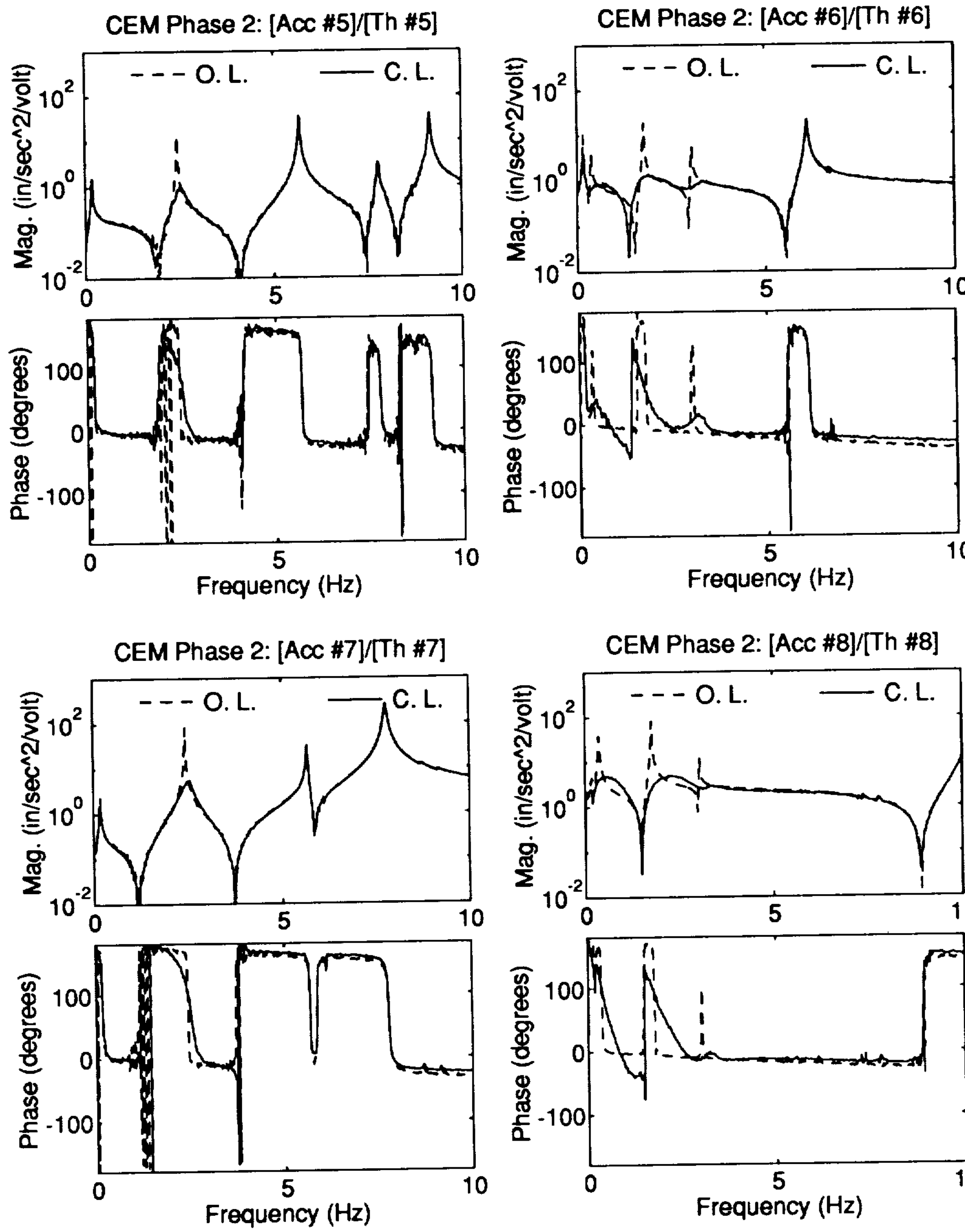

Figure D.5: Phase 2 CEM H_2/LQG A1.4 Measured Open and Closed Loop Accelerometer Frequency Responses

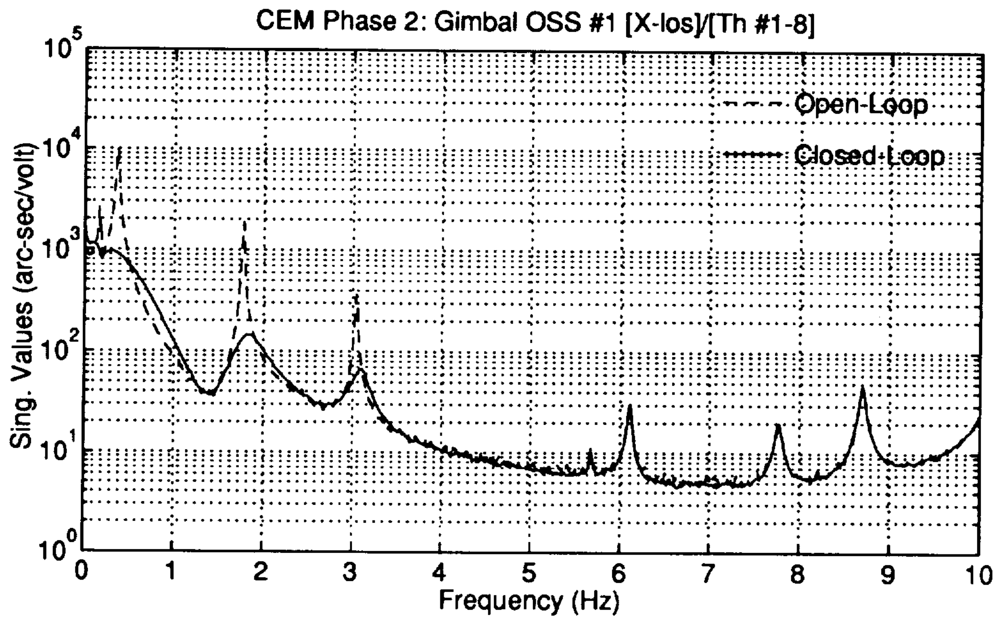

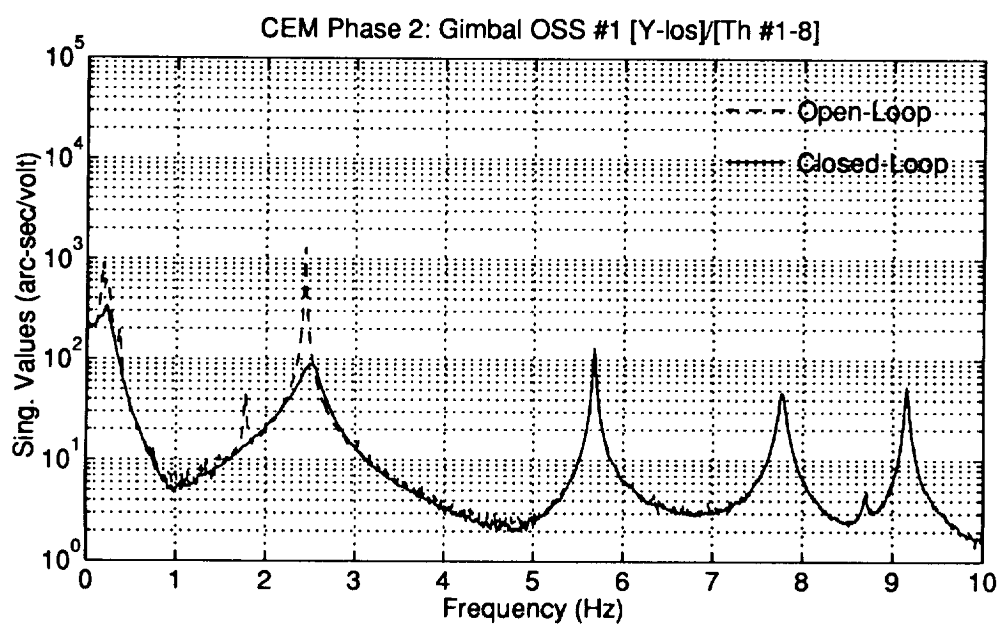

Figure D.6: Phase 2 CEM H_2/LQG V1.1 Measured Open and Closed Loop OSS #1 LOS Frequency Responses

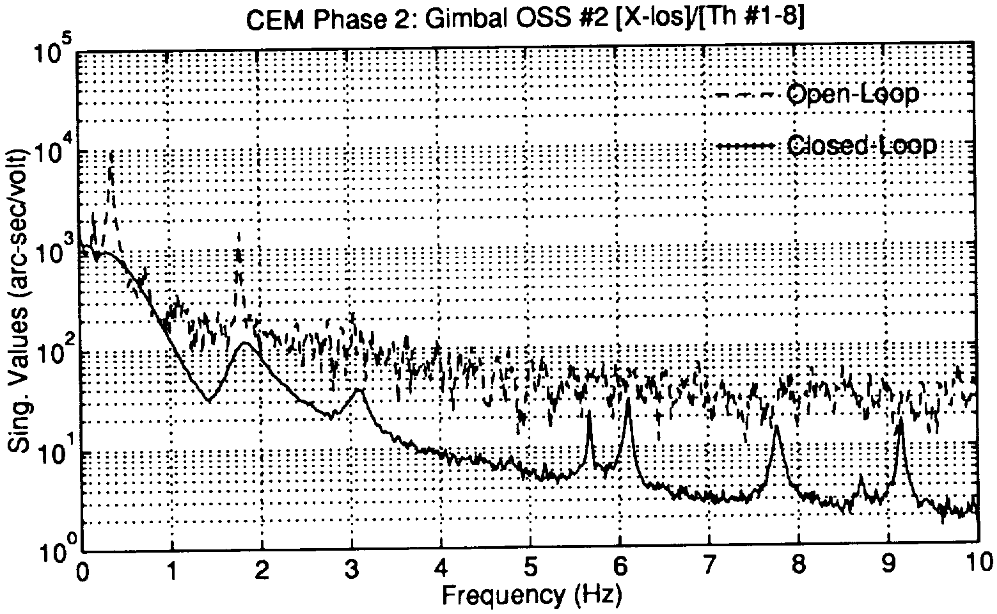

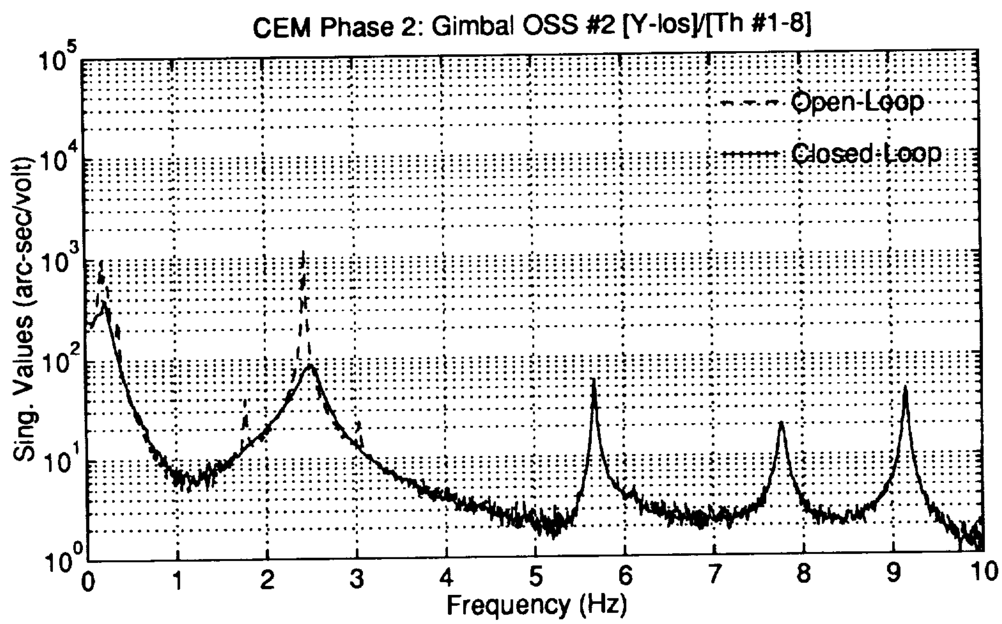

Figure D.7: Phase 2 CEM H_2/LQG V1.1 Measured Open and Closed Loop OSS #2 LOS Frequency Responses

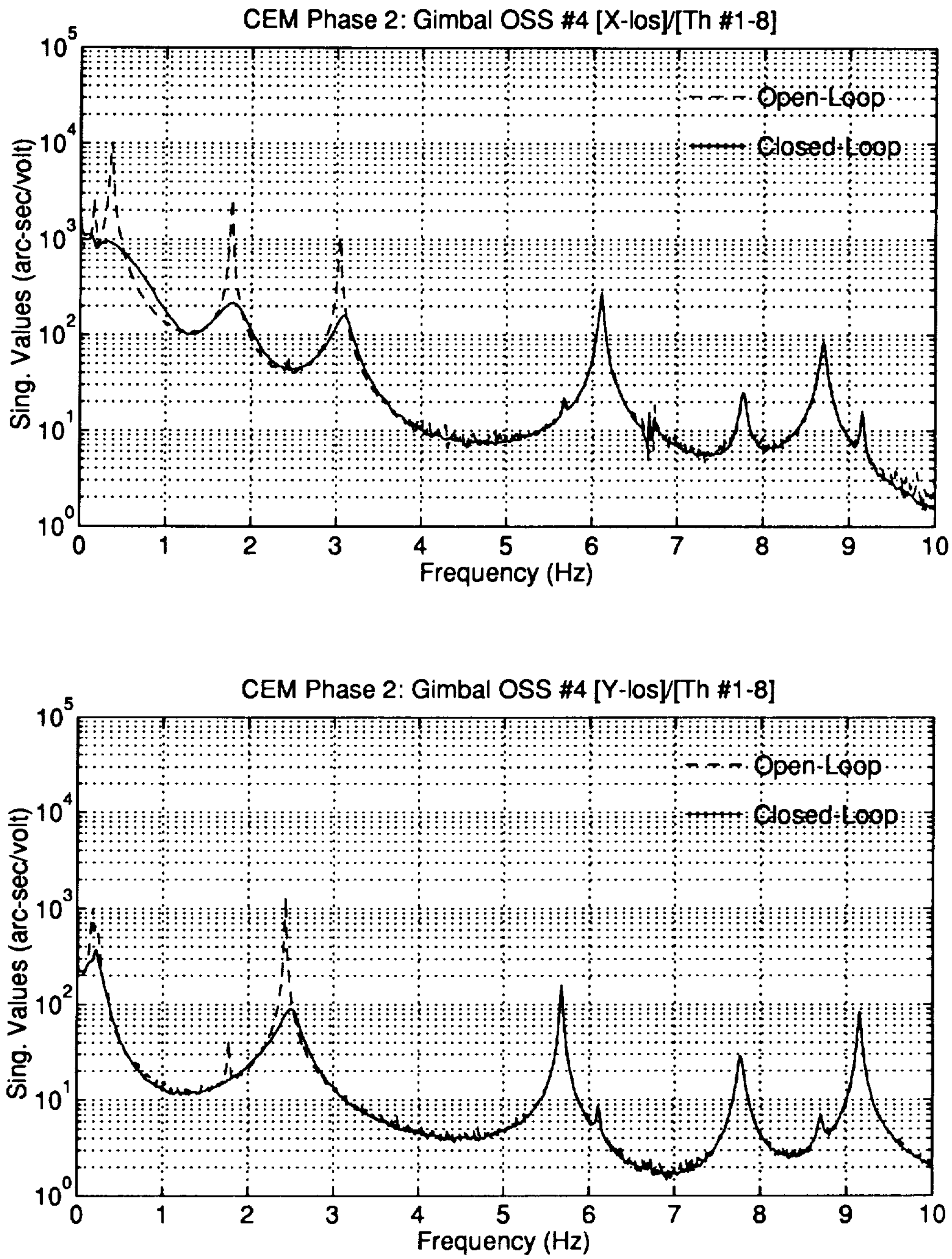

Figure D.8: Phase 2 CEM H_2/LQG V1.1 Measured Open and Closed Loop OSS #4 LOS Frequency Responses

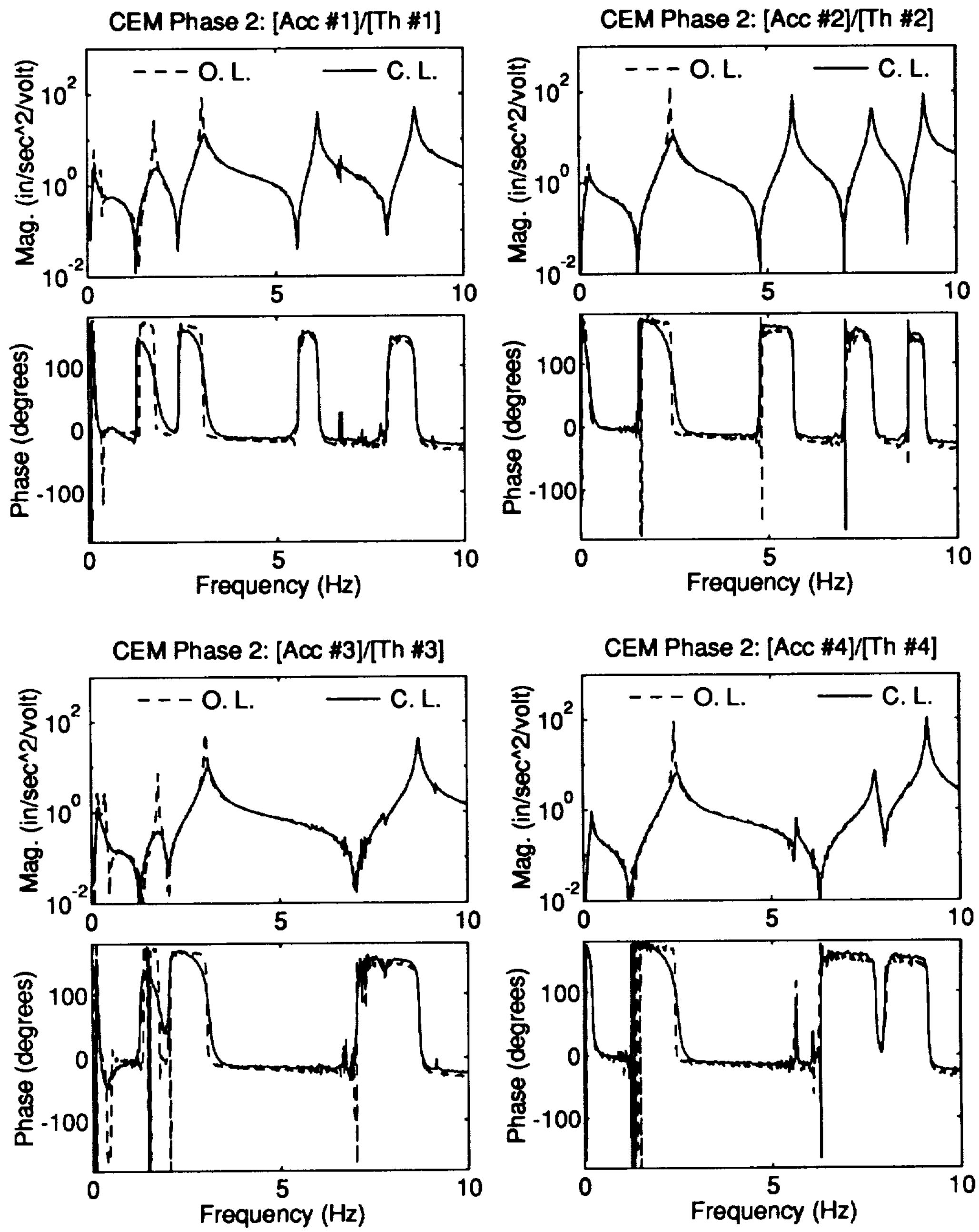

Figure D.9: Phase 2 CEM H_2/LQG V1.1 Measured Open and Closed Loop Accelerometer Frequency Responses

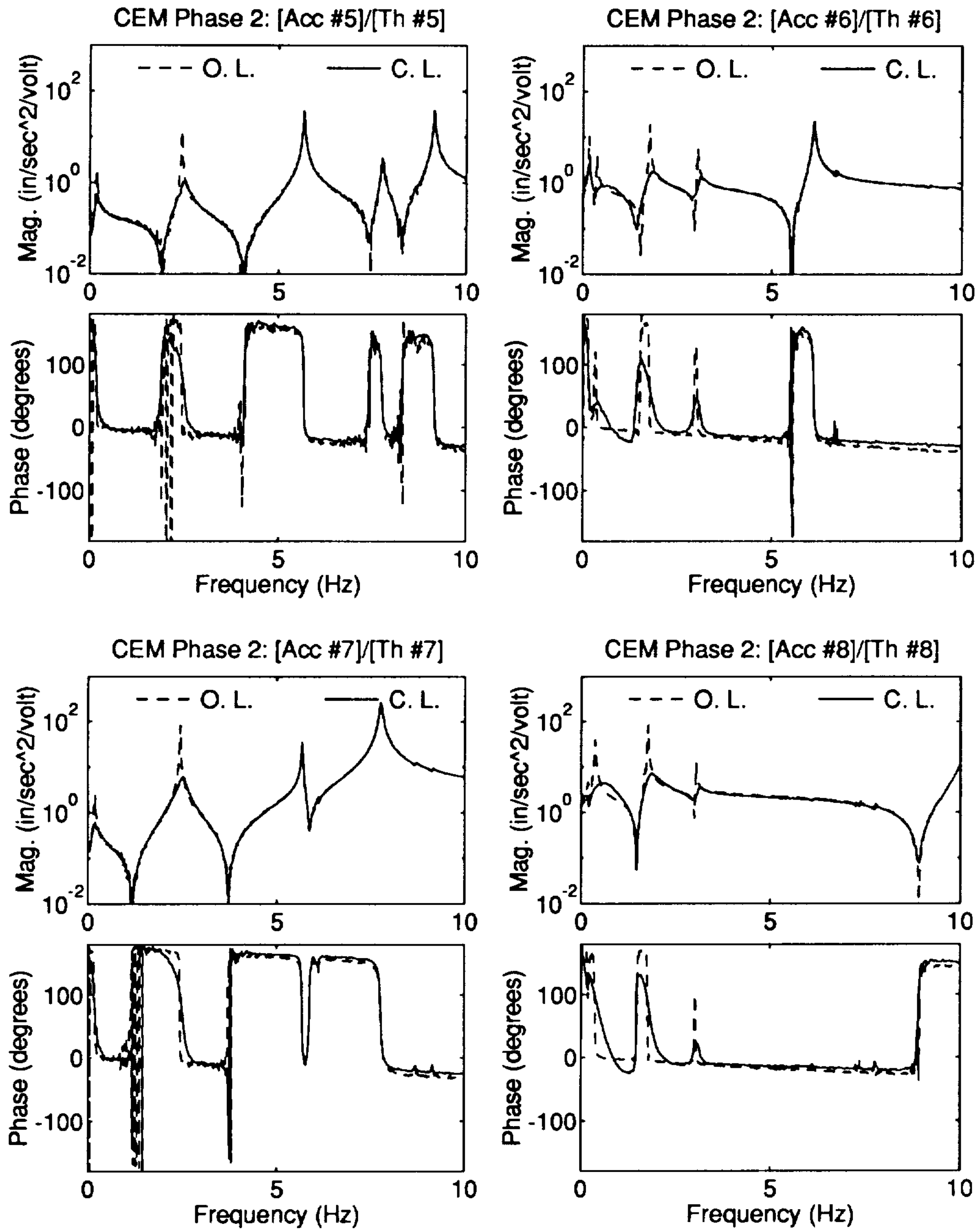

Figure D.10: Phase 2 CEM H_2/LQG V1.1 Measured Open and Closed Loop Accelerometer Frequency Responses

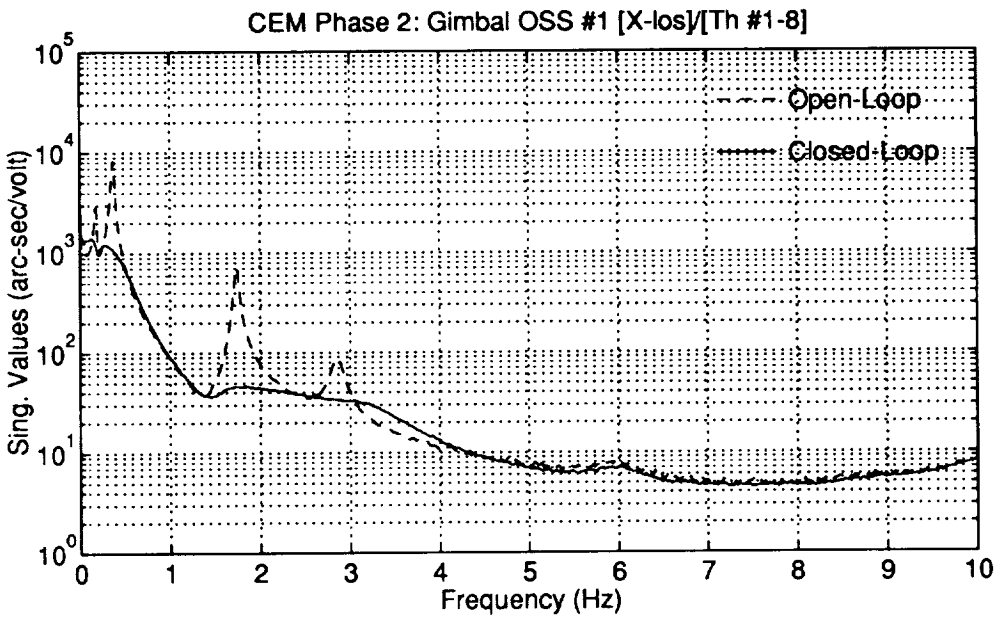

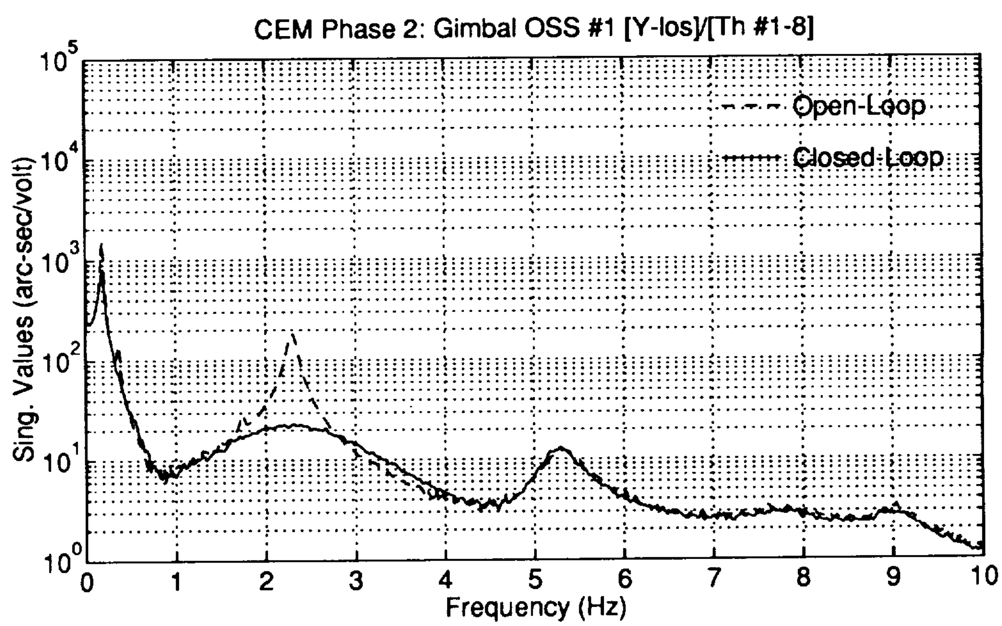

Figure D.11: Phase 2 CEM HAC/LAC 1.1 Measured Open and Closed Loop OSS #1 LOS Frequency Responses

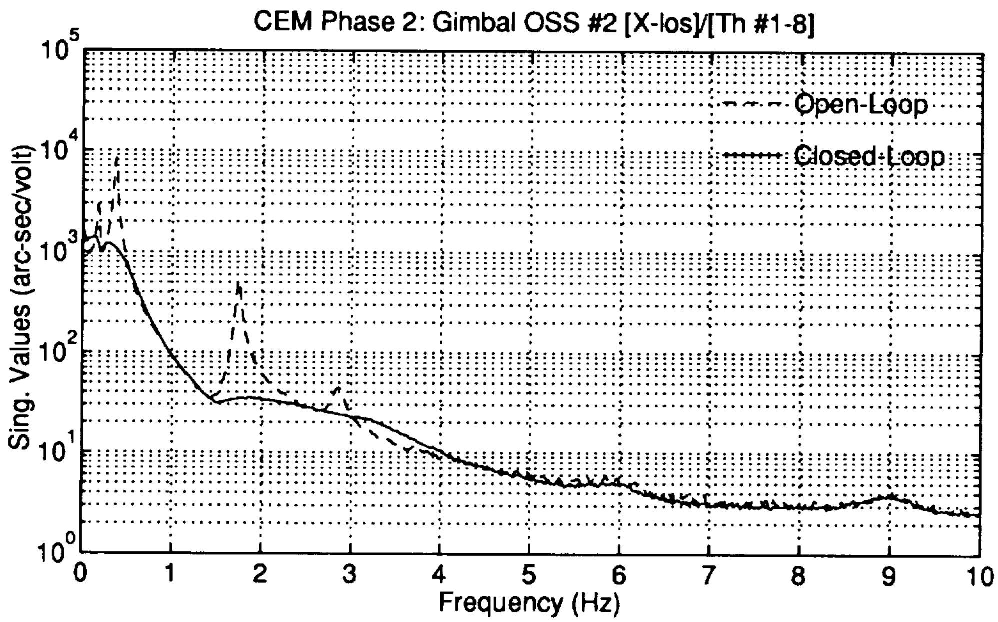

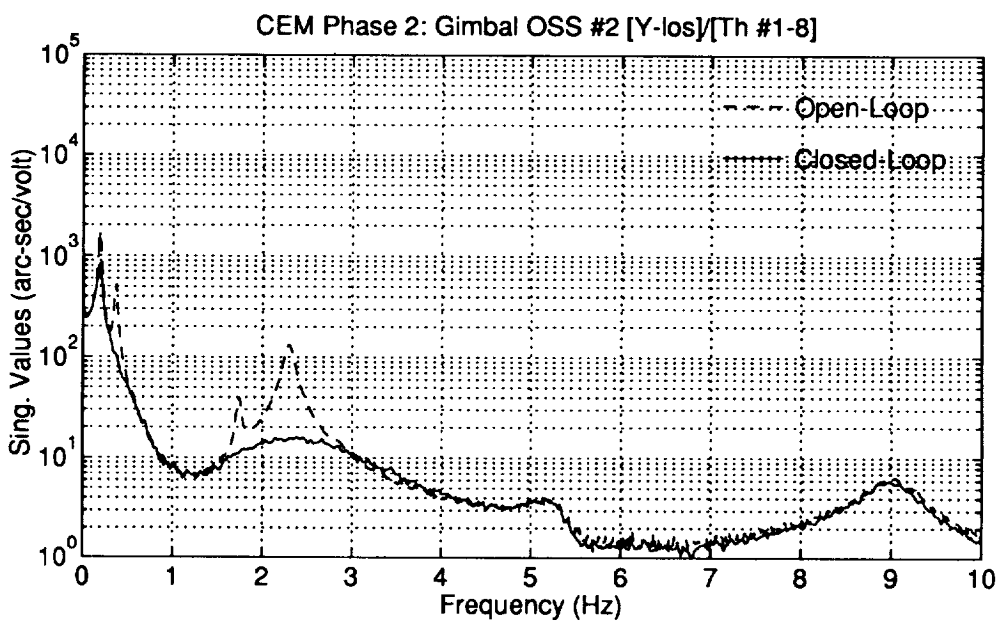

Figure D.12: Phase 2 CEM HAC/LAC 1.1 Measured Open and Closed Loop OSS #2 LOS Frequency Responses

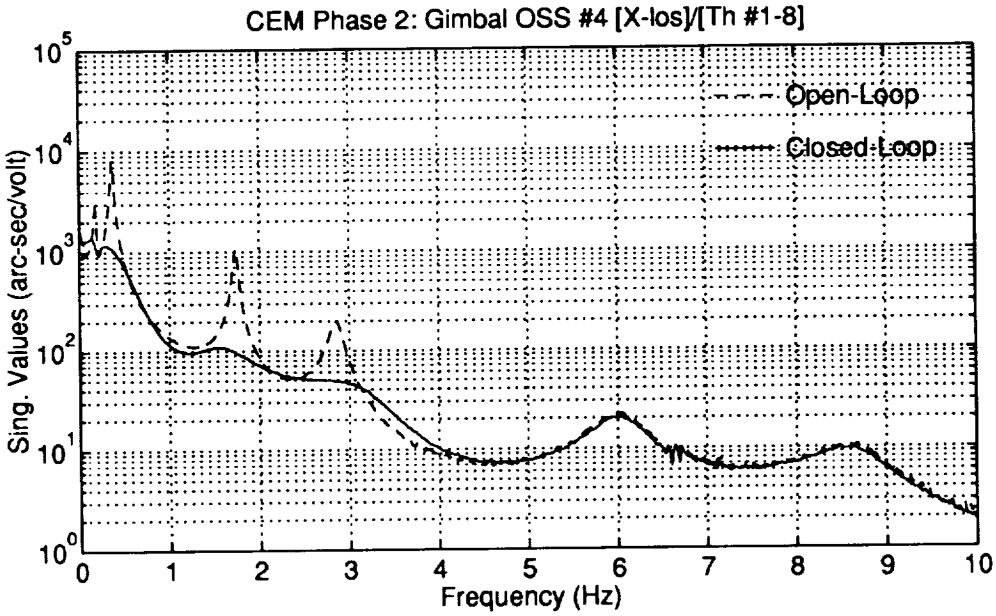

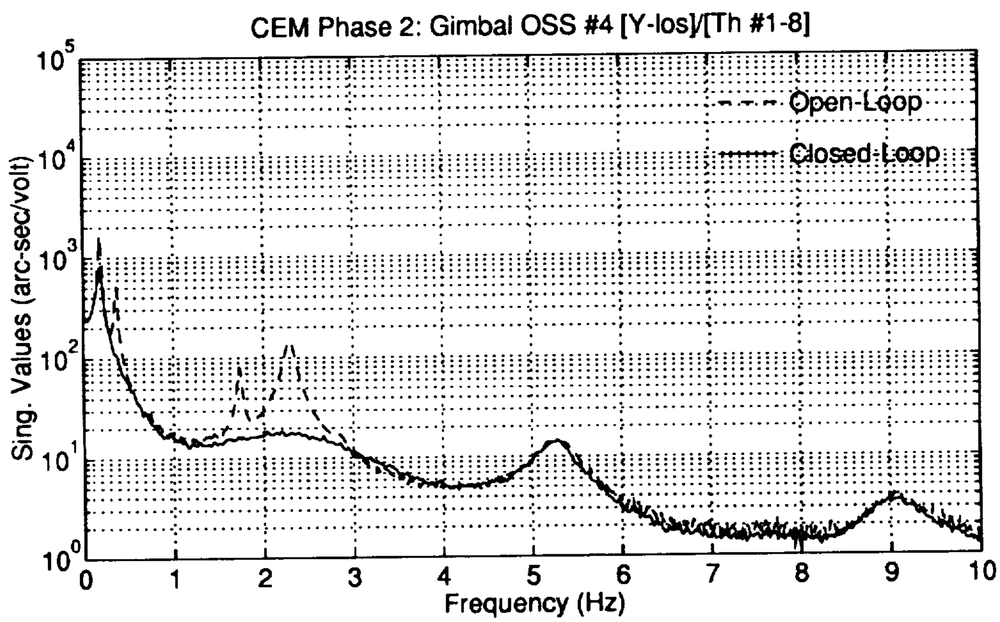

Figure D.13: Phase 2 CEM HAC/LAC 1.1 Measured Open and Closed Loop OSS #4 LOS Frequency Responses

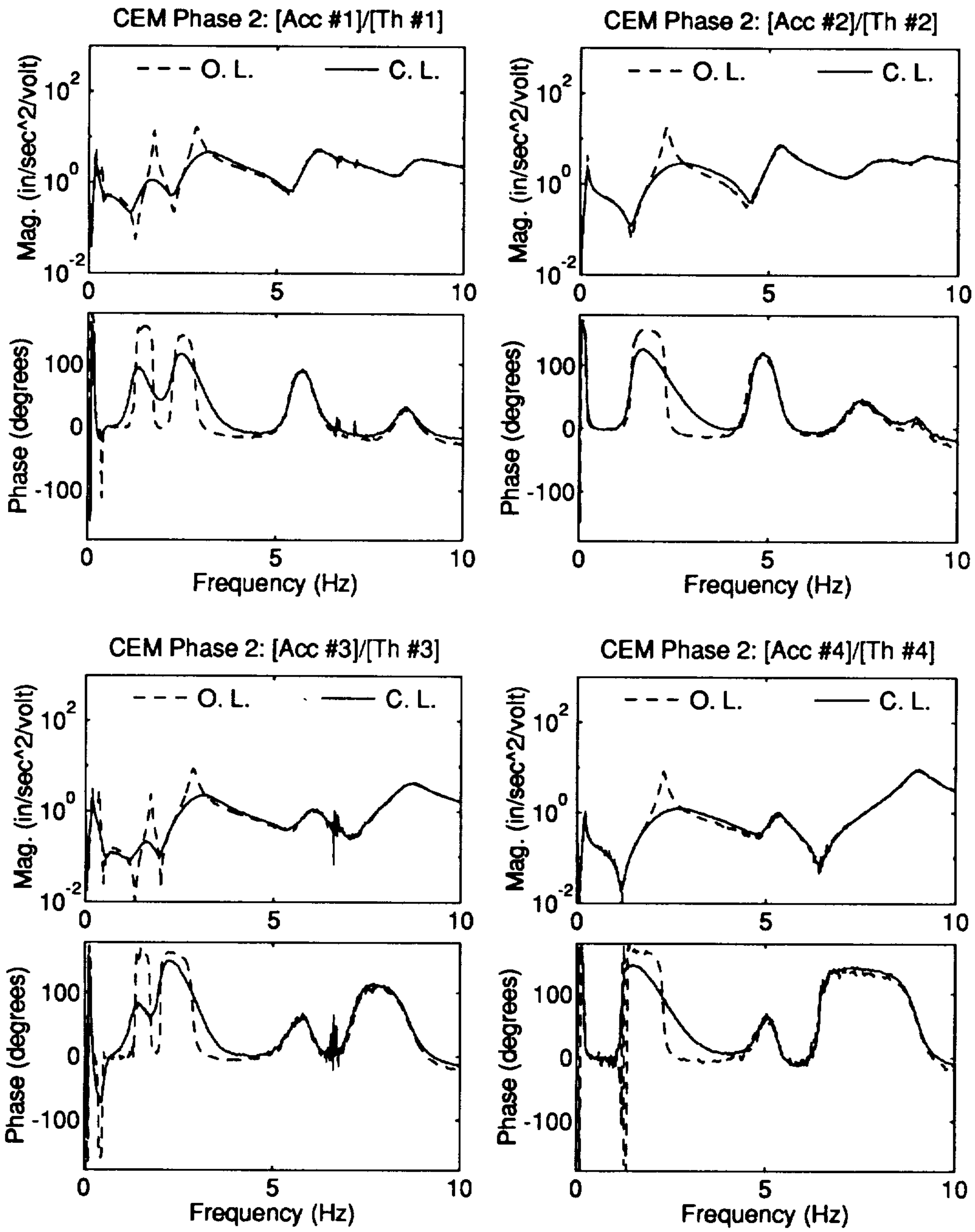

Figure D.14: Phase 2 CEM HAC/LAC 1.1 Measured Open and Closed Loop Accelerometer Frequency Responses

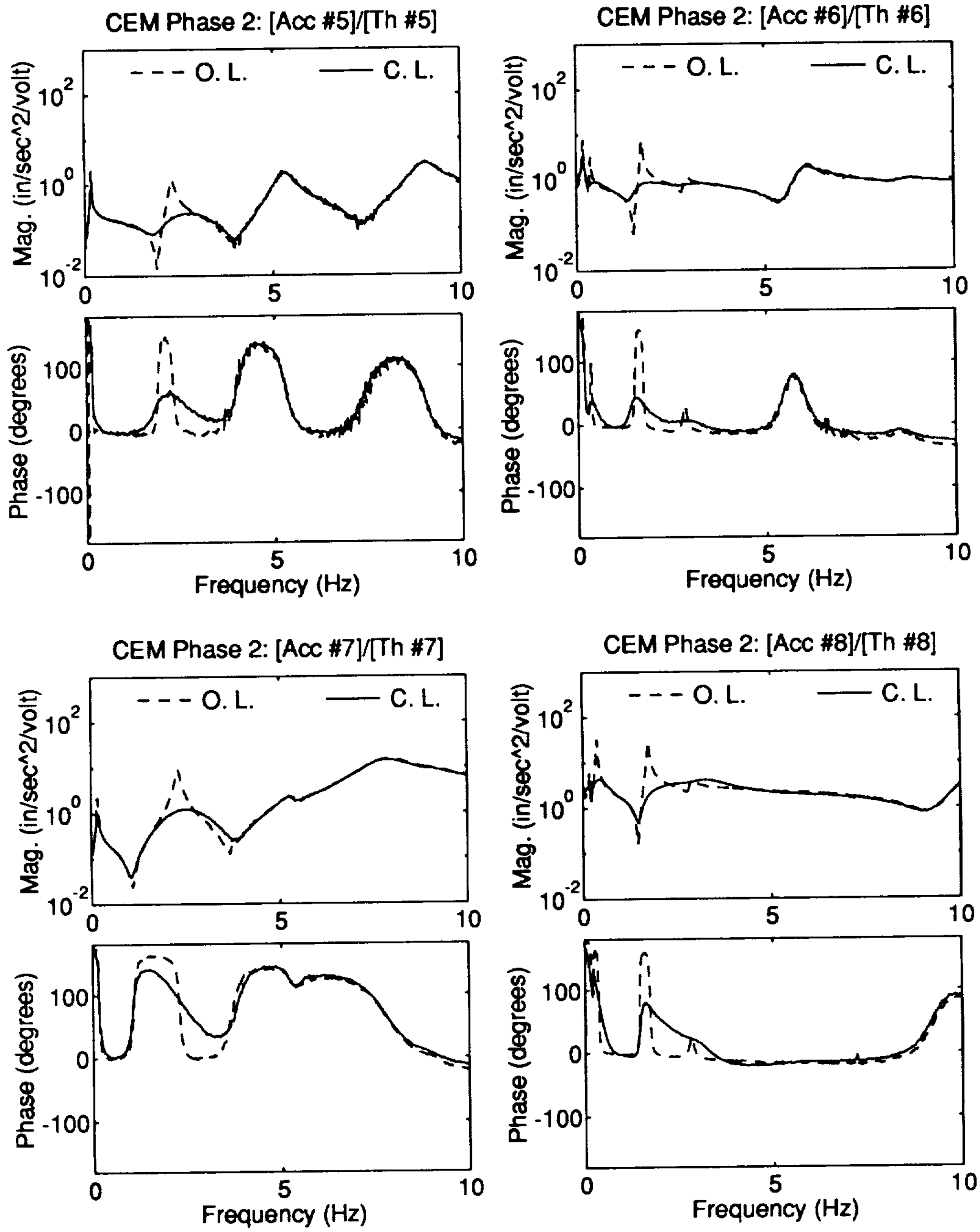

Figure D.15: Phase 2 CEM HAC/LAC 1.1 Measured Open and Closed Loop Accelerometer Frequency Responses

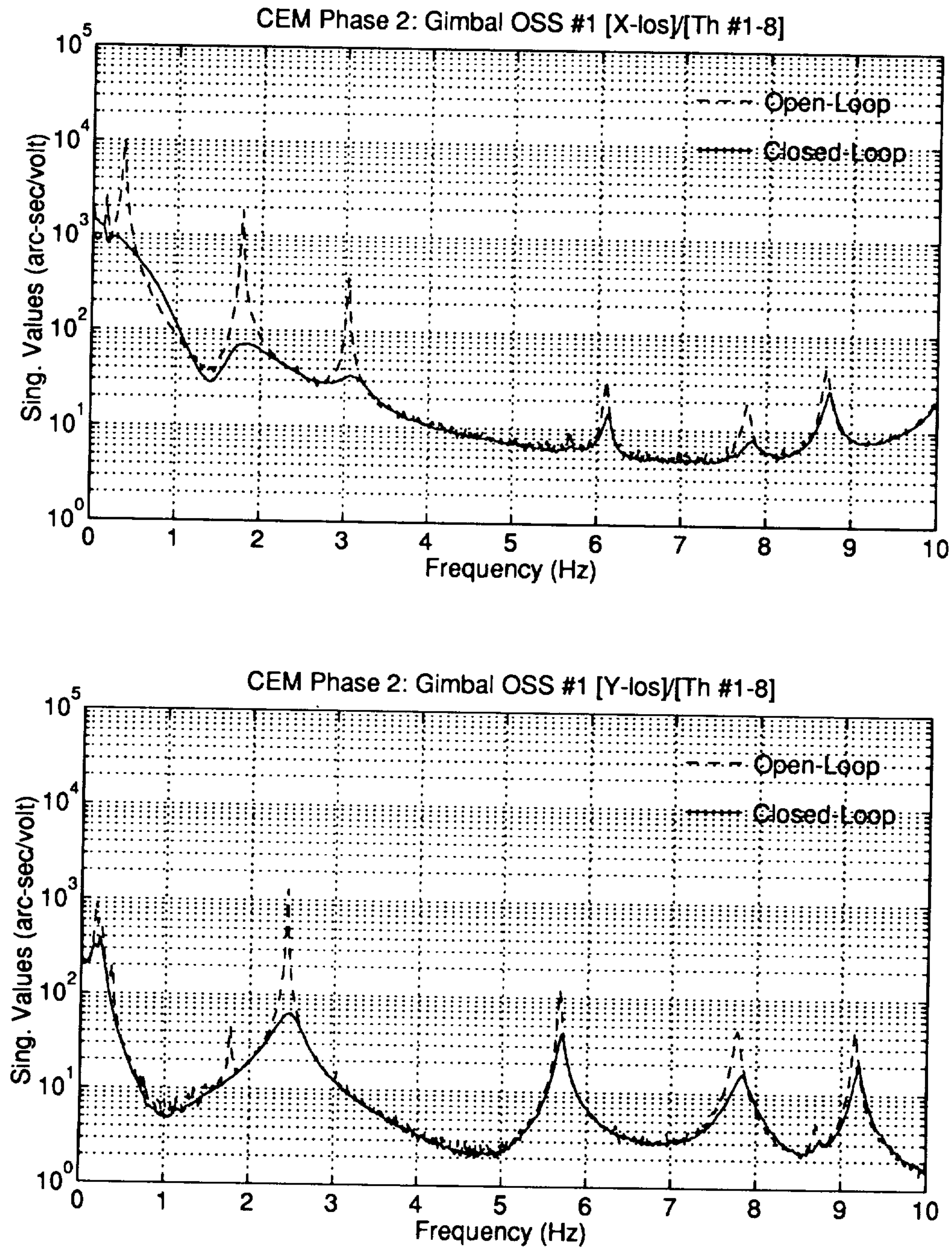

Figure D.16: Phase 2 CEM HAC/LAC 1.2 Measured Open and Closed Loop OSS #1 LOS Frequency Responses

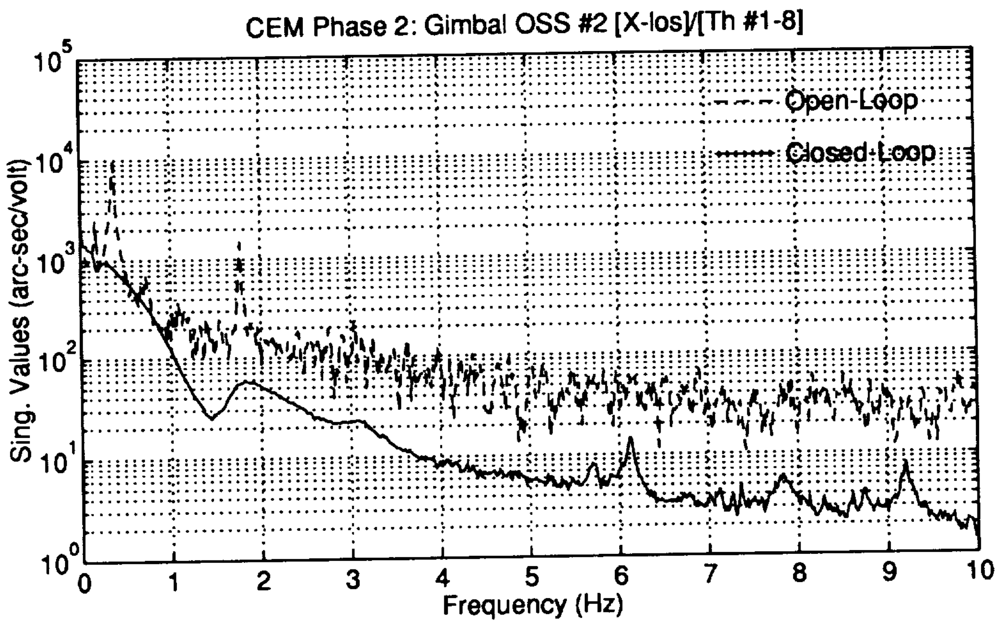

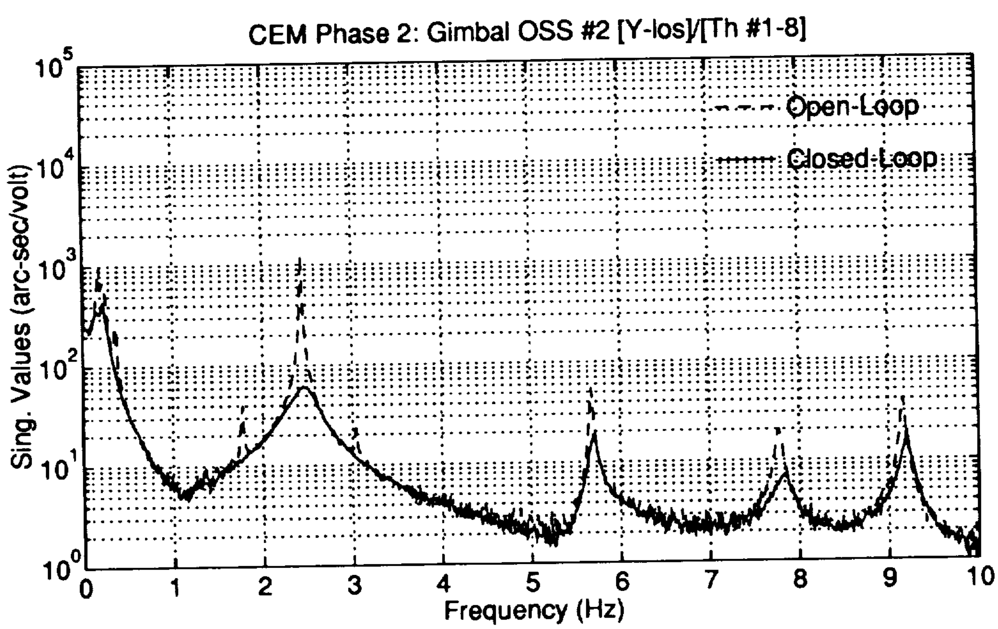

Figure D.17: Phase 2 CEM HAC/LAC 1.2 Measured Open and Closed Loop OSS #2 LOS Frequency Responses

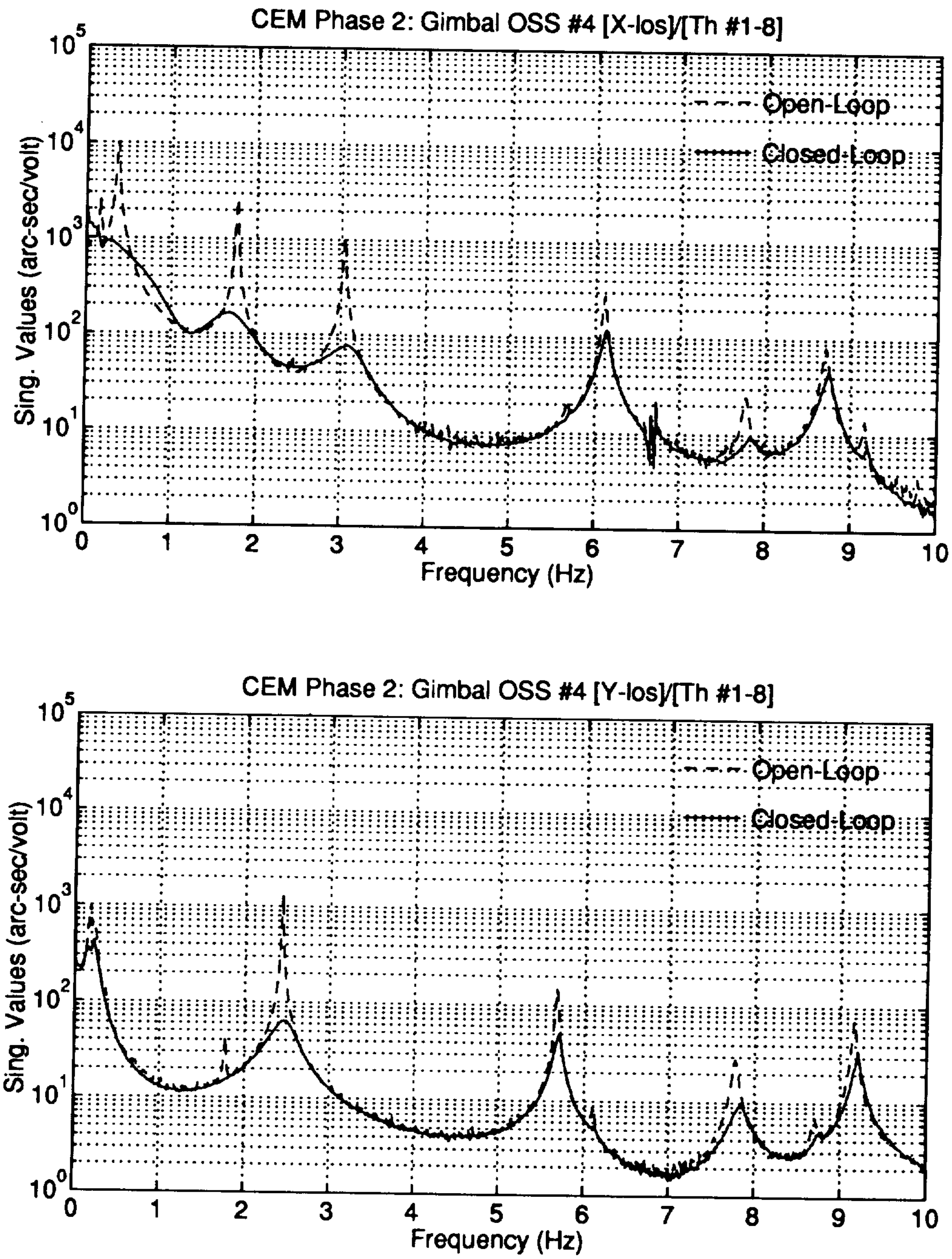

Figure D.18: Phase 2 CEM HAC/LAC 1.2 Measured Open and Closed Loop OSS #4 LOS Frequency Responses

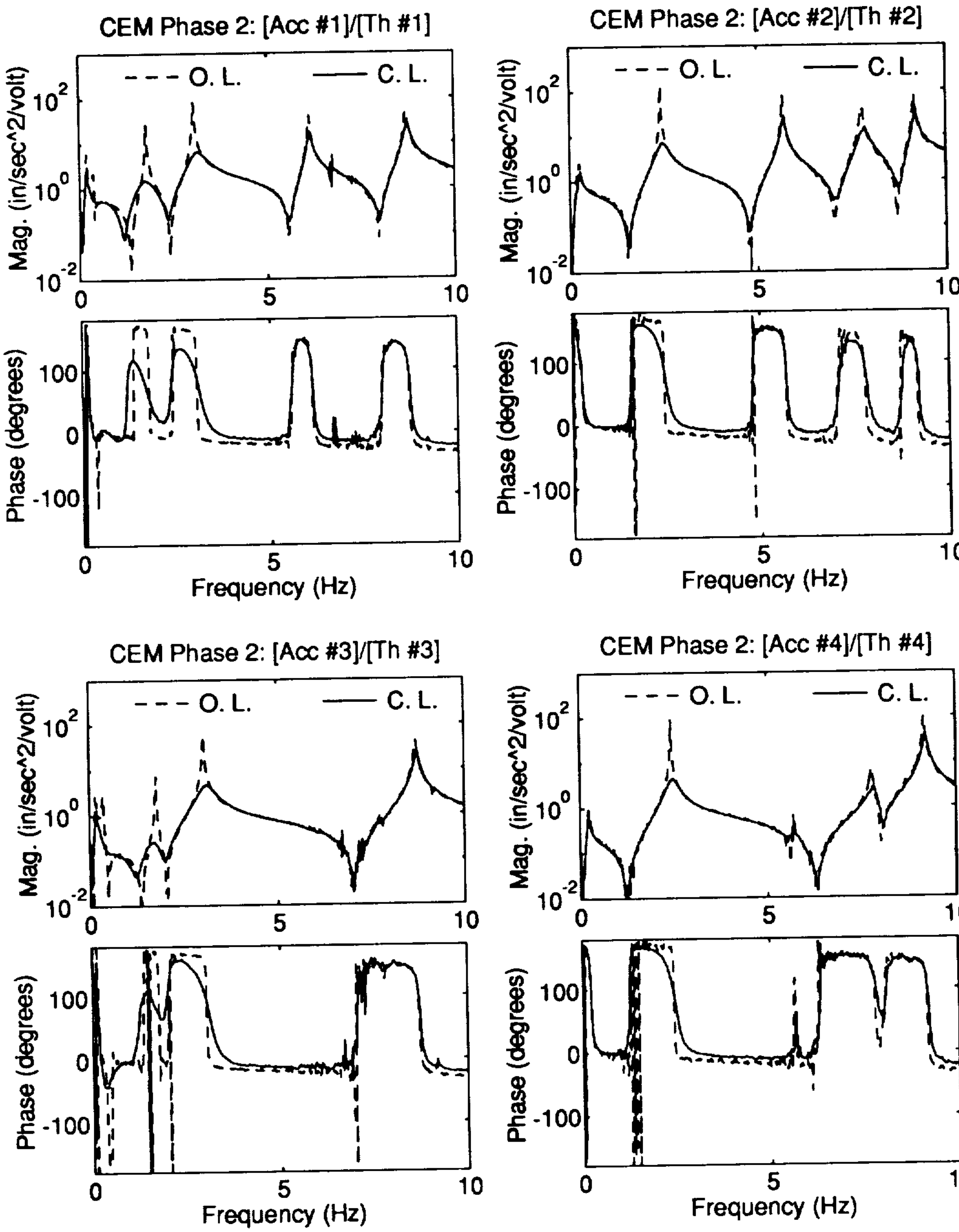

Figure D.19: Phase 2 CEM HAC/LAC 1.2 Measured Open and Closed Loop Accelerometer Frequency Responses

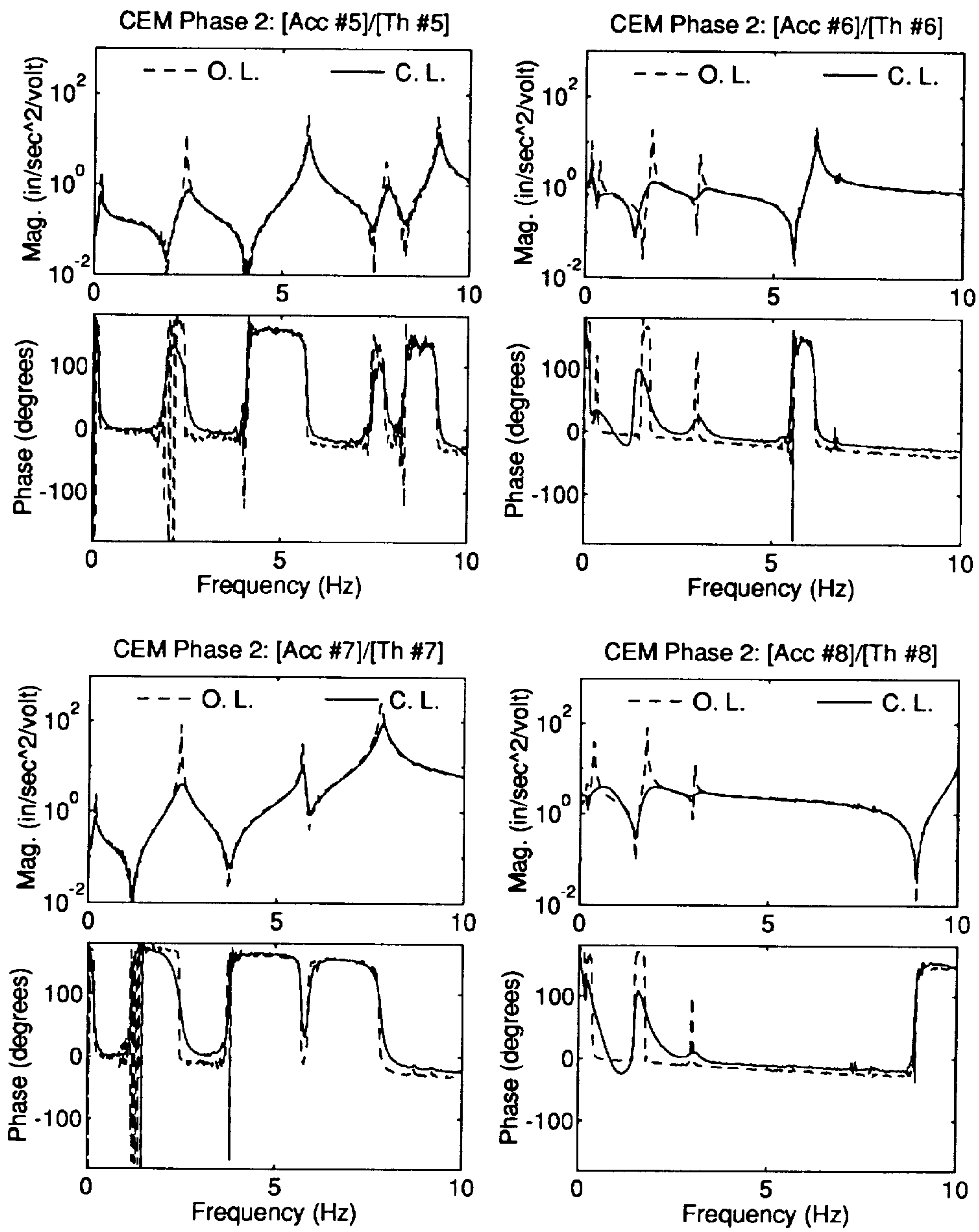

Figure D.20: Phase 2 CEM HAC/LAC 1.2 Measured Open and Closed Loop Accelerometer Frequency Responses

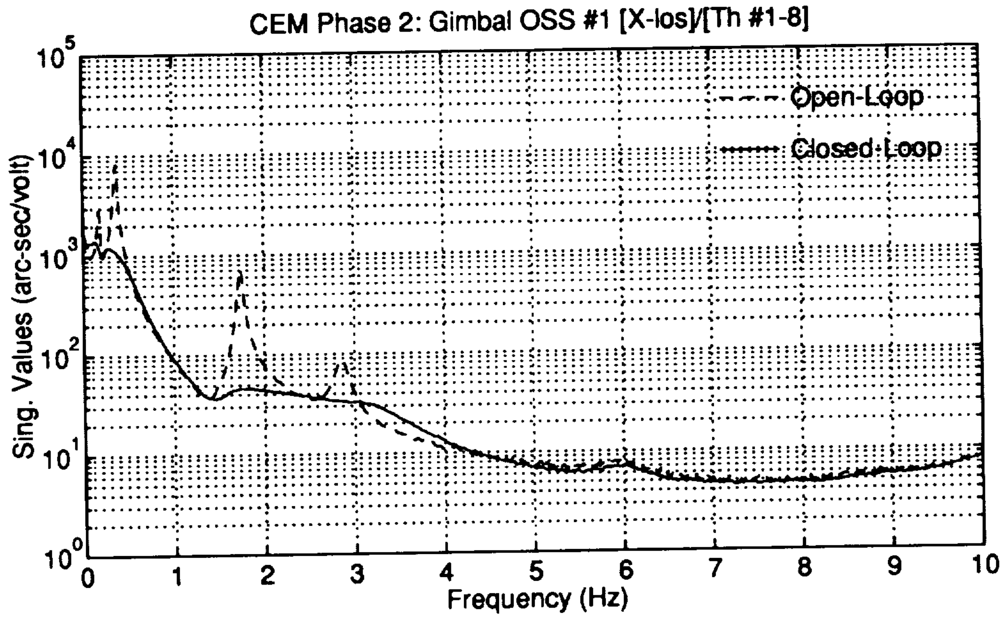

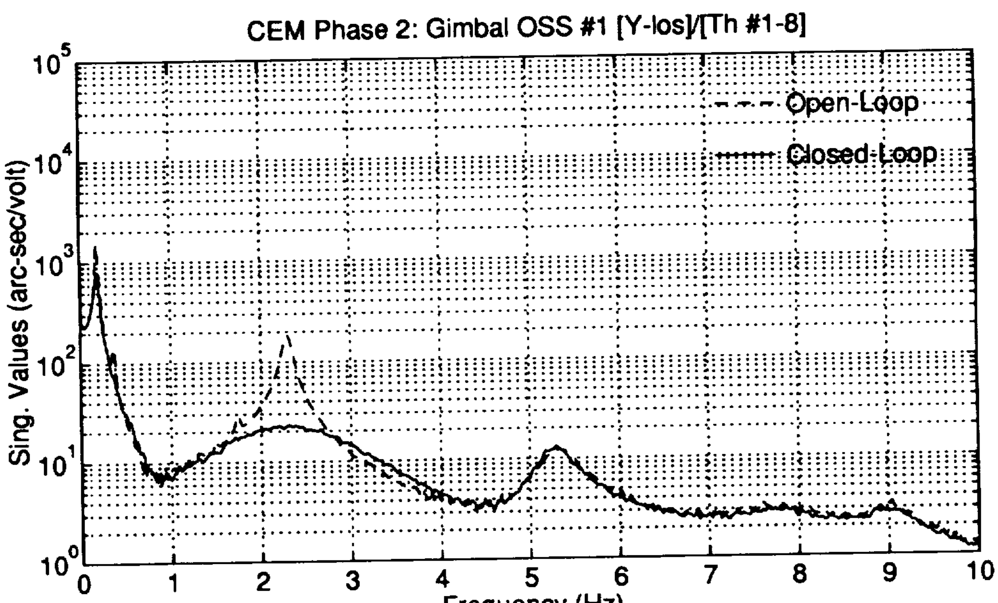

Figure D.21: Phase 2 CEM HAC/PAS 1.6.1.2 Measured Open and Closed Loop OSS #1 LOS Frequency Responses

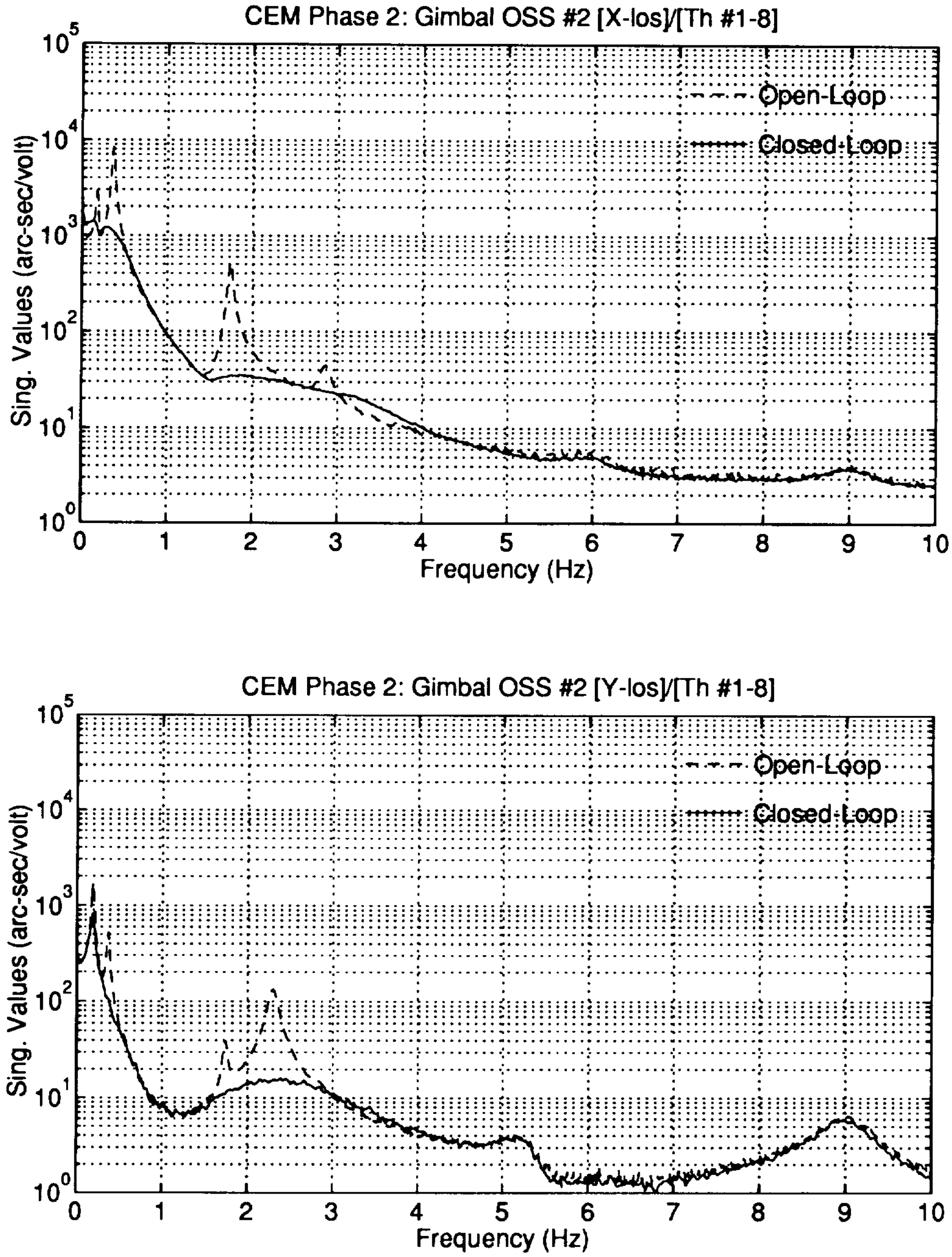

Figure D.22: Phase 2 CEM HAC/PAS 1.6.1.2 Measured Open and Closed Loop OSS #2 LOS Frequency Responses

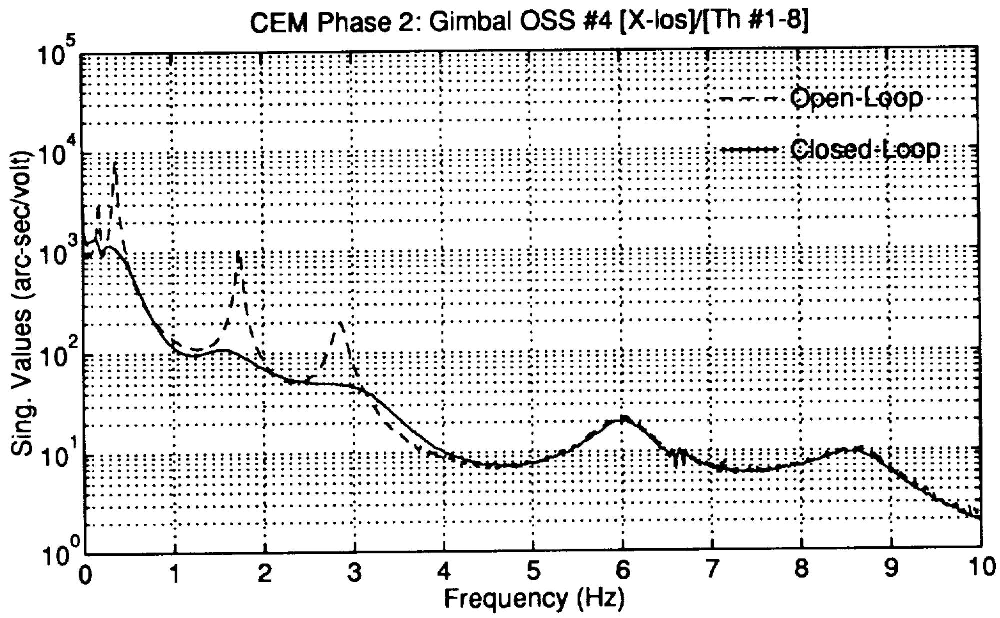

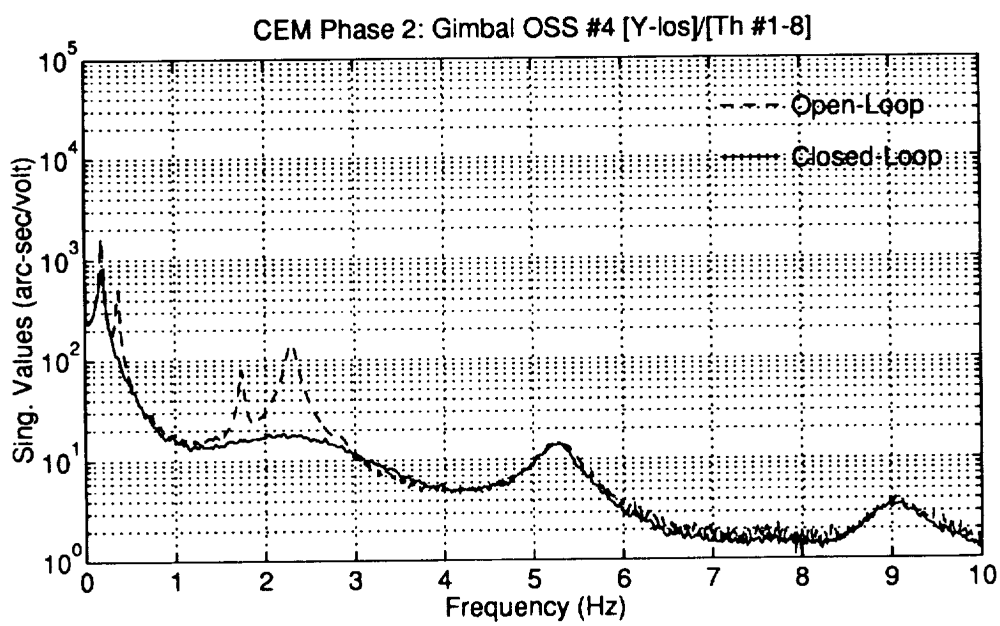

Figure D.23: Phase 2 CEM HAC/PAS 1.6.1.2 Measured Open and Closed Loop OSS #4 LOS Frequency Responses

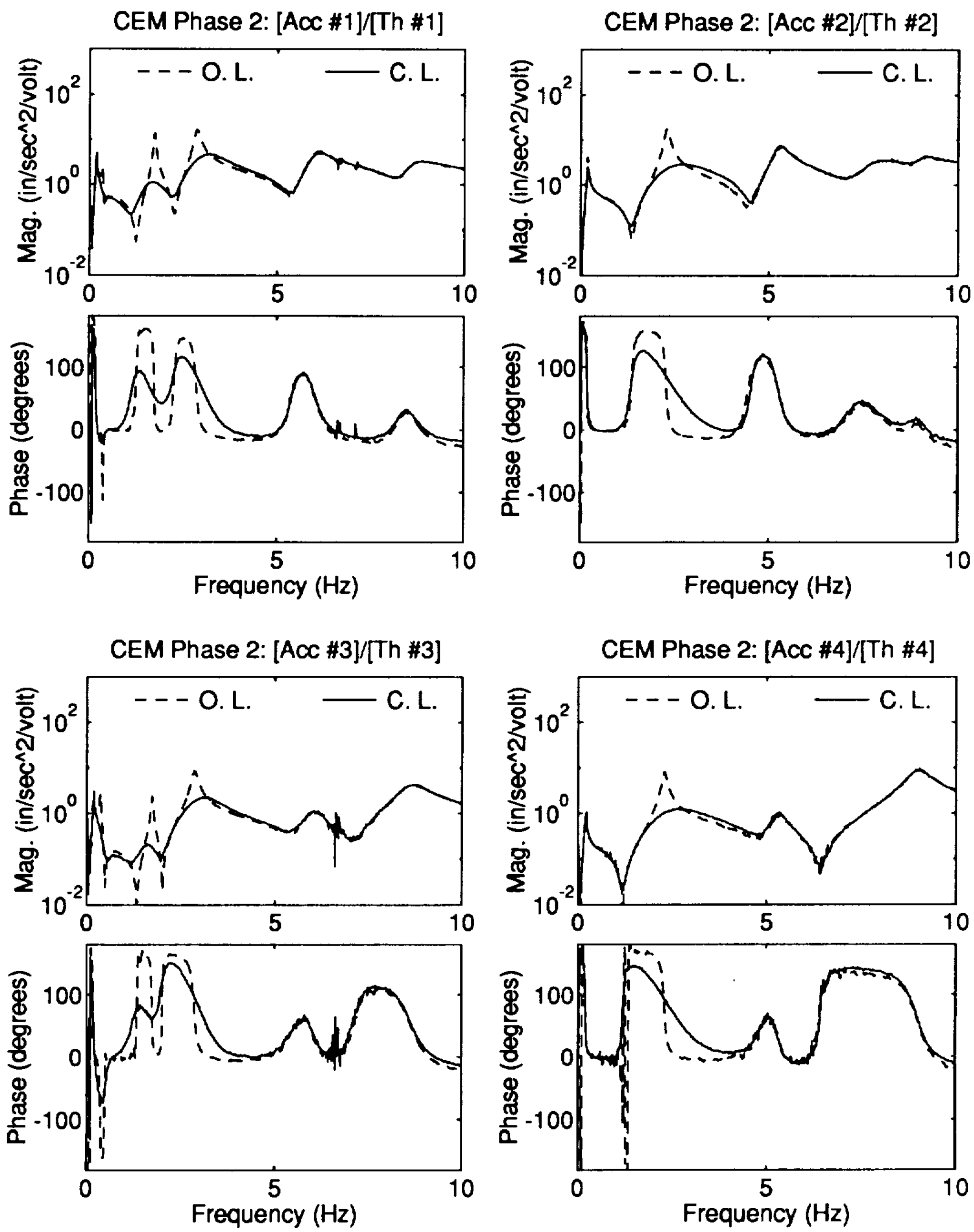

Figure D.24: Phase 2 CEM HAC/PAS 1.6.1.2 Measured Open and Closed Loop Accelerometer Frequency Responses

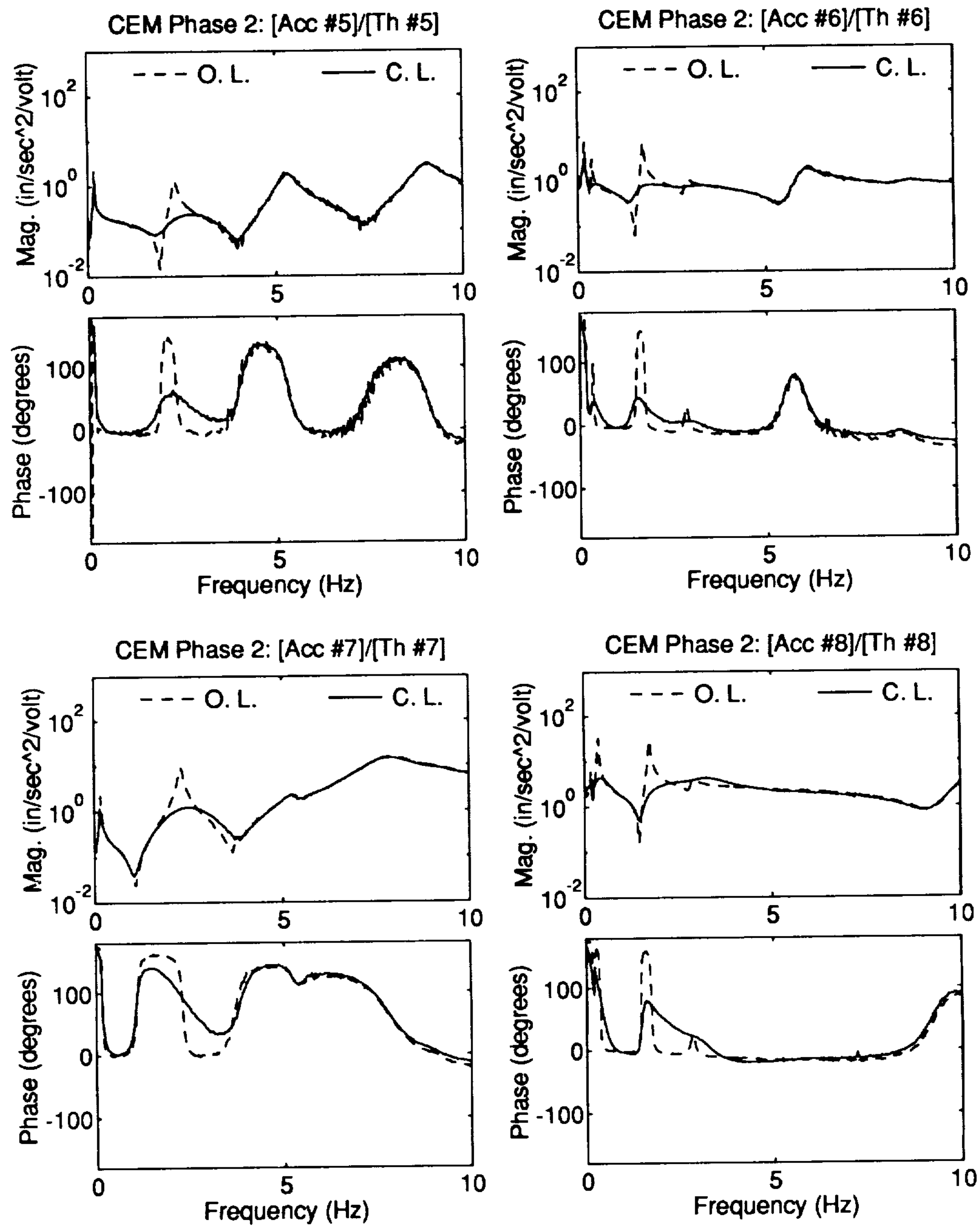

Figure D.25: Phase 2 CEM HAC/PAS 1.6.1.2 Measured Open and Closed Loop Accelerometer Frequency Responses

Appendix E

Phase 2 CEM Modal Strain Energy Distributions

Table E.1: Phase 2 CEM Model P2090992 Modal Strain Energy Distribution For Modes 10, 11, and 20

Set Name	Percent Elastic Strain Energy In Set		
	Mode #10	Mode #11	Mode #20
Main Truss,20 Bays,Longerons	20.56	13.57	22.15
Main Truss,42 Bays,Longerons	62.35	37.12	3.08
Main Truss,20 Bays,Battens	0.29	0.05	7.88
Main Truss,42 Bays,Battens	1.33	0.98	0.19
Main Truss,20 Bays,Batten Diagonals	0.01	0.01	0.18
Main Truss,42 Bays,Batten Diagonals	0.02	0.55	0.01
Main Truss,20 Bays,Top, Bottom Diagonals	0.02	0.69	0.29
Main Truss,42 Bays,Top, Bottom Diagonals	0.09	20.35	0.21
Main Truss,20 Bays,Side Diagonals	1.66	0.11	26.09
Main Truss,42 Bays,Side Diagonals	6.51	18.23	1.17
Laser Tower Truss Longerons	1.22	0.04	33.87
Laser Tower Truss Battens	0.00	0.00	0.03
Laser Tower Truss Batten Diagonals	0.00	0.00	0.00

continued on next page

continued from previous page

Set Name	Percent Elastic Strain Energy In Set		
	Mode #10	Mode #11	Mode #20
Laser Tower Truss Front, Back Diagonals	0.11	0.00	3.20
Laser Tower Truss Side Diagonals	0.01	0.00	0.09
Reflector Truss Longerons	3.99	2.65	0.78
Reflector Truss Battens	0.00	0.01	0.00
Reflector Truss Batten Diagonals	0.00	0.02	0.00
Reflector Truss Side Diagonals	0.52	0.10	0.11
Reflector Truss Front,Back Diagonals	0.01	0.45	0.00
Front Suspension Truss Longerons $+Y$	0.01	0.03	0.02
Front Suspension Truss Longerons $-Y$	0.01	0.02	0.03
Front Suspension Truss Battens $+Y$	0.00	0.00	0.00
Front Suspension Truss Battens $-Y$	0.00	0.00	0.01
Front Suspension Truss Batten Diagonals $+Y$	0.00	0.00	0.00
Front Suspension Truss Batten Diagonals $-Y$	0.00	0.00	0.00
Front Suspension Truss Front, Back Diagonals $+Y$	0.01	0.00	0.02
Front Suspension Truss Front, Back Diagonals $-Y$	0.01	0.00	0.02
Front Suspension Truss Top, Bottom Diagonals $+Y$	0.02	0.03	0.04
Front Suspension Truss Top, Bottom Diagonals $-Y$	0.02	0.04	0.06
Back Suspension Truss Longerons $+Y$	0.05	0.47	0.00
Back Suspension Truss Longerons $-Y$	0.04	0.42	0.00
Back Suspension Truss Battens $+Y$	0.01	0.02	0.00
Back Suspension Truss Battens $-Y$	0.00	0.01	0.00
Back Suspension Truss Batten Diagonals $+Y$	0.00	0.01	0.00
Back Suspension Truss Batten Diagonals $-Y$	0.00	0.01	0.00
Back Suspension Truss Front,			

continued on next page

continued from previous page

Set Name	Percent Elastic Strain Energy In Set		
	Mode #10	Mode #11	Mode #20
Back Diagonals $+Y$	0.04	0.12	0.00
Back Suspension Truss Front, Back Diagonals $-Y$	0.03	0.12	0.00
Back Suspension Truss Top,Bottom Diagonals $+Y$	0.06	0.21	0.00
Back Suspension Truss Top,Bottom Diagonals $-Y$	0.06	0.12	0.00
Reflector Support Brackets	0.08	0.01	0.01
Front Suspension Cables	0.02	0.03	0.03
Front Cable Standoffs	0.00	0.00	0.00
Back Suspension Cables	0.10	1.47	0.01
Back Cable Standoffs	0.00	0.00	0.00
Gimbal 1 Supports	0.00	0.00	0.02
Gimbal 1 Rings	0.02	0.00	0.01
Gimbal 1 Posts	0.00	0.00	0.00
Gimbal 1 Laser Supports	0.00	0.00	0.00
Gimbal 1 Plate Backup	0.00	0.00	0.00
Gimbal 1 Plates	0.00	0.00	0.03
Gimbal 1 Control Board	0.00	0.00	0.05
Gimbal 2 Supports	0.02	0.05	0.01
Gimbal 2 Rings	0.20	0.02	0.00
Gimbal 2 Posts	0.00	0.00	0.00
Gimbal 2 Laser Supports	0.00	0.00	0.00
Gimbal 2 Plate Backup	0.00	0.00	0.00
Gimbal 2 Plates	0.01	0.09	0.01
Gimbal 2 Control Board	0.00	0.00	0.00
Gimbal 3 Supports	0.01	0.24	0.00
Gimbal 3 Rings	0.19	0.25	0.00
Gimbal 3 Posts	0.00	0.00	0.00
Gimbal 3 Laser Supports	0.00	0.00	0.00
Gimbal 3 Plate Backup	0.00	0.00	0.00
Gimbal 3 Plates	0.01	0.76	0.01
Gimbal 3 Control Board	0.00	0.06	0.00

continued on next page

continued from previous page

Set Name	Percent Elastic Strain Energy In Set		
	Mode #10	Mode #11	Mode #20
Small Reflector Plate	0.00	0.00	0.00
Forward Thruster Plate	0.00	0.00	0.00
Tower Thruster Plate	0.00	0.00	0.01
Middle Thruster Plate	0.00	0.00	0.01
Reflector Thruster Plate	0.01	0.00	0.00
Laser Plate	0.00	0.00	0.00
Controller Board Plate	0.00	0.00	0.00
Weightless Beams	0.00	0.00	0.00
Reflector Spacer Plate	0.00	0.00	0.00
Spacer Plate	0.00	0.00	0.00
PESD Springs	0.02	0.22	0.00
Thruster Tubes	0.04	0.01	0.07

Appendix F

Phase 2 CEM Beam Element Group Definitions

Table F.1: Phase 2 CEM Beam Element Group Definitions

Beam Element Set	First Element	Last Element
Main Truss,20 Bays,Longeron Group	1	80
Main Truss,20 Bays,Bay 1 Longerons	1	4
Main Truss,20 Bays,Bay 2 Longerons	5	8
Main Truss,20 Bays,Bay 3 Longerons	9	12
Main Truss,20 Bays,Bay 4 Longerons	13	16
Main Truss,20 Bays,Bay 5 Longerons	17	20
Main Truss,20 Bays,Bay 6 Longerons	21	24
Main Truss,20 Bays,Bay 7 Longerons	25	28
Main Truss,20 Bays,Bay 8 Longerons	29	32
Main Truss,20 Bays,Bay 9 Longerons	33	36
Main Truss,20 Bays,Bay 10 Longerons	37	40
Main Truss,20 Bays,Bay 11 Longerons	41	44
Main Truss,20 Bays,Bay 12 Longerons	45	48
Main Truss,20 Bays,Bay 13 Longerons	49	52
Main Truss,20 Bays,Bay 14 Longerons	53	56
Main Truss,20 Bays,Bay 15 Longerons	57	60

continued on next page

continued from previous page

Beam Element Set	First Element	Last Element
Main Truss,20 Bays,Bay 16 Longerons	61	64
Main Truss,20 Bays,Bay 17 Longerons	65	68
Main Truss,20 Bays,Bay 18 Longerons	69	72
Main Truss,20 Bays,Bay 19 Longerons	73	76
Main Truss,20 Bays,Bay 20 Longerons	77	80
Main Truss,42 Bays,Longeron Group	81	248
Main Truss,42 Bays,Bay 1 Longerons	81	84
Main Truss,42 Bays,Bay 2 Longerons	85	88
Main Truss,42 Bays,Bay 3 Longerons	89	92
Main Truss,42 Bays,Bay 4 Longerons	93	96
Main Truss,42 Bays,Bay 5 Longerons	97	100
Main Truss,42 Bays,Bay 6 Longerons	101	104
Main Truss,42 Bays,Bay 7 Longerons	105	108
Main Truss,42 Bays,Bay 8 Longerons	109	112
Main Truss,42 Bays,Bay 9 Longerons	113	116
Main Truss,42 Bays,Bay 10 Longerons	117	120
Main Truss,42 Bays,Bay 11 Longerons	121	124
Main Truss,42 Bays,Bay 12 Longerons	125	128
Main Truss,42 Bays,Bay 13 Longerons	129	132
Main Truss,42 Bays,Bay 14 Longerons	133	136
Main Truss,42 Bays,Bay 15 Longerons	137	140
Main Truss,42 Bays,Bay 16 Longerons	141	144
Main Truss,42 Bays,Bay 17 Longerons	145	148
Main Truss,42 Bays,Bay 18 Longerons	149	152
Main Truss,42 Bays,Bay 19 Longerons	153	156
Main Truss,42 Bays,Bay 20 Longerons	157	160
Main Truss,42 Bays,Bay 21 Longerons	161	164
Main Truss,42 Bays,Bay 22 Longerons	165	168
Main Truss,42 Bays,Bay 23 Longerons	169	172
Main Truss,42 Bays,Bay 24 Longerons	173	176
Main Truss,42 Bays,Bay 25 Longerons	177	180
Main Truss,42 Bays,Bay 26 Longerons	181	184
Main Truss,42 Bays,Bay 27 Longerons	185	188

continued on next page

continued from previous page		
Beam Element Set	First Element	Last Element
Main Truss,42 Bays,Bay 28 Longerons	189	192
Main Truss,42 Bays,Bay 29 Longerons	193	196
Main Truss,42 Bays,Bay 30 Longerons	197	200
Main Truss,42 Bays,Bay 31 Longerons	201	204
Main Truss,42 Bays,Bay 32 Longerons	205	208
Main Truss,42 Bays,Bay 33 Longerons	209	212
Main Truss,42 Bays,Bay 34 Longerons	213	216
Main Truss,42 Bays,Bay 35 Longerons	217	220
Main Truss,42 Bays,Bay 36 Longerons	221	224
Main Truss,42 Bays,Bay 37 Longerons	225	228
Main Truss,42 Bays,Bay 38 Longerons	229	232
Main Truss,42 Bays,Bay 39 Longerons	233	236
Main Truss,42 Bays,Bay 40 Longerons	237	240
Main Truss,42 Bays,Bay 41 Longerons	241	244
Main Truss,42 Bays,Bay 42 Longerons	245	248
Main Truss,42 Bays,Top,Bottom Diagonal Group	604	687
Main Truss,42 Bays,Bay 1 Top,Bottom Diagonals	604	605
Main Truss,42 Bays,Bay 2 Top,Bottom Diagonals	606	607
Main Truss,42 Bays,Bay 3 Top,Bottom Diagonals	608	609
Main Truss,42 Bays,Bay 4 Top,Bottom Diagonals	610	611
Main Truss,42 Bays,Bay 5 Top,Bottom Diagonals	612	613
Main Truss,42 Bays,Bay 6 Top,Bottom Diagonals	614	615
Main Truss,42 Bays,Bay 7 Top,Bottom Diagonals	616	617
Main Truss,42 Bays,Bay 8 Top,Bottom Diagonals	618	619
Main Truss,42 Bays,Bay 9 Top,Bottom Diagonals	620	621
Main Truss,42 Bays,Bay 10 Top,Bottom Diagonals	622	623
Main Truss,42 Bays,Bay 11 Top,Bottom Diagonals	624	625
Main Truss,42 Bays,Bay 12 Top,Bottom Diagonals	626	627
Main Truss,42 Bays,Bay 13 Top,Bottom Diagonals	628	629
Main Truss,42 Bays,Bay 14 Top,Bottom Diagonals	630	631
Main Truss,42 Bays,Bay 15 Top,Bottom Diagonals	632	633
Main Truss,42 Bays,Bay 16 Top,Bottom Diagonals	634	635
Main Truss,42 Bays,Bay 17 Top,Bottom Diagonals	636	637
		continued on next page

continued from previous page

Beam Element Set	First Element	Last Element
Main Truss,42 Bays,Bay 18 Top,Bottom Diagonals	638	639
Main Truss,42 Bays,Bay 19 Top,Bottom Diagonals	640	641
Main Truss,42 Bays,Bay 20 Top,Bottom Diagonals	642	643
Main Truss,42 Bays,Bay 21 Top,Bottom Diagonals	644	645
Main Truss,42 Bays,Bay 22 Top,Bottom Diagonals	646	647
Main Truss,42 Bays,Bay 23 Top,Bottom Diagonals	648	649
Main Truss,42 Bays,Bay 24 Top,Bottom Diagonals	650	651
Main Truss,42 Bays,Bay 25 Top,Bottom Diagonals	652	653
Main Truss,42 Bays,Bay 25 Top,Bottom Diagonals	654	655
Main Truss,42 Bays,Bay 27 Top,Bottom Diagonals	656	657
Main Truss,42 Bays,Bay 28 Top,Bottom Diagonals	658	659
Main Truss,42 Bays,Bay 29 Top,Bottom Diagonals	660	661
Main Truss,42 Bays,Bay 30 Top,Bottom Diagonals	662	663
Main Truss,42 Bays,Bay 31 Top,Bottom Diagonals	664	665
Main Truss,42 Bays,Bay 32 Top,Bottom Diagonals	666	667
Main Truss,42 Bays,Bay 33 Top,Bottom Diagonals	668	669
Main Truss,42 Bays,Bay 34 Top,Bottom Diagonals	670	671
Main Truss,42 Bays,Bay 35 Top,Bottom Diagonals	672	673
Main Truss,42 Bays,Bay 36 Top,Bottom Diagonals	674	675
Main Truss,42 Bays,Bay 37 Top,Bottom Diagonals	676	677
Main Truss,42 Bays,Bay 38 Top,Bottom Diagonals	678	679
Main Truss,42 Bays,Bay 39 Top,Bottom Diagonals	680	681
Main Truss,42 Bays,Bay 40 Top,Bottom Diagonals	682	683
Main Truss,42 Bays,Bay 41 Top,Bottom Diagonals	684	685
Main Truss,42 Bays,Bay 42 Top,Bottom Diagonals	686	687
Main Truss,20 Bay,Side Diagonal Group	690	727
Main Truss,20 Bay,Bay 2 Side Diagonals	690	691
Main Truss,20 Bay,Bay 3 Side Diagonals	692	693
Main Truss,20 Bay,Bay 4 Side Diagonals	694	695
Main Truss,20 Bay,Bay 5 Side Diagonals	696	697
Main Truss,20 Bay,Bay 6 Side Diagonals	698	699
Main Truss,20 Bay,Bay 7 Side Diagonals	700	701
Main Truss,20 Bay,Bay 8 Side Diagonals	702	703

continued on next page

continued from previous page

Beam Element Set	First Element	Last Element
Main Truss,20 Bay,Bay 9 Side Diagonals	704	705
Main Truss,20 Bay,Bay 10 Side Diagonals	706	707
Main Truss,20 Bay,Bay 11 Side Diagonals	708	709
Main Truss,20 Bay,Bay 12 Side Diagonals	710	711
Main Truss,20 Bay,Bay 13 Side Diagonals	712	713
Main Truss,20 Bay,Bay 14 Side Diagonals	714	715
Main Truss,20 Bay,Bay 15 Side Diagonals	716	717
Main Truss,20 Bay,Bay 16 Side Diagonals	718	719
Main Truss,20 Bay,Bay 17 Side Diagonals	720	721
Main Truss,20 Bay,Bay 18 Side Diagonals	722	723
Main Truss,20 Bay,Bay 19 Side Diagonals	724	725
Main Truss,20 Bay,Bay 20 Side Diagonals	726	727
Main Truss,42 Bay,Side Diagonal Group	728	811
Main Truss,42 Bay,Bay 1 Side Diagonals	728	729
Main Truss,42 Bay,Bay 2 Side Diagonals	730	731
Main Truss,42 Bay,Bay 3 Side Diagonals	732	733
Main Truss,42 Bay,Bay 4 Side Diagonals	734	735
Main Truss,42 Bay,Bay 5 Side Diagonals	736	737
Main Truss,42 Bay,Bay 6 Side Diagonals	738	739
Main Truss,42 Bay,Bay 7 Side Diagonals	740	741
Main Truss,42 Bay,Bay 8 Side Diagonals	742	743
Main Truss,42 Bay,Bay 9 Side Diagonals	744	745
Main Truss,42 Bay,Bay 10 Side Diagonals	746	747
Main Truss,42 Bay,Bay 11 Side Diagonals	748	749
Main Truss,42 Bay,Bay 12 Side Diagonals	750	751
Main Truss,42 Bay,Bay 13 Side Diagonals	752	753
Main Truss,42 Bay,Bay 14 Side Diagonals	754	755
Main Truss,42 Bay,Bay 15 Side Diagonals	756	757
Main Truss,42 Bay,Bay 16 Side Diagonals	758	759
Main Truss,42 Bay,Bay 17 Side Diagonals	760	761
Main Truss,42 Bay,Bay 18 Side Diagonals	762	763
Main Truss,42 Bay,Bay 19 Side Diagonals	764	765
Main Truss,42 Bay,Bay 20 Side Diagonals	766	767

continued on next page

continued from previous page

Beam Element Set	First Element	Last Element
Main Truss,42 Bay,Bay 21 Side Diagonals	768	769
Main Truss,42 Bay,Bay 22 Side Diagonals	770	771
Main Truss,42 Bay,Bay 23 Side Diagonals	772	773
Main Truss,42 Bay,Bay 24 Side Diagonals	774	775
Main Truss,42 Bay,Bay 25 Side Diagonals	776	777
Main Truss,42 Bay,Bay 26 Side Diagonals	778	779
Main Truss,42 Bay,Bay 27 Side Diagonals	780	781
Main Truss,42 Bay,Bay 28 Side Diagonals	782	783
Main Truss,42 Bay,Bay 29 Side Diagonals	784	785
Main Truss,42 Bay,Bay 30 Side Diagonals	786	787
Main Truss,42 Bay,Bay 31 Side Diagonals	788	789
Main Truss,42 Bay,Bay 32 Side Diagonals	790	791
Main Truss,42 Bay,Bay 33 Side Diagonals	792	793
Main Truss,42 Bay,Bay 34 Side Diagonals	794	795
Main Truss,42 Bay,Bay 35 Side Diagonals	796	797
Main Truss,42 Bay,Bay 36 Side Diagonals	798	799
Main Truss,42 Bay,Bay 37 Side Diagonals	800	801
Main Truss,42 Bay,Bay 38 Side Diagonals	802	803
Main Truss,42 Bay,Bay 39 Side Diagonals	804	805
Main Truss,42 Bay,Bay 40 Side Diagonals	806	807
Main Truss,42 Bay,Bay 41 Side Diagonals	808	809
Main Truss,42 Bay,Bay 42 Side Diagonals	810	811
Tower Truss Longeron Group	812	855
Tower Truss Longerons Bay 1	812	815
Tower Truss Longerons Bay 2	816	819
Tower Truss Longerons Bay 3	820	823
Tower Truss Longerons Bay 4	824	827
Tower Truss Longerons Bay 5	828	831
Tower Truss Longerons Bay 6	832	835
Tower Truss Longerons Bay 7	836	839
Tower Truss Longerons Bay 8	840	843
Tower Truss Longerons Bay 9	844	847
Tower Truss Longerons Bay 10	848	851

continued on next page

continued from previous page

Beam Element Set	First Element	Last Element
Tower Truss Longerons Bay 11	852	855
Reflector Truss Longerons Group	955	970
Reflector Truss Longerons Bay 1	955	958
Reflector Truss Longerons Bay 2	959	962
Reflector Truss Longerons Bay 3	963	966
Reflector Truss Longerons Bay 4	967	970

Appendix G

Phase 2 CEM Beam Modal Strain Energy Distributions By Bay And Member Type

Table G.1: Phase 2 CEM Model P2090992 Beam Modal Strain Energy Distribution By Bay And Member Type For Modes 10, 11, and 20

Beam Element Set	Percent Elastic Strain Energy In Set		
	Mode #10	Mode #11	Mode #20
Main Truss,20 Bays,Longeron Group	20.56	13.57	22.15
Bay 1	0.00	0.00	0.00
Bay 2	0.01	0.01	0.01
Bay 3	0.02	0.02	0.05
Bay 4	0.05	0.04	0.11
Bay 5	0.10	0.08	0.20
Bay 6	0.16	0.13	0.33
Bay 7	0.25	0.20	0.50
Bay 8	0.35	0.28	0.71
Bay 9	0.48	0.39	0.96
Bay 10	0.62	0.50	1.25
Bay 11	0.79	0.63	1.59
Bay 12	0.98	0.78	1.97
Bay 13	1.07	0.79	2.32
continued on next page			

PRECEDING PAGE BLANK NOT FILMED

290

continued from previous page

Beam Element Set	Percent Elastic Strain Energy In Set		
	Mode #10	Mode #11	Mode #20
Bay 14	1.20	1.02	2.81
Bay 15	1.42	1.35	4.33
Bay 16	2.14	1.50	3.14
Bay 17	2.90	1.47	1.28
Bay 18	2.86	1.50	0.32
Bay 19	2.72	1.47	0.18
Bay 20	2.42	1.41	0.11
Main Truss,42 Bays,Longeron Group	62.35	37.12	3.08
Bay 1	2.70	1.60	0.09
Bay 2	2.34	1.40	0.06
Bay 3	2.00	1.22	0.03
Bay 4	1.68	1.03	0.02
Bay 5	1.38	0.86	0.01
Bay 6	1.10	0.69	0.01
Bay 7	0.84	0.54	0.02
Bay 8	0.61	0.40	0.03
Bay 9	0.42	0.28	0.04
Bay 10	0.26	0.18	0.06
Bay 11	0.14	0.11	0.08
Bay 12	0.06	0.05	0.10
Bay 13	0.00	0.00	0.00
Bay 14	0.01	0.02	0.14
Bay 15	0.04	0.04	0.14
Bay 16	0.10	0.07	0.14
Bay 17	0.20	0.13	0.14
Bay 18	0.32	0.21	0.14
Bay 19	0.47	0.30	0.13
Bay 20	0.65	0.41	0.13
Bay 21	0.84	0.54	0.12
Bay 22	1.05	0.66	0.10
Bay 23	1.25	0.79	0.09
Bay 24	1.47	0.91	0.07
Bay 25	1.68	1.04	0.05

continued on next page

continued from previous page

Beam Element Set	Percent Elastic Strain Energy In Set		
	Mode #10	Mode #11	Mode #20
Bay 26	1.89	1.17	0.04
Bay 27	2.10	1.29	0.02
Bay 28	2.30	1.40	0.01
Bay 29	2.49	1.51	0.01
Bay 30	2.67	1.61	0.01
Bay 31	2.83	1.70	0.01
Bay 32	2.99	1.78	0.01
Bay 33	3.13	1.86	0.02
Bay 34	3.28	1.95	0.04
Bay 35	3.06	1.70	0.05
Bay 36	2.85	1.36	0.06
Bay 37	2.78	1.72	0.09
Bay 38	2.38	1.40	0.14
Bay 39	2.06	1.17	0.13
Bay 40	1.72	1.01	0.19
Bay 41	1.51	0.93	0.20
Bay 42	0.68	0.08	0.11
Main Truss,42 Bays,Top, Bottom Diagonal Group	0.09	20.35	0.21
Bay 1	0.00	0.09	0.00
Bay 2	0.00	0.09	0.00
Bay 3	0.00	0.09	0.00
Bay 4	0.00	0.09	0.00
Bay 5	0.00	0.09	0.00
Bay 6	0.00	0.09	0.00
Bay 7	0.00	0.10	0.00
Bay 8	0.00	0.10	0.00
Bay 9	0.00	0.11	0.00
Bay 10	0.00	0.11	0.00
Bay 11	0.00	0.11	0.00
Bay 12	0.00	0.10	0.00
Bay 13	0.00	0.00	0.00
Bay 14	0.00	0.10	0.00

continued on next page

continued from previous page			
Beam Element Set	Percent Elastic Strain Energy In Set		
	Mode #10	Mode #11	Mode #20
Bay 15	0.00	0.10	0.00
Bay 16	0.00	0.10	0.00
Bay 17	0.00	0.10	0.00
Bay 18	0.00	0.09	0.00
Bay 19	0.00	0.09	0.00
Bay 20	0.00	0.09	0.00
Bay 21	0.00	0.08	0.00
Bay 22	0.00	0.07	0.00
Bay 23	0.00	0.07	0.00
Bay 24	0.00	0.07	0.00
Bay 25	0.00	0.06	0.00
Bay 25	0.00	0.06	0.00
Bay 27	0.00	0.06	0.00
Bay 28	0.00	0.05	0.00
Bay 29	0.00	0.05	0.00
Bay 30	0.00	0.05	0.00
Bay 31	0.00	0.05	0.00
Bay 32	0.00	0.04	0.00
Bay 33	0.00	0.04	0.00
Bay 34	0.00	0.03	0.00
Bay 35	0.00	0.00	0.00
Bay 36	0.00	0.70	0.00
Bay 37	0.01	3.42	0.04
Bay 38	0.01	3.56	0.04
Bay 39	0.01	3.47	0.04
Bay 40	0.01	3.40	0.04
Bay 41	0.02	2.89	0.03
Bay 42	0.01	0.29	0.00
Main Truss,20 Bay, Side Diagonal Group	1.66	0.11	26.09
Bay 2	0.02	0.00	0.05
Bay 3	0.03	0.00	0.07
Bay 4	0.04	0.00	0.08
			continued on next page

continued from previous page

Beam Element Set	Percent Elastic Strain Energy In Set		
	Mode #10	Mode #11	Mode #20
Bay 5	0.04	0.00	0.08
Bay 6	0.05	0.00	0.09
Bay 7	0.05	0.00	0.10
Bay 8	0.05	0.00	0.11
Bay 9	0.05	0.00	0.11
Bay 10	0.05	0.00	0.11
Bay 11	0.06	0.00	0.11
Bay 12	0.05	0.00	0.11
Bay 13	0.01	0.00	0.08
Bay 14	0.02	0.00	0.12
Bay 15	0.03	0.02	0.07
Bay 16	1.02	0.02	24.59
Bay 17	0.01	0.00	0.08
Bay 18	0.00	0.00	0.07
Bay 19	0.03	0.01	0.05
Bay 20	0.04	0.06	0.02
Main Truss,42 Bay, Side Diagonal Group	6.51	18.23	1.17
Bay 1	0.05	0.05	0.02
Bay 2	0.06	0.06	0.02
Bay 3	0.06	0.06	0.02
Bay 4	0.06	0.06	0.02
Bay 5	0.07	0.05	0.01
Bay 6	0.07	0.05	0.01
Bay 7	0.08	0.06	0.01
Bay 8	0.08	0.06	0.01
Bay 9	0.08	0.06	0.01
Bay 10	0.08	0.06	0.01
Bay 11	0.09	0.06	0.01
Bay 12	0.08	0.05	0.01
Bay 13	0.00	0.00	0.00
Bay 14	0.07	0.05	0.00
Bay 15	0.08	0.05	0.00

continued on next page

continued from previous page

Beam Element Set	Percent Elastic Strain Energy In Set		
	Mode #10	Mode #11	Mode #20
Bay 16	0.07	0.05	0.00
Bay 17	0.07	0.05	0.00
Bay 18	0.07	0.05	0.00
Bay 19	0.06	0.05	0.00
Bay 20	0.06	0.05	0.00
Bay 21	0.05	0.05	0.00
Bay 22	0.04	0.04	0.00
Bay 23	0.04	0.05	0.00
Bay 24	0.04	0.05	0.00
Bay 25	0.03	0.05	0.00
Bay 26	0.03	0.05	0.01
Bay 27	0.02	0.05	0.01
Bay 28	0.02	0.05	0.01
Bay 29	0.02	0.04	0.01
Bay 30	0.01	0.04	0.01
Bay 31	0.01	0.04	0.01
Bay 32	0.01	0.05	0.01
Bay 33	0.01	0.05	0.01
Bay 34	0.01	0.06	0.01
Bay 35	0.01	0.00	0.00
Bay 36	0.01	0.13	0.01
Bay 37	0.06	2.94	0.04
Bay 38	0.07	3.17	0.04
Bay 39	0.07	3.19	0.04
Bay 40	0.06	3.33	0.05
Bay 41	0.10	3.58	0.06
Bay 42	4.45	0.21	0.69
Tower Truss Longeron Group	1.22	0.04	33.87
Bay 1	0.36	0.02	10.19
Bay 2	0.28	0.01	7.76
Bay 3	0.21	0.01	5.80
Bay 4	0.15	0.00	4.13
Bay 5	0.10	0.00	2.78

continued on next page

continued from previous page

Beam Element Set	Percent Elastic Strain Energy In Set		
	Mode #10	Mode #11	Mode #20
Bay 6	0.06	0.00	1.72
Bay 7	0.04	0.00	0.94
Bay 8	0.02	0.00	0.42
Bay 9	0.00	0.00	0.13
Bay 10	0.00	0.00	0.00
Bay 11	0.00	0.00	0.00
Reflector Truss Longerons Group	3.99	2.65	0.78
Bay 1	2.11	1.48	0.41
Bay 2	1.25	0.78	0.24
Bay 3	0.64	0.38	0.12
Bay 4	0.00	0.00	0.00

Appendix H

Damper Assembly Procedure

This appendix documents the assembly procedure for the damping struts fabricated under this contract. The same procedure is used for all three types of dampers. The best photo available for each step has been selected for use in this report; thus dampers of all three types are shown in this documentation.

Complete details of all damper components are provided in the drawings in Appendix J. A sufficient number of each type plus a few extras for spoilage should be fabricated prior to beginning the assembly process, as it is easier to maintain consistency in the various assembly steps if the step is completed for all units prior to proceeding to the next step.

Assembly of the ISICLSS dampers involves bonding, both with epoxy adhesive and Loctite adhesive. The first requirement of any bonding process is cleanliness of the surfaces to be bonded. Thus, in addition to normal shop degreasing procedures, it is recommended that all surfaces to be bonded should be cleaned by a thorough wiping with MEK followed by a thorough wiping with isopropyl alcohol to remove the residual MEK. This cleaning is in addition to other steps described below. Clean parts should be handled wearing gloves or with clean cloths.

Step 1 — Clean Hub

Brush the hubs with Scotch-Weld 3911 Degreasing Primer. Allow the primer to dry for a minimum of five minutes. A white powder will form as the primer drys. After the primer drys, brush off the white powder with a clean brush.

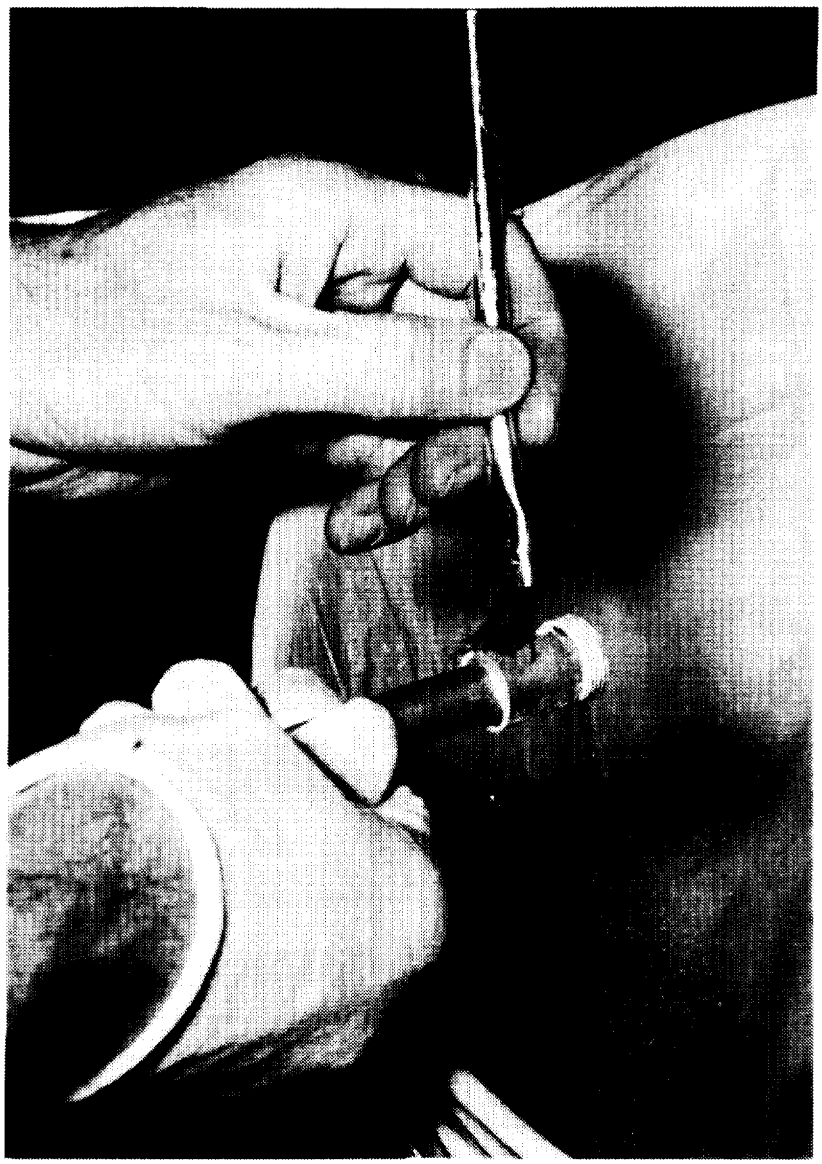

ORIGINAL PAGE
BLACK AND WHITE PHOTOGRAPH

Step 2 — Wipe Hub

Wipe any residual primer powder from the hubs with a clean, lint-free cloth.

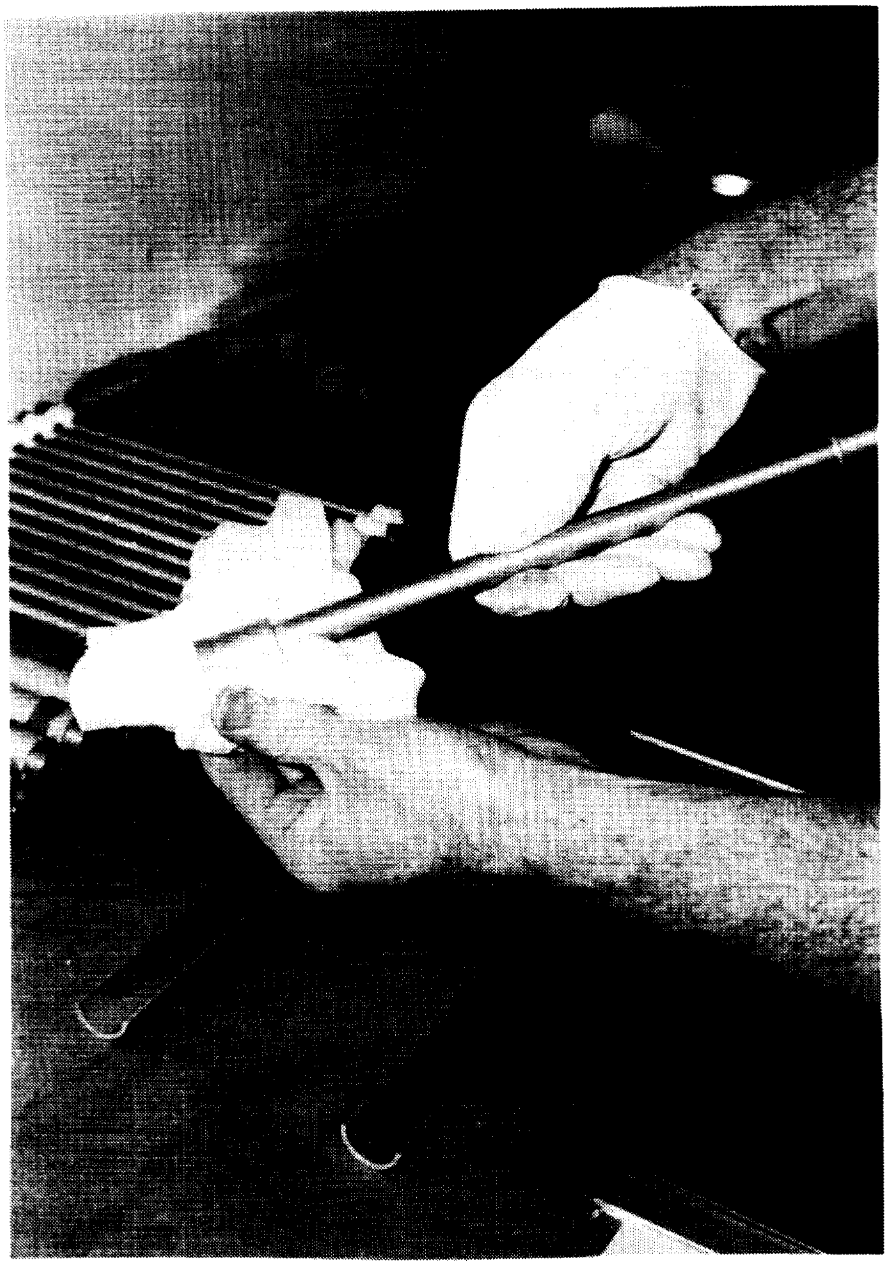

Step 3 — Mix Epoxy

Mix the Scotch-Weld 1838 Epoxy Adhesive according to the manufacturers instructions. It is important to mix the adhesive without whipping to avoid entrapping air. The work life of this adhesive is approximately 60 minutes at room temperature. As the work life is approached, the residual adhesive should be discarded and a fresh batch mixed.

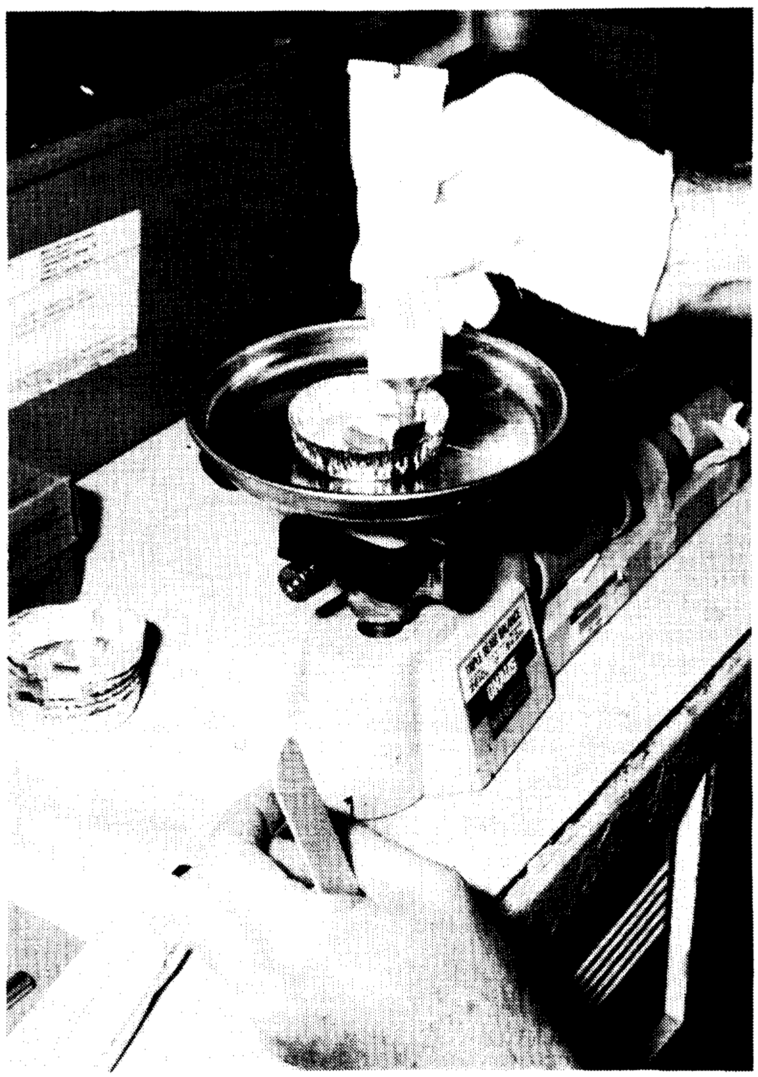

ORIGINAL PAGE
BLACK AND WHITE PHOTOGRAPH

Step 4 — Apply Epoxy To VEM

Apply a thin layer of epoxy to a clean aluminum plate, and press a strip of VEM into the epoxy. A roller can be used to roll the VEM onto the epoxy, in a manner similar to that shown in the photo for Step 5. Carefully peel the VEM strip from the wet epoxy as shown, avoiding getting any epoxy on the upper surface of the VEM.

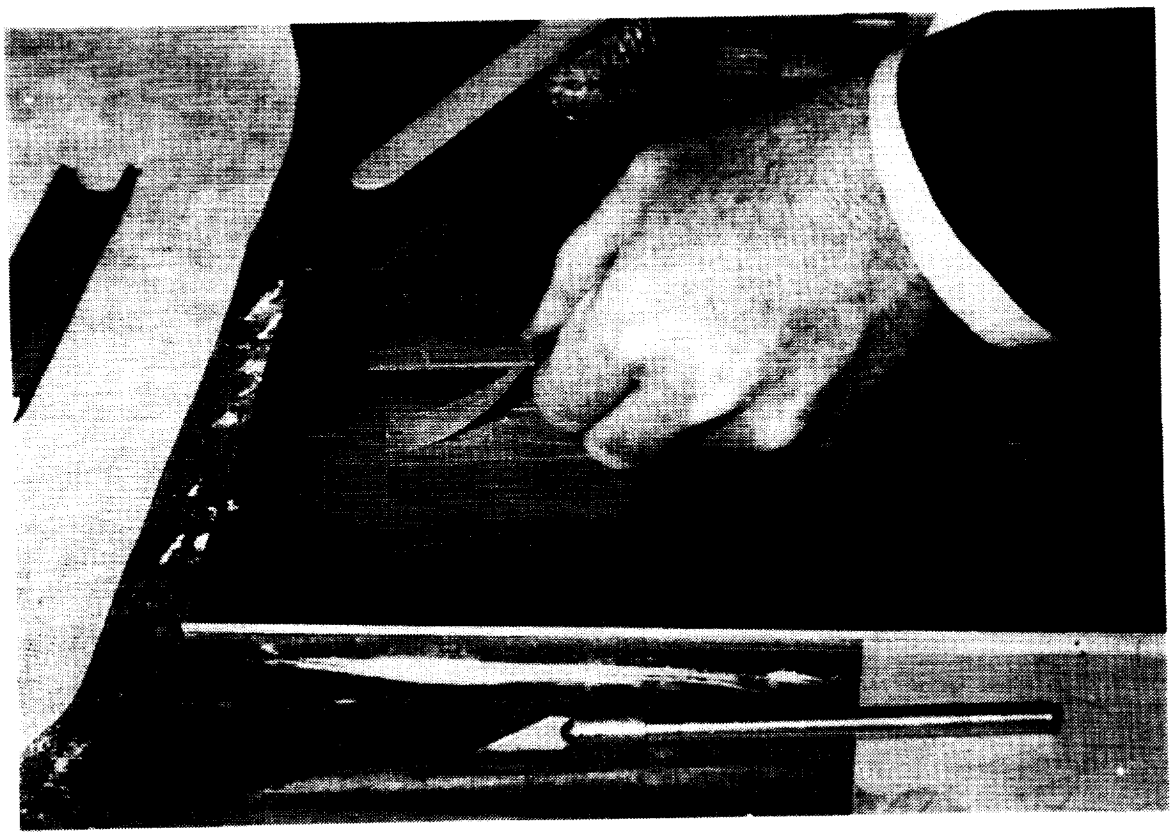

Step 5 — Remove Excess Epoxy

Place the VEM strip on a clean portion of the aluminum plate, epoxy side down. Lightly roll the VEM to remove excess epoxy. Only a very light, uniform coat should remain. Peel the strip from the plate as in Step 4.

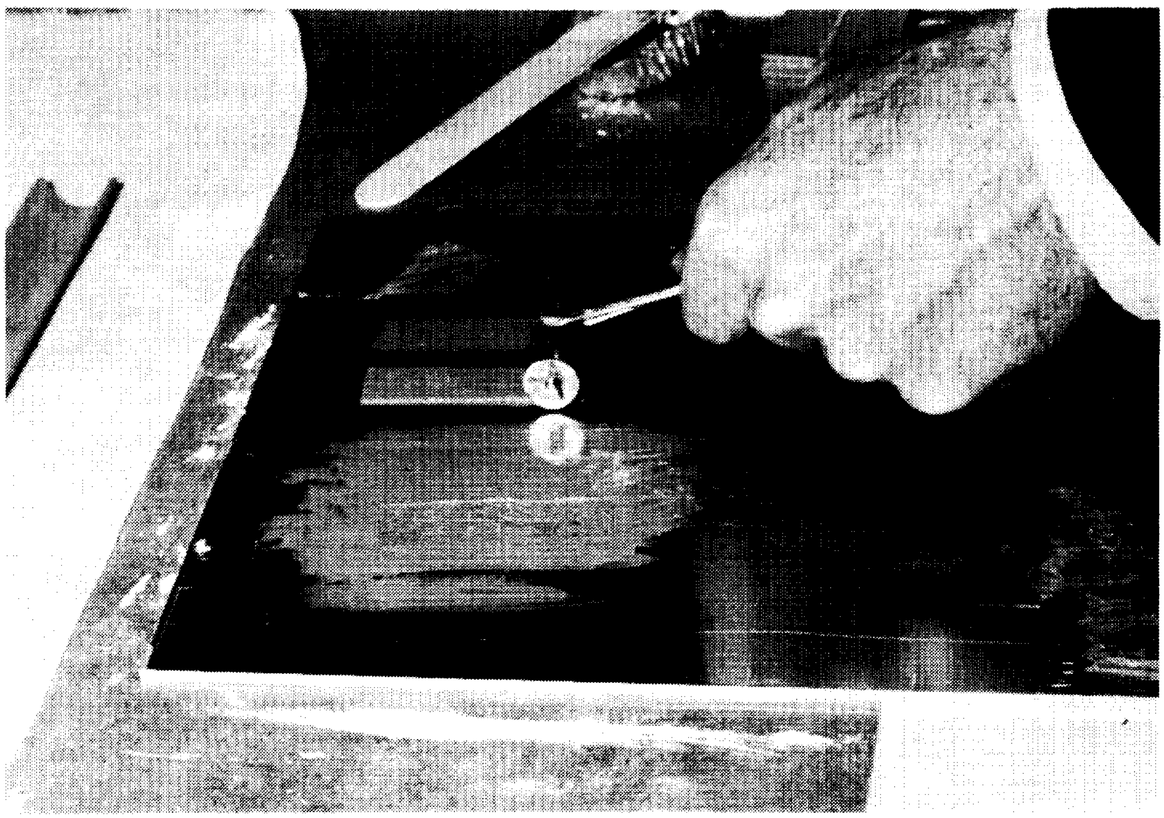

Step 6 — Wrap VEM On Hubs

Wearing clean gloves, wrap the VEM strip on the hub, maintaining the 0.1 inch protrusion of the VEM over the inner lip of the hub as indicated in the assembly drawing. This overlap is important to prevent the epoxy from flowing around the end of the VEM and starting a bridge that could form between the inner tube and the clamshell. Such a bridge will short out the VEM, seriously degrading damper performance.

Take care to avoid creating voids in the adhesive. This is a critical point in the process. The epoxy layer must be very thin but uniform, allowing the metal to show through clearly. A general guideline is to make the adhesive as thin as possible without creating voids. Too much adhesive will ruin the part. If the adhesive appears too thick, remove the VEM, clean the part, and start again.

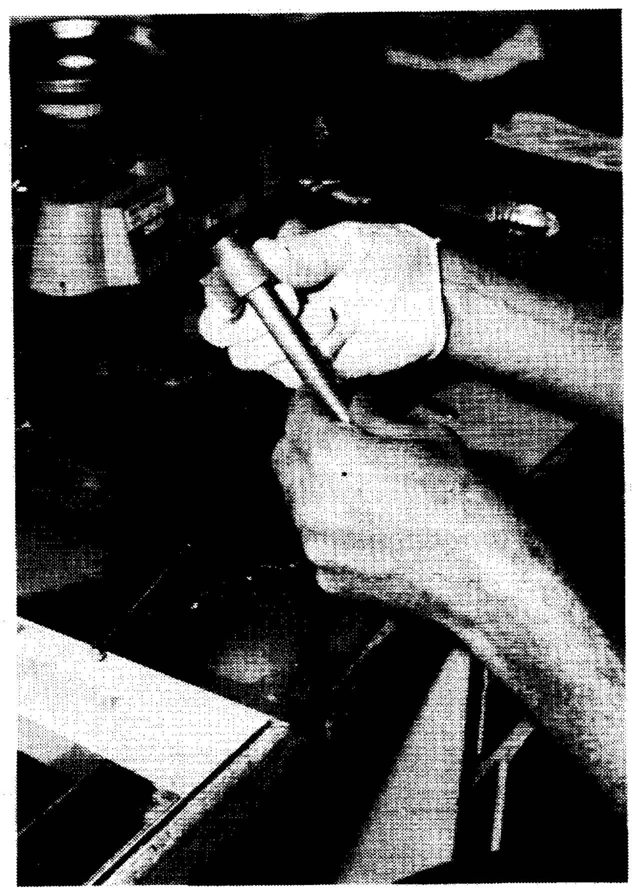

ORIGINAL PAGE
BLACK AND WHITE PHOTOGRAPH

Step 7 — Insert Hub/VEM Assembly Into Clamshell

This step utilizes the clamshells to hold the VEM onto the hubs while the epoxy bonding the VEM to the hubs cures. Verify that no epoxy has gotten onto the outer surfaces of the VEM wraps, or remove any traces of stray adhesive if necessary. At this point in the process, the clamshells serve only to hold the VEM in place while the epoxy cures.

Place the hub/VEM assembly into the clamshells, aligning the gap between the clamshells with the gap in the VEM wrap to avoid contact between the clamshell edge and epoxy on the edge of the VEM wrap.

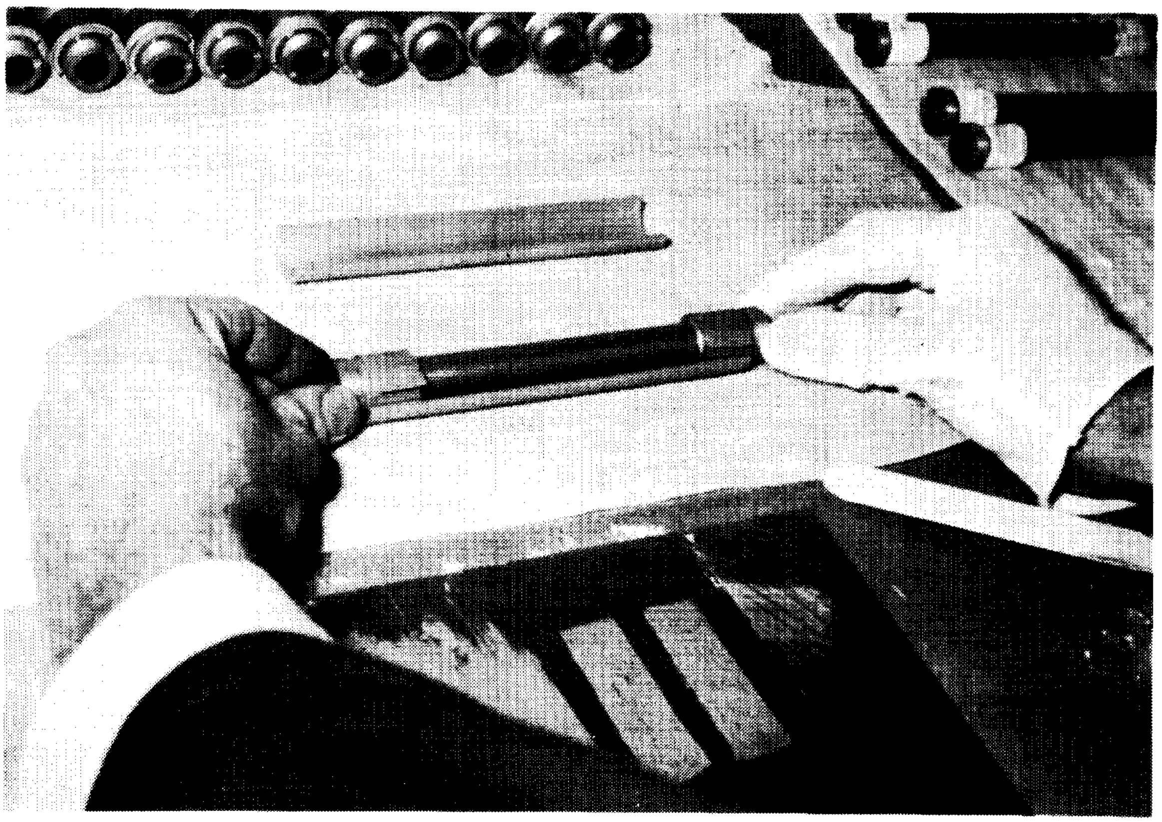

ORIGINAL PAGE
BLACK AND WHITE PHOTOGRAPH

Step 8 — Clamp Clamshells

Carefully slip hose clamps onto hub/VEM/clamshell assembly, being careful not to disturb the VEM. Tighten the clamshells lightly with a screwdriver. Apply only light pressure to avoid squeezing the epoxy out from between the VEM and the hub. Again, inspect to make sure that the VEM has not slipped out of alignment and that no epoxy has bridged the end of the VEM.

Allow the epoxy to cure for 24 hours. Remove the hose clamps and clamshells and verify that the VEM is in place. Inspect the bond thickness, verifying that the bond is thin, uniform, and without voids. Verify that no epoxy bridging has occurred either on the inner or outer edges of the hubs.

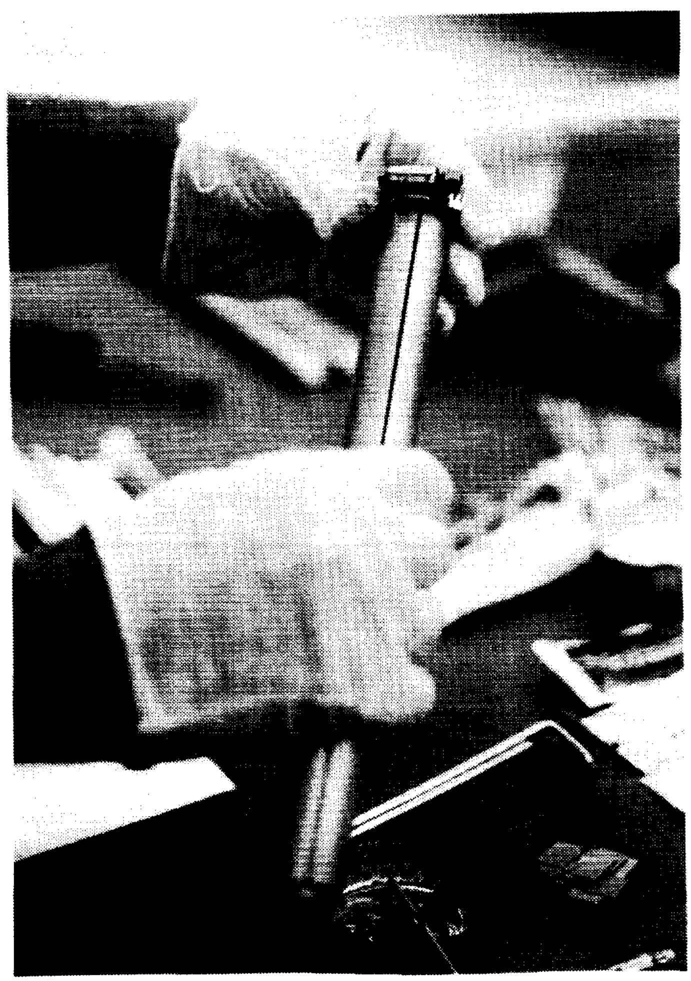

Step 9 — Clean Clamshells

Brush the last 1.5 inches of the inner surface of each end of each clamshell with Scotch-Weld 3911 Degreasing Primer, covering the portions that will be bonded to the VEM. Allow the primer to dry for a minimum of five minutes. After the primer drys, brush off the white powder with a clean brush. Wipe any residual primer powder from the clamshells with a clean, lint-free cloth.

ORIGINAL PAGE
BLACK AND WHITE PHOTOGRAPH

Step 10 — Spread Adhesive On Plates

This step utilizes a simple tool made of two 10 inch long sheets of aluminum clamped together. The width of the top sheet is about 0.3 inch narrower that the distance between the inner edges of the hubs, the exact distance depending on which damper is being manufactured. The width of the bottom sheet is the same as the distance between the outer edges of the hubs.

The top sheet is clamped on the bottom sheet, centered from side to side. A thin layer of epoxy is spread on the portions of the bottom sheet not covered by the top sheet.

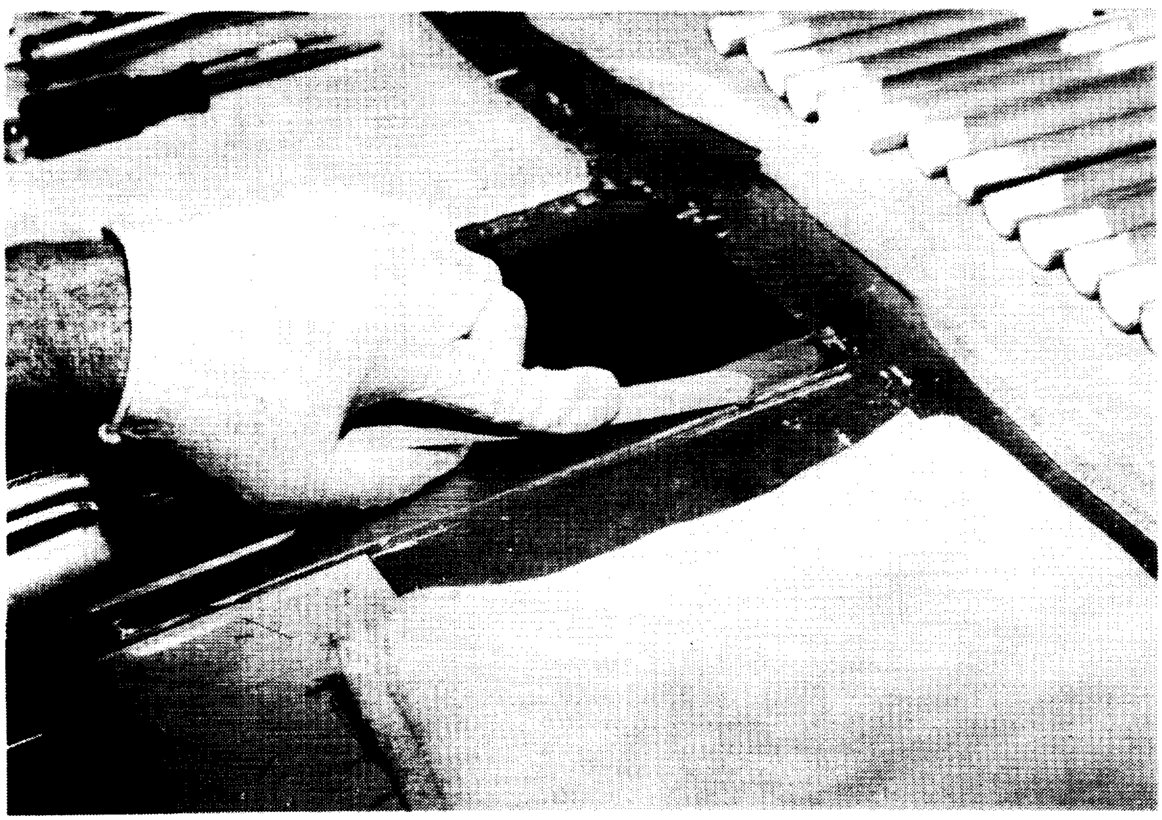

Step 11 — Apply Epoxy

The VEM/hub assembly is placed on the tool as shown. Note that the top plate serves as a guide, just fitting between the VEM wraps. The assembly is lightly rolled to coat the VEM wrap in preparation for bonding the clan shells. The assembly can be rolled on a dry portion of the plate to remove excess adhesive if required.

It is critical that only a thin coat of adhesive is used. Too much adhesive can cause bridging, thereby degrading the damping properties of the damper. Bridging around the VEM on the outside of the hubs can be seen and corrected, but bridging on the inside is covered by the clamshells and cannot be detected.

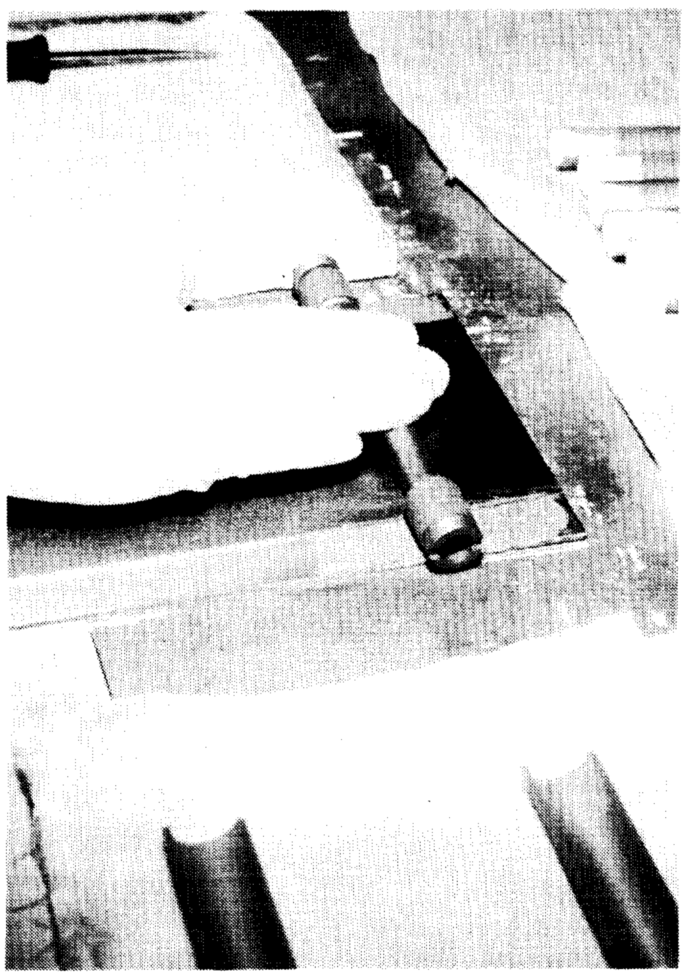

ORIGINAL PAGE
BLACK AND WHITE PHOTOGRAPH

Step 12 — Insert Assembly Into Clamshells

Insert the hub/VEM assembly into the clamshells, taking care to avoid sliding the assembly in the clamshells, which might form voids in the epoxy.

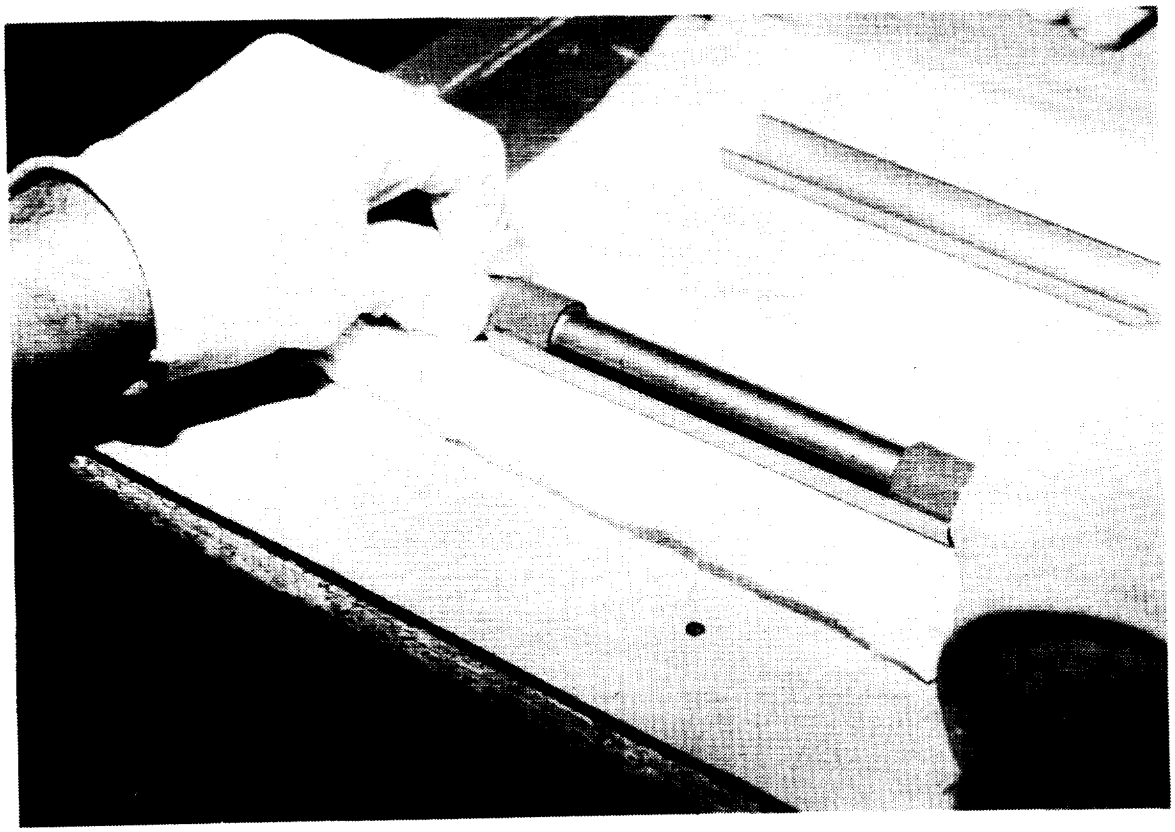

Step 13 — Apply Clamps and Spacers

Apply loose hose clamps to hub/VEM/clamshell assembly. Use thin plastic spacers to maintain gaps between clamshells as shown. These spacers prevent the clamshells from moving when the hose clamps are tightened.

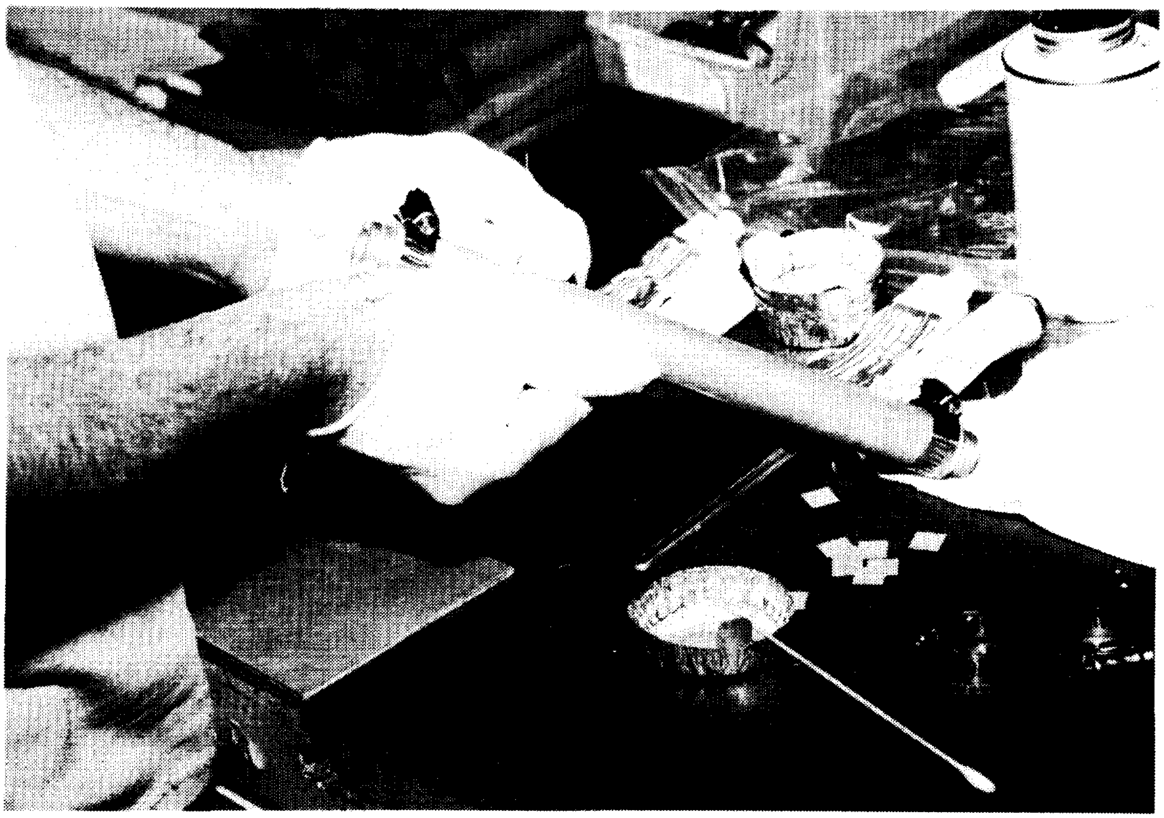

Step 14 — Tighten Clamps

Lightly tighten the clamps. Take this opportunity to make sure all parts are properly aligned and that no bridging has occurred. Allow the epoxy to cure for 24 hours, and then remove the hose clamps.

Step 15 — Apply Loctite To Sleeve

The sleeve will be bonded to the hub/VEM/clamshell assembly by Loctite RC/609, an adhesive specifically formulated for bonding cylindrical parts. Loctite RC/609 cures when placed in an anaerobic state. As long as it is exposed to oxygen, it will not cure. Thus, it is important that a sufficient quantity be placed on the parts to form a liquid barrier seal so curing can take place.

Paint the inner surfaces of each end of a clean sleeve generously with Loctite over a length of about three inches on each end.

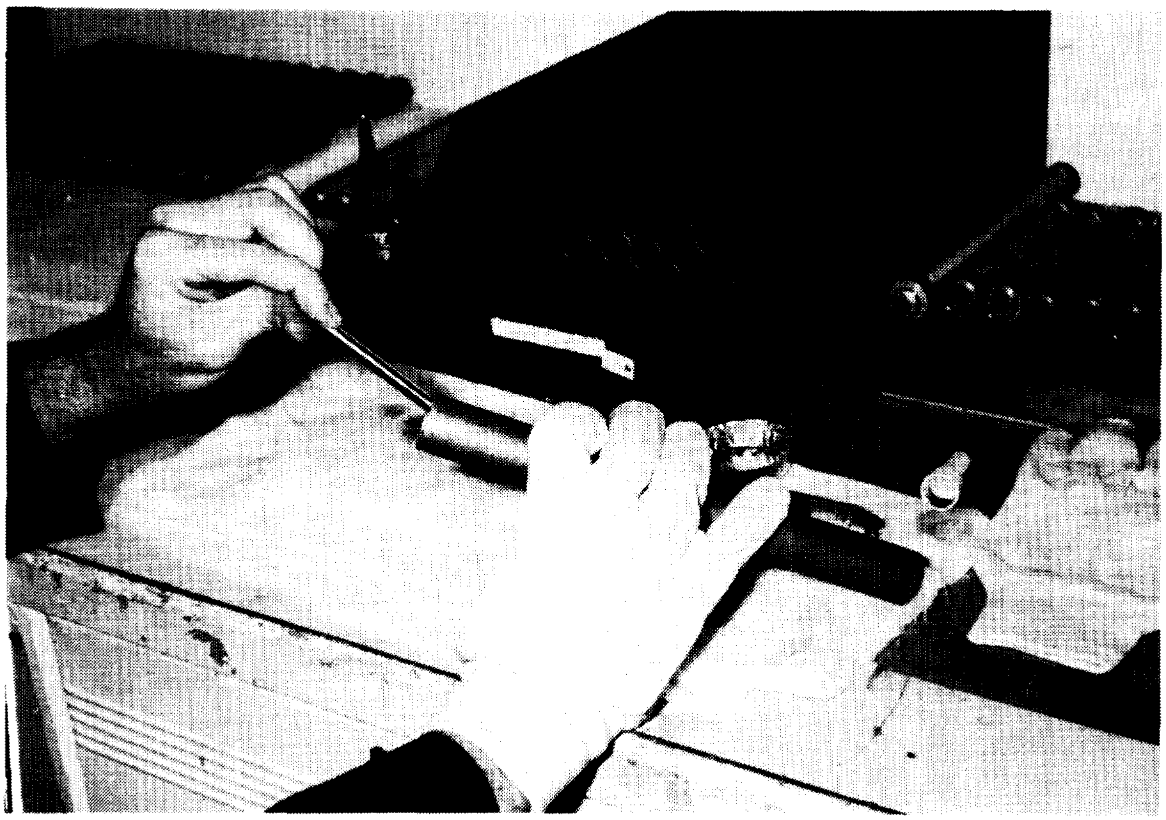

Step 16 — Apply Loctite To Assembly

If there is any chance that the outer surfaces of the clamshells have been contaminated, repeat the MEK/isopropyl alcohol cleaning process.

Paint the outer surfaces of the clamshells with Loctite over a length of three inches on each end.

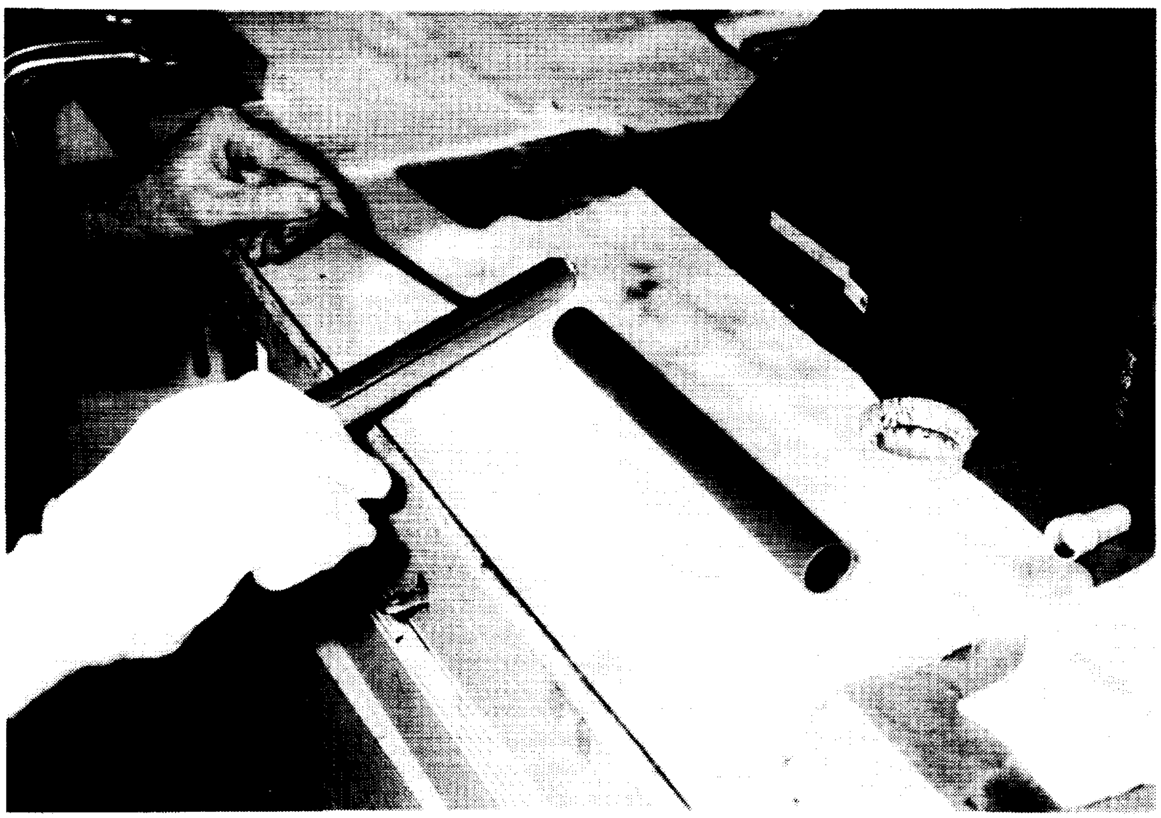

Step 17 — Insert Assembly Into Sleeve

Place the hub/VEM/clamshell assembly into the sleeve. Quickly tap the assembly into the tube. A tool consisting of two metal blocks clamped to the bench upon which the sleeve can be rested, but with sufficient clearance between them to accommodate the threaded end but not the hubs is helpful. The blocks act as a stop for the clamshells, resulting in proper alignment of the ends of the damper parts.

Allow the Loctite to cure for 24 hours. Wipe off excess, uncured Loctite. Inspect the bond strength by attempting to twist the sleeve off the assembly by hand. If a weak bond is detected, remove the sleeve, reclean the sleeve and the clamshells, and rebond.

Step 18 — Completed Dampers

The photo below shows the Phase 1 longeron damper (short light colored), the Phase 2 longeron damper (short dark colored), and the Phase 2 diagonal damper (long, light colored).

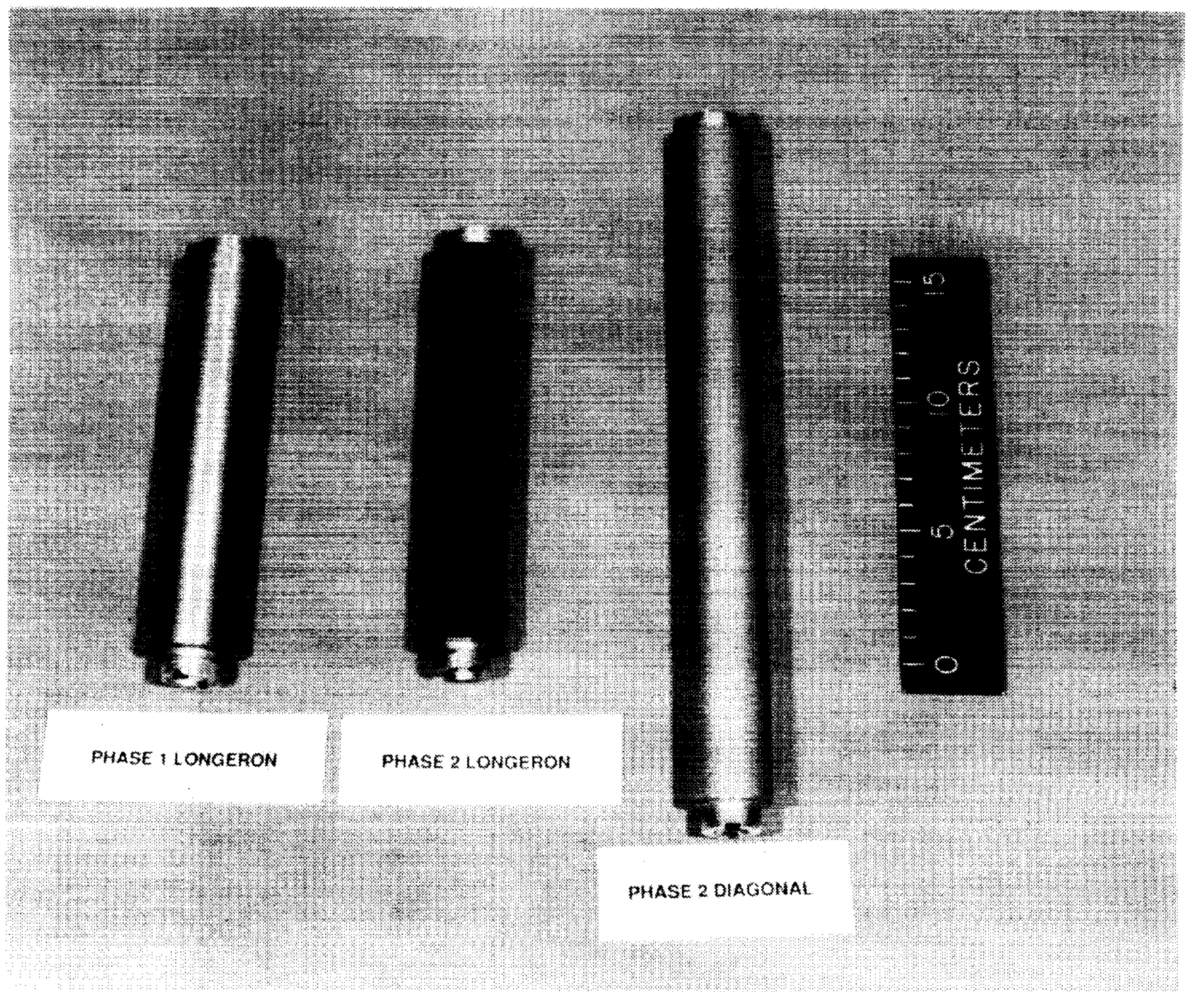

Appendix I

Damped Struts Unit Testing

This appendix documents the setup and results of dynamic and failure tests performed on viscoelastic shear dampers developed under this program. Testing for the Phase 1 dampers was conducted during July and August 1992 on the first 16 dampers fabricated by Martin Marietta for the ISICLSS program. Testing for the Phase 2 dampers was completed in July 1993. The Phase 1 testing is described first, followed by a description of enhancements made for the Phase 2 testing.

These tests had several objectives:

- Determine damper modulus and loss factor over 1 to 25 Hz frequency band.
- Determine linearity with respect to dynamic load level.
- Determine effects (if any) of static preload on dynamic characteristics.
- Determine failure loads and modes.

The following sections describe the setup, fixture characterization, data reduction, and results of the testing performed to accomplish the objectives listed above.

I.1 Test Setup and Procedure

All testing was conducted using the MTS 22 kip machine at the Materials Test Laboratory (MTL). Special fixture hardware was fabricated to interface the test articles with the MTS machine. The following sections describe the two distinct test setups and procedures used for the dynamic impedance tests and the static failure tests.

I.1.1 Impedance Tests

The damper impedance test setup is shown in Figures I.1 through I.3. Note that the hydraulic grips were removed from the MTS to allow use of the test fixture hardware. The fixture hardware was machined from 2.25 in. diameter steel bar stock to obtain a very stiff fixture arrangement. Subsequent test results indicated that additional compliance observed in the overall test setup was due to the MTS load frame flexibility.

In order to minimize instrumentation phase error, a PCB-208A03 force gauge powered by a Kistler coupler, and a Kaman proximity probe were used to make the impedance measurements. Previous testing has shown this instrumentation to produce virtually zero phase error in the 1 to 25 Hz range. As shown in Figure I.1, a QA-1400 accelerometer was installed inline with the damper to serve as a proximity probe calibration check. Table I.1 lists the instrumentation calibration factors.

Data acquisition was accomplished using an HP3562A analyzer. The analyzer source output was input to the MTS controller as a force command, and the scaling was set as 100 lb per Volt commanded. All impedance measurement data were stored on 3.5 inch floppy disks.

Damper impedance measurements were performed using random excitation over a 0 to 25 Hz band with the HP 3562A analyzer source output set to 2 V peak. This resulted in about 50 lb RMS applied to the damper, and about .0002 inches RMS displacement. Higher excitation levels tended to saturate the QA-1400 accelerometer output which was necessary for accurate proximity probe calibration. However, other random excitation levels, as well as sinusoidal excitation were applied to determine the effect of load level.

Dampers were generally preloaded with 10 lb static compression during impedance tests. Greater compressive preloads were applied to determine any effects on the measured data.

Two series of impedance tests were run. The first series was performed prior to system testing at Langley and the second was conducted following the system tests. During the first test series, temperature was not closely monitored, and varied from 71 to 74 Deg.F during the two days of impedance measurements. However, during the second test series, damper temperature was closely monitored via thermocouple measurements on the damper sleeves, and all testing was completed while the ambient temperature remained between 71 and 72 Deg. F. Due to this uniform temperature, unit-to-unit impedance data from the second test series was somewhat more consistent compared to data from the first test series. Damper impedance data presented in the results section of this report are from the second test series.

During initial test setup characterization, it became evident that the position measurement provided by the proximity probe differed from the QA-1400 accelera-

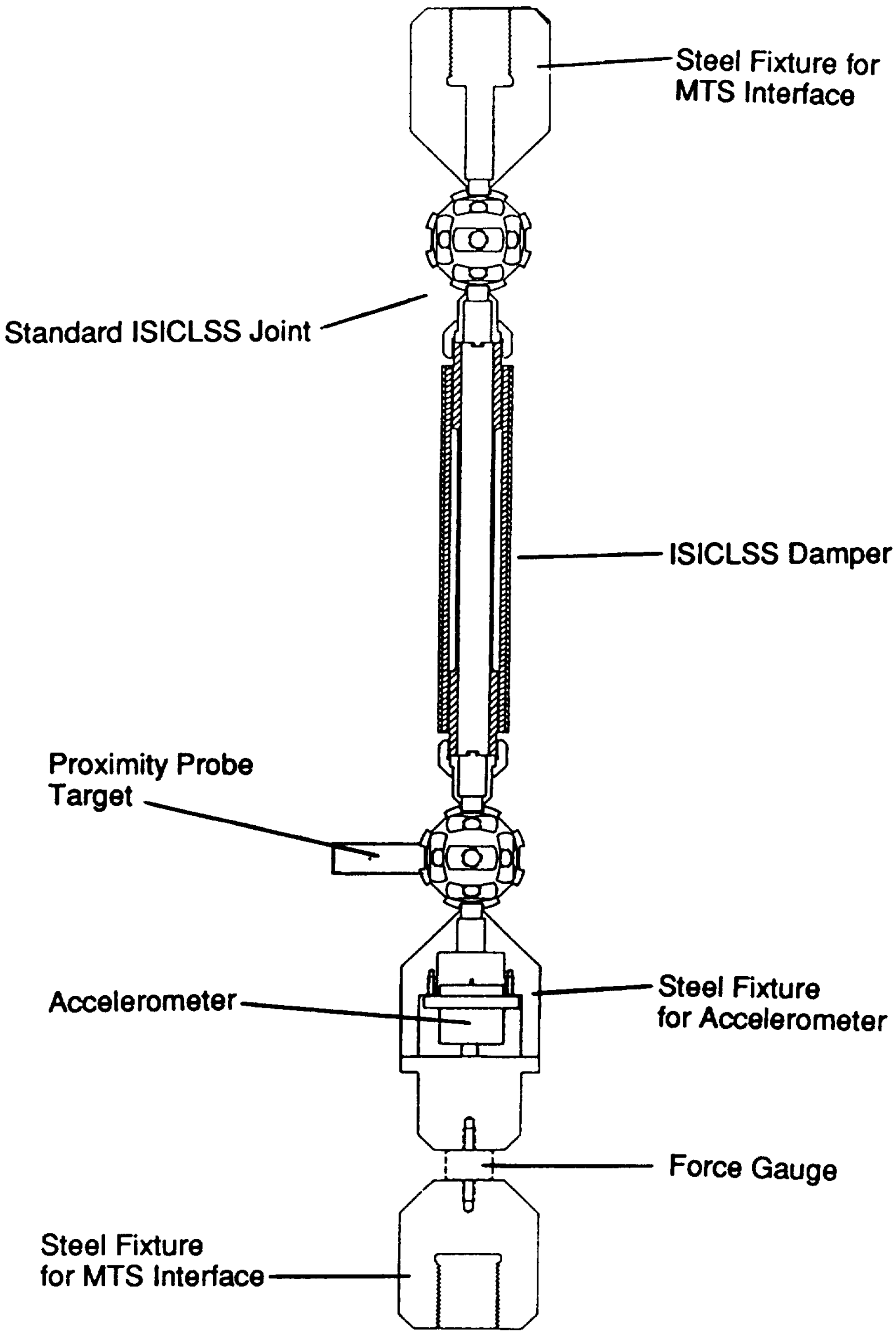

Figure I.1: Damper Test Fixture Schematic

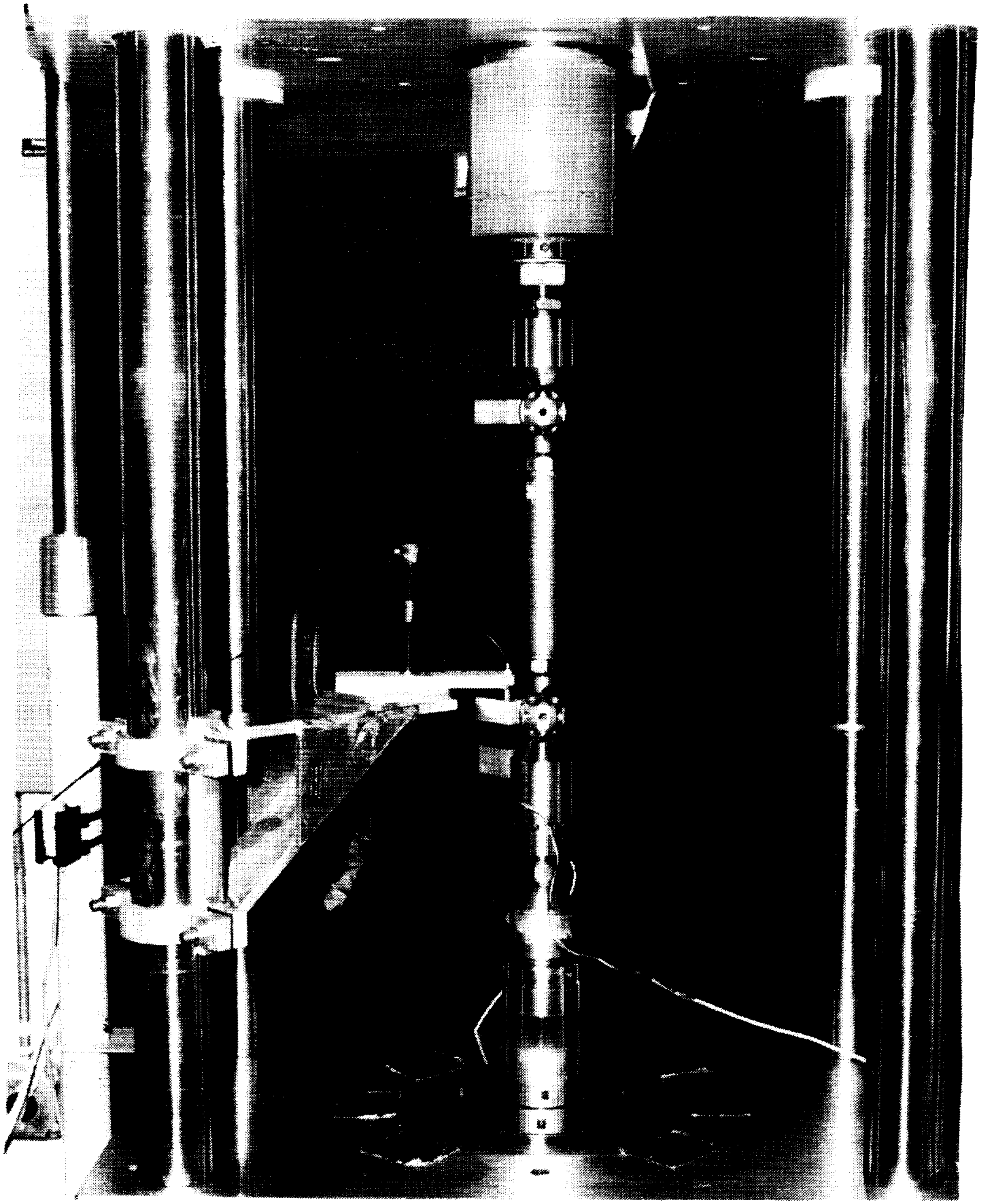

Figure I.2: Photo of Damper Test Fixture

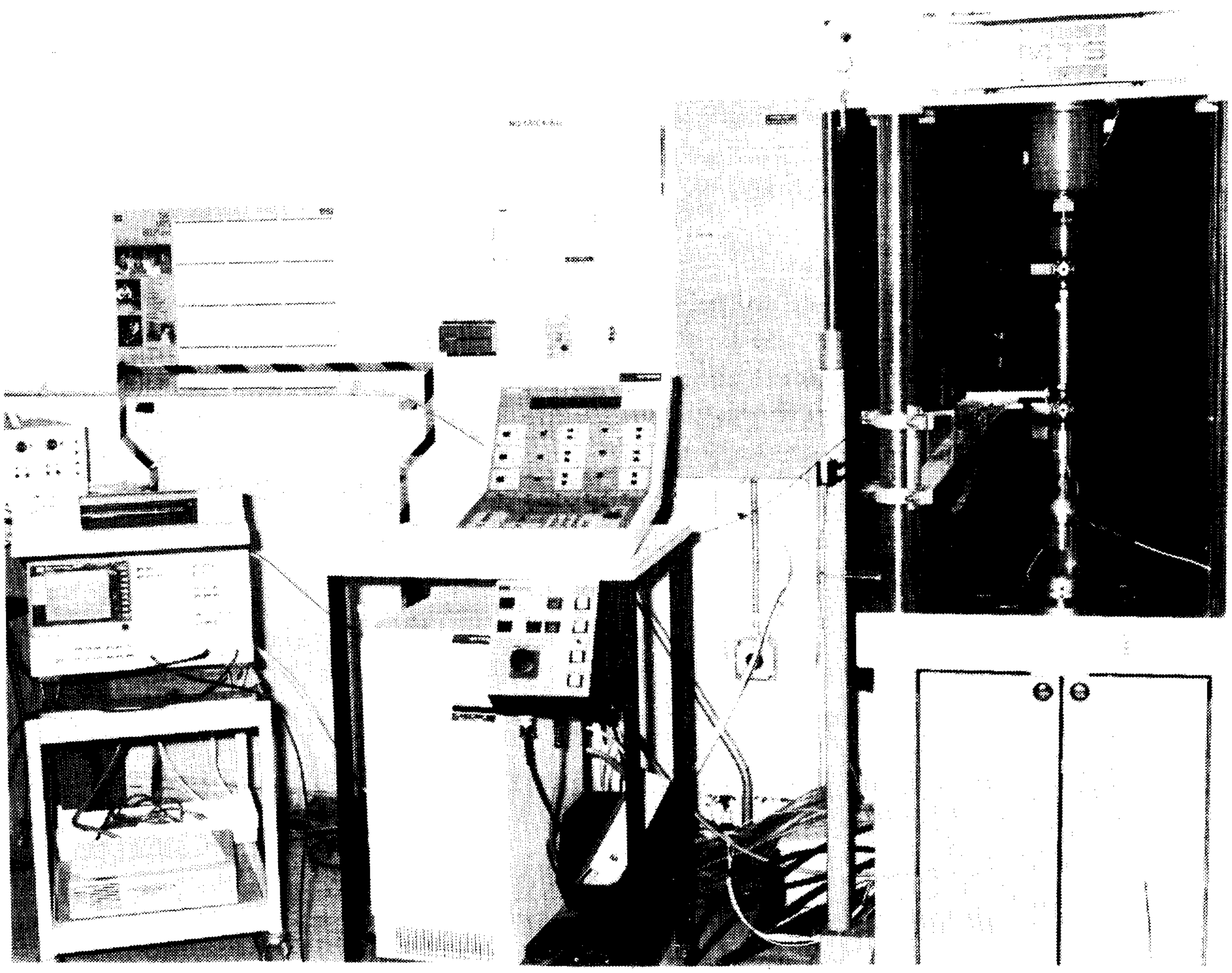

Figure I.3: Photo of Damper Test Equipment tion measurement by up to 10 percent (i.e. $accel = displ \times \omega^2 \times 1.1$). This was attributed to small rotation of the proximity probe target during test excitation. To correct for the rotation, the proximity probe output was scaled according to the acceleration output. The correction was accomplished by measuring the transfer function between measured position and acceleration (A/D), and curve fitting that measurement. Figure I.4 shows a typical measurement and fit. As shown, the relationship closely follows ω^2, but is off by about 4 percent in terms of absolute magnitude for this case ($fit/\omega^2 = 1.04$). Assuming the on-axis acceleration measurement is correct, this result indicates that the proximity probe measurement must be increased by 4 percent to obtain the true displacement at the accelerometer location.

Since the proximity probe scaling changed somewhat from specimen to specimen, the calibration procedure described above was performed for each specimen impedance measurement, and the Force / Displacement impedance scaled appropriately.

Both Force/Displacement (F/D) and Force/Acceleration (F/A) frequency response functions (FRF) were measured. The F/D and F/A measurements agreed in terms of modulus in the 5 to 10 Hz range, but roll-off and phase shift of the accelerometer degraded agreement above about 15 Hz. Also, the very low acceleration levels below 5 Hz resulted in very noisy F/A data. Therefore, the F/D measurements were used to determine specimen modulus and loss factor, with the F/A data used as a check. As described above, the F/D data were scaled by the A/D measurement.

I.1.2 Failure Tests

Failure tests were performed on the damper only (no standoffs or node balls). To accomplish these tests, special steel grip ends were fabricated which threaded onto the damper specimens, and clamped into the MTS hydraulic grips. The test setup is sketched in Figure I.5.

The standard MTS outputs (load cell and LVDT) were recorded on an X-Y plotter as displacement (strain) was increased at a controlled constant rate.

I.2 Fixture Characterization

The approach for determining damper modulus and loss factor was to measure the damper impedance (F/D FRF) at the forced end and assume the opposite damper end was fixed. The validity of this assumption was investigated through fixture characterization tests. These tests were performed to determine the flexibility and loss factor of the fixture so as to account for their influence on measured damper impedance.

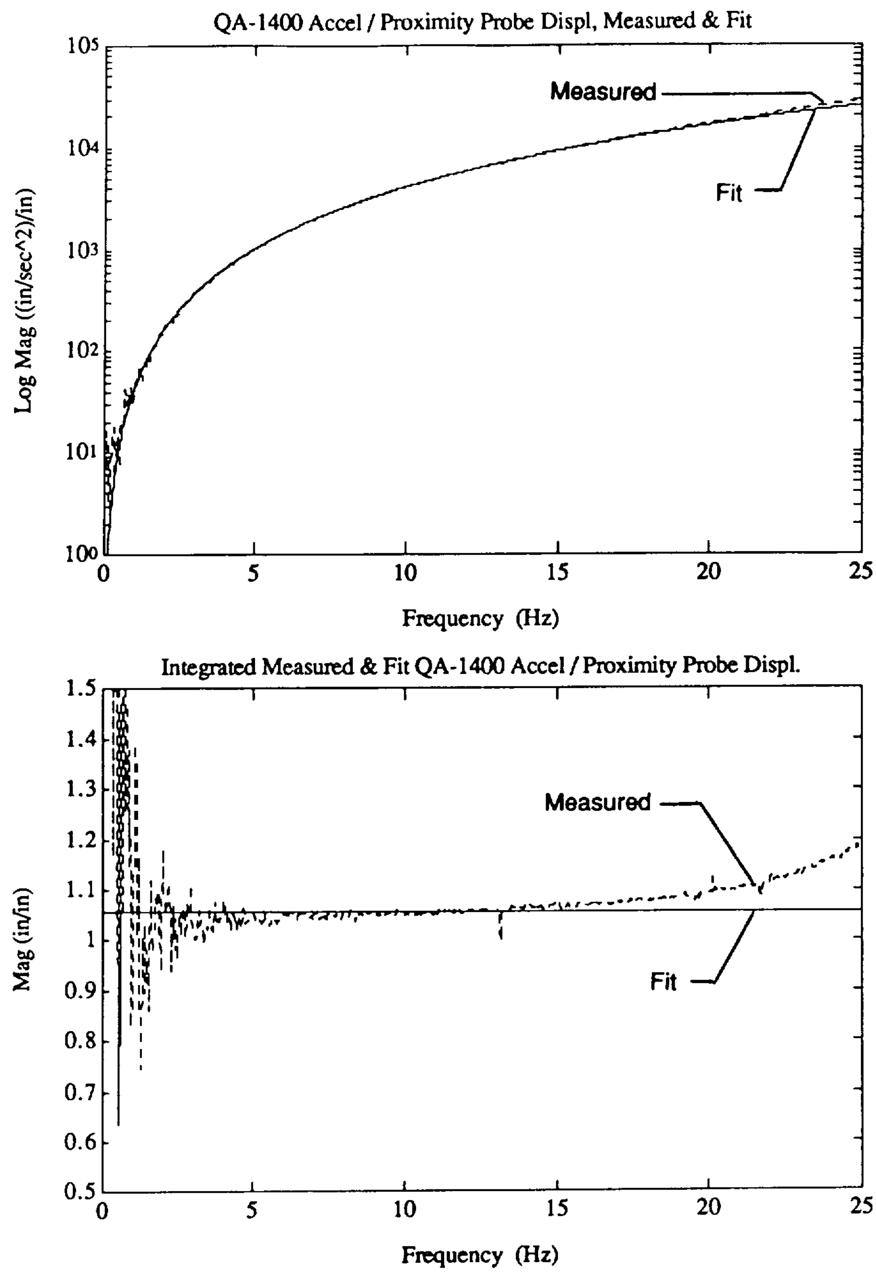

Figure I.4: Proximity Probe Calibration Using Curve Fit of Measured Acceleration / Displacement FRF

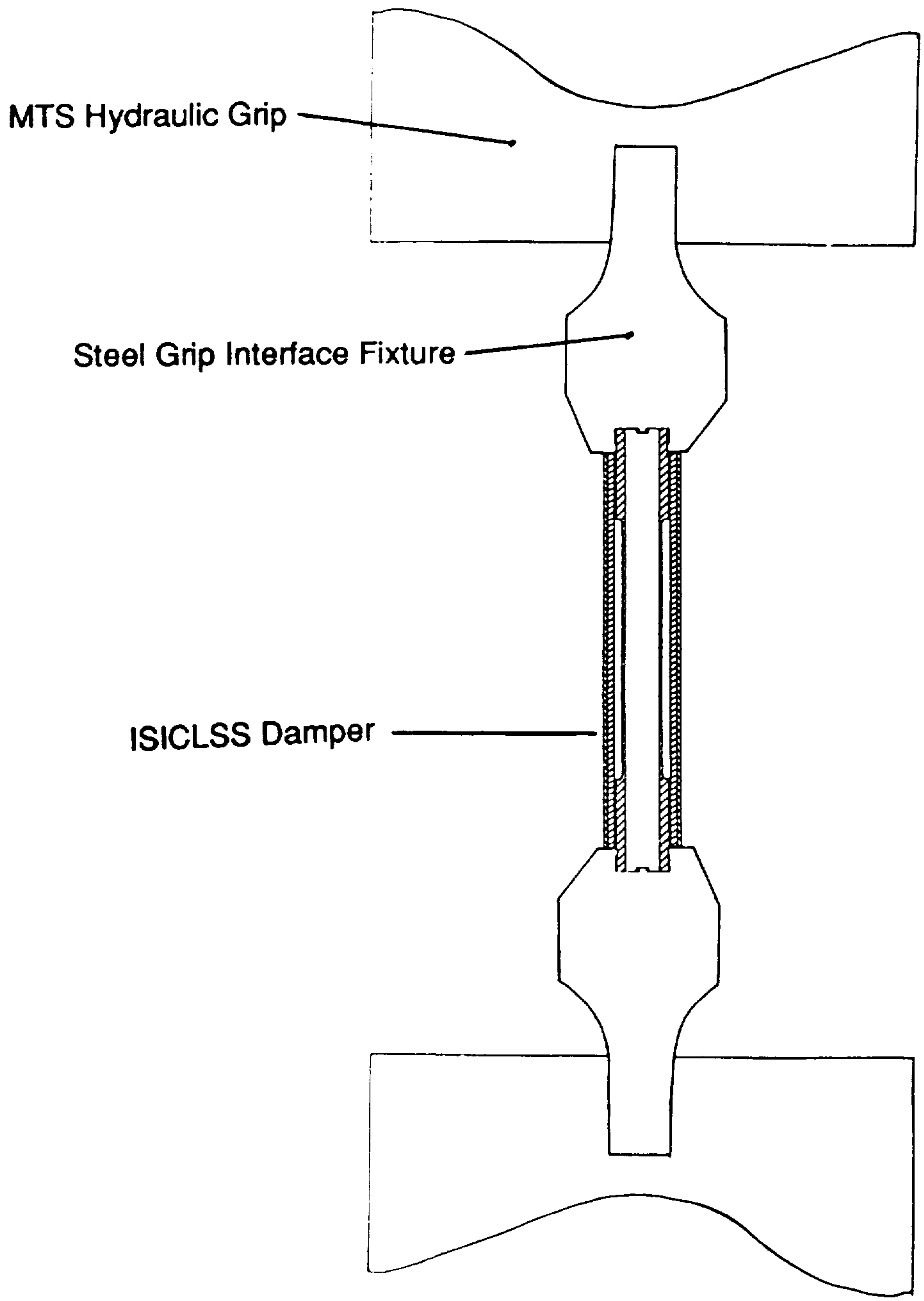

Figure I.5: Damper Failure Test Setup

Several tests were performed to characterize the test setup. These tests included the following:

1. Fixture hardware alone (Figure I.6)
2. Single ball (Figure I.7)
3. 0.5 inches aluminum bar (Figure I.8)
4. Baseline Langley 4 member (Figure I.9)

Results from these tests are shown in Figures I.10 through I.13 and summarized in Table I.2. The impedance measurements generally demonstrated flat response to 25 Hz, with less than 0.25 degrees of phase shift for the aluminum bar (Figure I.11) and baseline strut (Figure I.13, thereby verifying that little loss existed in the setup with a specimen stiffness less than 300 kip/in. Impedance of the fixture alone did show several degrees of phase shift (Figure I.10 since all strain energy was in the fixture and MTS load frame. The stiffness results listed in Table I.2 indicate a fixture stiffness (MTS machine, steel interface hardware) of 1200 to 1400 kip/in. This agrees with previous characterization of the MTS load frame stiffness performed by MTL personnel. Inclusion of a single ball lowered the measured stiffness to about 800 kip/in (Figure I.11). The nominal baseline member stiffness of 264 kip/in is from node to node. Therefore, the damper test setup includes the compliance of an extra ball in addition to the fixture's compliance. The combined stiffness of the fixture with extra ball may be derived from the measured value by modeling the setup as springs in series, and solving for the combined stiffness.

$$\left(\frac{1}{K_{total}} - \frac{1}{K_{strut}}\right) - 1 = K_{fixture} \tag{I.1}$$

Performing this calculation using 264 kip/in as the strut stiffness and 208 kip/in as the measured overall stiffness gives a combined stiffness of 981 kip/in. This agrees well with the measured combined stiffness of 817 kip/in considering the high sensitivity inherent to this calculation. For example, if K_{strut} is assumed to be 260 kip/in, $K_{fixture}$ becomes 1040 kip/in.

Based on the setup measurements, the damper measurements were corrected to account for fixture flexibility. The modulus and loss factor were corrected using the following relations:

$$K(\omega)_{damper} = \left(\frac{1}{K(\omega)_{total}} - \frac{1}{K_{fixture}}\right) - 1$$

Table I.1: Instrumentation Calibration Factors

Transducer	Calibration Factor
QA-1400 Accelerometer S/N 2037	9.557 $in/sec^2/V$
Kaman Proximity Probe Model KD2310-1S	0.02532 in/V
PCB 208A03 Force Gauge S/N 3232	85.72 lb/V

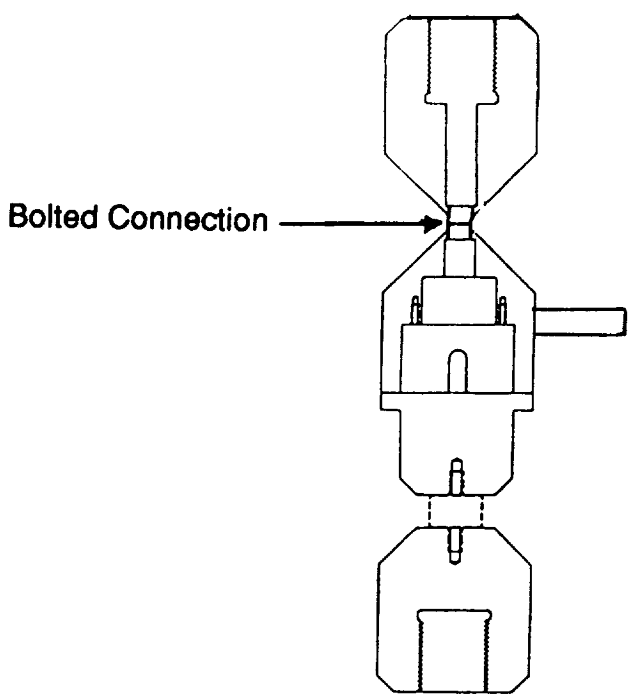

Figure I.6: Fixture Characterization Test: Fixture Hardware Alone

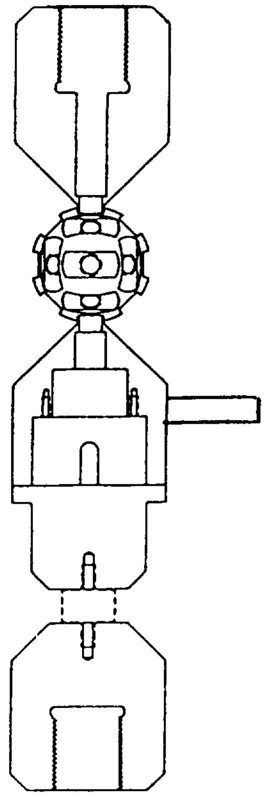

Figure I.7: Fixture Characterization Test: Single Ball

Table I.2: Results of Fixture Characterization Tests

Test Configuration	Nominal Element Stiffness (kip/in)	Measured Overall Stiffness (kip/in)	Derived Fixture Stiffness (kip/in)
Fixture Alone	unknown	1460	–
Fixture with Single Ball	unknown	817	–
Fixture with Aluminum Bar	160	142	1260
Fixture with Baseline Strut	264[1]	208[2]	981[3]

[1]Ball center to ball center
[2]Averaged over several tests
[3]Includes extra ball + 2 bolted connections

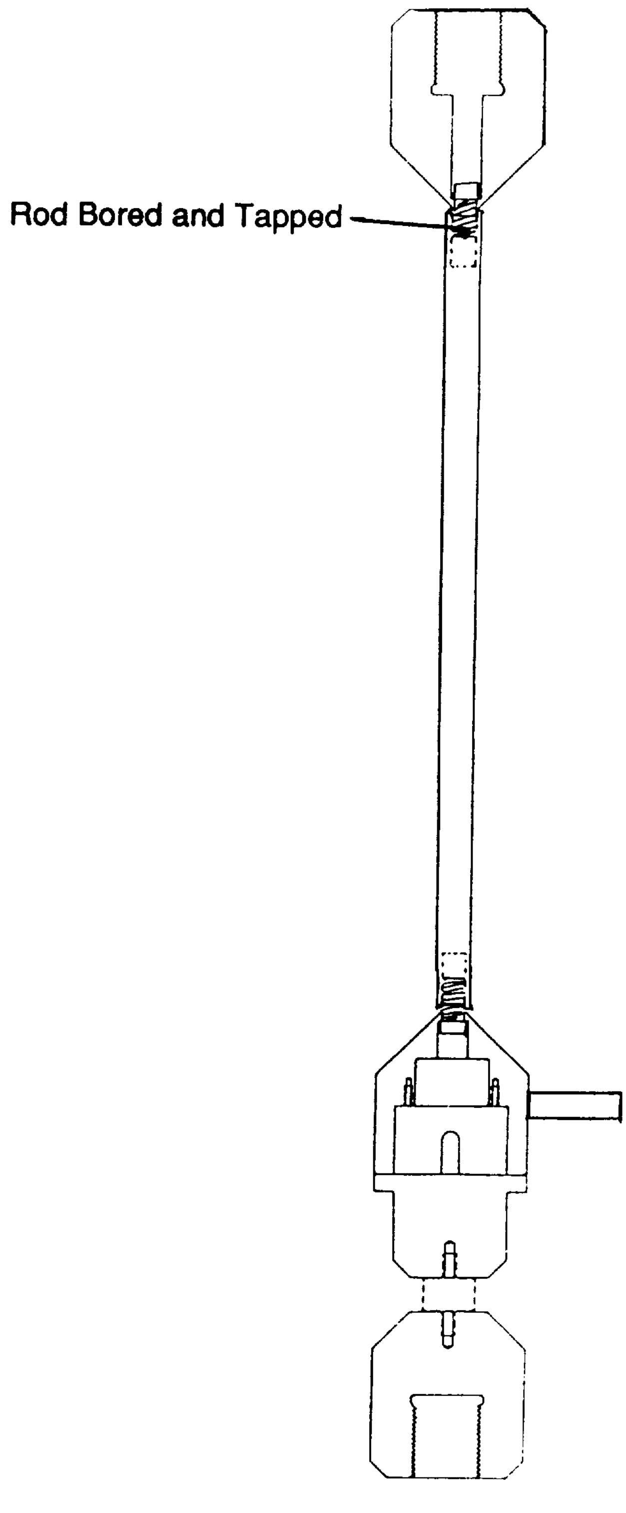

Figure I.8: Fixture Characterization Test: 0.5" Aluminum Bar

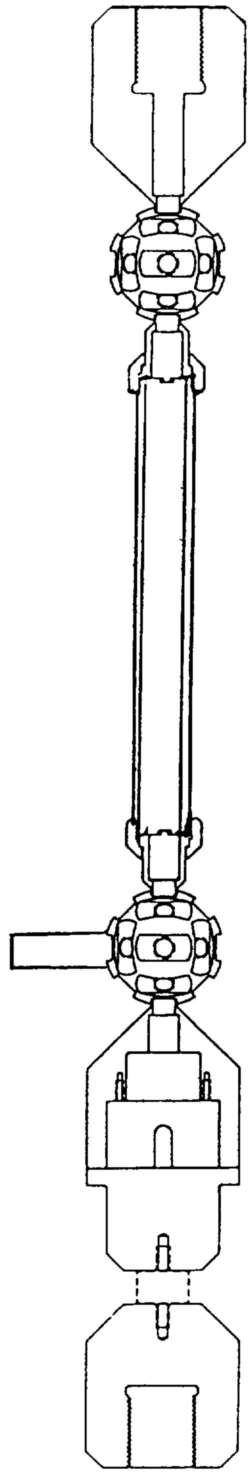

Figure I.9: Fixture Characterization Test: Baseline Langley 4 Member

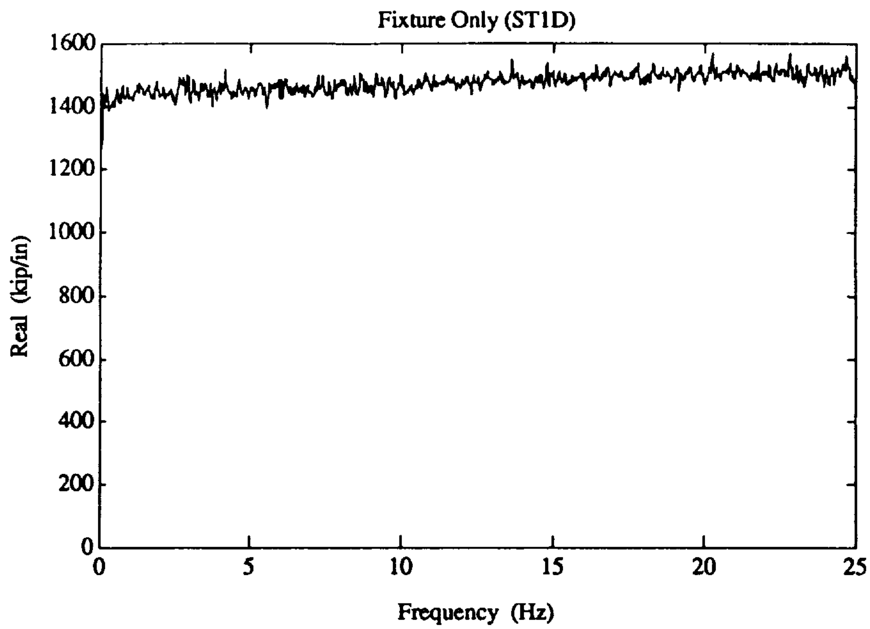

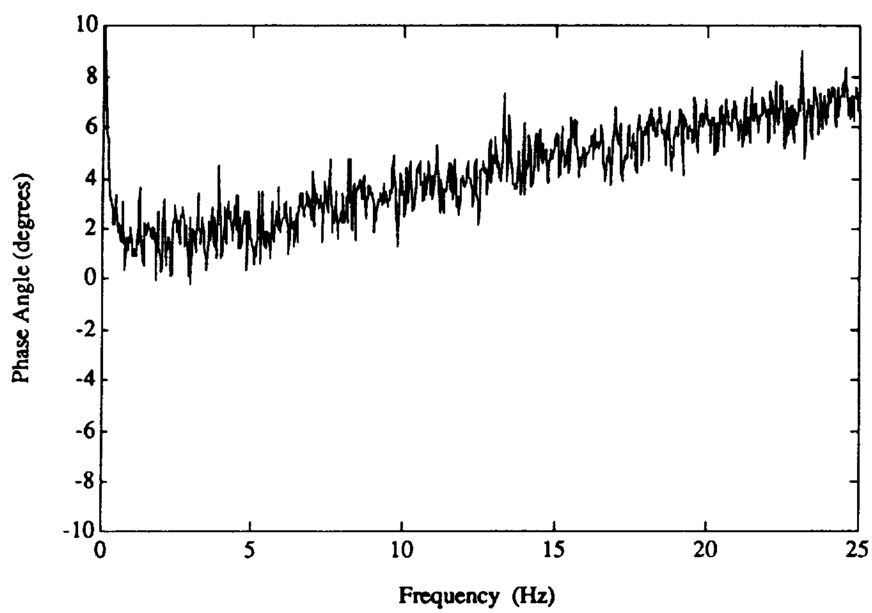

Figure I.10: Force/Displacement FRF for Fixture Hardware Alone

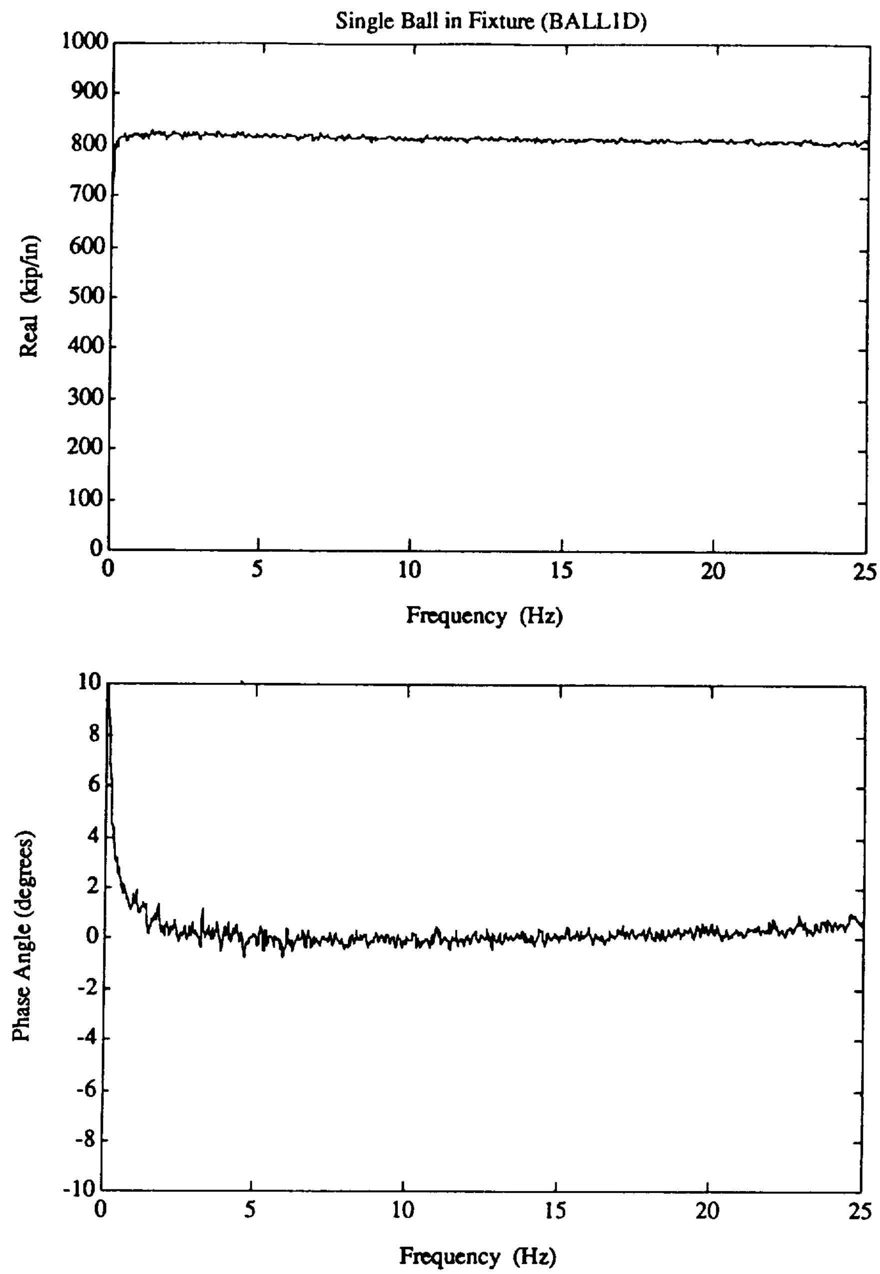

Figure I.11: Force/Displacement FRF for Single Ball

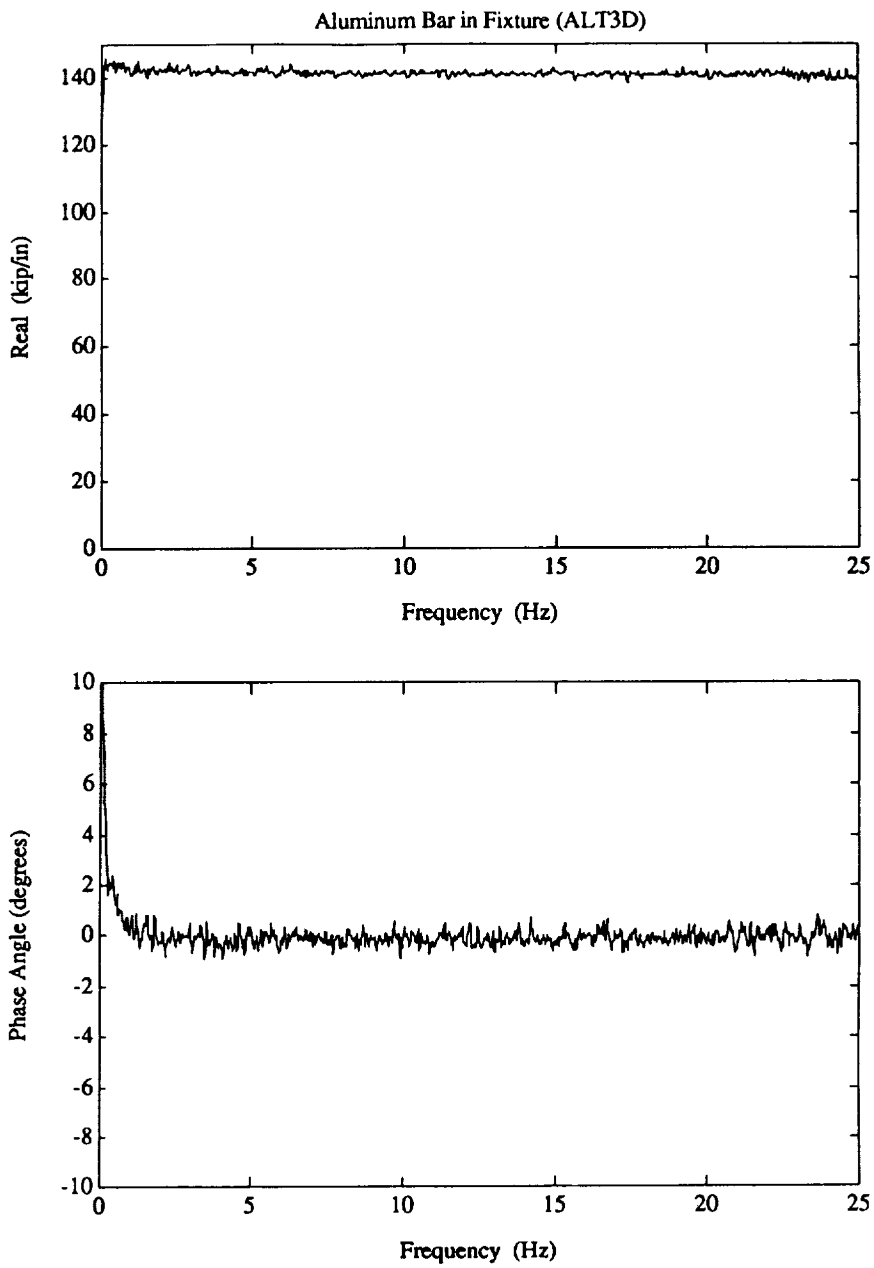

Figure I.12: Force/Displacement FRF for Aluminum Bar

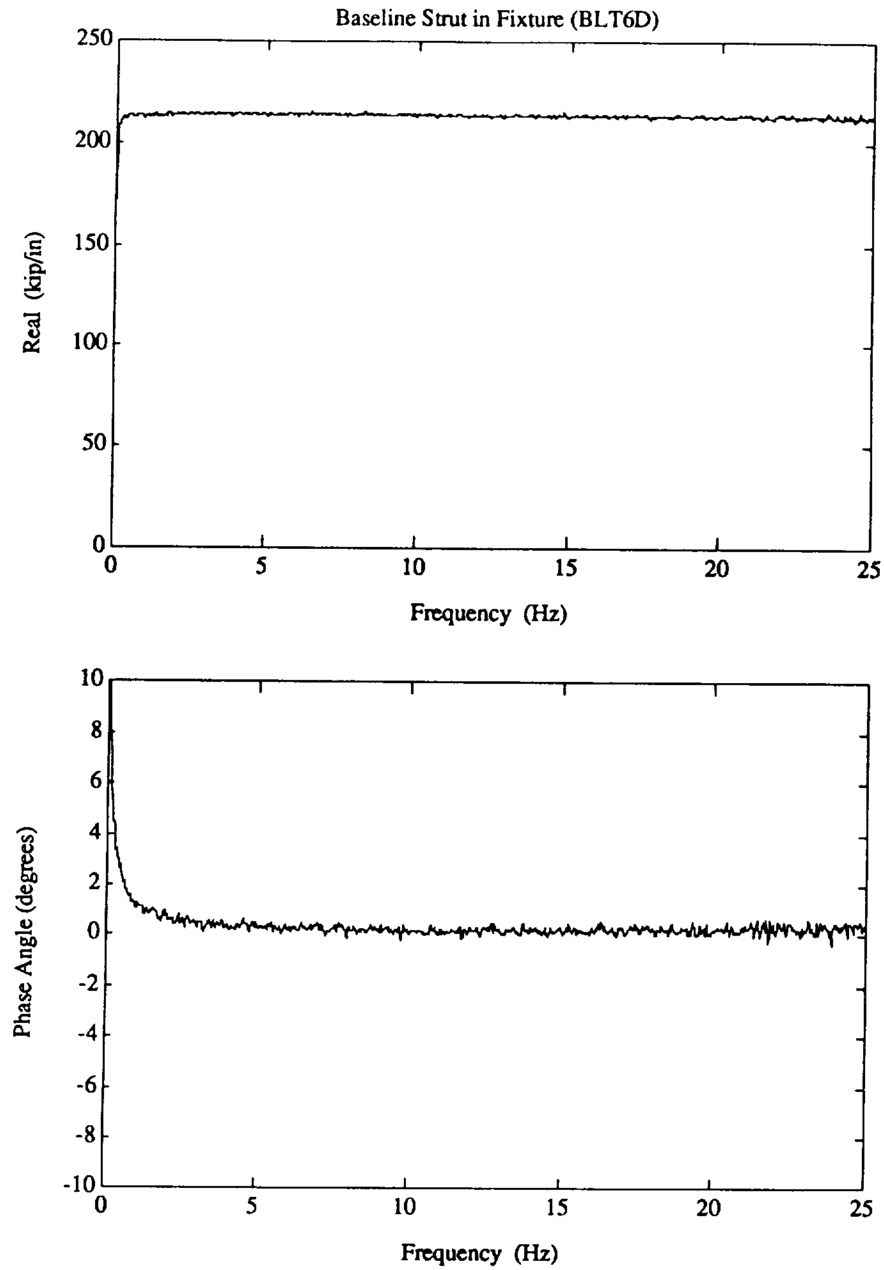

Figure I.13: Force/Displacement FRF for Baseline Langley 4 Member

$$\eta(\omega)_{damper} = \eta(\omega)_{total} \times \frac{K(\omega)_{damper}}{K(\omega)_{total}}$$

The value for $K_{fixture}$ used to correct damper impedance measurements was the average of values from the single ball test and derived from several baseline strut tests: 900 kip/in. Since roughly 80 percent of the strain energy is in the damper, the small loss factor of the fixturing contributes a negligible loss to the overall test as evidenced by the measured impedance of the aluminum bar and baseline strut (see Figures I.11 and I.13). The sensitivity of the corrected results to fixture stiffness is shown in Figure I.14. Here, typical damper data has been corrected using 900 and 800 kip/in fixture stiffnesses — resulting in a nearly 5% shift of corrected damper modulus and loss factor values.

I.3 Test Results

In this section, the impedance tests are presented first followed by the failure tests.

I.3.1 Impedance Tests

Impedance test results are summarized in Figures I.15 through I.18. As previously mentioned, the measurements presented here are from the second test series and therefore do not include data for dampers 5 and 11 which were used for failure testing following the first impedance test series. The impedance measurements are presented as modulus (real part of FRF) and loss factor (tangent of FRF phase angle), and can be considered as the damper properties at 72 F. The raw data shown in Figures I.15 and I.16 are "as measured" (not corrected for fixture flexibility effects), while the corrected data plotted in Figures I.17 and I.18 were computed from the measurements using the fixture stiffness correction method described above. The raw data is presented for reference, while the corrected data more accurately represents the damper characteristics.

Impedance measurements showed very little change (less than 2 percent) for input force levels ranging from 30 to 300 lb RMS. Also, damper preloads up to 100 lb compression had no measurable effect on the impedance measurements.

I.3.2 Failure Tests

Tensile failure tests were performed on dampers 5 and 11. These units were selected for failure tests since they exhibited somewhat lower modulus and loss factor respectively than the other dampers.

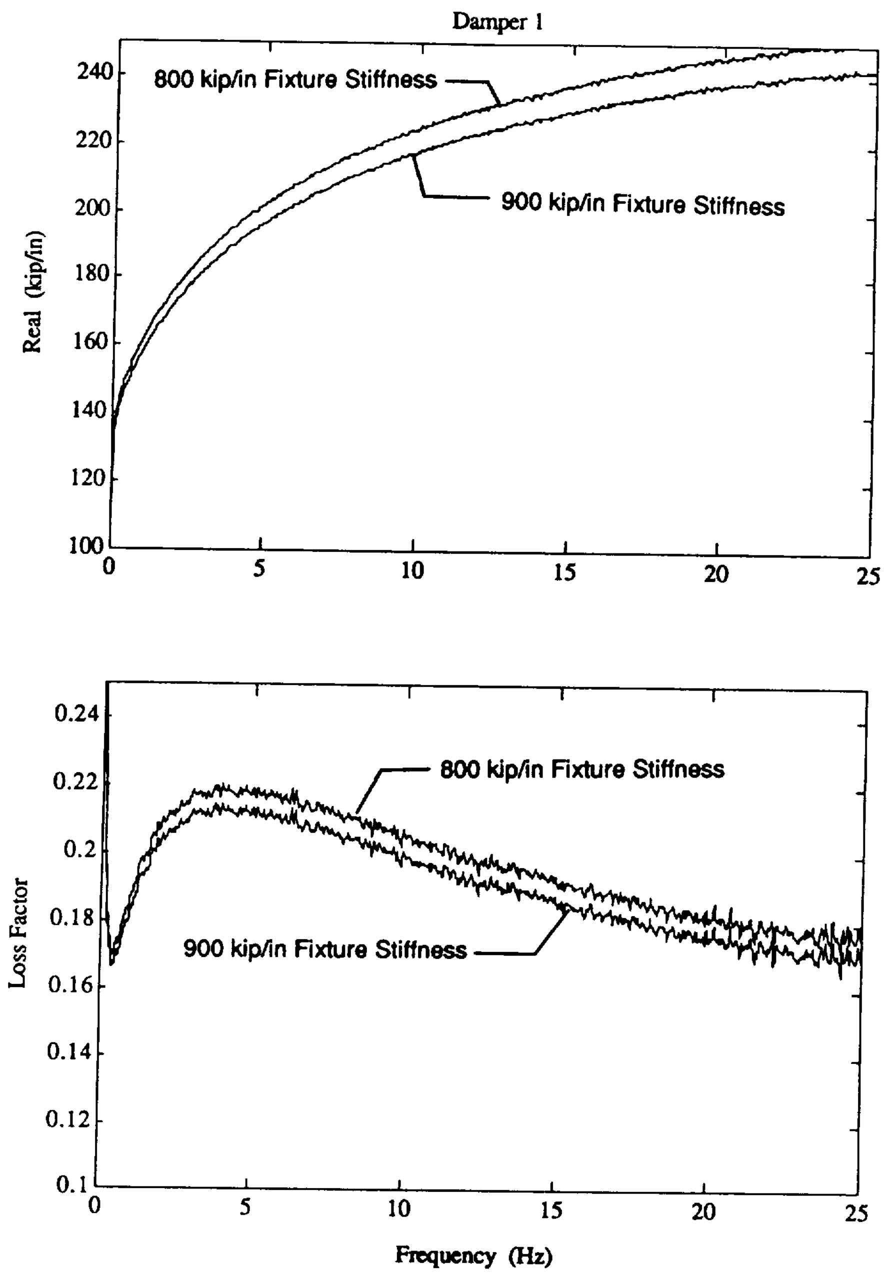

Figure I.14: Comparison of Corrected Damper Modulus Using 800 and 900 kip/in Fixture Stiffness

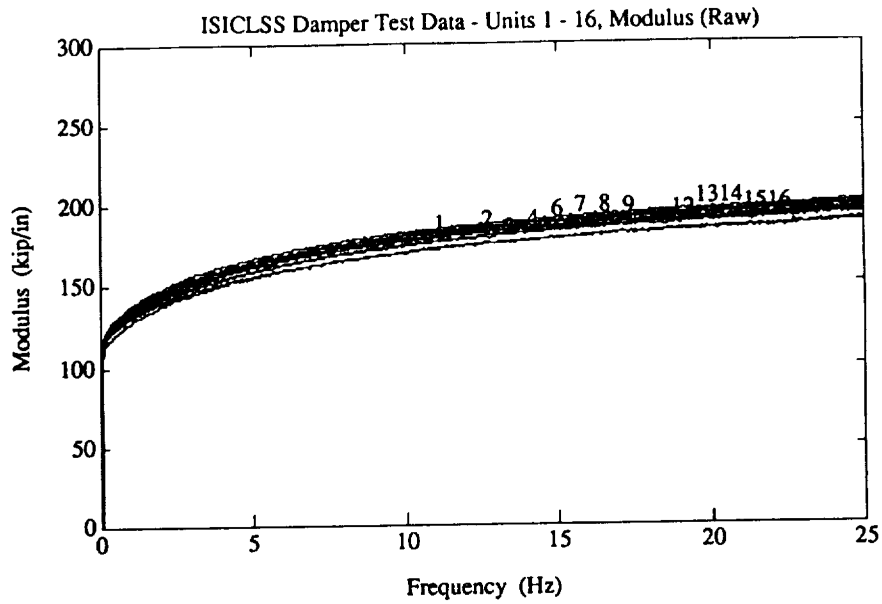

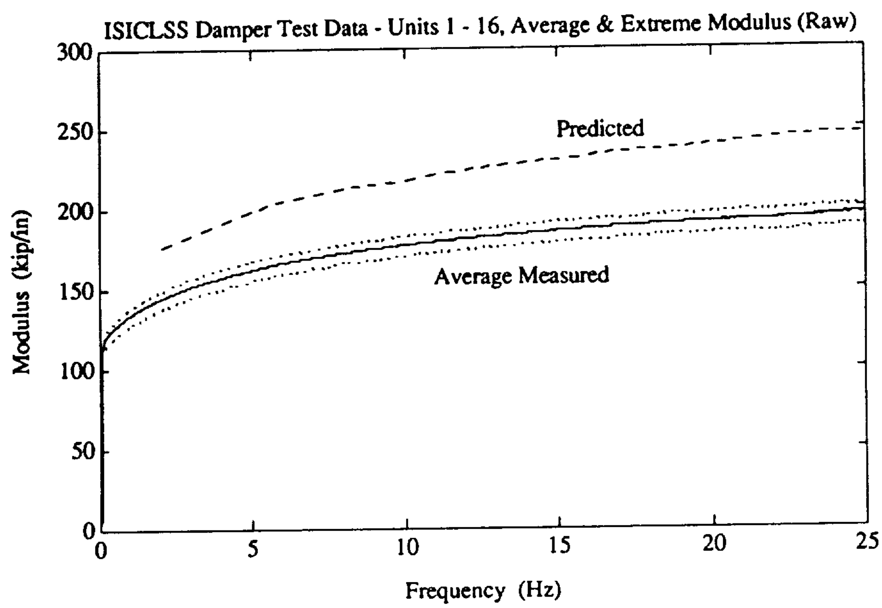

Figure I.15: Damper Modulus Data Not Corrected For Fixture Stiffness

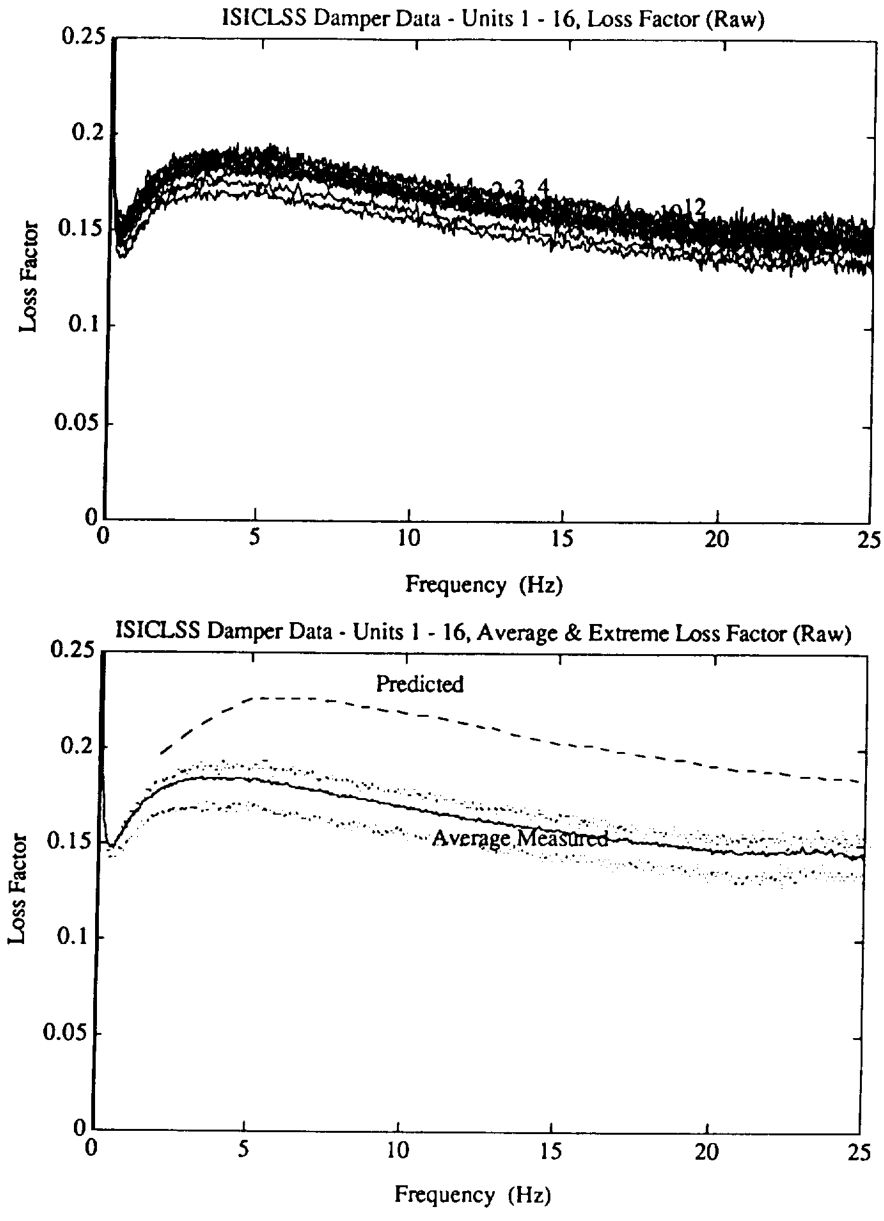

Figure I.16: Damper Loss Factor Data Not Corrected For Fixture Stiffness

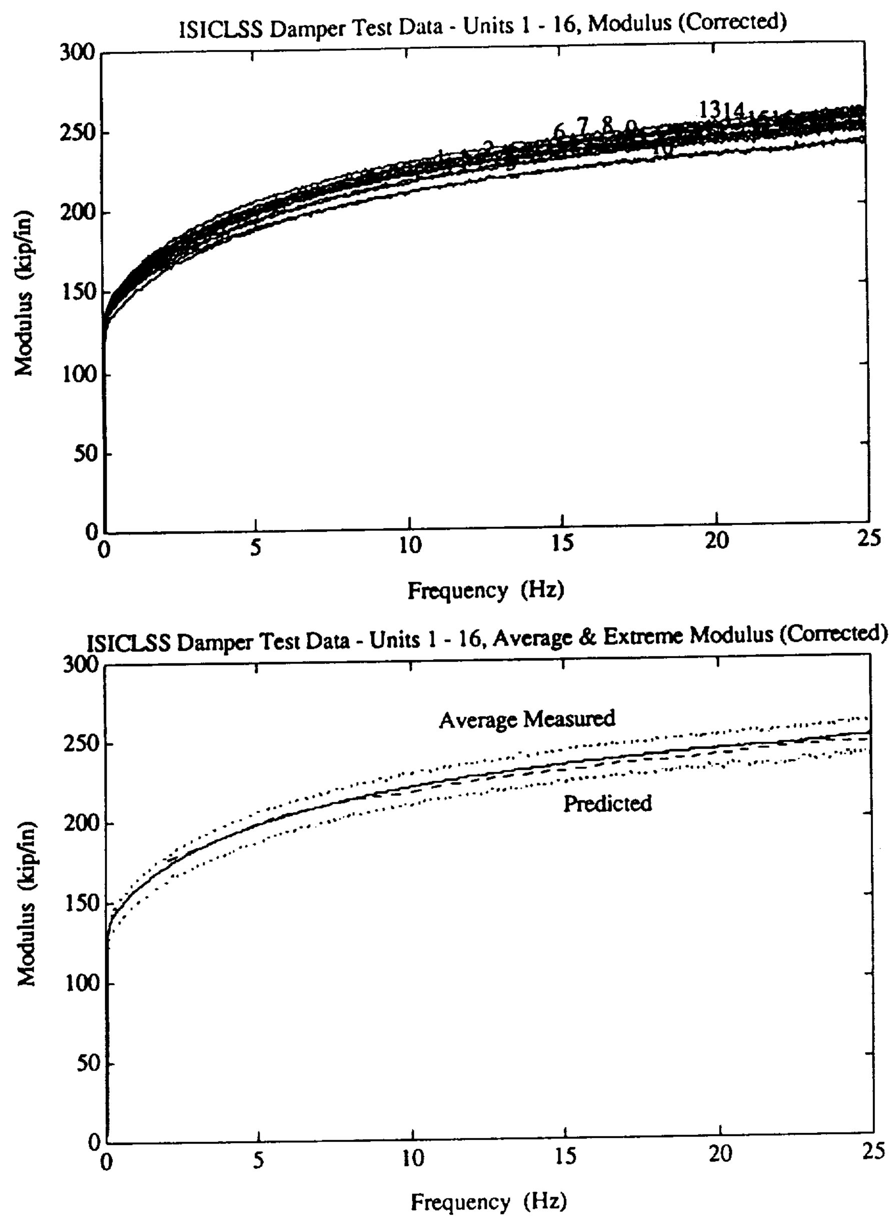

Figure I.17: Damper Modulus Data Corrected For Fixture Stiffness of 900 ksi

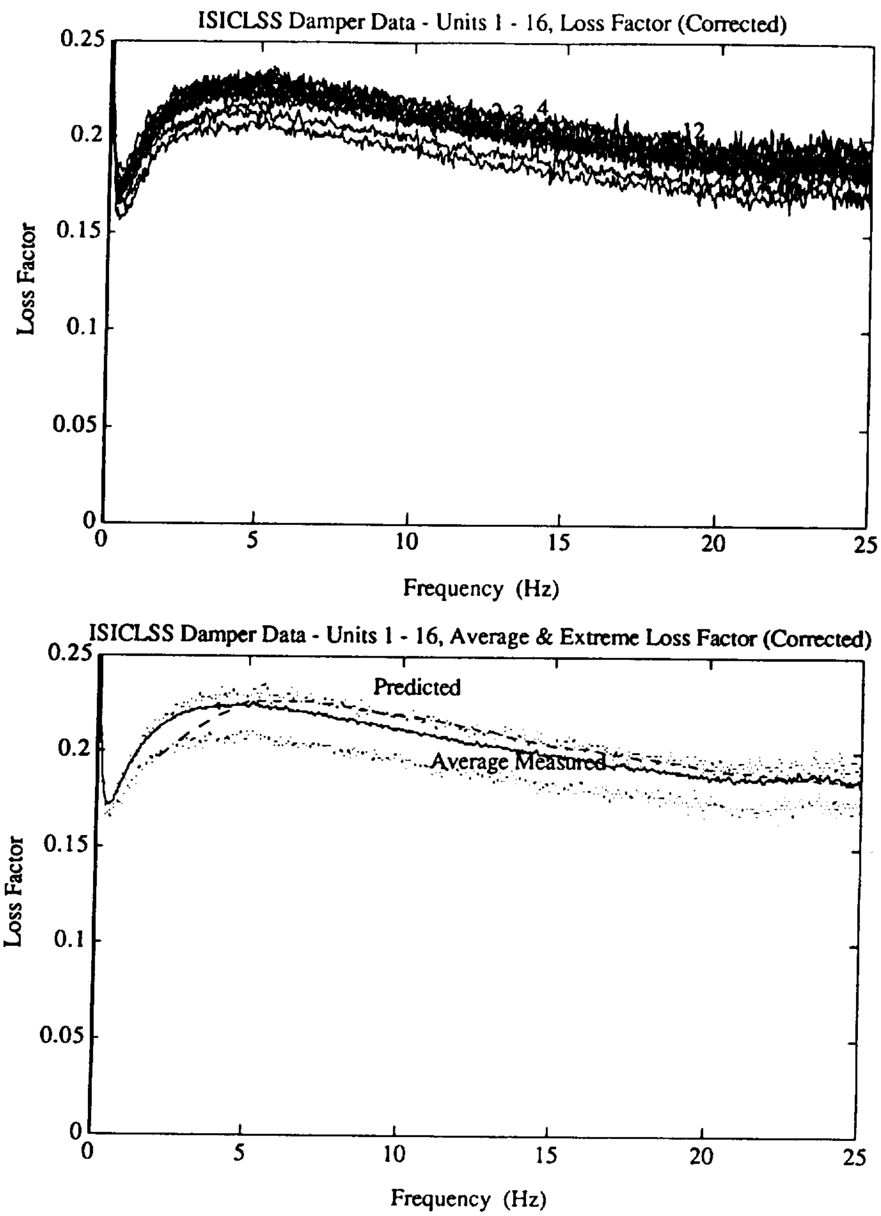

Figure I.18: Damper Loss Factor Data Corrected For Fixture Stiffness of 900 ksi

Table I.3: Damper Failure Test Results

Failure Mode	Load (Lb)	
	Damper # 5	Damper # 11
Sleeve-to-Clamshell Bond Failure	2600	2600
Initial VEM/Epoxy Failure	5100	5400
Center Tube Yield	4400	5500
Center Tube Fracture	not measured	6400

From a detailed examination of the failure test plots, four distinct changes in behavior can be identified:

1. At roughly 0.001 in., the stiffness decreases due to overcoming a preload caused by the grip end fixture being tightened against the damper sleeve during test setup assembly.

2. After remaining very linear from 50 to 2500 lbs load, the stiffness again falls off in a smooth fashion. This is attributed to a gradual failure of the sleeve-to-clam shell Loctite bond. Failure of this bond significantly decreases the damper loss factor and therefore is considered the maximum allowable damper load.

3. At roughly 5000 lbs, a sudden failure occurs as the VEM and associated epoxy bond fail. This failure occurred on only one end for damper 5, and in several steps on both ends of damper 11.

4. Finally, yielding of the center tube begins near 5000 lbs and ultimate fracture occurs near 6000 lb. Only damper 11 was taken to ultimate failure, while the damper 5 test was halted prior to failure to allow investigation of the failure modes.

The actual displacements and loads of the various failures for both dampers are listed in Table I.3.

I.4 Phase 2 Damper Testing

Testing of the revised designs for the Phase 2 damping elements was undertaken using test procedures identical to those described in the previous sections. When the test apparatus was reassembled and impedance tests of the Phase 2 designs were performed, however, the agreement between the test data and the analysis was poor compared with those obtained for the Phase 1 design. Therefore, testing of the undamped baseline members and of the previously tested Phase 1 dampers was performed to determine if the poor agreement was due to problems with the test apparatus or the damping members themselves.

Testing of the undamped truss members provided good agreement in magnitude with the previously determined values and very small impedance phase angles, implying that the test setup was providing the same results as the previous test series. The newly acquired test data for the previously tested Phase 1 damping members, however, resulted in values which were significantly different from those previously obtained. Figure I.19 provides a comparison of the 1992 and 1993 test data for damper 9. The damper appears to be stiffer than during the initial test series, and the loss factor is seriously degraded in the 2 to 10 Hz region where high damping of the CEM is required.

Good agreement for the undamped member with significant differences for damper 9 1992 and 1993 test results suggested degradation of the VEM had occurred during the 6 months between test series. VEM properties used for the Phase 1 analysis were available from a previous program and were not verified by retesting, but were believed to be accurate due to the good agreement between Phase 1 predicted and test results. Therefore, complex modulus tests on the viscoelastic material used for the Phase 2 damping members were undertaken to determine if degradation of the material had occurred, with the results showing that the viscoelastic had not degraded and its properties were within normal batch-to-batch or experimental variations associated with viscoelastic materials. Efforts to explain this apparent anomaly focused on the damper test data and impedance test setup, as the variation over time could only be explained by inaccurate measurements during either the 1992 or 1993 impedance test series.

I.4.1 Phase 2 Test Setup Checkout and Modification

Numerous check cases on the test apparatus were undertaken to determine if an instrumentation error was providing the variation between test series. The only known difference between the Phase 1 and Phase 2 tests was that a calibration procedure for the proximity sensor was performed during setup for the Phase 1 test series whereas only a secondary calibration was performed for the initial Phase 2 testing. This secondary calibration was provided by the repeatability of the test data for the baseline undamped members, producing the known stiffness and a small phase angle. The proximity sensors were calibrated by the normal procedure and Phase 1 dampers were then installed and tested in the MTS test machine, with these results resembling the Phase 1 test data. Apparently, the nonlinear circuitry which must be used to calibrate the proximity sensor had changed between the Phase 1 and initial Phase 2 testing in such a manner so as to maintain small phase errors for the undamped members but produce very significant errors for the damped elements. Solving this problem cost considerable resources. Rather than expend further efforts to verify this hypothesis, we concentrated on improving the test setup.

During the test apparatus checkout procedure, multiple transducers of various types were used to check calibration factors and consistency of data. As a result of this investigation, several improvements in the test setup were made to eliminate potential sources of error in the data. An improved test setup and procedure was then used to obtain final Phase 2 test data. During the checkout procedure, the modulus and loss factor data were found to be dependent on the location of the proximity sensor in the test. This was believed to be due to rotation of the node ball, and was quantified by placing an auxiliary accelerometer on the proximity probe target on opposite sides of the lower node ball. The frequency response between the QA accelerometer mounted coaxially with the specimen and these acceleration output was then measured and is given in Figure I.20. There are significant differences in both magnitude and phase for the two tests, while no variation was noted when the specimen was removed from the machine and identical measurements were taken. These differences can produce errors on the order of 10% in both magnitude and loss factor and are attributable to rotations of the lower node ball during the test due to slightly eccentric loading conditions.

To eliminate this error, two proximity sensors were used for the final test series and their outputs were summed using a summing junction so that the contributions due to member rotation were removed (Figure I.21). In the Phase 1 testing and the the initial Phase 2 testing, the accelerometer mounted coaxially with the specimen was used to determine the member stiffness while the phase angle (loss factor) was measured using the proximity sensor. Therefore, the results were similar between the various test series for member stiffness, while member loss factor was significantly different. The additional flexibility provided by the upper node ball and the MTS fixture apparatus were removed by installing two proximity sensors on the upper node ball and measuring the motion of the center of the upper node ball while cycling the specimen (Figure I.22). The MTS/fixture impedance was shown to be constant over frequency and invariant for the various member types, having a value of 1400

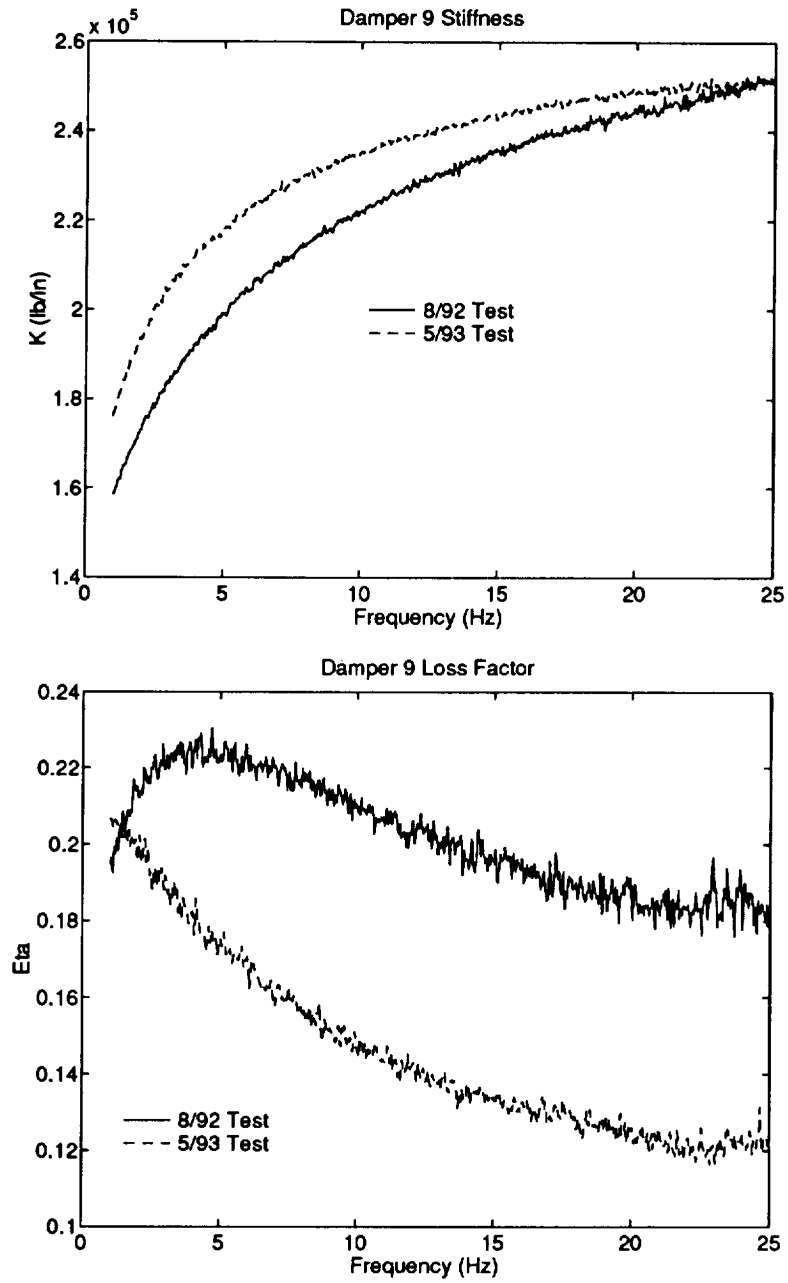

Figure I.19: Comparison of Phase 1 and Initial Phase 2 Stiffness and Loss Factor for Unit #9 kips/in and a very small phase angle. This direct measurement provides a fixture impedance value which can be removed from the lower proximity probe measurements to directly determine the behavior of the damped element. For the second Phase 2 testing series, only one measurement was required to determine the impedance of the members — the applied force versus the sum of the two calibrated proximity sensors. The fixture flexibility was removed subsequent to data acquisition to provide the measured member moduli and loss factors.

I.4.2 Impedance Tests

The impedance of the Phase 2 damping members and the previously tested Phase 1 members was measured using the modified test apparatus and procedures described above. Figure I.23 provides a comparison of the measured impedance for damper 9 for the various test series and the analytical predictions. The measured dynamic stiffness of the damping member is relatively constant throughout the various test series, however a large variation in member loss factor is present. The improved test procedures and apparatus used for the final Phase 2 testing provides the most accurate test data, although the loss factor is somewhat low when compared to the analytical data.

The final Phase 2 testing provided relatively consistent data between the various damper types, with only small unit-to-unit variation. Figures I.24 through I.29 provide the measured impedances of the members after correcting for the fixture flexibility and removing outlying elements from the group. Also provided is a comparison between the analytic predictions using the complex modulus data measured during the Phase 2 effort. The results are relatively close to their analytic counterparts, with the loss factor being generally lower than the predictions. These consistently low loss factor measurements may be attributable to a DYAD-606 loss factor which is lower than that measured using the complex impedance apparatus.

I.4.3 Member Failure Testing

To ensure that the Phase 2 damper designs would have the required load carrying capability, load-deflection data were taken for several members to determine their behavior and ultimate strength. The load-deflection data for two Phase 2 diagonal members and one Phase 2 longeron member are provided in Figures I.30 to I.32. Dampers 104 and 126 are Phase 2 diagonal damping members, while damper 71 is a Phase 2 longeron member. The strength of the Loctite bonds, the epoxy bonds used to mount the VEM and the inner member are summarized in Table I.4. These strengths were shown to be adequate for the Phase 2 testing, and the members were

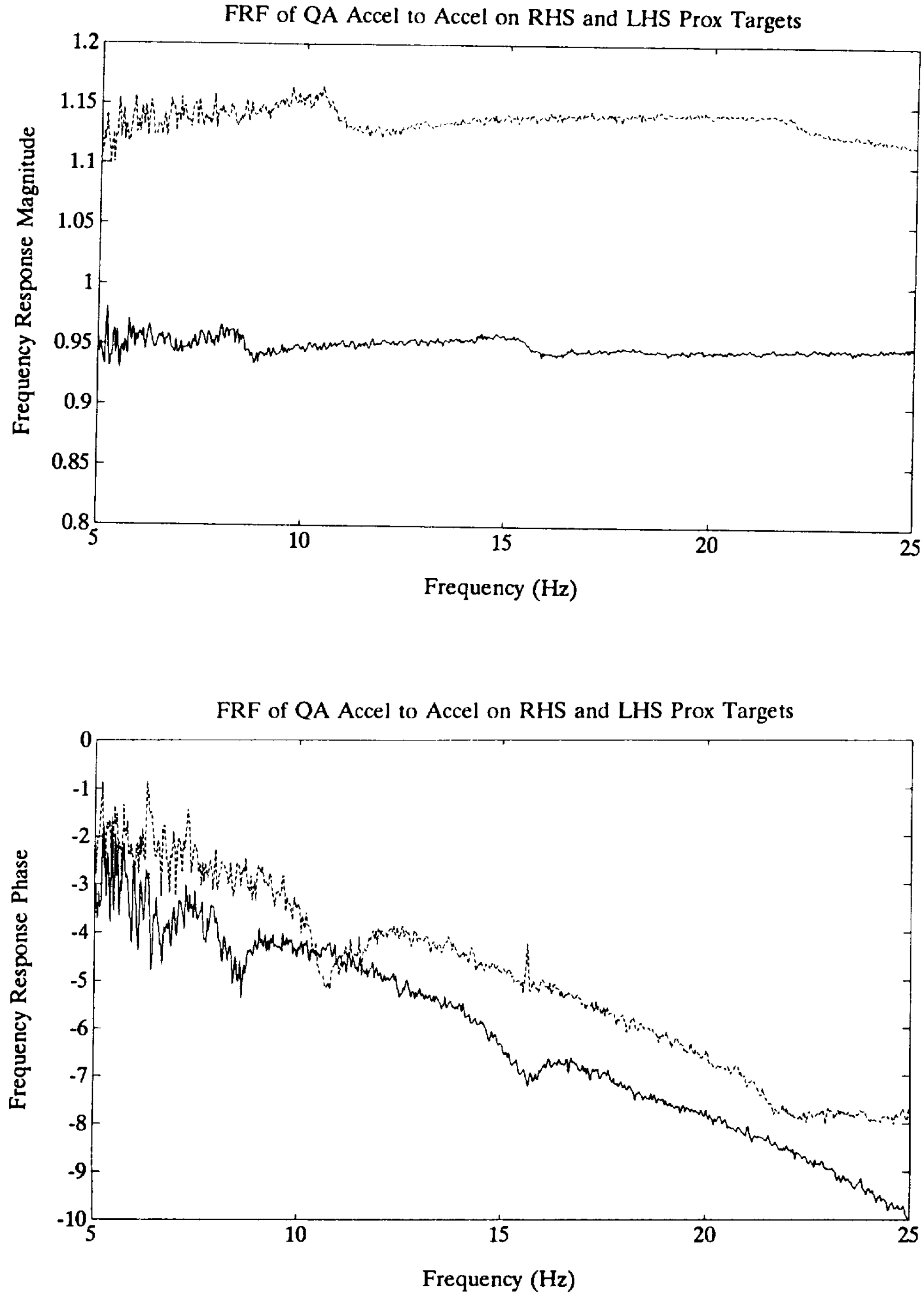

Figure I.20: QA Accel to RHS and LHS Accel Frequency Response

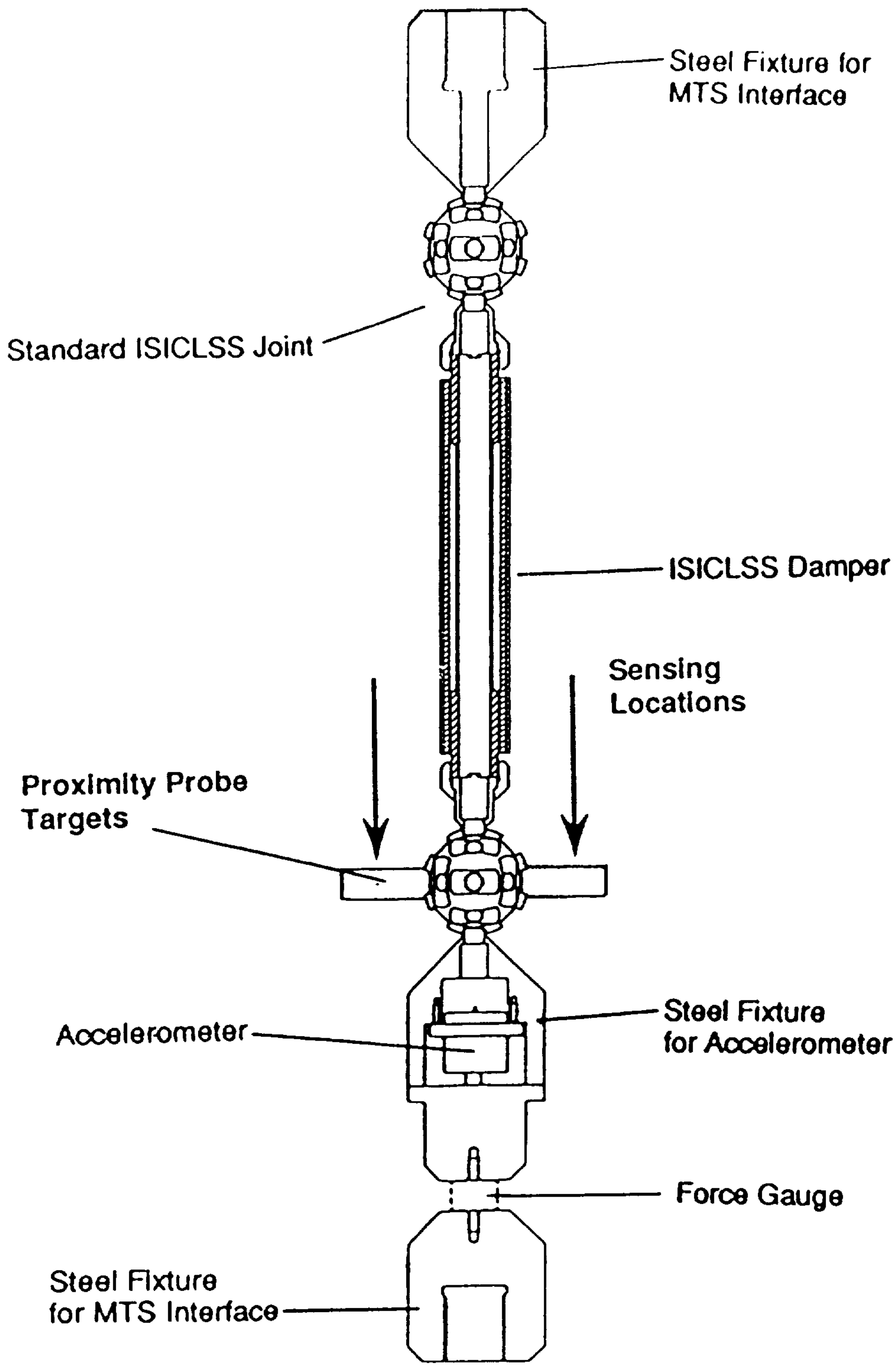

Figure I.21: Revised Test Setup Using Two Proximity Sensors

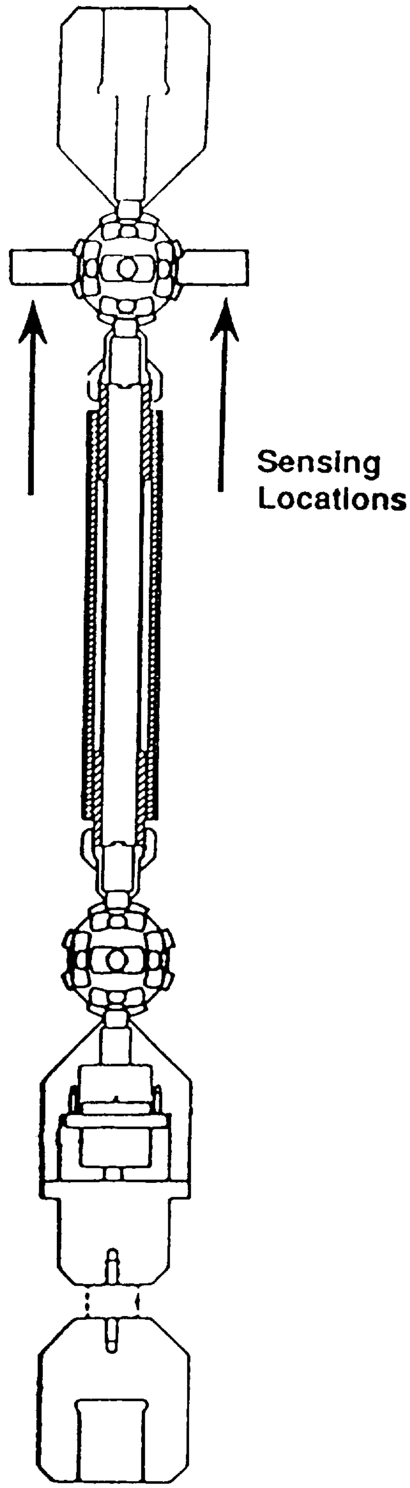

Figure I.22: Measurement of Fixture Impedance Using Two Sensors Phase 2 Test Results

Table I.4: Phase 2 Damper Failure Test Results

Failure Mode	Load (Lb)		
	Damper # 104	Damper # 126	Damper # 71
Sleeve-to-Clamshell Bond Failure	2300	2400	2600
Initial VEM/Epoxy Failure	2700	2900	3900
Center Tube Yield	2500	2600	3300
Center Tube Fracture	2900	3000	3500

then delivered to LARC for the Phase 2 system tests.

I.5 Conclusions

The test results show excellent unit-to-unit consistency of the dampers and good agreement with design predictions for damper modulus and loss factor. High sensitivity to temperature was expected due to the strong temperature dependency of DYAD 606 VEM and indeed was observed. The modified Phase 2 test setup and procedures provide an accurate measurements of the impedance of the damping members which were used to compute the expected damping for the Phase 2 CEM system tests.

Damper failure for all member types begins at over 2000 lb, and occurs gradually, thereby allowing discovery of the failure before any catastrophic failure occurs. Of particular importance is the consistency of bond failure loads and impedance data, indicating that the fabrication procedures control bond properties very well.

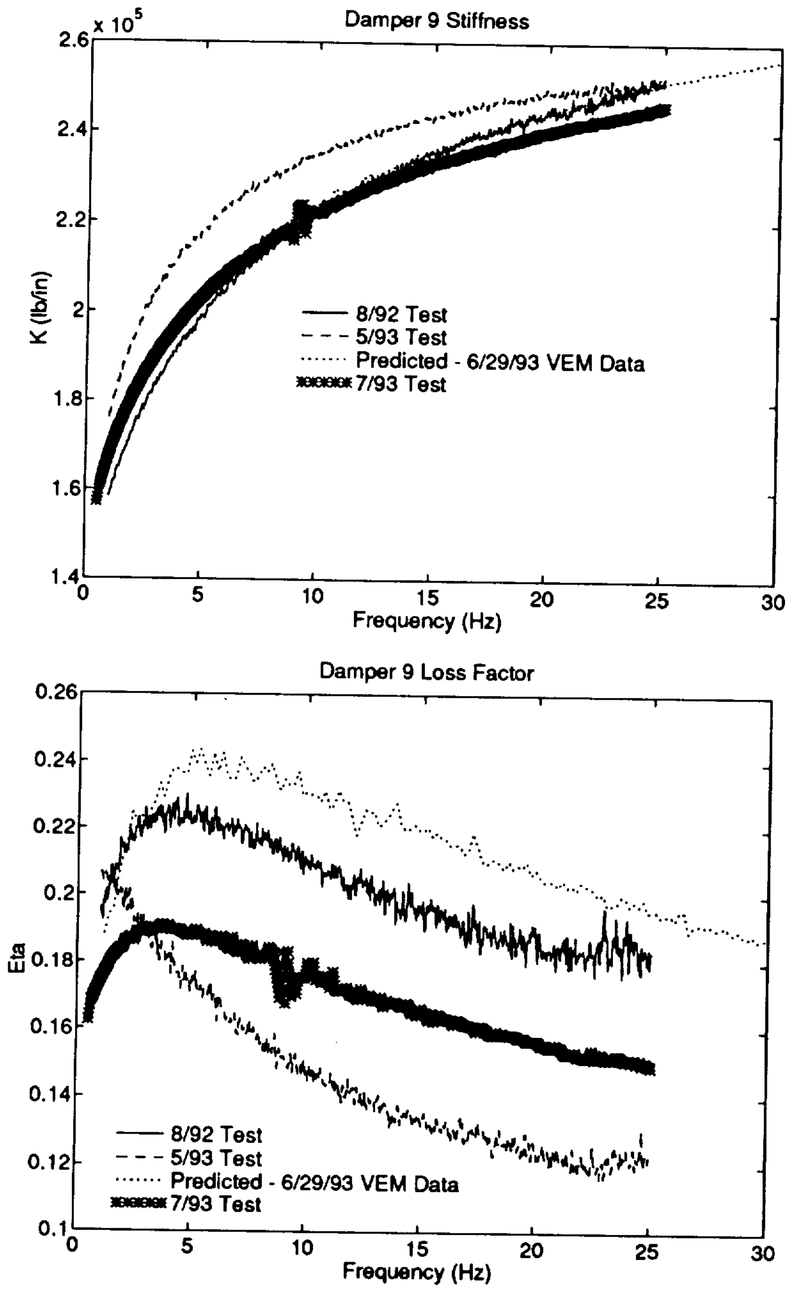

Figure I.23: Comparison of Stiffness and Loss Factor Data for Damper Unit #9

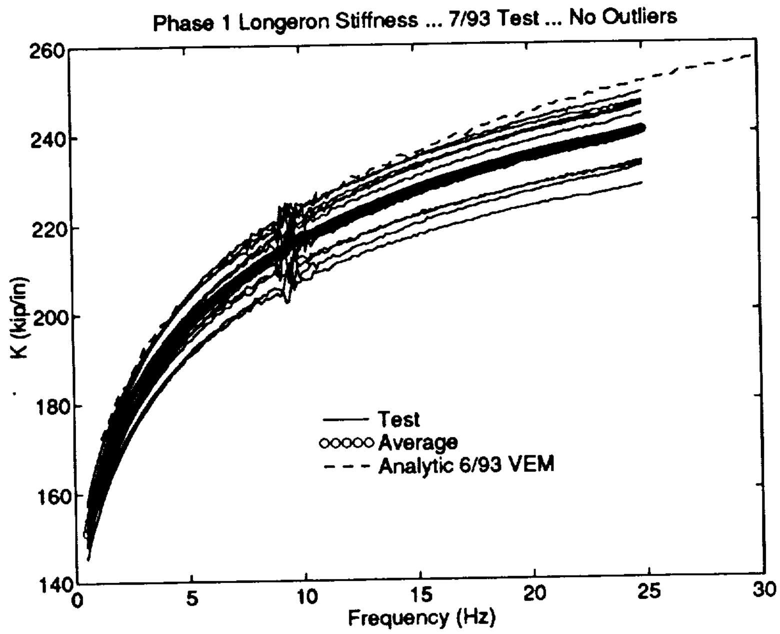

Figure I.24: Phase 1 Longeron Stiffnesses

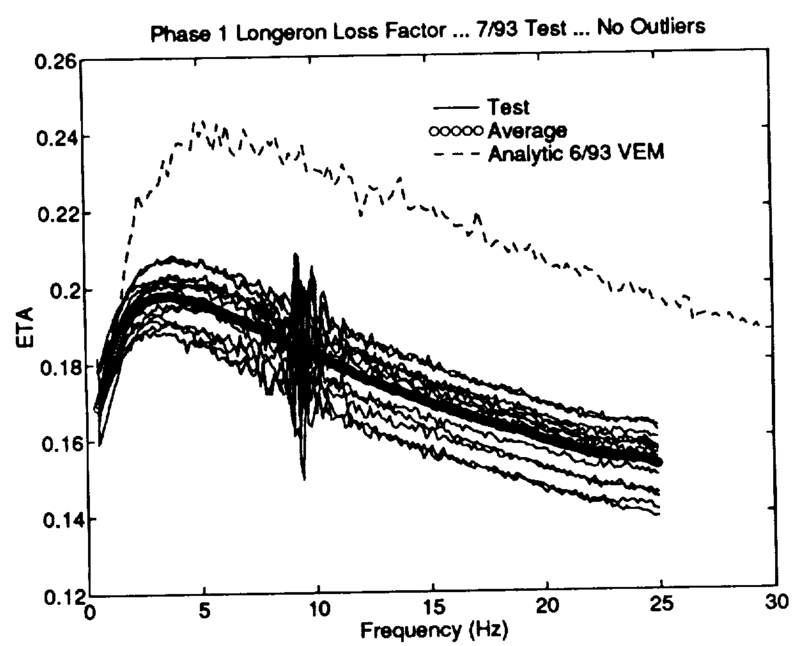

Figure I.25: Phase 1 Longeron Loss Factors

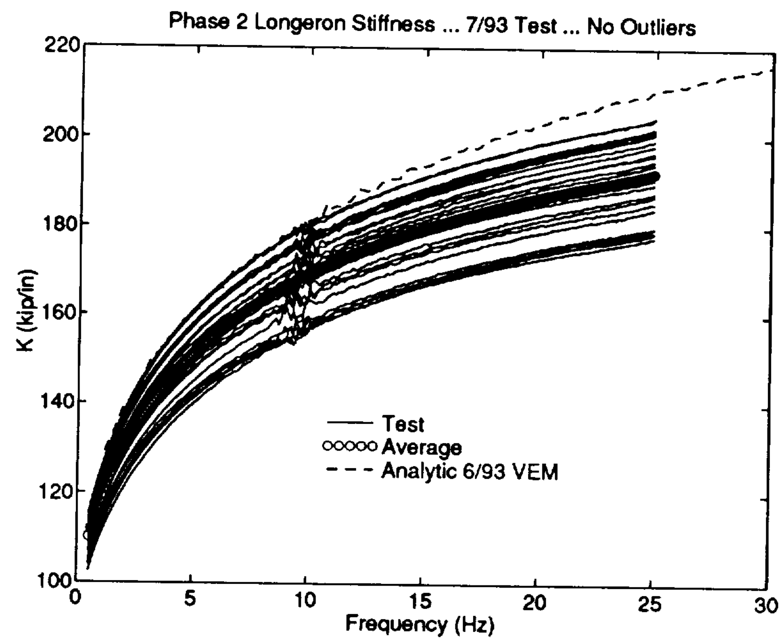

Figure I.26: Phase 2 Longeron Stiffnesses

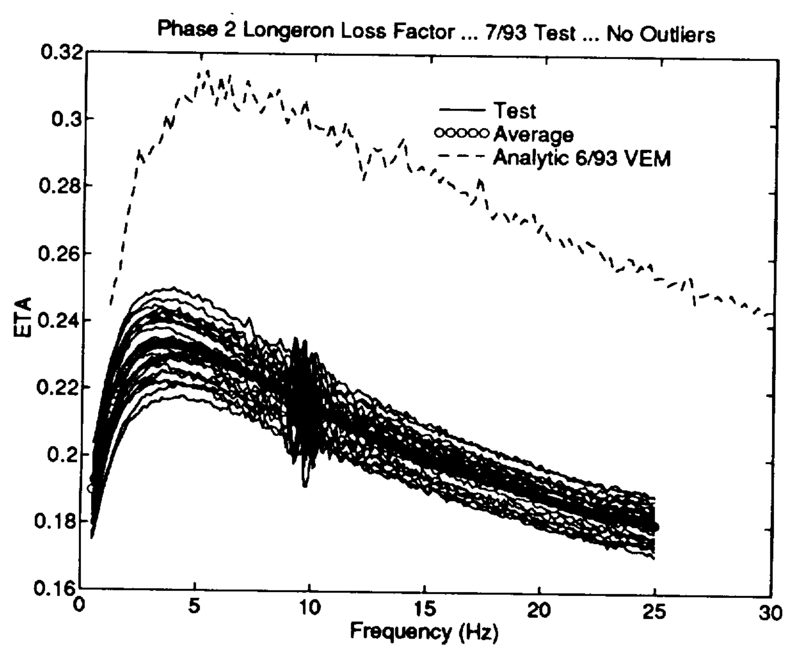

Figure I.27: Phase 2 Longeron Loss Factors

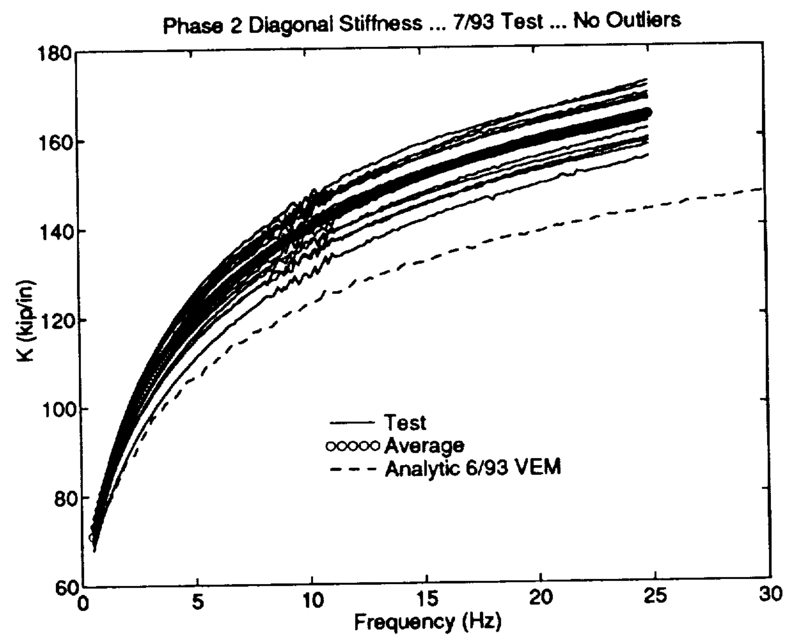

Figure I.28: Phase 2 Diagonal Stiffnesses

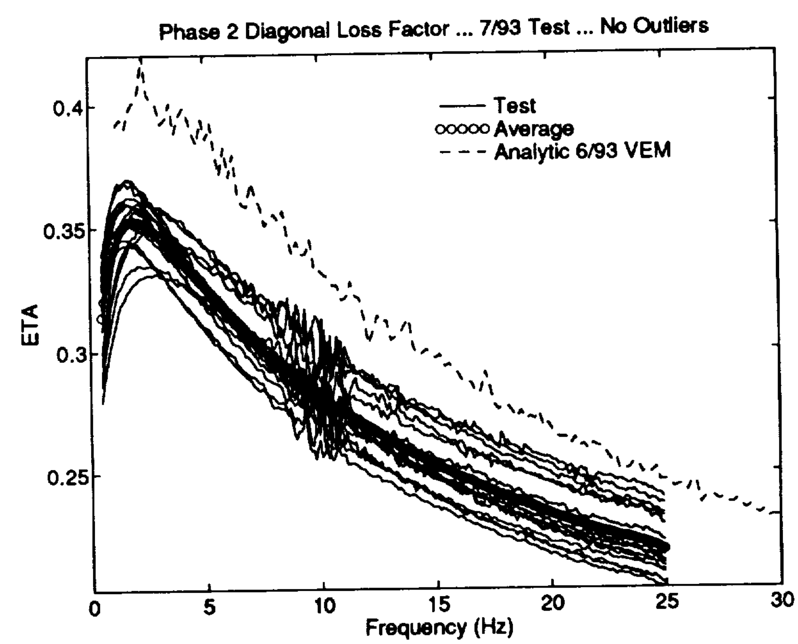

Figure I.29: Phase 2 Diagonal Loss Factors

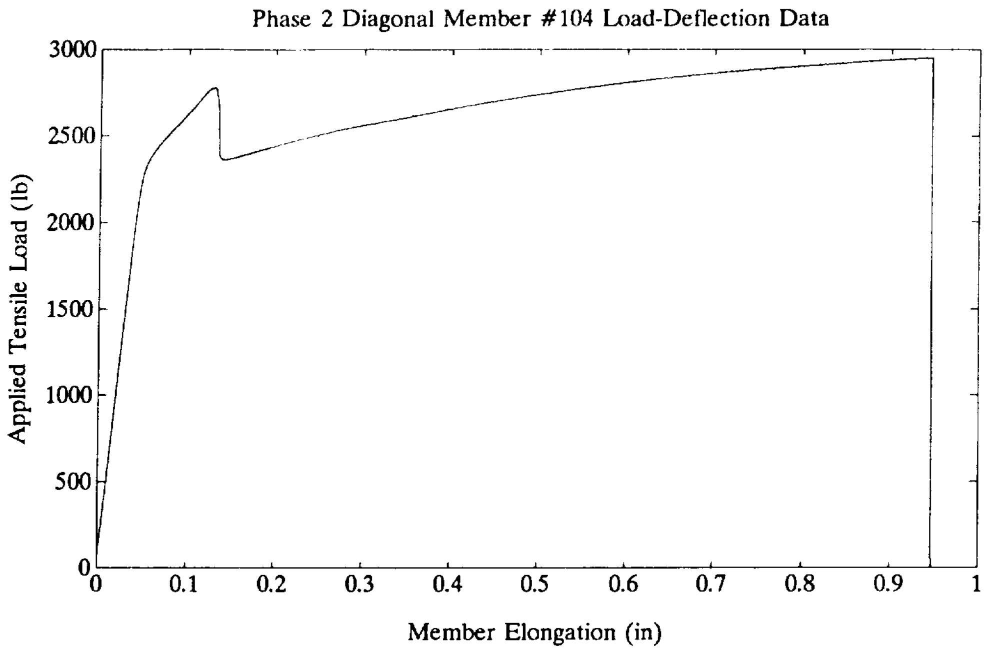

Figure I.30: Load Deflection Measurement for Damper Unit #104

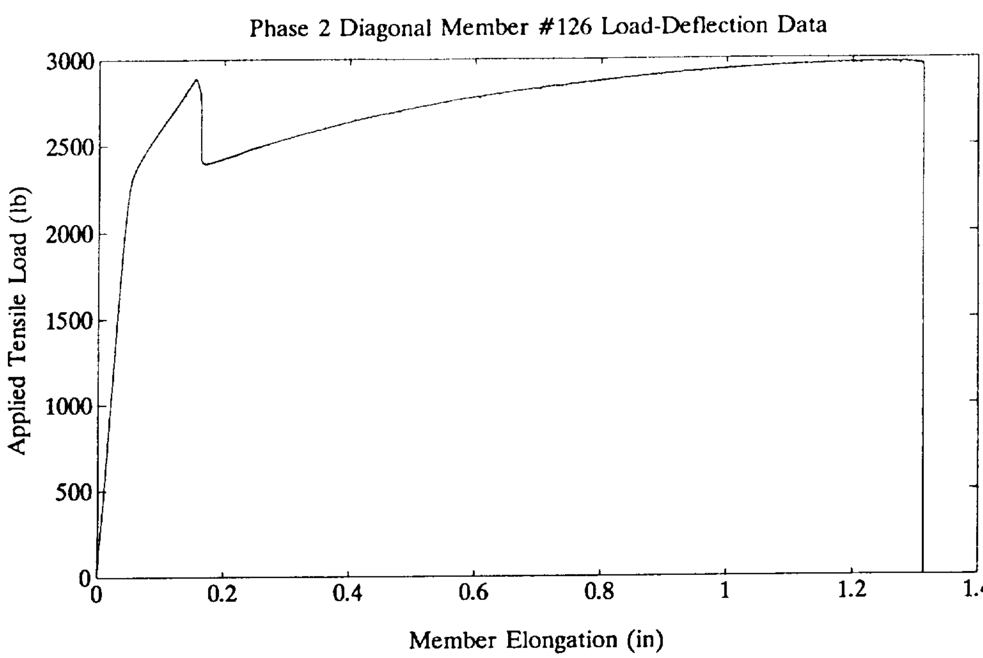

Figure I.31: Load Deflection Measurement for Damper Unit #126

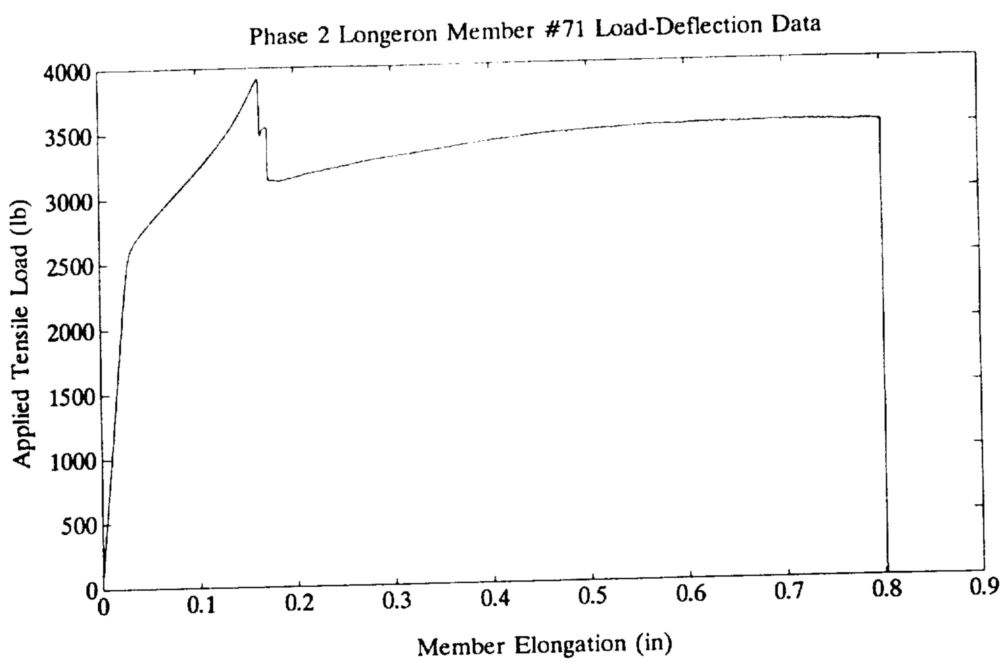

Figure I.32: Load Deflection Measurement for Damper Unit #71

Appendix J

Damped Struts Documentation

This appendix contains the design drawings for each type of damped struts fabricated for the CEM, including the Phase 1 longeron, the Phase 2 longeron and the Phase 2 diagonal dampers. For each damper type, sheet 1 is the assembly drawing; sheet 2 is inner strut drawing; sheet 3 is the drawing for the 2 clamshells; sheet 4 is the sleeve drawing.

Change not documented in the drawings:

For the Phase 2 longeron and diagonal dampers the external radius of the hub shown as 0.7620 in sheets 2 of the ISIC 3000 and 4000 drawings was adjusted down to 0.7610. This was done to accomodate the tolerances on the aluminum tubing stock purchased to manufacture the Phase 2 damper sleeves.

REV	ZONE	DESCRIPTION	DATE	APPROVED
A	C-4	ADDED MORE INFORMATION ABOUT BONDING TO NOTE 6	11-2-92	
A	C-2	VEM WIDTH INCREASED FROM 1.000 TO 1.100	11-2-92	

NOTES:

1. INTERPRET DRAWING IN ACCORDANCE WITH ANSI Y14.5
2. INSIDE CORNER (FILLET) RADII ARE .020 MAX. UNLESS SPECIFIED OTHERWISE
3. REMOVE BURRS AND BREAK SHARP CORNERS

4▷ FINISH: IRIDITE PER EPS 30063, TYPE II

5▷ FINISH: GOLD ANODIZE PER MIL-A-8625, TYPE II, CLASS 2

6▷ APPLY EPOXY PER MANUFACTURER'S INSTUCTIONS FROM PRODUCT SPECIFICATION SHEET. APPLY EPOXY TO FLAT METAL SURFACE FIRST, AND THEN TO SURFACES TO BE BONDED BY ROLLING ON APPLIED AREA. MINIMUM BOND THICKNESS FOR FULL PART COVERAGE IS DESIRED

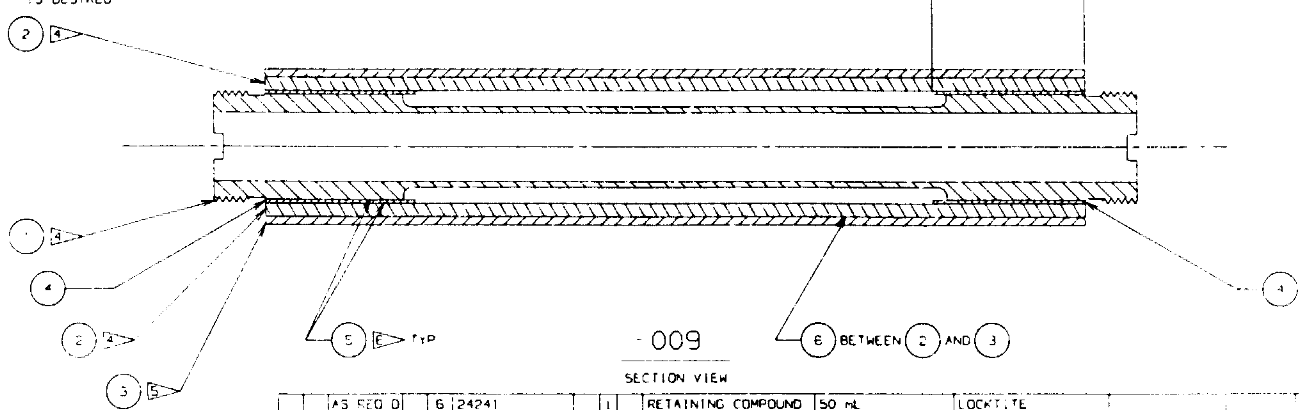

-009

SECTION VIEW

QUANTITY/DASH NO				FIND NO	PART NO	ZONE	SH	SER SYM	DESCRIPTION	STOCK SIZE	MATERIAL OR VENDOR	MATERIAL SPECIFICATION	MATERIAL CODE	FINISH OR MFR CODE	REV
		AS REQ D		6	24241		1		RETAINING COMPOUND	50 mL	LOCKTITE				
		AS REQ D		5	1838B/A GREEN		1		EPOXY, TWO PART	3.6 FL OZ	3M				
		AS REQ D		4	DTOA 606		1		VISCOELASTIC MAT'L	.023 THICK	SOUNDCOAT DYAD				
		1		3	ISIC 1001-003		4		SLEEVE, COVER	Ø1.125 X .058W	2024-T3 ALUM			5▷	
		2		2	ISIC 1001-002		3		SHELL, HALF	Ø1.000 X .095W	2024-T3 ALUM			4▷	
		1		1	ISIC 1001-001		2		STRUT, THIN SECTION	Ø.875 X .188W	2024-T3 ALUM			4▷	
		009													

LIST OF MATERIAL

DASH NUMBER	NEXT ASSY	USED ON	FINAL ASSY	TEST
-009	LNG 590-000	CSI TRUSS	12	4
	APPLICATION		QTY REQD	

INTERPRET DWG PER DOD-STD-100. UNLESS OTHERWISE SPECIFIED DIMENSIONS ARE IN INCHES AND ARE AFTER PLATING. TOLERANCES ON: DECIMALS .X ±.1, .XX ±.03, .XXX ±.010; ANGLES ±.5

MACHINED SURFACES 32√

DRAWN BY SCOTT MICKEY, DEPT 3312, DATE 06-22-92
CHECKER
CP ENGR
PROJECT
RELEASE DATE
CONTRACT NO 203631

3RD ANG PROJ

MARTIN MARIETTA
ASTRONAUTICS GROUP, POB 179, DENVER, COLORADO 80201

ISICLSS

DAMPED STRUT - PHASE I

SIZE C | FSCM NO 04236 | DRAWING NO ISIC 1001 | REV A

SCALE 2/1 | SHEET 1 OF 4

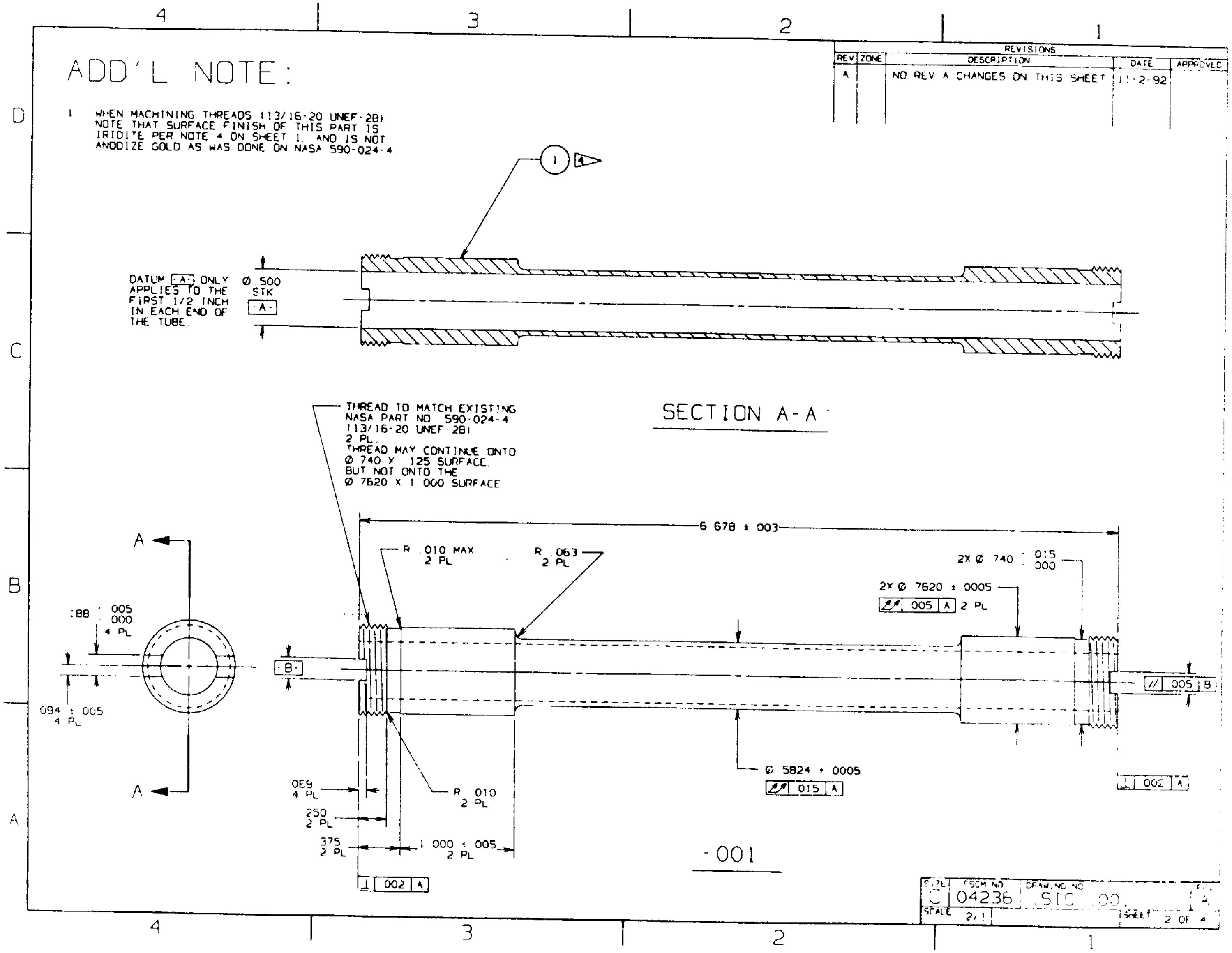

ADD'L NOTE:
1 WHEN MACHINING THREADS (13/16-20 UNEF-2B) NOTE THAT SURFACE FINISH OF THIS PART IS IRIDITE PER NOTE 4 ON SHEET 1. AND IS NOT ANODIZE GOLD AS WAS DONE ON NASA 590-024-4.
REVISIONS
REV ZONE DESCRIPTION DATE APPROVED
A NO REV A CHANGES ON THIS SHEET 11-2-92
DATUM -A- ONLY APPLIES TO THE FIRST 1/2 INCH IN EACH END OF THE TUBE.
Ø .500 STK -A-
SECTION A-A
THREAD TO MATCH EXISTING NASA PART NO. 590-024-4 (13/16-20 UNEF-2B) 2 PL. THREAD MAY CONTINUE ONTO Ø .740 X .125 SURFACE. BUT NOT ONTO THE Ø .7620 X 1.000 SURFACE
6.678 ± .003
R .010 MAX 2 PL
R .063 2 PL
2X Ø .740 +.015 -.000
2X Ø .7620 ± .0005 .005 A 2 PL
.188 +.005 -.000 4 PL
.094 ± .005 4 PL
-B-
// .005 B
Ø .5824 ± .0005 .015 A
⊥ .002 A
.063 4 PL
.250 2 PL
.375 2 PL
R .010 2 PL
1.000 ± .005 2 PL
⊥ .002 A
-001
SIZE C FSCM NO 04236 DRAWING NO SIC .001 REV A
SCALE 2/1 SHEET 2 OF 4

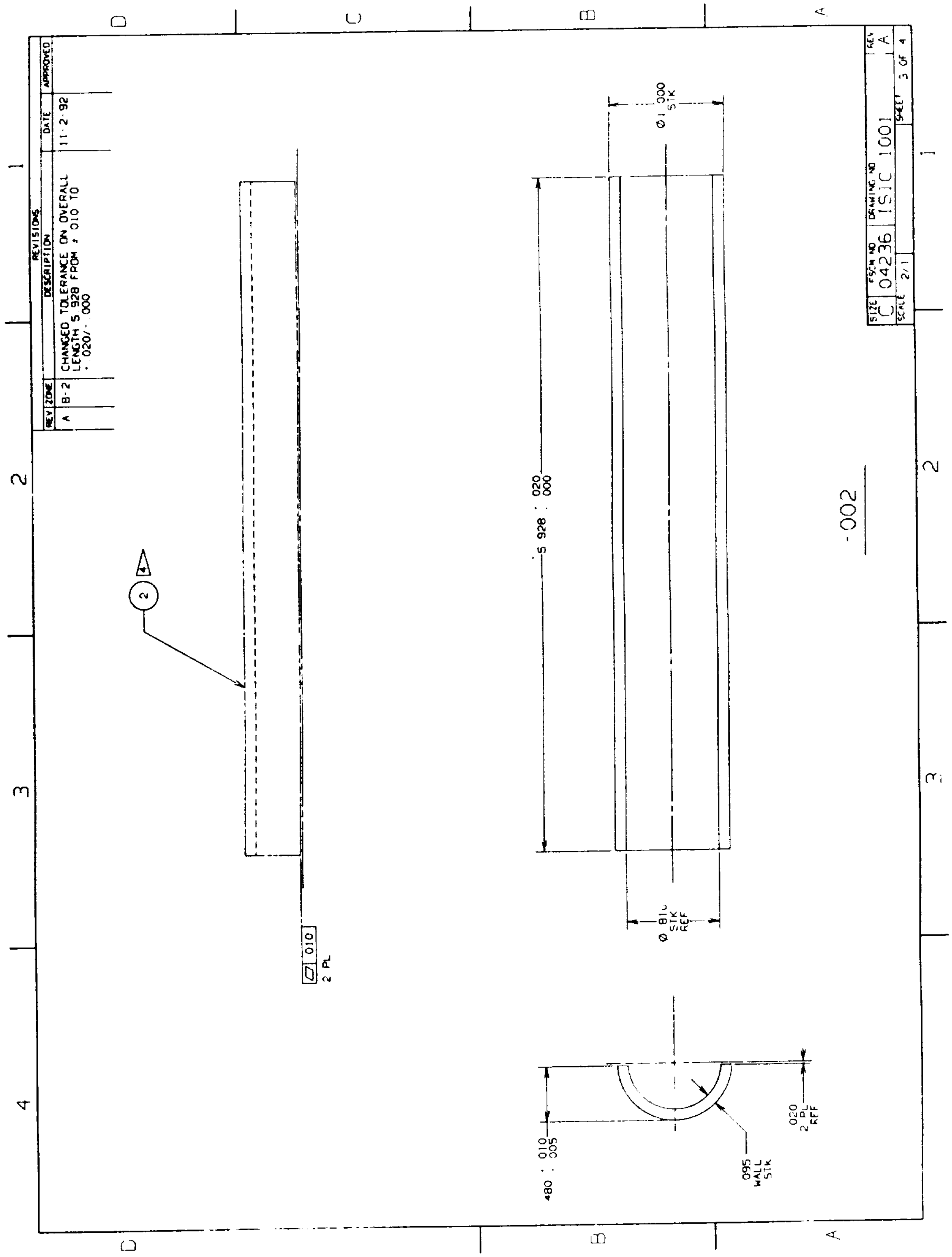
REVISIONS
REV
ZONE
DESCRIPTION
DATE
APPROVED
A
B-2
CHANGED TOLERANCE ON OVERALL LENGTH 5.928 FROM ±.010 TO +.020/-.000
11-2-92
-002
SIZE
C
FSCM NO
04236
DRAWING NO
ISIC 1001
REV
A
SCALE
2/1
SHEET
3 OF 4
2 PL
.095 WALL STK
.020 2 PL REF

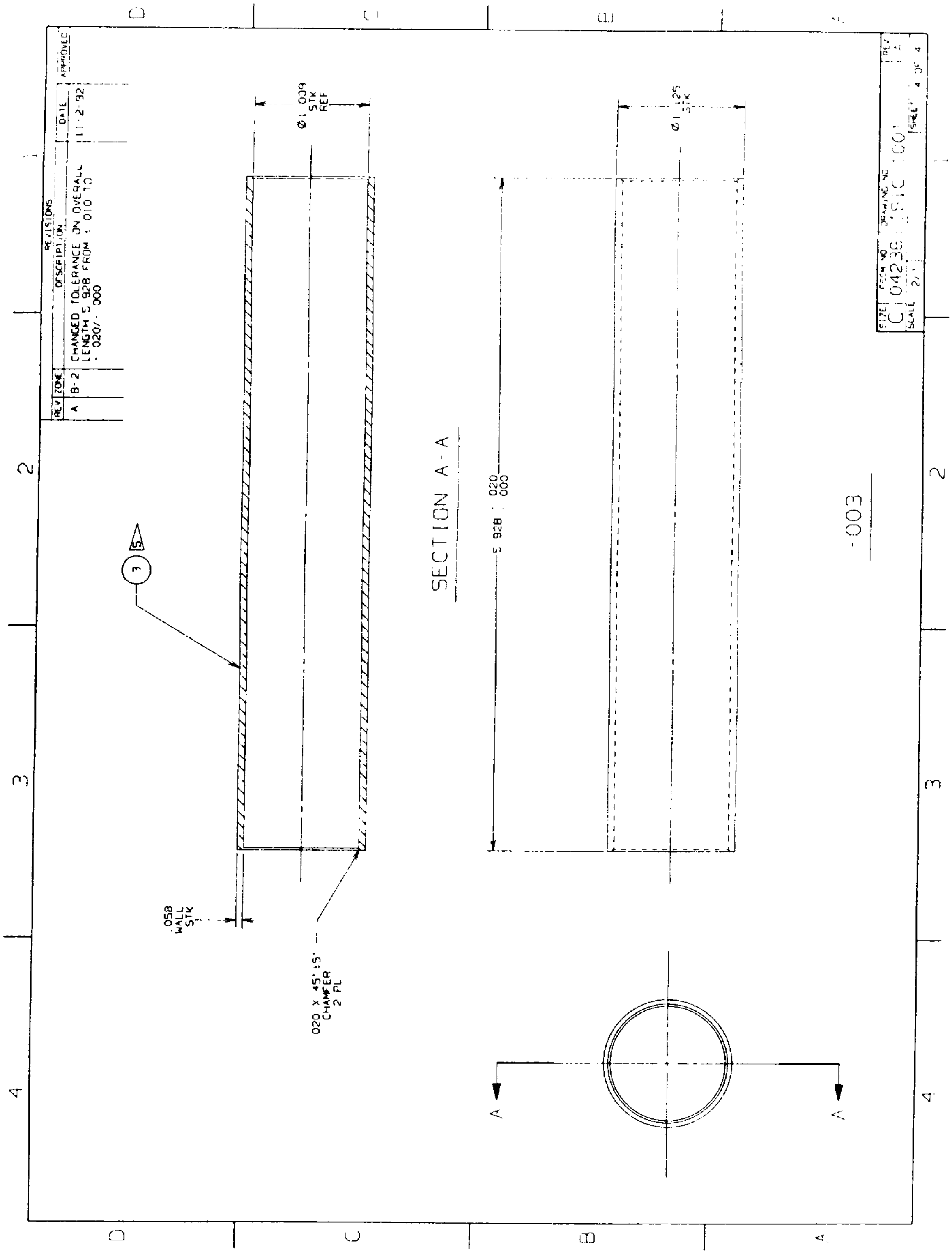
REVISIONS
REV ZONE DESCRIPTION DATE APPROVED
A B-2 CHANGED TOLERANCE ON OVERALL LENGTH 5.928 FROM ±.010 TO +.020/-.000 11-2-92
.058 WALL STK
.020 X 45°±5° CHAMFER 2 PL
Ø1.009 STK REF
SECTION A-A
5.928 +.020 -.000
Ø1.125 STK
A
A
-003
SIZE C
FSCM NO 04236
DRAWING NO
SCALE 2/1
REV A
SHEET 4 OF 4

NOTES:

1. INTERPRET DRAWING IN ACCORDANCE WITH ANSI Y14.5
2. INSIDE CORNER (FILLET) RADII ARE .020 MAX. UNLESS SPECIFIED OTHERWISE.
3. REMOVE BURRS AND BREAK SHARP CORNERS.

4 FINISH: IRIDITE PER EPS 30063, TYPE II.

5 FINISH: BLACK ANODIZE PER MIL-A-8625, TYPE II, CLASS 2.

6 APPLY EPOXY PER MANUFACTURER'S INSTUCTIONS FROM PRODUCT SPECIFICATION SHEET. APPLY EPOXY TO FLAT METAL SURFACE FIRST, AND THEN TO SURFACES TO BE BONDED BY ROLLING ON APPLIED AREA. MINIMUM BOND THICKNESS FOR FULL PART COVERAGE IS DESIRED.

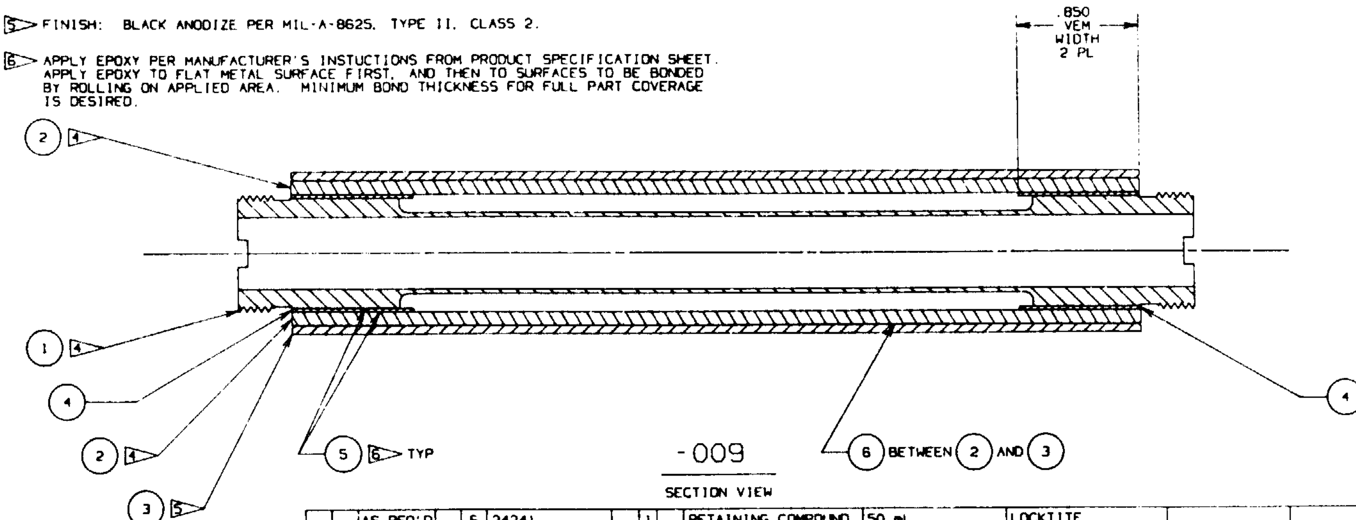

-009
SECTION VIEW

QUANTITY/DASH NO	FIND NO	PART NO	ZONE	SH	SER STR	DESCRIPTION	STOCK SIZE	MATERIAL OR VENDOR	MATERIAL SPECIFICATION	MATERIAL CODE	FINISH OR MFR CODE
AS REQ'D	6	24241		1		RETAINING COMPOUND	50 mL	LOCKTITE			
AS REQ'D	5	18388/A GREEN		1		EPOXY, TWO PART	3.6 FL OZ	3M			
AS REQ'D	4	DTOA 606		1		VISCOELASTIC MAT'L	.023 THICK	SOUNDCOAT DYAD			
1	3	ISIC 3000-003		4		SLEEVE, COVER	Ø1.125 X .058W	2024-T3 ALUM			5
2	2	ISIC 3000-002		3		SHELL, HALF	Ø1.000 X .095W	2024-T3 ALUM			4
1	1	ISIC 3000-001		2		STRUT, THIN SECTION	Ø.875 X .188W	2024-T3 ALUM			4
009											

LIST OF MATERIAL

DASH NUMBER	NEXT ASSY	USED ON	FINAL ASSY	TEST
-009	LNG 590-000	CSI TRUSS	52	10
	APPLICATION		QTY REQD	

INTERPRET DWG PER DOD-STD-100. UNLESS OTHERWISE SPECIFIED DIMENSIONS ARE IN INCHES AND ARE AFTER PLATING

TOLERANCES ON:

DECIMALS .X	.XX	.XXX	ANGLES
±.1	±.03	±.010	±.5

MACHINED SURFACES 32√

DRAWN BY | DEPT | DATE
CHECKER
GP ENGR
PROJECT
3RD ANG PROJ
RELEASE DATE
CONTRACT NO 203631

MARTIN MARIETTA
ASTRONAUTICS GROUP, POB 179, DENVER, COLORADO 80201

ISICLSS
DAMPED LONGERON - PHASE 2

SIZE C | FSCM NO 04236 | DRAWING NO ISIC 3000 | REV -
SCALE 2/1 | SHEET 1 OF 4

REVISIONS: REV | ZONE | DESCRIPTION | DATE | APPROVED

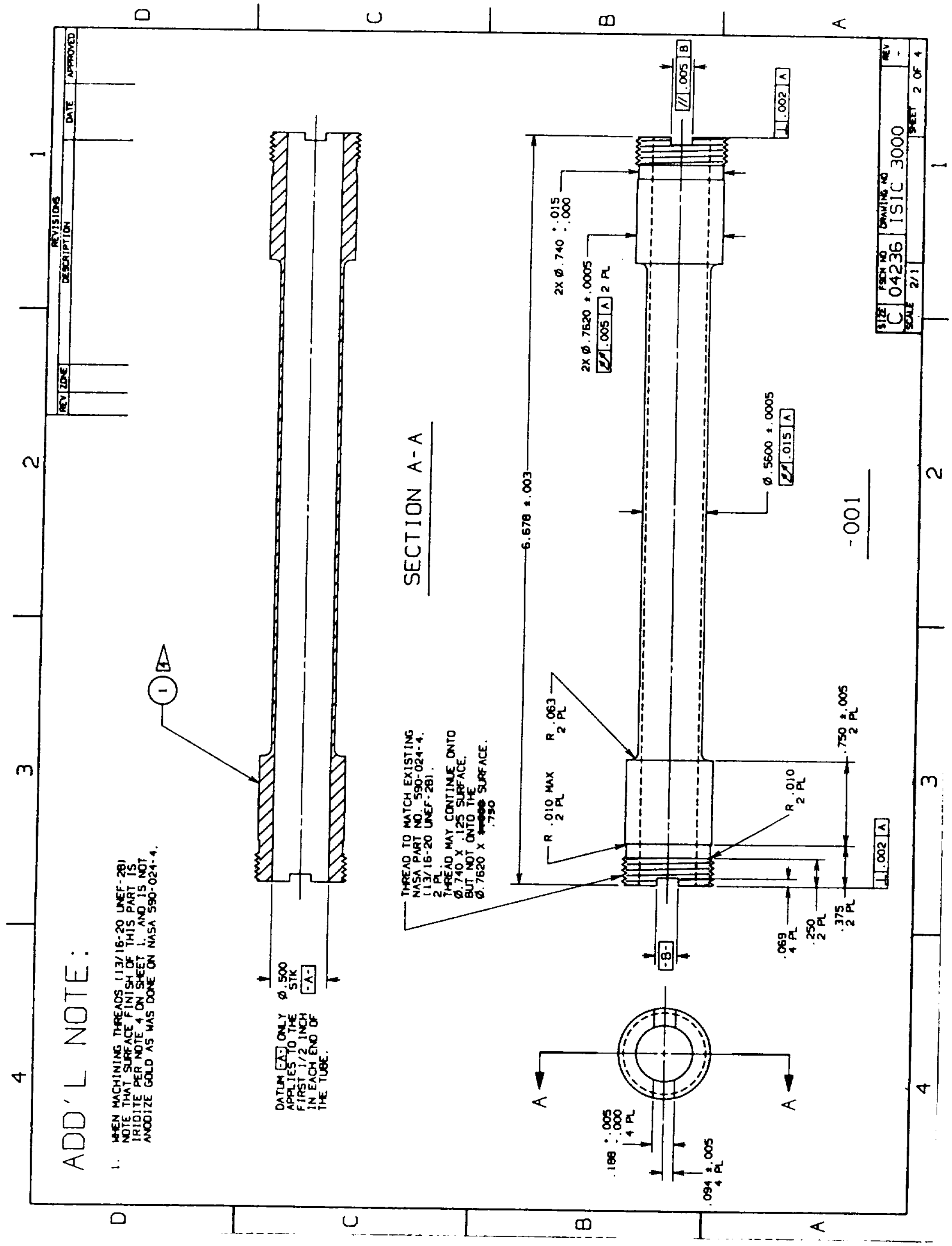
ADD'L NOTE:
1. WHEN MACHINING THREADS (13/16-20 UNEF-28) NOTE THAT SURFACE FINISH OF THIS PART IS IRIDITE PER NOTE 4 ON SHEET 1. AND IS NOT ANODIZE GOLD AS WAS DONE ON NASA 590-024-4.
DATUM -A- ONLY APPLIES TO THE FIRST 1/2 INCH IN EACH END OF THE TUBE.
Ø.500 STK -A-
SECTION A-A
THREAD TO MATCH EXISTING NASA PART NO. 590-024-4. (13/16-20 UNEF-28). 2 PL.
THREAD MAY CONTINUE ONTO Ø.740 X .125 SURFACE, BUT NOT ONTO THE Ø.7620 X .750 SURFACE.
R .010 MAX 2 PL
R .063 2 PL
R .010 2 PL
6.678 ± .003
.750 ± .005 2 PL
.069 4 PL
.250 2 PL
.375 2 PL
-B-
.188 +.005 -.000 4 PL
.094 ± .005 4 PL
2X Ø.740 +.015 -.000
2X Ø.7620 ± .0005 .005 A 2 PL
Ø.5600 ± .0005 .015 A
.002 A
// .005 B
-001
REVISIONS
REV ZONE DESCRIPTION DATE APPROVED
SIZE C FSCM NO 04236 DRAWING NO ISIC 3000 REV -
SCALE 2/1 SHEET 2 OF 4

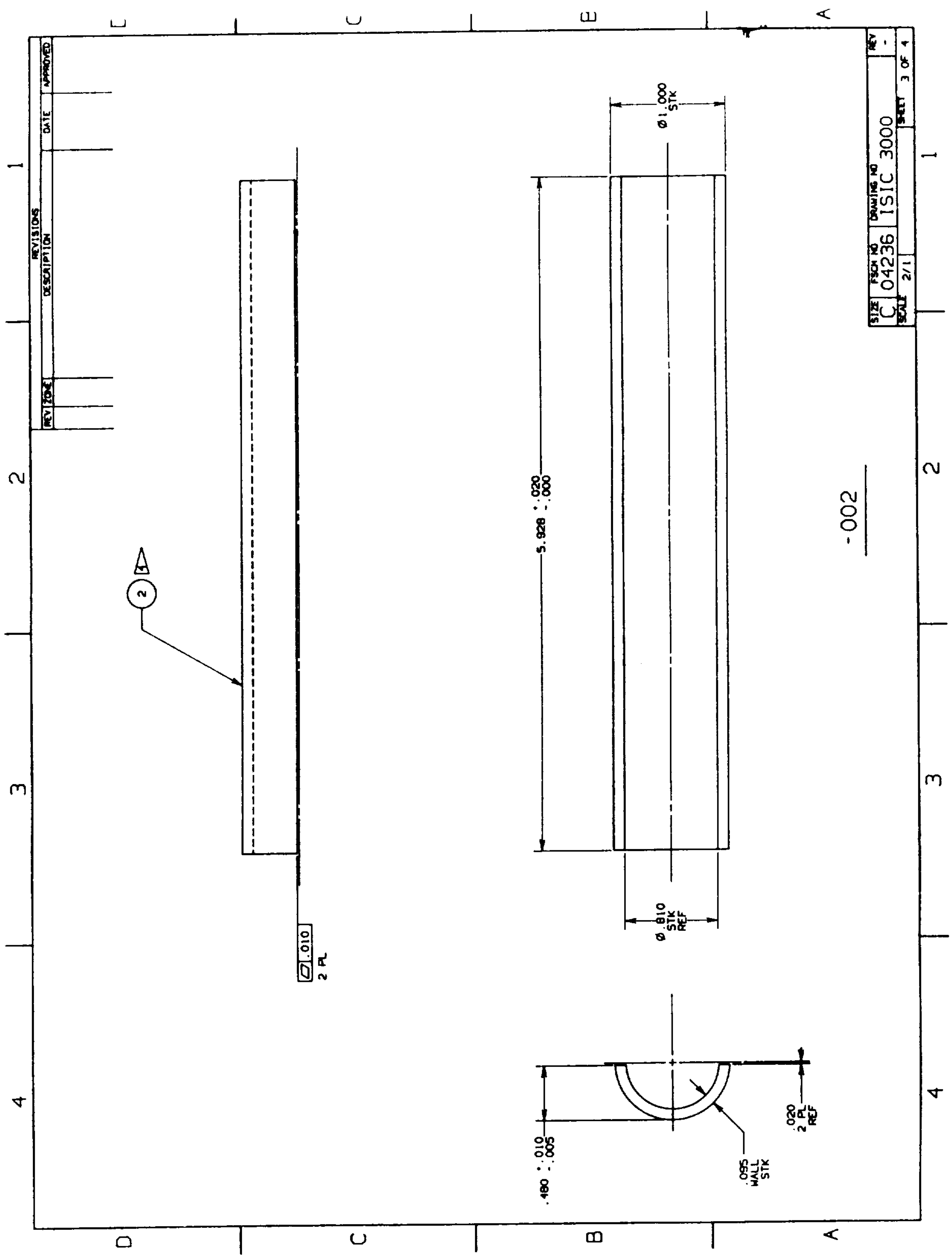
REVISIONS
REV
ZONE
DESCRIPTION
DATE
APPROVED
SIZE
C
FSCM NO
04236
DRAWING NO
ISIC 3000
REV
-
SCALE 2/1
SHEET 3 OF 4
-002
5.928 +.020 -.000
Ø 1.000 STK
Ø .810 STK REF
.010
2 PL
2
.480 +.010 -.005
.095 WALL STK
.020 2 PL REF
1
2
3
4
A
B
C
D

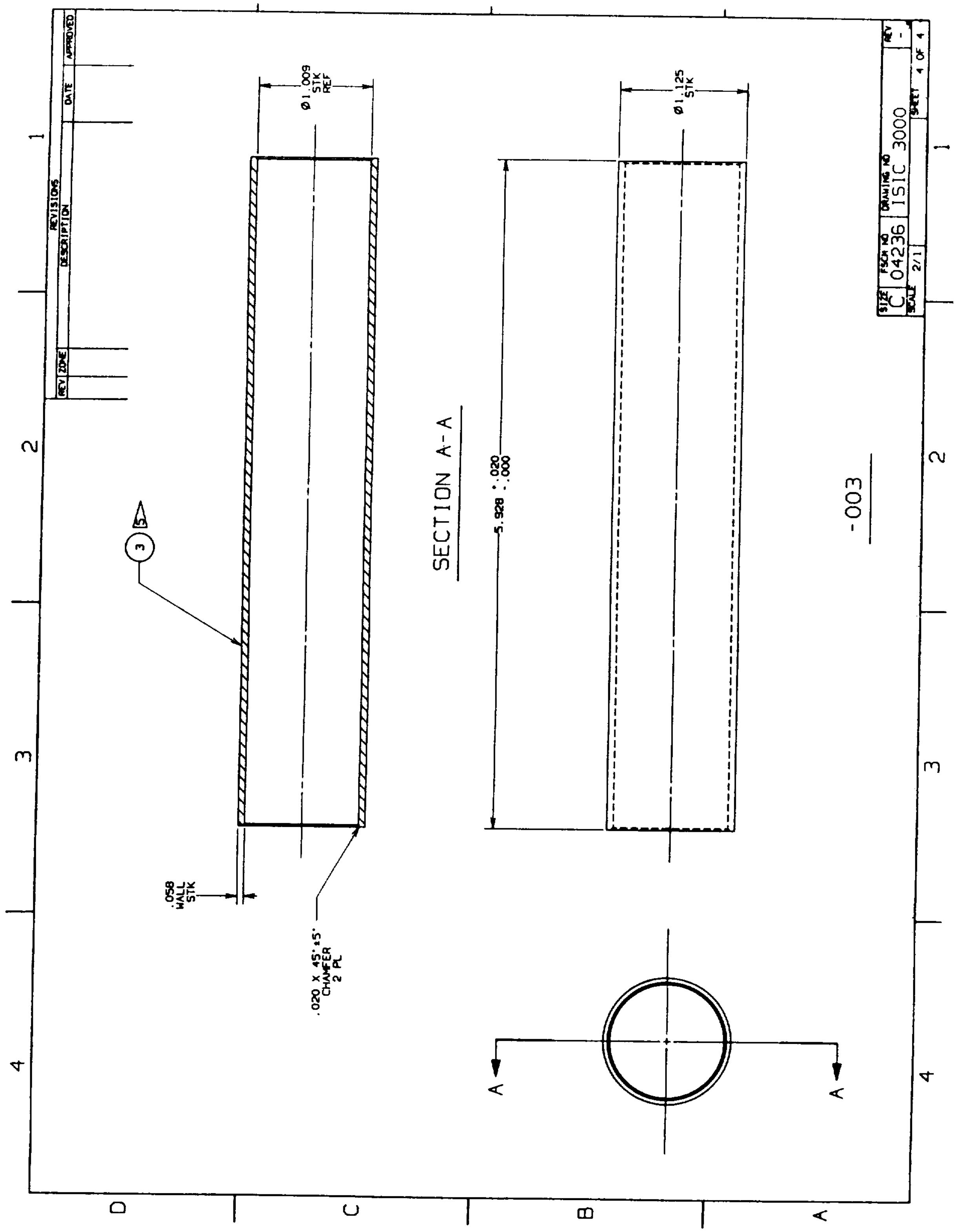

REVISIONS
REV
ZONE
DESCRIPTION
DATE
APPROVED
Ø1.009 STK REF
Ø1.125 STK
3
5
SECTION A-A
5.928 +.020 -.000
-003
.058 WALL STK
.020 X 45°±5° CHAMFER 2 PL
A
A
SIZE C
FSCM NO 04236
DRAWING NO ISIC 3000
REV -
SCALE 2/1
SHEET 4 OF 4

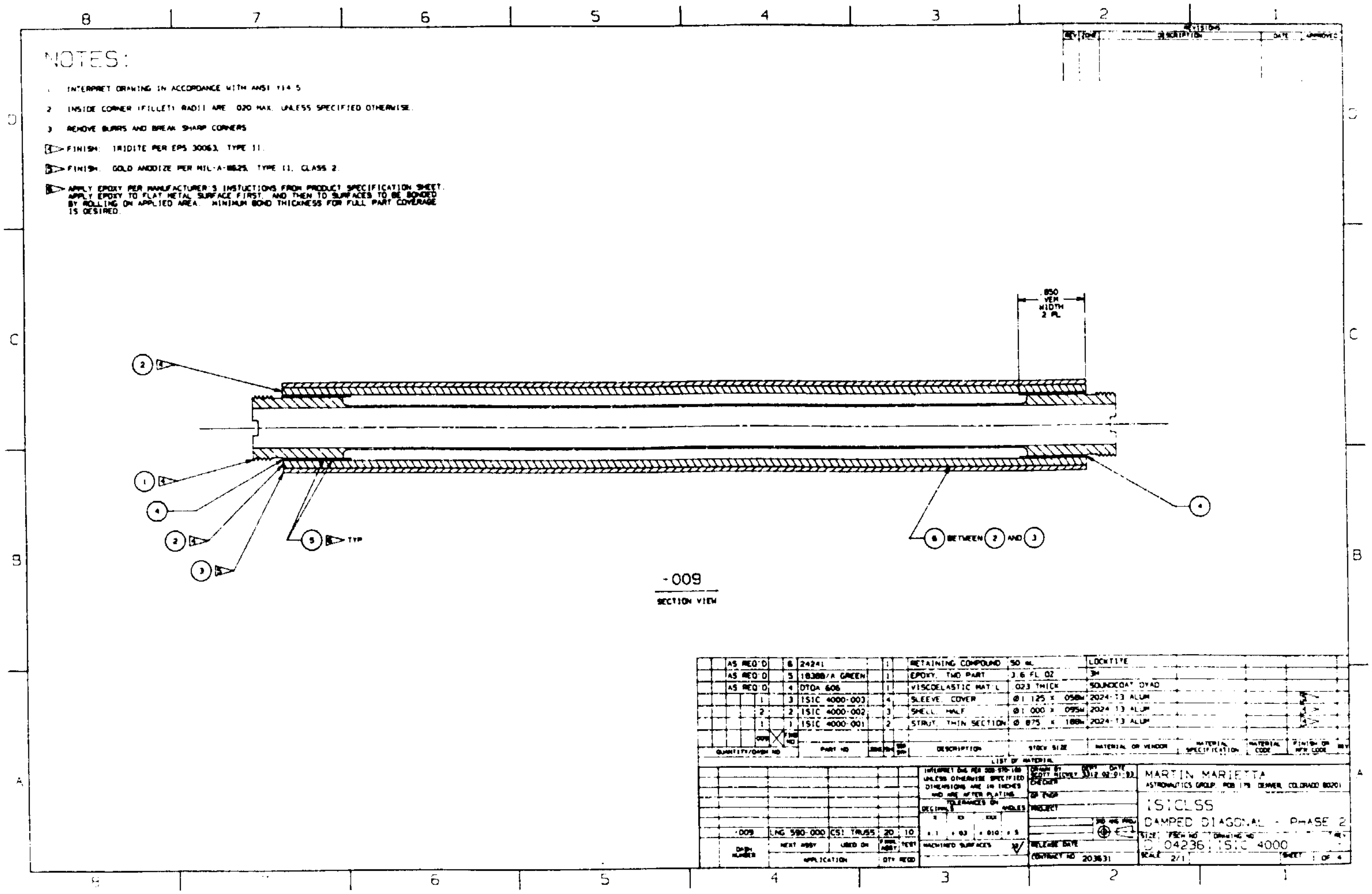
NOTES:
1 INTERPRET DRAWING IN ACCORDANCE WITH ANSI Y14.5
2 INSIDE CORNER (FILLET) RADII ARE .020 MAX. UNLESS SPECIFIED OTHERWISE.
3 REMOVE BURRS AND BREAK SHARP CORNERS
FINISH: IRIDITE PER EPS 30063, TYPE II.
FINISH: GOLD ANODIZE PER MIL-A-8625, TYPE II, CLASS 2.
APPLY EPOXY PER MANUFACTURER'S INSTUCTIONS FROM PRODUCT SPECIFICATION SHEET. APPLY EPOXY TO FLAT METAL SURFACE FIRST, AND THEN TO SURFACES TO BE BONDED BY ROLLING ON APPLIED AREA. MINIMUM BOND THICKNESS FOR FULL PART COVERAGE IS DESIRED.
.850 WIDTH 2 PL
TYP
BETWEEN 2 AND 3
-009
SECTION VIEW
AS REQ'D 6 24241 RETAINING COMPOUND 50 ML LOCKTITE
AS REQ'D 5 18388/A GREEN EPOXY, TWO PART 3.6 FL OZ 3M
AS REQ'D 4 DTOA 606 VISCOELASTIC MAT'L .023 THICK SOUNDCOAT DYAD
1 3 ISIC 4000-003 SLEEVE, COVER Ø1.125 X .058W 2024-T3 ALUM
2 2 ISIC 4000-002 SHELL, HALF Ø1.000 X .095W 2024-T3 ALUM
1 1 ISIC 4000-001 STRUT, THIN SECTION Ø.875 X .188W 2024-T3 ALUM
QUANTITY/DASH NO
PART NO
DESCRIPTION
STOCK SIZE
MATERIAL OR VENDOR
MATERIAL SPECIFICATION
MATERIAL CODE
FINISH OR MFR CODE
LIST OF MATERIAL
-009 LNG 590-000 CSI TRUSS 20 10
DASH NUMBER
NEXT ASSY
USED ON
APPLICATION
QTY REQD
INTERPRET DWG PER 500-STD-100 UNLESS OTHERWISE SPECIFIED DIMENSIONS ARE IN INCHES AND ARE AFTER PLATING
TOLERANCES ON
DECIMALS
ANGLES
MACHINED SURFACES
DRAWN BY SCOTT
DATE
CHECKER
PROJECT
RELEASE DATE
CONTRACT NO 203631
MARTIN MARIETTA
ASTRONAUTICS GROUP, POB 179 DENVER, COLORADO 80201
ISICLSS
DAMPED DIAGONAL - PHASE 2
SIZE D
FSCM NO 04236
DRAWING NO ISIC 4000
SCALE 2/1
SHEET 1 OF 4

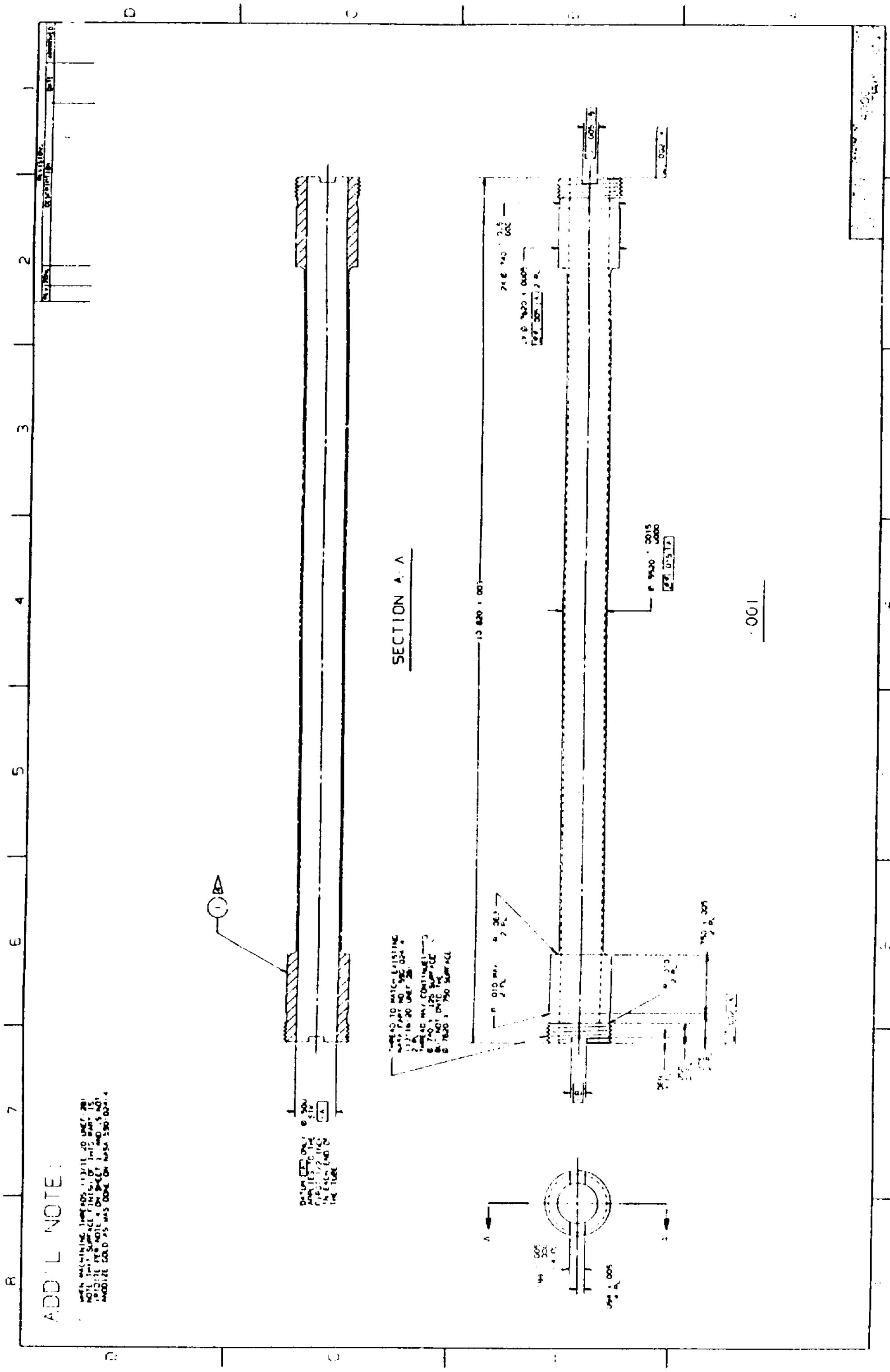
ADD'L NOTES
SECTION A-A

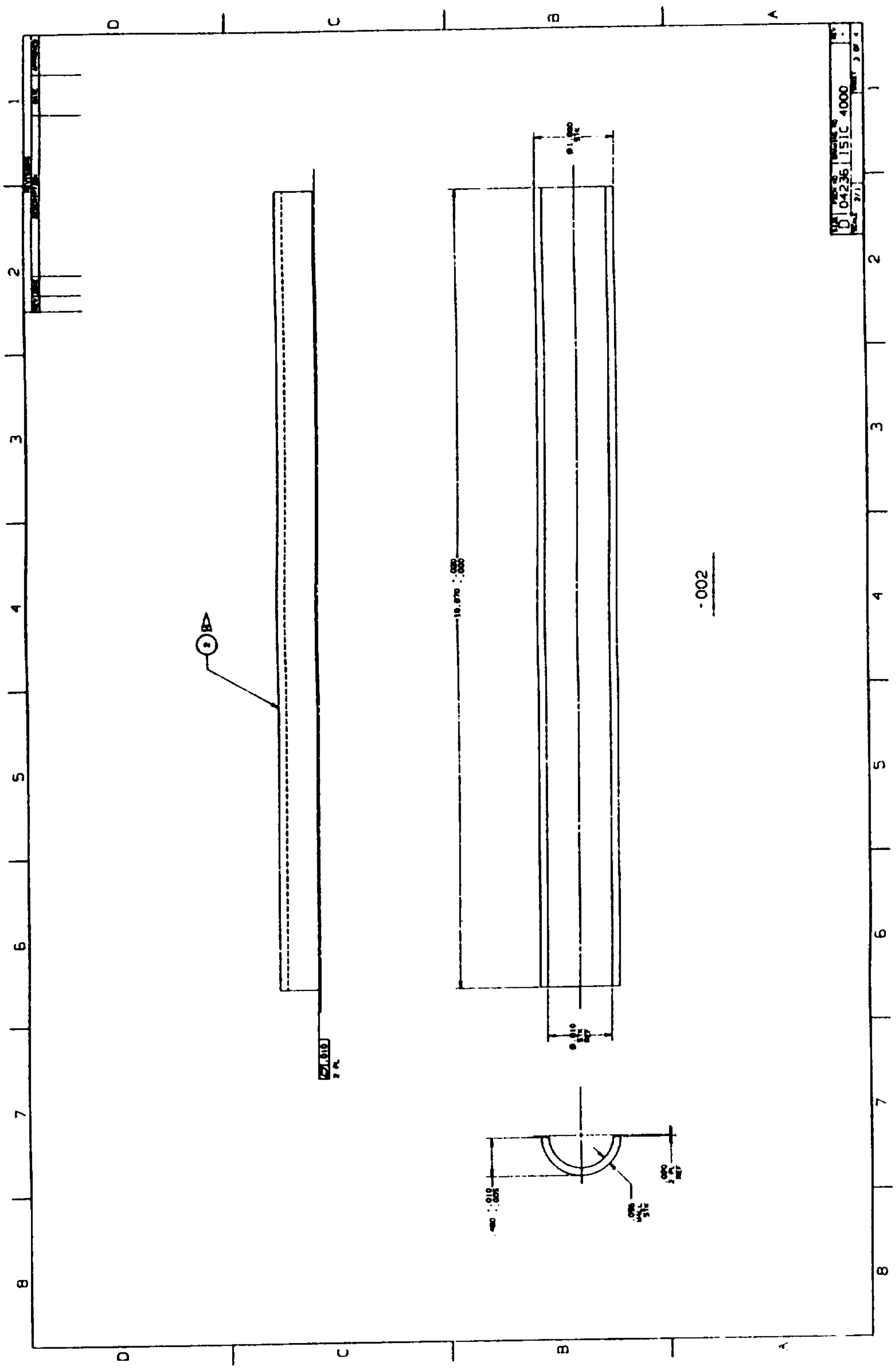
-002

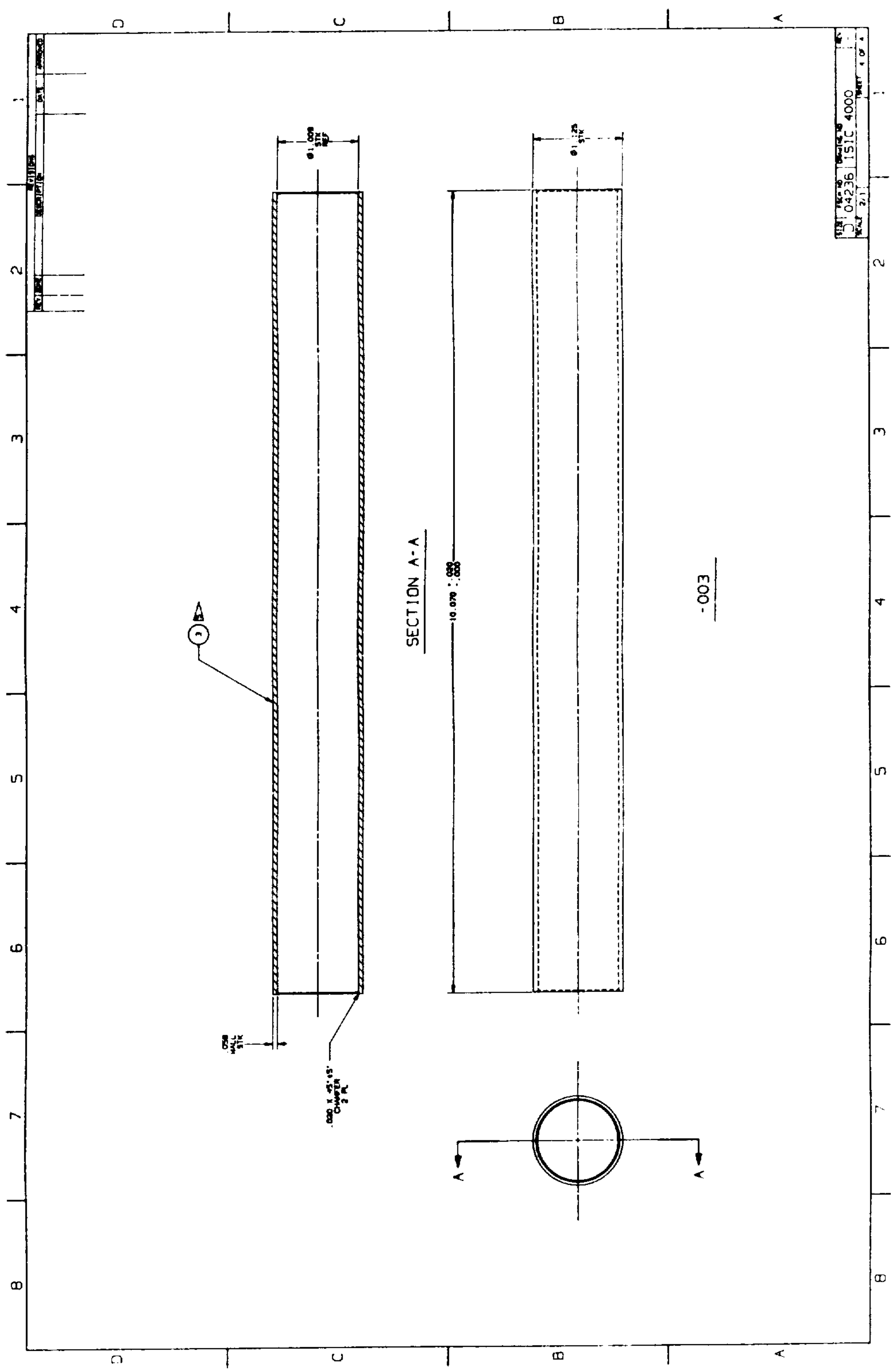
SECTION A-A
-003
D
04236
151C 4000
2/1
4 OF 4

REPORT DOCUMENTATION PAGE	Form Approved OMB No. 0704-0188

Public reporting burden for this collection of information is estimated to average 1 hour per response, including the time for reviewing instructions, searching existing data sources, gathering and maintaining the data needed, and completing and reviewing the collection of information. Send comments regarding this burden estimate or any other aspect of this collection of information, including suggestions for reducing this burden, to Washington Headquarters Services, Directorate for Information Operations and Reports, 1215 Jefferson Davis Highway, Suite 1204, Arlington, VA 22202-4302, and to the Office of Management and Budget, Paperwork Reduction Project (0704-0188), Washington, DC 20503.

1. AGENCY USE ONLY *(Leave blank)*

2. REPORT DATE
April 1994

3. REPORT TYPE AND DATES COVERED
Contractor Report

4. TITLE AND SUBTITLE
Integrated Active and Passive Control Design Methodology for the LaRC CSI Evolutionary Model

5. FUNDING NUMBERS
NAS1-19371
WU 590-14-91-52

6. AUTHOR(S)
Christopher T. Voth, Kenneth E. Richards, Jr., Eric Schmitz, Russel N. Gehling, and Daniel R. Morgenthaler

7. PERFORMING ORGANIZATION NAME(S) AND ADDRESS(ES)
Martin Marietta
Astronautics Group
P.O. Box 179
Denver, CO 80201

8. PERFORMING ORGANIZATION REPORT NUMBER

9. SPONSORING / MONITORING AGENCY NAME(S) AND ADDRESS(ES)
National Aeronautics and Space Administration
Langley Research Center
Hampton, VA 23681

10. SPONSORING / MONITORING AGENCY REPORT NUMBER
NASA CR-4580

11. SUPPLEMENTARY NOTES
Langley Technical Monitor: Rudeen Smith-Taylor
Final Report

12a. DISTRIBUTION / AVAILABILITY STATEMENT
Unclassified-Unlimited
Subject Category 18

12b. DISTRIBUTION CODE

13. ABSTRACT *(Maximum 200 words)*
A general design methodology to integrate active control with passive damping has been demonstrated on the NASA LaRC CSI Evolutionary Model (CEM), a ground testbed for future large, flexible spacecraft. Vibration suppression controllers designed for Line-of-Sight (LOS) minimization have been successfully implemented on the CEM. A frequency-shaped H2 methodology was developed, allowing the designer to specify the roll-off of the MIMO compensator. A closed-loop bandwidth of 4 Hz, including the six rigid-body modes and the first three dominant elastic modes of the CEM was achieved. Good agreement was demonstrated between experimental data and analytical predictions for the closed-loop frequency response and random tests. Using the Modal Strain Energy (MSE) method, a passive damping treatment consisting of 60 viscoelastically damped struts was designed, fabricated and implemented on the CEM. Damping levels for the targeted modes were more than an order of magnitude larger than for the undamped structure. Using measured loss and stiffness data for the individual damped struts, analytical predictions of the damping levels were very close to the experimental values in the (1-10) Hz frequency range where the open-loop model matched the experimental data. An integrated active/passive controller was successfully implemented on the CEM and was evaluated against an active-only controller. A two-fold increase in the effective control bandwidth and further reductions of 30% to 50% in the LOS RMS outputs were achieved compared to an active-only controller. Superior performance was also obtained compared to a High-Authority/Low-Authority (HAC/LAC) controller.

14. SUBJECT TERMS
Active Control
Passive Damping
CSI Evolutionary Model
Analytical Predictions
Experimental Results
HAC/LAC Controller
Multi-Input Multi-Output

15. NUMBER OF PAGES
372

16. PRICE CODE
A16

17. SECURITY CLASSIFICATION OF REPORT	18. SECURITY CLASSIFICATION OF THIS PAGE	19. SECURITY CLASSIFICATION OF ABSTRACT	20. LIMITATION OF ABSTRACT
Unclassified	Unclassified	Unclassified	

NSN 7540-01-280-5500

Standard Form 298 (Rev. 2-89)
Prescribed by ANSI Std. Z39-18
298-102